# In Situ Full-Field Characterisation of Strain Concentrations (Deformation Twins, Slip Bands and Cracks)


Abdalrhaman Mohamed Koko

St Cross College, University of Oxford

A thesis submitted for the degree of

Doctor of Philosophy

Trinity 2022

# Abstract

**Title:** In Situ Full-Field Characterisation of Strain Concentrations (Deformation Twins, Slip Bands and Cracks)

**Author:** Abdalrhaman Mohamed Saeed Mohamed, St Cross College

**Supervisors:** Professor Thomas James Marrow and Professor Angus J Wilkinson

**Date of Submission**: Trinity Term 2022

This thesis has developed novel methods to characterise the deformation field, in and ex situ, of strain concentrations (i.e., deformation twins, slip bands and cracks) using diffraction methods to map the local elastic deformation field, and calculate elastic strain energy release rate (*J*-integral) and stress intensity factors (SIFs) to parametrise the field under conditions of small-scale yielding.

To calculate the *J*-integral from an elastic strain field, the field was integrated to equivalent displacement to use the finite element formulation for high accuracy. The method was validated against two and three dimensional synthetic crack fields and then applied to strain fields measured using synchrotron energy-dispersive X-ray diffraction (EDXD) for a fatigue crack propagating in the heat affected zone (HAZ) of a welded bainitic steel. The integrated displacement field was then used to calculate the *J*-integral and mode I, showing a good agreement with the standard analytical solution and results obtained using displacement fields of the same crack measured using Digital Image Correlation (DIC). The parametrisation via the *J*-integral and SIFs was extended to use the finite element solver's equivalent domain integration (EDI), and anisotropic elastic and elasto-plastic material properties.

The high-resolution electron backscatter diffraction technique (HR-EBSD) was employed to map the elastic strain field. The effect of the unknown deformation conditions at the electron

backscatter reference pattern ($EBSP_0$) were investigated to select an optimum $EBSP_0$. The developed analytical techniques were then applied to study deformation twinning, slip band and crack local fields, in situ. First, an age-hardened duplex stainless steel (DSS) sample was deformed in tension, promoting plastic deformation by deformation twinning in the ferrite phase. The local in-plane strain fields ahead of a loaded deformation twin were measured, in and ex situ, and decomposed to the opening mode I and in-plane shear mode II SIFs. The analysis showed that the increase in twin lateral thickness correlates with mode I, while the elastic recovery when the load was removed was mainly in mode II.

By estimating the EBSP depth resolution using Monte Carlo (MC) simulation, the analysis was extended to the third dimension and applied to study, in situ, intragranular slip bands in the ferrite phase of an age-hardened DSS. The integrated displacement fields gave information about the in- and out-of- plane movement of the surface, which was decomposed to the three dimensional stress intensity factors, $K_{I,II,III}$. This showed that constraint of the topological changes due to out-of-plane shear induces additional tensile stresses, and the ratio of mode II to mode III depends on the direction of the slip band Burgers vector relative to the observed surface.

Finally, a simplified method that did not rely on FE solvers to calculate the *J*-integral and SIFs was derived and used to investigate mixed-mode cleavage crack propagation in (001) single silicon crystal. The mixed-mode crack field was consistent with a constant maximum potential energy release rate (MPERR) criterion for crack propagation and the expected cleavage toughness of silicon.

# Research output

## Literature Review

Part of the literature review included in this thesis was incorporated into Wikipedia articles written under '*Abdo2905*'. These pages include:

- Energy release rate (fracture mechanics) page, which was extensively updated and referenced to include other conservation of energy integrals (L and M), *J*-integral page, including the history, limitations, and vectorial nature of the integral,
- Electron backscatter diffraction, which was updated to include the physics of patterns formation and HR-EBSD,
- Crystal twinning was updated to highlight the different types of twinning, including deformation twinning,
- Geometrically necessary dislocations (GND), which was extensively updated, and
- Other topics, e.g., slip bands, and age-hardened stainless steel, were created (drafted).

## Publications

**A. Koko**[1], P. Earp, T. Wigger, J. Tong, and T.J. Marrow, "J-integral analysis: An EDXD and DIC comparative study for a fatigue crack," International Journal of Fatigue 2020, 134:105474. https://doi.org/10.1016/j.ijfatigue.2020.105474.

[1] 'Koko' is the author's family name (or nisbah/نسبة) based on the Arabic naming system contrary to the one adopted by the United Kingdom.

**A. Koko**, J. Marrow, and E. Elmukashfi, “Computation of the three-dimensional displacements from the elastic deformation field: application to indentation cracks in silicon,” To Appear, July 2021. https://doi.org/10.48550/arXiv.2107.10330.

**A. Koko**, E. Elmukashfi, K. Dragnevski, A.J. Wilkinson, and T.J. Marrow, “J-integral analysis of the elastic strain fields of ferrite deformation twins using electron backscatter diffraction,” Acta Materialia 2021, 218:117203. https://doi.org/10.1016/j.actamat.2021.117203.

**A. Koko**, E. Elmukashfi, T.H. Becker, P.S. Karamched, A.J. Wilkinson, and T.J. Marrow, “In situ characterisation of the strain fields of intragranular slip bands in ferrite by high-resolution electron backscatter diffraction,” Acta Materialia 2022, 239:118284. https://doi.org/10.1016/j.actamat.2022.118284.

**A. Koko**, T.H. Becker, E. Elmukashfi, N. M. Pugno, A.J. Wilkinson, and T.J. Marrow, “HR-EBSD analysis of in situ stable crack growth at the micron scale,” Under review by Journal of the Mechanics and Physics of Solids. https://doi.org/10.48550/arXiv.2206.10243.

**A. Koko**, A.J. Wilkinson, and T.J. Marrow, “An iterative method for reference pattern selection in high resolution electron backscatter diffraction (HR-EBSD),” Under review by Ultramicroscopy. https://doi.org/10.48550/arXiv.2206.10242.

**A. Koko**, S. Singh, S. Barhli, T. Connolley, N.T. Vo, T. Wigger, D. Liu , Y. Fu, J. Réthoré, J. Lechambre, J.-Y. Buffiere, T.J. Marrow, “3-dimensional analysis of fatigue crack fields and crack growth by in situ synchrotron X-ray tomography,” International Journal of Fatigue (to appear).

T.J. Marrow, D. Scotson, X. Jin, H. Chen, Y. Chen, **A. Koko**, P. Earp, H. Wu, "Small specimen testing, with image-based analysis, for crack propagation resistance in polygranular nuclear graphite," Accepted for publication in *ASTM International*.

## Conference Presentations

*J*-Integral analysis of EDXD and DIC data to quantify the strain and displacement fields of a fatigue crack in a weld HAZ, *The 5th IJ Fatigue and FFEMS Joint Workshop on Characterisation of Crack Tip Fields*, Heidelberg, Germany, 8–10 April 2019.

Deformation twinning in age-hardened duplex stainless steel, University of Oxford, March 2020.

*J*-integral analysis of the strain fields of micro-cracks in single silicon crystal using HR-EBSD, *15th International Conference on Advances in Experimental Mechanics*, Virtual event, 07-09 Sep. 2021.

In situ HR-EBSD analysis of quasi-static crack propagation in single crystal silicon, *The 6th IJ Fatigue and FFEMS Joint Workshop on Characterisation of Crack/Notch Tip Fields*, Dubrovnik, Croatia, 11–13 April 2022.

**Poster:** "Characterisation of Crack fields in Indented Single Silicon Crystal," University of Oxford, November 2020 and *23rd European Conference on Fracture – ECF23,* 27 June 2022.

3D analysis of HR-EBSD fields of indentation micro-cracks in (001) silicon, *23rd European Conference on Fracture – ECF23*, Madeira Island, Portugal, 27 June 2022.

## Other Contributions

Codes presented throughout this thesis are available at https://github.com/Shi2oon.

# Acknowledgements

I want to express utmost gratitude to my supervisor, Professor (Thomas) James Marrow, for giving me the space to be creative and explore my ideas while devoting an enormous amount of time for discussion, reviewing, guidance and pushing me beyond my limits. Thank you for being an excellent supervisor, teacher, and scientific role model. I am forever captivated by your work ethic, patience, knowledge, and passion for science. To my 2nd supervisor, Professor Angus J. Wilkinson, thank you for creating an enjoyable working environment in OMG! and for your insightful views and suggestions on my work.

Besides my supervisors, I would like to thank Dr Elsiddig Elmukashfi and Dr Phani Karamched for their precious support, guidance, innovative ideas, patiently answering my (sometimes spontaneous) questions, and making the past few years the most intellectually stimulating of my life. My thanks must also go to the people who have helped me overcome technical and scientific hurdles over the past few years, especially Professor Thorsten Becker (University of Cape Town), and the DCCEM and LIMA staff. I thank TJM group members and Materials' IT staff (Paul, Chris, and Rob) for their calm and patience as I cluttered the entire IT system for months. Thanks to Ms Carole Souter, Ms Suzy Hodge, Dr Jo Ashbourn, and Ms Lorraine Laird for providing food for thought.

I want to thank my mom, Layla, and sisters, Eman and Alaa, for their unconditional love. Thank you Christine for being a fabulous godmother. Ayad Khalid and Mohamed Almujtaba Nizam Aldeen for your positivity and altruism. In no particular order, I cannot forget to thank Marin Vukšić, Shraddha Singh, Hamid Kisha, Leena El-Hussein, Mohamed Tarig, Mohamed Saif, Israa Alazreg (Bulbul), and Dalia Yousif for your friendship and the beautiful memories we share.

Last but not least, I am grateful to the Materials department and EPSRC for providing a generous PhD studentship (EP/N509711/1) and to the examiners, Professor David Armstrong and Professor David Nowell, for taking the time to read my thesis; looking forward to discussing my work with you.

# Table of Contents

44,828 words excluding title page, abstract, table of contents, figures caption, cited literature and appendices.

# Chapter 1. Literature Review

Contents



## 1.1 Introduction

Understanding fracture at the micro-scale is critical for understanding materials' strength. For structural materials' strength improvement and failure prediction (i.e., integrity), particularly of anisotropic metals such as magnesium zirconium and uranium, it is critical to understand the role of certain microstructural features (e.g., grain boundaries) and deformation-induced features (i.e., deformation twinning, slip bands and cracks), and their interactions (i.e., strain concentrations). Characterising and understanding the deformation of materials at the micro-scale also enables microstructure-informed design using modelling tools (e.g., crystal plasticity).

This has motivated incremental progress to develop characterisation tools and techniques. However, at the micro-scale, that progress was hindered due to the lack of reliable quantitative measurement techniques, the difficulty of conducting an in-situ experiment, and the complexity of the problem itself. Nevertheless, high-resolution X-ray synchrotron image and diffraction, digital image correlation (DIC) and electron backscatter diffraction (EBSD) have emerged and enabled microscale in-situ measurement of elastic strain, elastic deformation gradient, and total in-plane displacements, respectively. Typically, these techniques are complemented by numerical analysis and computational simulation built around continuum mechanics theories.

This project aimed to develop a novel method to observe and acquire in-situ quantified deformation data at strain concentrations (i.e., deformation twins, slip bands and micro-cracks), and parametrise these by characterising the mechanical conditions at these strain concentrators.

Therefore, through this literature review, I will discuss the history of brittle fracture theories, advances in the local measurement of fracture parameters, and their relevance to this study. Then each section will be self-contained, including the required literature review in the introduction, incorporated directly into the chapters, as I have done with topics like (HR) EBSD in Chapter 3 and deformation twinning in Chapter 4.

## 1.2 Parameterising a crack's deformation field

Measurement of materials strength can be dated back to Leonardo da Vinci and Galileo Galilei, but Robert Hooke's book titled 'of Spring' is considered the manifesto that paved the way for the mechanics of materials [1,2]. Hooke assumed a linear approximation response to the material under load (i.e., like springs). The fracture is brittle in a perfect crystal with no imperfections in this linear relation between deformation (i.e., strain) and stress. Savart [3], in 1829, established that a perfect crystal almost does not exist. Furthermore, although plastic deformation has been known since Tresca's 1864 paper [4] (also see the discussion in [5]), the fracture mechanics theories up to the 1920s were only applicable to the linear elastic behaviour of materials.

In 1921, a century ago, motivated by the contradiction between the actual stress required to fracture bulk glass and that to break the glass interatomic bonds; Griffith [6] concluded that as the material dimension decreases, the fracture stress increases due to the loss of stress

concentrations (corners and scratches). This led him to infer that a crack will extend when the available material's global energy (thermodynamic energy balance) is enough to overcome the material's elastic resistance/energy relating the fracture strength to the specific surface energy rather than the tensile strength of the material. Griffith's theory was based on the earlier works of Kirsch and Kolosoff [1] in 1898 and Inglis [5] in 1913, who solved the problem of an infinite tensile plate with circular and elliptical holes, respectively.

Taylor [7], Orowan [8], and Polanyi [9] – independently – suggested in 1934 that, essentially, line defects (i.e., dislocations) lower the required stress as the interatomic bond breakage occurs in sequences rather than simultaneously. The sequence and simultaneous deformation mechanisms came to be known as heterogeneous and homogeneous nucleation of shear, and the latter is highly unlikely to occur as it requires high stress (almost equivalent to the crystal's theoretical strength) [10]. For example, Frank-Read sources [11], grain boundaries [12], and precipitate interfaces [13] are easy-to-activate sources of dislocations; thus, heterogeneous deformation is more favourable.

Griffith's surface energy criterion is strictly only suitable for ideally brittle materials with extremely sharp cracks (i.e., glass) and was further developed in 1949 by Irwin [14] and Orowan [15] – independently – to include plastic deformation as a form of the material's fracture resistance. Irwin [16,17] concluded that these plastic zones, which develop at the crack tip, cause energy to dissipate (i.e., as heat) as the surface is created. Hence, for a crack to propagate, the total energy of fracture should be enough to describe both the surface and dissipating energy. This total energy is calculated per unit area as the crack propagates and is known as the critical strain energy release rate ($G$). It is defined as the rate of change of potential elastic strain energy per unit area of the crack extension and is usually calculated

with the assumption of isotropic linear elasticity of the material outside the plastic zone. The critical value of the energy release rate (at the onset of fracture) is considered a measure of fracture toughness, with the – effective – crack length corrected to include the actual crack length. The plasticity effect on the crack stress field is illustrated in Figure 1-1. Irwin's plasticity correction does not address the phenomena 'physics' but instead compensates for the difference – in the stress response – between the plastic and elastic zones to satisfy equilibrium equations [18].

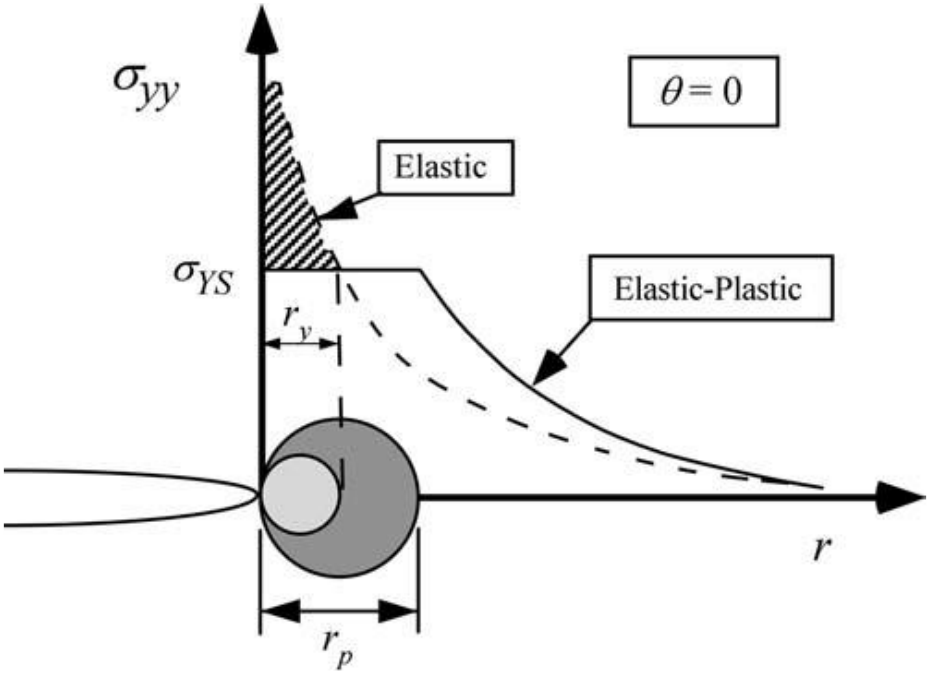


Figure 1-1: Estimate of 1st and 2nd order of plastic zone size ($r_y$ and $r_y$, respectively) ahead of a crack tip orientated at 0° (from [19]).

$$\sigma \approx \underbrace{\frac{G}{2\pi}}_{\text{Theoretical}} \approx \underbrace{\sqrt{\left(\frac{2E'\gamma_s}{\pi a}\right)}}_{\text{Griffith 1921}} \approx \underbrace{\sqrt{\left(\frac{2E'(\gamma_s+\gamma_p)}{\pi a_{eff}}\right)}}_{\text{Irwin \& Orowan 1949}} \approx \underbrace{\frac{K}{\sqrt{\pi a} * f\left(\frac{a}{W}\right)}}_{\text{Williams \& Irwin 1957}} \qquad 1—1$$

$$E' = \begin{cases} \dfrac{E}{1-\nu^2} & \text{for plane strain} \\ E & \text{for plane stress} \end{cases}$$

where $\sigma$ is the stress field for a centrally cracked sample, $\gamma_s$ is the surface energy per unit area, v is Poisson's ratio, $\gamma_p$ is the plastic energy, *K* is the stress-intensity factor, *G* is the shear modulus, *W* is the ½ sample width, $a_{eff}$ is the effective crack length = $a + r_y$, *a* is the ½ Crack length, $r_y$ is the Plastic Zone size, *E* is the modulus of elasticity and $f\left(\frac{a}{W}\right)$ is a dimensionless function, sometimes written as *Y* or *α*.

In the 1950s, from the Maxwell–Huber [20]–Hencky–von Mises [21] hypothesis and Westergaard solution [22], other [17,23–26] stress analyses to derive solutions for the stress field near a sharp crack tip under external forces were made, also assuming an isotropic linear elastic behaviour for materials. These analyses concluded that – regardless of crack body configuration in-plane strain conditions – the stress near the crack tip varies with $1/\sqrt{r}$, with ($r$) being the distance from the crack tip. This is described by the stress intensity factor ($K$). Daugdale [27] included a strain rate effect on the plastic zone hardening in his 'Plastic Strip Model' – also known as the cohesive zone model – and replaced the actual crack length with an effective length. He concluded that '*it is unwise*' to attach any significance to the strain hardening rate if it produces a smaller plastic zone due to the bulk material capable of withstanding higher stresses with less stress redistribution.

In 1961, Wells [28] proposed another parameter to measure the material's ability to resist crack propagation as a degree of crack tip blunting, known today as Crack Tip Opening Displacement (CTOD). Typically, CTOD is obtained by tracking the crack opening and extension using techniques such as digital image correlation DIC.

Meanwhile, non-local energy-based methods – based on the Noether theorem –evolved this isotropic linear elastic fracture mechanics to address anisotropic nonlinear problems. Noether [29] proved that within a Euclidean homogenous and isotropic reference frame (i.e., Noether frame) where energy and momentum are conserved, a path-independent integral describes the potential energy stored by the force field (i.e., an equivalent descriptor of forces). A mathematical formulation of the conservation laws, which originated from Günther [30], was applied to elastostatics in the form of path-independent integrals of some functionals of the elastic field over the bounding surface of a closed region. Some years earlier, Eshelby [31,32] represented the 'force on an elastic singularity or inhomogeneity' in the form of a surface integral that, in the absence of other defects, led to an elastostatic conservation law. James Rice introduced the two-dimensional analogue of this conservation law [33] as a path-independent line integral that could be applied to a stress concentration, although earlier investigations by Sanders [34] and Cherepanov [35] were closely related. Rice's integral has become known as the $J$-integral and is widely adopted in fracture mechanics.

In the late 1960s, Cherepanov [35] and Rice [33] showed (Figure 1-2) that the Riemann-summation of the nonlinear energy release rate could be written as a path-independent contour integral (known as *J*-integral) around the crack tip (known as the Hutchinson[36] Rice and Rosengren [37], HRR, singularity) using Green's theorem (seen in eq. 1—2), where $J$ integral (J for James Rice) is the strain energy release rate, $\sigma_{ij}$ and $\varepsilon_{ij}$ are the stress and strain tensors, respectively, $W$ is the strain energy density, $T_i$ is the components of the traction vector, $u_i$ is the displacement vector components, $n_j$ is the components of the unit vector normal to $\Gamma$ and $ds$ is the length increment along the contour $\Gamma$ .

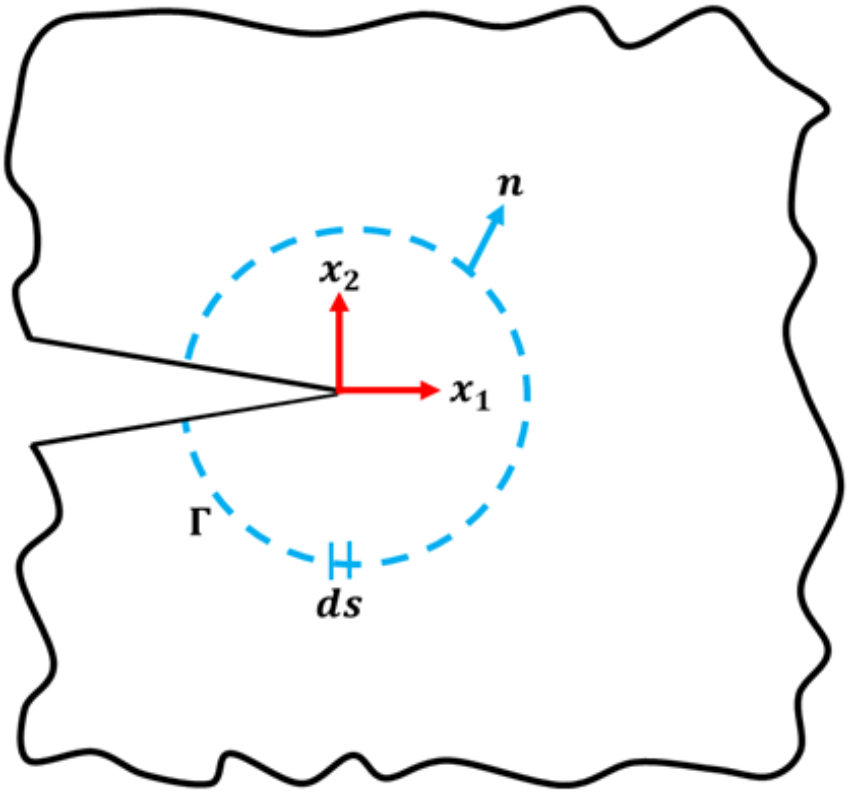


Figure 1-2: An arbitrary contour (Γ) of a crack tip's deformation field.

$$J = \int_{\Gamma} \left( W dx_2 - T_i \frac{\partial u_i}{\partial x_1} ds \right), \qquad W = \int_0^{\epsilon_{ij}} \sigma_{ij} d\epsilon_{ij}, \qquad T_i = \sigma_{ij} n_j, \tag{1—2}$$

$$\text{Small} - \text{scale yielding} \begin{cases} J = \underbrace{m\, \sigma_{YS}\, \delta}_{\text{CTOD}} & \text{1—3} \\ J = \underbrace{\left(\frac{1}{E'}\right)(K_I^2 + K_{II}^2) + K_{III}^2 \left(\frac{1+v}{E}\right)}_{\text{Mixed Loading Mode Stress-intensity factors}} & \text{1—4} \end{cases}$$

Hutchinson [36] and Rice and Rosengren [37] were the first to apply the *J*-integral as a criterion to describe the strain energy release rate for crack growth in linear elastic or elastic-plastic materials. This path-independent line integral, the *J*-integral, is defined by equation 1—4. In the context of crack fields, it is obtained by formulating a contour or domain-independent integral (Figure 1-2) that starts from the free surface of the crack tip to calculate the elastic energy release rate in the direction of a virtual crack extension [38]. Its

application was limited to loaded cracks with no internal stress/strains or edge tractions [39], no significant plasticity [40], and curved cracks or unloading [39–41], as these are the necessary conditions for the integral to be path-independent. Nevertheless, with modifications, the $J$-integral can be applied to other conditions, including significant plasticity [42]. The numerical character of the $J$-integral facilitates its evaluation with finite element (FE) methods, typically by application of the divergence theorem and equivalent domain integration (EDI) [43]. In addition, the *J*-integral can characterise strain and stress fields at the crack tip in conditions that obey the linear elastic or Ramberg-Osgood hardening relation [44]. Thus, non-local energy-based methods extended fracture mechanics to nonlinear problems of crack expansion. Whether localisation/concentration of strain can give rise to a singularity or not, the conservation/invariant integrals (e.g., *J*-integral) are capable of providing a path-independent description of the strain concentration (vector) field once the material's stress-strain constitutive law is defined (e.g., power-law hardening material) [45–47]. However, this description breaks down at the nanoscale [48].

The critical $J$-integral ($J_{IC}$) – at the condition of quasi-static crack propagation – is widely used as a fracture criterion for various materials [49–53] and test configurations [54,55], where it is coupled with analytical or finite element analyses that use knowledge of remote applied boundary conditions and specimen geometry to perform structural integrity assessments. Recently, methods have been developed that use experimental data for the displacement fields around cracks as local boundary conditions in finite-element models to solve the elastic strain field and calculate the $J$-integral. These analyses demonstrated that such local measurements could quantify the potential elastic strain energy release rate without knowledge of the external boundary conditions (i.e., load, crack length) [56,57]. Shih *et al.*

[58] showed that the *J*-integral field calculation could be modified to include thermal and residual stress. Additionally, Shih [59] derived a relationship between the energy release rate and Crack Tip Opening Displacement (CTOD) (see eq. 1—3) by exploiting the HRR singularity and assuming a small-scale yielding zone where $\delta$ is the CTOD value at the crack-tip, $\sigma_{YS}$ is the yield strength, and $m$ is a dimensionless constant depends on stress state and material properties.

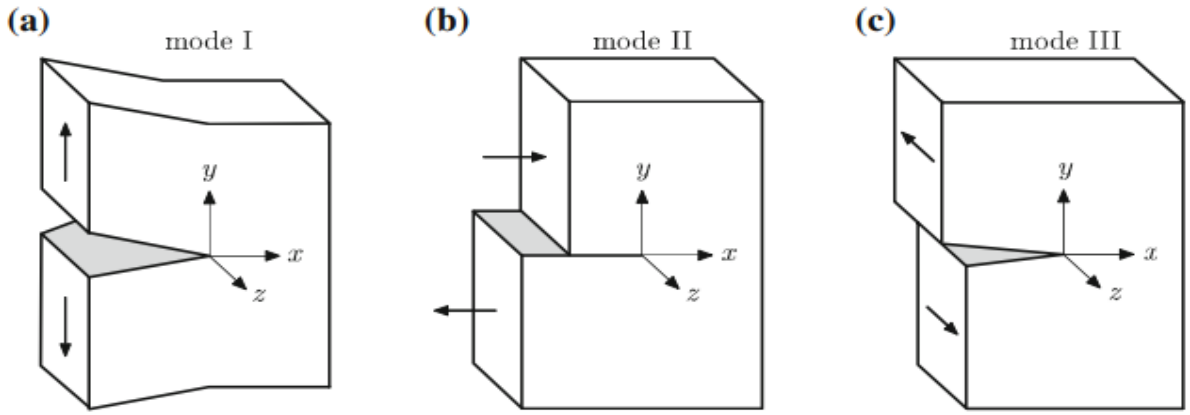


Figure 1-3: Three types of crack loading: (a) Mode (I) loading being applied parallel to the crack plane resulting in the crack opening up (tensile stress). (b) Mode (II) loading being in-plane shear loading results in sliding one crack face to the other. (c) Mode (III) loading being out-of-plane shear. These load modes can be applied individually or combined (adapted from [60]).

Application of the $J$-integral to mixed-mode crack problems (e.g., where crack kinking or deflection occurs, and the crack tip is not loaded purely by opening) is complex since the $J$-integral does not distinguish between the strain energy contributions from crack opening (mode I) and shearing (modes II and III). Thus, decomposition is needed to evaluate the two or three dimensional stress intensity factors that describe the equivalent elastic field. In the early 1970s, Bueckner [57] and Rice [58] used a weight function concept for 3D stress analysis of anisotropic linear elastic materials under combined mode I and II loading. Further analysis by Cottrell and Rice [61] showed that the total elastic strain energy release rate is the sum of the energy release rates of the independent modes in mixed mode loading, if the crack tip

retains the same configuration (i.e., no change in direction) and there is small-scale yielding. Shih and Asaro [62] introduced the interaction integral method to separate the deformation fields by superimposing an auxiliary field onto the actual tensor field; thus, decomposing the field in terms of its symmetric (mode I), in-plane antisymmetric (mode II), and out-of-plane antisymmetric (mode III) parts.

The integral nature of (*J*) eases the employment of finite element (FE) analysis, whether as a line or surface area (2D) or a volume (3D) integral, and the decomposition of modes of loading [63]. FEM is a computer-based numerical method for solving mathematical physics problems by imposing boundary conditions and meshing/segmenting the physical system as pieces or elements. Then, physical laws are applied to elements adjacent to the boundary, individually, which are linked to other elements. Theoretically, this solves complex physical equations by reducing them to a set of linear algebraic equations at each element [64]. This breakthrough allowed the strain energy release rate (i.e., *J*-integral) to be calculated and decomposed to stress intensity factors using finite elements (FE) either in 2D or 3D for complex crack configurations using (arbitrary) boundary conditions of the displacement field or applied loads [65] but with an increased computational complexity compared to line integration.

Path-independent *J*-integral is widely used to analyse the configurational forces in problems as diverse as dislocation dynamics [66,67], misfitting inclusions [68], propagation of cracks [69], shear deformation of clays [70], and co-planar dislocation nucleation from shear loaded cracks [71]. The integrals have been applied to linear elastic and elastic-plastic materials and have been coupled with processes such as thermal [72] and electrochemical [73] loading, and internal tractions [74]. Experimental fracture mechanics studies have recently used full-field

in situ measurements of displacements [56,75] and elastic strains [76,77] fields to parameterise the crack tip's local deformation field as a *J*-integral.

Digital image correlation (DIC) provided a method to measure the crack field and allowed for using FE for post-processing. Becker *et al.* [56] used a full field displacement obtained using DIC to calculate the *J*-integral using FEM with mode I crack lying on the x-axis. They noted that *J*-integral evaluation requires high-quality displacement field data for the integral to converge and only considers mode I loading, and Breitbarth *et al.* [78] included mode I and II. This method showed better accuracy than the least-square method of estimating the stress intensity factors from the displacement field [79] and less sensitivity (up to 7% [80]) to the accuracy in defining the crack tip location considering the uncertainty of finding the displacement vectors in the vicinity of discontinuities (i.e., near the crack) or edges which can be padded [81].

Further development of the method was conducted by Barhli *et al.* [76], who showed it was possible to calculate the *J*-integral using strain field data acquired using X-ray Diffraction. This opened the possibility of using the elastic displacement gradient tensors locally measured using High (angular) resolution electron backscattered diffraction to calculate the *J*-integral. Nevertheless, there are still difficulties determining the crack path and crack-tip, and masks/excludes the data at the crack vicinity.

Réthoré *et al.* [82] and Roux and Hild [80] separated the loading modes while assuming elastic properties (i.e., $K_{I\text{-}III}$) by using a crack field method and integrated approach, respectively. Stren *et al.* [83] proposed an interaction integral approach, and Ishikawa proposed a kinematic decomposition method to separate the loading modes without having to assume

an elastic fracture (i.e., $J_{I\text{-}III}$), which was further developed by Molteno and Becker [63] for 3D stereo DIC data.

Recently, Cinar *et al.* [84] introduced an autonomous, precise, and reliable crack detection algorithm based on the phase congruency method. By applying a refined FEM meshing (Poissant and Barthelat [85]) for the imported displacement data around the detected crack and using the commercial Abaqus software's [86] native capability to separate the different loading modes (mode III requires 3D data); Barhli *et al.* [75] achieved a precise calculation for *J*-integral (error less than 7% without considering error due to plasticity). His method could also include nonlinear material properties.

As this project aimed to develop a novel method to observe and acquire in-situ quantified deformation data of strain localisation at deformation twins, slip bands and micro-cracks; the potential energy-release rate (i.e., *J*-integral) appears to describe the complex mechanical conditions at the deformation twins, slip bands and micro-cracks, through the stress intensity factors, without knowledge of the sample loading history, or any other global parameters.

# Chapter 2. Computation of the displacement field from the measured elastic strain field

Contents

## 2.1 Introduction

Studying the interactions between the load and deformation at different scales is critical to understanding and improving engineering metals and alloys' structural properties (i.e., strength, ductility, and toughness). However, despite maturity in experimental and measurement techniques at both nano- and macro scales, the mesoscale (10-0.01 µm) is still in its infancy. This affects the ability to study, for example, how deformation-induced features (DIFs) (i.e., deformation twins, micro-cracks, and slip bands) and microstructural features (e.g., grain boundaries and other DIFs) interact during the deformation process and how that can produce local strain concentrations that may initiate fracture. This knowledge is crucial for the microstructure-informed design of materials using modelling tools such as crystal plasticity. Thus, there is a need for high-resolution data that will characterise the strain field, which may be approached by ex situ measurements; although, in-situ studies are the goal because ex-situ measurements can be affected by stress relaxation.

Previous work on the full-field analysis of the elastic strain fields around cracks has shown that elastic strain maps obtained by synchrotron X-ray diffraction [76] can be used to calculate the displacement field, which then can be analysed via a finite-element-based method (JMAN_S) to quantify the elastic strain energy field via the *J*-integral [33,35]. Hence, the strain energy release rate for crack propagation can be quantified by local measurements without knowing the external boundary conditions (i.e., load, crack length). However, these studies were done at a relatively large scale (cm-size specimens) on long cracks with low spatial resolution and a 2D uniform (i.e., rectangular) field of view with regularly spaced square elements.

With the apparent non-uniformity of the microstructural features (e.g., grains, twins) at the mesoscale, the challenge now is developing a robust, more sensitive, and accurate method to integrate the displacement field from a high-resolution strain field measured at the micro-scale. The method needs to be flexible to solve for a non-uniform field of view with non-square elements. This will allow the direct use of the high-resolution data as an input to commercial Finite Element software (e.g., ABAQUS® [86]) for models that do not ignore the residual deformation and full-field fracture studies (e.g., *J*-integral). This is pivotal to existing high-resolution techniques such as HR-EBSD (High-resolution Electron Backscatter Diffraction) [87]. It will pave the way for more efficient mapping strategies to capture the deformation field using techniques such as X-ray micro-Laue diffraction.

Here, a novel method for numerical integration of the elastic deformation field will be derived and implemented, which uses a finite element method for discretising the field before assembling the boundary system of equations and solving for the nodal displacement using a least square method. This chapter discusses two theoretical problems to explore 2D and 3D capabilities and computational time and accuracy using different mesh refinement and gaussian points using synthetic and experimental data to validate the proposed method and demonstrate potential applications.

## 2.2 Numerical method

Consider a class of problems in which the deformation field is given in the form of a deformation measurement, such as the engineering strain or deformation gradient, in the deformed configuration. Hence, the scope of the proposed formulation is to determine the displacement field by integrating the deformation measure at a given set of points (i.e., mesh nodes). Thus, consider a body subjected to mechanical loading, which results in a deformation defined by the deformation gradient.

$$F_{ij} = \frac{\partial x_i}{\partial X_j} = \delta_{ij} + \frac{\partial u_i}{\partial X_j} \qquad 2—1$$

where $X_i, x_i$, 1,2,3, is a standard Cartesian coordinate system for the reference and deformed configurations, $u_i = x_i - X_i$ is the displacement vector, $\delta_{ij}$ is the second-order identity tensor and $H_{ij} = \partial u_i / \partial X_j$ is the displacement gradient. Thus, the displacement gradient can be split into infinitesimal strain $\varepsilon_{ij}$ (symmetric part) and rotations $\omega_{ij}$ (asymmetric part) that are given by:

$$\varepsilon_{ij} = \frac{1}{2}\left(\frac{\partial u_i}{\partial X_j} + \frac{\partial u_j}{\partial X_i}\right), \qquad \omega_{ij} = \frac{1}{2}\left(\frac{\partial u_i}{\partial X_j} - \frac{\partial u_j}{\partial X_i}\right) \qquad 2—2$$

The body can be discretised using finite elements to determine the nodal displacement field. Thus, the displacement field is interpolated as:

$$u_i(X_j, t) = \sum_{I=1}^{N_{\text{nodes}}} N_I(X_j) u_{iI}(t) \qquad 2—3$$

where $N_I$ are the standard finite element shape functions, which can also be expressed in terms of the parent element coordinates $\xi_i \in (\xi, \eta, \zeta)$, $N_{\text{nodes}}$ is the total number of nodes in the mesh and $u_{iI}$ are the values of the displacement fields. The reference

($X_i$) and current configurations ($x_i$) are respectively interpolated as:

$$X_i(X_j) = \sum_{I=1}^{N_{\text{nodes}}} N_I(X_j) X_{iI}\,, \qquad x_i(X_j, t) = \sum_{I=1}^{N_{\text{nodes}}} N_I(X_j) x_{iI}(t) \tag{2—4}$$

where $X_{iI}$ and $x_{iI}$ are the coordinates of node $I \in \Omega$ in the reference and current configurations, respectively. Using the definitions in equations (2—1) and 2—3), the displacement gradient can be obtained by:

$$H_{ij}(X_k, t) = \frac{\partial u_i(X_k, t)}{\partial X_j} = \sum_{I=1}^{N_{\text{nodes}}} \frac{\partial N_I(X_k)}{\partial X_j} u_{iI}(t) = \sum_{I=1}^{N_{\text{nodes}}} \frac{\partial N_I}{\partial \xi_l} \underbrace{\frac{\partial \xi_l}{\partial X_j}}_{J_{jl}^{-1}} u_{iI}(t) \tag{2—5}$$

where $J_{ij} = \partial X_i / \partial \xi_j$ is the mapping gradient from a reference configuration to the parent domain that can be determined from equation (2—6) as:

$$J_{ij} = \frac{\partial X_i}{\partial \xi_j} = \sum_{I=1}^{N_{\text{nodes}}} \frac{\partial N_I}{\partial \xi_j} X_{iI} \tag{2—6}$$

The mapping gradient of the current configuration to the parent domain is similarly determined from equation (2—7) as:

$$j_{ij} = \frac{\partial x_i}{\partial \xi_j} = \sum_{I=1}^{N_{\text{nodes}}} \frac{\partial N_I}{\partial \xi_j} x_{iI} \tag{2—7}$$

where $F_{ij} = j_{ik} J_{kj}^{-1}$. Hence, the displacement gradient can be written in terms of the current configuration as follows:

$$H_{ij}(X_k, t) = \sum_{I=1}^{N_{\text{nodes}}} \frac{\partial N_I}{\partial \xi_k} \frac{\partial \xi_l}{\partial x_j} F_{lk} u_{iI}(t) \tag{2—8}$$

The expressions (2—5) or (2—8) contain a system of equations in which the unknowns are the nodal displacements $u_{iI}$ that are of a number $N_{\text{Un}} = N_{\text{nodes}} \times N_{\text{Dim}}$, where $N_{\text{Dim}}$ is the

number of dimensionality of the problem. The displacement gradient in the left-hand side can be prescribed anywhere within the element. Therefore, a set of computational points (i.e., $N_{\mathrm{P}}$ points) that lie within the element can be chosen. Thus, the total number of equations becomes $N_{\mathrm{Eq}} = N_{\mathrm{Ele}} \times N_{\mathrm{P}} \times N_{\mathrm{d}}$ , where $N_{\mathrm{Ele}}$ is the total number of elements in the mesh and $N_{\mathrm{d}}$ is the number of components of the deformation measure, e.g., in 3D problems, $N_{\mathrm{d}} = 9$. The system of equations can be written in the algebraic form in (2—9)[2].

$$A_{ij} d_j = b_i \qquad 2—9$$

where $A_{ij}$ is a $N_{\mathrm{Eq}}$ x $N_{\mathrm{Un}}$ coefficients matrix, $d_j$ is a vector that encapsulates the unknown nodal displacements $u_{iI}$, $b_i$ is a vector that encapsulates the displacement gradient $\partial u_i / \partial X_j$. The linear algebraic equations in (2—9) result in one of three solution sets:

(i) If $N_{\mathrm{Eq}} = N_{\mathrm{Un}}$ this will lead to a single unique solution. Thus, $A_{ij}$ has a full rank, and its inverse $A_{ij}^{-1}$ is unique.

(ii) If $N_{\mathrm{Eq}} > N_{\mathrm{Un}}$ this will make the system of equations overdetermined, and the solution can be best solved using the least-squares method. Thus, a minimization of the square error can be written as below:

$$\min \left\| A_{ij} d_j - b_i \right\|^2 \qquad 2—10$$

The solution to the minimisation problem of the values of the nodal displacements $d_j$ is then obtained by equation (2—11).

$$d_j = \left( A_{ij}^T A_{ij} \right)^{-1} A_{ij}^T b_i \qquad 2—11$$

[2] Equation (2—9) is the well-known $F = KU$ equation for the finite element method, where $F$ is the force vector, $K$ is the elements stiffness matrix and $U$ is the displacement vector. More details in Appendix (2.A) – FE-OOM code implementation.

(iii) If $N_{\mathrm{Eq}} < N_{\mathrm{Un}}$ this will make the system of equations underdetermined with an infinite number of solutions unless the problem is subjected to a constraint or regularisations (e.g., condition matrix when using pseudoinverse method ($\mathrm{cond}(A_{ij})) = \|A_{ij}\|\|A_{ij}^{+}\|$, where $A_{ij}^{+}$ is the Moore–Penrose inverse of an $A_{ij}$ matrix).

## 2.3 Benchmarking

### 2.3.1 2D Synthetic dataset

Firstly, a theoretical strain field will be used to predict the displacement field using the proposed Finite Elements method as implemented in MATLAB (https://mathworks.com/) using the Object-Oriented method (i.e., FE-OOM) with a detailed comparison between the predicted field, the only other method reported in the literature (JMAN_S [76]), and the actual displacement field to show the accuracy of the solution.

Briefly, in JMAN_S, the measured in-plane elastic strain field is discretised with a measurement point centred inside a square linear element with four nodes. The measurement point then becomes the Gauss point, as illustrated in Figure 2-1a.II for each element. The elastic field is then integrated into displacement using the finite difference method. Solving for the equations uses the Trust-Region-Reflective least squares algorithm [88] natively implanted in MATLAB® that uses the Cholesky factorisation method. The method works for full matrixes with a regularised grid. More details are in [89].

#### 2.3.1.1 Analytical dataset

A 2D square domain of $L \times L$ size was considered such that the crack is parallel to $x$-axis and its tip is located at the centre of the domain (i.e., $a = L/2$), where $L = 8$ mm. The displacement in $x$ and $y$-directions, $U_x$ and $U_y$, around a crack with a mode I stress intensity

factor ($K_I$) of 30 MPa $m^{0.5}$ was created using Westergaard-Solution [22] and assuming plane strain conditions as highlighted below in eq. 2—12 to 2—15 and shown in Figure 2-2a.I. The isotropic elastic modulus ($E$) and Poison's ratio ($v$) were 210 GPa and 0.3, respectively, similar to ferritic steel. The field of view was 8 x 8 mm Then, the 2D strain tensors ($\varepsilon_{xx}$, $\varepsilon_{yy}$ and $\varepsilon_{xy}$) were then calculated from the displacement numerical gradient (2—16).

$$U_x = \frac{K_I}{2\mu}\sqrt{\frac{r}{2\pi}}\cos\left(\frac{\theta}{2}\right)\left[k - 1 + 2\sin^2\left(\frac{\theta}{2}\right)\right] \qquad 2—12$$

$$U_y = \frac{K_I}{2\mu}\sqrt{\frac{r}{2\pi}}\sin\left(\frac{\theta}{2}\right)\left[k + 1 + 2\cos^2\left(\frac{\theta}{2}\right)\right] \qquad 2—13$$

$$\mu = \frac{E}{2(1+v)} \qquad 2—14$$

$$k = \begin{cases} 3 - 4v & \text{for plane strain} \\ \dfrac{3-v}{1+v} & \text{for plane stress} \end{cases} \qquad 2—15$$

$$\varepsilon_{xx} = \frac{\partial \mathrm{u}_x}{\partial x}, \qquad \varepsilon_{yy} = \frac{\partial \mathrm{u}_y}{\partial y}, \qquad \varepsilon_{xy} = \frac{1}{2}\left[\frac{\partial \mathrm{u}_x}{\partial y} + \frac{\partial \mathrm{u}_y}{\partial x}\right] \qquad 2—16$$

where $(x, y)$ and $(r, \theta)$ are the Cartesian and polar coordinates of coordinate systems, respectively, centred at the crack tip, and $\mu$ is the shear modulus.

The domain is discretised using a uniform square mesh of element length $l_e = 0.2$ mm (total of 1600 elements). In the discretisation, linear interpolation functions are adopted, i.e., 4-node linear element. The number of computational points is taken to be *one* at the centre of the element, as shown in Figure 2-1a.II.

A uniform grid mesh with four nodes was placed around the measurement point (depending on the element) with the aim for these measurement points to be the Gauss points. For example, a linear element has four nodes and one computational point. Thus, each

measurement point will be an element, as illustrated in Figure 2-1. No interpolation was needed, considering the uniform spacing between each point. Then the appropriate shape function is used to move from the physical coordinate (x, y) to a dimensionless local natural coordinate system ($\eta_1, \eta_2$). The Jacobian, which describes shape distortion where the area is stretched out by a factor of the Jacobian determinant [64], was calculated from the product of the shape function derivatives with respect to the natural coordinates (in equation 2—6) and nodal/physical coordinates (in equation 2—7). A set of linear equations (stiffness) matrix and the load/force matrix assembled at the Gauss points and solved to obtain the displacement at the nodes. See 'Appendix (2.A) – FE-OOM code implementation' for extensive details.

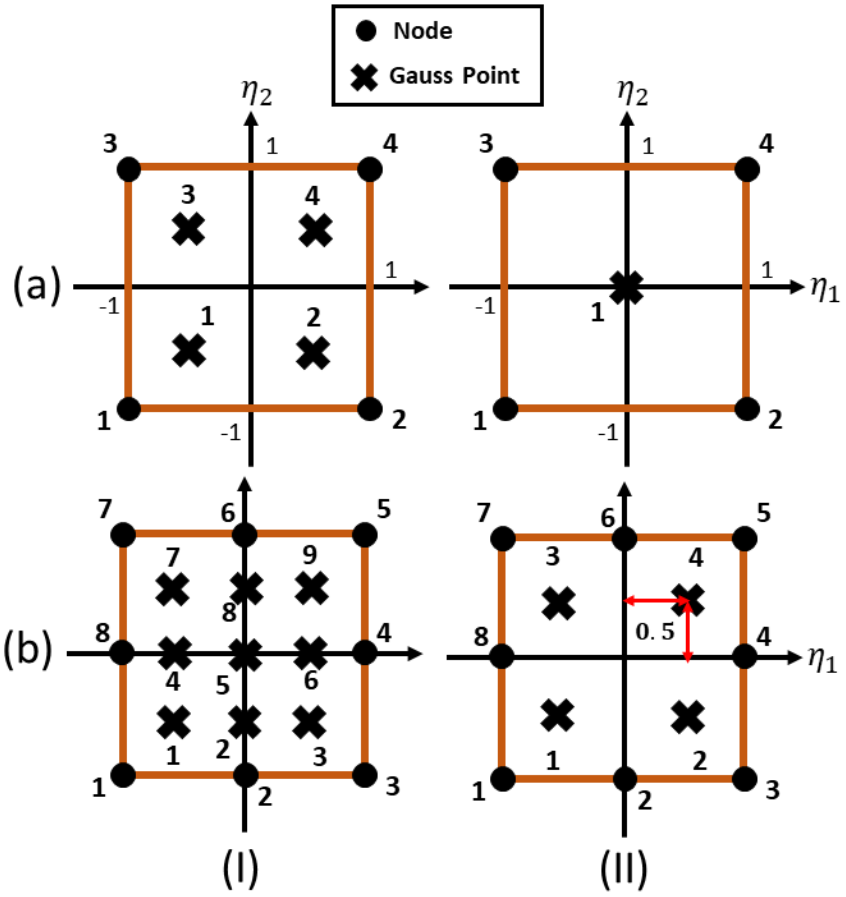


Figure 2-1: Schematic of (a) Linear and (a) Quadratic elements with a range of Gauss integration points used for (I) full or (II) reduced integration. A dimensionless local natural coordinate system ($\eta_1, \eta_2$) was defined with its origin located at the centre of the rectangular element.

### 2.3.1.2 Results and discussion

The synthetic strain field was applied to the JMAN_S method and the newly developed Finite Elements Object-Oriented method (FE_OOM) using only one Gauss point to allow for comparison. The displacement field in $y$-direction, $U_y$, from both methods and the original field are both presented in Figure 2-2, a.1-3. The variation between integrated fields and the original field around a boundary can be instantly spotted at the crack. A boundary in a deformed material creates a discontinuity in the field accompanied by incompatibility in the deformation field across the boundary. However, FE-OOM shows better accommodation for the incompatibility, which extends across two elements, compared to JMAN_S, which extends to three pixels. Results from FE-OOM can be improved by increasing integration points (i.e., Gauss points) which cannot be done in JMAN_S.

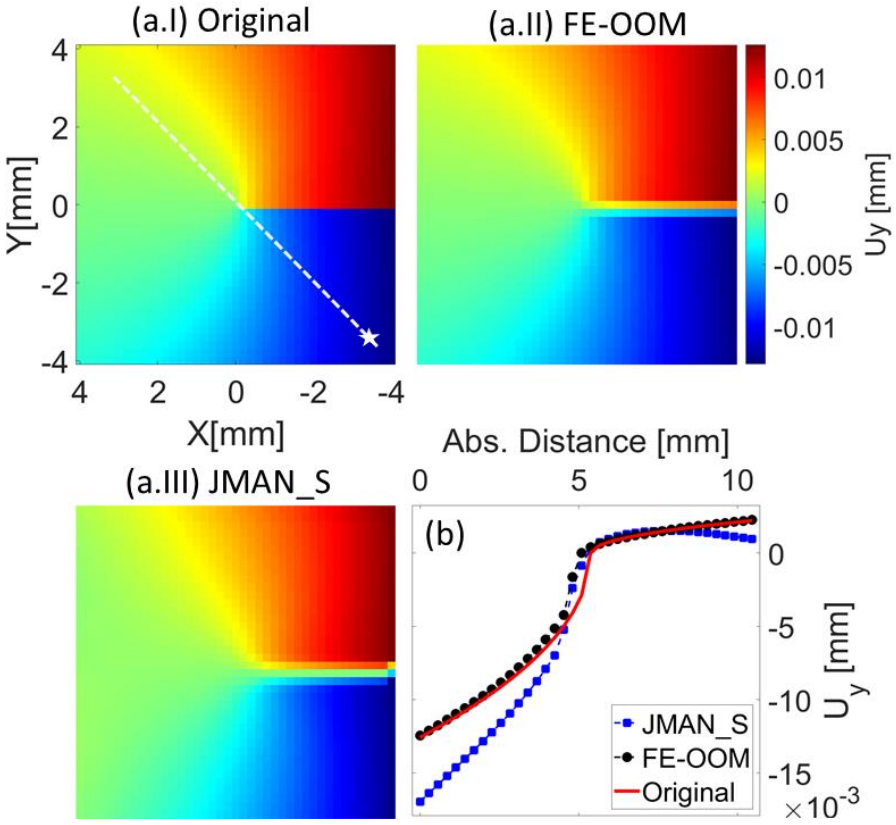


Figure 2-2: (a.I) An original $U_y$ displacement field created using Westergaard solution and integrated field obtained using (a.II) Finite element object-oriented method (FE-OOM) and (a.III) JMAN_S. (b) A diagonal line profile (along the white dotted line in a.I) was obtained from a.I-III.

Also, the shape of the field behaviour ahead of the crack-tip remains curved and consistent between FE-OOM and the original field, contrary to the JMAN_S field. A line profile was taken across the field to compare the actual integrated value to the original, as shown in Figure 2-2a.1 with white dotted lines. The results, presented in Figure 2-2b, show that the proposed method (FE-OOM) accurately predicts the displacement field with a small error value, i.e., $\approx 0.1\%$, less than the errors of the JMAN-S method [76]. This is because JMAN_S consider the problem as a finite difference (integration) problem that has a linear form (does not solve for higher-order polynomials), and it uses an optimal weighted sum implemented by the '*Isqlin*' function, a native MATLAB® Trust-Region-Reflective Linear Least Squares Algorithm [88], to solve for the nodal displacement. The function achieves global convergence by iterating over a formulated 2D trust-region sub-problem which adjusts in size – using an overall merit function – until an adequate solution is found within the allowed error range, prioritising efficiency/speed over accuracy. Also, JMAN_S assumes that the material is linearly elastic; thus, compatibility conditions are used to solve for displacement from the linear elastic material deformation field. This inhibits JMAN_S from analysing the vast majority of engineering materials (e.g., elastic-plastic or anisotropic-elastic materials).

In addition, in measured deformation fields, grain boundaries are typically surrounded by a higher level of noise and dead or zero values at the boundary, depending on the boundary width and measurement resolution. One can exclude these values, but this will change the 2D data from a fully dense matrix which cannot be used with the JMAN_S method. Alternatively, one can replace the empty pixels and noise with zeros (applying a median filter), adversely affecting the integrated field around a boundary. The FE-OOM method can solve

for non-dense matrixes, including sparse matrixes. This makes it suitable, for instance, to integrate a specific deformed grain in a polycrystal material.

Regardless of the accuracy of the solution obtained with the finite element method, it is only an approximation to the exact solution. Hence, the accuracy of this method was assessed by running the previous analysis but with different element sizes and integrating using a different number of gaussian points to show their effect on computational time and solution accuracy ($\delta$) using an Intel® Xeon® Gold 6130 CPU fitted with dual 2.10GHz processors, 512 GB RAM, 64-bit operating system and x64-based processor but only used half (32) of the nodes. The solution accuracy ($\delta$) is defined as in equation (2—17), where $n$ is total number of elements, $a_i^W$ is value of the $i$th element obtained directly from Westergaard solution $U_y$ displcement field and $S$ is for the integrated $U_y$ displacement field.

$$\delta = \frac{1}{n}\sum_{i=1}^{n}\left|\frac{a_i^W - a_i^S}{a_i^W}\right| \qquad 2—17$$

The computational time and accuracy using different resolutions (elements in the 8 x 8 mm$^2$ map) and Gauss points were then plotted in Figure 2-3. Here, the strain measurement point was centred inside an element and then interpolated to the Gauss point(s). From this computational experiment, it can be concluded that the number of Gauss points substantially affects accuracy while minimally changing the computational time. In contrast, when only using 1 Gauss point, a steep and gradual increase in accuracy with element quantity can also be observed. This is because, generally, Gauss quadrature integration using high order terms, i.e., Gaussian points, yields more accurate values with a higher number of orders improving the integration solution accuracy and yielding exact values for polynomials up to degree 2n-1

with n being the number of quadrature points [90]. However, as highlighted in Figure 2-3, this also increases the computational time.

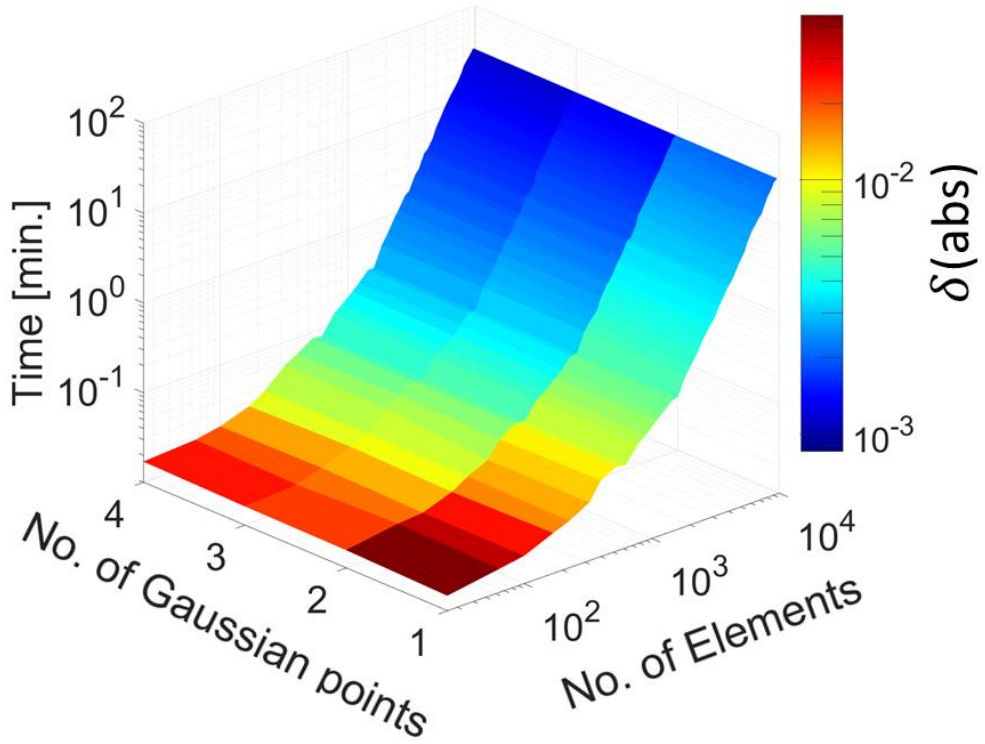


Figure 2-3: The computational time and accuracy of solving for nodal displacement using different elements with different integration points using Intel® Xeon® Gold 6130 CPU.

The relationship between the number of elements ($N_{el}$), number of Gauss points ($N_g$) and accuracy ($\delta$) can be estimated from Figure 2-3 as in equation (2—18) with $R^2 = 0.93$.

$$\delta = \frac{0.2}{\sqrt{N_{el} * N_g}} \qquad 2—18$$

This MATLAB® implementation (see Appendix (2.A) – FE-OOM code implementation) allows for various methods to be utilised to ensure efficient and accurate computation of the problem. The difference between the two types of element order is emphasised. The two-dimensional implementation allows using a linear, lower-order element (Figure 2-1a) and quadratic, higher/second-order element (Figure 2-1b) linked to appropriate linear and none-linear shape function and jacobian for full and reduced integration. As the name suggests, the

linear element, i.e., f(x) = ax+b, is more suitable and efficient for linear integration between two points and does not capture curvature (e.g., quadratic function in Figure 2-4). Higher-order elements, e.g., $f(x) = ax^2+bx+c$, on the other hand, are accurate for higher-order polynomial integration but are far more expensive. Cubic elements, i.e., $f(x) = ax^3 + bx^2 + cx + d$, were not implemented.

When implementing the quadratic element, one is faced with a problem: for full integration using a quadratic element, one needs 9 Gauss points, which means the element needs to engulf nine measurement points compared to 4 for full integration using a linear element. Then, looking at Figure 2-1b, when considering uniform spacing, the reader will notice that it can be easy to place the measurement points where the Gauss points are. Nevertheless, the problem arises when the integration for nodal displacement is completed because there is no integration for the centric point. Thus, the integrated map will have a missing point for each element constructed around nine measurement points. Of course, the reverse approach can be taken by placing the measurement point at the element's centre and then linearly interpolating to the Gauss points before octically[3] ($8^{th}$ degree polynomial) interpolating the displacement for the centric points from the values of the integrated eight nodes displacement surrounding the point. However, interpolating to enrich the map will negate the need to use high-order elements to achieve similar accuracy (similar to segmenting a curve into small lines). Another approach is to use reduced quadratic element integration, using nine measurement points, i.e., the 4-point numbered 1 to 4 in Figure 2-1b.II are 1, 3, 9, and 7 from Figure 2-1b.I. This leads to reduced accuracy compared to full integration. Note that 'full integration' here refers to the order (number of Gauss points) that is required to get

[3] James Cockle proposed the name in 1851 (Mechanics Magazine, Vol. LV, p. 171).

an exact solution for an undistorted (or regular shape) element which has straight edges that meet at edge nodes [91].

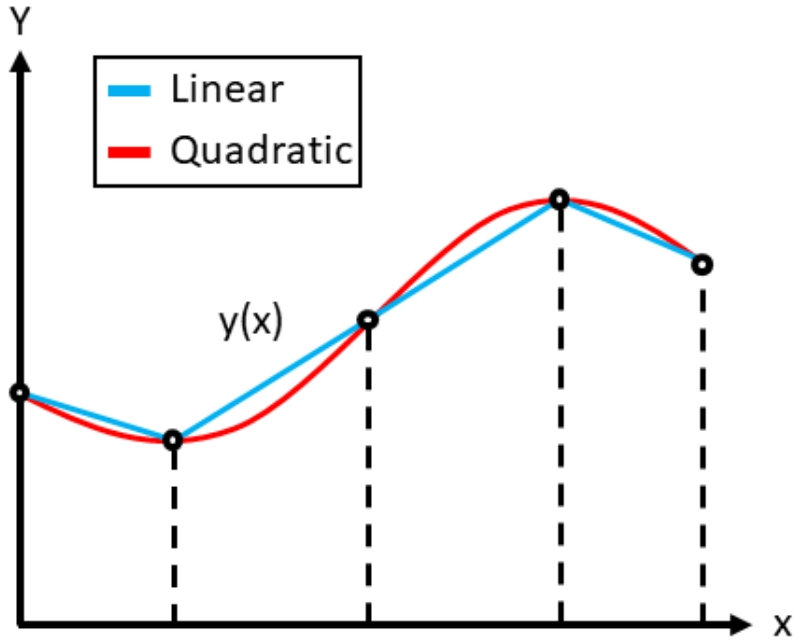


Figure 2-4: 4 element linear and quadratic approximation.

This relationship between element order (p) and the number of elements (h), where the accuracy between different element order converge at a higher number of elements, is not unique to our method but something that was explored by Babuška and Szabó [92] in the hp-adaptive finite element method that can efficiently solve similar problems. Considering the problem at hand and the number of points in most measured elastic strain fields; linear elements should be enough to approximate the problem accurately with careful consideration given to the number of Gauss points, especially in three-dimensional analysis where full integration is highly recommended as it will at least provide a (tri-) quadratic solution for 3 x 3 x 3 gaussian (points) integration.

### 2.3.2 2D Experimental dataset

The elastic strain data measured by X-ray diffraction was integrated and compared to the in-plane displacement field measured using digital image correlation (DIC). The *J*-integral and stress intensity factors are used for a detailed comparison between the two fields and to show the accuracy of the solution.

#### 2.3.2.1 Experiment

Full details of the experiment that provided the raw data analysed in this work have been published elsewhere [93][4] and are summarised briefly here. The test specimen was fabricated from an HSLA (high strength low alloy with yield strength ~800 MPa) steel weld joint (Cr2Ni4MoV), which had been annealed at 550°C for 40 hours to relieve the residual welding stresses. A standard compact tension geometry (notch depth of $a/W$ = 0.35, $W$ = 50 mm) was used, with a thickness of 6.5 mm to improve X-ray transmission (Figure 2-5). The specimen, which satisfied the ASTM E647 conditions for elastic deformation, was fatigued via a load-shedding scheme to a final $\Delta K$ of 13 MPa √m ($R$=0.1) to develop a pre-crack in the HAZ, parallel to the weld interface as shown in Figure 2-5a.

One surface of the specimen was metallographically polished, and a region of interest (10 × 10 mm) around the crack tip was etched (3% nitric acid-ethanol solution) to provide sufficient speckle for digital image correlation of optical images. These were recorded during the experiment using a LaVision DIC system (LaVision GmbH, Göttingen, Germany), equipped with

[4] The author of this thesis was not involved with the experiment design nor execution at the synchrotron facilities. The experiment provided the diffraction spectra and images which the author analysed to obtain the strain and displacement maps. Post-test analysis of the sample was also done by the author.

a 12-bit CCD camera attached to an optical microscope with a Schneider Kreuznach 50 mm lens and a 100 mm extension tube. The distance between the lens and the specimen surface was roughly 50 mm. Two LED flashlights were used to ensure appropriate lighting conditions. An area around the crack tip of about 1300 × 1100 $\mu m^2$ was imaged with a spatial resolution of 0.54 µm/pixel.

The Energy Dispersive X-ray Diffraction measurements (EDXD) were obtained in experiment EE13579, using a multi-wavelength 'white beam' and the 'Horseshoe' 23-element detector (Figure 2-7a) of beamline I12 (Joint Engineering, Environmental and Processing – JEEP) at the UK Diamond Light Source [94]. This provided the diffraction spectra from suitably oriented grains within a gauge volume defined by collimating slits and diffraction angle, which in this case was 100 µm × 100 µm x 4500 µm. Rastering the specimen position in the beam allowed mapping an area of 1.6 mm × 1.3 mm (~208 data points per map) around the crack tip.

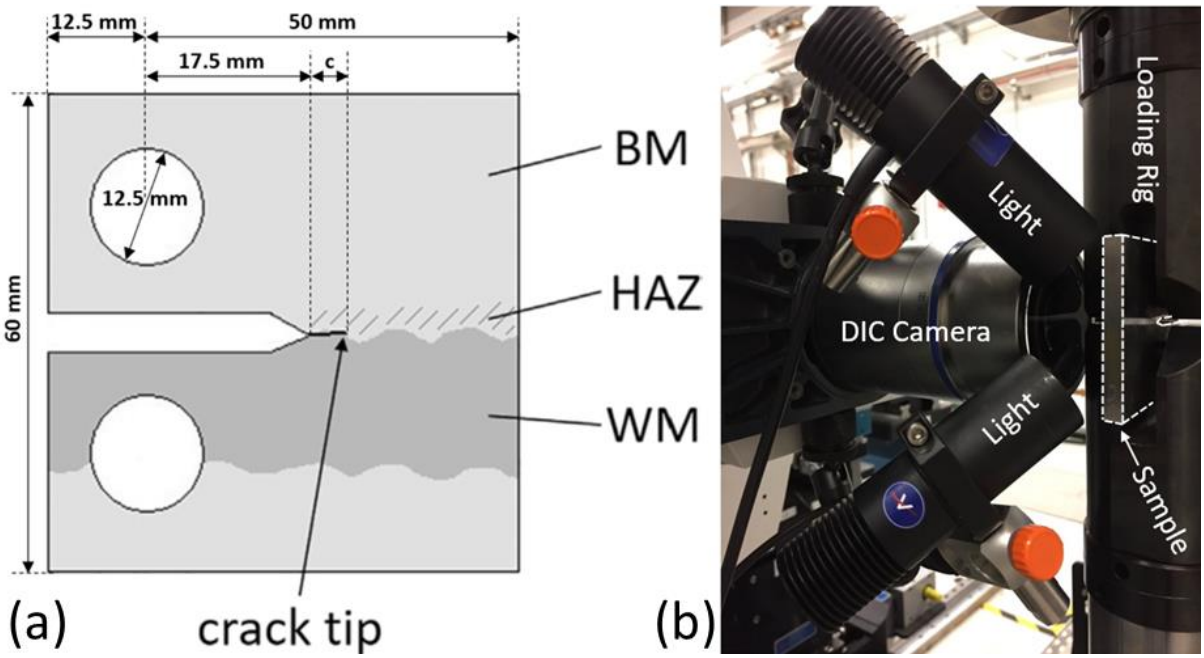


Figure 2-5: (a) Schematic of the compact tension (CT) specimen, identifying the weld metal (WM), heat affected zone (HAZ), base metal (BM) and the fatigue pre-crack location in the HAZ (adapted from [93]). (b) Experimental setup during DIC imaging acquisition.

Optical and EDXD data were obtained pseudo-simultaneously by installing the EDXD detector and the DIC microscope next to each other. The specimen was loaded by a 100 kN servo-hydraulic loading rig mounted on a translation stage, so the specimen could be positioned alternately in the X-ray beam for EDXD measurements and then in the view of the microscope for optical imaging (Figure 2-5b). The time required to change between optical and EDXD modes was less than 10 minutes. The translation stage positioning was performed using a calibrated digital encoder with a precision greater than ±10 μm.

The experiment was executed on a single test specimen in 3 phases. These are summarised in Figure 2-6, which presents the applied stress intensity factor as a function of the number of load cycles applied, where K:ASTM was calculated from the specimen geometry, measured crack length, and applied load using the ASTM standard E647 [95]. Here, $P$ is the applied load, $B$ the sample thickness, $a$ the crack length and $W$ the sample width.

$$K_I = \frac{P}{B}\sqrt{\frac{\pi}{W}}\left[\begin{array}{c} 16.7\left(\frac{a}{W}\right)^{\frac{1}{2}} - 104.7\left(\frac{a}{W}\right)^{\frac{3}{2}} + 369.9\left(\frac{a}{W}\right)^{\frac{5}{2}} \\ -573.8\left(\frac{a}{W}\right)^{\frac{7}{2}} + 360.5\left(\frac{a}{W}\right)^{\frac{9}{2}} \end{array}\right] \qquad 2—19$$

In the 1st phase, the specimen was cycled between upper ($P_{max}$) and lower ($P_{min}$) load values of 3.4 kN and 0.34 kN, respectively (stress intensity factor range $K_{max} - K_{min} = \Delta K$, where $\Delta K \approx$ 15 MPa √m, $R$=0.1) to observe the evolution of the crack field without substantial fatigue crack growth. Observations were obtained at intervals with the specimen under a static load, initially at $P_{min}$, then at $P_{max}$ for up to 1000 cycles. In the 2nd phase, the loads were increased to 6.6 kN and 0.66 kN values ($P_{max}$ and $P_{min}$, respectively) to provide a stress intensity factor range of $\Delta K \approx$ 30 MPa √m, $R$=0.1 to examine the crack field developed during steady-state fatigue crack propagation. Measurements were obtained initially at $P_{min}$, and

then at $P_{max}$ for up to 2000 cycles. In the 3rd phase, a single load cycle between 0.66 kN and 3.3 kN was examined as the load was incrementally increased and then decreased without any crack growth to examine the variation of the crack field within a single load cycle.

After the experiment, the specimen was sectioned metallographically by the author of this thesis and electron backscatter diffraction (EBSD) was used to investigate the microstructure surrounding the crack tip. EBSD maps at a step size of 43 nm, over an area of 0.5 mm x 0.5 mm, were obtained using a ZEISS Merlin FEG SEM microscope fitted with a Bruker EBSD system and plasma cleaner. The data was analysed using MTEX [96], and texture was calculated as an Orientation Distribution Function (ODF) with a halfwidth of 7.5° to minimise the estimation error to less than 0.1% [97].

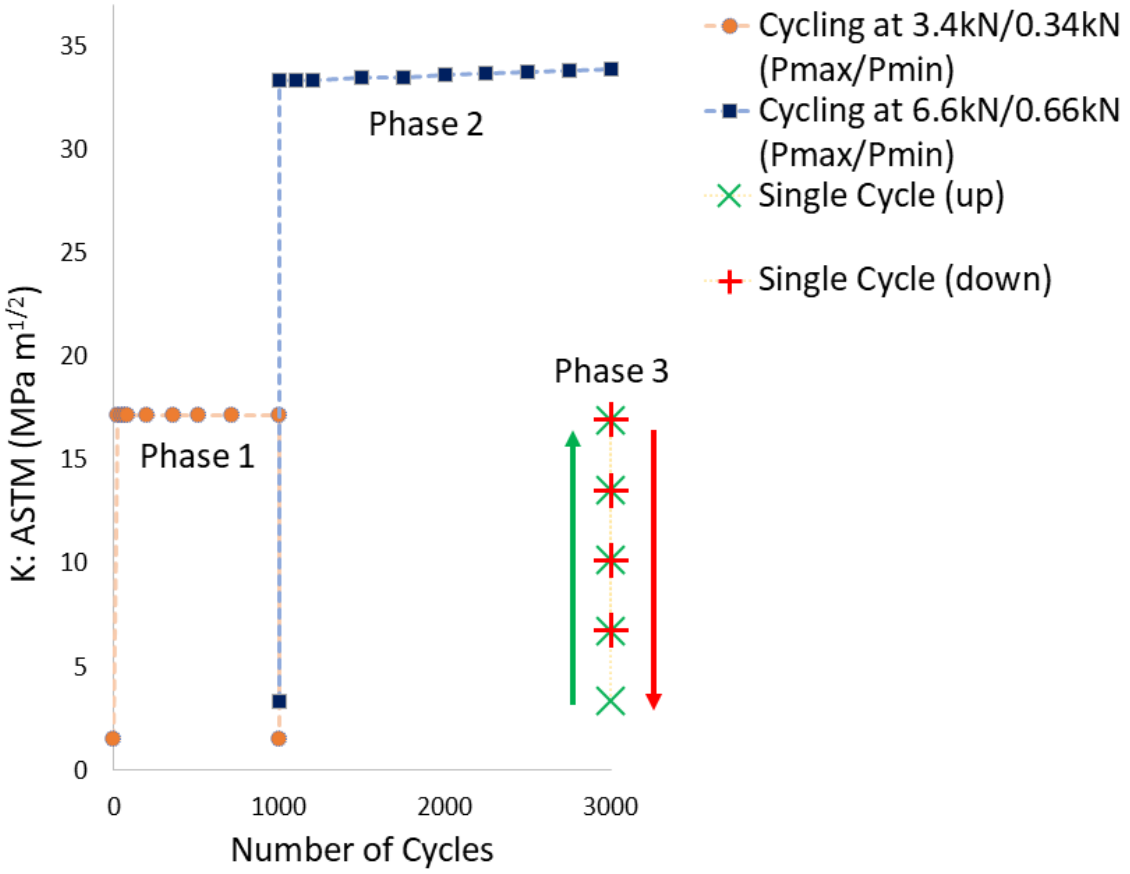


Figure 2-6: The phases of the experiment, identifying the applied stress intensity factor, K:ASTM (calculated from the crack length, specimen geometry and loads using the ASTM standard formula), for each observation as a function of the total number of fatigue cycles.

#### 2.3.2.2 Data Analysis

A typical X-ray spectrum from one element of the detector is illustrated in Figure 2-7a, which shows the diffracted intensity as a function of $q$, where $q = {}^{2\pi}/_{d}$ and $d$ is the diffracting lattice plane spacing. The most intense peak is from the {110} planes; an example of a single peak fit for the {110} peak with its FWHM (Full Width Half Maximum) intensity identified is shown as an inset in Figure 2-7a. To correct for different sensitivities of the elements in the detector, calibration data were obtained using an untextured Ceria powder ($Ce_2O$) sample using the same parameters (e.g. beam slits and collimation) and were used to normalise[5] the measured intensity for each of the 23 elements (see inset Figure 2-7a) with respect to one element, arbitrarily selected as number 12 at 90°. Normalised data from the complete set of 23 elements are shown in Figure 2-7b.

The EDXD spectra were fitted to obtain the peak positions ($q_n^{hkl}$) from which to calculate the strain ($\epsilon_n^{hkl}$) on each family of lattice planes relative to an unstrained reference value, $q_0$, using equation (2—20). Improving on Simpson [98] and Mostafavi *et al.* [99]; the overall lattice strain ($\epsilon_\varphi^{hkl}$), as a function of azimuthal angle ($\varphi$) at each detector, was weighted ($W_n^{hkl}$) for the contribution of each ($n$) diffraction peak, relative to all peaks ($N$) as described in equations (2—21) and (5), using a 'relative' peak intensity ($I_n^{hkl}$) that depends on the multiplicity of the diffracting planes [100]. The elastic strain variation across the detectors was then fitted using a single-term Fourier transform, and the in-plane elastic strain tensor ($\epsilon_{xx}$, $\epsilon_{xy}$ and $\epsilon_{yy}$) were obtained from the fitting parameters using equation 2—23 (Figure 2-8a) as it is more accurate compared to using specific detector values due to the additional information [98].

[5] The MATLAB code is available at https://doi.org/10.5281/zenodo.6411615.

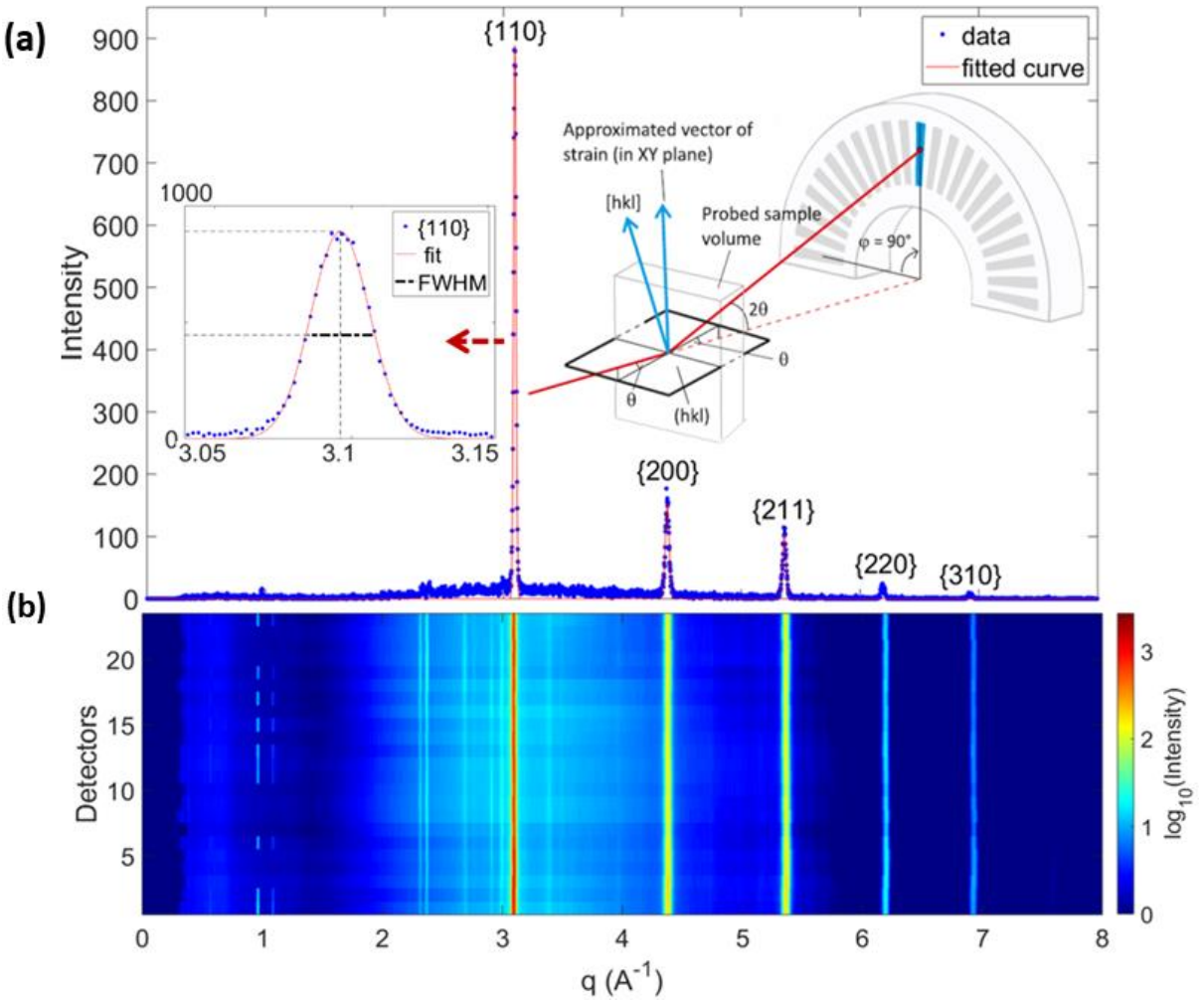


Figure 2-7: (a) Energy-dispersive X-ray diffraction (EDXD) spectrum obtained at 1 point from a single element of the 'Horseshoe' detectors; a Gaussian fit to extract peak position and FWHM from one detector is shown as an inset. (b) normalised data from all 23 elements of the detector.

$$\epsilon_n^{hkl} = \frac{q_0}{q_n^{hkl}} - 1 \qquad 2—20$$

$$\epsilon_\varphi^{hkl} = \sum_{n=1}^{N} \epsilon_n^{hkl} W_n^{hkl} \qquad 2—21$$

$$W_n^{hkl} = I_n^{hkl} / \sum_{n=1}^{N} I_n^{hkl} \qquad 2—22$$

$$\epsilon_\varphi^{hkl}(\varphi) = \left[\frac{\epsilon_{xx} + \epsilon_{yy}}{2}\right] + \left[\frac{\epsilon_{xx} - \epsilon_{yy}}{2}\right] \cos 2\varphi + \epsilon_{xy} \sin 2\varphi \qquad 2—23$$

The Full-Width Half Maxima ($FWHM_{\varphi}^{hkl}$) were calculated using the Gaussian-fit peak width ($c_n^{hkl}$) as in equation (2—24). The mean value across all the detectors was used to map $\mathrm{FWHM_{xy}}$ at each $(x, y)$ coordinate measurement point. The maximum value of FWHM was localised (Figure 2-8b), and a cross-correlation algorithm could be used for efficient subpixel image registration between the FMHM maps [93]. This allowed changes in the position of the FWHM peak (or maximum spatial value) to be tracked with subpixel accuracy (1 pixel = 100 µm).

$$FWHM_{\varphi}^{hkl} = \sum_{n=1}^{N} 2\sqrt{2\ln(2)}\; c_n^{hkl}\, W_n^{hkl} \qquad 2—24$$

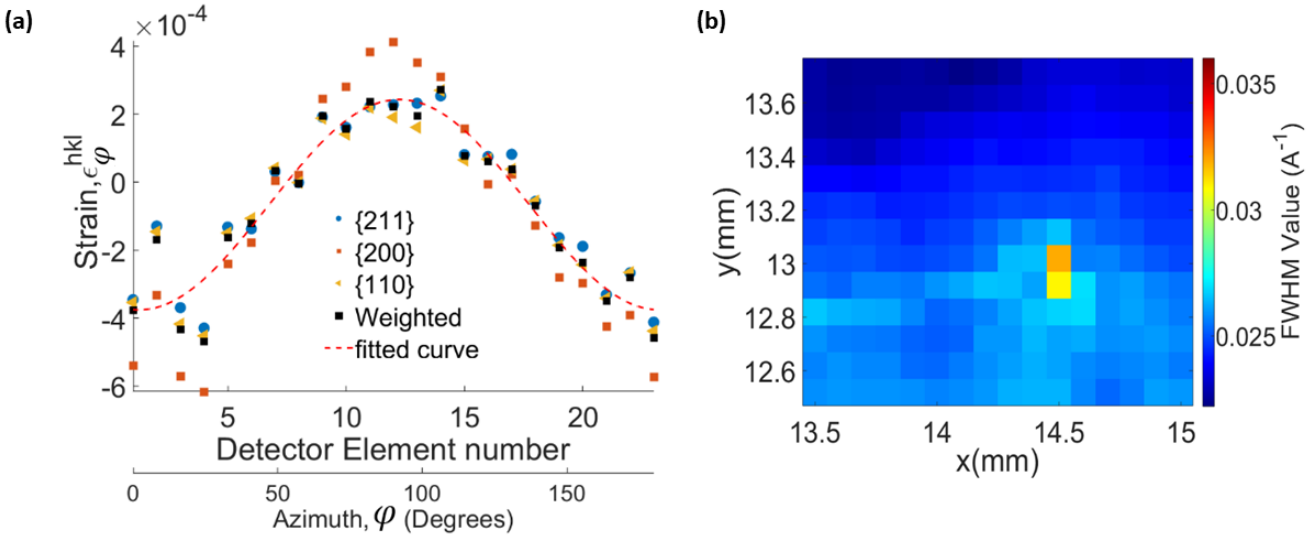


Figure 2-8: a) the variation of elastic strain with azimuth angle over the 23 detectors for the single dominant peaks, their weighted average, and the fitted curve to the weighted average; b) an example map of weighted FWHM (full width half maximum) value. The crack tip position can be tracked by cross-correlation analysis of the movement of the distribution of FWHM values between successive maps.

Maps of the effect of the change in load (i.e., from $P_{min}$ to $P_{max}$) on the strain tensor components were obtained by subtracting the apparent strains at each measurement point measured in the preceding observation of the specimen (i.e., at $P_{min}$). A set of typical strain maps is shown in Figure 2-9. The reference maps at $P_{min}$ are shown in Figure 2-9 (I-III); the

crosses show the positions of the individual measurements with interpolated contours of strain. The strain changes from $P_{min}$ to $P_{max}$ are shown in Figure 6 (IV-VI). Here, due to slight stage movements during the observations, the measurement window is not entirely the same, and some small regions at the margin do not have measurements at both $P_{min}$ and $P_{max}$. These are shown as white.

Typically, XRD data from an un-strained region of the sample would be used for the reference, with reference peak positions ($q_o$) obtained by Gaussian fitting to the most intense – also distinct – peaks (i.e., {110}, {200} and {211} in body centred cubic ferrite) to minimise fitting residuals and error. In this experiment, a satisfactory un-strained reference was not obtained. Hence, an alternative approach was required to find a suitable reference with minimum strain.

First, theoretical positions for the most intense peaks were calculated with a nominal lattice parameter ($a_o$ = 2.8665 Å for ferrite). Then, a set of measurement points remote from the crack tip (examples indicated in Figure 2-9. III) was identified, which had minimum absolute strains (i.e., minimum elastic deformation) and minimum FWHM (i.e., minimum plastic deformation). These points were averaged to provide a more representative reference for $q_o$, as shown in Table 2-1, which was used to recalculate the elastic strain tensor components in that experiment phase (the sample was removed and replaced in the loading rig between phases 2 and 3).

Table 2-1: Optimised $q_0$ values, used for the reference in strain maps for the most strongly diffracting planes. All were measured at $P_{min}$ (Phase I and Phase 3: 0.33 kN, Phase 2: 0.66 kN).

| Planes | $q_0^{\text{Theoretical}}\ (\text{Å}^{-1})$ | $q_0^{\text{Optimised}}\ (\text{Å}^{-1})$ | | |
|---|---|---|---|---|
| | | 1st Phase | 2nd Phase | 3rd phase |
| {110} | 3.10041 | $3.09560 \pm 8.8 \times 10^{-6}$ | $3.09633 \pm 1.1 \times 10^{-5}$ | $3.09570 \pm 9.5 \times 10^{-6}$ |
| {200} | 4.38464 | $4.37774 \pm 2.4 \times 10^{-5}$ | $4.37872 \pm 2 \times 10^{-5}$ | $4.37792 \pm 2.1 \times 10^{-5}$ |
| {211} | 5.37006 | $5.36173 \pm 2.8 \times 10^{-5}$ | $5.3630 \pm 2 \times 10^{-4}$ | $5.36202 \pm 2.3 \times 10^{-5}$ |

± in optimised $q_0$ values reflect the standard deviation from the mean in the selected points.

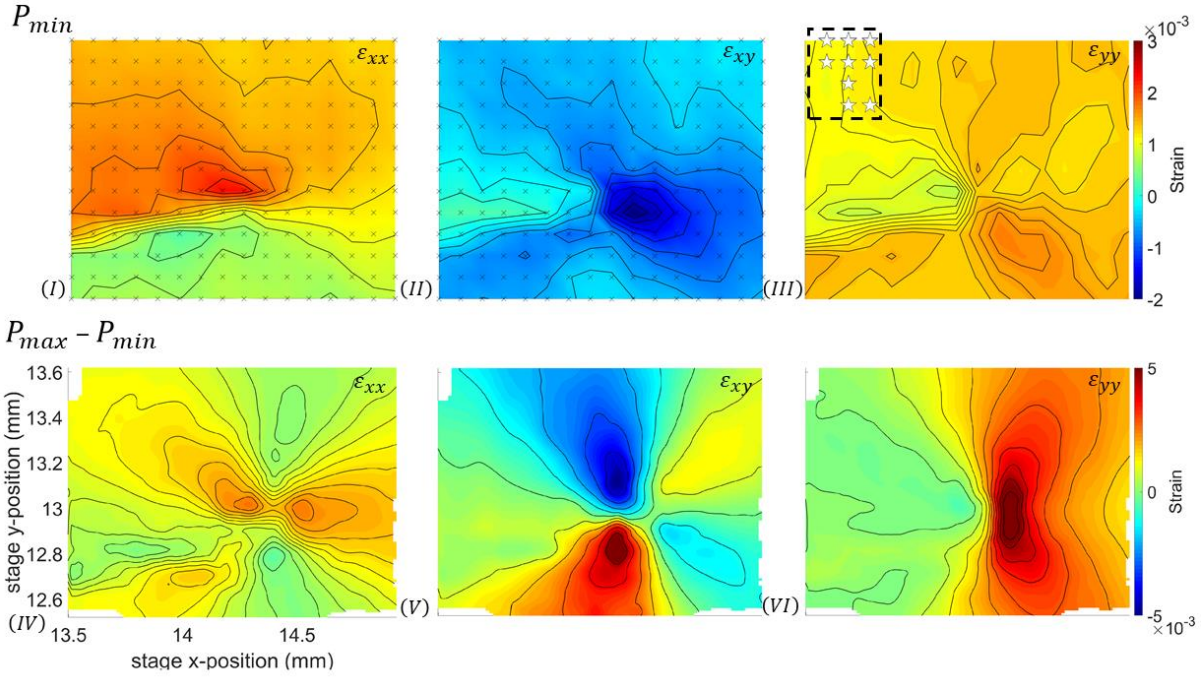


Figure 2-9: Examples of strain tensor maps obtained at (I-III) 0.66 kN ($P_{min}$) and (IV-VI) 6.6 kN ($P_{max}$) for $\varepsilon_{xx}$, $\varepsilon_{xy}$ and $\varepsilon_{yy}$. The strains at $P_{min}$ are calculated using the theoretical $q_0$ (see Table 2-1). The points selected for the optimised $q_0$ are indicated by the white stars inside the dashed black box (III).

The optical images allowed digital image correlation (DIC) to measure the movement between a reference and a distorted image [101]. Some repositioning of the lighting was necessary between observations, and despite the precision of the translation stage, the optical images

suffered from translational rigid body movements and changes in light intensity. The image was corrected using an image registration algorithm to improve the accuracy of subsequent DIC analysis, which was implemented via an efficient Fourier-space subpixel image registration MATLAB® algorithm using cross-correlation to calculate shifts [102]. The images were then processed using the DaVis Software (FFT DIC algorithm) using a subset size of 48 x 48 image pixels with 25% overlap to obtain the displacement field.

The crack length and tip position were identified using the displacement field by a method developed by Cinar *et al.* [84] for 3D cracks, and it was modified to allow for 2D crack analysis. The method is based on edge detection using phase congruency [103], which is contrast invariant and identifies where the Fourier components of the image are most in phase, such as edges. The displacement fields were interpolated to fill the few points with no data (NaN). The sequence of the data post-processing is summarised in Figure 2-10, where a phase congruency map (Figure 2-10e) of the smoothed (Figure 2-10b and d) and filtered (Figure 2-10c) displacement field is computed. A Hough transform is applied to autonomously detect the longest linear discontinuity (i.e., the crack) from the binarized map (Figure 2-10f).

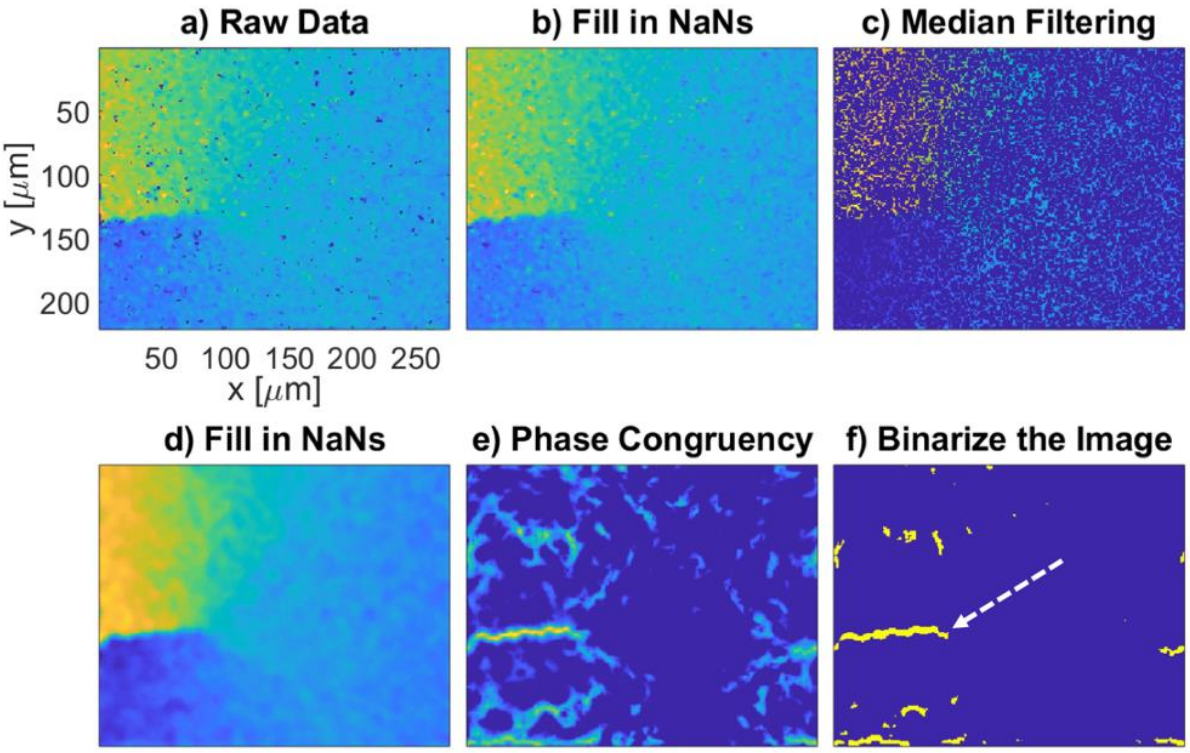


Figure 2-10: The post-processing steps of the phase congruency analysis [84]: to identify the crack from the DIC-measured displacement field: a) raw data (*y*-displacement field); b) interpolation to fill empty points with no DIC data (NaN: not a number); c) median filter to reduce noise; d) final interpolation to remove any remaining points with no data; e) calculation of phase congruency values; f) binary segmentation and identification of the most extended linear feature using Hough transform.

#### 2.3.2.3 Results and discussion

The developed fatigue crack, imaged by SEM, is shown in Figure 2-11a, and an EBSD grain orientation map of the same area is presented in Figure 2-11b. The pole figures, calculated from this field of view (Figure 2-11c), show a weak texture. This is consistent with the EDXD data (Figure 2-7b), which showed negligible variation between detectors after the Ceria normalisation for sensitivity. These data were used with the ISODEC software [104] to calculate the diffraction elastic constants in the direction normal to the crack plane, assuming $E_{110} = 220 \pm 2$ GPa, $E_{200} = 164 \pm 2$ GPa and $E_{310} = 175 \pm 1$ GPa [105]. A value of 212 ± 7 GPa was obtained for Young's modulus and 0.318 for Poisson's ratio using Hill's weighted average model [106]. The EBSD data also allowed mapping of the lower bound estimate of the

number density of geometrically necessary dislocations (GND) [107]; the increased GND density along the crack path is apparent (Figure 2-11d).

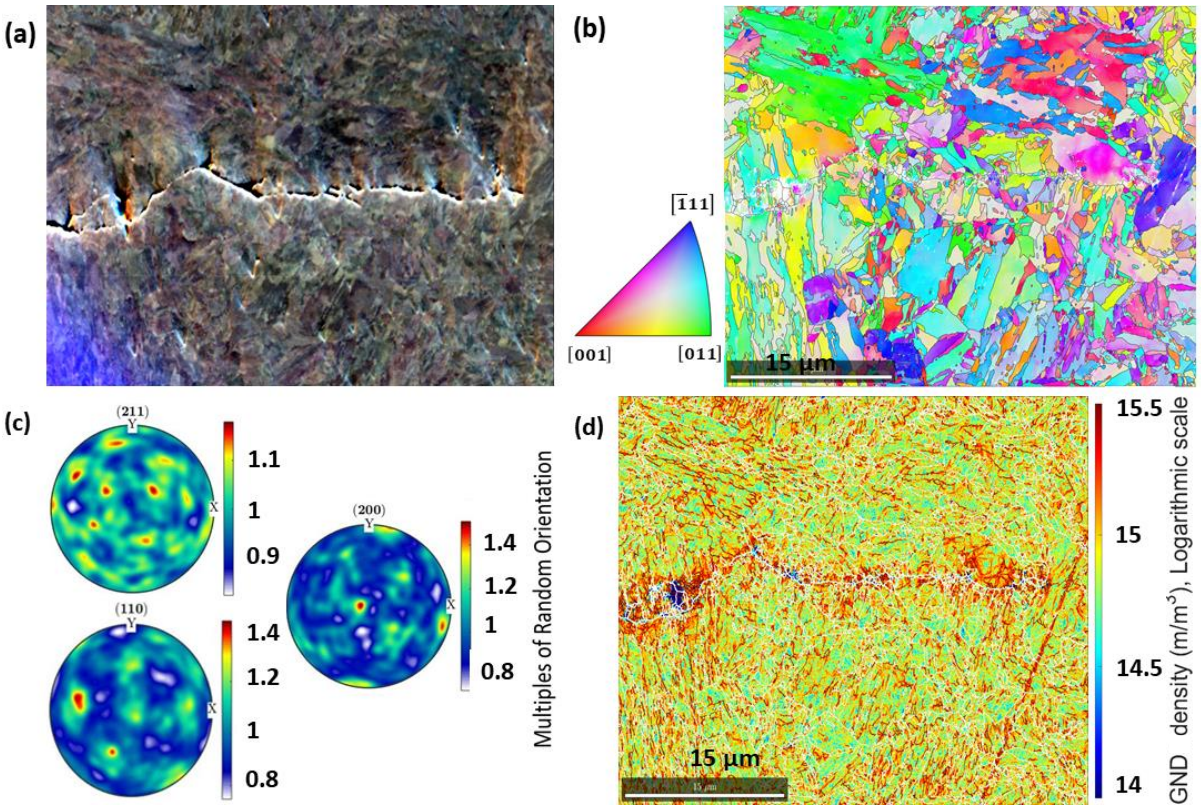


Figure 2-11: SEM examination of the fatigue crack: (a) secondary electron image; (b) EBSD map of the same area as (a). (c) Orientation Distribution Function (ODF) plots for the {211}, {200} and {110} planes; d) geometrically necessary dislocations (GND) density.

The GND distribution shows the limited extent of crack tip plasticity of the propagating fatigue crack. The localised increase of diffraction peak width (i.e. the weighted FWHM) can be attributed to the effect of plastic deformation at the crack tip, so the cross-correlation tracking of the position of the FWHM peak (e.g. Figure 2-8b) can be used to investigate changes in the crack tip position. The results are presented in Figure 2-12. The change in crack tip position identified via the phase congruency analysis of the DIC-measured surface displacement field is also shown.

In phase 1 of the experiment, DIC observed no change in the crack position. However, over the first 100 cycles, a meaningful change occurred in the position of the FWHM peak, measured at 3.4 kN $P_{max}$, before becoming essentially static. This may be related to a gradual evolution of the crack tip plastic zone with the increased applied maximum SIF relative to the lower value used to develop the pre-crack. Reduction of the load to 0.3 kN ($P_{min}$) at the end of phase I was accompanied by a retreat of the FWHM peak position, and increasing the load to 0.6 kN ($P_{min}$, phase 2) caused an increase in the position of the FWHM peak.

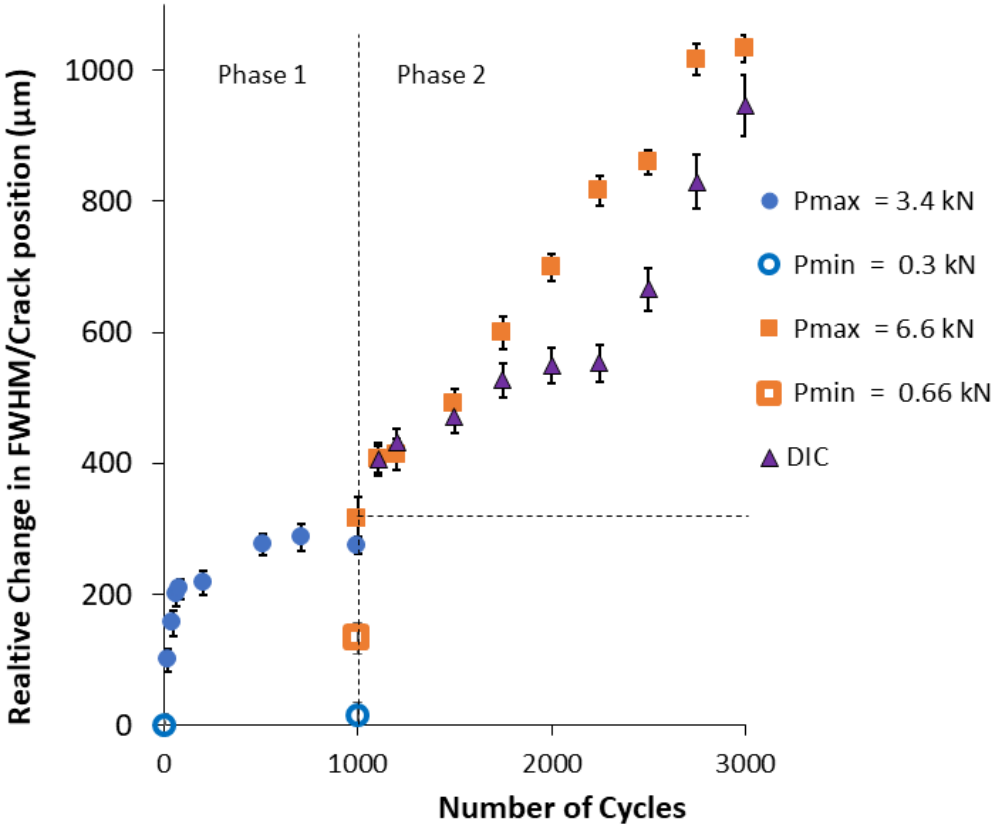


Figure 2-12: The change in crack tip position with the number of cycles, measured using EDXD and DIC. DIC showed no detectable change in the crack tip position in phase I. In phase 2, the DIC-measured change has been plotted relative to the position of the EDXD FWHM peak, measured at $P_{max}$ at the start of phase 2. (i.e., at the intersection of the orthogonal dotted lines).

In phase 2, the change in position of the FWHM peak, measured at 6.6 kN ($P_{max}$), was consistent with the change in position of the crack tip measured by DIC. Differences may be due to the shape of the crack front since the DIC measurement was made at the surface, while

the EDXD data are averaged across a thickness of 4.5 mm of the gauge volume of the diffracted beam within the specimen [93]. These data show that observations of the EDXD FWHM peak position at a nominally constant applied stress intensity factor may be used to detect and measure crack propagation.

#### 2.3.2.4 *J*-integral analysis

The EDXD elastic strain tensor maps were used to calculate the elastic displacement field, and then displacement fields from DIC and EDXD were used to calculate the *J*-integral using the JMAN method developed by Becker *et al.* [56]. *J*-integral evaluation using JMAN uses the displacement field as a boundary condition with the crack lying on the x-axis. For better accuracy and stable convergence, the *J*-integral is formulated as a surface/domain integral rather than a line integral as in equation (2—25), where $el$ is the number of elements, $A$ is the surface/domain enclosing the crack tip, $\sigma$ is the stress tensor, $U$ is the displacement, $W$ is the strain energy density, and $q$ is a (linear) smoothing function of the local direction of a virtual crack extension which is equal to unity at the tip and zeroes outside the domain.

$$J = \sum_{el}\left[\left(\sigma_{xx}\frac{dU_x}{dx} + \sigma_{xy}\frac{dU_y}{dx} - W\right)\frac{dq}{dx} + \left(\sigma_{xy}\frac{dU_x}{dx} + \sigma_{yy}\frac{dU_y}{dx}\right)\frac{dq}{dy}\right] * A_{el} \qquad 2—25$$

$$\because W = \frac{1}{2}\sigma_{ij}\epsilon_{ij}$$

The JMAN method requires high-quality displacement field data for the integral to converge and masking the crack path. Examples of the initial contour selection are shown in Figure 2-13. The outer contour extends to the bounds of the data, and the *J*-integral analysis uses the converged value with increasing contour size. The JMAN method is limited to mode (I) loading, and this was warranted by the sample geometry and loading and is verified by inspection of the displacement field. Using these 2D fields, the calculations assumed plane

stress conditions for the DIC analysis (i.e., surface measurements) and plane strain conditions for EDXD (i.e., bulk measurements within the specimen). The same ISODEC-calculated elastic properties were used in all analyses. Using the appropriate plane stress and plane strain relationships, the converged *J*-integral values were converted to linear elastic mode I.

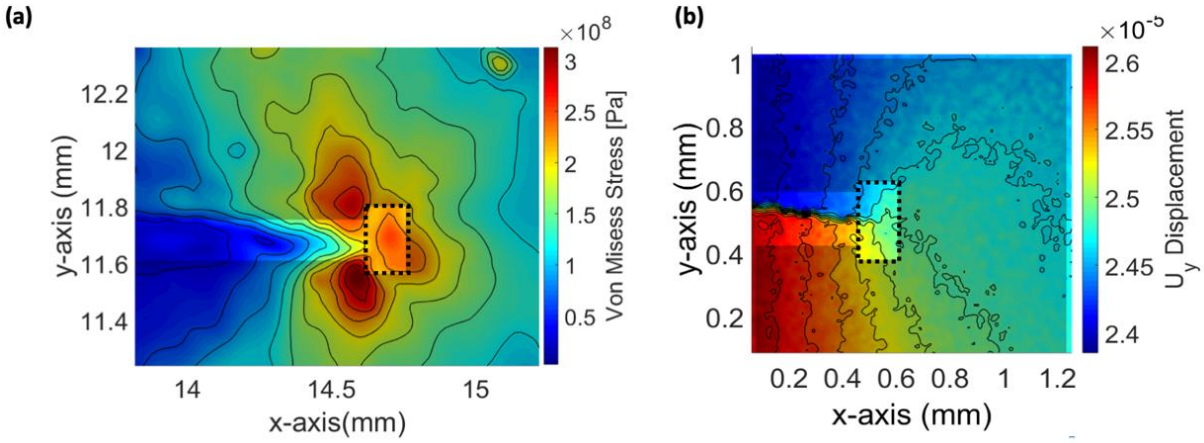


Figure 2-13: Examples of the selection of the initial *J*-integral contour (shown by black dotted box) and the excluded region (~0.2 mm wide) along the crack for a) analysis of EDXD data (Von Mises stress map shown); b) Analysis of DIC data (map of the displacement component perpendicular to crack plane shown).

The changes in the elastic stress intensity factor change experienced by the crack with the change in load within single cycles (i.e. at the same crack length for each map) are presented in Figure 2-14; data are presented from single cycles selected during phase 1, 2 and 3 of the experiment. The figure shows a good agreement between the stress intensity factor ranges obtained using EDXD, DIC, and ASTM. The *J*-integral analyses for the DIC and EDXD data assume linear elastic properties, which are also assumed in the ASTM calculation. Since the fatigue loading in a single cycle is essentially elastic, a good agreement should be expected between the applied stress intensity factor range (ASTM) and that extracted from the DIC-measured displacement field. Indeed, the agreement of the DIC analysis with the ASTM value verifies that the ASTM equation can be applied (i.e., elastic loading) in this case. The agreement between the DIC and EDXD analyses also confirms that strain mapping by EDXD

can measure the change in the elastic field and then extract the cyclic stress intensity factor range. Non-linear cyclic plasticity at the crack tip, which is indicated by the slight changes in the FWHM position (Fig 9), would tend to reduce the elastic strain field that is measured directly by diffraction; this may be the cause of the tendency for the EDXD analysis to provide slightly lower values than the DIC and ASTM values at high applied loads.

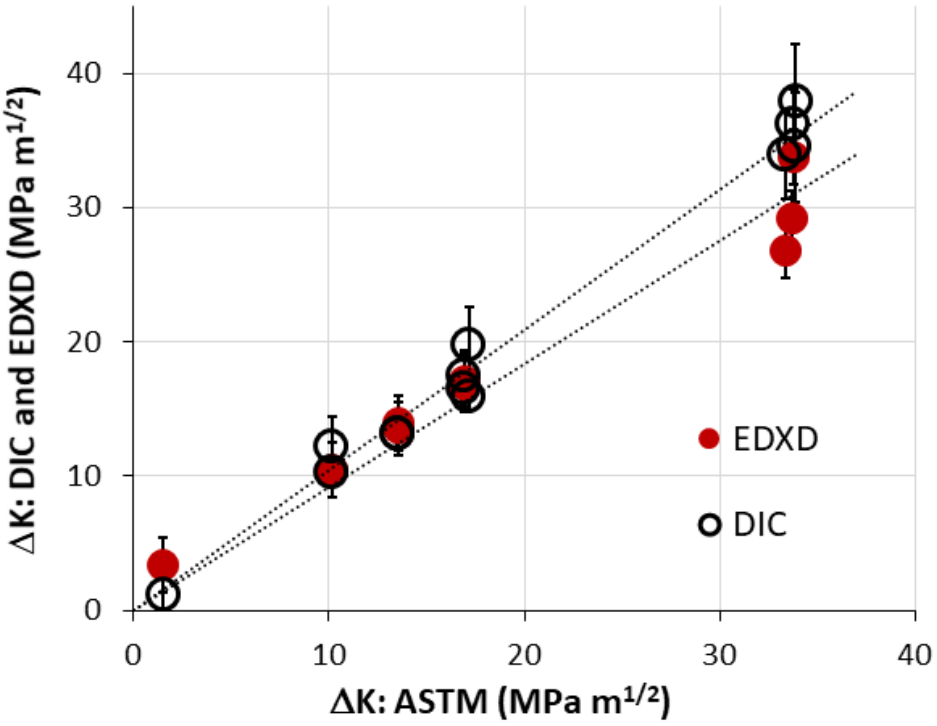


Figure 2-14: Stress intensity factor ranges obtained from DIC and EDXD and compared to analytical (ASTM solution).

Therefore, this methodology allows direct characterisation of the applied elastic strain energy field without requiring knowledge of the specimen geometry, crack length or applied loads. It may be used in future studies to investigate the effects of fatigue overloads, underloads, and phenomena such as crack closure on the crack field that acts on the crack tip to control crack propagation.

### 2.3.3 3D Synthetic dataset

Thirdly, having searched the existing literature, I did not find a method to integrate the three-dimensional (volumetric) strain field into the displacement field. Such data can be obtained using micro-Laue microdiffraction [108–110] and dark-field X-ray microscopy [111]. Therefore, a theoretical strain field was used to predict the displacement field using the proposed method, compared to the original field through the stress intensity factors to show the accuracy of the solution.

#### 2.3.3.1 Analytical dataset

A 3D cubic domain of $L$ x $L$ x $L$ size was considered such that the crack is parallel to $x$-axis and its tip is located at the centre of the domain (i.e., $a = L/2$) at (0,0,0) coordinate as seen in Figure 2-16, where $L = 8$ mm. The displacement in $x$, $y$ and $z$-directions around a crack with a mode I stress intensity factor ($K_I$) of 30 MPa m$^{0.5}$, mode II ($K_{II}$) of 40 MPa m$^{0.5}$, and mode III ($K_{III}$) of 10 MPa m$^{0.5}$ were created using analytical solution [28] and assuming plane stress conditions. The elastic modulus ($E$) and Poison's ratio ($v$) were 210 GPa and 0.3, respectively. Then, the full strain tensors were calculated from the numerical displacement gradient (2—29). The domain is discretised using a uniform square mesh of element length $l_e = 0.67$ mm (11 x 11 x 11 elements).

$$U_x = \frac{K_I}{2\mu}\sqrt{\frac{r}{2\pi}}\cos\left(\frac{\theta}{2\pi}\right)\left[k - 1 + 2\sin^2\left(\frac{\theta}{2}\right)\right] + \frac{K_{II}}{2\mu}\sqrt{\frac{r}{2\pi}}\sin\left(\frac{\theta}{2\pi}\right)\left[k + 1 + 2\cos^2\left(\frac{\theta}{2}\right)\right] \quad 2—26$$

$$U_y = \frac{K_I}{2\mu}\sqrt{\frac{r}{2\pi}}\cos\left(\frac{\theta}{2\pi}\right)\left[k + 1 - 2\cos^2\left(\frac{\theta}{2}\right)\right] - \frac{K_{II}}{2\mu}\sqrt{\frac{r}{2\pi}}\cos\left(\frac{\theta}{2\pi}\right)\left[k - 1 - 2\sin^2\left(\frac{\theta}{2}\right)\right] \quad 2—27$$

$$U_z = \frac{2K_{III}}{\mu}\sqrt{\frac{r}{2\pi}}\sin\left(\frac{\theta}{2\pi}\right) \quad 2—28$$

$$\varepsilon_{ij} = \frac{1}{2}\left(\frac{\partial U_i}{\partial x_j} + \frac{\partial U_j}{\partial x_i}\right), \qquad i = j = x, y, z \quad 2—29$$

After the linear mesh was created around each element using a custom-made meshing algorithm implanted in MATLAB®, which fits a uniform 3D 8 nodes hexahedron grid, the coordinates of the nodes and element connectivity matrix were passed to calculate the shape function and Jacobian for Isoparametric linear brick elements with 8 Gauss points (Figure 2-15). The basic idea is to use the shape/interpolation function to relate the strain/measurement point (centric point) to the Gauss integration points and then to the (integrated) nodal displacement. Element stiffness and force matrix at Gauss points are assembled in a sparse matrix to efficiently use the available memory and solve the nodal displacement equation (2—11) using the MATLAB® lsqminnorm algorithm, which is suitable for sparse matrixes and computationally less expensive. The nodal displacement is corrected for rigid body movement (translations and rotation) by selecting the point with absolute minimum displacement as the origin [112]. More details are in Appendix (2.A) – FE-OOM code implementation.

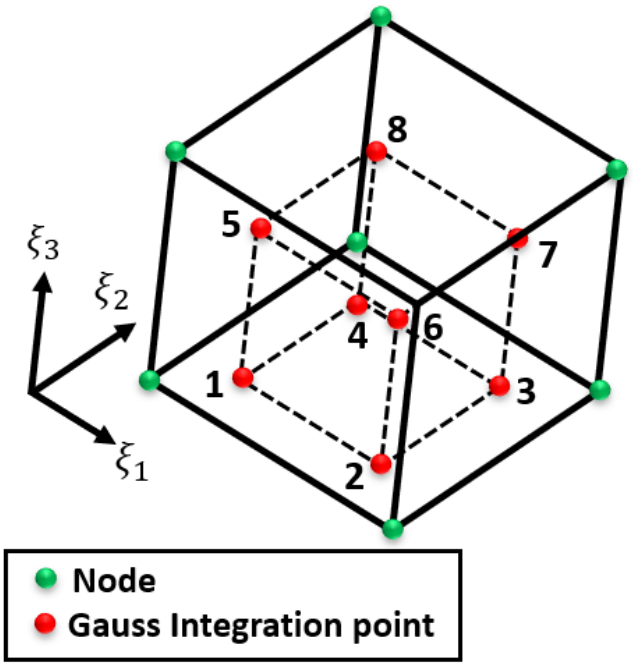


Figure 2-15: Schematic of a linear brick element with 8 Gauss points (full integration). A dimensionless local natural coordinate system ($\xi_1$, $\xi_2$, $\xi_3$) was defined with its origin located at the centre of the brick element.

With the material property, this field is used as a boundary condition in the ABAQUS® finite element solver for calculating (3D pointwise [113]) *J*-integral and stress intensity factor analysis along the crack front. The synthetic and integrated displacement fields were injected as boundary conditions in ABAQUS® to compare the two fields through the stress intensity factors.

#### 2.3.3.2 Results and discussion

For the mixed-mode synthetic data; the average mode I equalled 30.4 ± 0.5 MPa $m^{0.5}$, mode III was -38.5 ± 3.2 MPa $m^{0.5}$, mode III was 8.7 ± 0.5 MPa $m^{0.5}$ and overall energy release rate of 10,958 ± 1,050 J $m^{-2}$ (continuous lines in Figure 2-16). The variance is from the values obtained as the domain of integration expanded from the crack tip. These values are ~4% lower than the actual stress intensity factors used to calculate the synthetic field. This could be attributed to the sensitivity of stress intensity calculation (via the interaction integral method [62]) to the crack tip position, especially for mode I and mode II components [114] considering the very coarse field. A thorough analysis of this is out of the scope of this chapter.

The integrated displacement fields have an average stress intensity factor for mode I loading that equalled 31.7 ± 3 MPa $m^{0.5}$, mode II is -36.8 ± 1.1 MPa $m^{0.5}$, mode III is 8.6 ± 0.2 MPa $m^{0.5}$, and the overall energy release rate of 11,094 ± 502 J $m^{-2}$. There is good agreement between the overall results and across the sample thickness, as shown in Figure 2-16; the results from the synthetic data are plotted with a continuous line and the integrated field with points and dotted lines.

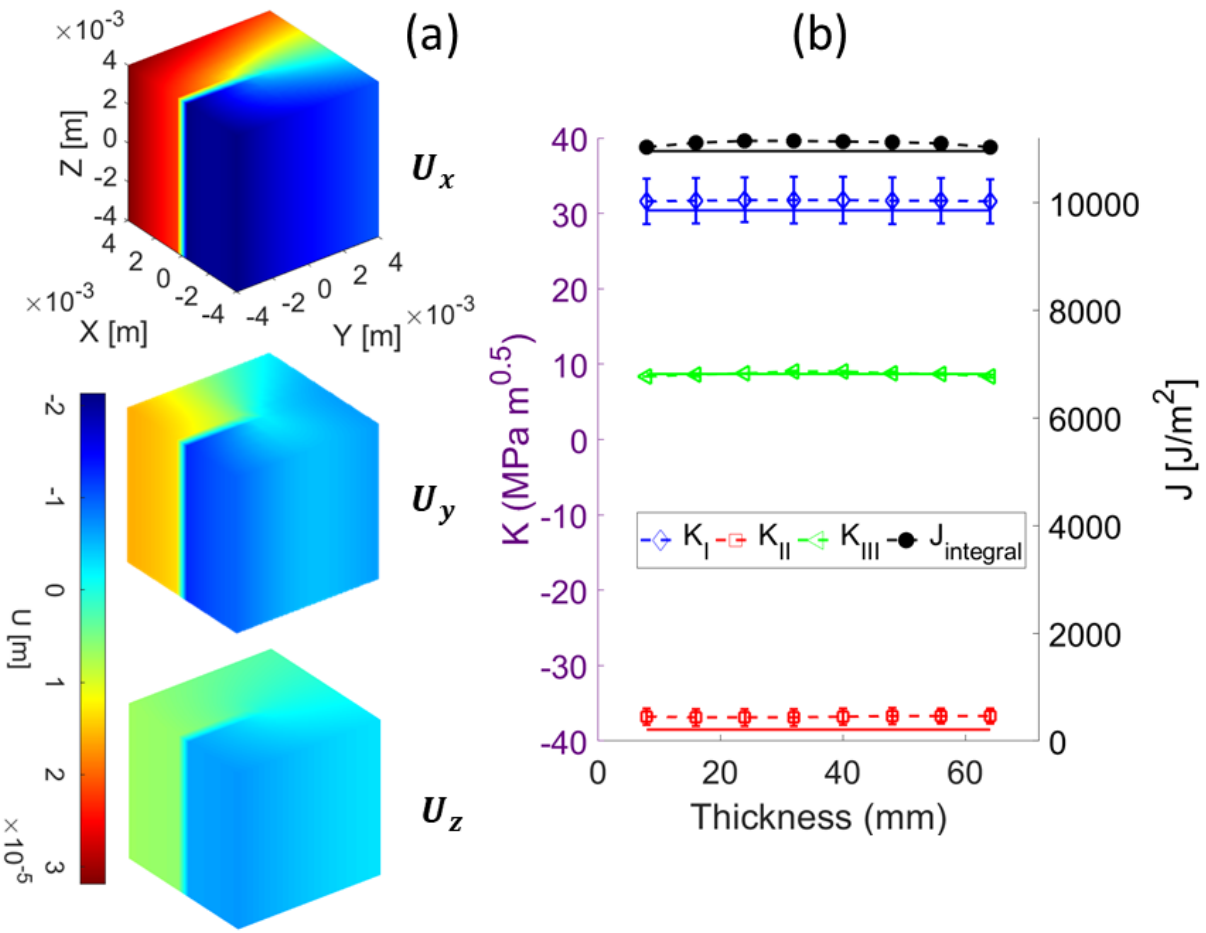


Figure 2-16: (a) Synthetic mixed mode crack field showing displacement in x, y, and z. (b) Comparison between the stress intensity factor and energy release rate values for synthetic data (continuous line) and the integrated field (point and dotted line), both calculated in ABAQUS®.

## 2.4 Conclusion

A novel approach was derived to compute the elastic displacement field from a measured elastic deformation field (i.e., deformation gradient or strain). The method is based on integrating the deformation field using finite element discretisation. Space and displacement fields are approximated using similar piece-wise interpolation functions. Hence, the full elastic deformation field can be expressed in terms of the nodal displacements, which are unknown. The nodal displacements are then obtained using a least square method.

The method is validated against the two-dimensional mode I stationary crack problem in an elastic solid and accurately predicted the Westergaard solution of the displacement field with a small value of error ($\approx 0.1\%$) compared to the more significant errors of another method found in the literature (JMAN_S [76]). The effect on the accuracy and computational time of using full and reduced integration (different Gauss points) with a linear and quadratic element while integration maps with a different number of elements are then thoroughly investigated. The method was also briefly validated for three-dimension by comparing the stress intensity factors – calculated via ABAQUS® – of synthetic and integrated data of a crack expressing mixed-mode conditions. Again, the results showed a low error (<~4%).

Then, the proposed 2D method was applied to an experimental dataset where synchrotron Energy Dispersive X-ray Diffraction (EDXD) and Digital Image Correlation (DIC) were applied to map, simultaneously, the 2D elastic strain and displacement fields of a propagating fatigue crack in the HAZ of a welded Cr2Ni4MoV bainitic steel. Both types of full-field data provided independent inputs to finite element/*J*-integral analyses that directly quantified the elastic cyclic stress intensity factor range applied to the crack. No knowledge was required of the specimen geometry, crack length or applied loads. The agreement between the two analyses in this controlled study shows the reliability of the proposed method and its potential application with synchrotron EDXD mapping to reliably measure the crack tip elastic field in more complex situations, such as interactions between crack closure, residual stresses, and applied load. This can also be expanded to 3D strain fields probed using micro-Laue microdiffraction [108–110] and dark-field X-ray microscopy [111].

# Chapter 3. Selection of cross-correlation reference pattern for HR-EBSD analysis

Contents



## 3.1 Introduction

Full-field displacements, elastic strains, and the geometrically necessary dislocation (GND) density provide quantifiable information about the crack and the material's elastic and plastic behaviour at the microscale. Measuring strain at the microscale requires careful consideration of other key details besides the change in length/shape (e.g., local texture, individual grain orientations). These micro-scale features can be measured using different techniques, e.g., hole drilling, monochromatic or energy-dispersive polychromatic X-ray diffraction (XRD) or neutron diffraction (ND). However, the electron backscattering diffraction

(EBSD) technique provides an impressive combination of sensitivity, spatial resolution and ease of use compared to other techniques [115–117].

For electron backscattering diffraction microscopy, a flat polished crystalline specimen is usually placed inside an SEM chamber, tilted 70° from SEM original specimen positioning and 110° to the diffraction camera (see Figure 3-1L) [118]. Tilting the sample elongates the interaction volume perpendicular to the tilt axis, allowing more electrons to leave the sample due to elastic scattering providing better contrast [119,120]. The high-energy electron beam (typically 20 kV) is focused on a small volume and scatters at a spatial resolution of ~20 nm at the specimen surface [121]. The spatial resolution varies with angular width [122], interaction volume [123], nature of the material under study [121], and in transmission Kikuchi diffraction with the specimen thickness [124]; thus, increasing the beam energy increases the interaction volume and decreases the spatial resolution [125].

As these backscattered electrons leave the sample, they interact with the crystal's periodic atomic lattice planes and diffract according to Bragg's law at a range of scattering angles ($2\theta_{hkl}$). The backscattered electrons form Kikuchi lines – having different intensities – on an electron-sensitive flat film/screen (commonly phosphor), gathered to form a Kikuchi band (see Figure 3-1R). These Kikuchi lines are the trace of hyperbola formed by the intersection of Kossel-cones with the plane of the phosphor screen. The width of a Kikuchi band is related to the scattering angles and, thus, lattice spacing ($d_{hkl}$) [126–129]. These Kikuchi lines and patterns were named after Seishi Kikuchi, who, together with Shoji Nishikawa, was the first to notice this diffraction pattern in 1928 using TEM [130] which is similar in geometry to X-ray's Kossel pattern [131]. Detailed information about the detection and indexing of diffraction patterns can be found in Ref. [132].

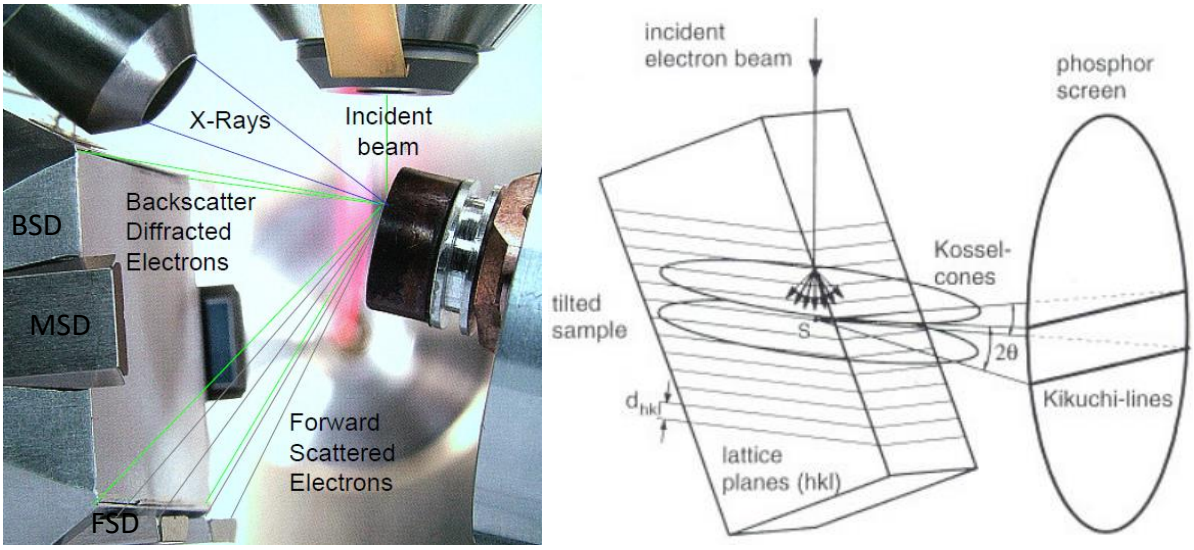


Figure 3-1: (L) EBSD (range between the green lines) and EDS (range between the purple lines) typical hardware configuration inside field emission gun scanning electron microscope (FEG-SEM) (adapted from [133]). (R) Origin of Kikuchi lines (from [126]).

The systematically arranged Kikuchi bands, which have a range of intensity along their width, intersect around the centre of the regions of interest (ROI), describing the probed volume crystallography [134]. These bands and their intersections form what are known as Kikuchi patterns or electron backscatter patterns (EBSPs). To improve contrast, the patterns' background is corrected by removing anisotropic/inelastic scattering using static background correction (see Figure 3-2) or dynamic background correction [135].

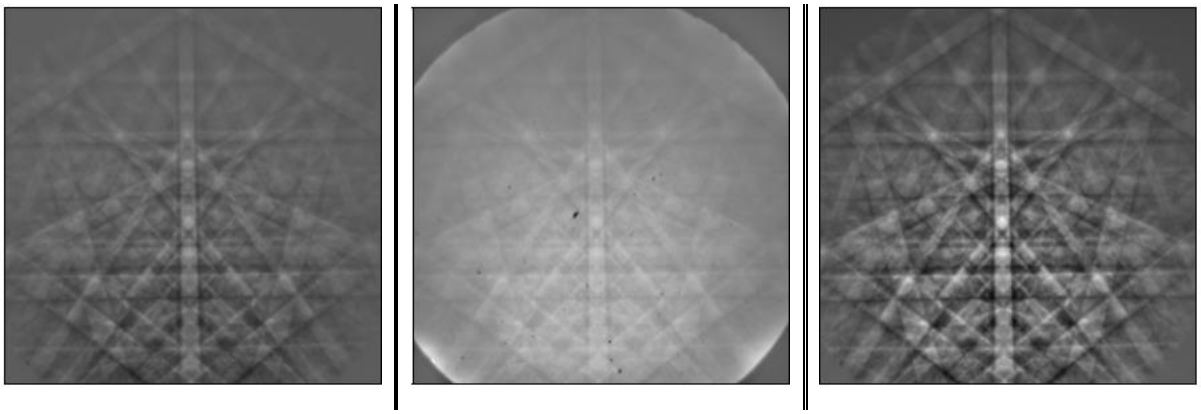

Figure 3-2: Single crystal 4H SiC (gnomically projected) EBSP collected using (left) conventional, (centre) dynamic, and (right) combined background correction [135].

The resulting Kikuchi pattern bands are detected using the Hough transform [136] and then individually indexed using Miller–Bravais indices (sometimes coupled with a voting scheme [137,138], fitting scheme [139,140], or/and neighbour pattern averaging and re-indexing NPAR [141]) to give a unique solution to the single crystal orientation that is related to the other crystal orientations within the field-of-view. However, microscope alignments, image shifts, scan distortion that increases with decreasing magnification, ill-prepared contaminated and rough specimen surface, changes in material, boundary indexing failure and detector quality can lead to uncertainties in determining the crystal orientation [142–144]. Fundamentally, the EBSD pattern's signal-to-noise (SNR) ratio is material dependent and decreases with high acquisition speeds and beam currents, which directly affects the angular resolution of the measurements [145].

EBSD maps can provide surface information about texture, grain size, misorientation across boundaries (e.g., grain or twin), and local misorientations of the crystal [115,146,147]. In addition, finer features (e.g., phase, polarity) can be adequately quantified from the intensity distribution within the Kikuchi bands [148]. Furthermore, the change and degradation in electron backscatter patterns (EBSPs) provide information about the diffracting volume. The pattern degradation (or diffusion) due to plastic deformation can be used to assess the level of plasticity through the pattern or image quality (IQ) [149], where IQ is calculated as the sum of the detected peaks (i.e., sharp patterns in Hough space) when using conventional Hough Transform. Wilkinson [150] used the changes in the high-order Kikuchi lines position to determine the elastic strains, but with low sensitivity (0.3% to 1%). Tracking the change in these higher-order Kikuchi lines is practical when the strain is small, as it is sensitive to changes in lattice parameters [151]. In the early 1990s, Troost *et al.* [152] and Wilkinson *et al.*

[153,154] used pattern degradation and change in the zone axis position to measure the residual elastic deviatoric strains and small lattice rotations with a 0.02% accuracy.

High (angular) resolution electron backscatter diffraction (HR-EBSD) – introduced by Wilkinson *et al.* [155,156] – increased the angular resolution by two orders of magnitude, without sacrificing the spatial resolution, by cross-correlating the EBSPs collected from a deformed sample with a reference pattern that was measured remotely from the stress concentration sites [87]. As shown in Figure 3-3, in high-quality EBSPs, (a) a region of interest (ROI) is first (b) extracted from the EBSP; the use of a smaller ROI reduces the computation time and is suitable for capturing the pattern's non-uniform shifts, (c) normalised and weighted to remove the background intensity gradients, (d) fast Fourier transformed, (e) filtered to remove low and high-frequency fluctuations (i.e., noise and background intensity gradients without blurring the pattern), then (f) transformed back to the real domain, and finally (g) correlated with a reference pattern in the Fourier domain. A Henning window function is typically applied before (d) to avoid the image edge effect.

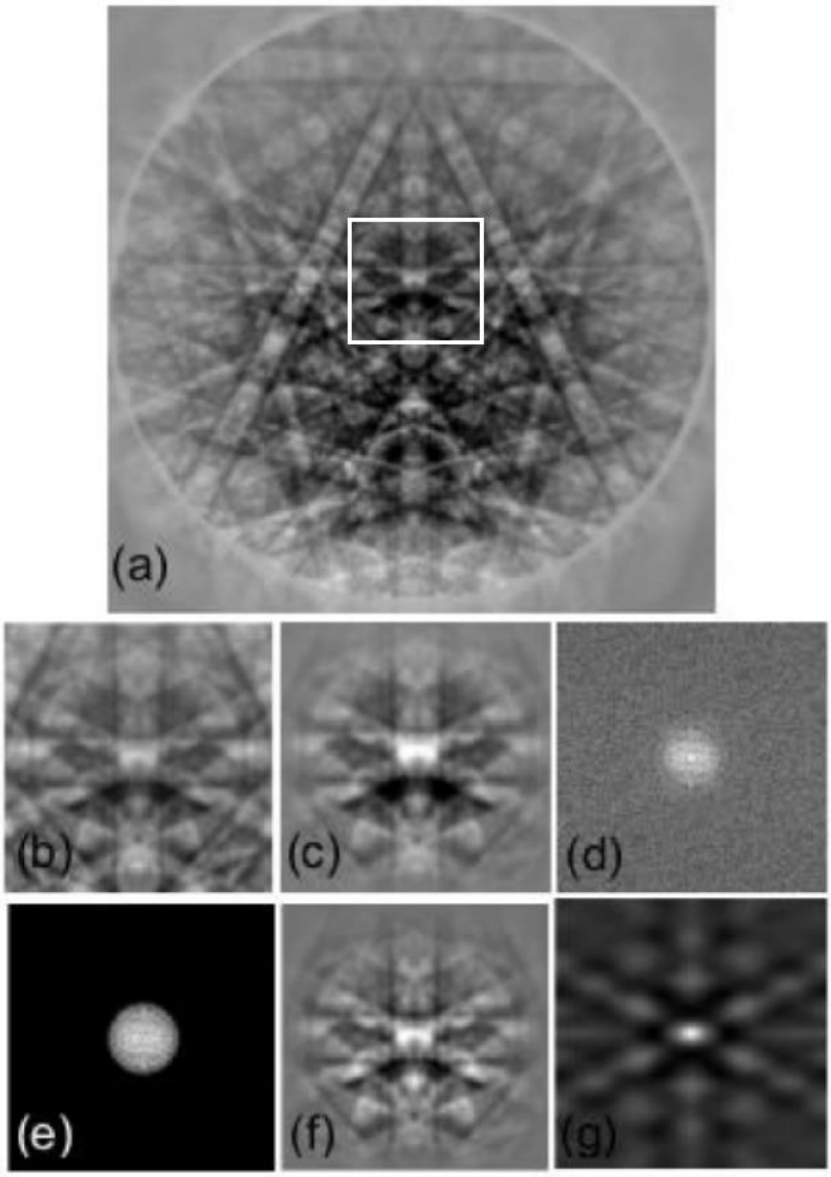


Figure 3-3: (a) HR-EBSD ROI, highlighted using a white box inside the EBSP, processing routine of (b) subtracting the ROI, (c) removing background intensity, (d) applying fast Fourier transform, (e) filter low and high-frequency fluctuations, before (f) transforming the ROI back to the real domain, and (g) correlate it with the reference pattern (from [157]).

The independent slight changes/shifts in at least four regions (i.e., changes in interplanar spacing or zone axes) are interpreted via geometry to quantify the relative elastic strain and lattice rotations between each point and the reference. Pattern shift is measured in more than 20 regions of interest (ROI) in one EBSP with a bilinear or bicubic interpolation method to find a best-fit solution [158,159]. The geometrical relationship between deformed and reference is described below.

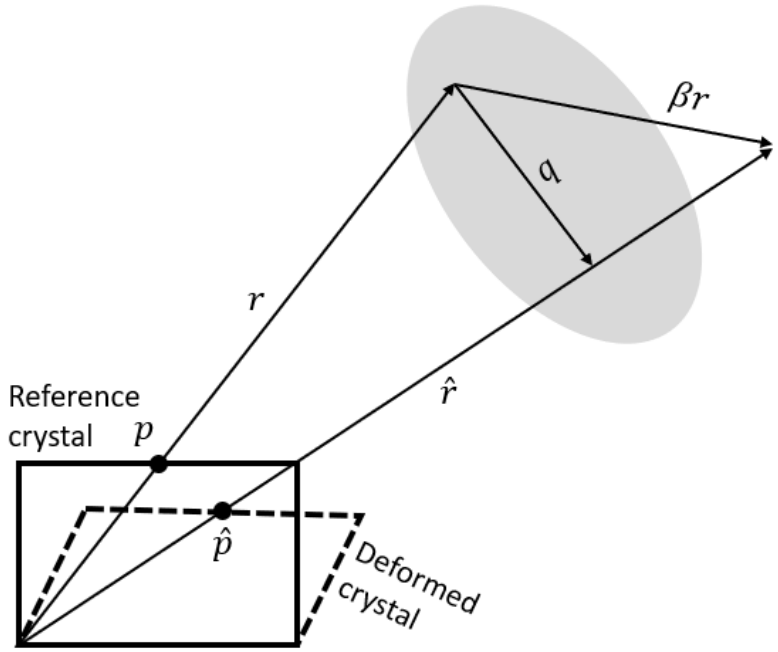


Figure 3-4: Schematic shifting between a reference and deformed crystals in the EBSP pattern projected in the phosphor screen.

As seen in Figure 3-4, the shifts in the pattern between the collected point ($\hat{p}$) and associate (non-coplanar) vector ($\hat{r}$), and reference point ($p$) pattern and associate vector ($r$). The displacement gradient tensor (β) (or local lattice distortion) relates the measured geometrical shifts from $r$ to $\hat{r}$ (see Figure 3-4). Thus, the (pattern shift) vector ($q$) can be written as in equations 3—1 and 3—2, where $x_i$ and $u_i$ are the direction and displacement in *i*th direction, respectively.

$$q = \beta r - (\beta r.\hat{r})\hat{r} \qquad 3—1$$

$$\beta = \begin{pmatrix} \frac{\partial u_1}{\partial x_1} & \frac{\partial u_1}{\partial x_2} & \frac{\partial u_1}{\partial x_3} \\ \frac{\partial u_2}{\partial x_1} & \frac{\partial u_2}{\partial x_2} & \frac{\partial u_2}{\partial x_3} \\ \frac{\partial u_3}{\partial x_1} & \frac{\partial u_3}{\partial x_2} & \frac{\partial u_3}{\partial x_3} \end{pmatrix}, \qquad r = \begin{pmatrix} r_1 \\ r_2 \\ r_3 \end{pmatrix} \qquad 3—2$$

The shifts are measured in the phosphor (detector) plane ($\beta_3 r_3 = 0$), and the relationship is simplified; thus, eight out of the nine displacement gradient tensor components can be calculated by measuring the shift ($\hat{r}$ and $q$) at four distinct, widely spaced regions on the EBSP

[143,156]. This shift is then corrected to the sample frame (flipped around Y-axis) because EBSP is recorded on the phosphor screen and is inverted as in a mirror. Then corrected around the X-axis by 24° (i.e., 20° sample tilt plus ≈4° camera tilt and assuming no angular effect from the beam movement [160]). Using infinitesimal strain theory, the deformation gradient is then split into elastic strain (symmetric part, where $ij = ji$), $e_{ij}$, and lattice rotations (asymmetric part, where $ii = jj = 0$), $\omega_{ij}$.

$$e_{ij} = \frac{1}{2}(\beta_{ij} + \beta_{ij}^{T}), \qquad \omega_{ij} = \frac{1}{2}(\beta_{ij} - \beta_{ij}^{T}) \tag{3—3}$$

These measurements do not provide information about the volumetric/hydrostatic strain tensors. By imposing a boundary condition that the stress normal to the surface ($\sigma_{33}$) is zero (i.e., traction-free surface [161], equation 3—4), and using Hooke's law with anisotropic elastic stiffness constants, the missing ninth degree of freedom can be estimated in this constrained minimization problem by using a nonlinear solver [156].

$$\sigma_{33} = C_{33kl}\, e_{kl} = 0 \tag{3—4}$$

where $C_{klij}$ is the crystal anisotropic stiffness tensor. These two equations are solved into (3—5) – (3—8) to re-calculate the refined elastic deviatoric strain ($\varepsilon_{kl}$) including the missing ninth (spherical) strain tensor. An alternative approach that considers the full β can be found in [161].

$$e_{ij} = \begin{pmatrix} e_{11} \\ e_{22} \\ e_{33} \\ 2e_{12} \\ 2e_{13} \\ 2e_{23} \end{pmatrix} \tag{3—5}$$

$$\begin{pmatrix} k_1 \\ k_2 \\ k_3 \end{pmatrix} = \begin{pmatrix} e_{11} - e_{33} \\ e_{22} - e_{33} \\ e_{12}C_{3312} + e_{13}C_{3313} + e_{23}C_{3323} \end{pmatrix} \tag{3—6}$$

$$\varepsilon_{33} = -\frac{k_1 C_{1133} + k_2 C_{2233} + k_3}{C_{1133} + C_{2233} + C_{3333}} \quad 3—7$$

$$\varepsilon_{kl} = \begin{pmatrix} k_1 + \varepsilon_{33} \\ k_2 + \varepsilon_{33} \\ \varepsilon_{33} \\ 2e_{12} \\ 2e_{13} \\ 2e_{23} \end{pmatrix} \quad 3—8$$

Finally, the stress and strain tensors are linked using the crystal anisotropic stiffness tensor ($C_{klij}$), as in equation (3—9) using Einstein summation convention with symmetry of stress tensors ($\sigma_{ij} = \sigma_{ji}$). More details in [158,162].

$$\sigma_{ij} = C_{ijkl}\, \varepsilon_{kl} \quad 3—9$$

The quality of the produced data can be assessed by taking the geometric mean of all the ROI's correlation intensity/peaks, and a value lower than 0.25 should indicate problems with the EBSPs quality [143].

The HR-EBSD method was reported [156,163–165] to achieve a sensitivity of $\pm 10^{-4}$ in components of the displacement gradient tensors (i.e., strain and rotation in radians) by measuring the shifts at an image resolution of ±0.05 pixels, but it was limited to small strains and rotations (>1.5°). Britton and Wilkinson [158] raised the rotation limit to ≈11° by using a remapping technique [166] that recalculated the strain after rotating the patterns using a rotation matrix (R in equation 3—10) calculated from the 1st cross-correlation iteration. However, further lattice rotation caused by severe plastic deformation will cause errors in the elastic strain calculations. Ruggles *et al.* [167] recently demonstrated an improved HR-EBSD sensitivity, even at 12° of lattice rotation, using the inverse compositional Gauss–Newton-based (ICGN) method instead of cross-correlation. Vermeij and Hoefnagels [168] also established a method that achieves a sensitivity of $\pm 10^{-5}$ in the displacement gradient tensors

components using a full-field integrated digital image correlation (IDIC) framework instead of dividing the EBSPs into small ROIs. Patterns in IDIC can be distortion corrected to negate the need for re-mapping up to ≈14° [169,170].

$$\mathrm{R} = \begin{pmatrix} \cos\omega_{12} & \sin\omega_{12} & 0 \\ -\sin\omega_{12} & \cos\omega_{12} & 0 \\ 0 & 0 & 1 \end{pmatrix} \begin{pmatrix} 1 & 0 & 0 \\ 0 & \cos\omega_{23} & \sin\omega_{23} \\ 0 & -\sin\omega_{23} & \cos\omega_{23} \end{pmatrix} \begin{pmatrix} \cos\omega_{31} & 0 & -\sin\omega_{31} \\ 0 & 1 & 0 \\ \sin\omega_{31} & 0 & \cos\omega_{31} \end{pmatrix} \quad 3—10$$

Accurate determination of pattern centre limits the accuracy of HR-EBSD [171]; thus, the recent development of AstroEBSD [172] and PCGlobal [173], open-source MATLAB® codes, increased the precision of determining the pattern centre (PC) and – consequently – elastic strains [174] by using a pattern matching approach [175] which simulates the pattern using EMSoft [176]. Although HR-EBSD cannot easily access the volumetric change in the object (i.e., hydrostatic strain) because there is no change in the plane or angles of the lattice planes (crystallographic directions) but only changes in the position/width of the Kikuchi bands (and their energetic correspondence) [177,178], it is still superior to the conventional surface Hough transform analysis [179] (see Table 3-1).

Table 3-1**:** Comparison of conventional Hough transform EBSD and HR-EBSD [156,180].

| | EBSD | HR-EBSD |
|---|---|---|
| Absolute Orientation | ∽2° | N/A |
| Misorientation | ∽0.1° to 0.5° | ∽0.006° (1 x $10^{-4}$ rad) |
| GND @ 1 µm step In lines/$m^2$ (b = 0.3 nm) | > 3 x $10^{13}$ | > 3 x $10^{11}$ |
| Relative Residual Strain | N/A | Deviatoric elastic strain 1 x $10^{-4}$ |
| Example Tasks | Texture, Microstructure, etc. | Deformation |

Nonetheless, in the HR-EBSD analysis, the elastic deformation field is still calculated relative to a reference pattern or point ($EBSP_0$) in the map, manually selected away from stress raisers, and assumed stress-free. Any deformation at this remote point can significantly influence the field magnitude and distribution [85], which creates a 'reference pattern problem' similar to the '$d_0$ problem' in X-ray diffraction [128]. Using a deformed $EBSP_0$ adds a phantom deformation gradient across the map, decreasing the accuracy [181,182]. Thus, selecting a reference pattern ($EBSP_0$) plays a key role even when a linear 'top-up' method is used; such a method is based on enhancing the probed field by predicting the strain at the $EBSP_0$ with crystal plasticity finite-element (CPFE) simulation used to estimate the absolute strain values [183]. Another alternative is to use a simulated strain-free $EBSP_0$. However, the use of simulated reference patterns for absolute strain measurement is still an active area of research [148,174,184–190] and scrutiny [174,181,191–195] as difficulties arise from the variation of inelastic electron scattering with depth causing intensity asymmetry in EBSPs, precise determination of the pattern centre, and accurate representation of the experimental geometry (e.g., lack of correct contrast at zone axis in crude kinematic simulations leading to phantom stresses and optical distortion). A current study [151] simulated an EBSP from a deformed volume of interaction. The reverse engineering of the problem by applying a deformation gradient to the EBSP helps separate what each deformation component does to the EBSP geometry, the deformation's effect on intensity distributions in the EBSP, pattern distortion from instruments, and can provide insights into how the correlation between sharp and blurred patterns can be used to estimate plastic strains.

As noted above, conventionally, one pattern with the highest image quality (IQ) in the grain is assumed to be least stressed and is selected from those furthest away from stress

concentrations. However, IQ does not carry a clear physical meaning [196], and the relative deformation distribution (i.e., strain, stress, rotation) is insensitive to the IQ of $EBSP_0$ [87]. IQ is sometimes combined with the geometrical necessary dislocations (GND) density calculated from the Hough-measured local grain misorientation to select the point with a high IQ and low dislocation activity. Selecting a reference pattern, where the point is also remote from stress concentrations, can produce accurate measurements up to $3.2 \times 10^{-4}$ strain compared to Laue microdiffraction measurement [164].

As an analysis of the HR-EBSD deformation field is sensitive to the selection of $EBSP_0$ within a deformed grain, here, a thorough investigation of the effect of $EBSP_0$ on the deformation maps was conducted to empirically find a new method to select the $EBSP_0$ since the image quality of the EBSP does not necessarily reflect the level of elastic strain, and selection of $EBSP_0$ based on image quality alone is insufficient.

## 3.2 Methodology

### 3.2.1 Materials and EBSPs collection

Two materials were used to create the samples to analyse ductile, quasi-brittle and brittle phases. The 1st set of samples was taken from a large (~200 mm thickness) forging of Zeron 100 duplex stainless steel (UNS: S32760 [197]) with a nominal composition of 25% Cr, 7% Ni, 3.6% Mo, 0.7% Cu, 0.7% W, 0.22% N that was 475 °C aged for 100 hrs in the air. During this heat treatment, spinodal decomposition of the supersaturated solid ferrite solution into Fe-rich nanophase ($\alpha'$) and Cr-rich nanophase ($\alpha''$) accompanied by G-phase precipitation occurs [198–200], increasing the ferrite hardness while the hardness of the austenite phase remains nearly unchanged [201–203] due to faster diffusivity in ferrite compared to the austenite [204]. This creates a sample with ductile (austenite) and quasi-brittle[6] (ferrite) phases.

100 hrs ageing time was chosen because the hardness of the ferrite phase hardly changed after 50 hrs of ageing (Figure 3-5a), as revealed by Vickers hardness testing of the ferrite phase in 11 widely separated locations in each sample. Modulated microstructure formed due to spinodal composition was confirmed using FEG-TEM with Cr-rich nanophase giving the bright image and Fe-rich darker image (Figure 3-5b[7]).

[6] Describing aged ferrite as quasi-brittle can be considered incorrect since it can deform plastically; however, aging significantly reduce the ferrite phase plasticity. For more details a review of age-hardened stainless steel metallurgy is available in Appendix (3.A) – Age-hardened duplex stainless steel.

[7] Sample preparations including FIB were made by the author. Thinning to electron transparency, sample lift-out and FEG-TEM imaging were done by Mr Marin Vukšić.

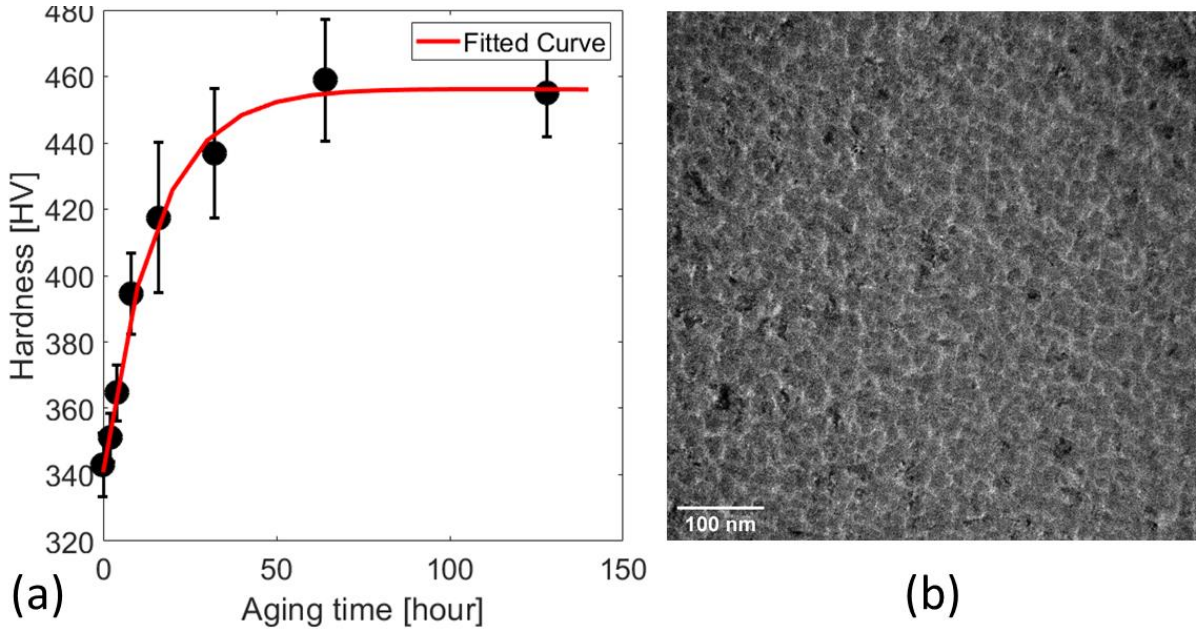


Figure 3-5: (a) Change of hardness (measured using diamond Vicker indent and expressed in Vickers Pyramid Number, HV) with 2, 4, 8, 16, 32, 64, and 128 hours aging time for the ferrite phase in super-duplex Zeron 100 alloy. (b) Bright-field FEG-TEM (at 200kV) showing the morphology of the modulated microstructure of the ferrite phase aged at 475 °C for 100 hrs.

EBSP quality is extremely sensitive to the surface preparation [205]; thus, the observed surface of the aged specimens was ground using SiC papers from 240 to 4000 grit and polished using diamond paste (from 9 to 1 µm), finishing with 50 nm colloidal silica for 2 hours (50 r.p.m speed and 5 N force) to produce a mirror-flat surface without artefacts. The specimens were ultrasonically cleaned for 20 minutes using ethanol, rinsed with deionised water, and dried with a hot air blower.

The 2$^{nd}$ set of samples was brittle (at room temperature [206]), cleaved from a pre-polished $(001)$ single-crystal silicon wafer with a thickness of 0.5 mm. These materials are suitable model materials for EBSD analysis as the polished surface does not oxidise further, and high-quality patterns can be acquired in a reasonable time.

The samples of both materials were positioned between the jaws of a 2 kN Deben® 70° pre-tilted loading stage inside a Carl Zeiss Merlin field emission gun scanning electron microscope

(FEG-SEM). The SEM chamber and loading stage were plasma cleaned and purged together before the sample was deformed in displacement control by the movement of one jaw. The Si samples were deformed in compression, and the DSS samples were deformed using simple tension and 3-point bending.

In each case, arrays of high-quality EBSPs were collected in situ with the sample under load to map the ROI at increasing levels of applied nominal strain. Before each observation, the setup was left to stabilise for 30 minutes at fixed crosshead displacement. The microscope conditions were 10 nA/20 kV beam current/voltage and 18 mm working distance for all materials. The collected high-quality EBSPs were recorded as an 800 × 600 pixel image, 16-bit depth, with 100 millisecond exposure time per pattern, and a step size of 75 nm for the DSS and 250 nm for the silicon. These conditions provided a practical time for measurement while avoiding sample drift [207–211].

### 3.2.2 $EBSP_0$ effect analysis

After excluding points with a high density of geometrical necessary dislocations (GND), which may be calculated using tools such as MTEX [107]; the reference $EBSP_0$ for each grain can be selected as a point that is remote to stress concentrations, has a high-quality pattern, low GND density and an orientation close to the grain's mean orientation. This conventionally selected $EBSP_0$ will be termed '*Native*' in this work. To assess HR-EBSD sensitivity to the selected $EBSP_0$, the patterns at 50 points were randomly selected from 25% of the highest-quality patterns (Figure 3-7). The IQ of these randomly selected patterns varied by less than 2% of the average value. Each of the 50 patterns was used in HR-EBSD calculations to map the stresses in the region of interest.

The HR-EBSD analysis was performed iteratively to minimise strain errors due to large misorientations (>1.5°); in the second pass, the EBSPs were remapped to an orientation close to $EBSP_o$ by using the local rotation matrix that is estimated from the first pass [212]. The elastic constants (in GPa) for the ferrite ($\alpha$) are: $C_{11} = 230, C_{44} = 117, C_{12} = 135$, the austenite ($\gamma$)are: $C_{11} = 231.4, C_{44} = 116.4, C_{12} = 134.7$ [213], and for (001) silicon are $C_{11} = 165.7, C_{44} = 79.6, C_{12} = 63.9$ in GPa [214], all were transformed to the crystal frame of reference via Euler angles [215]. The pattern centre (PC) shift due to beam movement during acquisition was corrected using AstroEBSD [172]. No further angular effect from drift was expected as the ROI was small (~20 x 15 $\mu m^2$), and the samples were all conductive [216].

The density of geometrically necessary dislocations (GND) was estimated from the local lattice curvature; the method used ideas based on Sun *et al.* [217] and El-Dasher *et al.* [218], implemented by Wilkinson and Randman [207] with a complete description of the rotation gradient that retains six measured terms. For a detailed review of the estimation of the geometrically necessary dislocations (GND) density, delving into the governing theories, implementation, estimation from different measurement methods, and required sensitivity, please see Appendix (3.B) – Geometrically necessary dislocations (GND) density estimation.

## 3.3 Results

### 3.3.1 Quasi-brittle material (ferrite)

The ferrite grain in the aged duplex stainless steel (DSS) sample was analysed using HR-EBSD to obtain the elastic deformation field. The grain's fields were calculated relative to different sample points/references, as shown in Figure 3-6a. These 6 references have a remarkably high IQ compared to other available patterns in the grain. Four of the points were selected randomly; the fifth is the '*Native*' reference point, as explained earlier, and the logic behind the sixth is to be explained later, but for now, it can also be assumed to be randomly selected.

The 1$^{st}$ point (Figure 3-6a.I) was selected near the grain boundary. Patterns near the grain boundary are expected to be highly deformed due to stress incompatibility between the grains as grains respond to the nominal load; however, that did not affect the 1$^{st}$ point IQ. By selecting this point, the relative stress in the grain was suppressed, and the line profile (in dark blue in Figure 3-6b) confirmed the stress magnitude reduction, at least in in-plane shear.

The 2$^{nd}$ point (Figure 3-6a.II) was selected in the centre of the grain and seemed to give a more realistic stress distribution inside the grain, with the left upper side of the grain expressing compressive stress and the other upper side experiencing tensile stress with a linear feature existing in the middle of the grain that seems to be induced by the incompatibility of the stress in the grain. The line profile (in light blue in Figure 3-6b) indicates that the selected point may be experiencing negative in-plane shear stress, which increases the in-plane shear of the field calculated for the grain.

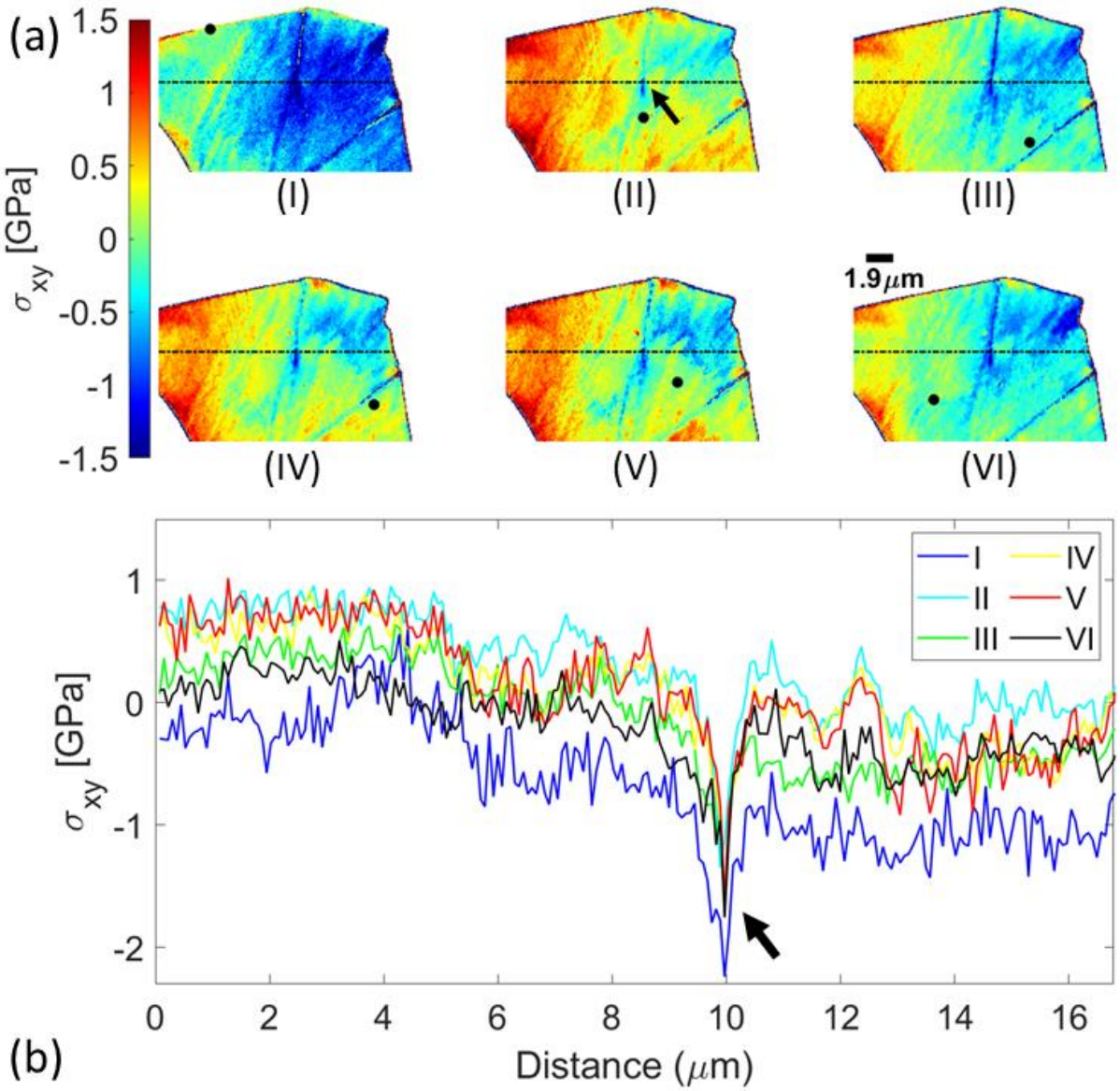


Figure 3-6: a) In-plane shear stress ($\sigma_{xy}$) fields produced using 6 different $EBSP_0$ in a ferrite grain. A black dot indicates the position of the reference pattern in each case. b) The line profile of the in-plane shear stress along the dotted line. The black arrow points to the value ahead of the linear feature observed in the middle of the grain (see Figure 3-7). V and VI are '*Native*' and '*Chosen*' $EBSP_0$, respectively. The IQ values of points I to VI are 0.4019, 0.4419, 0.4394, 0.4444, 0.4288 and 0.4419.

The 3rd and 6th points produced a field that shows the concentration of (negative in-plane shear) stress around the linear features (i.e., deformation twin) at the top-middle of the grain and the other linear feature (i.e., slip band) at the bottom right of the grain. Both features are continuous, and the negative nature of the in-plane shear does not change across both features compared to the field produced using other $EBSP_0$. However, the 6th was selected

away from the stress concentration compared to the 3rd point, which is not far away and can be affected by the deformation field induced by the nearby slip band. The line profile from the feature is similar to the 6th point, although the 6th point profile seems less noisy. Both points give profiles that are similar to the other points.

The 4th point (Figure 3-6a.III) has the highest IQ in the grain and has a similar (overall) stress distribution compared to the 5th/*Native* point. The line profile (yellow line in Figure 3-6b) confirms the previous observation with slight convergence between the point with the highest IQ and '*Native*'. Although there is a relationship between the point local conditions and the resultant deformation field, that does not translate when looking at the pattern IQ.

Regardless of the pattern choice, the line profile is similar near the stress concentrations at 10 µm (black arrow in both Figure 3-6a.II and Figure 3-6b[8]) but differs when describing the general distribution of stress. These different $EBSP_0$ show how the reference pattern of choice influences the HR-EBSD result, and there is a correlation between the assumed conditions at the pattern with the resultant map, which will be explored thoroughly by sampling $EBSP_0$ within the grain for HR-EBSD analysis, totalling 51 points (Figure 3-7) and 51 HR-EBSD maps.

[8] The field ahead of this feature (i.e., deformation twin) is analysed thoroughly in Chapter 4.

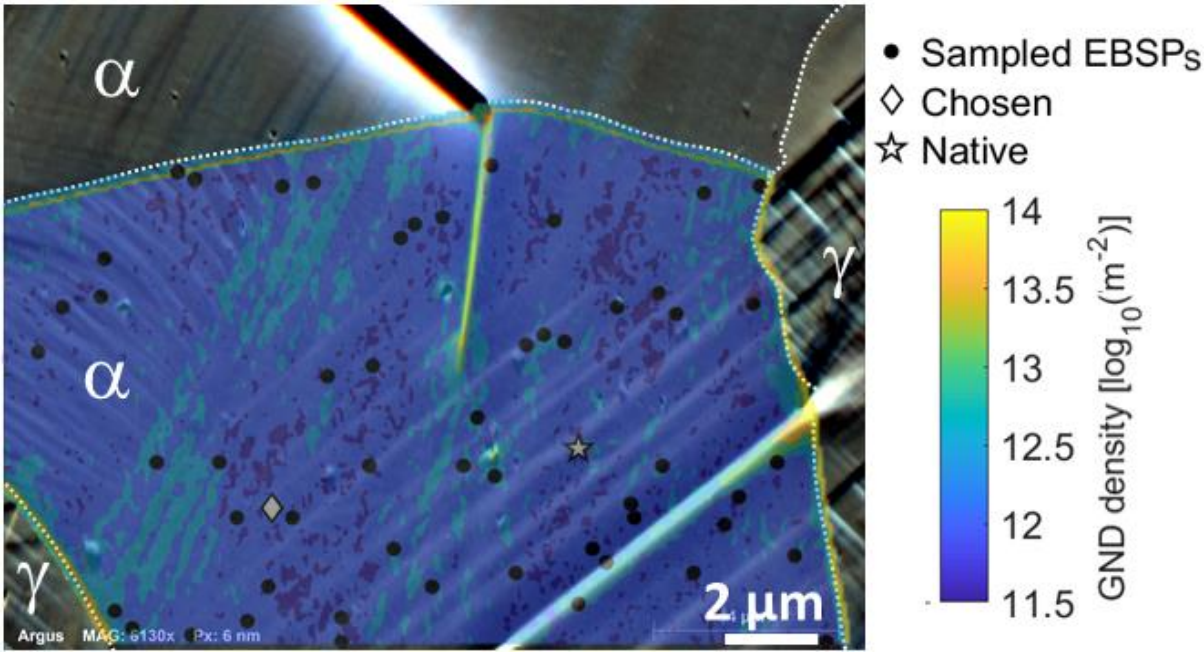


Figure 3-7: Geometrical necessary dislocation (GND) density map overlayed over a forescatter electron (FSD) image for the field of view with the location of 52 EBSPs. One '*Native'*-ly selected (grey star), 50 were randomly '*Sampled'* (black points), and another '*Chosen'* after further deliberation (white diamond).

The local conditions at each $EBSP_0$ can be approximated by averaging the results from the other 50 HR-EBSD maps. For each $EBSP_0$ and associated HR-EBSD map, these estimated conditions at the $EBSP_0$ were then correlated with the average deformation conditions at the grain. For example, in the point highlighted as '*Native*' in Figure 3-8, the x-axis coordinate is the average stress in the grain calculated using the '*Native*' EBSP, and the y-axis is the estimated stress conditions at the '*Native*' point, which was averaged across the 50 other points. The linear-inverse relationships clearly show the sensitivity of the HR-EBSD map on the reference pattern choice, even from a set of high-quality possible references. Figure 3-8 shows the different estimated stress states at each reference point which linearly affect the HR-EBSD calculated map based on the reference pattern. Averaging the stress across all the reference patterns for all points in the map should reduce the noise level, but there will still be an unknown offset.

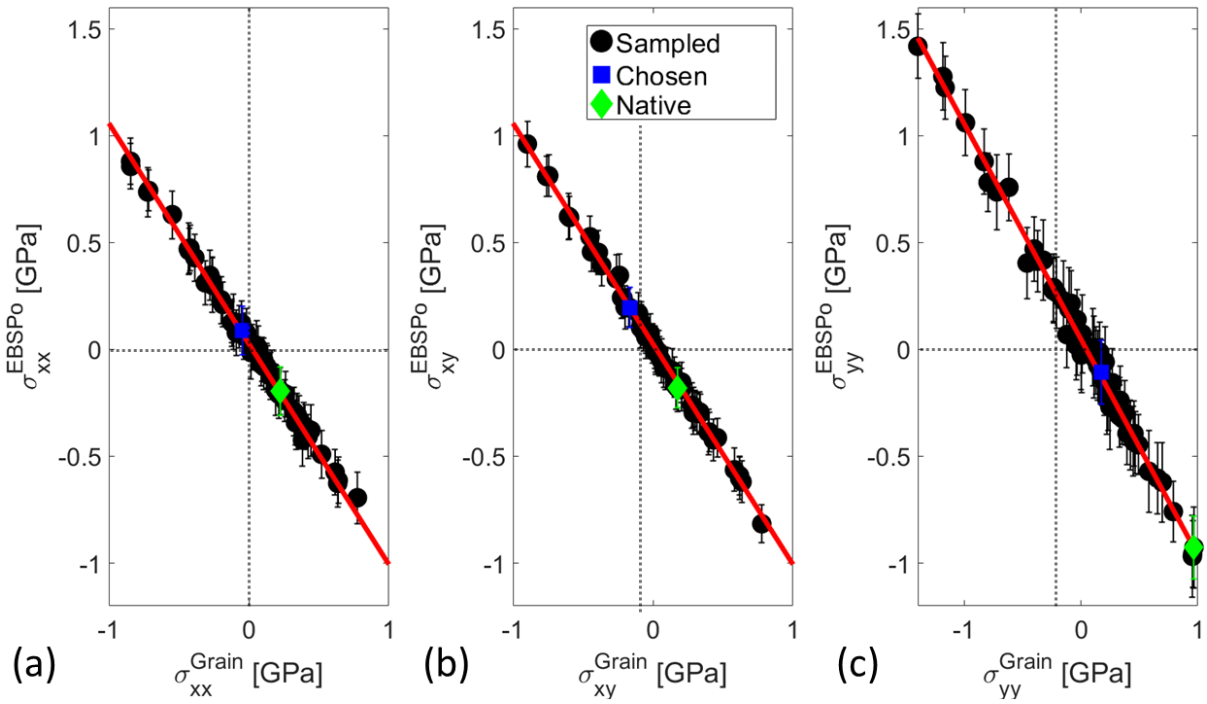


Figure 3-8: Grain and EBSP$_0$ averaged (a) $\sigma_{xx}$, (b) $\sigma_{xy}$, and (c) $\sigma_{yy}$ stresses for the randomly selected reference patterns.

Other parameters were then also averaged per map (labelled grain Figure 3-9) and per point across maps (labelled EBSP$_0$ Figure 3-9) to deduce the relationship between image and cross-correlation related parameters (IQ, the mean angular error (MAE), and correlation peak height (PH)) and calculated deformation field components – e.g., determinant of the deformation gradient tensor ($A^o$), in equation (3—11), strain $\varepsilon_{ij}$, rotation $\omega_{ij}$, and GND density – in both the grain and randomly selected EBSP$_0$.

$$A^o = \frac{1}{n}\sum_{el=1}^{n}\left|F_{ij}\right|_{el}, \qquad i=j=x,y,z \qquad 3—11$$

where $n$ is the total of points in the map for the 'Grain' calculation and the total number of maps (=51) for the 'EBSP$_0$' calculation, PH is the cross-correlation peak height normalised by the value from the reference self-correlation in each case, and the mean angular error (MAE) is a quantitative measure of the difference between the pattern shift at each segmented ROI from the EBSP and the best fit solution, all obtained after remapping.

For the set of values obtained with each reference pattern, the correlations between grain-average and reference point-averages were quantified through Pearson's correlation coefficient [219] implanted in the MATLAB® *corrcoef* function (eq. 3—12). Each dataset $(A, B)$ was first normalised using the mean ($\sigma$) and standard deviation ($\mu$) before finding the linear correlation coefficient ($\rho$) of two datasets with $N$ number of observations.

$$\rho(A,B) = \frac{1}{N-1}\sum_{i=1}^{N}\left(\overline{\frac{A_i - \mu_A}{\sigma_A}}\right)\left(\overline{\frac{B_i - \mu_B}{\sigma_B}}\right) \qquad 3—12$$

The same analysis was applied across 9 different ferrite-grain maps (9 grains x 51 sampled $EBSP_0$ = 459 maps). The correlation coefficients are shown in Figure 3-9.

The diagonal of Figure 3-9 shows the strong inverse correlation between the grain and local reference pattern status in each tensor of the strain and rotation components. The correlation is strong for rotation components as they are estimated from the 1st iteration, where strain (and consequently stress) tensors are corrected in the 2nd iteration and then refined. A reference pattern that is deformed in a specific manner (e.g., experiences a dominate $\varepsilon_{xx}$) exacerbates the same component in the resultant HR-EBSD maps and influences the distribution in other components. The diagonal correlation also shows the strong dependency of the resultant grain field on the PH and MAE, whereby high local PH produce a high PH field and low local MAE produces a less erroneous field. The inverse relationship extends between local PH and MAE to grain MAE and PH. There is also considerable interaction between the local $EBSP_0$ PH MAE and estimated GND density and the resultant grain, where high plasticity reduced the PH and increased the angular error.

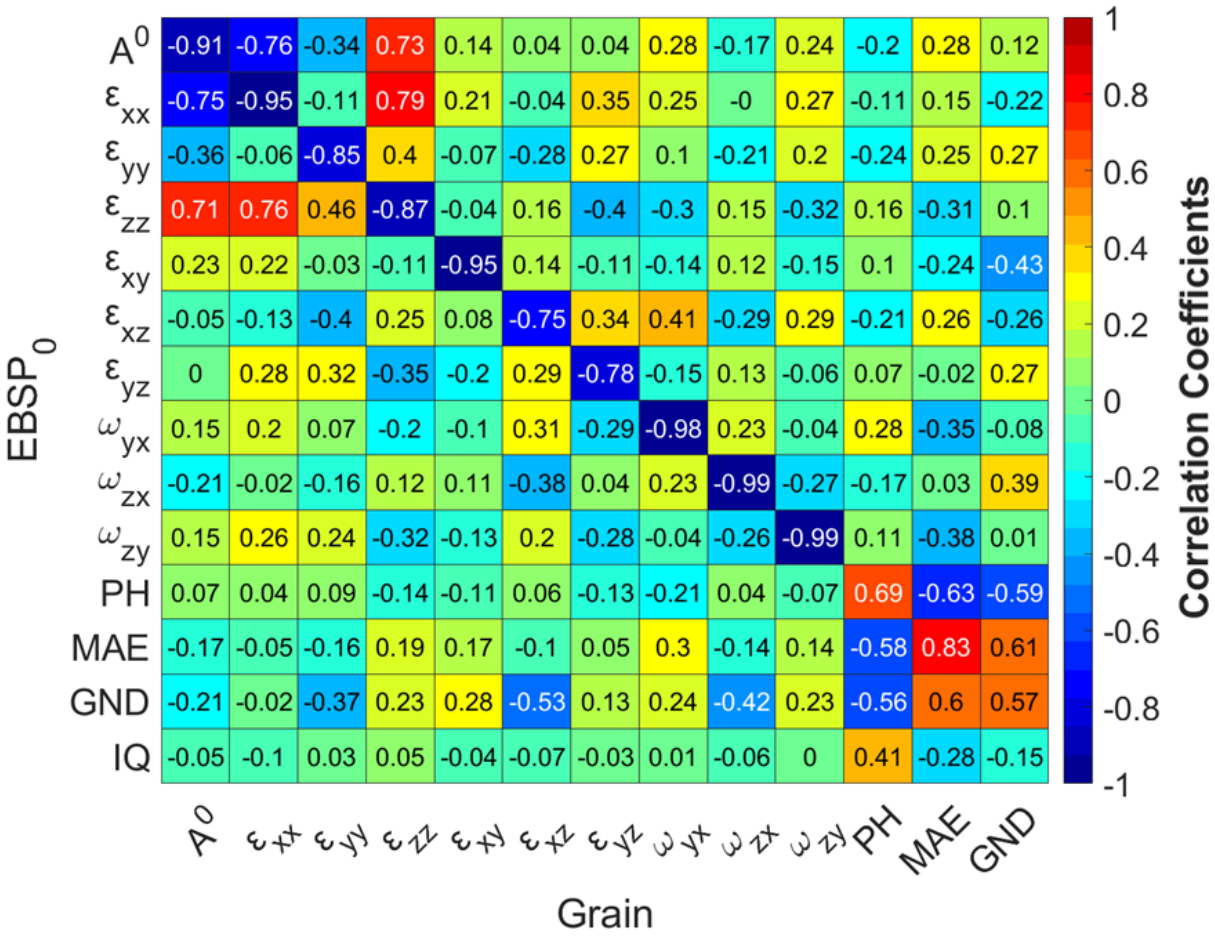


Figure 3-9: Correlation coefficients for the grain average (Grain) and reference point-average ($EBSP_0$) across 9 different datasets for the ferrite grain in aged duplex stainless steel. The minus sign indicates an inverse relationship.

Figure 3-9 shows the insensitivity of the $EBSP_0$ deformation components to the cross-correlation parameters (i.e., PH and MAE), although the point-average PH and MAE affect the grain average PH and MAE, which captures the fact that using a reference point that does not correlate well with available patterns will reduce the overall correlation quality. The grain's PH and MAE were averaged across the 51 HR-EBSD maps and plotted in Figure 3-10a. These values can be fitted by (empirical) equation (3—13), where $a$ and $c$ are 0.014 and 0.16, respectively. The same fit was applied to the other data sets and then the relationship coefficients $a$ and $c$ were plotted in Figure 3-10b which shows an inverse relationship where the value of $c$ changes with PH quality and $a$ relates to MAE quality.

$$\mathrm{PH} = {}^{a}/_{\sqrt{\mathrm{MAE}}} + c \qquad 3—13$$

It is postulated that the optimum $EBSP_0$, i.e., the least deformed of the available patterns, should offer the highest cross-correlation (PH) with the lowest errors (MAE) since such a pattern has high quality and is close to the average grain orientation. Objectively, this is the point on the EBSD map with the highest PH value and low MAE value. This was identified using an algorithm that finds the point with the lowest MAE in the grain and then searches for the point with the highest PH. If these are not the same point, the 2nd lowest MAE is located and compared to 1st and 2nd until they coincide. This point, termed '*Chosen*', is indicated in Figure 3-7, Figure 3-8, and Figure 3-10 with a PH of 0.8 and MAE of 4.7 x $10^{-4}$ rad (for the collect EBSPs shown in Figure 3-7), was used as the reference pattern for the HR-EBSD calculations.

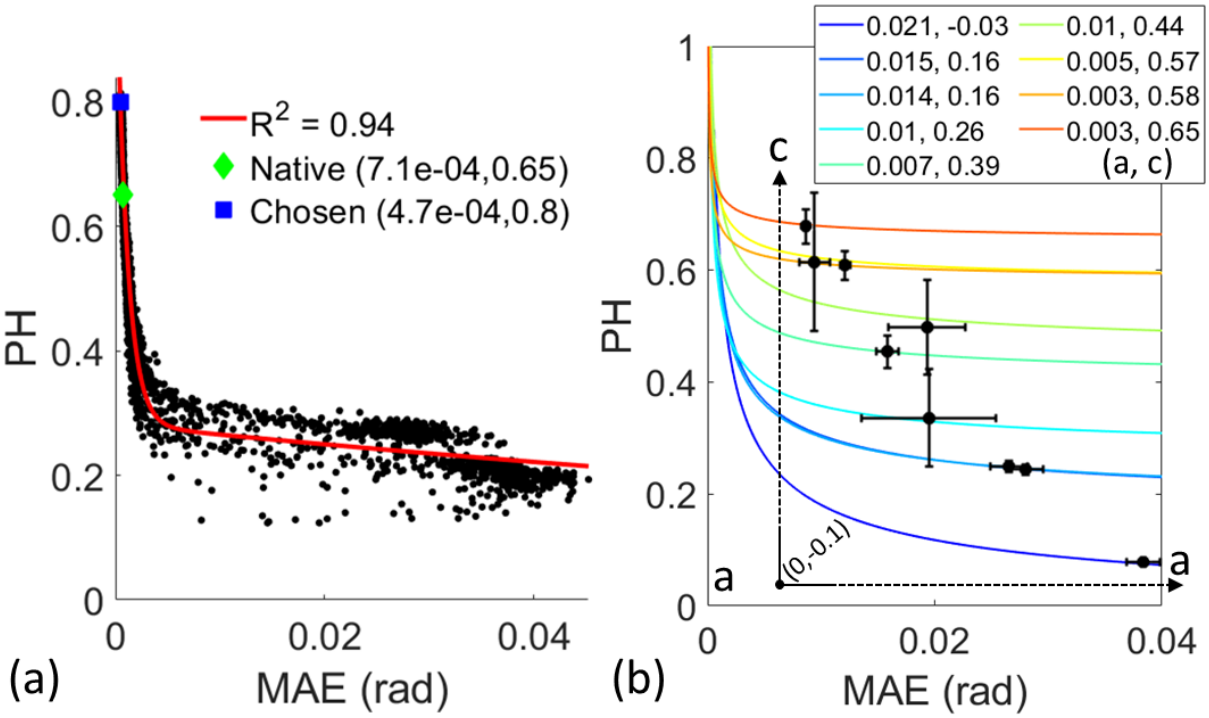


Figure 3-10: (a) Cross-correlation peak height (PH) and mean angular error (MAE) averaged across all 51 different HR-EBSD maps and fitted with an inverse square root function. (b) Fitting coefficients were obtained by applying the analysis to 9 HR-EBSD maps. The variance was calculated from the goodness of fit ($R^2$).

The 6th map (labelled IV) shown in Figure 3-6 was produced using the '*Chosen*' $EBSP_0$. The field and line profile accentuated existing stress concentrations and showed a less noisy line profile and stress distribution in general. The calculated field PH and MAE are 0.76 and 6 x $10^{-4}$ rad compared to '*Native',* which gave a PH of 0.76 and MAE of 8 x $10^{-4}$ rad. Although the difference in overall improvement is not huge in terms of cross-correlation parameters, the difference in magnitude and distribution can be seen clearly in Figure 3-6b, V and IV, especially at 5 µm, where the difference reaches ~450 MPa, which shows the criticality of the $EBSP_0$ problem.

### 3.3.2 Ductile material (austenite)

This example analysed an austenite grain in the age-hardened duplex stainless steel (coloured in Figure 3-11). The austenite phase shows significant plastic deformation, with planar slip, compared to the harder ferrite; the mean GND density is 12.44 ± 0.43 $\log_{10}(m^{-2})$, compared to 11.85 ± 0.74 $\log_{10}(m^{-2})$ in the ferrite example. As for the previous ferrite example, 52 $EBSP_0$ were selected, with 1 being the '*Native*', 50 sampled randomly from the points with the highest IQ, and one '*Chosen*' using the algorithm to find the map point with the lowest MAE and highest PH after averaging the values from the 51 maps. The locations of the points are marked on the map of GND density, which also shows significant plastic strain concentrations at some grain junctions. Due to the ductility of the austenite, larger lattice rotations are expected, but the phantom strains were minimised by the remapping process [158].

Similar to the previous analysis, the overall distribution of the in-plane shear stress is similar regardless of the reference choice, as highlighted by the stress peak at the sub-boundary (highlighted by an arrow in Figure 3-11 and Figure 3-12 and has misorientation to the parent grain that is less than 0.5°). However, the finer details of the distribution of stress and magnitude, and the gradual increase near 10 µm, are dependent on the $EBSP_0$ location/status,

where a more positively deformed point is located near the ferrite-austenite grain boundary (4th point in Figure 3-12a.IV) which renders the grain field as being compressed even when the test was done in tension. The shear direction can be inferred from the topography at that corner compared to the topography at the other edges in the vicinity of the ferrite-austenite grain boundary.

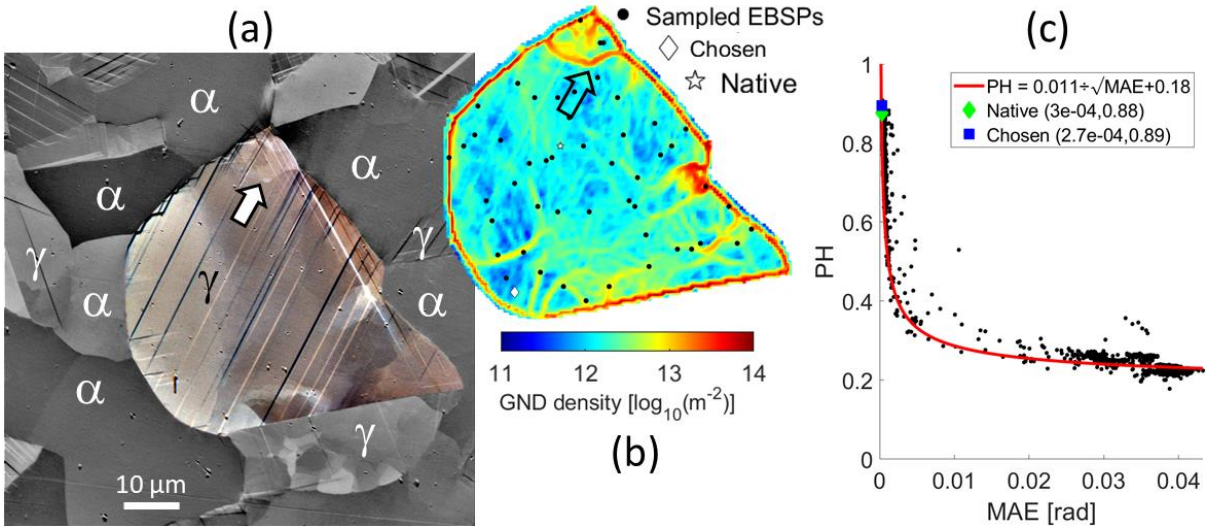


Figure 3-11: (a) Forescatter electron (FSD) image with the other grain grey-scaled to accentuate the grain understudy. (b) Estimated geometrically necessary dislocations (GND) density map with the location of the 52 $EBSP_0$. (c) Cross-correlation peak height (PH) and mean angular error (MAE) were averaged across 51 HR-EBSD maps and fitted with an inverse square root function.

A similar observation can be made for the 1st point, but the field is less compressed than the 4th point in-plane shear stress field. A more positive in-plane shear is induced when the point was selected inside the sub-grain (3rd point), which appears to be compressed judging from the FSD image topography at the intersection between the ferrite grains and the austenite grain. Neutral axes (where the 6th point or '*Chosen*' is located) appear in Figure 3-12a maps except for the 4th point's map. GND density distribution is unaffected by conditions at the $EBSP_0$, but the magnitude doubled in some points when using '*Chosen*'.

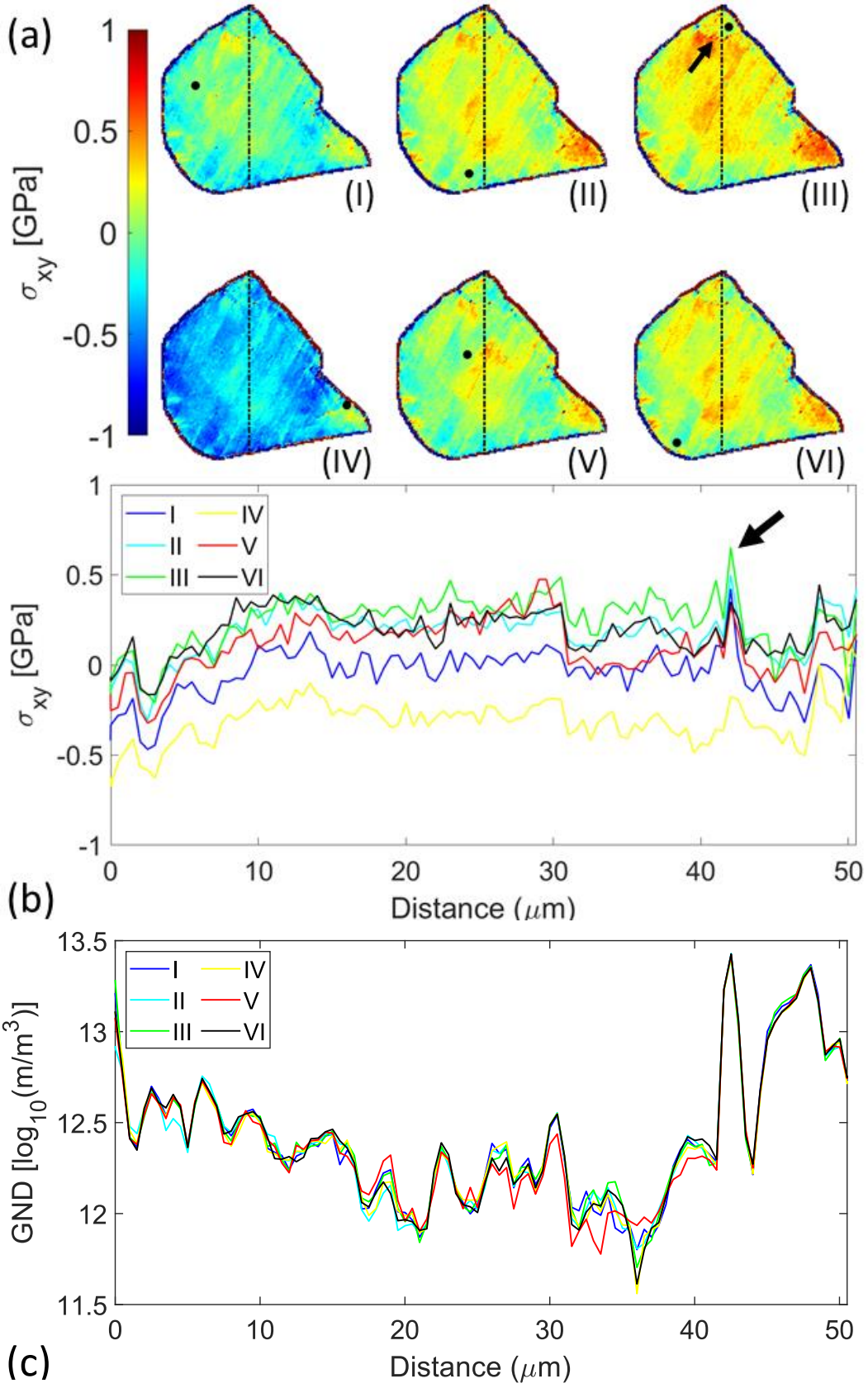


Figure 3-12: a) In-plane shear stress ($\sigma_{xy}$) fields produced using 6 different EBSP$_0$ in an austenite grain. A black dot indicates the position of the reference pattern. The line profile along the dotted for (b) the shear stress and (c) GND density. The arrow points to the sub-boundary, also seen in Figure 3-11. V and VI are '*Native*' and '*Chosen*' EBSP$_0$.

The same correlative analysis applied to the ferrite was applied to the austenite (Figure 3-13), revealing a weaker relationship between the in-plane shear strain (and consequently the stress) tensor (as indicated by the -0.32 correlation coefficient). The inverse correlation between the grain and local reference pattern status in deformation-related tensors along the diagonal correlation is less pronounced than in the ferrite phase. The local MAE strongly influences the resultant field MAE, PH, and estimated GND density but the influence of IQ of the reference pattern on the resultant field, similarly to the ferrite example, is less obvious.

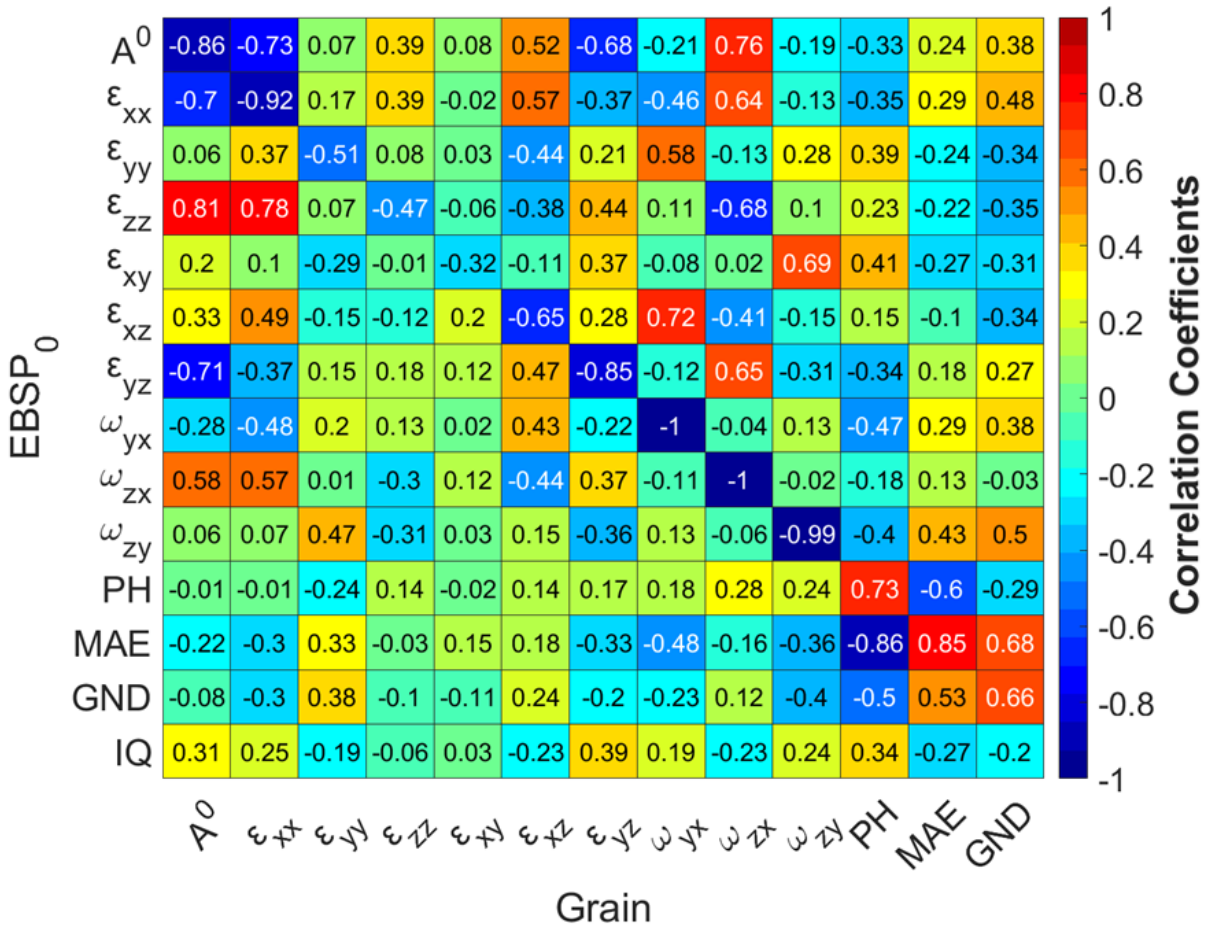


Figure 3-13: Correlation coefficients for the grain average (Grain) and reference point-average ($EBSP_0$) for the austenite grain in aged duplex stainless steel. The minus sign indicates an inverse relationship.

Fitting equation 3—13 to the PH and MAE data for the austenite grain gave $a$ and $c$ of 0.011 and 0.18, respectively (Figure 3-11c). The algorithm '*Chosen*' $EBSP_0$ gave an average local PH

of 0.89 and MAE of 2.7 x $10^{-4}$ rad compared to the '*Native*' local PH of 0.88 and MAE of 3 x $10^{-4}$. The overall calculated field PH and MAE were then 0.85 and 13 x $10^{-4}$ rad, marginally different from the fields cross-correlated with the '*Native',* which gave a PH of 0.85 and MAE of 14 x $10^{-4}$ rad. However, as for the ferrite example, although the mean improvement in correlation parameters does not seem substantial, the effect on the stress magnitudes and distribution cannot be ignored. This is observed in Figure 3-12, comparing V and VI, especially at 11 µm and 36 µm, where the difference in the in-plane shear stress reaches ~250 MPa.

### 3.3.3 Brittle material (silicon)

For the silicon sample, 12 EBSP arrays were collected around a crack[9]. Applying the same correlative analysis to 12 datasets (12 datasets x 52 sampled $EBSP_0$ = 624 maps) gives Figure 3-14. The diagonal correlation for the deformation components is similar to that observed in the ferrite, with an inverse correlation between the grain and local reference pattern status in each tensor of the strain and rotation components. This strong correlation is also seen in MAE, but the estimated GND density is not influenced by EBPS0 image quality, PH, MAE, or the deformation status at the $EBSP_0$ because at room temperature Silicon is brittle and deforms with no significant plasticity [220].

[9] Analysed thoroughly in Appendix (6.B) – In situ $EBSP_0$ selection.

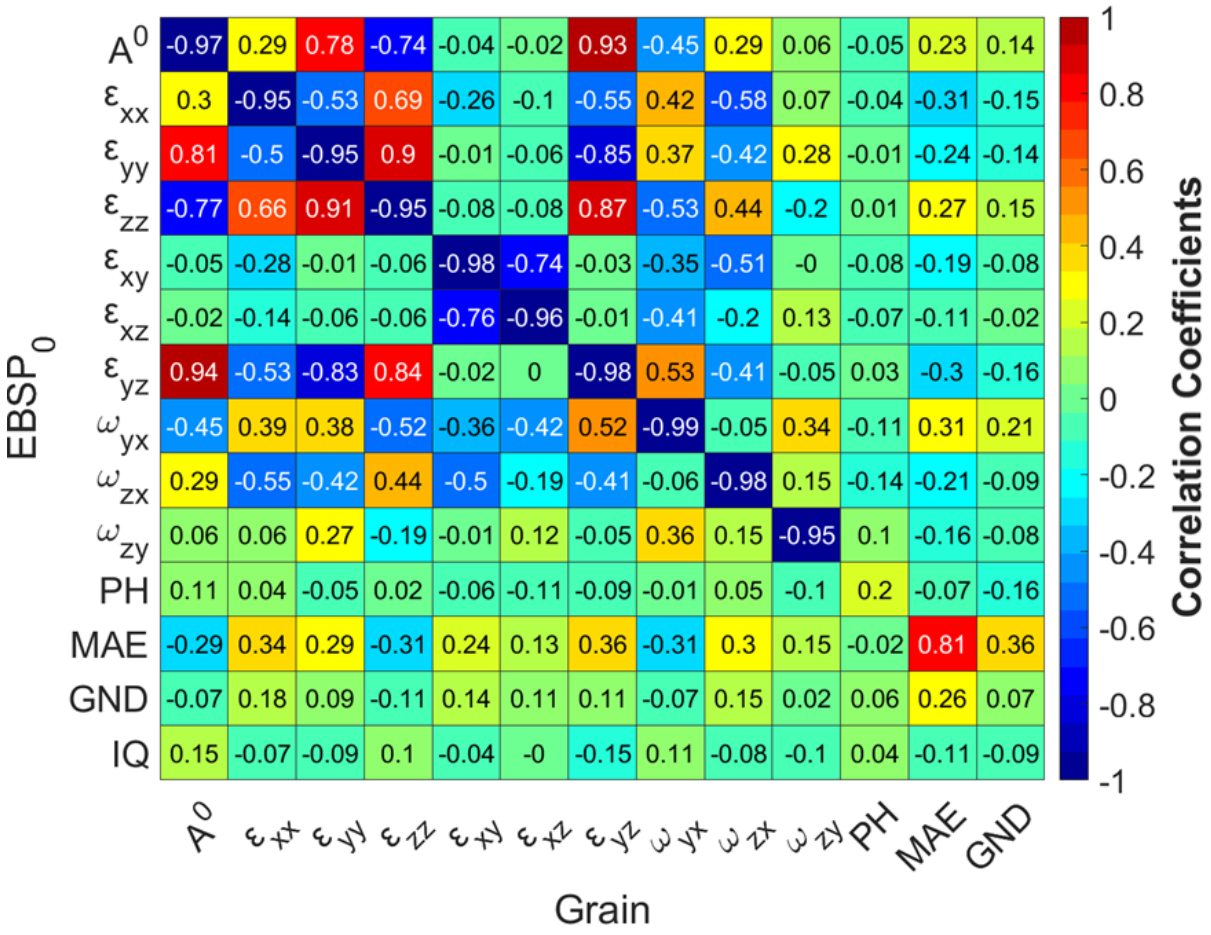


Figure 3-14: Correlation coefficients for the grain average (Grain) and reference point-average ($EBSP_0$) averaged for 12 Si maps. The minus sign indicates an inverse relationship.

The '*Chosen*' $EBSP_0$, for the 12 intervals, was then taken as the point with the highest PH and lowest MAE after exploring the relationship between PH and MAE, which was consistent with the previous analysis, as shown in Figure 3-15. '*Chosen*' compared to '*Native*' (like the previous analysis) did not show a consistently reduced elastic strain or deformation but insignificantly improved PH and MAE in the calculated field (more details can be found in Appendix (6.B) – In situ $EBSP_0$ selection).

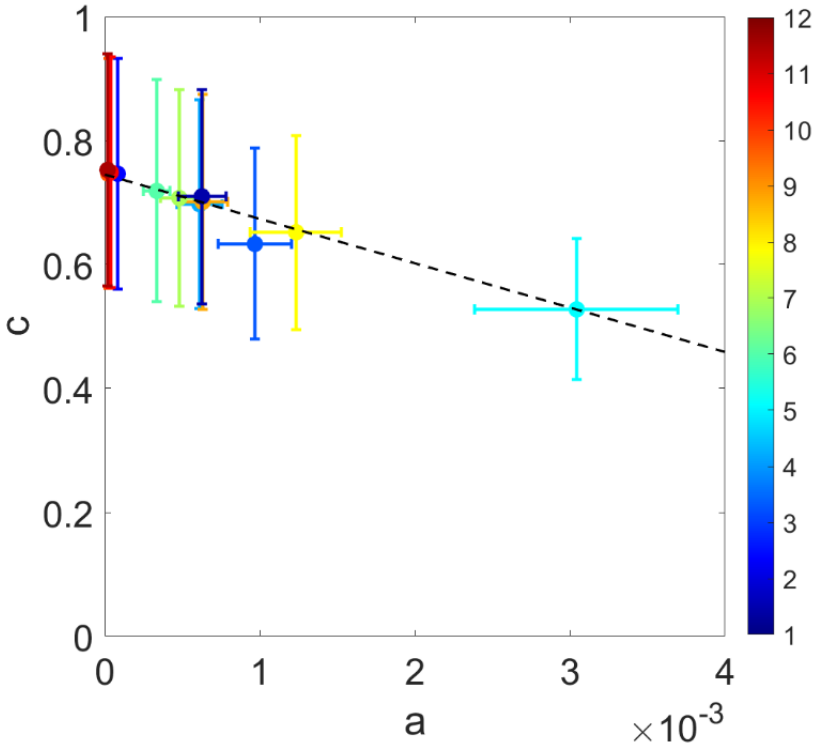


Figure 3-15: Fitting coefficient for $\mathrm{PH} = {a}/{\sqrt{\mathrm{MAE}}} + c$ for the 12 measurements in silicon, indicated by legend colour.

## 3.4 Discussion

The strong inverse diagonal correlations (Figure 3-9, Figure 3-13 and Figure 3-14) indicate that the $\mathrm{EBSP_0}$ deformation status (component by component) inversely impacts the calculated field except for the GND density. Figure 3-16 summarised how the local conditions in the $\mathrm{EBSP_0}$ influence the same component in the calculated field across the brittle silicon (Si) sample, quasi-brittle ferrite (Fe-$\alpha$) phase, and the ductile austenite (Fe-$\gamma$) phase, in terms of deformation gradient average determinant ($A^0$), Von Mises stress ($\sigma_{\mathrm{VM}}$), rotation magnitude ($\omega_T = \sqrt{\omega_{32}^2 + \omega_{13}^2 + \omega_{21}^2}$), maximum in-plane principal strain ($\varepsilon_{\mathrm{Max}}$), PH, MAE and GND density.

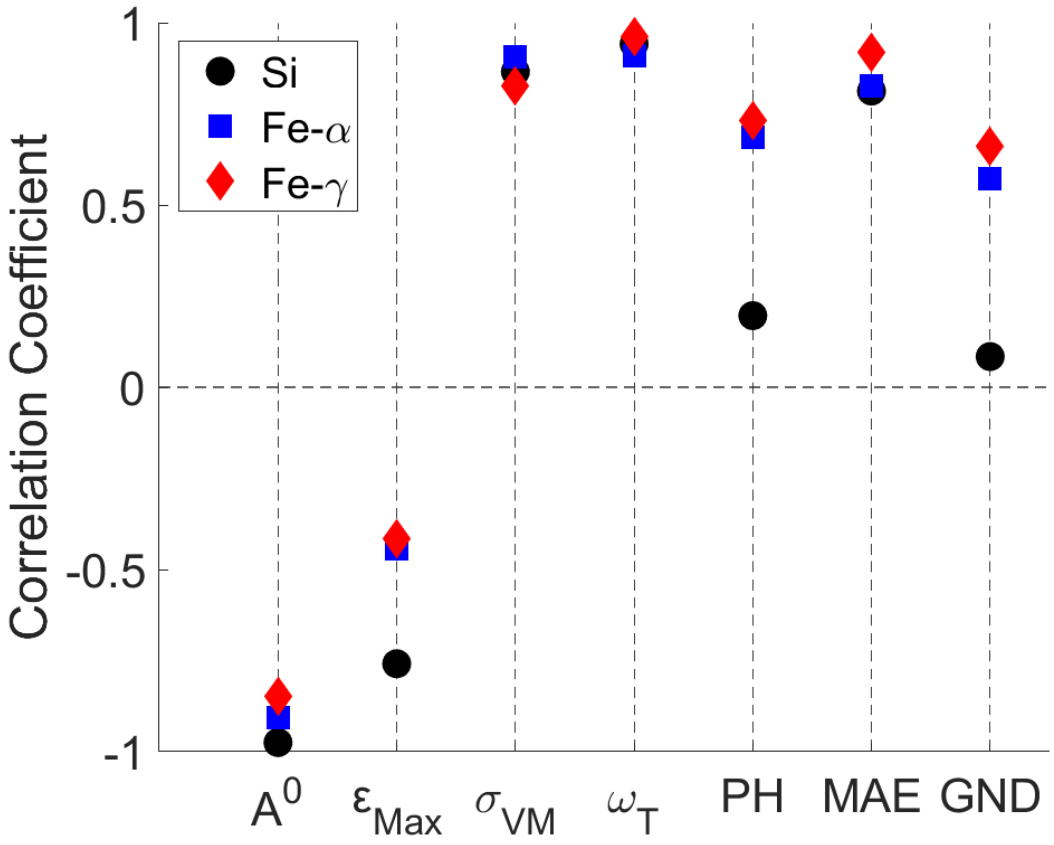


Figure 3-16: Linear correlation coefficient of $EBSP_0$ local status with the same parameter in the calculated grain field for Silicon (Si), the ferrite (Fe-α) and austenite (Fe-γ) phases of age-hardened DSS. The analysis considers the deformation gradient average determinant ($A^0$), Von Mises stress ($\sigma_{VM}$), rotation magnitude ($\omega_T = \sqrt{\omega_{32}^2 + \omega_{13}^2 + \omega_{21}^2}$), maximum in-plane principal strain ($\varepsilon_{Max}$), correlation peak height (PH), mean angular error (MAE) and GND density.

The elastic deformation gradient and (Von Mises[10]) stress are strongly inversely dependent on the $EBSP_0$ deformation state, but the latter correlation is reduced with increased plasticity. The rotation magnitude ($\omega_T$) and the mean angular error (MAE) have a high correlation coefficient unaffected by the material plasticity. This shows that a reference pattern from a highly deformed point will reduce the magnitude of the strains in the inferred total deformed field and induce more (angular) error, which demonstrates the strong effect of the choice of $EBSP_0$ and the adverse consequence on both magnitude and distribution in

[10] Von Mises stress and the rotation magnitude are a positive square root of the tensors; hence, it does not show the inverse relationship.

each component of the calculated elastic field. This is because the elastic tensors vary with direction, as the lattice is distorted directionally with consequent effects on the EBSD pattern; thus, the elastic strains cause small shifts in the zone axes whilst plastic strains cause blurring of the bands' edges due to incoherent scattering [221,222].

This is clear when looking at the correlation between the estimated GND density and $EBSP_0$ characteristics which is material-dependent. For example, the ferrite showed a considerable correlation between the resultant map's PH and MAE with the $EBSP_0$ image quality (IQ) and plasticity level, where an $EBSP_0$ with high IQ and low GND density produced a map with high PH and low MAE. This is consistent with the widespread use of the '*Native*' selection across the literature [163,223–228]. $EBSP_0$ affects GND density, contrary to the literature [87,228,229], where HR-EBSD is assumed to accurately determine the lattice distortion gradient independently of the $EBSP_0$. However, as the GND density is typically reported in log scale maps, this influence ($\leq \pm 0.04$ $\log_{10}$ ($m/m^{-3}$)) is relatively unimportant (Figure 3-12c). This further shows the significance of plastic-induced perturbations on patterns, increasing with the materials' ability to deform plastically. Thus, the deformation conditions at the reference point affect the PH and MAE, as plasticity reduces PH and increases MAE, and elasticity mainly increases MAE. Note that the correlation coefficient discussed here (i.e., Pearson correlation coefficient) is a linear correlation coefficient that ignores any other types of relationship, which may exist.

The relative deformation distribution is independent of $EBSP_0$ characteristics (i.e., IQ, PH, and MAE) with no apparent connection to elastic deformation components. This may contradict qualitative studies that used pattern characteristics as indicators of elastic strain gradient [230]; however, in this study, only high-quality patterns were selected as the set of potential

reference patterns. Furthermore, Wright *et al.* [221] indicated that qualitative IQ analysis and correlation between electron beam spot size and probed pattern degradation is adequate for a tungsten filament scanning electron microscope and not a FEG (field emission gun) microscope.

The PH and MAE of the grain were then averaged across the 51 HR-EBSD maps; the result can be fitted to an (empirical) equation (eq. 3—13) where the PH is related to the inverse of the square root of MAE through two coefficients, $a$ and $c$. The inverse relationship between the PH and MAE encapsulates the effect of the plastic deformation blurring of the patterns and the elastic deformation changing of the zone axes.

From the previous analysis, the optimum $EBSP_0$, i.e., the least deformed of the available patterns, should offer the lowest errors (low MAE) with the highest cross-correlation (high PH). Such a pattern naturally has high quality and is close to the average grain orientation. High PH indicates low plastic deformation, which would otherwise cause rapid fluctuation of plastic strain across the diffracting volume and blurring with diffused low-indexed pattern [222]. Low MAE relates to the consistent description of the strain state, i.e., it reduces the uncertainty that arises from the unknown deformation conditions at the $EBSP_0$ on the calculated deformation field while improving the deformation field precision (less random point-to-point noise) and accuracy. Thus, the search algorithm applied to select the optimum $EBSP_0$ gives more weight to MAE as the induced noise (from pattern acquisition or due plasticity) is directly affected by the local MAE. PH is also more affected by MAE as plasticity increases, with the correlation between local MAE and grain PH increasing from -0.13, and -0.58, to as high as -0.86 for the Si, Fe-$\alpha$, and Fe-$\gamma$, respectively. The need for remapping

increases due to significant lattice rotation; thus, the suitability of the $EBSP_0$ becomes more critical while reducing phantom strains [181,182].

Arguments can be made against the efficacy of randomly iterating for 50 maps to determine the 'chosen' reference, as this is time-consuming. Using 50 points is arbitrary but provides more robust statistics when analysing the correlations. An optimal $EBSP_0$ can be achieved with less sampling. Looking at Figure 3-17, the optimality of the $EBSP_0$ is substantially increased just after one iteration (excluding the '*Native*' $EBSP_0$ iteration), where at each iteration, the HR-EBSD maps are averaged (Figure 3-10), then the point with the highest PH and lowest MAE is selected to calculate the deformation maps. Even in quasi-brittle material, a similar '*Chosen*' $EBSP_0$ was achieved after 3 iterations, and the other 19 iterations had similar $EBSP_0$ characteristics to a '*Chosen*' $EBSP_0$. Thus, the reader can safely iterate 3 times to achieve comparable results in selecting the optimal $EBSP_0$ from the patterns available in the grain.

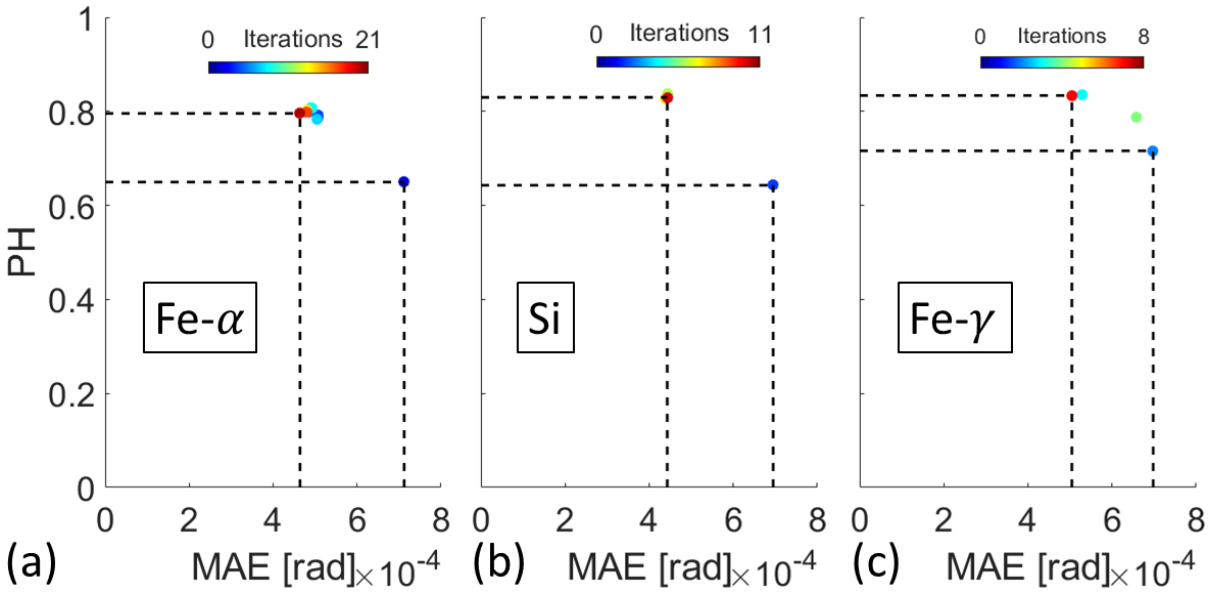


Figure 3-17: Number of iterations required to find the optimal $EBSP_0$ for (a) ferrite, (b) silicon, and (c) austenite.

## 3.5 Conclusion

Selecting a reference pattern ($EBSP_0$) for high (angular) resolution electron backscatter diffraction (HR-EBSD) significantly limits strain mapping due to the unknown conditions at the reference point. Randomly selected $EBSP_0$ were used for HR-EBSD analysis for plastic, quasi-brittle, and brittle materials. These patterns have high image quality (IQ), low geometrical necessary dislocations (GND) density estimated from point-to-point misorientation, and orientation close to the grain's mean orientation. From analysing over 1,000 HR-EBSD maps, it can be concluded that:

A) The local conditions at $EBSP_0$ influence the resultant HR-EBSD map with highly deformed $EBSP_0$, hugely reducing the deformation field magnitude and mildly changing its distribution.

B) Choosing a point/$EBSP_0$ with an elevated level of plasticity (i.e., higher GND density) reduces the cross-correlation quality and induces error compared to choosing a point/$EBSP_0$ with an elevated level of elasticity which exacerbates only the error.

C) There was no direct relationship between (high quality) $EBSP_0$ image/correlation characteristics and the reference point deformation state.

D) By exploring and identifying an empirical relationship ($\mathrm{PH} = {}^{a}/_{\sqrt{\mathrm{MAE}}} + c$) between the cross-correlation peak height (PH) and the mean angular error (MAE), an objective process was used to select the least strained reference point.

# Chapter 4. *J*-Integral analysis of HR-EBSD elastic strain fields of ferrite deformation twins

Contents

## 4.1 Introduction

Deformation or mechanical twinning is the homogeneous change of orientation of part of a crystalline grain due to shear [231]. It is an important mechanism to accommodate plastic strains by changing crystal shape when sufficient independent slip systems cannot be activated, such as crystals with low symmetry [232] or deformation at low temperatures [233]. There are several general differences between deformation by slip and twinning, which can be summarised as follows:

(1) Slip occurs across several relatively separated, parallel planes, involving a simple movement along a slip plane as one rigid portion moves relative to the other. However, twinning shifts atoms synchronically with different magnitudes and directions, undergoing a significant affine reorientation without movement along the twinning plane [232,234]. The reorientation can be seen as a change in contrast in Figure 4-1a,

(2) Both modes of deformation cause a change in the texture of a polycrystalline material, but the effect of slip is gradual compared to twinning, which affects the texture characteristic and hardening during deformation [232]. Twin boundaries can block the propagation of dislocations (i.e., Hall–Petch effect), and the decrease in the slip barrier spacing due to the high density of stacking faults leads to an increase in the required stress for further plastic flow (i.e., delayed localised deformation) [235–237],

(3) Twinning has strong polarity (e.g., some variants within a specific twin mode operate only in compression) with easy activation across different grains, which require a small shear or a simple shuffle step to accommodate their movement [232,234,238] and,

(4) While the slip is sensitive to temperature and strain rate, twinning is more sensitive to microstructural aspects (e.g., texture and grain size) [232,238].

A deformation twin embryo forms in BCC metal by accumulating stacking faults, with a variant selection governed by the local stress state [239–241]. Variation of the stress field close to twins inferred from HR-EBSD experimental [242,243] and CPFE simulation data indicated that twins nucleate on sites with maximum strain energy density and twin resolved shear stress; thus, reducing the total elastic energy after formation. This relaxation depends on the twin thickness and is a deciding factor in the spacing between twins [244]. Experimental [245] and three-dimensional [246] analysis has focussed on the (stored) strain energy density measured along a path. This highly localised stress field can provide a sufficient driving force for concurrent twin nucleation [247,248] and inter/intra-granular crack nucleation [249,250].

The growth of a deformation twin can be perceived as a two-step process of i) thickening that is mediated by the interaction between the residual and mobile twin partials at the coherent twin-parent interface [251], and ii) dislocation mobility along the twin shear direction [252,253]. The twin propagates when the homogeneous shear stress reaches a critical value, and a twin-parent interface advances inside the parent grain [241]. The propagating deformation twin generates a stress field due to its confinement by the surrounding parent crystal, and deformation twins develop a 3D oblate spheroid shape (which appears in 2D sections as a bi-convex lens) with a mixed coherent and non-coherent interface (Figure 4-1b) [254–256].

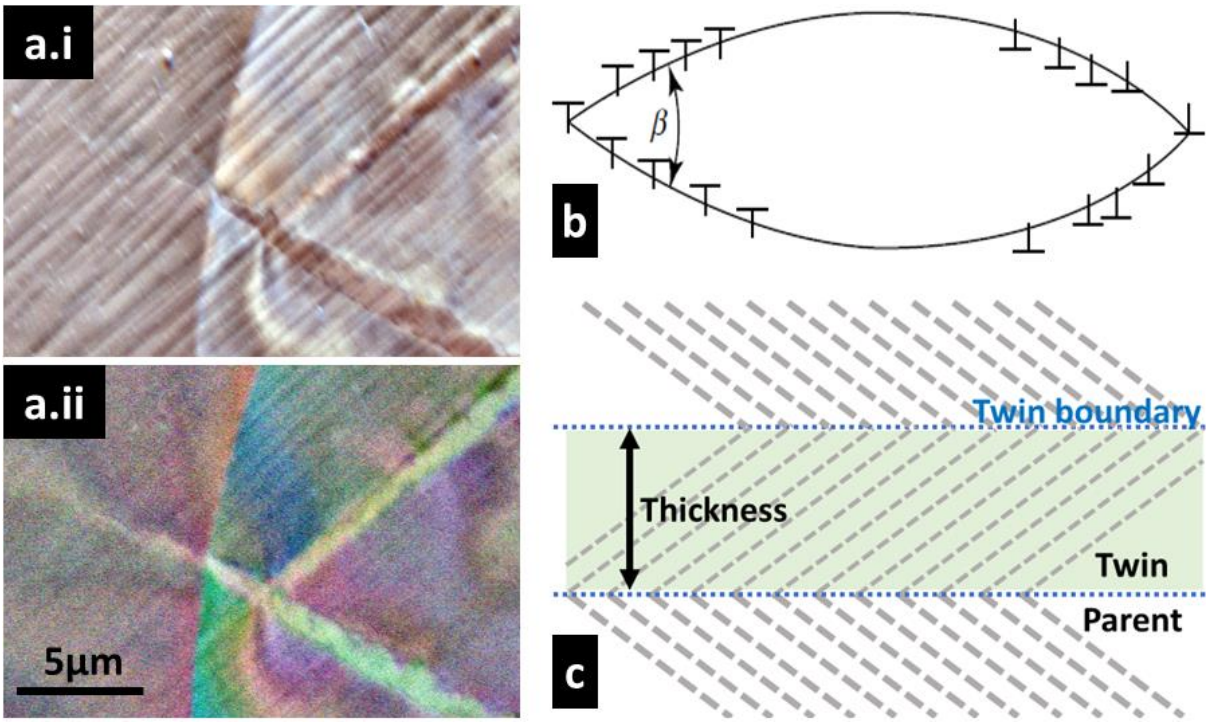


Figure 4-1: (a) forescatter diode (FSD) image for deformation twins at grain boundary in age-hardened ferrite at I) 18mm working distance and II) 38mm working distance. (b) Schematic of a lenticular twin with interface dislocations and (c) Twin band.

Kannan *et al.* [257] found, using in-situ ultra-high-speed optical imaging, that twin nucleation in single-crystal magnesium is stress-driven accompanied by instantaneous propagation at a speed of 1km/s (initially) that prioritises volume lateral thickening over forward propagation, past a critical width where growth is then become faster along the shear direction [256]. Barnett [258] also indicated that growth is due to twin tip extension. Furthermore, elastic simulations of the local stress field surrounding the ellipsoidal twin tip find that the field can be described using its lens angle ($\beta$) and that the stress field magnitude increases with twin thickness [239,244,248].

In practice, plastic accommodation occurs in the parent crystal; thus, it also depends on the material's yield stress, the anisotropic elastic stiffness of the parent crystal lattice, and the deformation twinning shear magnitude [259,260]. This can also be accompanied by long-range diffusion of elements and elemental segregation (e.g., Cr and Co in single crystal Ni-

based superalloy MD2), which occurs at the twin boundary to facilitate twin growth by lowering the critical stacking fault energy [261,262]. A linear variation has been observed between twin thickness, stacking fault energy [263] and grain size [264,265], and to a lesser degree, the stress state of the twinning grain (Schmid factor) [266]. The twin thickness saturated once a critical residual dislocations' density reached the coherent twin-parent crystal boundary [267,268].

Significant attention has been paid to the crystallography [233,264,269–271], morphology [272–274] and macro mechanical effects [275–277] of deformation twinning. Although the criterion for deformation twin growth is not entirely understood, it is a tip-controlled phenomenon linked to the interaction between the residual and mobile twin partials at the twin interface; thermodynamically, this involves the elastic energy of the strained lattice, the interface and volume free-energy of the twin, and the dissipated energy of the growth mechanism [277,278]. To fully understand the interactions between microstructure (i.e., grain size, texture), temperature and strain rate on deformation twinning, it is crucial to characterise the (high) local stress and strain field associated with twin thickening and propagation. This is especially important for materials where cleavage fracture can be initiated by twinning (e.g., iron-silicon [279], the ferrite phase of age-hardened duplex stainless-steel [280], and single-crystal magnesium [249]) as a stress-relieving mechanism.

Early studies of deformation twins arrested within grains of niobium [281] and iron [282] visualised the highly local strain concentration at the twin tip using an etch-pit procedure. More recently, high-resolution electron backscatter diffraction (HR-EBSD) has been used to investigate the strain 'singularity' ahead of a twin tip in hexagonal close-packed (HCP) zirconium alloy [222]. A deformation twin in commercial purity titanium was characterised

similarly and then quantified using a local Schmid factor (LSF) at the twin tip [157,283], as described in eq. (4—1).

$$\mathrm{LSF} = \frac{\sigma : S}{\|\sigma\|}, \qquad \text{Schmid matrix } \left(S_0^i\right) = d^i \otimes n^i \tag{4—1}$$

where $\|\sigma\|$ is the maximum principal stress, $d^i$ is the shear direction and $n^i$ is the plane normal for the $i^{\text{th}}$ slip system. The authors concluded that conditions at the twin tip control thickening and propagation in a manner analogous to the operation of dislocation sources ahead of a crack-tip [284]. In the analysis, a broad region of high LSF ahead of the twin tip favoured propagation, whereas a narrow region of high LSF promoted thickening. Since then, it has been argued [285] that the LSF firmly controls the twin variant selection, as twinning has strong polarity.

The LSF novelty – compared to other criteria to describe conditions at the twin [286–288] – lies in combining a geometrical criterion with the deformation field in the parent grain to provide an approximate indication of the local twin mode (i.e., thickening or propagation). However, the LSF analysis does not take advantage of the available full-field data, relies on global information on the applied stress, and does not consider the energy balance that drives twin growth. To the author's knowledge, there have been no in-situ experiments to quantify the strain field ahead of a propagating deformation twin. Such observations might validate geometrical [287] or hybrid geometrical-energy-based criteria [288–290] for growth. Nanoscale testing (i.e., transmission electron microscopy) may not represent the behaviour in bulk samples due to plasticity starvation, i.e., large surface area to volume ratio [291], so a suitable analysis method is needed.

Lloyd [266] described the stress concentration field ahead of the twin tip using a two-dimensional dislocation-based model within a single magnesium grain. Wang and Li [292], who considered microscopic phase-field (MPF) models of cracks, noted that the stress fields were similar for dislocations, deformation twinning and martensitic transformations, with differences only in the traction of the created surface, i.e., there is 100% traction recovery for dislocations and a traction-free surface for a crack. They highlighted that the stress field singularity regulates the advancement of the crack-tip and dislocations. This stress concentration can be characterised using a path-independent line integral, as shown by Eshelby for dislocations considering the contribution from the surface traction and ellipsoidal inclusions [293,294], and Rice [33] for cracks and stress concentrations with traction-free surfaces. Furthermore, Venables [295] noted that the oblate spheroid shape of the twin tip is the ideal example of an ellipsoid inclusion or a notch.

Previous analyses that used HR-EBSD to measure the strain field ahead of blocked slip-bands [296–298] and deformation twins [299] have demonstrated their singularity-like behaviour. Here, a full-field 2-dimensional *J*-integral analysis and the interaction integral have been applied to HR-EBSD data for the first time to quantitatively characterise the mechanical conditions surrounding the tips of intragranular twins. The objective is to ultimately develop an experimental methodology to investigate the criteria for twin growth and the mechanical interactions between twins and other microstructure features (twins, grain boundaries, precipitates), which affect the plasticity and fracture of polycrystalline metals.

The chapter is structured as follows: Following a brief description of the experimental methodology, the analysis of the *J*-integral from HR-EBSD data is presented as it is applied to an intragranular twin in a ferrite grain that is observed as the twin thickens and extends when

the applied tensile strain is increased. Ex situ analyses of several ferrite twins are then presented to examine the characteristic stress intensity factors $K_I$ and $K_{II}$ of the elastic fields around unloaded twins. The limitations of the current 2D analysis are discussed.

## 4.2 Methodology

### 4.2.1 Experiment

Specimen with a dog-bone geometry (Figure 4-2, nominally 30 × 14 × 1.5 $mm^3$) was electrical discharge machined (EDM) from a large (~200 mm thickness) forging of super-duplex Zeron 100 alloy (UNS: S32760, https://bit.ly/2ZdBdBe) with a nominal composition of 25% Cr, 7% Ni, 3.6% Mo, 0.7% Cu, 0.7% W, 0.22% N, before being aged in air at 475°C for 100 hrs to cause age-hardening of the ferrite by spinodal decomposition to encourage ∑3 {211} <111> ferrite deformation twinning in the coarse-grained ferrite (Figure 4-3), at room temperature, with no meaningful change in the austenite properties [196,302]. Duplex stainless steel is a suitable model material for EBSD analysis as the polished surface does not oxidise quickly, and high-quality patterns can be acquired in a reasonable time.

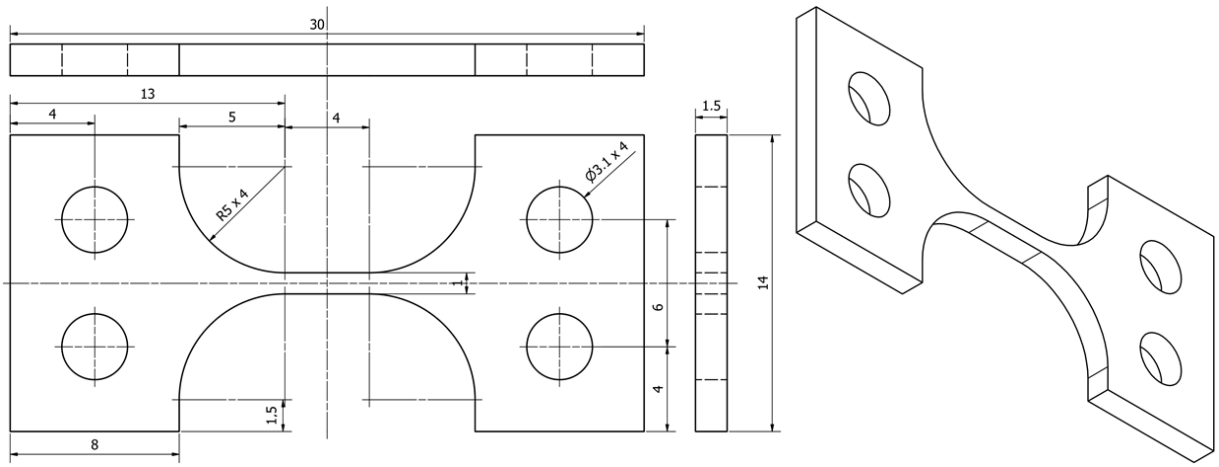


Figure 4-2: Zeron 100 duplex stainless-steel tensile specimen (dimensions in mm).

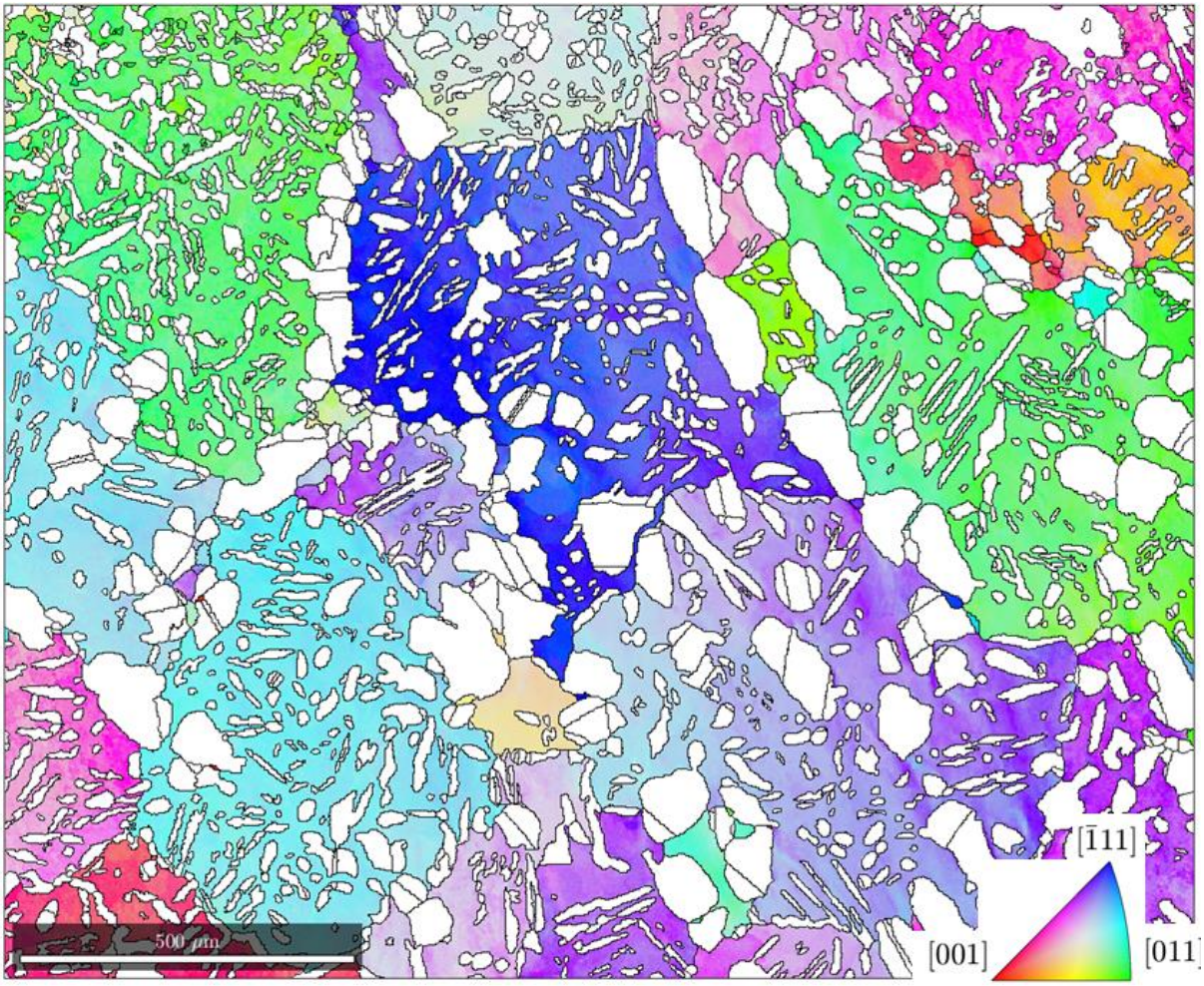


Figure 4-3: EBSD map for age-hardened duplex stainless-steel ferrite phase with excluded austenite grains. The scale bar is 500 µm.

The observed surface of the aged specimens was ground using SiC papers from 240 to 4000 grit, polished using diamond paste (from 9 to 1 µm), finishing with 50 nm colloidal silica for 2 hours (50 rpm speed and 5 N force) to produce a mirror-flat surface without artefacts. The specimens were ultrasonically cleaned for 20 minutes using ethanol, rinsed with deionised water, and dried with a hot air blower.

The specimens were loaded using a 70° pre-tilted 2 kN Tensile Deben® stage in a Carl Zeiss Merlin FEG-SEM system equipped with Bruker e-flash high-resolution EBSD detector. Before observations were made, the stage and specimen were plasma cleaned within the microscope for 4.5 hours (3 cycles of 45 minutes of plasma cleaning followed by purging). The deformation

was performed in tension using a motor speed of 0.1 mm/min. For the in situ test, the nominal engineering stress and strain were evaluated using the tensile load and initial cross-section dimension and the change in crosshead displacement for the nominal gauge length of 4 mm.

The in situ specimen was observed using both secondary electron (SE) and forescatter diode (FSD) imaging (similar to Figure 4-1a) until a suitable region of interest (ROI) was identified for higher resolution analysis. Arrays of electron backscatter diffraction patterns (EBSPs) were then collected to map the ROI at increasing levels of nominal applied strain. Before each observation, the setup was left to stabilise for 30 minutes at fixed crosshead displacement. The microscope conditions were 10 nA/20 kV beam current/voltage and 18 mm working distance. The high-quality EBSPs were recorded as an 800 × 600 pixel map, with 100 millisecond exposure time per pattern and a step size of 75 nm. These conditions provided a reasonable time for measurement (75 minutes for an 18.6 × 14 $\mu m^2$ map) while avoiding sample drift [206,207]. After unloading, the same conditions were used to analyse regions of interest in the ex situ specimen, selected by a deformed gauge length region survey using FSD and secondary electron imaging. These EBSPs were then used for HR-EBSD analysis through the objective process outlined in Chapter 3.

The subsurface geometry of the twin was revealed using Focused Ion Beam (FIB) slicing. The sample was placed inside a Zeiss Auriga dual-beam SEM-FIB system that has a Schottky field emission Gemini electron column coupled with an Orsay Physics 'Cobra' Ga+ ion FIB. The sample was tilted after achieving eccentricity at 54° before moving to a working distance of 5 mm. FIB and SEM coincided by adjusting the stage-beam working distance and spatial stage movement, allowing simultaneous milling and imaging. Once eccentricity and coincidence were achieved, a protective ~1.5 µm platinum and ~1.5 µm carbon layers were deposited over

the feature using a 240 pA/ 30 kV beam to protect the surface and give better contrast. A 35 µm deep trapezium was then milled using 16 nA/ 30 kV to allow for easy viewing of the feature in the 3rd dimension In-lens and Secondary Electron (SE) Imaging conditions with 36° titled correction (effective 90° viewing) set for fine milling using ATLAS 3D with a 600 pA/ 30kV milling conditions. The obtained image stacks were 16-bit with a voxel size of 10*10*25 $nm^3$ for FIB slicing of a volume of 28.29*12.09*23.35 $\mu m^3$. 3D image drift was corrected using Fiji ImageJ [301] before manually training a Weka Segmentation classifier [302] on 20 frames to detect cracks from the matrix and the protective Pt layer and then applying the trained classifier to the entire image stack. The segmented stack was then visualised using AVIZO (version 2020.3.1).

### 4.2.2 Trace analysis

Body-centred cubic ferrite has two active slip systems {110} <111>, {112} <111> ({123} <111> can also occur, but rarely activates [303]) and one twinning system {112} <111> that has the {112} habit plane. EBSD-assisted trace analysis [304] is achieved by examining the slip trace, a straight-line resultant from the intersection of the active slip plane with the sample surface, creating the surface step. A deformation twin trace is defined by the twin-long axis. All possible traces/lines formed by the slip plane and twin habit plane of each of the {110}<111> and {112}<111> variants (listed in Figure 4-7) were transformed into the Cartesian reference frame of the (parent) grain of interest using the rotation matrix ($R_{\varphi_1,\Phi,\varphi_2}$) which was constructed from the mean grain's Euler angle ($\varphi_1, \Phi, \varphi_2$), (Table 4-1).

The use of MTEX [96] libraries, which are implemented for crystallographic operations, reduces the steps required for $[h, k, l](u, v, w)$ transformation to (x, y, z) of the sample. Then the traces (vectors) can be visualised using the MATLAB® *quiver* function to plot the

theoretical slip trace into the EBSD map, which was visually compared to the traces of the features observed in the forescatter diode (FSD) image to help identify the best match slip system or twin variant (code available at https://doi.org/10.5281/zenodo.6411600). In the case of multiple slip planes having the same trace, the one with the highest Schmid factor (SF) was selected.

Table 4-1: Twin, parent, and adjacent grain Euler angles for Figure 4-6.

| Type | $\varphi_1$ | $\Phi$ | $\varphi_2$ |
|---|---|---|---|
| Deformation Twin | 253 | 152 | 278 |
| Ferrite (α, 2) | 12 | 151 | 354 |
| Ferrite (α, 1) | 252 | 151 | 277 |

The Schmid factor was calculated using equations 4—3), where $n^i$ is the slip or twin plane normal and $d^i$ is the shear direction after rotating the load direction matrix from the sample frame ($L_S$, loading in x-direction) to the crystal frame ($L_c$). In addition, in case of multiple twin variants having a similar trace, one can plot pole figures of all competing variants with the parent, and the true twin will coincide with the parent (Figure 4-6b) [215].

$$L_c = R_{\varphi_1,\Phi,\varphi_2} L_S \qquad 4—2$$

$$SF = \left|\left(L_c * n^i\right)\left(L_c * d^i\right)\right| \qquad 4—3$$

### 4.2.3 *J*-integral analysis

To simplify the *J*-integral analysis, the elastic strain field ($\varepsilon$) at the tip of the deformation twin (white box in Figure 4-11b in $\varepsilon_{xy}$) was transformed to a new reference frame ($\varepsilon'$) using a 2D rotation matrix, so the twin trace was parallel to the horizontal x-axis of the new coordinate

frame. The elastic nodal displacement field in the new coordinate system was computed by integrating the measured elastic strain field (one datum per EBSD measurement point). This employed a method implemented in MATLAB® to create a uniform rectangular grid with four nodes (equivalent to a CPS4 element in ABAQUS®) around each element, with 4 Gaussian points (full Gaussian quadrature integration) per element to increase integration accuracy (Figure 4-4, see Chapter 2). The remaining 2D (planar) rigid body motions (translations and a 0.01° rotation) were then removed from the integrated displacement field, selecting the point with absolute minimum displacement as the origin [112]. At each level of applied strain, Figure 4-13 shows the field of the integrated displacement magnitude (after rotation and rigid body motion correction).

Using a MATLAB® code[11], these nodal displacements were injected into the ABAQUS® finite element solver as boundary conditions which applied an anisotropic elastic model (ferrite elastic constants) oriented to the crystal frame of reference using a rotation matrix ($R_{\varphi_1,\Phi,\varphi_2}$) constructed from the Euler angles ($\varphi_1, \Phi, \varphi_2$) of the reference pattern ($EBSP_0$) as in equation (4—4) [305].

$$R_{\varphi_1,\Phi,\varphi_2} = \begin{bmatrix} \cos\varphi_1\cos\varphi_2 - \cos\Phi\sin\varphi_1\sin\varphi_2 & \cos\Phi\cos\varphi_1\sin\varphi_2 + \sin\varphi_1\cos\varphi_2 & \sin\Phi\sin\varphi_2 \\ -\cos\varphi_1\sin\varphi_2 - \cos\Phi\sin\varphi_1\cos\varphi_2 & \cos\Phi\cos\varphi_1\cos\varphi_2 - \sin\varphi_1\sin\varphi_2 & \sin\Phi\cos\varphi_2 \\ \sin\Phi\sin\varphi_1 & -\sin\Phi\cos\varphi_1 & \cos\Phi \end{bmatrix} \quad 4—4$$

[11] Code is available at https://doi.org/10.5281/zenodo.6411605.

The local crystal anisotropic elastic stiffness matrix, C, is defined as [306]:

$$C = \begin{bmatrix} 230 & 135 & 135 & 0 & 0 & 0 \\ & 230 & 135 & 0 & 0 & 0 \\ & & 230 & 0 & 0 & 0 \\ & & & 117 & 0 & 0 \\ & & Sym. & & 117 & 0 \\ & & & & & 117 \end{bmatrix} GPa \qquad 4—5$$

Then by using the rotation matrix, the anisotropic elastic stiffness matrix, $C_{EBSP_0}$, can be mapped from the reference crystal coordinate system to the local coordinate system as below [213,309]:

$$C_{EBSP_0} = T_\sigma^{-1}\, C\, T_\varepsilon \qquad 4—6$$

where:

$$T_\sigma = \begin{bmatrix} R_{11}^2 & R_{12}^2 & R_{13}^2 & 2R_{12}R_{13} & 2R_{11}R_{13} & 2R_{11}R_{12} \\ R_{21}^2 & R_{22}^2 & R_{23}^2 & 2R_{22}R_{23} & 2R_{21}R_{23} & 2R_{21}R_{22} \\ R_{31}^2 & R_{32}^2 & R_{33}^2 & 2R_{32}R_{33} & 2R_{31}R_{33} & 2R_{31}R_{32} \\ R_{21}R_{31} & R_{22}R_{32} & R_{23}R_{33} & R_{22}R_{33}+R_{23}R_{32} & R_{21}R_{33}+R_{23}R_{31} & R_{21}R_{32}+R_{22}R_{31} \\ R_{11}R_{31} & R_{12}R_{32} & R_{13}R_{33} & R_{12}R_{33}+R_{13}R_{32} & R_{11}R_{33}+R_{13}R_{31} & R_{11}R_{32}+R_{12}R_{31} \\ R_{11}R_{21} & R_{12}R_{22} & R_{13}R_{23} & R_{12}R_{23}+R_{13}R_{22} & R_{11}R_{23}+R_{13}R_{21} & R_{11}R_{22}+R_{12}R_{21} \end{bmatrix}$$

4—7

$$T_\varepsilon = \begin{bmatrix} R_{11}^2 & R_{12}^2 & R_{13}^2 & R_{12}R_{13} & R_{11}R_{13} & R_{11}R_{12} \\ R_{21}^2 & R_{22}^2 & R_{23}^2 & R_{22}R_{23} & R_{21}R_{23} & R_{21}R_{22} \\ R_{31}^2 & R_{32}^2 & R_{33}^2 & R_{32}R_{33} & R_{31}R_{33} & R_{31}R_{32} \\ 2R_{21}R_{31} & 2R_{22}R_{32} & 2R_{23}R_{33} & R_{22}R_{33}+R_{23}R_{32} & R_{21}R_{33}+R_{23}R_{31} & R_{21}R_{32}+R_{22}R_{31} \\ 2R_{11}R_{31} & 2R_{12}R_{32} & 2R_{13}R_{33} & R_{12}R_{33}+R_{13}R_{32} & R_{11}R_{33}+R_{13}R_{31} & R_{11}R_{32}+R_{12}R_{31} \\ 2R_{11}R_{21} & 2R_{12}R_{22} & 2R_{13}R_{23} & R_{13}R_{23}+R_{13}R_{22} & R_{11}R_{23}+R_{13}R_{21} & R_{11}R_{22}+R_{12}R_{21} \end{bmatrix}$$

4—8

Descriptions and notations for rotation, and $T_\sigma$, $T_\varepsilon$ and $T$ matrices may be different across the literature. The transformation ($Q$) matrix is used for the rotation of the coordinate system,

and this differs from the rotation ($R$) matrix to rotate tensors (counterclockwise) in a fixed coordinate system. Also, the Bunge rotation (X Z' X'') where Bunger-Euler rotation (Z X' Z'') is conventionally used for EBSD [160]. For stiffness rotation, there are differences in the notation for ordering the shear components [212,310,311]. A comparison between rotations in the example of silicon (111), using Voigt [310], Reuss [311], Hill [106], Lekhnitskii [214] and Salvati *et al.* [307], and Dunne *et al.* [308] methods (which is available here https://doi.org/10.5281/zenodo.6411619) showed that Dunne *et al.* [308] method has the most significant inconsistency, with ±4%, from known values [213], and Lekhnitskii [214] and Salvati *et al.* [307] having the most accurate value; hence, it was used.

ABAQUS® was used as an FE solver, which uses the equivalent domain integration (EDI) [38,43,58] for *J*-integral calculation as described in equations (4—9) to (4—11) as the domain starts at the deformation twin tip and expands in the local direction of a virtual (twin) extension with the linear spatial variation across nodes calculated using a smoothing function ($q$) that equals unity at the tip and zero outside the domain (Figure 4-4a).

$$J_x = \frac{\Delta\Pi}{\Delta q} = \sum_{el=1}^{N_{el}} \left( \sum_{g=1}^{N_g} \left\{ \left[ \left( \sigma_{ij} \frac{\partial u_j}{\partial x} - W_s \delta_{1i} \right) \frac{\partial q_1}{\partial x_i} \right] \underbrace{\det\left( \frac{\partial x_k}{\partial \eta_k} \right)}_{J_{kj}} \right\}_g W_g \right)_{el} \qquad 4—9$$

$$\because \frac{\partial q_1}{\partial x_j} = \sum_{I=1}^{N_n} N_I(x)\, Q_{1I} = \sum_{I=1}^{N_n} \frac{\partial N_I}{\partial x_j} Q_{1I} = \sum_{I=1}^{N_n} \sum_{k=1}^{N_D} \frac{\partial N_I}{\partial \eta_k} \frac{\partial \eta_k}{\partial x_j} Q_{1I} \qquad 4—10$$

$$W_s = \int_0^{\varepsilon_{kl}} \sigma_{ij} d\varepsilon_{kl}\,, \qquad i = j = x, y, z \qquad 4—11$$

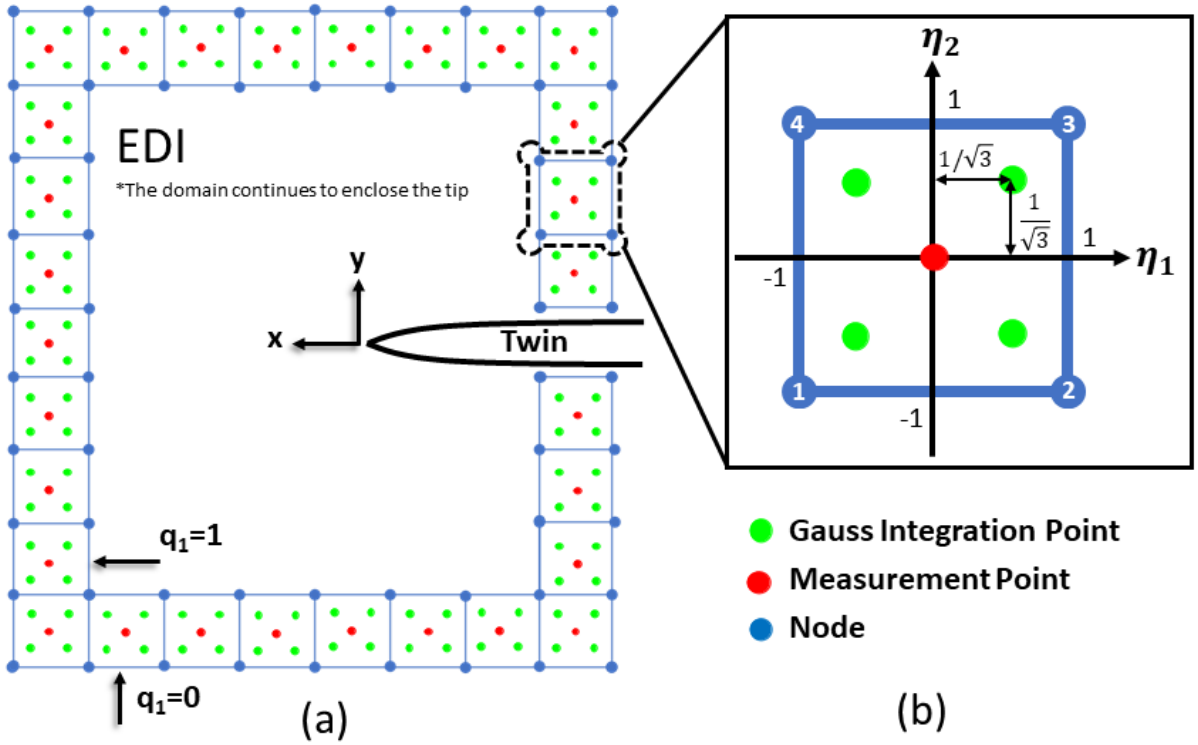


Figure 4-4: Schematic of the finite element method (a) discretisation of the problem using a uniform rectangular grid with four nodes around each element, with 4 Gaussian points (full Gaussian quadrature integration) per element and (b) mapping of reference configuration.

where $N_{el}$, $N_g$, $N_n$ and $N_D$ are the number of elements, Gauss points (=4), nodes (=4) and dimensions (=2), respectively. $\varepsilon_{kl}$ and $\sigma_{ij}$ are the strain and stress calculated from the displacement field ($u_i$) and the material's linear anisotropic elastic constants ($C_{ijkl}$). $W_s$ and $W_g$ are the strain energy density and Gauss weight factor. $\delta$ is the Kronecker delta equals unity inside the domain and zeroes outside the domain. And $q_1$ equals the summation of $Q_I$ in the $I$th node, with nodal values multiplied by the Lagrangian shape function ($N_I$). $\partial\eta_k/\partial x_j$ is the inverse Jacobian matrix ($J_{kj}^{-1}$) of the transformation from ($x_1$, $x_2$) physical space to nodal coordinate ($\eta_1$, $\eta_2$) in Figure 4-4b.

## 4.3 Results

### 4.3.1 In situ tensile test: Region of interest selection

The nominal applied stress and strain of the in-situ test specimen are presented in Figure 4-5a. During the experiment, the sample first undergoes plastic deformation of the austenite at low strain due to the higher hardness of the aged ferrite. Observable synergetic plasticity was activated, consisting of a planar slip-band formed in the austenite phase and deformation twinning in the ferrite phase (Figure 4-5b). The twinning was initiated in relatively big grains and propagated to a boundary instantaneously (~2.5 mm/μs [312]) in a direction close to the loading direction without noticeable load drop nor apparent slip activities in the parent grains.

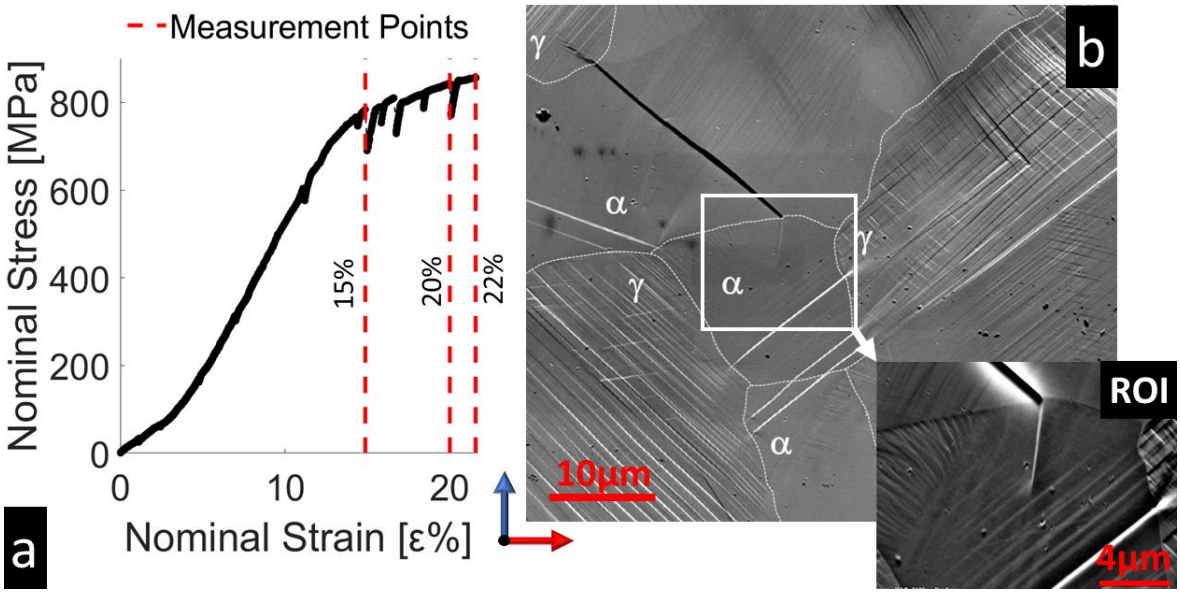


Figure 4-5: a) Nominal stress-strain curve for DSS sample deformed in tension and observed in situ. Stress relaxation occurred during the hold before each HR-EBSD measurement, and the highlighted points (dashed red lines) show the strains at which HR-EBSD measurements were analysed; b) secondary electron (SE) image to show the Region of Interest (ROI) and a forescatter diode (FSD) close-up taken at 15% nominal strain with white dotted grain boundaries.

Wavy slip near interfaces and slip-bands were also detected but predominately in small grains. As the test continued, the density of planar-austinite and wavy-ferrite slip increased with a visible planar-to-wavy transition. The average stress relaxation during every 30 minutes

stabilising period, which occurred mainly at the start, was 54 MPa and was negligible (average 0.44 MPa) during HR-EBSD mapping of the region of interest (ROI). This stress relaxation can be due to the Deben® stage stiffness, system compliance and load re-distribution. The subsequent analysis considers data obtained at 15, 20 and 22% nominal strains.

The selected ROI contains a linear feature that is blocked by ∑3 {60°} ferrite-ferrite grain boundary (Figure 4-6a and b) (The two grains will be designated α,1 and α,2). There is no change in crystal orientation across the linear feature, and it is identified by trace analysis as a (121) $[1\bar{1}1]$ slip-band. The Luster and Morris [313] *m'* parameter for the blocking ferrite-ferrite grain boundary is ~1, which indicates a '*soft'* boundary that can accommodate slip transfer. However, this criterion is only relevant for the statistical analysis of slip-to-slip transfer [314], and it has no reported association with slip-to-microcrack transfer [315] and, in this instance, slip-to-twin transfer. Due to the applied tensile stress, the slip band is predicted to have a 0.30 Schmid factor. From a Taylorian point of view [316,317], the single grain response to the global boundary conditions (i.e., uniaxial tensile) is complicated in polycrystalline materials by the constraints that are imposed by the neighbouring crystals, so this Schmid factor (SF) may not necessarily represent the actual local stress state. An alternative method to calculate the SF is discussed in Appendix (5.B) – HR-EBSD based Schmid factor.

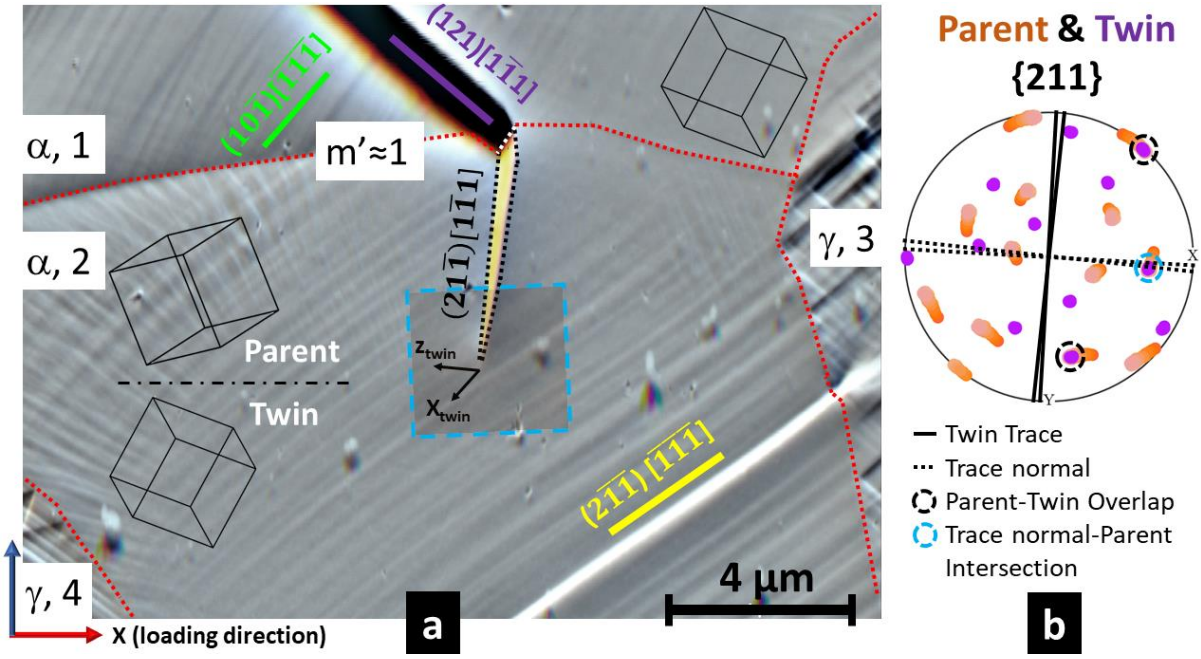


Figure 4-6: a) Forescatter diode (FSD) image for the ROI, at 22% nominal strain, with grain boundaries delineated with red dots, purple green and yellow lines define the slip-band traces, and dotted black lines outline the twin interfaces. The crystal unit cell orientation for the parent, twin and neighbouring ferrite grains are superimposed. b) Stereographic projection pole figure for {211} in the tensile direction projecting the parent and twin of ferrite grain ($\alpha$,2), with traces of the twin/parent GB shown by solid black lines and the planes containing the poles of the interfaces shown by dotted solid lines. The normal to the identified twin invariant plane is circled (pale blue).

A deformation twin developed in the ferrite grain (α,2) at the head of the blocked slip band in the other ferrite grain (α,1). EBSD analysis confirmed its 60° misorientations to the parent grain. The trace analysis of the deformation twin and slip-bands (yellow line) in the parent grain (α, 2) is presented in Figure 4-7, where the trace length is proportional to the Schmid factor. The twin trace is parallel to the habit plane of the $(21\bar{1})[1\bar{1}1]$ variant, with the pole of its twin invariant plane inclined at 56 ± 2° to the surface normal. The projection on the specimen surface of the twin shear direction in the twin invariant plane is at 48° to the loading direction ($X_{twin}$ in Figure 4-6a, where $Z_{twin}$ is the projection of the twin plane normal [157]). By a similar analysis, the slip traces that are visible in grains α,1 and α,2 are $(10\bar{1})$ $[\bar{1}\bar{1}\bar{1}]$ with 0.47 Schmid factor (green line), and $(2\bar{1}\bar{1})$ $[\bar{1}\bar{1}\bar{1}]$ with 0.48 Schmid factor (yellow line), the highest Schmid factor (0.48) of the {112} <111> slip system, respectively.

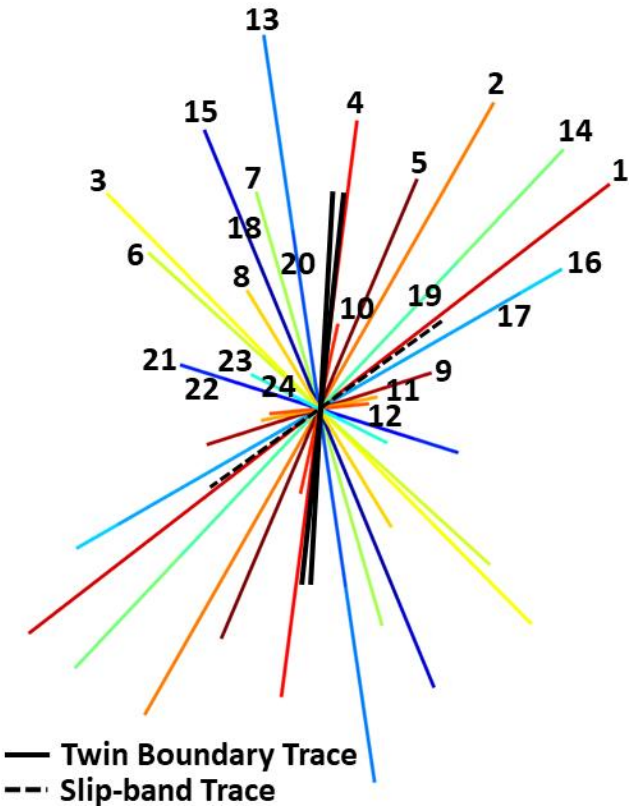


BCC – Slip/Twin Variants

| No. | Direction $< 111 >$ | Plane $\{211\}$ | SF @Parent | Legend |
|---|---|---|---|---|
| 1 | $[\bar{1}\bar{1}\bar{1}]$ | $(2\bar{1}\bar{1})$ | 0.476 | |
| 2 | $[1\bar{1}1]$ | $(2\bar{1}1)$ | 0.457 | |
| 3 | $[11\bar{1}]$ | $(112)$ | 0.392 | |
| 4 | $[1\bar{1}1]$ | $(21\bar{1})$ | 0.377 | |
| 5 | $[\bar{1}\bar{1}\bar{1}]$ | $(\bar{1}\bar{1}2)$ | 0.324 | |
| 6 | $[1\bar{1}1]$ | $(121)$ | 0.300 | |
| 7 | $[\bar{1}11]$ | $(211)$ | 0.293 | |
| 8 | $[\bar{1}11]$ | $(12\bar{1})$ | 0.180 | |
| 9 | $[\bar{1}\bar{1}\bar{1}]$ | $(\bar{1}2\bar{1})$ | 0.153 | |
| 10 | $[\bar{1}11]$ | $(1\bar{1}2)$ | 0.113 | |
| 11 | $[1\bar{1}1]$ | $(\bar{1}12)$ | 0.077 | |
| 12 | $[11\bar{1}]$ | $(\bar{1}21)$ | 0.065 | |

BCC - Slip Variants

| No. | Direction $< 111 >$ | Plane $\{011\}$ | SF @Parent | Legend |
|---|---|---|---|---|
| 13 | $[11\bar{1}]$ | $(101)$ | 0.490 | |
| 14 | $[\bar{1}\bar{1}\bar{1}]$ | $(10\bar{1})$ | 0.462 | |
| 15 | $[1\bar{1}1]$ | $(110)$ | 0.391 | |
| 16 | $[\bar{1}\bar{1}\bar{1}]$ | $(\bar{1}10)$ | 0.363 | |
| 17 | $[11\bar{1}]$ | $(\bar{1}10)$ | 0.301 | |
| 18 | $[\bar{1}11]$ | $(110)$ | 0.273 | |
| 19 | $[1\bar{1}1]$ | $(10\bar{1})$ | 0.262 | |
| 20 | $[\bar{1}11]$ | $(101)$ | 0.234 | |
| 21 | $[11\bar{1}]$ | $(011)$ | 0.189 | |
| 22 | $[1\bar{1}1]$ | $(011)$ | 0.129 | |
| 23 | $[\bar{1}\bar{1}\bar{1}]$ | $(0\bar{1}1)$ | 0.099 | |
| 24 | $[\bar{1}11]$ | $(0\bar{1}1)$ | 0.039 | |

Figure 4-7: Trace analysis of Deformation Twin and Slip-bands in BCC ferrite grain 2.

FIB and high-resolution in-lens SEM imaging provide an in-depth look at the geometry of the twin. Grain boundaries were emphasised using dotted red lines except for deformation twin boundaries, as they are easy to spot due to the different electron channelling caused by the twin having a different orientation than the parent grain. Identified slip bands are given the exact colour identification in Figure 4-6a. Unknown slip traces are highlighted with a white dotted line. The $(21\bar{1})$ twin is enclosed in a blue ellipse. A secondary twin that has different contrast is enclosed in a maroon ellipse. Constructed geometry revealed that the $\gamma$-4 austenite grain (Figure 4-6) is a shallow grain with deformation twins (which can be spotted in Figure 4-5b) that were deflected at a ferrite-ferrite grain boundary and continued to grow in (an apparent) different direction. A dashed white slip was noticed to change (apparent) direction when crossing the twin and continued beyond the twin until the boundary. Deformation twins have a non-uniform twin boundary.

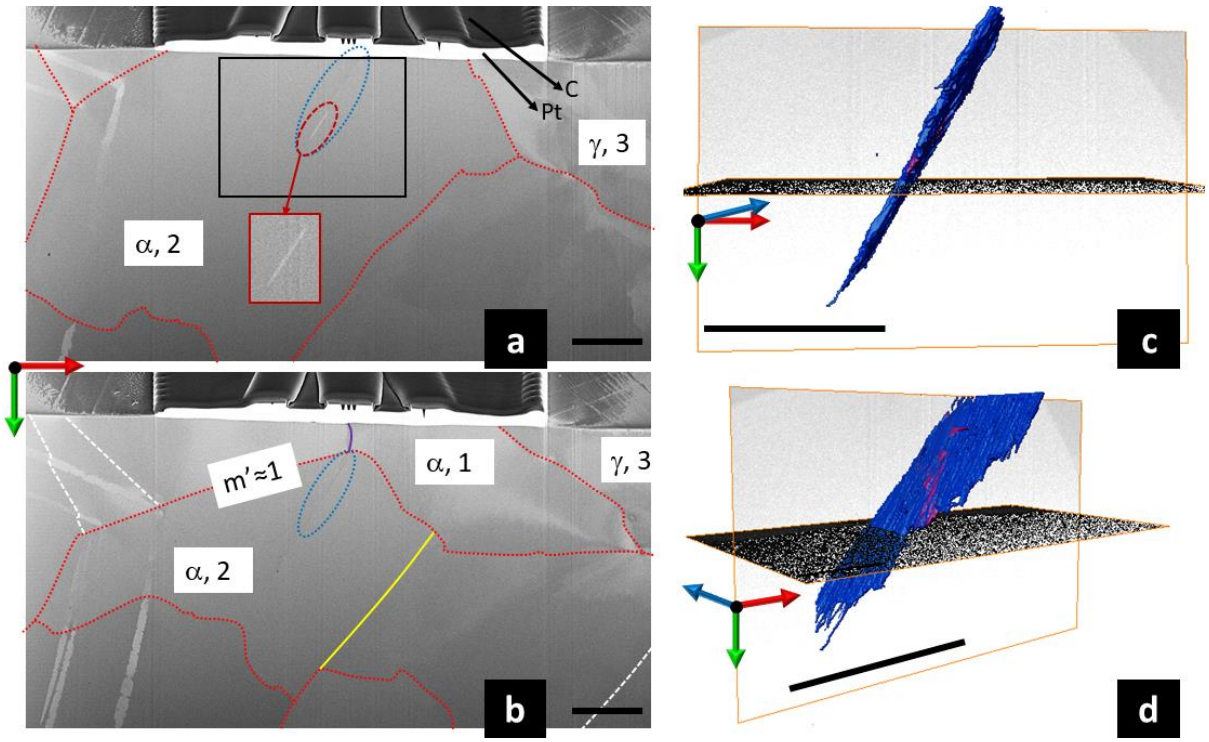


Figure 4-8: (a-b) The FIB field of view imaged using in-lens SEM imaging. (c-d) $(21\bar{1})$ Twin geometry. The scale bar is 5 µm. The blue ellipse indicates the initial twin, and the maroon ellipse is the secondary twin.

Then using AVIZO® on the region highlighted with the black box in Figure 4-8a, the $(21\bar{1})$ twin and secondary twin geometry were constructed (blue colour) using a watershed algorithm combined with manual tracing and removal of (background) noise. The twin's overall width is thin (>0.3 μm), slightly narrowing with the depth. The twin length is constant near the surface but rapidly decreases after ~1 μm. The feature (assumed as a secondary twin) with different contrast (maroon colour) extends across the primary twin geometry. The twin is inclined at 30 ± 1° from the z-axis.

### 4.3.2 In situ tensile test: Twin surface length and width

To determine whether the twin thickness and length changed with the increase in applied strain, which would indicate twin thickening and propagation in equilibrium with the surrounding field, the surface widths of the $(21\bar{1})[1\bar{1}1]$ twin and (121)[$1\bar{1}1$] slip band (purple line in Figure 4-6a) were measured near the ferrite/ferrite grain boundary (dotted white line in Figure 4-6b) and normal to the slip band's apparent edges, respectively. Repeat measurements (at least 5 times) were made manually using the ImageJ [318], and the results were averaged (Figure 4-9c).

An edge-detection method was used to measure the twin length objectively. After alignment of the FSD images (pixel size 6 nm) with an efficient Fourier-space subpixel image registration algorithm (section 2.3.2.2) and cropping and rotating the region of interest (blue dashed square in Figure 4-6a), the images (Figure 4-9a) were interpolated to fill the few points with no data (NaN). A median filter was applied to reduce noise before mapping the phase congruency of the image intensity. Phase congruency [84,103] is contrast invariant and identifies where the Fourier components of the image are most in phase, such as edges. The phase congruency map was threshold segmented to obtain a binary image that identified the

regions of high phase congruency, and the Hough transform was used to detect and measure the largest linear feature (i.e., the deformation twin) (Figure 4-9b). The slip band surface width, twin length and twin surface width increased with the applied strain (Figure 4-9c) by up to 450 nm, 60 nm, and 335 nm, respectively. At the initial observation of 15% strain, the slip band width was 0.51 ± 0.01 µm, whereas the twin had a length of 5.63 ± 0.01 µm and a width of 0.4 ± 0.01 µm.

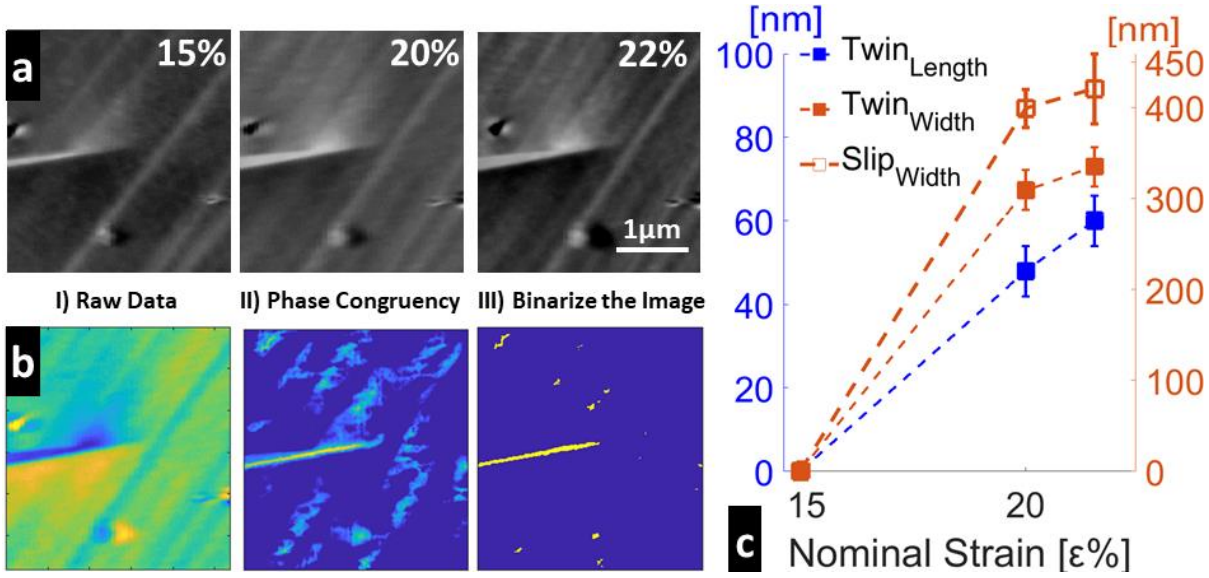


Figure 4-9: (a) FSD images of the ROI with increasing applied nominal strain. (b) Post-processing (false colour image intensity) to segment the twin from the FSD image using phase congruency (for example, at 15% nominal strain). (c) The change in slip band width, twin width, and twin length (the variance is the measurement resolution) with strain, relative to the initial observation at 15% nominal strain.

### 4.3.3 HR-EBSD analysis

In the in situ experiment analysis, the *Chosen* reference $EBSP_0$ (i.e., pattern with the least deformation selected with the method described in Chapter 3) was taken from the 1$^{st}$ ROI observation at the nominal applied strain of 15%. This same pattern was then used as the reference for the subsequent observations, obtained under the same imaging/beam conditions without interruption, re-focusing, or stage movement. The below figure shows the effect of swapping the reference pattern on the quality of HR-EBSD analysis. As the quality of

other grains remains as it was, the ferrite grain (which contains the deformation twin being analysed in this chapter) exhibits a significant improvement in both mean angular error (MAE) and peak height (PH) when using a (relatively) undeformed pattern for the 1st measurement. Unifying the reference pattern across the three in situ analyses guarantees the reduction of the 'relativity' of the HR-EBSD field to one point and not three (Figure 4-10). Maps of the in-plane components of the calculated elastic strain tensors ($\varepsilon_{xx}, \varepsilon_{yy}$ and $\varepsilon_{xy}$) are presented in Figure 4-11 for the three observations at 15%, 20% and 22% nominal applied strain, together with maps of the GND density.

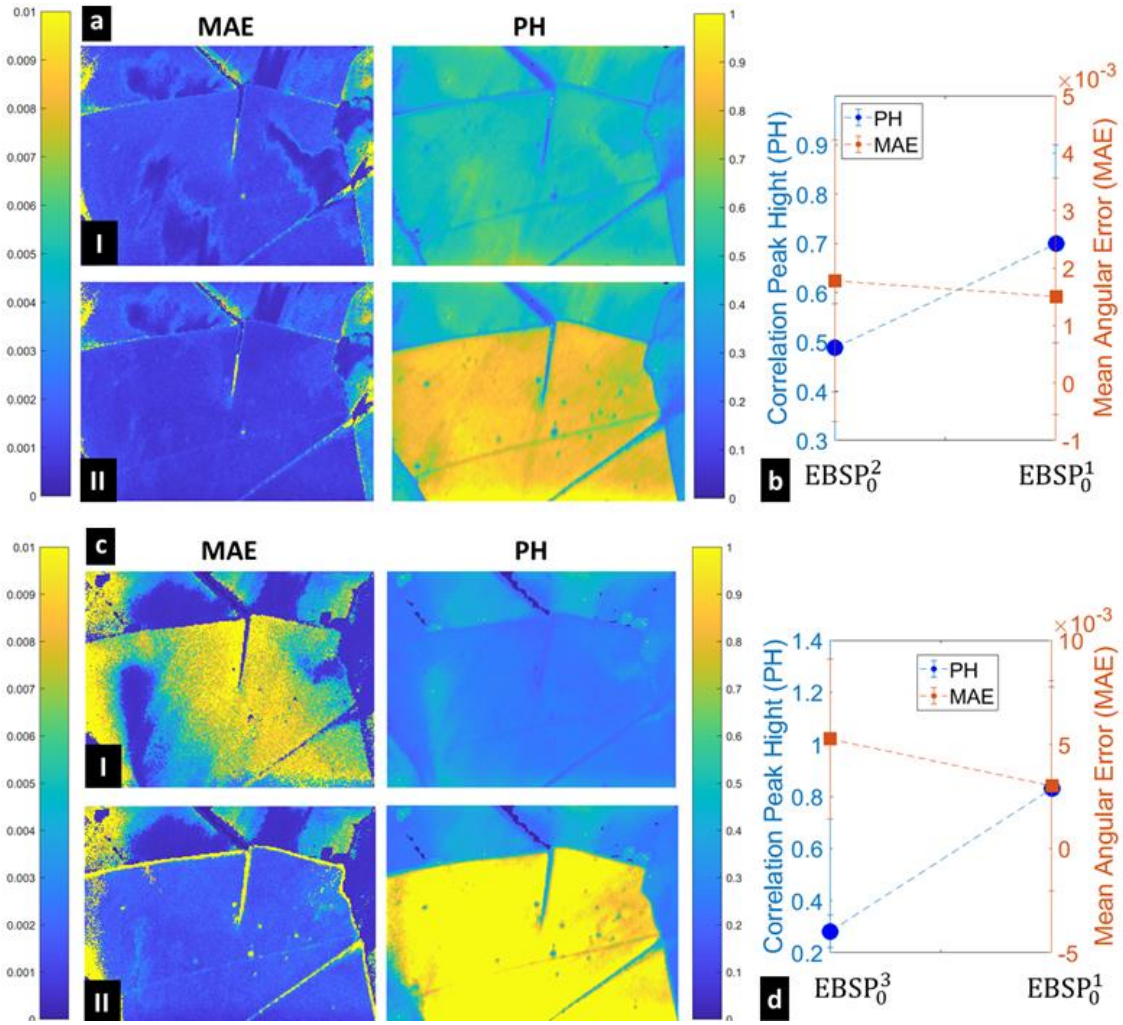


Figure 4-10: The effect on HR-EBSD analysis quality for the (a) 2nd and (c) 3rd in situ measurement when using a reference pattern selected from the (I) measured field ($\mathrm{EBSP}_0^2$ in b and $\mathrm{EBSP}_0^3$ in d) and (ii) from 1st in situ measurements ($\mathrm{EBSP}_0^1$). (b and d) Comparing the mean value of peak height (PH) and mean angular error (MAE) in the ferrite grain when using different reference patterns.

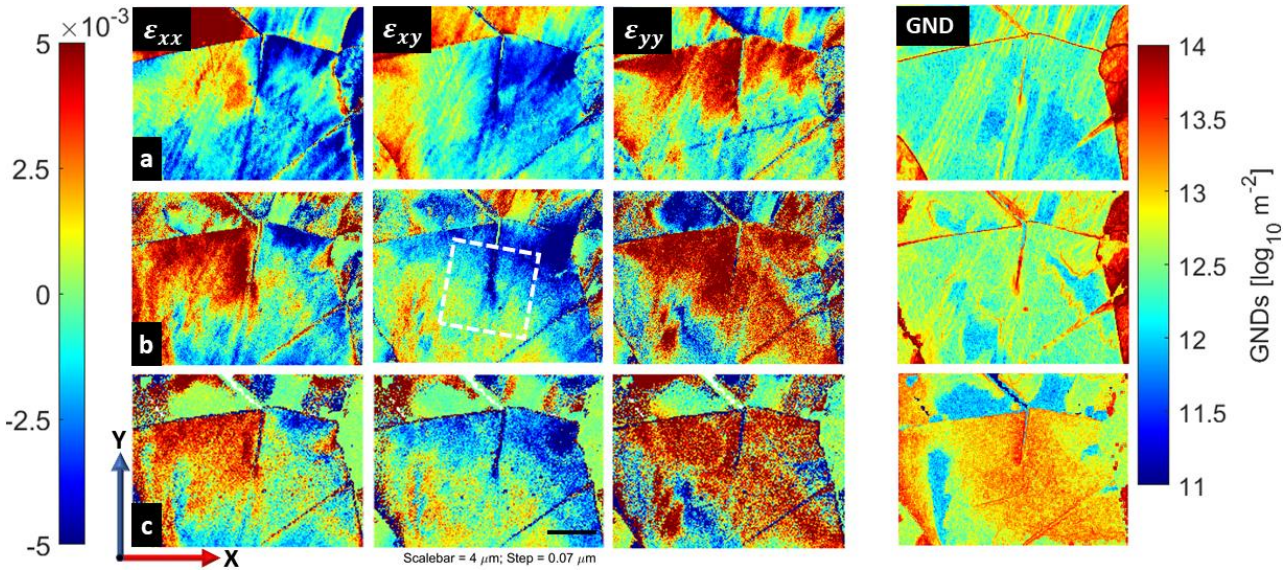


Figure 4-11: Maps of the in-plane components of the elastic strain tensors ($\varepsilon_{xx}$, $\varepsilon_{yy}$ and $\varepsilon_{xy}$) and GND density in the ROI, calculated using HR-EBSD at applied nominal strains of a) 15%, b) 20%, and c) 22%.

The effect of applied strain on the average stress (parallel and perpendicular to the applied loading) in grain (α,2) was investigated. First, the mapped strain field was censored to exclude points that were close to strain concentrations using GND density, i.e. four iterations of removing points with GND density higher than the iteration's mean; the remaining points that comprised 4% of the 33,178 measurement points in each map (Figure 4-12a) with an average MAE of 3.5 x $10^{-4}$, 3.4 x $10^{-4}$, and 3.2 x $10^{-4}$, and PH of 0.74, 0.70 and 0.84 at 15%, 20%, and 22% nominal strain, respectively. The statistical distributions of stress, parallel ($\sigma_{xx}$) and perpendicular ($\sigma_{yy}$) to the direction of loading, are presented in Figure 4-12b as a function of the nominal applied strain. The data describing the stresses relative to the reference pattern is quite scattered. Nonetheless, the mean parallel stress increased with applied nominal strain, whereas there was no significant change in the perpendicular stress.

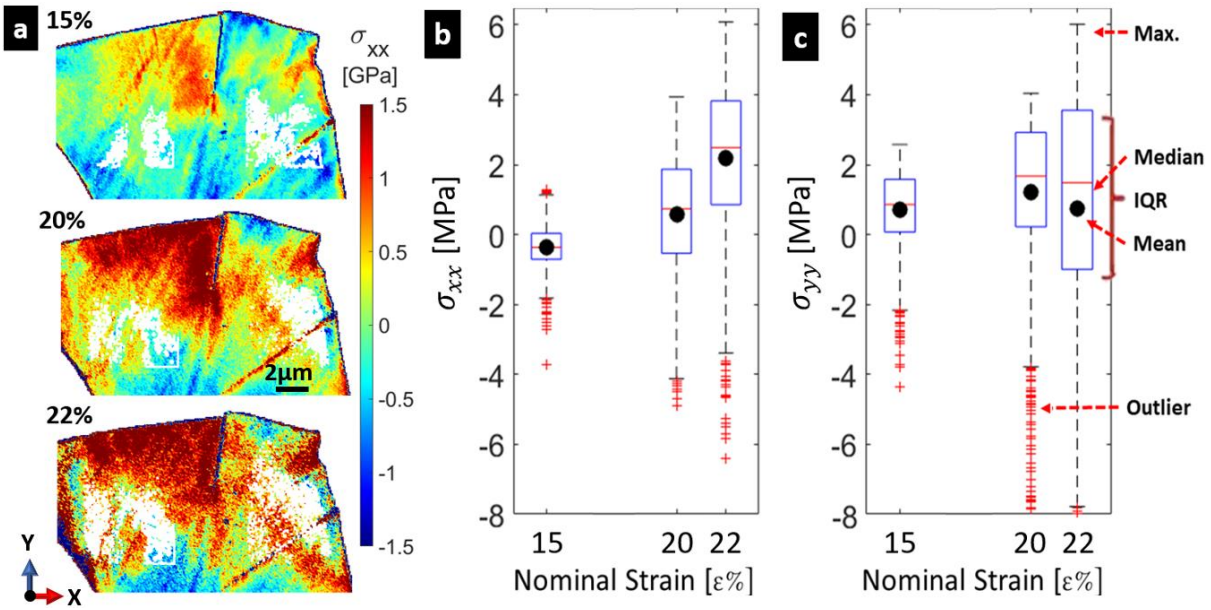


Figure 4-12: Maps of $\sigma_{xx}$ in grain (α,2) at nominal strains of 15% to 22%, obtained using the *Chosen* reference pattern at 15% straining. The white regions show where data for the background stresses have been selected that are remote from stress concentrations (see main text for criteria). The orthogonal stresses $\sigma_{xx}$ (parallel to loading) and $\sigma_{yy}$ (perpendicular to loading) are plotted in b) and c), where the mean, median, and interquartile range (IQR) are shown. Outliers are identified as values 1.5 times more than the interquartile range.

### 4.3.4 *J*-integral analysis

The ABAQUS® solver calculated the *J*-integral (treating the twin as a traction-free interface), assuming plane stress conditions. The mode I and II stress intensity factors (SIF), $K_I$ and $K_{II}$, were then obtained using the interaction integral method implemented natively in ABAQUS® [62,114]. In this analysis, the equivalent domain integral (EDI) [43] was defined by an inner contour that enclosed the twin-tip and outer contours that expanded outwards (in intervals of 3 nodes).

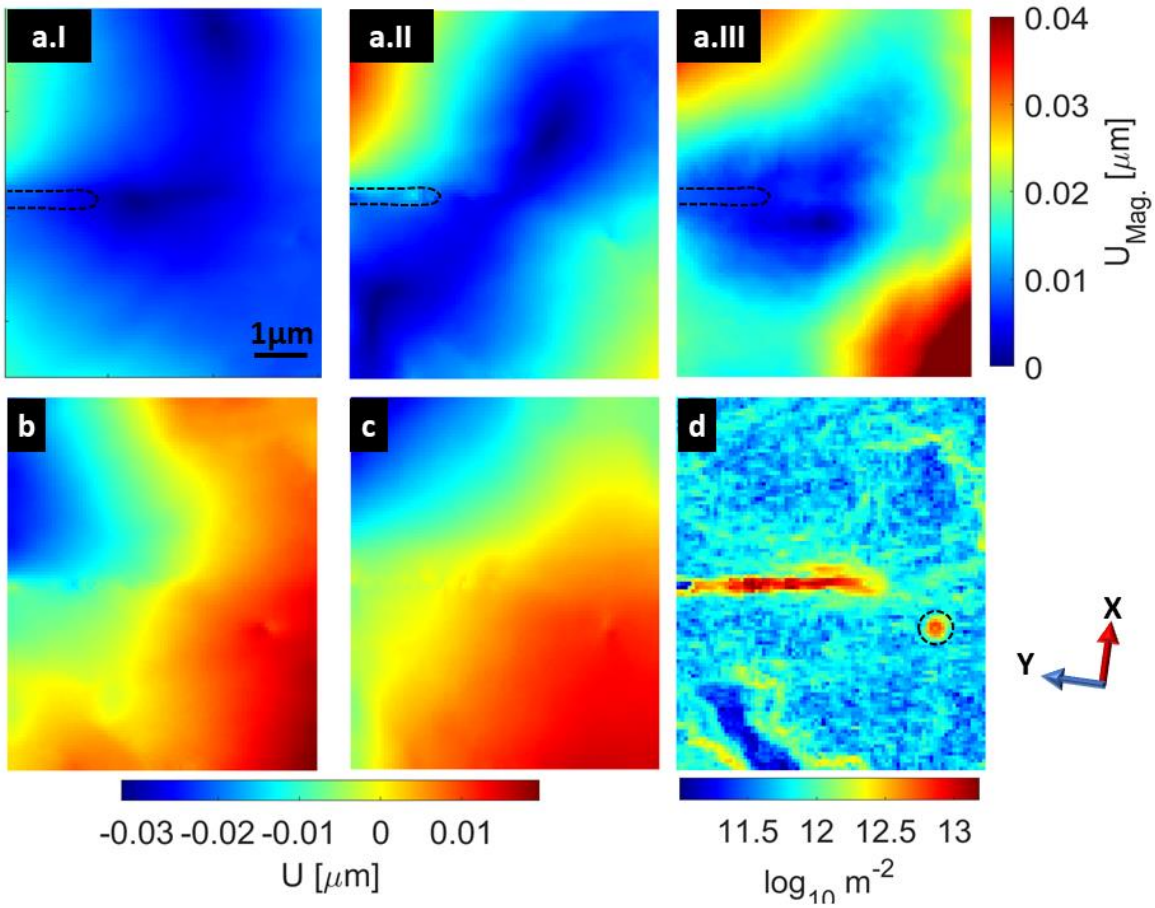


Figure 4-13: (a) Integrated displacement field (displacement magnitude) around the twin-tip (dashed black lines) at applied nominal strains of I) 15%, II) 20%, and III) 22%. Integrated (b) Ux, (c) Uy and (d) GND density at 20% applied nominal strain. The axes X and Y are parallel to those in Figure 4-11.

The *J*-integral analysis is only valid (path independent) under small-scale yielding conditions where excessive plasticity is not present [40,42]. In principle, the convergence of the *J*-integral may be achieved in the region of plastic deformation (i.e., the HRR, Hutchinson [36], and Rice and Rosengren [37], singularity) and beyond where linear elastic behaviour dominates. Inaccurate knowledge of the twin tip location would influence the convergence [79,80,319], but the tip location was quite precisely located, as shown in Figure 4-9. Non-convergence near the twin tip is observed in all the analyses, particularly in regions of high GND density (Figure 4-13d). The presented values of the *J*-integral and the $K_I$ and $K_{II}$ SIFs are the converged results. This is illustrated in Figure 4-14, where the evolution of the *J*-integral as the contour expands from the twin-tip is shown for each applied strain. The *J*-integral stabilises with increasing

domain size, and the stable value was evaluated using the mean and the variance for the values between the 11$^{th}$ and 18$^{th}$ domain (i.e., beyond ~ 1.3 µm from the twin tip) as highlighted in Figure 4-14a. The maximum number of contours (or domain size) was restricted to 22 (~ 2.6 µm) as a further extension of the domain reduced the stability of the convergence due to adjacency to other strain concentrators, such as a $(2\bar{1}\bar{1})[\bar{1}\bar{1}\bar{1}]$ slip band. Table 4-2 summarises the average *J*-integral and the mode I and II SIFs ($K_I$ and $K_{II}$). The values of twin thickness (calculated from the surface width using the twin orientation relative to the surface [320]) and length, correlation peak height (PH), mean angular error (MAE), and the density of geometrically necessary dislocations (GND) evaluated within the displacement integration window are also presented in Table 4-2.

The *J*-integral increased with applied strain between the 1$^{st}$ and 2$^{nd}$ observation stages (15% and 20% strain) and did not change significantly in the 3$^{rd}$ stage (22% strain). The twin thickness increased significantly only between the 1$^{st}$ and 2$^{nd}$ stages. Overall, the twin length increased slightly by roughly 40 nm from an initial length of ~5.6 µm. The mean angular error (MAE) of the EBSPs in the displacement integration window increased significantly in the 3$^{rd}$ observation, with a corresponding decrease in correlation peak height (PH) (Figure 4-14b). This was judged to be due to contamination from deposited carbon caused by the electron-beam-induced decomposition of gaseous hydrocarbons, which can accumulate during the EBSD scan [321]. The effect of this deposition can be seen in contour 13 (~ 1.5 µm from the twin tip) for the 1$^{st}$ observation (Figure 4-14a), which coincides with the visible carbon deposition in the FSD image (Figure 4-6a and Figure 4-13d). As the integration domain expands, it becomes less sensitive to local errors in the displacement field. Nonetheless, the increase in contamination in the 3$^{rd}$ observation increased the noise in the displacement field

and increased the uncertainty in the *J*-integral. The mode I SIF ($K_I$) increased with applied strain, whereas the mode II SIF ($K_{II}$) was almost constant and then increased in the 3rd observation at 22% applied strain (Table 4-2). The mean GND density value was calculated inside the integration window (Figure 4-13) while excluding non-indexed regions from the EBSD map. This GND density increased by a factor of ~3 (i.e., 0.50 ± 0.16 $\log_{10}$ $m^{-2}$) between the first and second observation and by a factor of ~6 (i.e., 0.8 ± 0.14 $\log_{10}$ $m^{-2}$) between the second and third observations.

Table 4-2: Summary of the numerical results for in situ observation of the twin as a function of nominal applied strain.

| Nom. Strain % | Twin Thickness (nm) | Twin Length (nm) | *J* (J $m^{-2}$) | $K_I$ (MPa $m^{0.5}$) | $K_{II}$ (MPa $m^{0.5}$) | GND density ($\log_{10}$ $m^{-2}$) | PH | MAE ($10^{-4}$ rad) |
|---|---|---|---|---|---|---|---|---|
| 15 | 401 ± 11 | 5630 ± 12 | 3.6 ± 0.3 | 0.47 ± 0.09 | 0.66 ± 0.03 | 11.5 ± 0.11 | 0.78 ± 0.01 | 0.8 ± 0.3 |
| 20 | 710 ± 19 | 5678 ± 6 | 11.1 ± 0.9 | 2.71 ± 0.11 | 0.60 ± 0.14 | 11.9 ± 0.12 | 0.69 ± 0.01 | 2.5 ± 0.8 |
| 22 | 736 ± 12 | 5690 ± 6 | 11.0 ± 1.3 | 3.25 ± 0.16 | 1.93 ± 0.14 | 12.7 ± 0.08 | 0.57 ± 0.04 | 8.2 ± 1.8 |

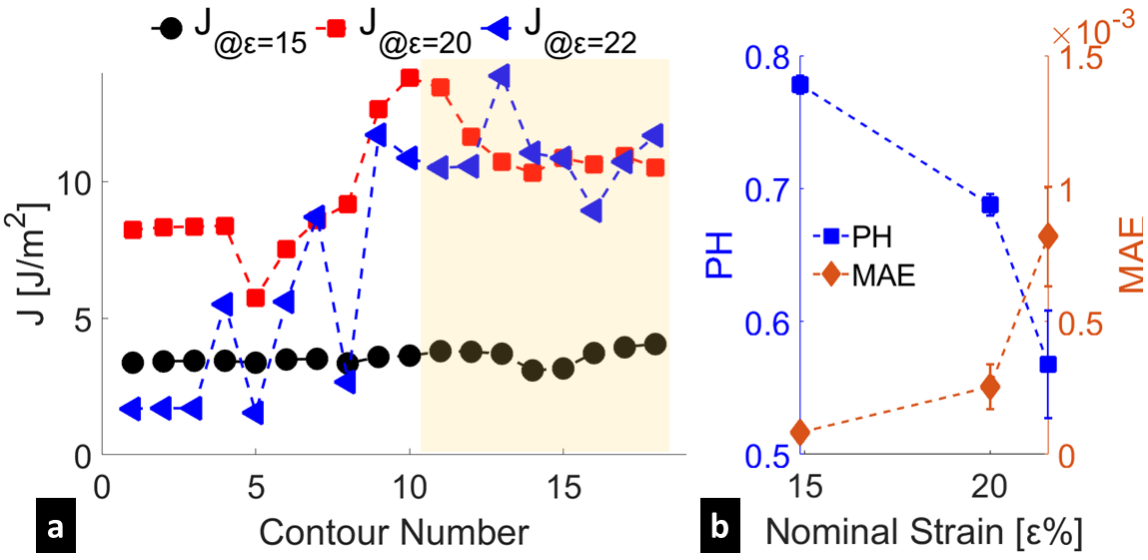


Figure 4-14: (A) Strain energy release rate (*J*-integral) with contour number at nominal strains of 15, 22 and 25%. (B) Mean angular error (MAE) and cross-correlation peak height (PH) as a function of the applied nominal strain.

### 4.3.5 Ex situ analysis of ferrite deformation twins

An ROI was identified in an unloaded specimen with three deformation twins of different thicknesses within the exact ferrite grain (Figure 4-15a). HR-EBSD maps of the stress field (Figure 4-15b) were calculated relative to the least deformed reference pattern ($EBSP_0$) in the grain. The twins, identified by trace analysis as $\sum 3\ (\bar{1}2\bar{1})[\bar{1}\bar{1}\bar{1}]$, have their tips within the grain, with the twin habit plane inclined at 33° to the surface of the specimen. The projection of the twin shear direction is at 77° to the applied loading ($X_{twin}$ in Figure 4-15a). The in situ tests obtained the twin thickness from the measured surface width and twin plane orientation.

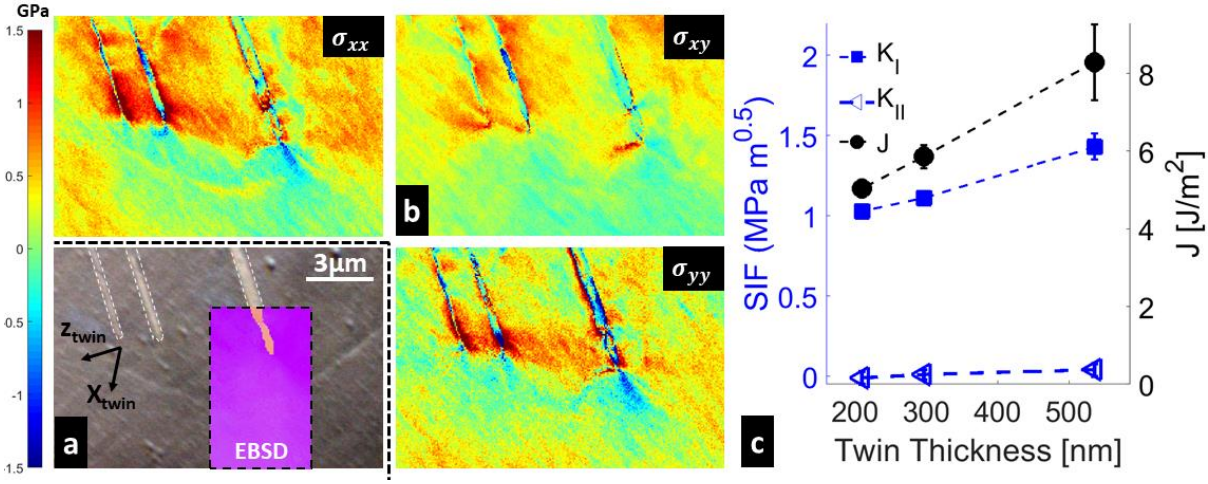


Figure 4-15: a) FSD image (with inset EBSD map of grain orientation) of three $\sum 3\ (\bar{1}2\bar{1})[\bar{1}\bar{1}\bar{1}]$ ferrite deformation twins in age-hardened duplex stainless-steel. b) HR-EBSD calculated stress tensors. c) *J*-integral, and mode I and II stress intensity factors ($K_I$ and $K_{II}$) as a function of twin thickness. Strains were calculated using the least deformed reference pattern ($EBSP_0$) with a mean MAE value of 3.5 ± 0.6 x $10^{-4}$ rad and PH of 0.86 ± 0.02.

Analysis of the *J*-integral for each twin was performed following the rotation of the HR-EBSD data and its integration into the displacement field. As for the in situ analysis, the number of contours (or domain size) was limited to a domain where stable convergence was achieved. The analysis found an increase in J from 5.04 ± 0.07 J $m^{-2}$ to 8.29 ± 0.98 J $m^{-2}$ with increasing twin thickness (Figure 4-15c). Decomposition of the *J*-integral into mode I and mode II SIFs ($K_I$ and $K_{II}$) shows an increase in $K_I$ with increasing twin thickness (from 1.03 ± 0.01 to 1.43 ± 0.08

MPa $m^{1/2}$). Both $K_{II}$ and the GND density are small and nearly constant with twin thickness; between -0.01 ± 0.00 to 0.04 ± 0.01 MPa $m^{1/2}$, and between 11.98 ± 0.22 to 12.17 ± 0.19 $\log_{10}$ $m^{-2}$, respectively.

The *J*-integral obtained from ex situ observations of other intragranular twins analysed by the same method are summarised in Figure 4-16 and detailed in Table 4-3, including orientations, width, thickness (i.e., calculated using the angle between the twin plane and surface). The SIFs were also decomposed from the *J*-integral. The values of $K_{II}$ are generally small for all twins, with no systematic relationship to the value of the *J*-integral. No relation was also found between the mode II SIF and the orientation of the twin (e.g., the orientation of the twin plane normal and shear direction relative to the observed surface). There is a good correlation between $K_I$ and the square root of the *J*-integral (Figure 4-16) since $K_I$ dominates the strain energy field for small $K_{II}$.

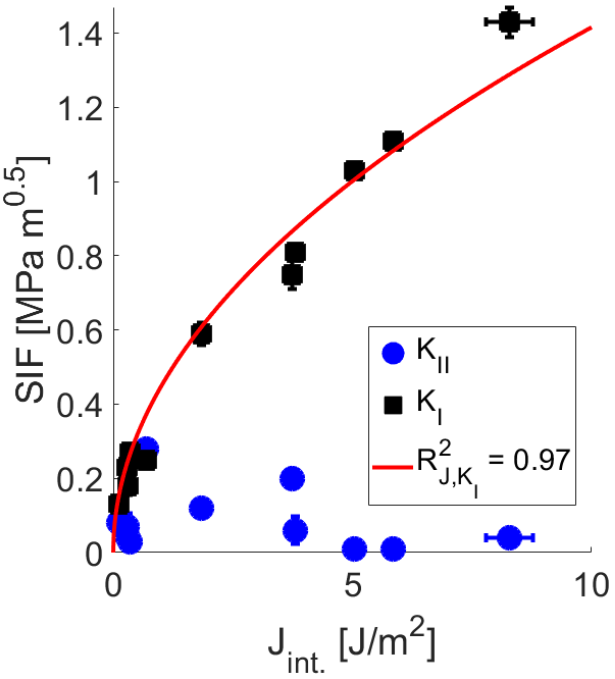


Figure 4-16: The *J*-integral and decomposed stress intensity factors (SIF, $K_I$ and $K_{II}$) obtained by HR-EBSD measurements of the elastic strain field ahead of intragranular ferrite deformation twins in different grains, observed ex-situ with no loading. The fitted relationship is $K_I = \sqrt{0.2J}$ for K in MPa $m^{0.5}$ and J in $Jm^{-2}$.

Table 4-3: Additional Ex Situ Results

| No. | Parent $(\varphi_1, \Phi, \varphi_1)$ | Twin $(\varphi_1, \Phi, \varphi_1)$ | Trace | $J$ (J m$^{-2}$) | $K_I$ (MPa m$^{0.5}$) | $K_{II}$ (MPa m$^{0.5}$) | No. of Contours | Width (μm) | Thickness (μm) | GND density ($\log_{10}$ m$^{-2}$) |
|---|---|---|---|---|---|---|---|---|---|---|
| 1 | (243, 140, 235) | (345, 157, 6) | $[1\bar{1}1](121)$ | 0.12 ± 0.00 | 0.14 ± 0.00 | 0.14 ± 0.00 | 7 | 0.95 ± 0.09 | 0.042 ± 0.013 | 11.85 ± 0.14 |
| | (243, 140, 235) | (345, 157, 6) | $[1\bar{1}1](121)$ | 0.62 ± 0.00 | -0.35 ± 0.00 | -0.03 ± 0.00 | 8 | 1.02 ± 0.10 | 0.086 ± 0.008 | 12.13 ± 0.21 |
| 2 | (332, 128, 313) | (44, 167, 56) | ?? | 3.12 ± 0.00 | -0.78 ± 0.00 | -0.20 ± 0.00 | 8 | 1.10 ± 0.10 | 1.036 ± 0.094 | 11.89 ± 0.09 |
| 3 | (149, 148, 181) | (269, 157, 258) | $[1\bar{1}1](\bar{1}12)$ | 0.35 ± 0.04 | -0.27 ± 0.01 | -0.03 ± 0.00 | 16 | 0.71 ± 0.05 | 0.440 ± 0.031 | 12.32 ± 0.13 |
| 4 | (241, 156, 247) | (55, 155, 25) | $[11\bar{1}](112)$ | 0.92 ± 0.05 | 0.25 ± 0.02 | -0.27 ± 0.03 | 12 | 0.36 ± 0.00 | 0.283 ± 0.001 | 12.12 ± 0.13 |
| 5 | (311, 162, 289) | (190, 143, 227) | $[\bar{1}11](211)$ | 3.80 ± 0.29 | -0.81 ± 0.02 | 0.06 ± 0.07 | 29 | 0.30 ± 0.03 | 0.102 ± 0.01 | 11.65 ± 0.13 |
| | (311, 162, 289) | (142, 149, 158) | $[11\bar{1}](112)$ | 3.75 ± 0.29 | -0.75 ± 0.82 | -0.20 ± 0.05 | 27 | 0.34 ± 0.02 | 0.189 ± 0.011 | 12.27 ± 0.11 |
| 6 | (216, 143, 224) | (341, 163, 21) | $[\bar{1}\bar{1}\bar{1}](\bar{1}2\bar{1})$ | 8.29 ± 0.98 | 1.43 ± 0.08 | 0.04 ± 0.04 | 13 | 0.53 ± 0.08 | 0.422 ± 0.064 | 12.17 ± 0.19 |
| | (216, 143, 224) | (341, 163, 22) | $[\bar{1}\bar{1}\bar{1}](\bar{1}2\bar{1})$ | 5.86 ± 0.29 | 1.11 ± 0.03 | 0.01 ± 0.03 | 12 | 0.30 ± 0.04 | 0.238± 0.032 | 12.04 ± 0.23 |
| | (216, 143, 224) | (341, 163, 22) | $[\bar{1}\bar{1}\bar{1}](\bar{1}2\bar{1})$ | 5.04 ± 0.07 | 1.03 ± 0.01 | 0.01 ± 0.04 | 13 | 0.21 ± 0.04 | 0.167 ± 0.035 | 11.98 ± 0.22 |
| 7 | (292, 144, 305) | (83, 169, 38) | ?? | 1.81 ± 0.00 | -0.56 ± 0.00 | 0.27 ± 0.00 | 8 | 0.36 ± 0.09 | 0.327 ± 0.082 | 14.77 ± 0.06 |

## 4.4 Discussion

The in situ analysis focused on a ferrite grain in which a deformation twin propagated slightly as the load was increased and thickened noticeably (Figure 4-9c). The thickening of the twin was accompanied by the thickening of the slip band associated with the twin. This indicates that the two features interacted as the grains deformed under the applied tensile strain.

The average change measured in the background stress in the ROI, parallel to the applied remote tensile loading, was about 2.6 MPa (Figure 4-12b), which is small compared to the change in applied tensile stress of 72.5 MPa (Figure 4-5a). The points used to calculate Figure 4-12b were selected to be remote from stress concentrations (Figure 4-12a) to monitor the response of the background stress to tensile loading and to verify the set-up stability as correlated changes in $\sigma_{xx}$ and $\sigma_{yy}$ would indicate sample movement. Systematic bias might arise from microscope stability issues or sample movement and could induce errors of up to $10^{-3}$ strain (i.e., ~200 MPa) [322]. A more negligible bias might arise from changes in EBSP acquisition configuration (between observations) induced by surface movements due to sample necking. However, this would be expected to affect both stress components similarly.

The observed increase in mean background $\sigma_{xx}$ with negligible change in the mean background $\sigma_{yy}$ shows the tensile background stress increased with increasing applied tensile strain. The significant difference between the increase in mean background $\sigma_{xx}$ and the applied stress is due to the residual stresses that arise in ferrite (compression) and austenite (tension) due to the difference in the thermal expansion of ferrite and austenite in duplex steel when cooled from elevated aging temperature [323]. In addition, Significant differences have been reported between the average stress in a plastically yielding grain and the average stress on a polycrystalline bulk sample [324,325]. The elevated levels of stress at grain

boundaries (Figure 4-12a) show that the average stress on the grain is much higher than the background stress. Strain hardening in duplex stainless steel occurs primarily in the austenite phase [326], reducing the stress carried by ferrite grains.

The in situ study finds that the mode I SIF increased with twin thickness. The mode II SIF did not change significantly between the 1st and 2nd observations but increased substantially in the 3rd observation. There was a corresponding increase in the mean GND density ahead of the twin by a factor of 3 between the first and second observations and a larger factor of 6.3 between the second and third observations. The GND density should be considered the lower plasticity limit since EBSD cannot probe the total dislocation density, including statistically stored dislocations. The increased GND density indicates an increase of the plastic deformation (i.e., zone of interaction between residual and mobile dislocations) ahead of the twin-tip, and this would be consistent with the shear strain of twin growth [267,327]. The twin shear direction is not parallel to the trace of the twin, but the shear deformation in the plane of the analysed surface is represented by $K_{II}$, which increases correspondingly. The current 2D analysis may lack sufficient sensitivity to detect the change in $K_{II}$ between the 1st and 2nd observations.

The ex situ observation of twins of the same orientation within the exact grain also reveals a strong correlation between $K_I$ and twin thickness (Figure 4-15c). The ex situ values of $K_{II}$ are minor compared to the in situ study. Low values of $K_{II}$ indicate that the twin shear has been relaxed by removing the mechanical load, leading to elastic recovery of the surrounding grain, leaving a direct relationship between the mode I SIF and the strain energy release rate, as indicated in Figure 4-16. However, de-twinning is prevented by the pinning effect of the residual dislocations at the twin-parent boundaries [241]. The mode I stress intensity factor,

$K_I$, which dominates the description of the strain field when $K_{II}$ is small, is also expected to be decreased by removing the applied load. This agrees with studies where magnitude increased with the twin length as seen between intervals. This 'step-wise' mechanism of growth – also observed by Song and Gray [328] and Liu *et al.* [255]– explains the surface irregularity occasionally seen at one or both sides of the twin-parent interface (e.g., Figure 4-8) and the straighter twin boundaries observed in shock-loaded samples. The tip movement leaves residual dislocation in the vicinity of the newly created twin lamella.

The difficulty of detailed interpretation of these two-dimensional results is apparent, and no attempt will be made – using the current analysis – to reconcile current ideas about twin propagation in BCC materials (e.g., [329,330]). The limitations are mainly because the current 2D analysis provides only a semi-quantitative assessment of the 3D deformation field. For instance, differences between the measured fields of twins of different orientations cannot be quantified using the current analysis; for an inclined twin plane, where the twin out-of-plane shear is significant, this shear will contribute to the $K_I$ field measured in a 2D analysis [331]. This is without considering the probable existence of a second twin, as highlighted in Figure 4-8. Nonetheless, the observations are consistent with the simulations that the stress field of twins is related to their ellipsoidal shape and that the magnitude of the stress concentration increases with twin lateral thickness [243].

The significant difference in the magnitude of the elastic fields from in situ and ex situ observations shows that ex situ analysis of unloaded material does not measure the conditions that pertain at the tip of a propagating twin and cannot quantify the criterion for twin propagation. In situ analysis methods, such as HR-EBSD, are required to quantify the critical elastic strain field around the twin as it propagates. The 2D analysis methodology

presented here could be applied to investigate the criterion for twin growth in observations of carefully selected twins (e.g., where the twin shear is parallel to the surface). Twins of more general orientations, with a similar 3D analysis of the elastic strain field, might be examined using a technique such as Laue microdiffraction that, unlike HR-EBSD, can measure absolute strain [108–110,332].

It is worth noting that the crack-like *J*-integral analysis strictly requires the contour to start and end from a traction-free surface, and therefore does not consider any internal pressure that might be exerted at the twin-parent boundary. Thus, to maintain the path independence of the integral, the *J*-integral definition of the contour path should be extended to include the twin-parent boundary traction [333] (similar to hydraulic fracture [334]), as described by the 2nd term of the equation (4—12) and Figure 4-17.

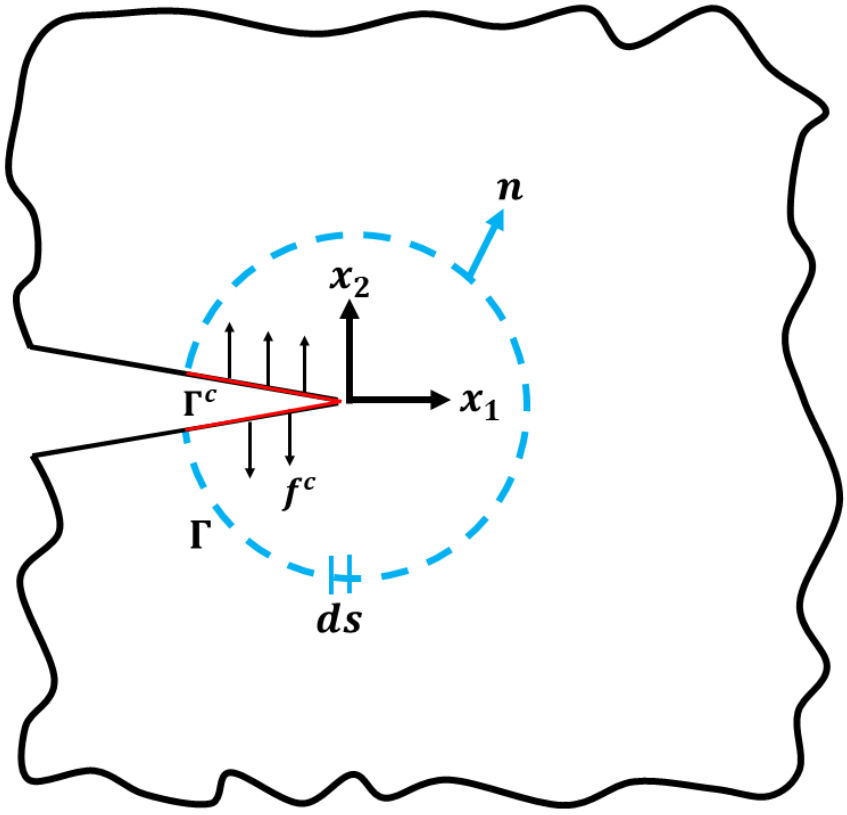


Figure 4-17: An arbitrary contour (Γ) encloses the deformation field at the twin tip with traction at the twin boundaries.

$$J = \int_{\Gamma} \left( W dx_2 - \sigma_{ij} n_j \frac{\partial u_i}{\partial x_1} ds \right) - \int_{\Gamma_c} \mathrm{f}^c \frac{\partial u_i}{\partial x_1} ds, \qquad W = \int_0^{\varepsilon_{ij}} \sigma_{ij} d\epsilon_{ij} \qquad 4—12$$

where $\sigma_{ij}$ and $\epsilon_{ij}$ are the stress and strain tensors, respectively, $W$ is the strain energy density, $u_i$ are the displacement vector components, $n_j$ are the components of the unit vector normal to $\Gamma$, $ds$ is the length increment along the contour $\Gamma$, $\mathrm{f}^c$ is the twin surface traction vector, and $\Gamma_c$ is the portion (in red in Figure 4-17) of the arbitrary contour ($\Gamma$) that contains the non-equilibrated (loading) forces that arise from the twin at the twin-matrix boundary/interface.

To address the parent-twin boundary traction, we need to look at the mechanism for the lateral expansion of twins, which remains a topic of debate [260,335], and there are no available three-dimensional models for twin propagation that relate the twin-tip morphology to twin propagation and thickening [157], and the interaction between the residual dislocations at twin-parent grain boundary during thickening [266] which can be then expressed as an explicit force, i.e., $\mathrm{f}^c$. Recently, an iterative model has been suggested. This method assumes a linear proportionality of stress at the interface to the twin thickness with a potential energy barrier as the rate-determining step [267,336]. For the current in situ analysis, it is judged by the *J*-integral convergence that there is a minimal effect of neglecting $\mathrm{f}^c$ on the path independency could be because the internal stresses (at the twin boundary) arising from the twin are balanced by the surface traction ($T_i$) [337]. As for the ex situ analysis, removal of the load leaves the twin-parent grain boundary in an equilibrium state with no force available for twin thickening or detwinning (i.e., $\mathrm{f}^c$=0).

There are arguments for the insufficiency of an elastic field-based criterion (i.e., energy release rate) for twin nucleation and growth as a criterion for stored (dislocation structure)

energy that have been recently proposed [244,338]. Indeed, the local field near the twin-tip is further complicated by plastic deformation. However, the *J*-integral analysis describes the elastic strain field in the wider envelope of material that acts on the twin tip. This field mediates between the applied remote loading and twin propagation to provide a local boundary description of the critical conditions, which can inform more detailed modelling. The conservation integrals treatment (as amplified by Eshelby [294]) is straightforward and without fitting approaches based on assumed fields [339,340].

## 4.5 Conclusion

The strain fields ahead of ferrite deformation twins have been quantified in a study of the ferrite matrix of Zeron 100 (25%Cr, 7%Ni) duplex stainless steel (DSS), which was age hardened for 100 hours, then deformed in tension and characterised in situ and ex situ by high-resolution electron backscatter diffraction (HR-EBSD). For the first time, the elastic strain field surrounding the twin-tip was integrated into a 2D displacement field and injected into a plane stress finite element simulation (ABAQUS®) to calculate the elastic strain energy release rate (*J*-integral), which was then decomposed into mode I and II stress intensity factors.

As perceived from these surface measurements, the strain field described by the mode I stress intensity factor increased with twin thickness. This is judged to accommodate the dimensional change of the ellipsoidal twin. The strain field, shown mainly by the in-plane shear mode II stress intensity factor, relaxed significantly when unloaded in the ex situ studies compared to the in situ case. Some current limitations of the 2D analysis are discussed, which aims to provide an experimental methodology to quantify the fields that describe the local boundary conditions for twin thickening and propagation.

# Chapter 5. HR-EBSD analysis of strain localisation ahead of intragranular slip bands in ferrite

Contents

## 5.1 Introduction

Deformation twins, slip bands and micro-cracks are deformation-induced features (DIFs) that can locally concentrate stress and strain in the microstructure of crystalline materials, particularly metals. Understanding their interactions, distribution, and accumulation is critical for the microstructural engineering of materials [341]. Few experimental studies have quantified the localised stress fields of DIFs, despite their importance to crystal plasticity finite element (CPFE) microstructure-sensitive models for mechanisms such as fatigue crack propagation [338,342,343] and deformation twin propagation [267]. CPFE can, to some extent [344], predict the local stress and strain distributions but currently omits finer details at the micro-scale [345–347]. The emerging phase-field approach is a promising way to simulate localised fields [348,349], and improved experimental methods to quantify the fields of DIFs, principally in situ studies, are needed to inform, validate, and calibrate such models.

Slip band height extends to the surface, a marking that appears when the active slip plane intersects the sample-free surface due to the difficulty of dislocation movement [350]. Thus, contrary to 2D line defects, the field at the slip-band tip is due to three-dimensional interactions where the slip band extrusion stretches the grain surface and stimulates intervals of dislocation blooming/avalanche from an active source, i.e., a Frank-Read source lying in the slip plane and pinned at both ends [11,351]. The stress concentration ahead of a slip band is important as it affects the transfer of plastic deformation across grain boundaries [296,297,352], and an understanding of this is needed to study yield and inter/intra-granular fracture [313,353,354], as the concentrated shear at the slip band can nucleate cracks in the plane of the slip band [258,355]. Persistent slip bands (PBS) that lead to intragranular fatigue crack initiation and growth may also form under cyclic loading conditions [356,357]. Thus, it

is crucial to quantify the local deformation fields associated with their propagation to properly characterise slip bands and validate mechanistic models for their interactions with microstructure. However, little attention has been given to intragranular slip band propagation (i.e., in the absence of grain boundary interaction).

The long-range stress field (i.e., the elastic strain field) around the tip of a stress concentrator, such as a slip band, can be considered a singularity, equivalent to that of a crack [358,359]. This singularity can be quantified using a path independent integral since it satisfies the conservation laws of elasticity. Slip bands form due to plastic deformation, and in plasticity, the analysis of the force on a dislocation considers the two-dimensional nature of the dislocation line defect. General definitions of the Peach–Koehler configurational force ($P_{kj}$) (or the elastic energy-momentum tensor [32]) on a dislocation, in the arbitrary $x_1$, $x_2$, $x_3$ coordinate system (Figure 1), decompose the Burgers vector ($b$) to orthogonal components [360], which leads to the generalised definition of the *J*-integral in equations (5—1) and (5—2). For a dislocation pile-up, the *J*-integral is the summation of the Peach–Koehler configurational force of the dislocations in the pile-up [360–362] (including out-of-plane, $\overrightarrow{b_3}$ [40]).

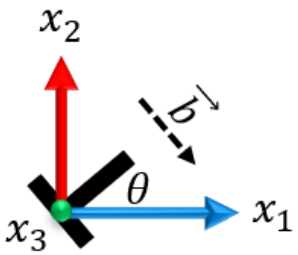


$$J_k = \int_S P_{kj} n_j dS = \int_S (W_s n_k - T_i u_{i,k}) dS \qquad 5—1$$

$$J_k^x = R_{kj} J_j, \qquad i,j,k = 1,2,3 \qquad 5—2$$

where $S$ is an arbitrary contour around the dislocation pile-up with unit outward normal $n_i$, $W_s$ is the strain energy density, $T_i = \sigma_{ij} n_j$ is the traction on $dS$, $u_i$ are the displacement vector components, $J_k^x$ is $J$-integral evaluated along the $x_k$ direction, and $R_{kj}$ is

a second-order mapping tensor that maps $J_k$ into $x_k$ direction. This vectorial $J_k$-integral leads to numerical difficulties in the analysis since $J_2$ and, for a three-dimensional slip band or inclined crack, the $J_3$ terms cannot be neglected.

This is also of practical importance in the direct asymptotic analysis of the geometrically induced singular stress concentrations at cracks and notches in elastic and inelastic materials [45]. Budiansky and Rice [46] and Hussain *et al.* [363] argued that for two-dimensional defects (i.e., $J_3$ neglected), the two components of the $J_k$ vector represent specific energy release rates related to the movements of the crack surfaces along the $x_1$-axis and the $x_2$-axis, respectively. However, if a contour enclosing a single crack tip is considered, the calculated energy release includes the contribution to $J_2$ arising from the traction-free surface. This will make $J_2$ path dependent [364], although it can still be related to the stress intensity factors as shown in equations (5—3) to (5—5) by treating $J_k$ as vectors. With vectorial $J_k$, the values of $K_{I,II,III}$ can be calculated using the Young's ($E'$) and shear ($\mu$) moduli but this method does not capture compressive fields, which is critical to the description of mode I loading. Thus, to simplify the *J*-integral analysis in a way that makes $J_1$ precisely the energy release rate, whilst avoiding the difficulty of the physical interpretations of $J_2$ and $J_3$ [45,46,363–367], the field can be resolved to a coordinate system consistent with the crack or slip band geometry (Figure 5-1) and its direction of propagation. Note that typically, a 'three-dimensional' $J$-integral analysis in the finite element method is achieved as a series of two-dimensional approximations at nodes along the (curved or straight) crack front, dealing with the 3D field in layers of $x_1$ and $x_2$ that are one element thick [43,58,368]; thus, $J_3$ is typically disregarded.

$$K_I = \frac{\sqrt{E'}}{2}\left[\sqrt{J_1 - J_2 - J_3} + \sqrt{J_1 + J_2 - J_3}\right] \qquad 5—3$$

$$K_{II} = \frac{\sqrt{E'}}{2}\left[\sqrt{J_1 - J_2 - J_3} - \sqrt{J_1 + J_2 - J_3}\right] \quad 5—4$$

$$K_{III} = \sqrt{2\mu J_3} \quad 5—5$$

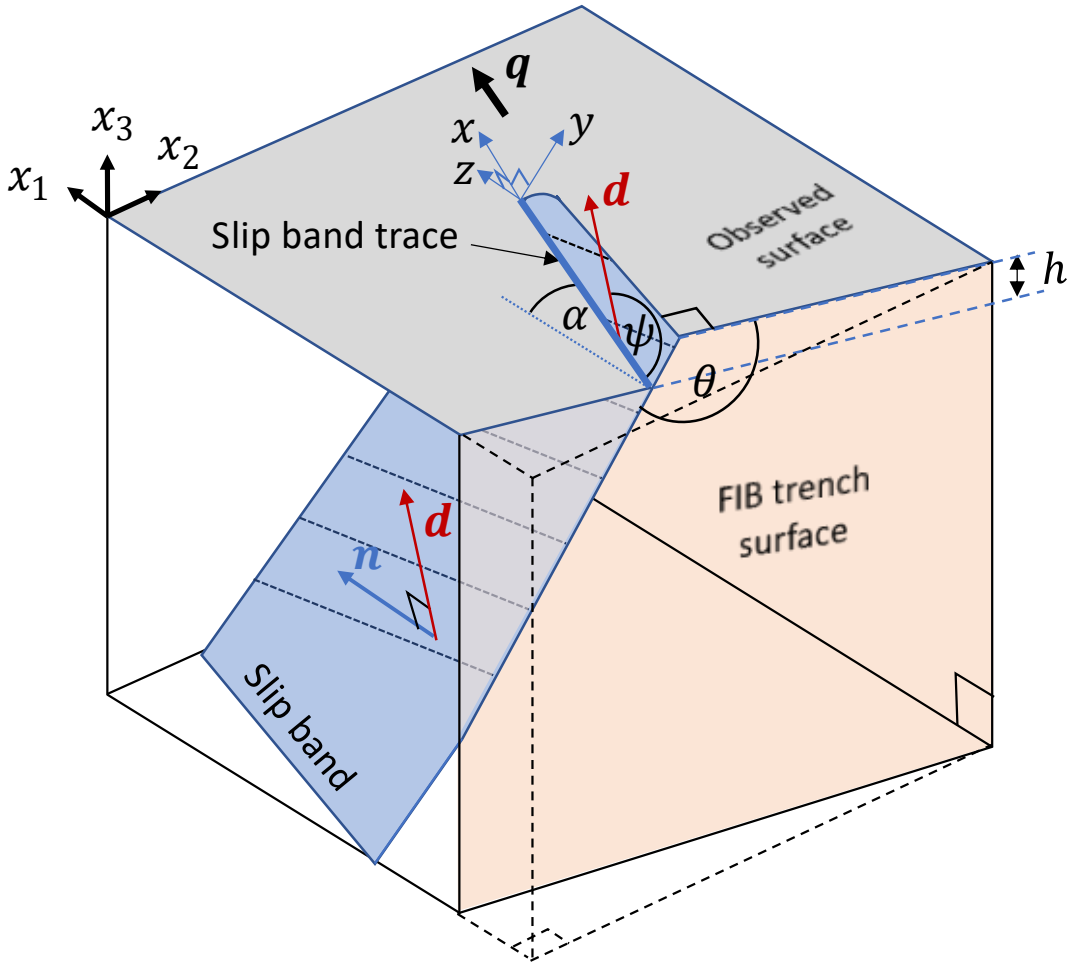


Figure 5-1: Schematic of a slip band relative to the measurement axes ($x_1$, $x_2$, and $x_3$), and axes related to the slip-band ($x$, $y$, and $z$), showing the angles that describe the relationship between these axes and the traces of the slip band ($\alpha$, $\theta$), and the inclination angle ($\psi$) of the slip trace ($x$) and the slip ban direction ($d$) relative to the surface. $h$ is the slip band height, and $q$ is the slip band propagation direction assumed for *J*-integral calculation when using the virtual extension method [38]. $n$ is the slip band plane normal.

The analysis of energy release rates cannot distinguish between the portions contributed by opening and shearing modes, which would be a disadvantage when studying mixed-mode crack propagation, for example. However, this singular $J$-integral can be related to the three-dimensional elastic stress intensity factors using a mode-decomposition technique such as

the interaction integral method [62]. The elastic strain field may then be described in terms of mixed-modes of mode I (tensile/compression), mode II (in-plane shear) and mode III (out-of-plane shear). In fracture mechanics, their interactions can affect the direction of propagation [369]. In plasticity, quantifying the fields of slip bands to extract the magnitudes of the shear modes II and III may aid the interpretation of criteria for slip band propagation and slip band interactions with microstructure features such as precipitates, inclusions, and grain boundaries.

This work aims to quantify the full elastic strain field around mechanically loaded slip bands, observed in situ, using high-resolution (HR) electron-backscatter diffraction (EBSD), which has the necessary spatial resolution and sensitivity to measure the field close to the surface. Previously, the *J*-integral and decomposed stress intensity factors could be used to analyse the *in-plane* elastic strain field (Chapter 4) of a surface observed by HR-EBSD. Here, the full elastic strain field is quantified using the *J*-integral (implemented in the finite element method) as a descriptor for the modes of deformation that contribute to the stress field. This chapter describes the experimental methodology, the HR-EBSD analysis, and the finite element integration of the strain field to the equivalent three-dimensional displacement field, from which the *J*-integral analysis is performed. With the assumption of small-scale plasticity, the *J*-integral is decomposed into the linear elastic stress intensity factors to express deformation modes. The analysis has been applied in a series of in situ studies, comprising an incipient slip band, an array of slip bands, and the loading/unloading of a slip band in ferrite (body-centred cubic) grains that comprise the matrix of an age-hardened duplex stainless steel.

## 5.2 Experimental method

### 5.2.1 Material and in situ mechanical deformation

The sample from a large (~200 mm thickness) forging of Zeron 100 duplex stainless steel (25% Cr, 7% Ni, 3.6% Mo, 0.7% Cu, 0.7% W, 0.22% N, wt.% nominal composition), measuring 1.5 x 12 x 0.8 $mm^3$, was aged in the air at 475°C for 100 hr. The surface for observation (1.5 x 12 $mm^2$) was ground using silicon carbide papers (100 to 4000 grit), polished on medium (PSU-M) pads with Kemet diamond compounds (9 to 0.25 µm), then a Nap-type cloth with colloidal silica suspension for 1 hour to mirror-finish, before ultrasonic cleaning for 20 minutes each in acetone, ethanol, and deionised water with final drying by hot air.

Mechanical deformation was done in 3-point bending (9 mm span) using a 2 kN Deben® 70°pre-tilted loading stage within a Carl Zeiss Merlin FEG-SEM. The chamber and stage were plasma cleaned and purged for 15 hours before testing the specimen at a displacement rate of 1 mm $min^{-1}$ (Figure 5-2a and b). The test was paused (positions marked by dotted red lines in Figure 5-2c) at fixed displacement to acquire electron backscatter patterns (EBSPs). The examined locations were selected by secondary electron (SE) and back- and fore- scatter electron (VFSD, Virtual Forward-scattered Electron Detector [370]) imaging. Given the sample dimensions and ferrite grain sizes, the selection of the slip bands to analyse was not influenced by the nominal distribution of strain and stress across the sample. Instead, the focus was on finding intragranular slip bands with a localised field that did not interact with other stress raisers, such as other slip bands, grain boundaries or phase boundaries.

In situ mapping was done by collecting an array (800 x 600) of EBSPs in a conventional EBSD setup employing a Bruker eFlash CCD camera with 10 nA/20 kV beam conditions, 100

millisecond exposure time per pattern, and 75 nm step size. These conditions were selected as being practical with little drift [206,207], that give Kikuchi bands with sharp contrast [154], and adequate step size [371] and pattern binning [207] for dislocation type convolution. Some load relaxation (<13%) occurred during the pattern acquisition.

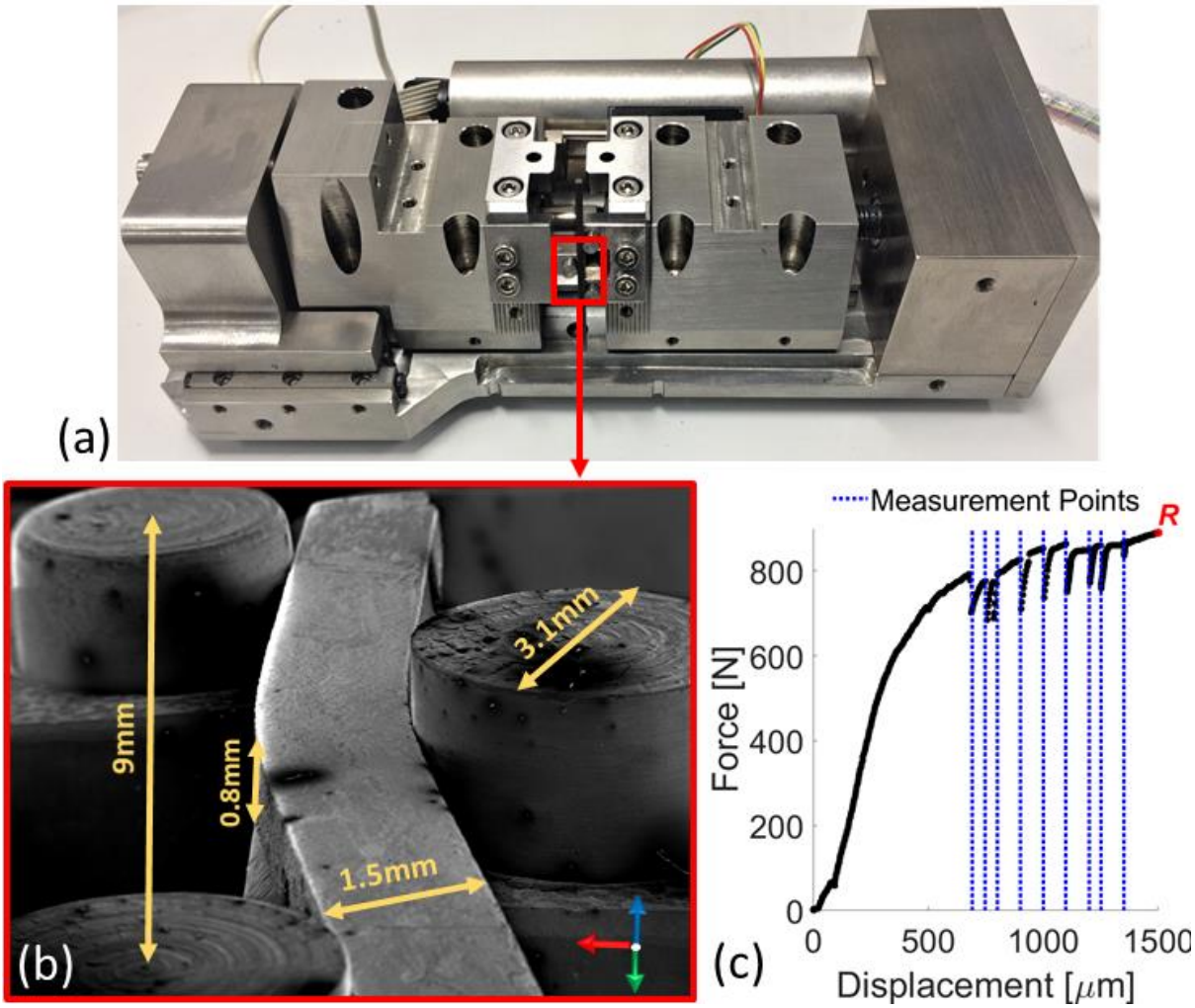


Figure 5-2: (a) 2 kN Deben® 70° pre-tilted mechanical loading stage for in situ EBSD. A schematic for the 3-point bending grip is in Appendix (5.A) – Additional figures. (b) Secondary electron image of the age-hardened duplex stainless-steel sample deformed in 3-point bending. (c) Applied force and measured displacement, with blue-dotted lines marking the in situ collections of electron backscatter diffraction maps. The sample was unloaded at point R for ex situ observation.

After a total applied monotonic displacement of 1.5 mm (red R in Figure 5-2), the sample was unloaded and mounted on an aluminium stub, and then ex situ EBSD mapping of selected features was done by collecting EBSPs using the same settings. Selected slip bands were then

sectioned orthogonally to their trace and the surface, using a Zeiss Auriga dual-beam SEM-FIB system that has a Schottky field emission Gemini electron column coupled with an Orsay Physics 'Cobra' Ga+ ion FIB with 1 nA/ 30 kV, after depositing a protective Pt layer on the surface at 240 pA/ 30 kV. The milled surface was observed using in-lens secondary electron (SE) imaging (Figure 5-1).

### 5.2.2 HR-EBSD analysis

These EBSPs were then used for HR-EBSD analysis through an objective process (Chapter 3), selecting the least strained reference pattern (i.e., the *Chosen* $EBSP_0$), using the empirical relation between MAE and PH to identify the reference pattern with the highest PH and lowest MAE. The spatial maps were segmented into grains, using a 5° misorientation criteria via MTEX [372]; this shows that the ferrite grains are massive compared to the austenite and contain subgrains with low-angle grain boundaries (>2°). These low-angle grain boundaries have a high GND (geometrically necessary dislocation) density content due to low indexing from diffraction pattern overlaps as the probed volume extends across the boundary [373]. Choosing a reference pattern within these subgrains to perform HR-EBSD on the parent grain affects the rotation components but does not influence the strain components due to the remapping on the $2^{nd}$ iteration [211]. Pattern centre shifts due to beam movement during EBSP acquisition were minimised using AstroEBSD [171]. Changes in the sample topography do not affect the strain due to the remapping in the $2^{nd}$ cross-correlation iteration [374] but may lead to reduced signal by shadowing in extreme cases [128].

The 3D elastic deformation tensor was calculated from the measured pattern shifts, assuming zero stress normal to the surface [375] and was decomposed to the lattice rotation and elastic deviatoric strain at an estimated strain sensitivity of $\pm 10^{-4}$ [156,163]. Deformation can affect

the correlation quality and, consequently, the MAE by blurring the EBSP, so inadequate quality points (PH < 0.3 and MAE > $10^{-3}$ rad [128]) were removed from the map. These did not exceed 0.1% of the map area.

### 5.2.3 Local Schmid factor by HR-EBSD ($xSF$)

For interpretation of the plastic deformation, it is helpful to determine the Schmid factor for each slip system in the grain. This requires knowledge of the stress acting within the grain. Uniaxial stress cannot be assumed due to the multiaxial deformation of the plastic bending of the beam. However, the full elastic stress field is obtained in the sample frame using HR-EBSD. The GND density may be used to identify strain concentrations, and such outliers, including the sub-grain boundary, were removed from the stress map. Using the remaining points (<40% of the total), the normalised mean values of the stress components (i.e., $\sum\|\sigma_{ij}\| = 1$) were used to determine the local stress state of the grain. The matrix of the normalised stress components was rotated to the crystal frame using a rotation matrix ($R_{\varphi_1,\Phi,\varphi_2}$) constructed from the Euler angles ($\varphi_1, \Phi, \varphi_2$) of the reference pattern ($EBSP_0$), as in equation (5—6), to construct a loading direction matrix ($r$), as in equation (5—7). From this, the HR-EBSD based Schmid factor ($xSF$) in the grain was calculated – using MTEX [96] – for the $i$th slip system's plane normal ($n$) and shear direction ($d$) (Figure 5-1). These were ranked according to their probability of occurrence, which was determined by the magnitude of the Schmid factor. The tracing algorithm is in section 4.2.2, and an extended introduction to this analysis with other examples is available in Appendix (5.B) – HR-EBSD based Schmid factor.

$$R_{\varphi_1,\Phi,\varphi_2} = \begin{bmatrix} \cos\varphi_2 & -\sin\varphi_2 & 0 \\ \sin\varphi_2 & \cos\varphi_2 & 0 \\ 0 & 0 & 1 \end{bmatrix} \begin{bmatrix} 1 & 0 & 0 \\ 0 & \cos\Phi & -\sin\Phi \\ 0 & \sin\Phi & \cos\Phi \end{bmatrix} \begin{bmatrix} \cos\varphi_1 & -\sin\varphi_1 & 0 \\ \sin\varphi_1 & \cos\varphi_1 & 0 \\ 0 & 0 & 1 \end{bmatrix} \quad 5—6$$

$$r = \left\| R_{\varphi_1,\Phi,\varphi_2} \sigma_{ij} \, R^T_{\varphi_1,\Phi,\varphi_2} \right\| \qquad 5—7$$

$$xSF_i = \left| \frac{r.n^i}{|r||n^i|} \cdot \frac{r.d^i}{|r||d^i|} \right| \qquad 5—8$$

### 5.2.4 Characterisation of dislocations by GND density estimation

Plastic deformation by dislocations in the body-centred cubic ferrite crystal can be characterised by 28 characteristic edge or screw dislocation types (4 <111> screw dislocations plus 24 edge dislocations of $<\bar{1}11>\{110\}$ and $<11\bar{1}>\{112\}$; the <111> {123} dislocations were neglected as they are rarely activated [303]), tabulated in Table 5-1. GND density estimation using HR-EBSD data can resolve the density of individual dislocation types [371,376,377].

Table 5-1: Description and labelling of the 28 characteristic edge and screw dislocations for body-centred cubic (BCC) ferrite, where $b$ is Burgers vector and $t$ is the line vector (parallel to $b$ for screw dislocations, and perpendicular to $b$, i.e., $t \cdot b = 0$ for edge dislocations). For dislocations of screw character, the Burgers vector is parallel to the dislocation line.

| Label | Edge | | Label | Edge | | Label | Edge | | Label | Screw |
|---|---|---|---|---|---|---|---|---|---|---|
| | $b$ | $t$ | | $b$ | $t$ | | $b$ | $t$ | | $b$ |
| 1 | $[\bar{1}11]$ | $[\bar{1}1\bar{2}]$ | 9 | $[\bar{1}11]$ | $[211]$ | 17 | $[1\bar{1}1]$ | $[\bar{1}\bar{1}0]$ | 25 | $[1\bar{1}1]$ |
| 2 | $[1\bar{1}1]$ | $[\bar{1}12]$ | 10 | $[\bar{1}\bar{1}\bar{1}]$ | $[\bar{2}11]$ | 18 | $[11\bar{1}]$ | $[0\bar{1}\bar{1}]$ | 26 | $[\bar{1}\bar{1}\bar{1}]$ |
| 3 | $[1\bar{1}1]$ | $[\bar{2}\bar{1}1]$ | 11 | $[1\bar{1}1]$ | $[121]$ | 19 | $[11\bar{1}]$ | $[101]$ | 27 | $[\bar{1}11]$ |
| 4 | $[11\bar{1}]$ | $[2\bar{1}1]$ | 12 | $[\bar{1}\bar{1}\bar{1}]$ | $[1\bar{2}1]$ | 20 | $[\bar{1}11]$ | $[110]$ | 28 | $[11\bar{1}]$ |
| 5 | $[\bar{1}11]$ | $[12\bar{1}]$ | 13 | $[\bar{1}11]$ | $[01\bar{1}]$ | 21 | $[1\bar{1}1]$ | $[011]$ | | |
| 6 | $[11\bar{1}]$ | $[1\bar{2}\bar{1}]$ | 14 | $[1\bar{1}1]$ | $[\bar{1}01]$ | 22 | $[\bar{1}\bar{1}\bar{1}]$ | $[0\bar{1}1]$ | | |
| 7 | $[11\bar{1}]$ | $[112]$ | 15 | $[11\bar{1}]$ | $[1\bar{1}0]$ | 23 | $[\bar{1}\bar{1}\bar{1}]$ | $[10\bar{1}]$ | | |
| 8 | $[\bar{1}\bar{1}\bar{1}]$ | $[11\bar{2}]$ | 16 | $[\bar{1}11]$ | $[\bar{1}0\bar{1}]$ | 24 | $[\bar{1}\bar{1}\bar{1}]$ | $[\bar{1}10]$ | | |

As in [376], the analysis assumes pure characteristics of dislocations (edge or screw) and ignores partial and mixed dislocation characters. The Burgers and line vectors (equation 5—

9) were transformed to the grain crystal frame (equation 5—10) before the estimation of their GND density [206].

$$\hat{t} = \frac{t}{|t|}, \qquad \hat{b} = \frac{b}{|b|}a \tag{5—9}$$

$$t' = R_{\varphi_1,\Phi,\varphi_2}\begin{bmatrix}1 & 0 & 0\\ 0 & 1 & 0\\ 0 & 0 & 1\end{bmatrix}\hat{t}, \qquad b' = R_{\varphi_1,\Phi,\varphi_2}\begin{bmatrix}1 & 0 & 0\\ 0 & 1 & 0\\ 0 & 0 & 1\end{bmatrix}\hat{b} \tag{5—10}$$

The normal direction (ND), parallel to $x_3$, of the plane $(hkl)$ that is parallel to the sample surface was estimated from the grain mean orientation. The angle ($\Phi$) between the Burgers vector of each dislocation type and the normal direction was then obtained using equation 5—11. In the analysis of the GND density at the slip bands, the orientations ($\Phi_i$) at each of the measured points in the slip band were weighted by the relative contribution of each dislocation type to the total GND density to calculate a weighted average angle ($\bar{\Phi}$, Figure 5-1) for the dislocations (i.e., the dot product of both $b$ and $t$ with the slip plane normal should equal zero) [378]. A function with an example is available at https://bit.ly/3vT2DJC.

$$\Phi_i = \tan^{-1}\left(\frac{\|b_i' \times (hkl)\|}{b_i'.(hkl)}\right) \tag{5—11}$$

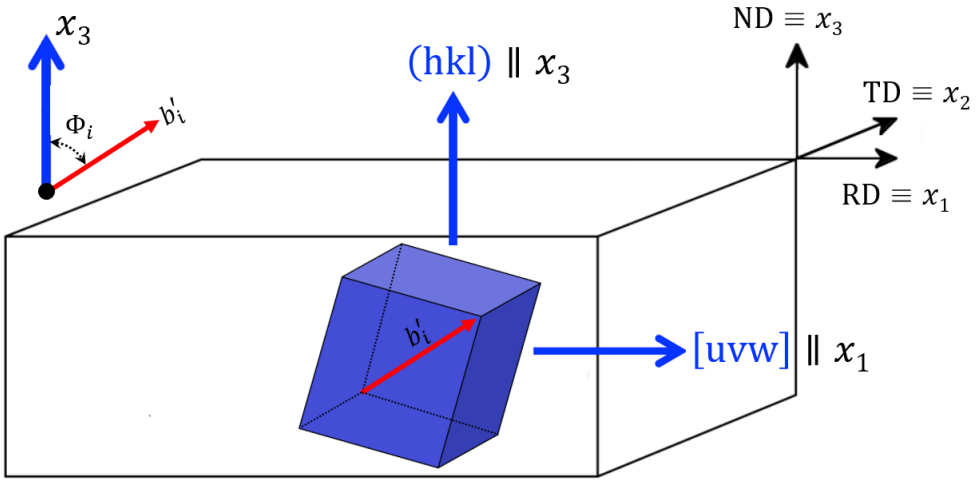


Figure 5-3: Schematic of $\Phi_i$ calculation showing an arbitrary orientated crystal (blue) in the sample.

### 5.2.5 Resolving the strain field to the slip-band frame of reference

The elastic deviatoric strain field, obtained in HR-EBSD analysis using measured shifts and distortions between EBSPs and a reference EPSP, was integrated into its equivalent displacement field to enable *J*-integral analysis by the finite element method. The analysis was simplified by performing a rotational transformation of the elastic strain tensors obtained from HR-EBSD to resolve them to the slip band geometry using a $Q_{z(\alpha)}$ and $Q_{x(\theta)}$; thus, making $x$ and $y$ the horizontal and vertical axes of the image frame, respectively. The necessary angles (Figure 5-1) were obtained by EBSD-based trace analysis (Chapter 4) of the slip band at the specimen surface and on the orthogonal wall of a focused ion beam (FIB)-milled trench on which the sub-surface slip trace was observed by secondary electron microscopy. Equation 5—14 follows the Einstein summation convention.

$$Q_{z(\alpha)} = \begin{bmatrix} \cos\alpha & \sin\alpha & 0 \\ -\sin\alpha & \alpha & 0 \\ 0 & 0 & 1 \end{bmatrix} \qquad 5—12$$

$$Q_{x(\theta)} = \begin{bmatrix} 1 & 0 & 0 \\ 0 & \cos\theta & \sin\theta \\ 0 & -\sin\theta & \cos\theta \end{bmatrix} \qquad 5—13$$

$$\varepsilon'_{pq} = Q_{pi} Q_{qj}\, \varepsilon_{ij} \qquad 5—14$$

These transformations resolve the strain field to the slip band; thus, $J_3$ is directly equivalent to the out-of-surface energy release rate ($G^{III}$) since the slip band normal is perpendicular to the slip trace on the surface ($x_3 \perp q$). The slip band resolved axes, $x$, $y$, and $z$, are shown in comparison with the sample observation axes, $x_1$, $x_2$, and $x_3$ in Figure 5-1. The sample axes, $x_1$, $x_2$, and $x_3$, are shown in all figures in this chapter using blue, red, and green arrows, whereas $x$ and $y$ refer the image/frame axes (horizontal and vertical, respectively) that are resolved to the slip band.

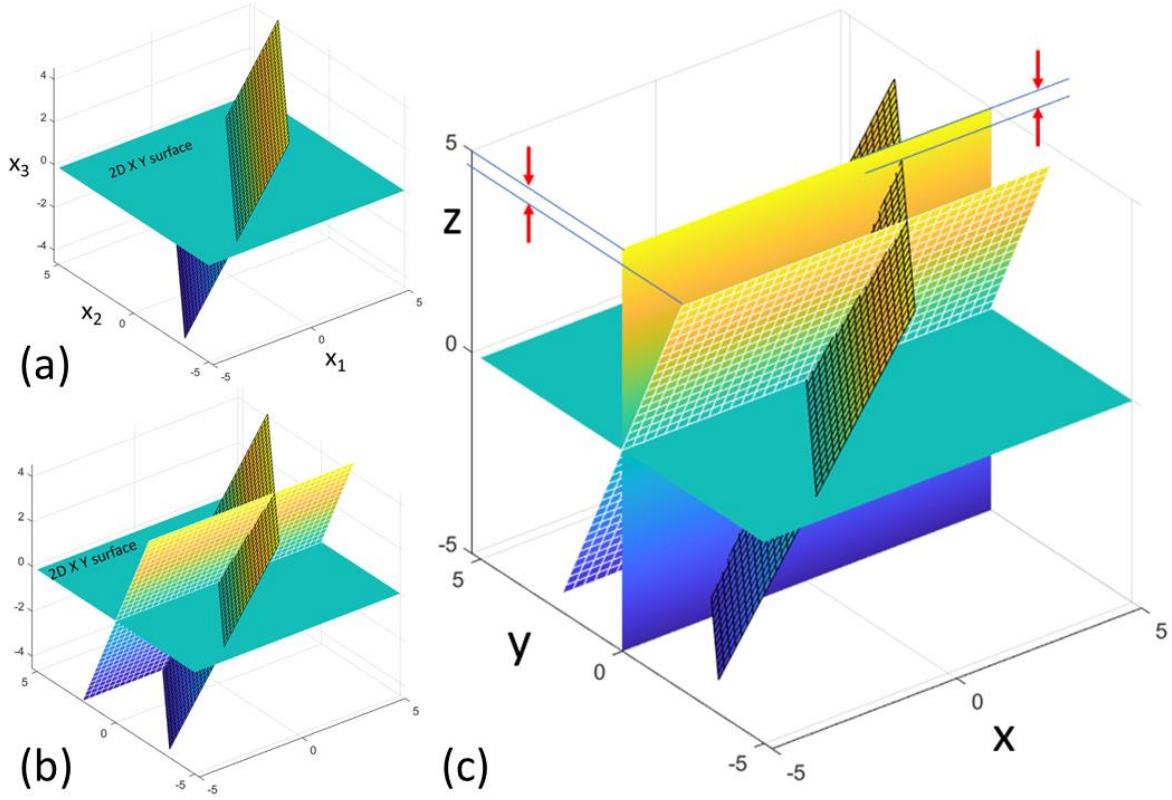


Figure 5-4: Slip-band transformation from (a) $x_1$, $x_2$, and $x_3$ axis to $x$, $y$, $z$ using (b) $Q_{z(\alpha)}$ and (c) $Q_{x(\theta)}$.

However, there is a change in the $z$ as indicated by the red arrows in Figure 5-4c. This Δz which will be the (physical) change between the measured field in $x_3$ and the transformed field in $z$ (coordinates). The question here is whether $\Delta z$ is a constant unit change (no correction needed) or a gradient? $\Delta z$ is a constant if it is assumed that all points in the measured field have the same $x_3$,and if it is assumed the EBSD depth of information is uniform even across topographies (Figure 5-5). A claim is accepted by authors [128,374] and refuted by Weiss and Klement [373] for a deformed sample.

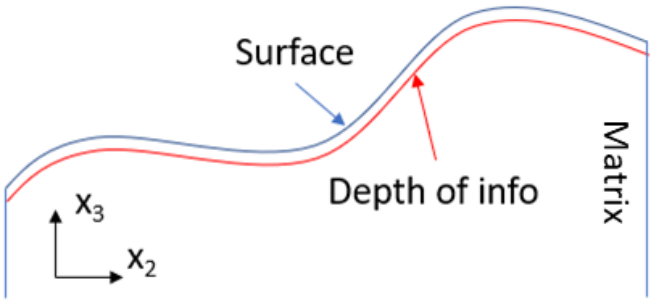


Figure 5-5: Assumed depth of information for EBSD.

An alternative route is to reconstruct a rotation matrix based on assuming, with no ambiguity, that the slip band is primarily made up of a specific edge dislocation, as described in equation (5—15), where $b$ is the Burgers vector, $t$ is the line direction, and $n$ is their cross product [157] before rotating the field using $Q_{z(\theta)}$ to align with $x_1$-axis ($x_1 \parallel q_1$). Users of these methods [296,297] did not clarify whether they rotated the field using Euler angles to the Crystal Cartesian frame before using slip band trace. In addition, this method might be valid for low symmetry materials, but – as it can be realised (later) from GND density analysis – this assumption is not valid, plus the slip trace is not readily distinguishable. Thus, as the HR-EBSD field is measured at the sample frame, the field is transformed to be consistent with the conventional three-dimensional *J*-integral analysis [58] described above.

$$R = \begin{bmatrix} b_1 & t_1 & n_1 \\ b_2 & t_2 & n_2 \\ b_3 & t_3 & n_3 \end{bmatrix} \qquad 5—15$$

### 5.2.6 HR-EBSD depth of information

The electron beam of Merlin FEG-SEM has an averaged mean-radius at the specimen surface of about ~25 nm at the 20 kV/10 nm beam condition [379]. The elliptical intersection of the beam on the 70° tilted surface means that the longitudinal resolution is 3 times higher than the lateral [380]. This geometry was used in a Monte Carlo (MC) simulation (Casino v2.48 [381]) of the trajectories of 5 x $10^6$ electrons into a bulk ferrite phase of 25% Cr, 5.4% Ni, 3.9% Mo, 0.6% Mn, 0.6% Cu, wt.% nominal composition [382]. The simulation was used to determine the probability for electrons to backscatter to the surface from a certain depth. The effective (mean) depth of information (50% probability) was estimated to be about 46 nm (red dashed line in Figure 5-6b), which defined the membrane finite element model used to analyse the *J*-integral from the deformation field.

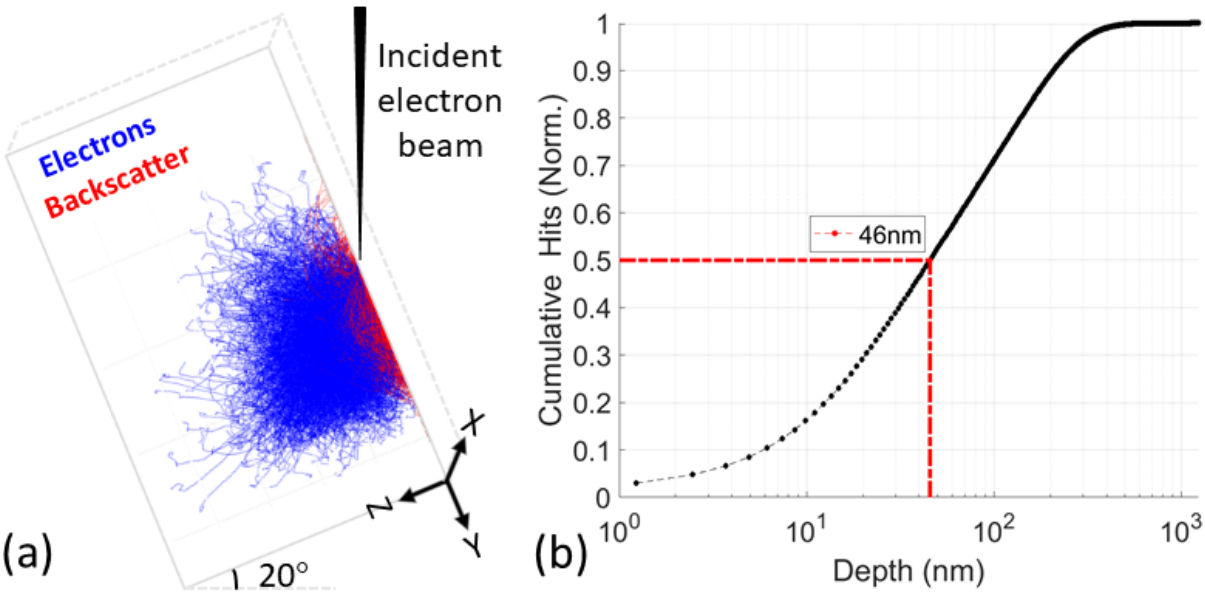


Figure 5-6: (a) Monte Carlo simulation of electron trajectories modelled using a screened Rutherford potential and the Mott-Bethe (power) model [381]. (b) cumulative probability of backscattered electron detection vs depth from the surface. The dashed red line indicates the mean of the distribution at 46 nm depth.

### 5.2.7 *J*-integral and three-dimensional stress intensity factors

The finite element method was used to obtain the displacement field from the measured elastic strains and extract the *J*-integral and three-dimensional stress intensity factors. To obtain the displacement field, a finite element model was defined in MATLAB® using hexahedron (brick) elements with 8 nodes to structurally mesh a 3D volume of 46 nm thickness (i.e., the HR-EBSD probed membrane layer). As an approximation, it was assumed that the plane of the slip band was perpendicular to the thin membrane by considering the rotational transformations of the stress field executed earlier. The coordinates of the nodes and element connectivity matrix were used to calculate the shape function and Jacobian for isoparametric linear brick elements with 8 Gauss points (full integration, see Chapter 2). The concept of the analysis is to use the shape/interpolation function to relate the strain at the measurement point (centric point) to the Gauss integration points and then to the (integrated) nodal displacement. The element stiffness and force matrix at the Gauss points

were assembled in a sparse matrix to efficiently use the available memory to solve nodal displacement (see Chapter 2). The resultant nodal displacements were corrected for rigid body movement (translations and rotation), and the point with absolute minimum displacement was defined as the origin [112]. These integrated displacement fields may be regarded as similar to those obtained by stereo digital image correlation (3D DIC) [383] since the analysis provides information on the in-plane and out-of-plane movements of the surface.

The (nodal) elastic displacements ($u$) were then examined using a mode-decomposition technique [368,384–388] that separates the field into components of symmetric ($u^I$), in-plane anti-symmetric ($u^{II}$) and out-of-plane anti-symmetric ($u^{III}$) fields by superimposing an auxiliary field onto the actual field with mirroring along the $x_1$-axis (equation 5—16). The auxiliary field was used to enlarge the actual field, forming a representation of symmetry while satisfying both the equilibrium equation and an assumed traction-free boundary condition on the slip plane surface (detailed in [389]).

$$u = u^I + u^{II} + u^{III} = \frac{1}{2}\begin{Bmatrix} u_x + \bar{u}_x \\ u_y - \bar{u}_y \\ u_z + \bar{u}_z \end{Bmatrix} + \frac{1}{2}\begin{Bmatrix} u_x - \bar{u}_x \\ u_y + \bar{u}_y \\ 0 \end{Bmatrix} + \frac{1}{2}\begin{Bmatrix} 0 \\ 0 \\ u_z - \bar{u}_z \end{Bmatrix} \qquad 5—16$$

$$u = u^I + u^{II} + u^{III} = \frac{1}{2}\begin{Bmatrix} u_x + \bar{u}_x \\ u_y - \bar{u}_y \end{Bmatrix} + \frac{1}{2}\begin{Bmatrix} u_x - \bar{u}_x \\ u_y + \bar{u}_y \end{Bmatrix} + \frac{1}{2}\begin{Bmatrix} u_z + \bar{u}_z \\ u_z - \bar{u}_z \end{Bmatrix} \qquad 5—17$$

The potential strain energy release rate ($J^{I,II,III}$) and corresponding stress intensity factors for each decomposed field were evaluated using the ABAQUS® finite element solver by applying the nodal displacements of each of the $u^I$, $u^{II}$ and $u^{III}$ fields as boundary conditions for a two-dimensional geometry, as simplified in equation (5—17). The $u^I$ and $u^{II}$ fields provide $K_I$ and $K_{II}$. By injecting the fields in this way, there is no need to assume that $u_z + \bar{u}_z = 0$; that assumption has been made previously where 3D stereo-DIC surface measurements [63] (citing [390]) provided only the two-dimensional displacements. For $u^{III}$, by using the mode

decomposition algorithm implemented in ABAQUS, the anti-symmetric shear $K_{III}$ and its associated symmetric out-of-plane mode I contribution (i.e., $K_I^r$) can be calculated.

The calculations were executed while maintaining the same rectangular grid spacing with 4 nodes for each plane stress element (ABAQUS® CPS4). The slip band was defined with its tip position located within the displacement field using the information from the maps of GND density and VFSD images with a precision of ~75 nm. The application of ABAQUS as the FE solver also allows the use of linear elastic, anisotropic elastic, and elasto-plastic material properties and the implementation of equivalent domain integration (EDI) [38,43,58] - rather than line integration – to calculate the magnitude and sign of the three-dimensional stress intensity factors [114]. The EDI starts at the slip band tip and propagates in the local direction of a virtual extension, with the linear spatial variation across nodes calculated using a smoothing function ($q$) that equals unity at the tip and zero outside the domain.

In the present elastic analysis, the anisotropic linear elastic properties of the ferrite crystal were used, and the slip band was defined as a traction-free surface (i.e., an equivalent crack) orthogonal to the membrane. The stiffness matrix was calculated by rotating the ferrite orthotropic stiffness tensor ($C_{11} = 230, C_{44} = 117, C_{12} = 135$ in GPa [212]) to the crystal orientation of the $EBSP_0$ [308]. A rotation matrix ($R_{\varphi_1,\Phi,\varphi_2}$) was constructed from the Euler angles ($\varphi_1, \Phi, \varphi_2$) of the reference pattern ($EBSP_0$) as below [305,391–393] following the conventional EBSD rotation Z X' Z'' scheme [160]. By using the rotation matrix, the anisotropic elastic stiffness matrix, $C_{EBSP_0}$, was mapped from the reference crystal coordinate system to the local coordinate system [213,309]; see section 4.2.3 for more details.

The resultant *J*-integral and stress intensity factor values were obtained using the $u^I$ displacement field gives $J^I$ and $K_I$, whereas the $u^{II}$ displacement field gives $J^{II}$ and $K_{II}$. The

$u^{III}$ displacement field gives the anti-symmetric out-of-plane shear, $K_{III}$, and the symmetric out-of-plane, $K_I^r$, components. Moreover, Cotterell and Rice [61] showed that for mixed-mode crack loading, the total strain energy release rate, $J$, is the sum of the energy release rates for each mode, as in equation (5—19). The code for this analysis and (synthetic) benchmarking datasets are available at https://doi.org/10.5281/zenodo.6411569. Extensive error analysis for the method is in Appendix (5.C) – Decomposed *J*-integral: Error analysis.

$$K_I^T = K_I + K_I^r \qquad 5—18$$

$$J = J^I + J^{II} + J^{III} \qquad 5—19$$

## 5.3 Results and discussion

The analyses were applied to a series of in situ observations, comprising an incipient slip band, an array of slip bands, and a slip band studied under an increasing, then decreased, load to investigate their stress fields. During deformation, the austenite phase first showed planar slip, with secondary slip developing as the applied displacement was increased. In ferrite, wavy slip was observed, accompanied by linear deformation bands that mostly terminated at grain or phase boundaries (Figure 5-7). These could be readily distinguished as deformation twins and slip bands using VFSD imaging, as in the far-field condition (38 mm working distance) the CCD camera diodes have high sensitivity to changes in diffraction angle [370,394]; the change in orientation of twins gives colour contrast, whereas the local plastic deformation of slip bands gives higher intensity contrast (i.e., highly-saturated, or low-intensity pixels). As loading progressed, there was an increase in the amount of wavy slip (Figure 5-7, box 1), an increase in the number of ferrite slip bands (Figure 5-7, box 2), and an increase in the width (i.e., height) '*h*' of slip steps (Figure 5-7, box 3). The slip band propagation was accompanied by increased step height (Figure 5-7, box 4) with a smooth or sharply kinked transition to slip systems of different orientations in an adjacent grain (Figure 5-7, box 5). Some slip bands terminated at sub-grain boundaries (misorientation <1°), and others terminated mid-grain with no apparent obstacle.

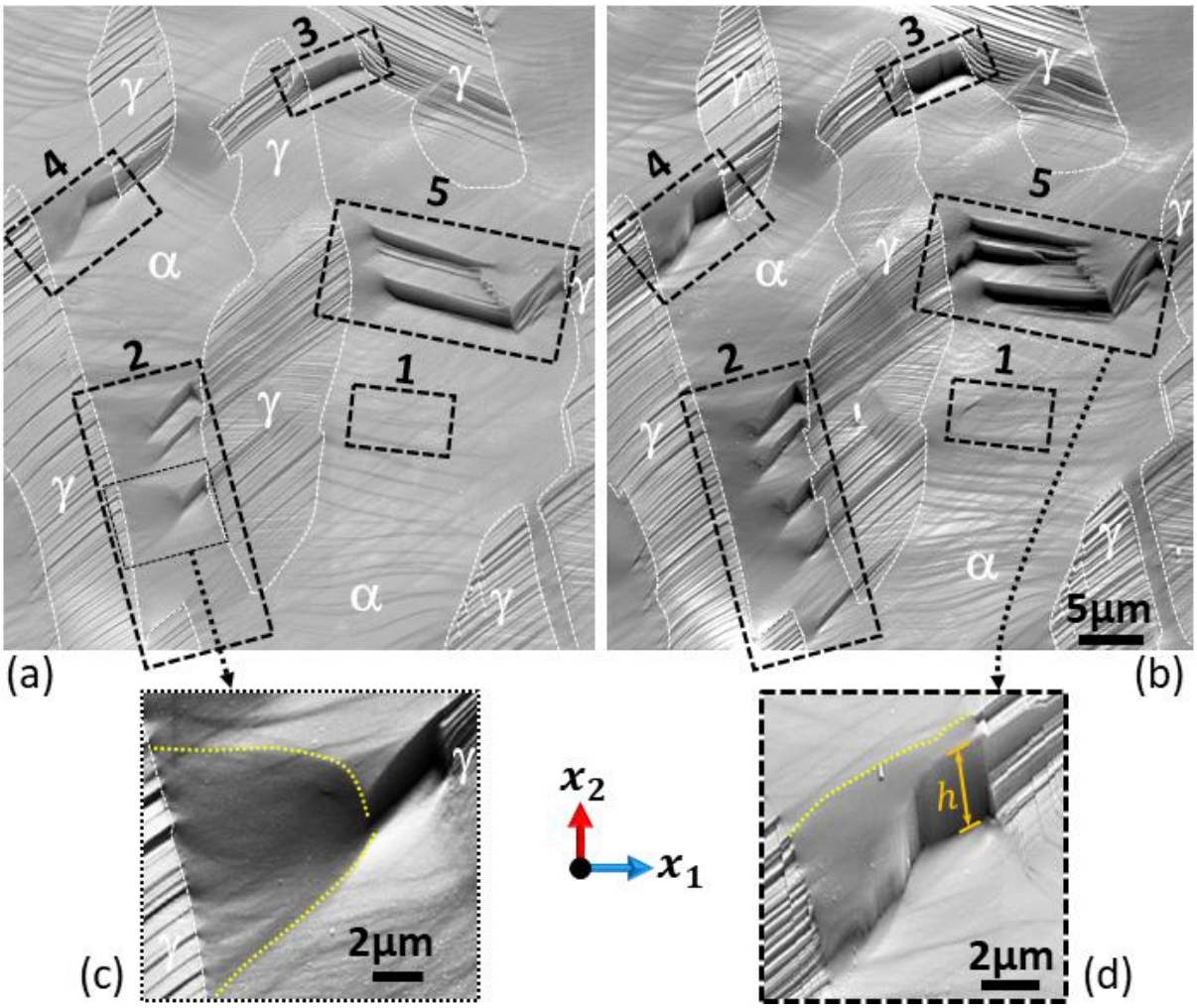


Figure 5-7: Secondary electron images of age-hardened duplex stainless-steel observed in situ in three-point bending at applied crosshead displacements of (a) 1.2 mm and (b) 1.5 mm. Selected regions (2 and 4) are shown with higher magnification in (c) and (d). The apparent slip band height is marked as '$h$.' Ferrite ($\alpha$) and austenite ($\gamma$) phases are labelled.

Some slip bands were found terminated at sub-grain boundaries (misorientation <1°), and others terminated mid-grain with no apparent obstacle. No precise observation was made of slip bands' incremental propagation (while maintaining both direction and plane) with the load. The analyses were applied to a series of in situ observations, comprising an incipient slip band, an array of slip bands, and slip bands studied under an increasing, then decreased, load to investigate the evolution of their stress fields. Nevertheless, due to high magnification and slow pattern acquisition, carbon deposition accumulation was rapid, introducing noise to the measurement and limiting additional acquisition at the exact location after further straining.

### 5.3.1 Incipient slip band

An array of parallel slip bands in a ferrite subgrain, $\alpha_1$, is shown in Figure 5-8a. The slip bands are blocked by a low-angle grain boundary (misorientation < 1°). The secondary electron image shows a 'bloom-like' contrast variation at each of the blocked slip band tips, indicating a gradual change in height that accommodates the out-of-plane shear displacement of the slip band; the latter is apparent from the sharp height change within the subgrain $\alpha_1$. A small step-like feature has also developed parallel to the slip traces within the adjacent subgrain $\alpha_2$. Analysis of the grain orientation by EBSD [395] shows its trace is consistent with the (112) slip plane that is inclined at 88° to the surface (Figure 5-8c). Thus, the step is on a slip band nearly normal to the specimen surface (Figure 5-8c).

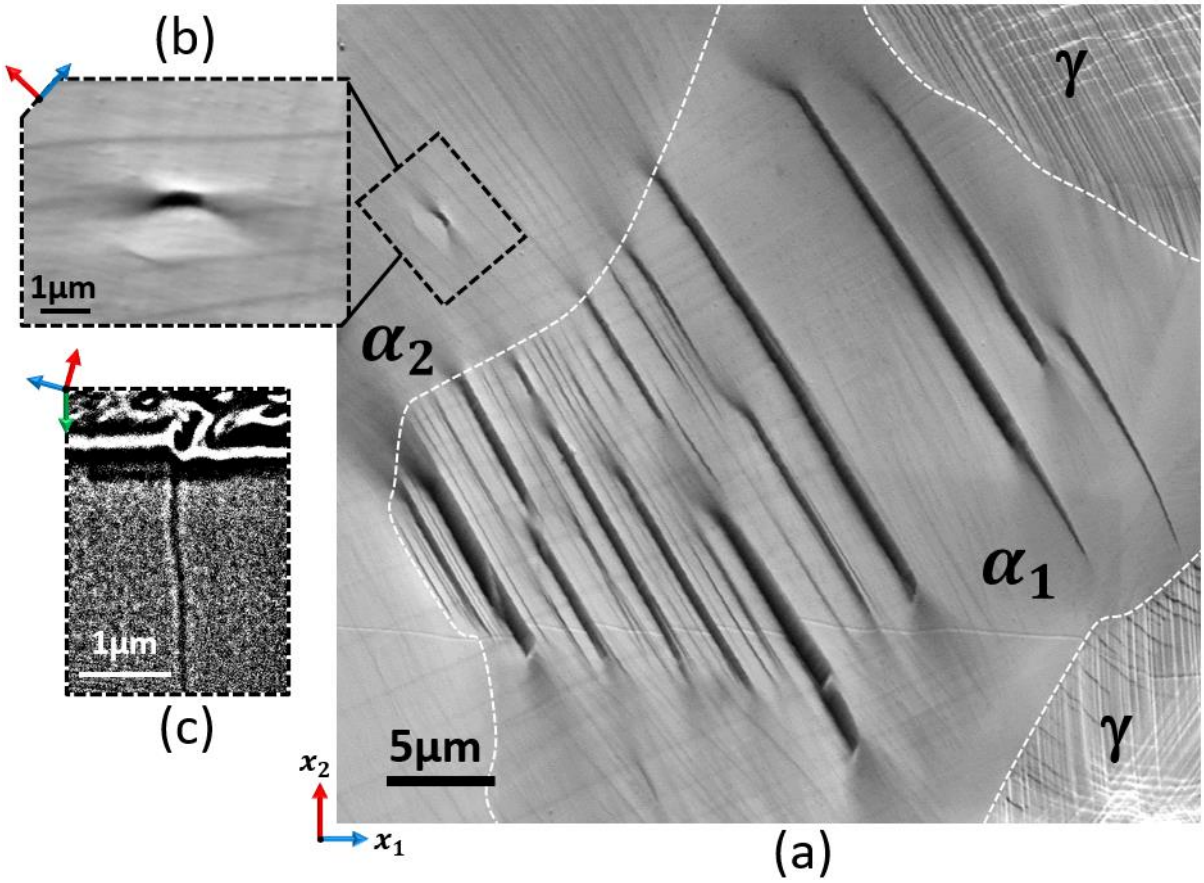


Figure 5-8: (a) SEM image of an array of slip bands and (b) $(112)$ trace and (c) focused ion beam sliced view in a ferrite grain of age-hardened duplex stainless steel.

If the simple normal stress in the direction of the maximum bending moment ($x_1$-axis direction) were assumed to act within the subgrain, the expected slip system with maximum shear stress would be $[1\bar{1}1](110)$ (Table 5-2). Nevertheless, this is not consistent with the observed plane. A loading direction matrix ($L_c$) was constructed from the HR-EBSD stress field of subgrain $\alpha_2$, as described in section 5.2.3, and it was found that the $[11\bar{1}](112)$ slip system has the highest $xSF$ of the {112} planes (Table 5-2), and its trace is within 2° of the trace of the observed slip band and the other parallel slip traces in this grain. This analysis demonstrates the importance of knowledge of the local stress state at the grain to define the Schmid factor [396].

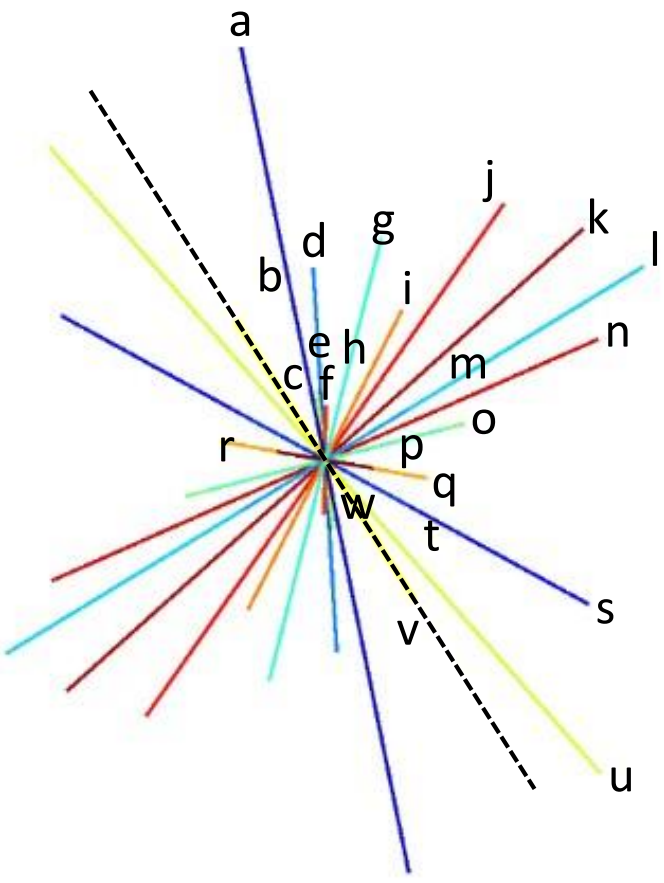


Figure 5-9: Traces of the possible slip systems for this ferrite grain (see Table 5-2). The trace length is proportional to the Schmid factor, calculated from the local stress tensor. The surface trace of the observed slip band is shown as a dashed black line, which is parallel to the traces of $(112)$ and $(12\bar{1})$.

Table 5-2: Slip variants (see Figure 5-9) with the relative Schmid factor (1 is highest), calculated with the assumption of i) tensile loading ($x_1$) and ii) local stress state of the grain ($xSF$). Systems ('v' and 'w') with traces parallel to that of the observed slip band in the subgrain $\alpha_2$ are **bold**. The system ('v') with the highest Schmid factors is highlighted with a double lined square. EBSD maps are in Appendix (5.B) – HR-EBSD based Schmid factor.

| Label | Trace | $x_1$ | $xSF$ | Label | Trace | $x_1$ | $xSF$ | Label | Trace | $x_1$ | $xSF$ |
|---|---|---|---|---|---|---|---|---|---|---|---|
| a | $[1\bar{1}1](110)$ | 1 | 22 | i | $[11\bar{1}](2\bar{1}1)$ | 10 | 15 | q | $[1\bar{1}1](\bar{1}12)$ | 14 | 10 |
| b | $[\bar{1}11](110)$ | 20 | 7 | j | $[1\bar{1}1](21\bar{1})$ | 5 | 19 | r | $[\bar{1}\bar{1}\bar{1}](\bar{1}\bar{1}2)$ | 21 | 14 |
| c | $[\bar{1}11](211)$ | 18 | 3 | k | $[\bar{1}\bar{1}\bar{1}](\bar{1}2\bar{1})$ | 4 | 21 | s | $[1\bar{1}1](011)$ | 6 | 11 |
| d | $[11\bar{1}](101)$ | 9 | 5 | l | $[\bar{1}\bar{1}\bar{1}](\bar{1}10)$ | 3 | 24 | t | $[11\bar{1}](011)$ | 16 | 1 |
| e | $[\bar{1}11](101)$ | 17 | 5 | m | $[11\bar{1}](\bar{1}10)$ | 15 | 12 | u | $[1\bar{1}1](121)$ | 2 | 18 |
| f | $[\bar{1}11](1\bar{1}2)$ | 19 | 8 | n | $[\bar{1}\bar{1}\bar{1}](2\bar{1}\bar{1})$ | 7 | 20 | v | $[\mathbf{11\bar{1}}](\mathbf{112})$ | 11 | 2 |
| g | $[\bar{1}\bar{1}\bar{1}](0\bar{1}1)$ | 8 | 17 | o | $[\bar{1}\bar{1}\bar{1}](10\bar{1})$ | 12 | 16 | w | $[\mathbf{\bar{1}11}](\mathbf{12\bar{1}})$ | 23 | 9 |
| h | $[\bar{1}11](0\bar{1}1)$ | 22 | 23 | p | $[1\bar{1}1](10\bar{1})$ | 13 | 13 | x | $(\bar{1}21)[11\bar{1}]$ | 24 | 4 |

The EBSD analysis provides the crystallographic directions of the slip band trace (i.e., $x$-axis in Figure 5-1, which is the cross product of the slip band plane normal, $n$, and sample normal) and the local Schmid factor analysis also provides the expected shear direction of the Burgers vector ($b$) of the most highly stressed slip system of the slip band. Both provide the information required to calculate the slip inclination angle ($\psi$) [397] (Figure 5-1) for the $[11\bar{1}](112)$ slip band, which is 79.3 ± 1.4°, consistent with the significant height of the slip band steps in the subgrain $\alpha_1$ that has essentially the same crystal orientation as subgrain $\alpha_2$. The step-like feature in subgrain $\alpha_2$ is therefore identified as an incipient slip band where the diffuse deformation (indicated by the multiple slip traces with a low surface profile elsewhere in the subgrain) has become localised, with a significant out-of-plane shear due to the high slip inclination angle. With continued deformation, it would be expected to develop to a more extended slip band, such as observed in subgrain $\alpha_1$.

The GND density analysis of the incipient slip band showed higher edge dislocation activity than screw dislocations (Figure 5-10a). By weighting the relative contribution of the identified dislocation systems (Figure 5-10b), $\bar{\Phi}$ is 50.9 ± 1.2°; the variance was obtained from 4 repeat measurements (within the blue-shaded region in Figure 5-10a). Whilst this direction indicates both a significant out-of-surface shear and shear parallel to the surface, none of the slip systems identified in the GND density analysis (see Table 5-1) are mobile on the (112) plane (i.e., $\bar{\Phi}$ is not in the plane of the slip band). This suggests that the GND density arises from slip systems other than the identified slip band and is necessary to accommodate the deformation caused by the localisation of shear and the complex local strains from the resulting step at the specimen surface.

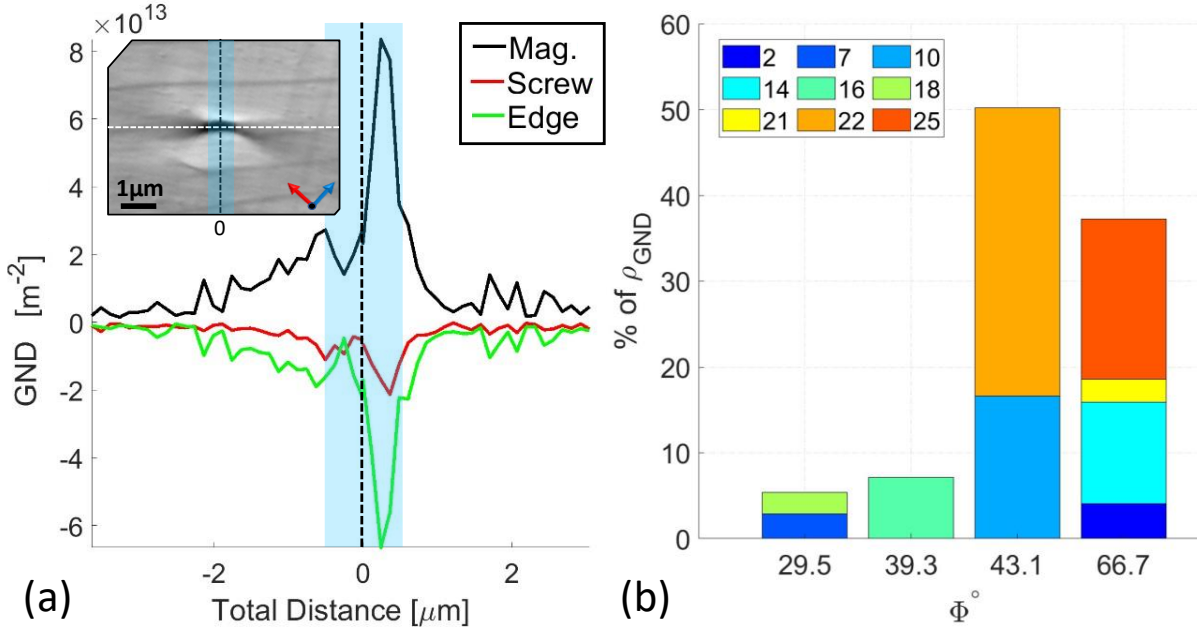


Figure 5-10: (a) Dislocation activity across $[11\bar{1}](112)$ slip band. The dislocations sign indicates the misorientation direction, with negative values representing sink-like activities and positive pile-up activities [371]. (b) Angle ($\Phi$) of each dislocation system of the Burgers vector relative to the surface with the relative contribution of each system stacked at the related angle. The dislocations forming the slip band are from the measurements shaded in blue in (a). The dislocation system associated with each label is listed in Table 5-1.

The HR-EBSD data and the integrated in-plane elastic displacement field, which were resolved and rotated to align the incipient slip band with the horizontal $x$-axis, both show the effect of the surface stretching that accommodates the out-of-plane shear of the slip band(Figure 5-11). The highest strains exist at the incipient slip band tips. The integrated elastic displacements show opposing $U_x$ displacements at each tip (i.e., shear) with a positive $U_y$ gradient across the grain (i.e., tension). The out-of-plane $U_z$ elastic displacement field also shows a step-change in height consistent with the topography, although the calculated elastic displacement is significantly smaller than the observed plastic displacement in Figure 5-8c.

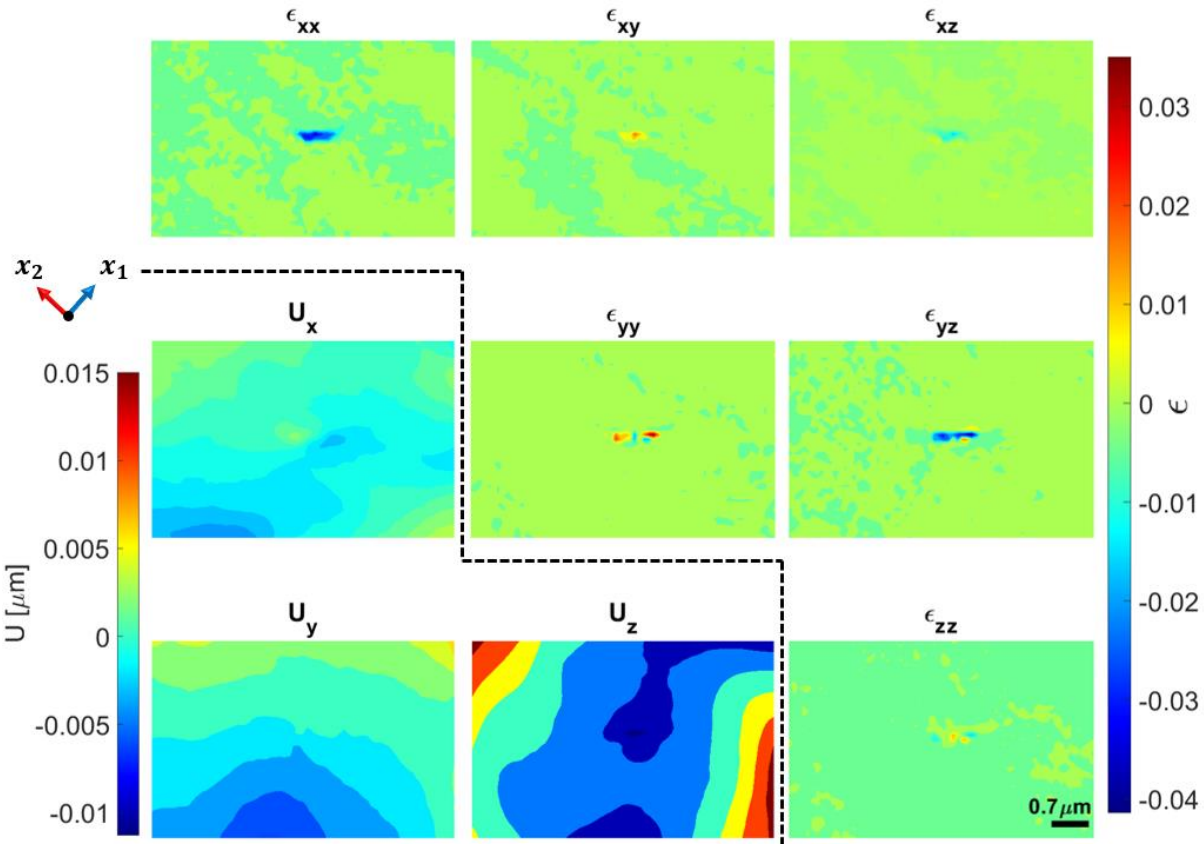


Figure 5-11: Components of the elastic deformation field of $[11\bar{1}](112)$ slip band, at the figure centre.

The strain energy field around the incipient slip band was then evaluated. The *J*-integral is only appropriate for strain energy release rate analysis of one singularity. The *J*-integral was thus evaluated by considering the tips of the slip band independently by splitting the

measured field at its centre along the vertical axis. The $q$ vectors (Figure 5-12a) were chosen to parallel the slip band trace, and the integration domain was expanded in ~100 nm intervals. Values obtained immediately at the tip were ignored since the assumption of elasticity breaks down [31], and stable convergence of the *J*-integral was achieved for both ends of the slip band once the displacement singularity was engulfed by the integration domain (Figure 5-12b). The initial non-convergence of the *J*-integral can be attributed to the elevated level of plasticity close to the slip band [31], which is illustrated by the high GND density. Convergence also began to fail when the domain expanded to interact with the peripheral fields of other stress raisers, such as the array of slip bands in the adjacent subgrain, as their contribution to the gradient field makes the vector field non-conservative (path independent) unless fully engulfed by the integration domain [40,42].

The characteristic *J*-integral values were taken as the average from the stable converged region (shaded area in Figure 5-12.I and II), with the variance indicating the convergence stability. The *J*-integrals at either end of the slip band are 0.82 ± 0.03 J $m^{-2}$ and 0.51 ± 0.00 J $m^{-2}$. Decomposition to stress intensity factors show the stress field singularity is equally dominated by opening in-plane mode I (0.25 ± 0.01 MPa $m^{0.5}$ and 0.21 ± 0.01 MPa $m^{0.5}$) and opposing mode III out-of-plane shears (0.21 ± 0.01 MPa $m^{0.5}$ and -0.11 ± 0.01 MPa $m^{0.5}$). The mode II in-plane shear is small (0.05 ± 0.01 MPa $m^{0.5}$ and 0.01 ± 0.00 MPa $m^{0.5}$). The small symmetrical out-of-plane (compressive) contribution to mode I ($K_I^r$ in equation 5—18) is neglected (-0.01 MPa and 0.00 MPa $m^{0.5}$). The (negative) sign of the in-plane $K_{II}$ and out-of-plane $K_{III}$ shear depends on the chosen arrangement of the nodes at the tip and does not carry any physical meaning [86]. The incipient slip band formed an out-of-plane step with its shear direction ($\psi$ at 79.3° to the surface trace) in a slip plane that is practically normal to the

surface; this shear would be expected to lead to a high mode III stress intensity factor with negligible mode II. The mode I stress intensity factor is deduced to be due to the surface stretching necessary to accommodate the emergence of the step.

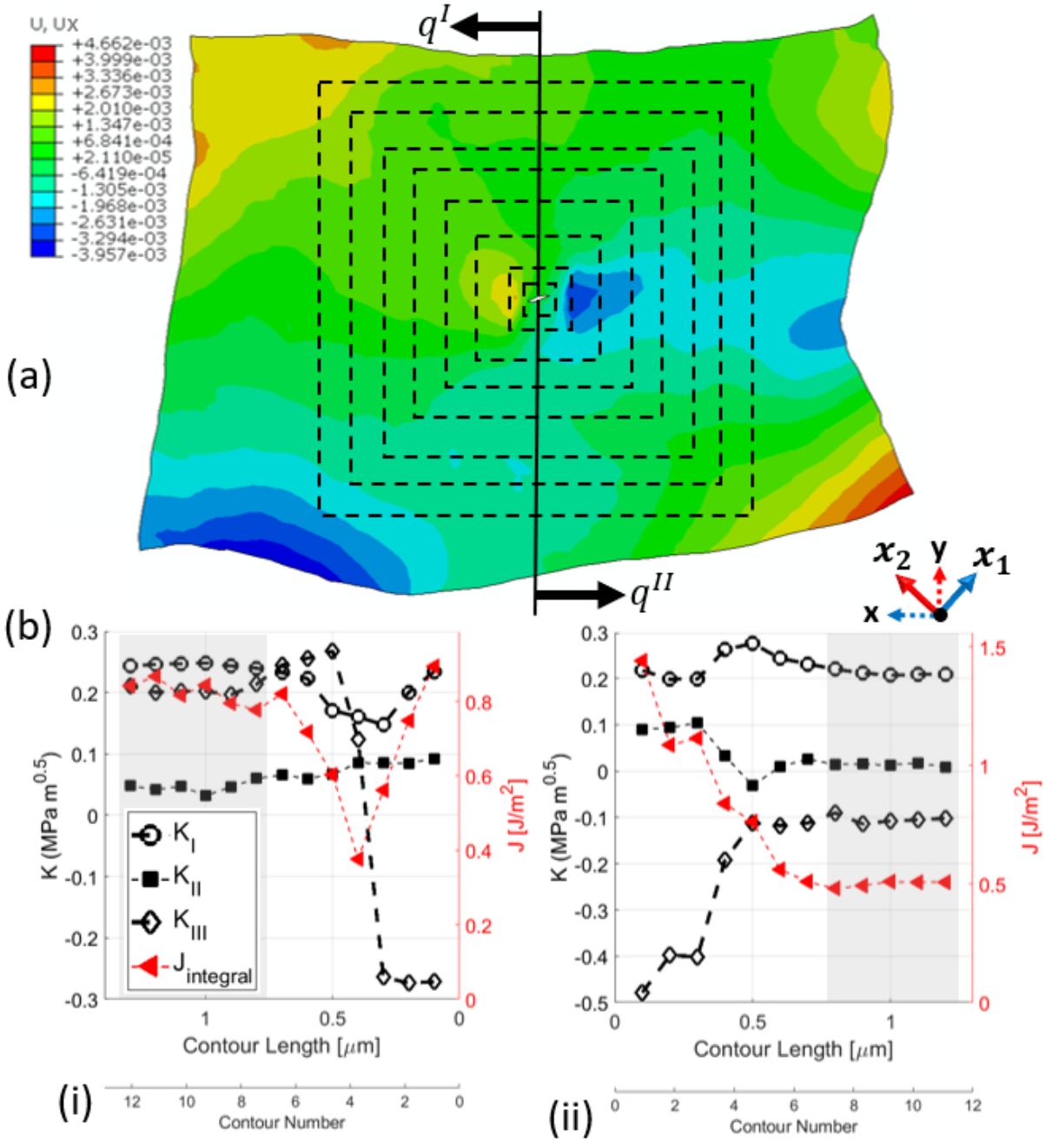


Figure 5-12: (a) The deformed configuration (exaggerated, with colour contours showing only the $U_x$ component of the displacement field) around the feature on the $[11\bar{1}](112)$ slip band with expanding EDI (dashed squares). (b) *J*-integral analysis was conducted at both ends of the feature using opposing vectors, $q^I$ and $q^{II}$.

In summary, the analysed feature is an incipient slip band where plastic deformation has started to localise to cause a step-like feature with a shear displacement out of the surface. The dominant slip system is consistent with the HR-EBSD based Schmid factor ($xSF$) in the grain, which was determined by local analysis of the stress tensor. The analysis to parameterise the elastic strain field has shown how the surface deforms to accommodate the shearing of the step, and this leads to the observed mode I and III stress intensity factors. The GND density analysis finds that these are not due to mobile dislocations of the same slip system as the slip band, and they are deduced to be due to the localised plastic deformation to accommodate the step.

### 5.3.2 An array of slip bands

An array of slip bands within a ferrite grain is shown in Figure 5-13. A 'blooming zone' of diffuse slip can be observed at the tip of each of these slip bands. The blooming zone increased in size as the load was increased and was also accompanied by a gradual increase in the slip band length and its apparent width, i.e., height (Figure 5-13d FIB sectioning orthogonal to the trace of one of the slip bands found the slip plane is inclined by 60 ± 1° to the surface ($\theta$ in Figure 5-1). The surface trace analysis, using the highest Schmid factor calculated via the local stress field from HR-EBSD, $xSF$, (see Appendix (5.B) – HR-EBSD based Schmid factor), identified the array as $[1\bar{1}1](\bar{1}12)$ slip bands with a slip inclination angle ($\psi$) of the Burgers vector that was 107.6 ± 9.5° from the surface trace (i.e. significant out of the surface shear). The average slip band widths (reported in Table 5-3) were measured using Fiji ImageJ [301] at several locations on the surface SEM image and GND density map (Figure 5-16b) at a 1.1 mm extension.

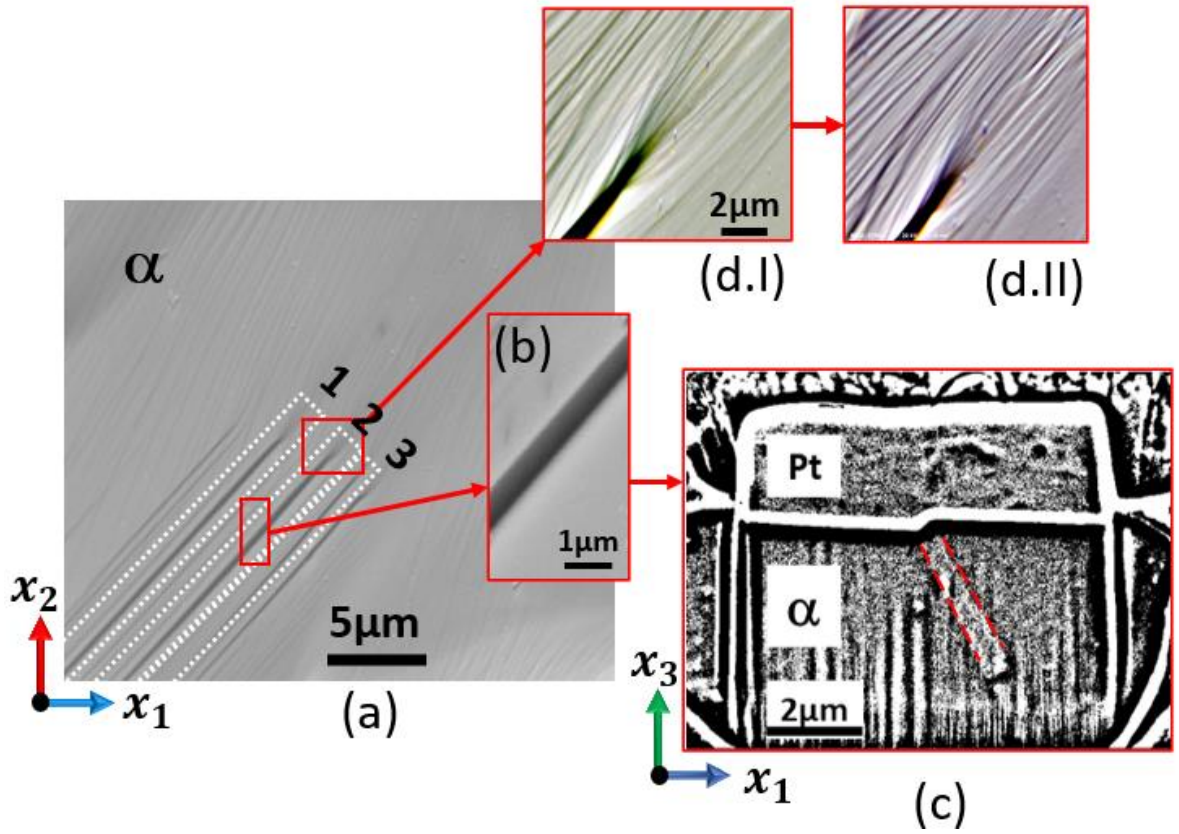


Figure 5-13: An array of $[1\bar{1}1](\bar{1}12)$ slip bands within a ferrite grain; (a) SEM image with (b) zoomed image of slip band no. 2; c) Contrast-enhanced image of FIB-sliced trench wall, at the location marked with red-square in a and magnified in b, to show the slip-plane (highlighted with dashed red lines). A Niblack local threshold [398] was applied to the in-lens secondary electron detector image to increase the image contrast of the slip band on the FIB trench surface (Pt is deposited platinum, and the vertical lines are FIB artefacts). (d) SEM image of the tip of slip band no.2 at applied displacements of (I) 1.1 mm and (II) 1.25 mm.

The GND density, presented as a function of distance along the slip band and extending beyond its tip into the parent grain, is presented for each slip band in Figure 5-14a. There is a sharp drop in dislocations activity outside the slip band and no apparent correlation between dislocation density and the slip band height (represented by the apparent thickness in Table 3), although the GND density seems higher near the tip of the narrower slip band (no. 3). Analysis of the individual dislocation types using the estimated GND density inside the slip band finds that all dislocation types are active, particularly edge dislocations.

The weighted average angle between the Burgers vector and the surface normal for all dislocation types was 46.1 ± 2.4° (the variance was obtained with 4 repeat measurements for each slip band, i.e., 12 in total). If considering only the 3 dislocation types (2 edges and 1 screw) that were glissile on $(\bar{1}12)$, i.e., $[1\bar{1}1]b\ [\bar{1}\bar{1}0]t$, $[1\bar{1}1]b\ [110]t$, and $[1\bar{1}1]b\ [1\bar{1}1]t$ that comprise 2.4%, 3.0% and 12.0% of all total dislocations measured in slip band, respectively. The weighted Burgers vector ($\bar{\Phi}$) of the mobile dislocation is at 12.7° to the surface normal. These are dislocations of the $[1\bar{1}1](\bar{1}12)$ system of the highest Schmid factor, but it is also clear that most of the GND density is due to the accommodation of other deformations.

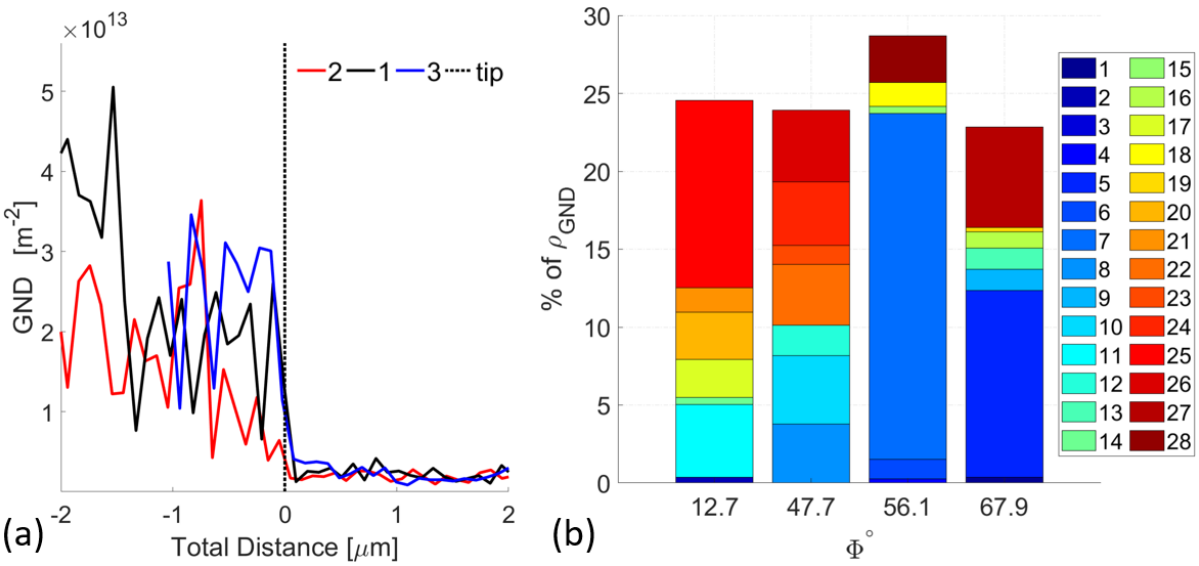


Figure 5-14: (a) Dislocation activity across three slip bands in the $(\bar{1}12)$ slip band array (0 is at each case's visually identified slip band tip). (b) Angle (Φ) of each dislocation type for the Burgers vector relative to the surface, averaged over the distance (-2 to 0) for the 3 slip bands. The dislocation types associated with each label are in Table 5-1.

Examination of the field before being resolved to the slip band can reveal the effect of the slip band height on the observed field, which allows the deformation field induced by the slip band to be directional. The integrated displacement field (Figure 5-15) shows an ellipsoidal distribution of the displacement/vector field at the slip tip (the geometry was extracted using GND density maps), and the magnitude increases outward. A dashed black line that presents

the ellipsoid (of diffused displacement vector field) long symmetry axis is aligned (± 0.5°) with the slip plane for slip band number three (dotted white line), which suggests that a predominant glide of the slip-plane causes the in-plane measured field. The misalignment increases to 6° and 10° as the slip band height (perceived width) increases. A similar ellipsoidal distribution of the displacement vector field was observed both in- and ex-situ. Thus, the field at the slip band tip is due to three-dimensional interactions between the matrix resistance and band out-of-plane step increment, and the proper way of parameterising this field can be accomplished using *J*-integral and stress intensity factors analysis on a field resolved on the slip band geometry.

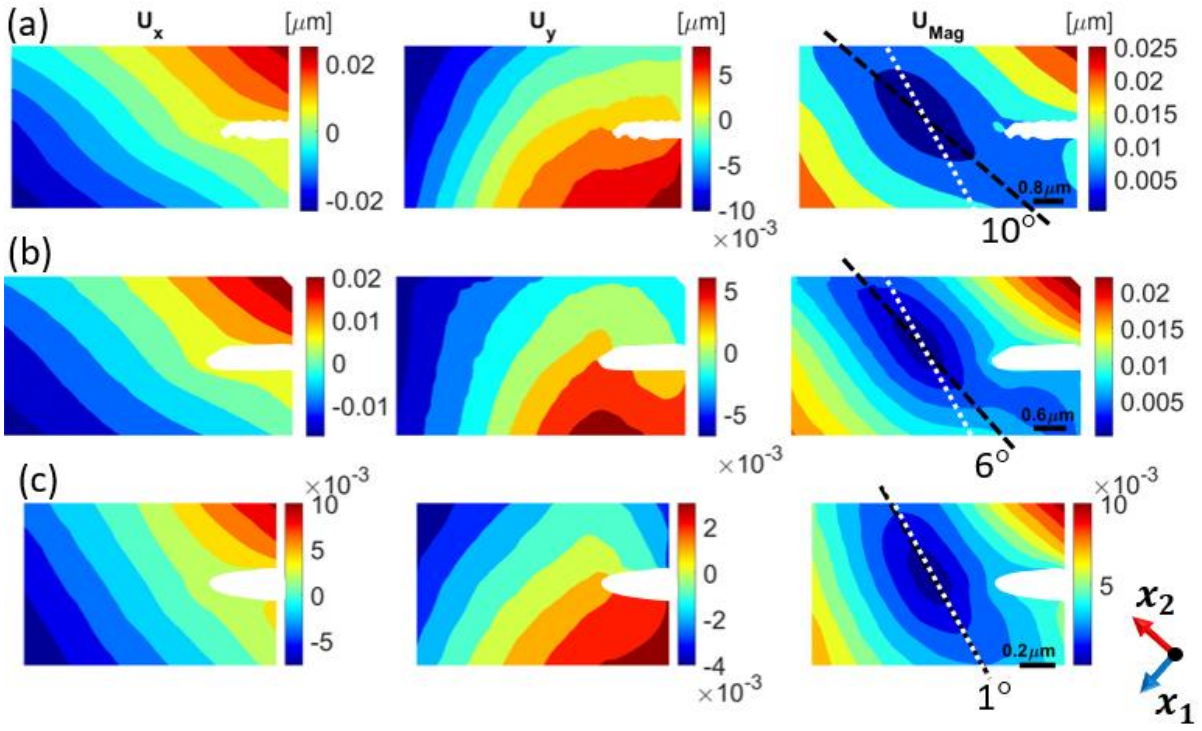


Figure 5-15: Integrated in-plane elastic displacement for $[1\bar{1}1](\bar{1}12)$ slip bands numbered (a) 2, (b) 1, and (c) 3 in Figure 5-13. The white dotted lines are the slip-plane revealed from FIB slicing (Figure 5-13c), and the dashed black lines are the ellipsoid long symmetry axis.

The elastic strain field was resolved to the slip band plane and integrated for the equivalent displacements. These are presented in Figure 5-16 and have the highest magnitude for the

thickest slip band (Table 5-3), where thickness is a proxy for the step height of the inclined slip band. There is a clear step in the in-plane $U_x$ and out-of-plane $U_z$ elastic displacements across the slip band, which increases with the slip band height. The opening $U_y$ displacement is more concentrated around the thinner slip band (i.e., smallest height step).

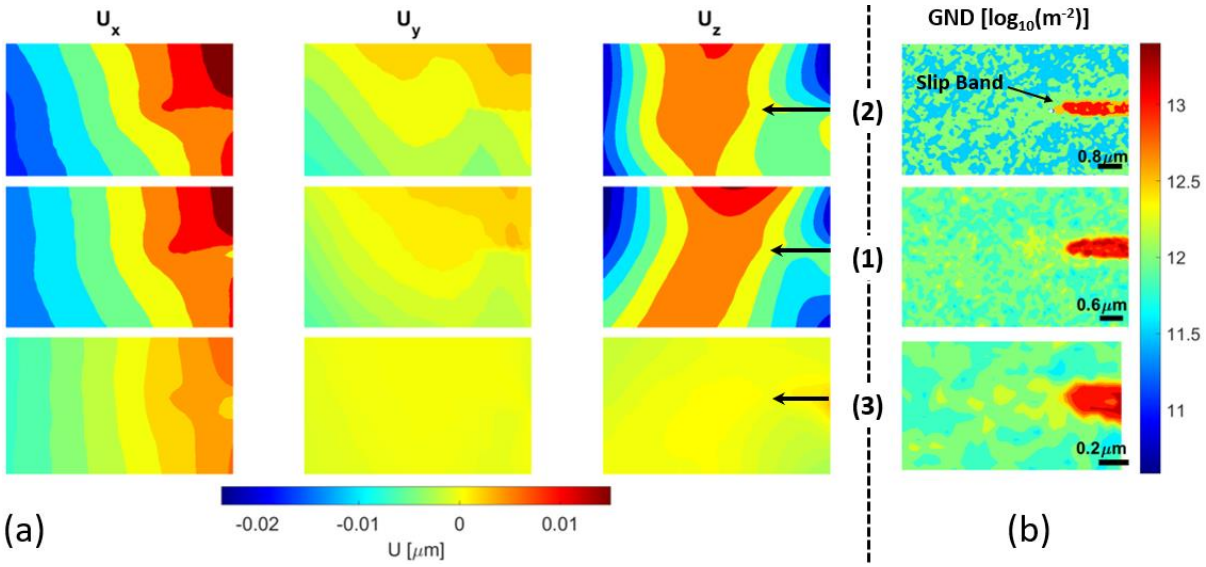


Figure 5-16: (a) integrated elastic displacement fields for the $[1\bar{1}1](\bar{1}12)$ slip bands (labelled 1, 2 and 3); (b) GND density for the same slip bands.

The *J*-integral analysis with mode decomposition to stress intensity factors was applied to the integrated elastic displacement fields, with a distance between consecutive contours of ~75 nm (Appendix (5.A) – Additional figures). The analysed region was chosen to exclude the deformation fields from neighbouring slip bands. The magnitude of all the strain field parameters is highest for the thicker slip bands (Table 5-3), and the mode II and III stress intensity factors were of similar magnitude. The existence of both shear modes is expected since the Burgers vector of the slip band describes shear in a direction at a high inclination angle ($\psi$ at ~107°, measured within the slip plane) from the surface trace, where the slip plane ($\theta$) is at ~60° to the surface. The mode I stress intensity factor, including the small contribution from out-of-plane deformation, has the highest magnitude. As with the incipient slip band,

the tensile mode I stress intensity factor arises from stretching the surface membrane that accommodates the increase in slip step height. Note that the sign of in-plane and out-of-plane shear (mode II and III) is considered irrelevant as it depends on the arrangement of the nodes at the tip and does not carry any physical meaning [86]; however, the sign of mode I is critical as it describes the tensile or compressive conditions at the slip band tip. Thus, the symmetrical out-of-plane (compressive) contribution to mode I ($K_I^r$) is not dependent on the mode III.

Table 5-3: Field parameters calculated for the $[1\bar{1}1](\bar{1}12)$ slip band array. The symmetrical out-of-plane (compressive) contribution to mode I, which is noted as $K_I^r$. The total mode I ($K_I^T$ in equation 5—18) is the summation of the in-plane mode I ($K_I$) and $K_I^r$. The (negative) sign of the in-plane $K_{II}$ and out-of-plane $K_{III}$ shear depends on the arrangement of the nodes at the tip and does not carry any physical meaning [86].

| Label | Thickness (μm) | $J$ (J m$^{-2}$) | $K_I$ (MPa m$^{0.5}$) | $K_{II}$ (MPa m$^{0.5}$) | $K_{III}$ (MPa m$^{0.5}$) | $K_I^r$ (MPa m$^{0.5}$) | $K_I^T$ (MPa m$^{0.5}$) |
|---|---|---|---|---|---|---|---|
| 2 | 0.61 ± 0.02 | 5.10 ± 0.08 | 1.20 ± 0.05 | 0.50 ± 0.03 | -0.69 ± 0.03 | -0.15 ± 0.06 | 1.05 ± 0.08 |
| 1 | 0.59 ± 0.02 | 2.98 ± 0.08 | 0.91 ± 0.01 | 0.15 ± 0.03 | -0.29 ± 0.07 | -0.21 ± 0.02 | 0.70 ± 0.02 |
| 3 | 0.44 ± 0.01 | 0.84 ± 0.02 | 0.37 ± 0.03 | 0.10 ± 0.00 | -0.15 ± 0.02 | -0.06 ± 0.03 | 0.31 ± 0.04 |

In summary, the analysis in this section has shown there is an effect of slip band height on the stress field by examining an inclined array of parallel slip bands under the same state of loading that established the highest Schmid factor on the $[1\bar{1}1](\bar{1}12)$ slip system. The magnitudes of the elastic field and integrated displacements increase with the slip band height, showing how the surface membrane deforms to accommodate the localised shear of the slip band. The elastic fields at the slip band tips, parametrised using the *J*-integral and stress intensity factors, have significant components in modes II and III. This agrees both with

the inclination angle of the slip bands. The effect of their heights is due to the shearing and stretching of the surface membrane surrounding the slip band tips.

### 5.3.3 Loading and unloading of a slip band

The effect of the change of load on a ferrite slip band that terminated mid-grain was investigated by in situ observation. The slip band crossed a low-angle grain boundary (dashed white line Figure 5-18a), and the slip band trace coincides with the $(112)$ plane inclined by 42 ± 1° to the surface ($\theta$ in Figure 5-1). A secondary slip band with the trace of (011) was also present in the field of view (Figure 5-18a.ii). Using the local loading direction matrix (as in section 5.2.3), the $[11\bar{1}](112)$ slip system has the highest Schmid factor, followed by $[11\bar{1}](011)$ (see Appendix (5.B) – HR-EBSD based Schmid factor). The inclination angle ($\psi$) of the shear direction in the $[11\bar{1}](112)$ slip system is 172.3 ± 2.7° (i.e., the Burgers vector lies almost parallel to the observed surface). The 'bloom' of diffuse contrast variation at the slip band tip increased in size as the applied loading was increased by the sample displacement (Figure 5-18a), but there was no measurable change in the slip band thickness (i.e., no measurable change in height), which was constant at 0.21 µm.

The total GND density, estimated using the average within the cropped field of view of Figure 5-18d that included the dislocations of the slip band, increased with the applied displacement and was 11.96 ± 0.03 log($m^{-2}$) at 1 mm, 12.15 ± 0.02 log($m^{-2}$) at 1.2 mm and 12.41 ± 0.03 log($m^{-2}$) after the load was removed following the 1.5 mm total displacement. The dislocation types in the slip band and at the tip vicinity were characterised using the example at the applied sample displacement of 1 mm. The dislocation activity was highest inside the slip band but was also significant in the diffuse zone ahead of the tip. The slip band had a high edge dislocation activity (79.8%), especially $[\bar{1}11]b\ [112]t$ that contributes 43.4% of the total GND

density. The weighted average angle ($\bar{\Phi}$) to the surface normal is estimated to be 41.6 ± 1.7°. However, $[11\bar{1}]b\ [11\bar{1}]t$ screw is the only dislocation type that is mobile on the plane of the slip band. As noted above, the inclination angle ($\psi$) of the $[11\bar{1}]$ Burgers vector is 172.3° to the slip trace, at 48.6° to the surface normal. These mobile screw dislocations comprise only 17.4% of the total dislocations forming the slip band. The 'blooming' zone had a much lower dislocation activity, especially the $[\bar{1}11]b\ [12\bar{1}]t$ edge dislocations.

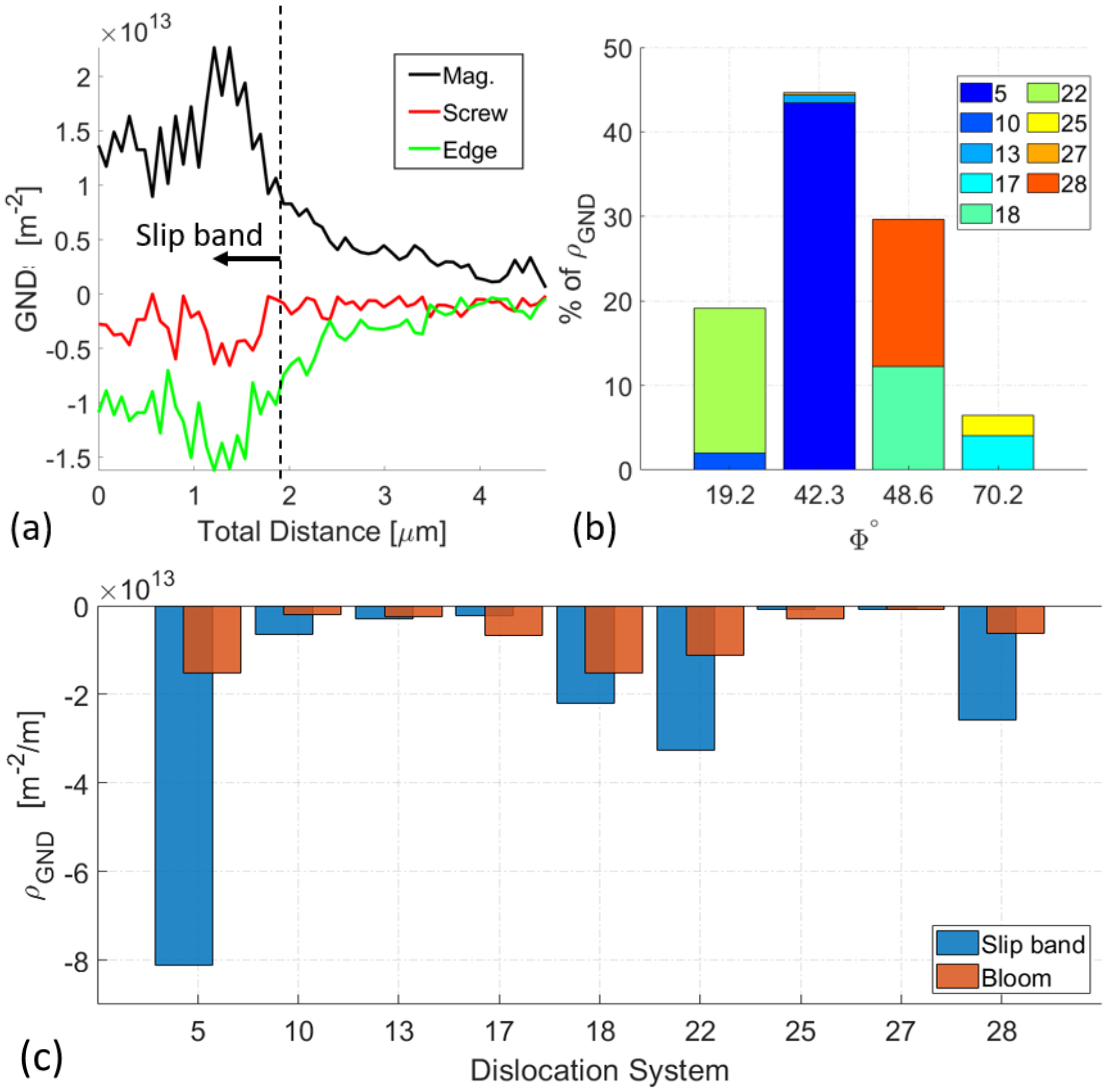


Figure 5-17: (a) Dislocation activity in $[11\bar{1}](112)$ slip band at an applied displacement of 1 mm. Inside the slip band (the area from 0 until the dashed line near the 2 µm marker) (b) the angle (Φ) of each dislocation system Burgers vector to the surface normal with their relative contribution. (c) The dislocation activity at the slip band and the blooming zone. The dislocation system associated with each label is in Table 5-1. The dislocations sign indicates the misorientation direction, with negative values representing sink-like activities and positive pile-up activities [371].

Due to the proximity of the austenite-ferrite phase boundary, the *J*-integral analysis was constrained to 13 contours at 0.75 nm intervals (~2 x 2 µm$^2$ region highlighted with the dashed white box in Figure 5-18b with the slip band tip at the centre). Convergence was achieved after the 6$^{th}$ contour (0.68 µm away from the slip band tip), with average value and variance taken from the 9$^{th}$ to 13$^{th}$ contours. The results (Table 5-4) show that the *J*-integral and mode I and mode II stress intensity factors increased as the specimen displacement was increased (i.e., increasing load) and then decreased when the load was removed. The mode III stress intensity factor and its additional contribution $K_I^r$ to the mode I stress intensity factor were negligible during loading but became significant when the load was removed.

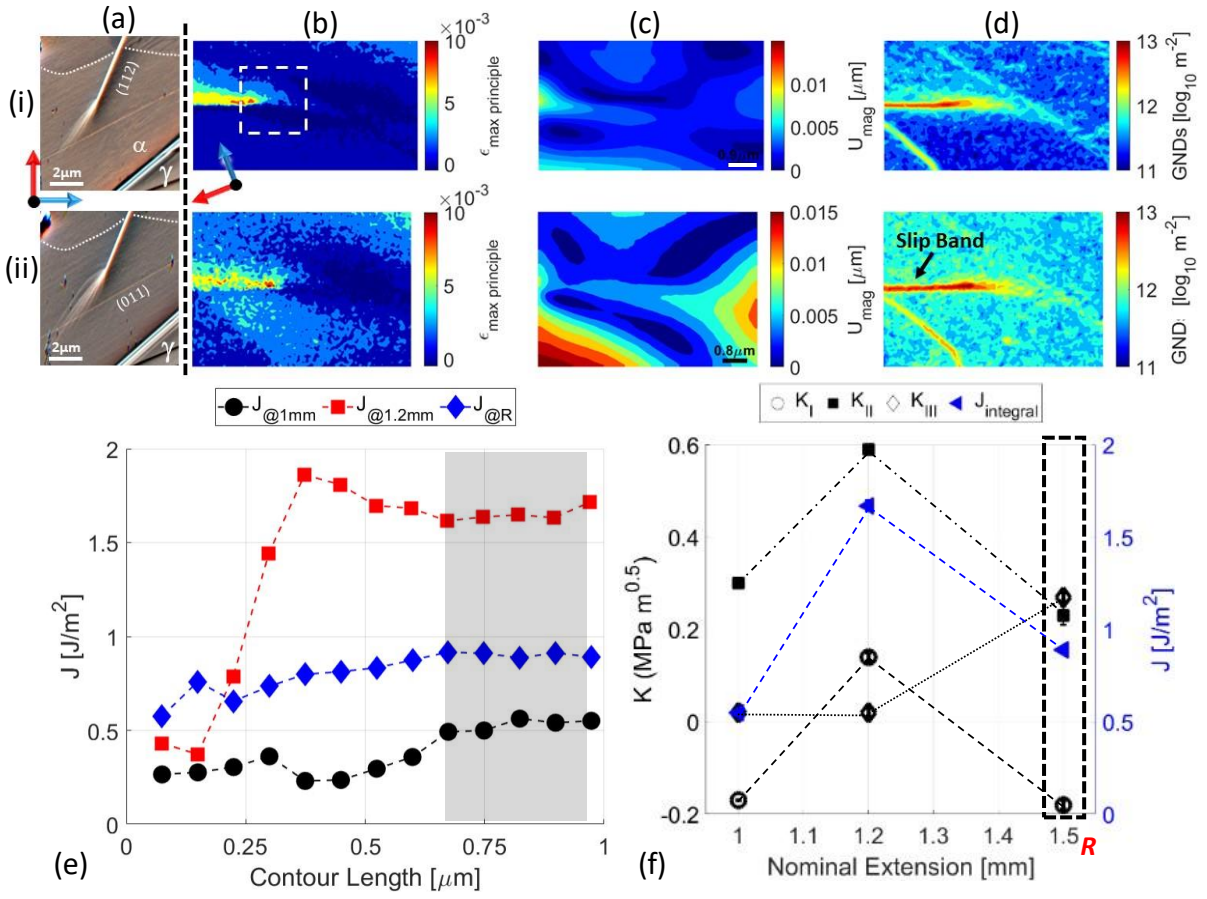


Figure 5-18: In situ loading of a $[11\bar{1}](112)$ slip band in a ferrite (a) grain using (a) VFSD imaging and (b) max principal strain, (c) integrated displacement magnitude, (d) GND density, (e) *J*-integral per contour values, (f) *J*-integral and decomposed $K_I$, $K_{II}$ and $K_{III}$. The notation (i) and (ii) indicate observations with (i) 1 mm and (ii) 1.2 mm extension. The **R** at 1.5 mm indicates that the field was measured ex situ (unloaded) following a 1.5 mm extension.

Table 5-4: Field parameters calculated for the $[\bar{1}11](211)$ Slip bands array when the (nominal) extension was increased from 1 to 1.2 mm before the sample was unloaded and scanned after (further) 1.5 mm extension. In-plane mode I is noted as $K_I$ and symmetrical out-of-plane contribution to mode I as $K_I^r$. The total mode I ($K_I^T$ in equation 5—18) is the summation of the in-plane mode I ($K_I$) and $K_I^r$. The (negative) sign of the in-plane $K_{II}$ and out-of-plane $K_{III}$ shear depends on the chosen arrangement of the nodes at the tip and does not carry any physical meaning [86]. Full convergence is shown in Appendix (5.A) – Additional figures.

| Extension (mm) | $J$ (J m$^{-2}$) | $K_I$ (MPa m$^{0.5}$) | $K_{II}$ (MPa m$^{0.5}$) | $K_{III}$ (MPa m$^{0.5}$) | $K_I^r$ (MPa m$^{0.5}$) | $K_I^T$ (MPa m$^{0.5}$) | GND density ($\log_{10}$ m$^{-2}$) |
|---|---|---|---|---|---|---|---|
| 1 | 0.55 ± 0.02 | -0.17 ± 0.00 | 0.30 ± 0.01 | 0.02 ± 0.00 | 0.02 ± 0.01 | -0.15 ± 0.01 | 11.96 ± 0.03 |
| 1.2 | 1.67 ± 0.03 | 0.14 ± 0.06 | 0.59 ± 0.01 | 0.02 ± 0.01 | 0.01 ± 0.00 | 0.15 ± 0.07 | 12.15 ± 0.02 |
| 1.5 (R) | 0.89 ± 0.00 | -0.18 ± 0.01 | 0.23 ± 0.02 | 0.27 ± 0.01 | -0.12 ± 0.03 | -0.30 ± 0.03 | 12.41 ± 0.03 |

This analysis of the effect of loading considered a slip band in a grain where the slip system of the highest Schmid factor had a Burgers vector at 172.3° to the surface. This direction would favour in-plane shear with minimal out-of-plane shear. Therefore, the slip band responded to load with no measurable change in its width, as there was no meaningful change in its height. The mode III stress intensity factor is low due to the in-plane shear, so it does not increase measurably with the applied load, and it significantly decreases on the removal of load is most probably an error from the analysis (see Appendix (5.D) – 3D integration and EBSP depth resolution). The in-plane mode II stress field increased significantly with loading, though this may have been relaxed by the 'bloom'' of diffuse plastic deformation. The mode I stress intensity factor is judged to arise from the constraint of the local mode II plastic deformation of the slip band tip and increases with the applied load.

## 5.4 General discussion

The stress field measured at the slip-band tip is due to the three-dimensional deformation that occurs as the concentrated plastic shear of the slip band locally stretches the surrounding surface membrane. Here, the 3D elastic field has been quantified by (HR) EBSD, leading to its parameterisation by mode I, II and III stress intensity factors. It is important to recognise that the elastic mode I stress intensity factor does not arise from any opening displacement (i.e., volume change) of the slip band since this cannot occur for dislocation glide. The mode I stress intensity factor is from the tensile stretching that accommodates the height change of the surface membrane due to the mode III shear, as it is constrained by the surrounding matrix [397]. Mode II plastic shear would similarly interact with the mode I field, and the constrained deformation would also affect the stress intensity factors in mode II and III. Hence, the surface characterisation by (HR)-EBSD does not accurately describe the stress field that would exist in a slip band embedded within a three-dimensional assembly of grains.

Nonetheless, the current elastic analysis provides a quantitative measure that may be useful in interpreting slip band behaviour and interactions with other microstructure features. In-plane and out-of-plane deformations have previously been observed, but could not be quantified, in a study that used digital image correlation of secondary electron images to examine the apparent strain concentrations of persistent slip bands that initiated fatigue cracks [397]. That analysis only provided the total strains on the surface (i.e., no elastic strain measurement), but the two-dimensional measurements found a relationship between the in-plane shear and tensile strains, which depended on the inclination angle of shear direction relative to the surface trace (i.e., $\psi$). Slip systems with in-plane shear (slight inclination angle, $\psi$) gave small tensile strains due to the lack of out-of-plane deformation, whereas out-of-

plane shear (larger inclination angle, $\psi$, approaching 90°) shows more significant tensile strains relative to the shear strains.

The relationship between the shear direction in the slip plane, measured by the slip inclination angle ($\psi$), and the shear modes II and III of the stress intensity factors, measured via (HR)-EBSD in this work, is presented in Figure 5-19. This plot includes data from the three exemplar studies above and additional in situ observations that were analysed similarly (see Appendix (5.A) – Additional figures). Figure 5-19 shows that mode II dominates at slip inclination angles closer to 0° or 180°, whereas mode III dominates near 90°. The mode ratio shows a clear trend with the slip inclination angle. The minor deviations from this trend may be attributed to variations in the slip plane orientation ($\theta$) with respect to the surface, which would be a secondary effect in these data due to its more limited range.

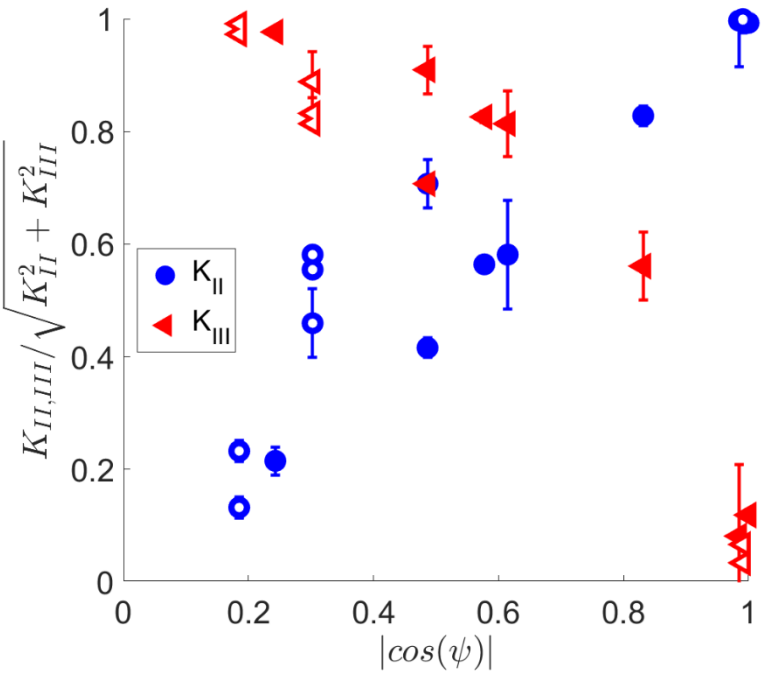


Figure 5-19: Slip inclination angle ($\psi$) relationship to the mechanical conditions at the slip band tip. Mode II and III contributions are presented relative to the magnitude of the effective shear stress intensity factor ($\sqrt{K_{II}^2+K_{III}^2}$). Data from the main text are presented as open symbols. The additional data points from in situ studies of other slip bands are described in Appendix (5.A) – Additional figures and are presented with solid symbols.

The elastic deformation field measured ahead of the slip band describes the stresses in the surface membrane of the observed grain. These are due to the plastic deformation at the tip of the slip band. The localisation of plastic deformation in the slip band is analogous to a mode II/III crack tip opening displacement, as the displacement is a shear that occurs only in a direction within the plane of the slip band. As noted above, this displacement is accommodated by diffuse plastic deformation (the observed 'bloom'), and the elastic field is, therefore, similar to the HRR singularity in the plastic zone of a crack [36,37]. The slip system that defines the slip band is the slip system of the highest Schmid factor due to the local stress tensor acting in the grain, which arises from the applied loading and interactions with adjacent grains. The Burgers vector of this slip system defines the direction of plastic shear in the slip band ($\psi$ in Figure 5-1). For shear directions with an inclination angle that is not close to the surface plane (i.e., $|\cos\psi| \gg 0$) , the slip band height increases as the magnitude of the shear increases. Hence, there is an increase in the magnitude of the elastic mode II and III stress intensity factors in the general case with increasing slip band height (Table 5-3). In the case where the Burgers vector is almost normal to the observed grain surface (Figure 5-12, i.e. (i.e. $|\cos\psi|\sim1$)), the stress field is mostly mode III, and in the case where the shear is almost parallel to the surface (Figure 5-18), the stress field is mostly mode II (i.e., $|\cos\psi|\sim0$). This leads to the general trend of the ratio of mode II to mode III stress intensity factors with the slip inclination angle (Figure 5-19).

Therefore, there is a direct connection between the calculated stress intensity factors and the mechanical conditions at the tip of the slip band. The stress field is affected by relaxation from plastic deformation close to the slip band tip and the constrained changes in the surface topography due to the out-of-plane shear of the slip band. However, the

quantitative analysis of the stress fields shows they are sensitive to the mode and magnitude of deformation of the slip band.

The observations provide insight into the propagation of slip bands, as these are terminated or arrested by the interaction of their emitted dislocations [351] with the surrounding crystal. Du *et al.* [399] showed that visible burst traces (Figure 5-20) at the surface are due to dislocation loops meeting the surface and acting as a stress-relaxing mechanism. New avalanches occur when the previous avalanche moves normal to the slip plane as the stress at sources reaches a critical value. Generation stops due to back-stress, which can be overcome by increasing the external stress [351]; thus, creating – jerky – intervals of (internal) short blooms and occasional (surface) large blooms/bursts at the slip band due to stress accumulation and (relaxation due to) repelling of (immobile) dislocation at the tip vicinity [399–401]. Thus, slip bands are sites where the shear deformation due to mobile dislocations is localised rather than diffused. Diffuse plastic deformation at the slip band tip acts to relax the (pressure) stress field [11,351] as the matrix yields near the slip band tip [402]. Due to this plastic deformation, the total in-plane and out-of-plane displacements are greater than the elastic displacements (Figure 5-18c) that cause the stress field, and the change in surface topology from diffuse plastic deformation is observed as the 'blooming' contrast (Figure 5-16a). The intensity of this topographical blooming and the elastic displacement magnitude increased with loading (Figure 5-20b) and slip band step height (Figure 5-13a) and is not directly linked to high GND density or change in lattice rotation. This is contrary to blooming observed ahead of slip bands impinged at grain boundaries [298,403], but it is somewhat similar to the surface displacement bursts due to internal movement of dislocations observed in nano-compression tests [350,400,401].

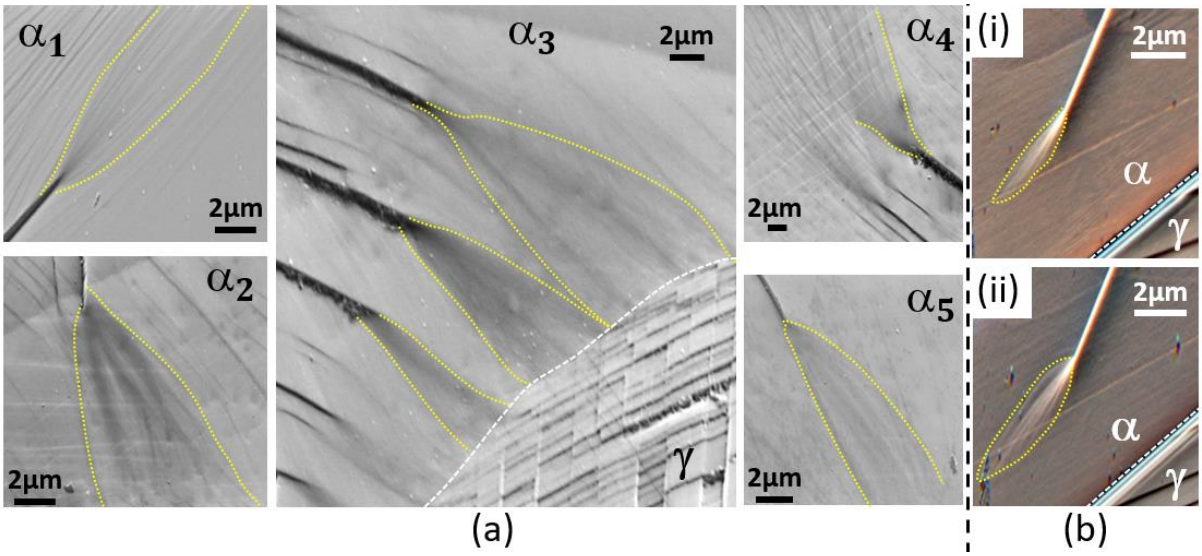


Figure 5-20: (a) In-lens images of plastic blooming from the tip of slip bands in the ferrite phase of age-hardened duplex stainless-steel material. (b) VFSD image of blooming/burst ahead of $[11\bar{1}](112)$ slip band at (i) 1 mm and (ii) 1.2 mm extension.

Resolving the individual dislocation types at the location of the slip band by using the mapped GND density was used to calculate the average orientation of their Burgers vector with respect to the sample surface. This dislocation activity was mainly from dislocations that were immobile on the slip band plane and necessary to maintain the geometrical distortion of the slip band [404]. A higher dislocation activity was observed at the slip band with more edge dislocations activity compared to screw dislocations which are associated with high-GND density (or hot) spots [405] and with lower slip band height (Figure 5-14a) in the array of slip bands. This is consistent with previous observations that found the thickness of the stress concentrations was inversely related to the dislocation density [406]. This length scale aspect is similar to the low GND density found around larger indents [407]. GND density abruptly decreased ahead of the slip band tip, similar to that observed at crack tips and linked to the intense strain gradient [408]. Therefore, the GND density relates to the plastic strain gradient that locally accommodates the slip band shear.

Some factors lead to quantitative limitations in the current analysis:

(1) The current method of selecting the least deformed pattern as a reference may still suffer from 'the reference pattern problem' [87,128], which will affect the magnitude of the strain component (and minimally GND density, see Chapter 3). Consequently, an incorrect reference would affect the integrated displacements field, calculated *J*-integral and decomposed stress intensity factors. An absolute three-dimensional lattice strain field can be obtained using micro-Laue microdiffraction [108–110] and dark-field X-ray microscopy [111], and future studies may employ such techniques.

(2) Experimental measurements [409,410] have shown that HR-EBSD is not accurate in estimating the out-of-plane shear strains components distribution or magnitude, which will affect the reliability of the integrated $U_z$ and consequently $K_{III}$ and $K_I^r$.

(3) $K_{III}$ and $K_I^r$ are dependent on the assumption made about the EBSPs' depth information but the in-plane mode I and mode II are not affected (see Appendix (5.D) – 3D integration and EBSP depth resolution).

(4) The integrated out-of-plane displacement ($U_z$) is also affected by the size of the selected window for integration. This will directly affect $K_{III}$ , with an effect also on mode I through the symmetrical out-of-plane field (i.e., $K_I^r$). However, it does not affect the in-plane displacement components ($U_x$ and $U_y$). This effect is apparent in the unloaded slip band after 1.5 mm straining (section 5.3.3).

(5) To a lesser extent, the assumption of surface traction-free ($\sigma_{33} = 0$) conventionally made for (HR)-EBSD analysis might not be accurate for the loaded slip band due to image forces at the free surface [411]. However, a counter-argument can be made by considering the $EBSP_0$ mean depth information (<200nm) and the material's atomic number [161].

Most of these limitations would apply to any assessment by HR-EBSD of the surface stress fields since they are affected by the out-of-plane deformations, and the limitation is not specific to their parameterisation as stress intensity factors.

The HR-EBSD technique provides a combination of sensitivity, spatial resolution, and ease of use compared to other techniques [115–117] used to study elastic and plastic deformation. Local mapping of the stress fields associated with slip bands and other stress-concentrating features provides an alternative to micro-mechanical experiments with pillars and cantilevers, which have drawbacks that include the adverse effect of FIB milling preparation including inducing residual stress and embrittlement [412], pre-strain [413], length-scale dependency [414], and the different behaviour between constrained and unconstrained crystals [415]. The (stereo) HR-EBSD analysis method to parameterise stress concentrations described here improves the in-plane method previously used to study deformation twinning in Chapter 4 as it extends the analysis to the third dimension. It does, however, require an approximate estimate of the EBSPs' depth resolution that might affect the reliability of the evaluation of the magnitudes of $K_{III}$ and $K_I^r$ (see Appendix (5.D) – 3D integration and EBSP depth resolution).

## 5.5 Conclusion

Slip bands that were terminated mid-grain in the ferrite phase of a 475 °C age-hardened duplex stainless-steel (Zeron 100: 25%Cr, 7%Ni) have been characterised in situ using electron backscatter diffraction (EBSD), high (angular) resolution (HR)-EBSD and secondary electron (SE) imaging. A novel analysis used the measured stress field to determine the local Schmid factors of the slip systems in the observed grains; this was validated by observing the slip band plane and shear direction.

The local measurements allowed a novel 3D parametrising of the stress fields at the slip band tip by evaluating the potential elastic strain energy release rate (*J*-integral). This was decomposed using auxiliary fields, with the assumption of small-scale plasticity, to obtain the three-dimensional stress intensity factors that described the magnitudes and modes of the stress concentration. The analysis was demonstrated by examining the mechanical conditions at an incipient slip band, the direct effect of the slip band height in an array of parallel slip bands, and the effect of loading of a slip band. The three-dimensional stress intensity factors were consistent with the magnitude and mode of the shear of the slip band; the ratio of the mode II to mode III stress intensity factors depended on the slip inclination angle relative to the observed surface.

The constraint of the topological changes of the surface due to shear induces additional tensile stresses; hence, this analysis provides a quantitative description of the stress fields of slip bands that affect their interaction with microstructure. GND density analysis indicated high edge dislocation activity at the slip band that abruptly decreased just ahead of the slip tip, with an inverse correlation between dislocation activity and slip band height near the slip tip.

# Chapter 6. HR-EBSD analysis of in situ stable crack growth at the micron scale in single-crystal silicon

Content



## 6.1 Introduction

Local analysis using *J*-integral used experimental data for elastic strain fields that were mapped by synchrotron X-ray diffraction; the elastic strains were integrated to find the equivalent elastic displacement field that provides the missing derivatives (i.e., $u_{2,1}$) required for $J$-integral analysis (Chapter 2). The strain mapping was done by diffraction at a relatively large scale (cm-size specimens with mm-size cracks) and with low spatial resolution. To study the criteria for crack growth at the micron scale within the microstructure, for instance, in local investigations of the toughness of brittle phases or coatings, there is a need for high-resolution data. It is also necessary to characterise the stress and strain fields in situ at, or

approaching, the critical state for crack propagation. Furthermore, the analysis needs to be appropriate to inclined crack planes that are not necessarily well-oriented for surface observations. Such an approach could replace or complement existing micro-mechanical test methods that rely on analytical solutions; these require knowledge of the applied loads and displacements, sample geometry, crack length, etc., [375,416] that can be difficult to obtain accurately. Micro-mechanical tests, which are primarily focused on mode I loading, may also be dependent on size and affected by FIB-milling damage [416,417], and can be influenced by non-symmetrical loading [418] and user bias [419].

In the previous chapters, it was shown that the $J$-integral could be used to parameterise the two-dimensional strain fields, measured by HR-EBSD, of the singularities of cracks (ex situ) [420], deformation twins (in situ) (Chapter 4). However, these analyses did not consider the three-dimensional nature of the stress concentrator, such as its inclined plane or the effect of out-of-surface displacements on the near-surface strain field.

This study presents a novel approach to calculating and decomposing the $J$-integral elastic energy release rate to the three-dimensional stress intensity factors directly from the elastic deformation gradient tensors obtained from the near-surface by membrane HR-EBSD. As a demonstration, the field ahead of cracks – observed in situ – was parametrised while propagating under quasi-static, mixed-mode conditions on inclined planes within (001) silicon single-crystal wafers.

## 6.2 Method

### 6.2.1 Materials and experimental details

A sample (Figure 6-5, Table 6-1), measuring 9.7 x 8.9 x 0.5 $mm^3$, was cleaved from a single crystal silicon wafer with a thickness of 0.5 mm. Its pre-polished surface was parallel to $(001)$ (Figure 6-1a). The loaded edges of the sample, parallel to $[110]$, were abraded manually. The sample was positioned between the jaws of a 2 kN Deben® 70° pre-tilted loading stage inside a Carl Zeiss Merlin field emission gun scanning electron microscope (FEG-SEM). The SEM chamber and loading stage were plasma cleaned and purged for 1 hour before the sample was loaded by compression in the $[\bar{1}10]$ direction in displacement-control by the movement of one jaw. The loading speed, initially 0.1 mm $min^{-1}$, was increased to 0.2 mm $min^{-1}$ after some initial damage occurred (see additional Figure 9-32, and the red line in Figure 6-1b indicates the change). Once a stable propagating crack was established, the loading was arrested at fixed displacement to allow the acquisition of electron backscatter patterns (EBSPs) to map the vicinity of the crack tip whilst under load. The exact loading and subsequent analysis methods were also used to test other specimens from (001) single-crystal silicon wafers, as described in Table 6-2.

The EBSPs were collected using a Bruker eFlash CCD camera using conditions of a 20 kV/10 nA beam, 18 mm working distance, and 200 millisecond exposure time per pattern. The step size was 0.25 µm, so the 800 x 600-pixel area mapped was about 20 x 15 $\mu m^2$. Load relaxation during the EBSD mapping was negligible (<2.8%). For the exemplar sample, the crack was propagated incrementally in 12 intervals (indicated by the dotted blue lines in Figure 6-1b).

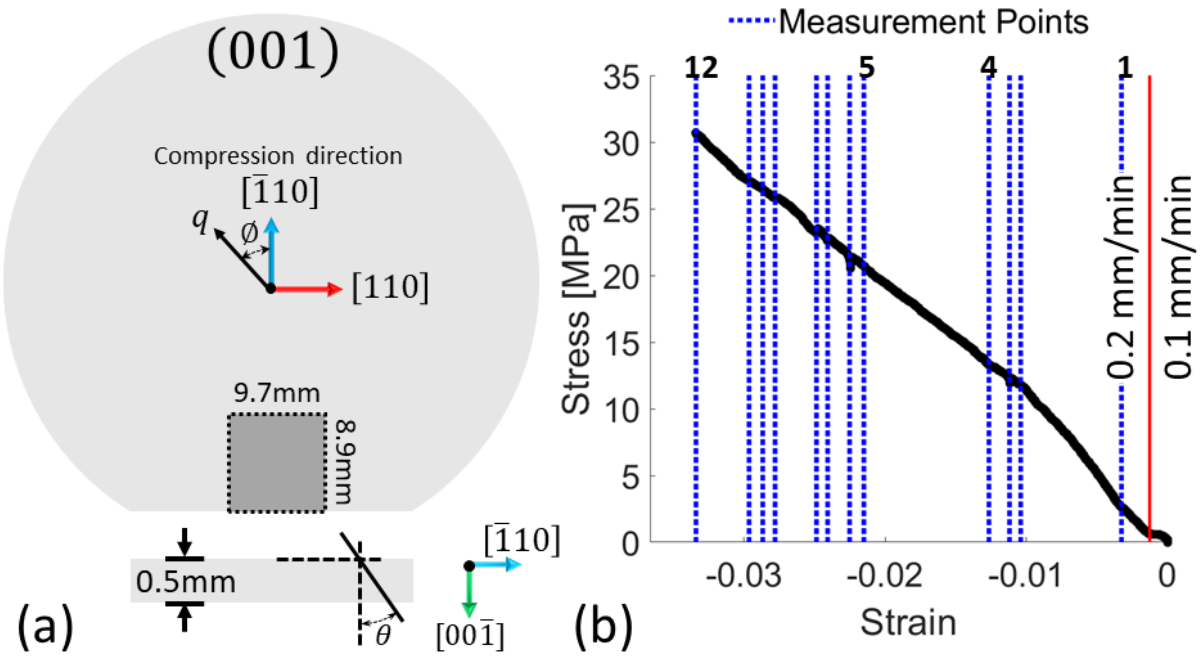


Figure 6-1: (a) Schematic of pre-polished Silicon (001) wafer with the 9.7 x 8.9 x 0.5 mm3 cleaved specimen that was loaded in compression parallel to $[\bar{1}10]$. The crack trace angles, ϕ, measured to the x-axis and θ, measured to the z-axis, are shown. (b) Nominal stress and strain (crosshead displacement/sample dimension). Loading started at a low speed of 0.1 mm $min^{-1}$, and the minor load dip near the red line in Figure 6-1b is due to the detachment of a small fragment at the loading contact. The speed was then increased to 0.2 mm min-1 (at the red line in b). The blue lines marked the collection of EBSD data when loading was suspended at fixed displacement.

Focused Ion Beam (FIB) milling was used to investigate the sub-surface orientation of the crack. This was done using a Zeiss Auriga dual-beam SEM-FIB system that has a Schottky field emission Gemini electron column coupled with an Orsay Physics 'Cobra' Ga+ ion FIB. The sample was tilted to 54° and positioned at a working distance of 5 mm. At each point of investigation, a 35 µm deep trench was cut by rough (16 nA/ 30 kV) and then fine milling (600 pA/ 30 kV). The crack trace on the trench wall, which is parallel to $[00\bar{1}]$ was measured with in-lens secondary electron (SE) imaging conditions at 36° tilt correction (i.e., an effective 90° view) over a depth of 15 µm (Figure 6-2c). All angles and distances were measured using ImageJ [318], and the uncertainties in angle and crack increment measurement were less than ±0.5° and ±0.5 µm, respectively.

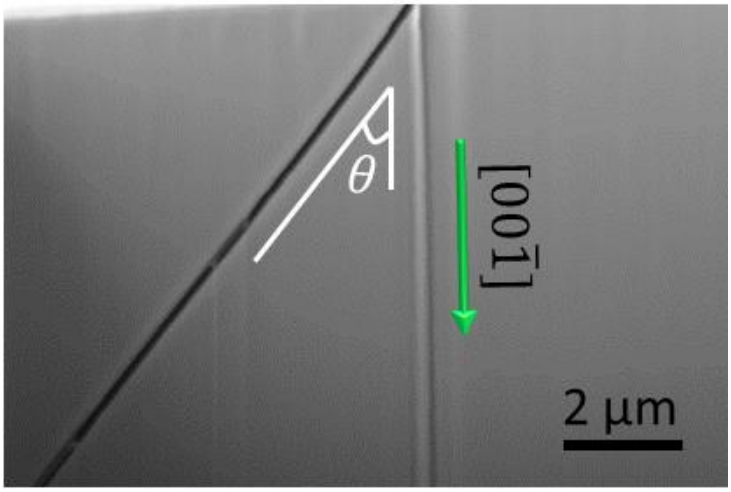


Figure 6-2: Secondary electron image for the crack labelled A in Figure 6-4g.

The elastic deformation field was calculated by cross-correlation of the EBSPs with a reference pattern ($EBSP_0$) acquired remotely from the crack and assumed stress-free (see Chapter 3). The interplanar spacing and zone axes changes were measured in 30 independent regions of interest in each EBSP, with bicubic interpolation to obtain the best-fit solution. The difference from the reference $EBSP_0$ was related to the elastic deformation gradient tensor ($F_{ij}$), which was polarly decomposed with an average sensitivity of 1.6 x $10^{-4}$ to deviatoric strains, $\epsilon_{ij}$, (symmetric part, where $ij = ji$) and lattice rotations $\omega_{ij}$ (asymmetric part, where $ii = jj = 0$) [156,158] even when the field of view hugely overlapped at a crack labelled 2. See Appendix (6.B) – In situ EBSP0 selection.

Conditions of a traction-free surface ($\sigma_{33} = 0$) was assumed [161], and anisotropic elastic properties were obtained using (001) Silicon orthotropic stiffness tensor ($C_{11} = 165.7, C_{44} = 79.6, C_{12} = 63.9$ in GPa [213]). The full deviatoric-strain and elastic stress components represent the surface membrane sampled by the backscattered electrons. The geometrically necessary dislocation (GND) distribution was estimated as detailed in Appendix (3.B) – Geometrically necessary dislocations (GND) density estimation.

### 6.2.2 Numerical evaluation of the $J$-Integral

To simplify the analysis of the $J$-integral energy release rate, the elastic deformation gradient tensor, $F_{ij}$, was transformed to resolve the field to axes relative to the plane of the crack that was defined by its trace on the FIB section and its propagation direction, $q_1$; the latter obtained from its trace on the pre-polished surface. The transformed elastic deformation gradient tensor, $F'_{ij}$, was obtained by $Q_z$ transformation and then $Q_x$ transformation of equations (6—1) to (6—3); thus, $x_3 \perp q_1 \parallel x_1$, where $\theta$ is the angle between the crack plane and the $z$-axis and $\emptyset$ is the angle between the surface crack trace and the $x$ axis (Figure 6-1a).

$$Q_{z(\emptyset)} = \begin{bmatrix} \cos\emptyset & \sin\emptyset & 0 \\ -\sin\emptyset & \cos\emptyset & 0 \\ 0 & 0 & 1 \end{bmatrix} \qquad 6—1$$

$$Q_{x(\theta)} = \begin{bmatrix} 1 & 0 & 0 \\ 0 & \cos\theta & \sin\theta \\ 0 & -\sin\theta & \cos\theta \end{bmatrix} \qquad 6—2$$

$$F'_{ij} = Q_{pi} Q_{qj} F_{ij} \qquad 6—3$$

For convenience, the superscript $F'_{ij}$ will be omitted in the subsequent discussion, such that $F_{ij}$ refers to the elastic deformation gradient tensor after transformation to the frame of reference of the crack. The same transformations were applied to the stiffness tensor [214].

Evaluating the $J$-integral required computation of the $q_1$-field and formulation of the equivalent domain integration (EDI) with the domain expanding from the crack tip. The $q_1$ vector undergoes a smooth linear spatial variation across the domain ($\frac{dq_1}{dx_1}$ in 6—4), with magnitude unity inside and zero outside the domain. The virtual crack propagation direction, $q_1$, is assumed to be in the positive $x_1$ direction and the crack tip is located centrally in a square contour of the mapped strain field, defined by elements (Figure 6-3) [63]. These conditions simplify the EDI $J$-integral analysis to equation (6—4) using a regularised mesh of

zero thickness (i.e., surface measurement assuming plane stress conditions) where no re-mapping to the element nodes is required.

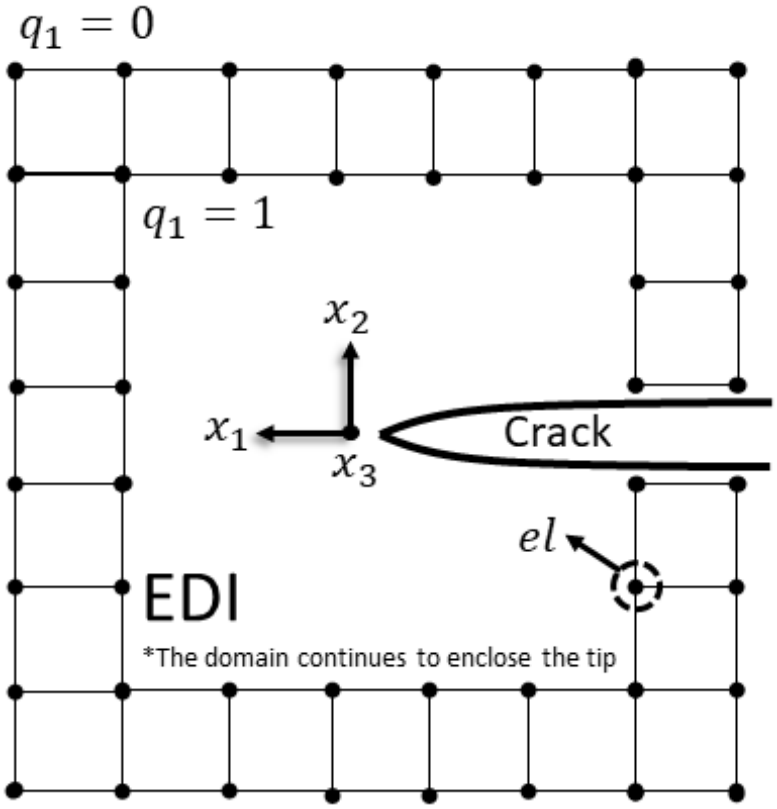


Figure 6-3: Schematic of the crack and the equivalent domain integral (EDI) method to calculate the potential elastic strain energy release rate or the $J_1$ or $J$-integral (so-named '$J$' for James Rice) for a monotonically loaded crack extending in $q_1$ direction as shown in equation (6—4), where $\sigma_{ij}$ is the stress tensors, $W$ is the elastic strain energy density, and $u_{i,j}$ is displacement/distortion gradient. The area increment along the equivalent domain is $dA$ and each element node $el$ is at a point on the EBSD acquisition grid (step size 0.25 µm).

$$J = \sum_{el=1}^{N_{el}} \left[ \left( \sigma_{11} u_{1,1} + \sigma_{12} u_{2,1} + \sigma_{13} u_{3,1} - W \right) \frac{dq_1}{dx_1} + \left( \sigma_{22} u_{2,1} + \sigma_{12} u_{1,1} + \sigma_{23} u_{3,1} \right) \frac{dq_1}{dx_2} \right] dA \qquad 6—4$$

As noted in the introduction, in linear-elastic materials (or with small-scale yielding conditions), the $J$-integral can be related to the three-dimensional elastic stress intensity factors using a mode-decomposition technique that separates the elastic field to symmetric

(mode I), in-plane skew-symmetric (mode II), and out-of-plane skew-symmetric (mode III) components. This is done by superimposing an auxiliary field onto the total field, mirrored along the $q_1$ vector (parallel to $x_1$-axis) with mesh symmetry due to the equally spaced grid. The stress intensity factors are directly related to the appropriate mode-specific $J$-integrals (i.e., $J^I$, $J^{II}$, and $J^{III}$) as in equation (6—5), using values of Youngs' modulus ($E$), shear modulus ($\mu$) and Poisson's ratio ($v$) estimated from the anisotropic stiffness tensor after being transformed to the crack plane normal [421]. The effective stress intensity factor $K_{\text{eff}}$ is directly calculated from the total energy release rate ($J$) as in equation (6—6) assuming plane stress conditions.

$$J = J^I + J^{II} + J^{III} = \frac{K_I^2}{E} + \frac{K_{II}^2}{E} + \frac{K_{III}^2}{2\mu} \qquad 6—5$$

$$K_{\text{eff}} = \sqrt{JE} \qquad 6—6$$

The deformation gradient tensors obtained from HR-EBSD are decomposed to solve equation (6—4) by following a similar derivation applied to displacement and stress fields [368,386,387,422]. The displacement derivatives ($u_{i,j}$) were expressed using $F_{ij}$ and the Kronecker delta ($\delta$) (which equals unity when $i = j$) as in equation (6—7). These derivatives were split into modes I, II and III. The mode decomposition of normal out-of-plane deformation components is debatable, where Nikishkov and Atluri [368], Shivakumar and Raju [387], Huber *et al.* [386], Rigby and Aliabadi [422] related the asymmetrical portion to mode III; Rigby and Aliabadi [388] showed that for mode III the strain $\varepsilon_{33}^{III}$ and stress $\sigma_{33}^{III}$ are both equal to zero at the crack front which is adopted when decomposing $F_{33}$; thus, equation (6—9) gives the displacement derivatives required for equation (6—4).

$$u_{i,j} = u_{i,j}^{I} + u_{i,j}^{II} + u_{i,j}^{III} = \sum_{M} F_{ij}^{M} - \delta_{ij}^{M}, \quad i,j = 1,2,3, \qquad M = I, II, III \tag{6—7}$$

$$\begin{aligned} u_{i,j} = {} & \frac{1}{2}\begin{pmatrix} u_{1,1} + \bar{u}_{1,1} & u_{1,2} + \bar{u}_{1,2} & u_{1,3} + \bar{u}_{1,3} \\ u_{2,1} - \bar{u}_{2,1} & u_{2,2} - \bar{u}_{2,2} & u_{2,3} - \bar{u}_{2,3} \\ u_{3,1} + \bar{u}_{3,1} & u_{3,2} + \bar{u}_{3,2} & u_{3,3} + \bar{u}_{3,3} \end{pmatrix} \\ & + \frac{1}{2}\begin{pmatrix} u_{1,1} - \bar{u}_{1,1} & u_{1,2} - \bar{u}_{1,2} & 0 \\ u_{2,1} + \bar{u}_{2,1} & u_{2,2} + \bar{u}_{2,2} & 0 \\ 0 & 0 & u_{3,3} - \bar{u}_{3,3} \end{pmatrix} \\ & + \frac{1}{2}\begin{pmatrix} 0 & 0 & u_{1,3} - \bar{u}_{1,3} \\ 0 & 0 & u_{2,3} + \bar{u}_{2,3} \\ u_{3,1} - \bar{u}_{3,1} & u_{3,2} - \bar{u}_{3,2} & 0 \end{pmatrix} \end{aligned} \tag{6—8}$$

$$\begin{aligned} u_{i,j} = {} & \frac{1}{2}\begin{pmatrix} (F_{11} + \bar{F}_{11}) - 1 & F_{12} + \bar{F}_{12} & F_{13} + \bar{F}_{13} \\ F_{21} - \bar{F}_{21} & F_{22} - \bar{F}_{22} & F_{23} - \bar{F}_{23} \\ F_{31} + \bar{F}_{31} & F_{32} + \bar{F}_{32} & (F_{33} + \bar{F}_{33}) - 1 \end{pmatrix} \\ & + \frac{1}{2}\begin{pmatrix} F_{11} - \bar{F}_{11} & F_{12} - \bar{F}_{12} & 0 \\ F_{21} + \bar{F}_{21} & (F_{22} + \bar{F}_{22}) - 1 & 0 \\ 0 & 0 & F_{33} - \bar{F}_{33} \end{pmatrix} \\ & + \frac{1}{2}\begin{pmatrix} 0 & 0 & F_{13} - \bar{F}_{13} \\ 0 & 0 & F_{23} + \bar{F}_{23} \\ F_{31} - \bar{F}_{31} & F_{32} - \bar{F}_{32} & 0 \end{pmatrix} \end{aligned} \tag{6—9}$$

Finally, to calculate the strain energy density, W, the Green-Lagrangian strain tensor, is split from the deformation gradient (or displacement gradient) tensors as in equations (6—10) and (6—11).

$$\varepsilon_{ij} = \frac{1}{2}\left(F_{is}^{T} F_{sj} - \delta_{ij}\right) \approx \frac{1}{2}\left(u_{i,j} + u_{j,i}\right) \tag{6—10}$$

$$\varepsilon_{ij} = \varepsilon_{ij}^{I} + \varepsilon_{ij}^{II} + \varepsilon_{ij}^{III}$$

$$\begin{aligned} \varepsilon_{ij} = {} & \frac{1}{4}\begin{Bmatrix} \varepsilon_{11} + \bar{\varepsilon}_{11} & \varepsilon_{12} - \bar{\varepsilon}_{12} & \varepsilon_{13} + \bar{\varepsilon}_{13} \\ \varepsilon_{21} - \bar{\varepsilon}_{21} & \varepsilon_{22} + \bar{\varepsilon}_{22} & \varepsilon_{23} - \bar{\varepsilon}_{23} \\ \varepsilon_{31} + \bar{\varepsilon}_{31} & \varepsilon_{32} - \bar{\varepsilon}_{32} & \varepsilon_{33} + \bar{\varepsilon}_{33} \end{Bmatrix} + \frac{1}{4}\begin{Bmatrix} \varepsilon_{11} - \bar{\varepsilon}_{11} & \varepsilon_{12} + \bar{\varepsilon}_{12} & 0 \\ \varepsilon_{21} + \bar{\varepsilon}_{21} & \varepsilon_{22} - \bar{\varepsilon}_{22} & 0 \\ 0 & 0 & \varepsilon_{33} - \bar{\varepsilon}_{33} \end{Bmatrix} \\ & + \frac{1}{4}\begin{Bmatrix} 0 & 0 & \varepsilon_{13} - \bar{\varepsilon}_{13} \\ 0 & 0 & \varepsilon_{23} + \bar{\varepsilon}_{23} \\ \varepsilon_{31} - \bar{\varepsilon}_{31} & \varepsilon_{32} + \bar{\varepsilon}_{32} & 0 \end{Bmatrix} \end{aligned} \tag{6—11}$$

The mode-specific full deviatoric-strain tensors ($\varepsilon_{ij}^{M}$) and elastic stress ($\sigma_{ij}^{M}$) are then related by Hooke's law with the anisotropic stiffness matrix. The MATLAB® code that implements this method and a benchmarking dataset are available at https://doi.org/10.5281/zenodo.6411485. For details of error analysis, see Appendix (6.C) – Analytical field benchmarking.

## 6.3 Results

After initial damage, a $[\bar{3}10](11\bar{1})$ ± 5.3° crack was nucleated near the centre of the moving jaw and propagated into the sample. A serrated parallel crack has also appeared along the main crack path while occupying the same main crack plane with (plane) bridging between the parallel crack and the main crack (Figure 6-5a and b). The crack changed plane while almost maintaining direction to $[\bar{3}10](12\bar{1})$ ± 2.3°, at the point labelled (B) in Figure 6-4 after 79.2 µm, before starting to curve and assuming the $[\bar{1}00](110)$ ± 6.0° at point (C), 122.1 µm away from the initiation site, until (D) after 229.7 µm. At (D), the crack zigzagged to $[\bar{3}\bar{1}0]$ and back to $[\bar{1}00]$ without changing the plane. The crack gradually changed plane, taking (031) ± 2.1° at point (E), 431.5 µm from the origin. At this point, the jaw was held at fixed displacement to allow for EBSD patterns acquisition at nominal stress of 2.6 MPa.

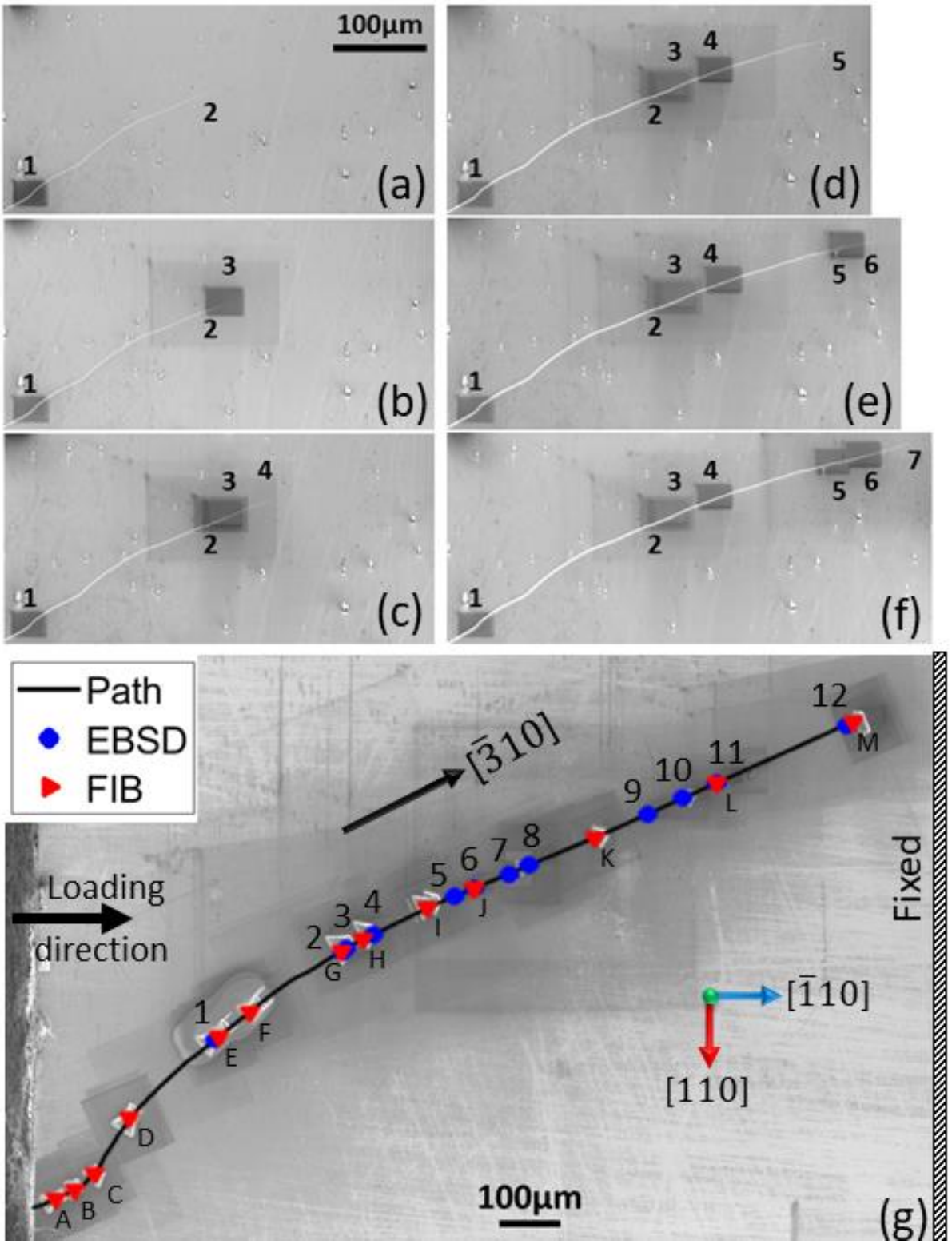


Figure 6-4: Example of crack propagation in a (001) silicon wafer loaded in compression parallel to $[\bar{1}10]$: a) showing the crack path, HR-EBSD mapping, and FIB cutting locations. The numbers mark the intervals of crack growth, after which the stable crack tip was observed under load by HR-EBSD. The sample surface was cleaned from the accumulated debris before FIB cutting of trenches parallel to $(110)$ at the marked locations to examine the sub-surface crack geometry (a-f) intervals for compressive crack growth. (g) Total crack path, including locations of EBSD mapping and FIB sectioning.

The crack was then propagated incrementally under quasi-static conditions by in-plane compression of the (001) single-crystal silicon wafer while acquiring EBSD patterns. Propagation was practically constant over ~700 µm (labels 5 to 12), with the propagation direction within 1° of $[\bar{3}10]$ and the crack plane within 4° of (131). Collected EBSD data was used to confirm the wafer orientation and to define $x$ and $y$ axis (see Appendix (6.A) – Additional figures, Figure 9-33). The pole figure was then used to identify the crack direction and (non-cleavage) plane by plotting the various poles of planes using a Wulff net to find the low index pole with an angle close to the measured $\theta$.

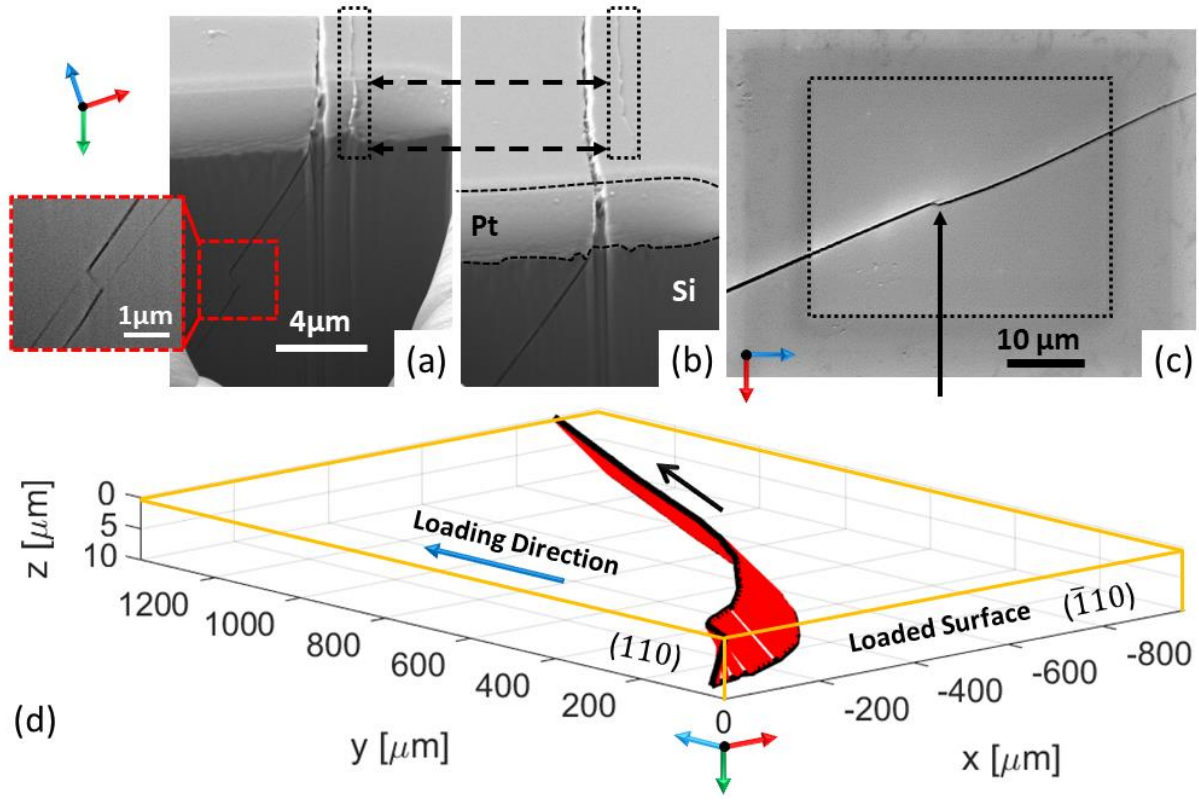


Figure 6-5: (a-b) FIB sliced of branched parallel cracks with a dashed box highlighting the serrated crack paralleled to the main crack as the two cracks bridge as shown in the (red-box) zoom. (c) kinked crack tip after EBSD acquisition (black dotted box) and increased load to grow the crack. (d) 3D visualisation of the crack geometry close to the surface, using the FIB slice traces and cubic interpolation between points.

Figure 6-5a to f shows incremental propagation of the crack until the 7th interval, and Figure 6-5g shows the fracture surface, the locations of the in situ HR-EBSD measurements, and subsequent FIB trench cuts that revealed its sub-surface inclination. The construction of crack path geometry using FIB slicing (and cubic extrapolation between points) can be seen in Figure 6-5d. The nominal applied stress and the orientation and crack length increment at each observation are summarised in Table 6-1.

After breaking open the sample, an inspection of the fracture surface (Figure 6-6) shows that the crack plane was generally smooth over the propagation region of interest following the complex initiation of fracture. Small steps (beach marks similar to 'Wallner' lines) indicate the crack front was essentially perpendicular to the EBSD-observed (001) surface. Wing cracks can be observed between locations 5 to 9 (Figure 6-6b). With torsion force being applied to fracture the sample open, some of these features (especially the twist hackles) were induced after the last EBSD scanned; the point labelled 12. Interestingly, the crack changed plane and direction after it was broken open by twisting one side, and the fracture surface was smoother but not completely flat/smooth, taking the $[\bar{1}10](110)$ ± 2° near the measurement surface $[\bar{1}10](111)$ ± 2° at the bottom.

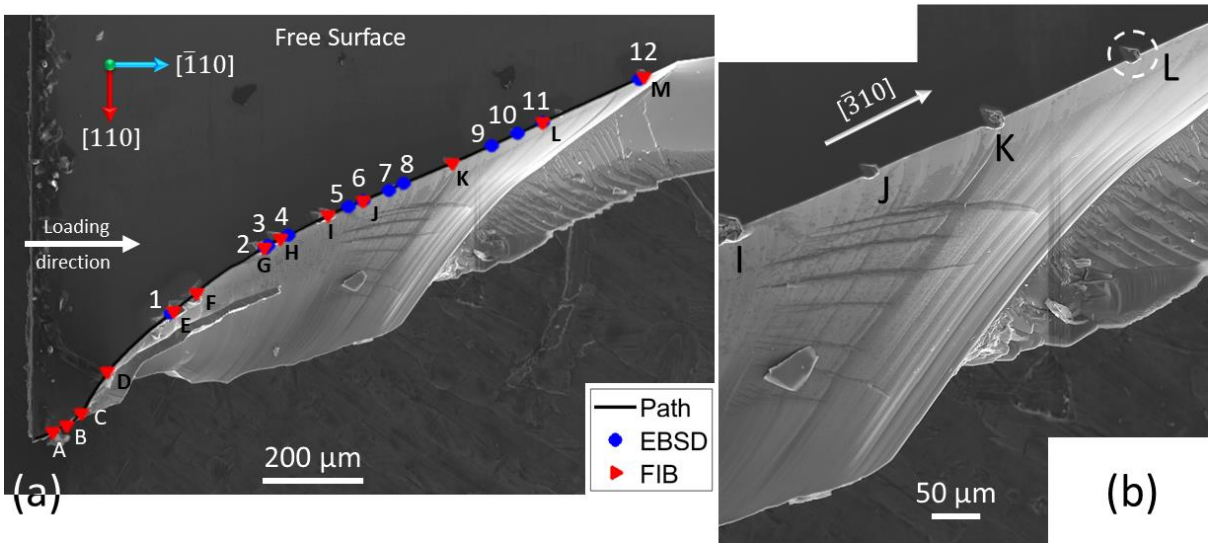


Figure 6-6: (a) SEM image of the specimen from Figure 2 after fracture with (b) highly magnified image of the small steps and wing cracks. The locations of the FIB sites are labelled similar to Figure 6-5. Exemplar damage at the fibbing site is circulated near L in (b).

The example of an in situ HR-EBSD observation of the crack (Figure 6-7) shows the elastic plane stress components (Figure 6-7a) and the decomposed mode I, II, III von Mises stresses after rotational transformations (Figure 6-7b). Here, the field has been rotated ($Q_z$) to align the crack trace with the $x_1$-axis and translated to place the crack tip at the centre of the map, which has been cropped to 15 x 15 µm$^2$. The same stress field is shown in Figure 6-7c after rotation ($Q_x$) to align $x_3$ perpendicular to the crack plane,. The most significant effect is observed in the shear components; the magnitude of in-plane shear ($\sigma_{xy}$) has increased and the out-of-plane shear ($\sigma_{xz}$) has decreased. The mode II von Mises stress is higher than the von Mises stresses of mode I and III.

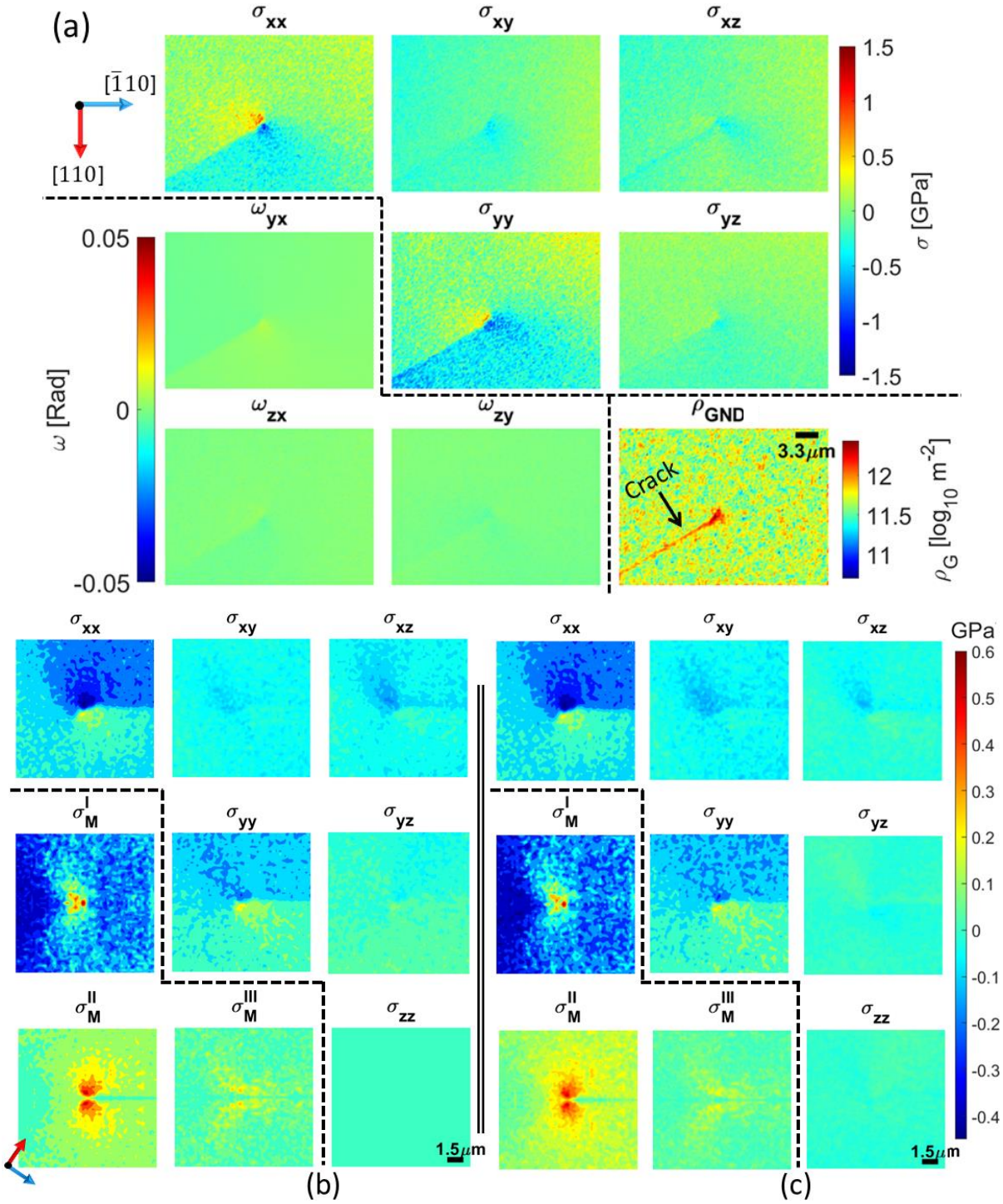


Figure 6-7: Example HR-EBSD data (Figure 6-6a, at label 1 - see Table 6-1): a) elastic stress components ($\sigma_{ij}$), rotation ($\omega_{ij}$) and GND density ($\rho_{GNDs}$) calculated in the microscope $xyz$ reference frame, showing high normal stresses in the surface plane. The stress normal to the surface is zero. The average GND density is low and is high only along the crack edges and at its tip; b) elastic stress components and decomposed mode I, II, III von Mises stresses after rotation by $\emptyset$ = 44.6°; and c) then by $\theta$ = 20.6° (define in Figure 6-1). The crack propagation is from left to right, compared to the reference frame data presented in (a). The rotations, coupled with regularised pattern acquisition (square meshing where $dA$ equals the step size), and centred crack tip ease the implementation of the domain equivalent integral (EDI) method of $J$-integral analysis.

$J$-integral values and the three-dimensional elastic stress intensity factors were calculated from each EBSD-measured field as the integration domain was advanced from the crack tip (Figure 6-8). The initial values with the smallest domain are erroneous due to noise and large strains close to the crack, and convergence is obtained as the domain expands. Contours larger than 2 μm correspond to encapsulation of the highly deformed field at the tip (i.e., the immediate singularity field), and these stable values were used. The mode-specific $J$-integral (or equivalent stress intensity) is the average of the 10 values in the converged shaded region (Figure 6-8). The total $J$-integral is the summation of the three mode-specific $J$-integrals (see method). The average values (and standard deviation) for each of the observations (labelled in Figure 6-5) of the quasi-static propagating cleavage cracks are given in Table 6-1.

The $[\bar{1}00](031)$ crack at locations labelled (1) and (2) experienced similar mechanical conditions and strain energy release rate with an effective stress intensity factor ($K_{\mathrm{eff}}$) of 0.6 ± 0.02 MPa $m^{0.5}$ and a slight increase in mode III with crack direction. As the crack changed plane (minimally) and direction to ($[\bar{7}10](173)$ crack (location 3, 704 μm from the crack initiation site), the mode I increased. This was followed by a significant change (~5°) in-plane and direction ($[\bar{4}10](142)$ (crack location 4 at 755 μm) that increased mode II. Initiation of the wing cracks (Figure 6-6b), near $[\bar{3}10](131)$ (crack location 5 at 902μm), can be linked to the increase of mode I, and further propagation until $[\bar{3}10](131)$ crack 8, at 1035 μm, proceeded with a fluctuating mode I. At $[\bar{3}10](131)$ crack 9 (at 1250 μm). Where there are wing cracks, mode III decreased while the strain energy release rate increases. Beyond the wing cracks, the surface crack assumed $(131)$ plane (between crack 10 to 12, from 1314 to 1615 μm) as mode I, mode III and the strain energy release rate slowly decreased, but mode II increased.

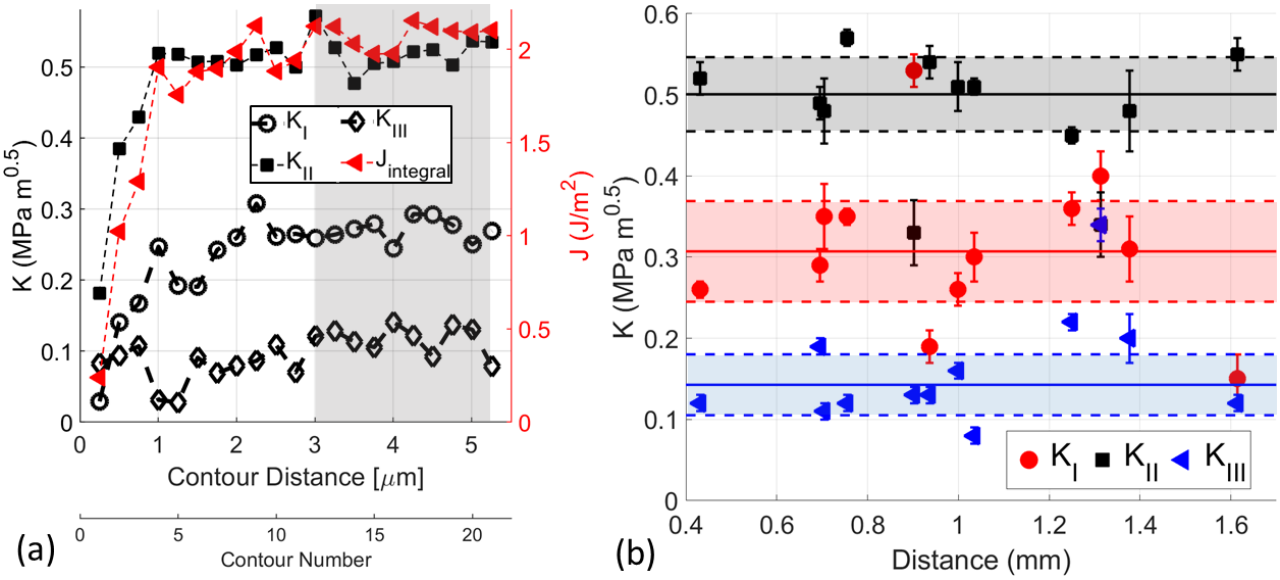


Figure 6-8: (a) $J$-integral and three-dimensional stress intensity factors as the contour of the integration domain expanded from the crack tip. The example is the crack tip position labelled 1 in Figure 6-6a. Values of the mode-specific $J$-integral (or equivalent stress intensity factor linked through the effective Youngs' modulus, shear modulus and Poisson's ratio estimated from the (001) silicon anisotropic stiffness tensor) are the average of the 10 values in the converged shaded region. The total $J$-integral is the summation of the mode-specific $J$-integrals. The values for all observations of this crack are given in Table 6-1. (b) Stress intensity factors through the observed intervals of the crack propagation. The horizontal axis is the total distance of crack propagation from initiation. The statistical bounds were obtained by the Bisquare weights method, implemented natively in MATLAB®, which uses an iterative reweighted least-square approach that minimises outliers' effect to calculate the mean and lower and upper bounds (shown above) or variant ($s^2$ in Figure 6-11).

The crack plane and propagation direction are effectively constant between locations 5 and 12 (Figure 6-4), as the crack propagated on the (131) plane in the $[\bar{3}10]$ direction with an average total energy release rate ($J$-integral) of 2.23 ± 0.17 J m$^{-2}$. The average mode I stress intensity factor is 0.31 ± 0.11 MPa m$^{0.5}$, with an average mode II stress intensity factor of 0.48 ± 0.06 MPa m$^{0.5}$. The average mode III stress intensity factor is small at 0.15 ± 0.06 MPa m$^{0.5}$. The average effective stress intensity factor, $K_{\text{eff}}$, for the (131) plane is 0.61 ± 0.02 MPa m$^{0.5}$. All means and variances are calculated using the bi-square weights method.

Data II, in Table 6-2, were collected via in situ observations (and post-test FIB sectioning) for another $[310](1\bar{3}1)$ crack also propagated under quasi-static conditions in (001) silicon single

crystal wafer, using the same experimental and analytical steps, as the crack propagated with an average total energy release rate ($J$-integral) of 2.50 ± 0.27 J m$^{-2}$. The average $K_I$ was 0.42 ± 0.15 MPa m$^{0.5}$, average $K_{II}$ was 0.38 ± 0.18 MPa m$^{0.5}$, average $K_I$ was 0.26 ± 0.21 MPa m$^{0.5}$, and average $K_{\text{eff}}$ was 0.65 ± 0.03 MPa m$^{0.5}$. See Appendix (6.A) – Additional figures.

Data were also collected via in situ observations for two specimens (III and IV) in (001) silicon single crystal wafers, in which cracks were also propagated under quasi-static conditions. FIB sectioning was impossible as the samples were fragmented on final failure. The crack plane has been assumed to be close to the {111} plane, inferred from trace analysis [304]. The data are given in Table 6-2.

Table 6-1: Geometrical information for the example crack (Figure 6-5) propagating in a $(001)$ silicon wafer (angles are defined in Figure 7). The elastic moduli are evaluated normal to crack plane. The evaluated $J$-Integral, three-dimensional stress intensity factors ($K_I, K_{II}, K_{III}$) and effective stress intensity factor ($K_{\text{eff}}$) are also shown.

| Label | Nominal stress (MPa) | Increment of crack (μm) | Crack Trace Angles (°) $\emptyset, \theta$ | Trace | $E$ (GPa) | $\mu$ (GPa) | $v$ | $J$ (J m$^{-2}$) | $K_{\text{eff}}$ (MPa m$^{0.5}$) | $K_I$ (MPa m$^{0.5}$) | $K_{II}$ (MPa m$^{0.5}$) | $K_{III}$ (MPa m$^{0.5}$) |
|---|---|---|---|---|---|---|---|---|---|---|---|---|
| 1 | 2.6 | 0 | 44.6, 20.6 | $[\bar{1}00](031)$ ± 2.1° | 177.2 | 79.6 | 0.113 | 2.03 ± 0.10 | 0.60 ± 0.02 | 0.26 ± 0.01 | 0.52 ± 0.02 | 0.12 ± 0.01 |
| 2 | 11.8 | 263.3 | 40.1, 18.7 | $[\bar{1}00](031)$ ± 0.2° | 176.8 | 79.2 | 0.116 | 2.08 ± 0.15 | 0.60 ± 0.02 | 0.29 ± 0.02 | 0.49 ± 0.02 | 0.19 ± 0.01 |
| 3 | 11.9 | 9.3 | 36.8, 19.0 | $[\bar{7}10](173)$ ± 3.9° | 176.0 | 78.4 | 0.122 | 2.26 ± 0.26 | 0.62 ± 0.04 | 0.35 ± 0.04 | 0.48 ± 0.04 | 0.11 ± 0.01 |
| 4 | 13.3 | 50.9 | 30.8, 23.7 | $[\bar{4}10](142)$ ± 2.2° | 173.9 | 76.4 | 0.138 | 2.71 ± 0.09 | 0.69 ± 0.01 | 0.35 ± 0.01 | 0.57 ± 0.01 | 0.12 ± 0.01 |
| 5 | 20.7 | 147.4 | 27.3, 23.3 | $[\bar{3}10](131)$ ± 5.8° | 172.3 | 74.9 | 0.150 | 2.48 ± 0.19 | 0.65 ± 0.03 | 0.53 ± 0.02 | 0.33 ± 0.04 | 0.13 ± 0.01 |
| 6 | 21.1 | 34.6 | 26.4, 25.5 | $[\bar{3}10](131)$ ± 8.0° | 171.8 | 74.5 | 0.154 | 2.07 ± 0.13 | 0.59 ± 0.02 | 0.19 ± 0.02 | 0.54 ± 0.02 | 0.13 ± 0.01 |
| 7 | 22.6 | 61.8 | 23.6, 24.7 | $[\bar{3}10](131)$ ± 7.1° | 170.4 | 73.2 | 0.164 | 2.15 ± 0.16 | 0.60 ± 0.02 | 0.26 ± 0.02 | 0.51 ± 0.03 | 0.16 ± 0.01 |
| 8 | 23.2 | 36.5 | 24.9, 23.7 | $[\bar{3}10](131)$ ± 6.1° | 171.1 | 73.8 | 0.159 | 2.12 ± 0.14 | 0.60 ± 0.02 | 0.3 ± 0.03 | 0.51 ± 0.01 | 0.08 ± 0.01 |
| 9 | 25.8 | 215.0 | 25.1, 20.6 | $[\bar{3}10](131)$ ± 3.1° | 171.2 | 73.9 | 0.158 | 2.28 ± 0.14 | 0.62 ± 0.02 | 0.36 ± 0.02 | 0.45 ± 0.01 | 0.22 ± 0.01 |
| 10 | 26.5 | 63.5 | 25.3, 19.6 | $[\bar{3}10](131)$ ± 2.1° | 171.3 | 74.0 | 0.158 | 2.52 ± 0.16 | 0.65 ± 0.02 | 0.40 ± 0.03 | 0.34 ± 0.04 | 0.34 ± 0.02 |
| 11 | 27.1 | 62.9 | 26.4. 17.9 | $[\bar{3}10](131)$ ± 0.4° | 171.8 | 74.5 | 0.154 | 2.39 ± 0.34 | 0.62 ± 0.05 | 0.31 ± 0.04 | 0.48 ± 0.05 | 0.20 ± 0.03 |
| 12 | 30.7 | 237.8 | 25.5, 14.9 | $[\bar{3}10](131)$ ± 2.6° | 171.4 | 74.1 | 0.157 | 2.04 ± 0.16 | 0.59 ± 0.02 | 0.15 ± 0.03 | 0.55 ± 0.02 | 0.12 ± 0.01 |

Table 6-2: Additional data obtained for in situ observations of cracks propagating assumed in (001) Si wafers (the results in Table 6-1 are 'Data $I'$'). For Data III and IV, the crack plane orientation was inferred from the surface trace.

| Data | | Nominal stress (MPa) | Crack Trace Angles (°) $\emptyset$, $\theta$ | Trace | $E$ (GPa) | $\mu$ (GPa) | $v$ | $J$ (J m$^{-2}$) | $K_{\mathrm{eff}}$ (MPa m$^{0.5}$) | $K_I$ (MPa m$^{0.5}$) | $K_{II}$ (MPa m$^{0.5}$) | $K_{III}$ (MPa m$^{0.5}$) |
|---|---|---|---|---|---|---|---|---|---|---|---|---|
| II | 1 | 8.2 | -26.7, 17.5 | $[310](1\bar{3}1)$ ± 0.1° | 169.4 | 72.3 | 0.172 | 2.61 ± 0.43 | 0.65 ± 0.05 | 0.40 ± 0.04 | 0.35 ± 0.04 | 0.32 ± 0.04 |
| | 2 | 11.5 | -23.5, 17.5 | $[310](1\bar{3}1)$ ± 3.0° | 172.0 | 74.6 | 0.152 | 2.71 ± 0.29 | 0.67 ± 0.04 | 0.36 ± 0.03 | 0.21 ± 0.04 | 0.47 ± 0.05 |
| | 3 | 13.4 | -26.8, 17.5 | $[310](1\bar{3}1)$ ± 0.2° | 170.4 | 73.2 | 0.164 | 2.42 ± 0.19 | 0.64 ± 0.02 | 0.50 ± 0.02 | 0.35 ± 0.02 | 0.18 ± 0.02 |
| | 4 | 15.4 | -23.8, 17.5 | $[310](1\bar{3}1)$ ± 2.8° | 172.0 | 74.6 | 0.152 | 2.39 ± 0.24 | 0.63 ± 0.03 | 0.32 ± 0.06 | 0.46 ± 0.01 | 0.22 ± 0.03 |
| III | | N/A | 17.1, -35.3 | [011] $(11\bar{1})$ ± 0.2° | 167.2 | 70.4 | 0.188 | 2.29 ± 0.1 | 0.62 ± 0.01 | 0.32 ± 0.02 | 0.46 ± 0.02 | 0.22 ± 0.02 |
| IV | 1 | N/A | 6.7, 64.8 | $[\bar{1}10](111)$ ± 6.7° | 163.4 | 67.1 | 0.218 | 2.90 ± 0.65 | 0.65 ± 0.07 | 0.47 ± 0.06 | 0.35 ± 0.06 | 0.22 ± 0.04 |
| | 2 | N/A | 2.8, 64.8 | [011] $(11\bar{1})$ ± 2.8° | 162.8 | 66.6 | 0.222 | 2.80 ± 0.40 | 0.65 ± 0.05 | 0.41 ± 0.05 | 0.43 ± 0.07 | 0.15 ± 0.03 |

## 6.4 Discussion

Single crystal silicon is a brittle material at room temperature [219] that most easily cleaves on the {110}, {111} [423] and {001} planes [424], with the lowest mode I fracture toughness ($K_{Ic}$) reported for {111} (Table 6-3) and favourably propagate in the <110>, resulting in a smooth fracture surface [424]. The (experimentally measured) fracture toughness varies with the crack plane and direction [425,426]. However, high strain gradients encourage higher-order planes fracture [427], and once the crack deviates from the <110>, it can propagate in any direction with hysteric and discontinuous transition between fracture modes [428–430]. The initially complex crack path, which was not analysed, may be due to multi-axial stresses from the Hertzian contact of the rough edge of the sample with the loading anvil. Note that complex stress distribution can cause crack path deviation [431].

Although the experiment was conducted under quasi-static conditions, the crack propagation is dynamic between the observations. A propagating crack in silicon can oscillate above a critical speed, independent of the applied stress and sample geometry, which is manifested by the spatial structure observed on the crack surface (Wallner lines [432,433], front wave and ridge pattern [434] in Figure 6-6), which relates to mode mixity and asymmetric stress distribution [431] causing energy dissipation [435] and modulation [436], and crack deflection [431]. A crack that does not propagate on a cleavage plane is expected to propagate by sudden jumps and not continuously, which further influences the crack surface [437].

Table 6-3: Recommended and reported mode I fracture toughness values for single crystal silicon cleavage at room temperature [424]. Discrepancies between reported results can be due to environmental effects and crack misalignment [438,439].

| Fracture Plane | {100} | {110} | {111} |
|---|---|---|---|
| Reported $K_{IC}$ (MPa m$^{1/2}$) | 0.75–1.29 | 0.68–1.19 | 0.62–1.22 |
| Recommended $K_{IC}$ (MPa m$^{1/2}$) | 0.75 | 0.71 | 0.62 |
| Recommended $J_{IC}$ (J m$^{-2}$) | 2.163 | 1.483 | 1.022 |

Bouscaud *et al.* [440] estimated that the electron beam could cause the local temperature to increase in the interaction volume due to dissipating energy created from inelastic scattering. However, while discussing inelastic scattering, the study focused on X-ray yield to calculate the interaction volume (e.g., 3 µm for Ge) rather than backscattered electrons. Thus, using Monte Carlo Simulation (Casino v2.48 [381]), a 173 nm effective volume of interaction (i.e., depth resolution, $r$) was calculated for 5 x 10$^6$ electrons bombarding a 70° titled Silicon sample placed inside a Merlin FEG-SEM that has a beam mean-radius of ~25 nm at 20 keV beam energy ($E_0$) of and 10 nm current ($I_0$)(Figure 6-9).

A negligible (mean) induced temperature ($\Delta T$) of 1.2 K was then estimated from equation (6—12), assuming a thermal conductivity ($\lambda$) of 149 W m$^{-1}$ K$^{-1}$ at 300 K [441], which is not high enough to induce an amorphous silicon layer known to occur during nano-pillar FIB ablation [442] and influencing the fracture toughness [443]. Thus, it is less likely that this instantaneous induced temperature coupled with minimal stress relaxation due to current pulsed induced from beam movement during EBSPs acquisition (electro-plastic effect, EPE [444,445] and electron beam irradiation [446]) and carbon disposition accumulated during the long EBSD scan can influence the calculated fracture toughness and the initial tip response to load (kink in Figure 6-5c).

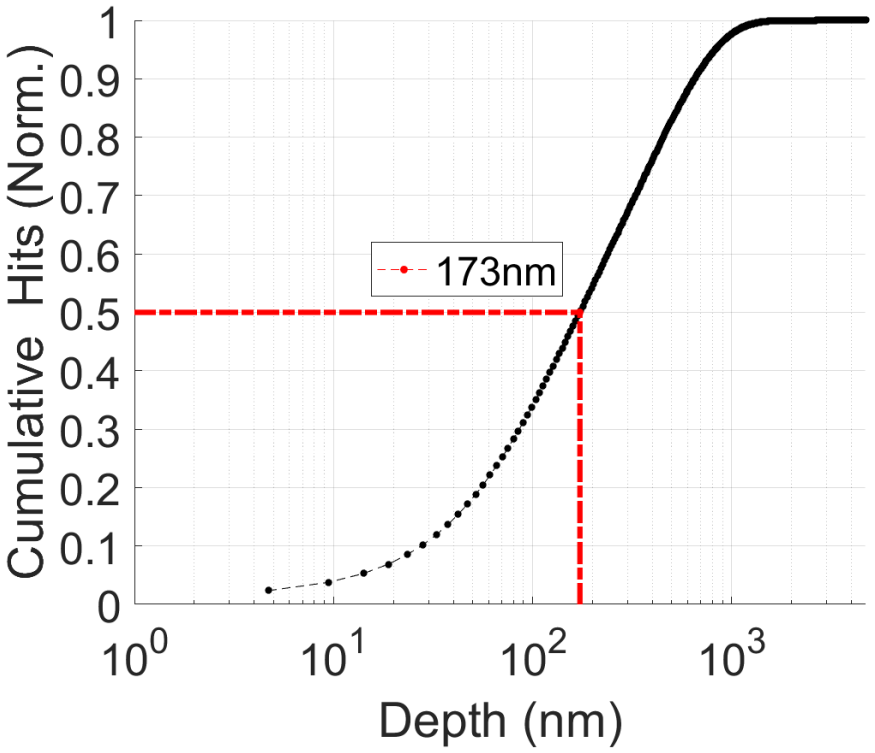


Figure 6-9: Cumulative probability of backscattered electron detection vs depth from the surface for Monte Carlo simulated electron trajectories in Silicon. A dashed red line indicates the mean of the distribution.

$$\Delta T = \frac{E_0 I_0}{2\pi\lambda r} \qquad 6—12$$

In addition, the local variations in the relative modes may be due to slight deviations in the direction of the crack when it arrests (Figure 6-10). The observed 'Wallner' lines are evidence of crack deviation at arrest and re-initiation. This may be due to plastic deformation local to the crack tip either from the electro-plastic effect (discussed earlier) or (asymmetrical) dislocations emission at the crack tip [447] and its effect on crack re-initiation [448]. Incorrect definition of the crack propagation direction ($q_1$), which is assumed to be the visible crack trace, would influence the symmetry of the field decomposition and, consequently, the SIFs. However, it would not significantly alter the effective stress intensity factor because loading modes are coupled, even if they differ in stress radial/tangential variation [429,449]. See Appendix (6.A) – Additional figures, Figure 9-35.

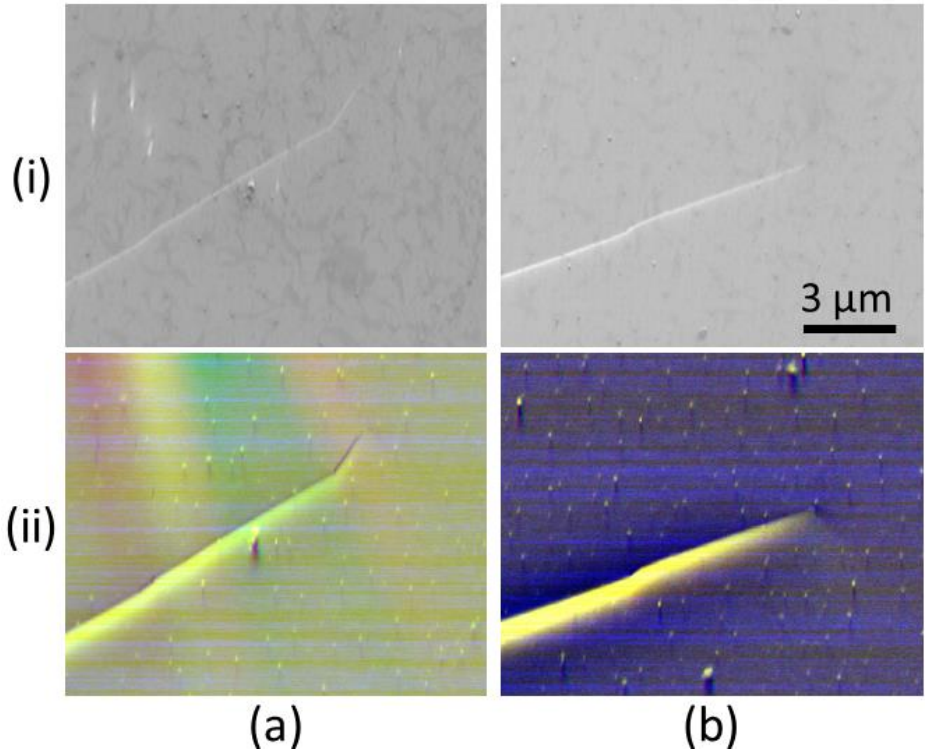


Figure 6-10: (i) Secondary electron, and (ii) forward scatter detector (FSD) images for the crack tip at the point labelled (a) 1 and (b) 4 in Figure 6-4 as the crack propagates in the (001) single silicon wafer (Table 6-1).

Significant observations were obtained for cracks that propagated close to $\{131\}$ plane in a quasi-static manner with no branching (Figure 6-5 and Table 6-1). The GND density map (e.g., Figure 6-7a) demonstrates that the fracture was brittle with no significant plastic deformation, unlike cleavage cracks observed in single-crystal metals [450,451]. For the three-dimensional stress intensity factors (Table 6-1 and Figure 6-8b), the crack shows that during quasi-static crack growth, the stress field surrounding the crack tip was almost constant, with negligible mode III and mixed-mode I/II loading dominated by mode II except when wing cracks were initiated (crack 5) and dissipated (crack 9) as wing cracks were reported to influence fracture characteristics in Silicon [452]. The average mode I stress intensity factor is lower than the mode I fracture toughness of the (weakest) {111} cleavage plane (Table 6-3); however, it is expected, as inclined cleavage cracks were reported to experience mixed-mode loading with higher shear compared to opening [439].

There are various criteria proposed for crack propagation under mixed-mode loading; for example, using the maximum circumferential/tangential stress (MSC) criterion [453], fracture occurs in the direction where the circumferential stress surrounding the crack tip is the maximum; however, mode III does not affect the circumferential stress; thus, cannot be extended to the third dimension. Two [454] and three [455] dimensional minimum strain energy density (MSED) criterion predicts that fracture occurs in the direction where the strain energy density is the minimum, i.e., a crack propagates along the minimum resistance path, but, in this criterion formulation mode III only effects loading and not direction. Two [363,456,457] and three [458] dimensional maximum potential energy release rate (MPERR) criterion emerges as the most robust criterion as it includes the influence of mode III, which decreases the fracture direction.

Chang *et al.* [458] used two-dimensional curves to represent the three-dimensional critical surface that described the mixed-mode contributions to the MPERR criterion (Figure 6-11a and c). The experimental SIFs (Table 6-1 and Table 6-2) were compared to this critical surface, constructed through equations (6—13) to (6—16), using values from 0.62 to 1.22 MPa $m^{0.5}$ for single crystal silicon cleaved in mode I for cleavage planes [424]. $K_{IC}$ of 0.70 MPa $m^{0.5}$ provided the best fitting surface for the experimental data with $R^2$ equals 0.89 (Figure 6-11b).

$$\left({\mathrm{K_I}}/{\mathrm{K_{IC}}}\right)^2 + \left({\mathrm{K_{II}}}/{\mathrm{K_{IIC}}}\right)^2 + \left({\mathrm{K_{III}}}/{\mathrm{K_{IIIC}}}\right)^2 = 1 \qquad 6—13$$

$$K_{IIC} = \frac{\sqrt{3}}{2}K_{IC}, \qquad K_{IIIC} = \frac{\sqrt{k+1}}{2}K_{IC} \qquad 6—14$$

$$k = \frac{(3-v)}{(1+v)} \text{ for plane stress} \qquad 6—15$$

$$\psi = \tan^{-1}\left(K_{III}/\sqrt{K_I^2 + K_{II}^2}\right) \qquad 6—16$$

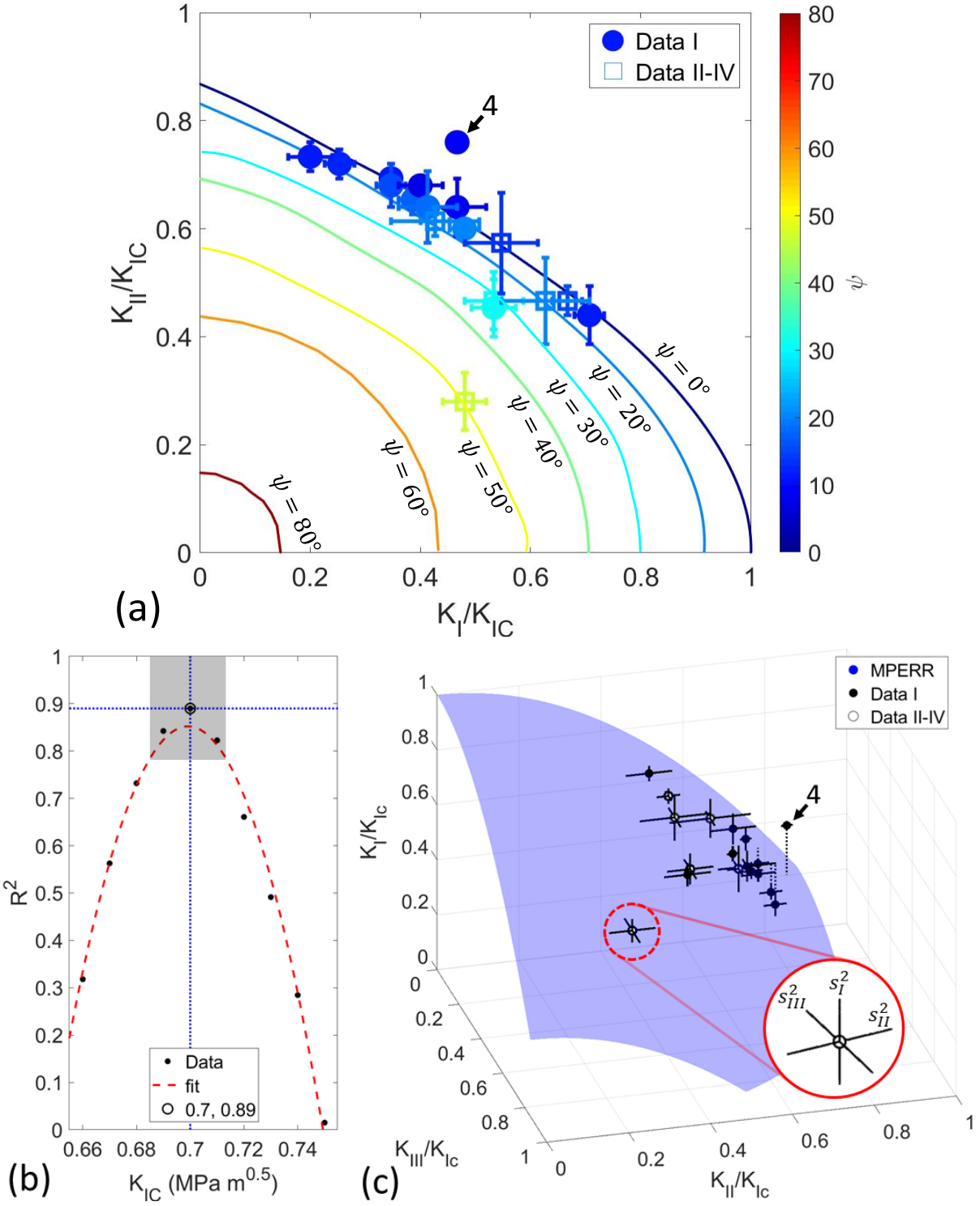


Figure 6-11: (a) Contour plot of the maximum potential energy release rate (MPERR) criteria (equations 6—13 to 6—16) using Experimental data from datasets I to IV (Table 6-1 and Table 6-2) are shown, with the best fit value ($R^2 = 0.89$) of $K_{IC} = 0.70$ MPa m$^{0.5}$ for the range of $K_{IC}$ found in literature [458]. (b) The goodness of the fit (R2) using different $K_{IC}$ values with the grey box being the weighted uncertainty.; and (c) the critical surface at a constant value of 0.70 MPa m$^{0.5}$ when applying equation (6—13) to the experimental data. The solid black lines are the measurement uncertainty. The vertical dotted black lines indicate the difference (parallel to the $K_I/K_{IC}$ axis) between the data and the surface.

Considering the quality of the fit (i.e., uncertainty in $K_{IC}$) weighted with the overall polynomial fit (i.e., rate of fit degradation as $K_{IC}$ changes), $K_{IC}$ is 0.70 ± 0.02 MPa $m^{0.5}$ (grey box in Figure 6-11b). Crack (4) is the outlier of the critical surfaces, and it has the highest (potential) energy release rate at 2.71 ± 0.09 J $m^{-2}$ as the crack experienced the most significant change in direction and plane (~5°).

Two [459,460] and three [461–463] dimensional maximum tensile (or principal) stress (MTS) criteria are alternatives to constructing a critical fracture surface based on the relation between the mode I, II, and III, which was experimentally examined [464,465]. However, the MPERR criterion is more consistent with the mode decomposition approach as both are energy-based.

This novel analysis method provides a straightforward and high-resolution solution to quantify the elastic fields acting on a crack tip, using local measurements without knowing the external boundary conditions (e.g., load, crack length). The analysis can be applied to mixed mode loading and the in situ studies of quasi-static crack propagation. The present analysis is suitable for elastic deformation or small-scale yielding conditions, but more advanced decomposition algorithms must be employed for significant elasto-plastic deformation [466].

This decomposition method is suitable for regulated mesh and localised crack field with no need to deploy finite element solvers, and it is computationally cheap. However, it is highly vulnerable to noise and uncertainties in the crack tip location (see Appendix (6.C) – Analytical field benchmarking), and it does not work for stress raisers with compressive mechanical conditions (especially mode I) as minus values are interpreted as imaginary. Also, the stress field needs to be linearly elastic and have the $r^{-0.5}$ form of singularity, where $r$ is the distance

from the crack tip. More complex and computationally expensive methods can be used as an alternative (see Chapter 2), which can be coupled with finite element solvers to get the most out of the measured field, including padding to address noise near the crack [75] and calculation of the crack probable extension direction (e.g., XFEM ABAQUS®). However, that analysis relies on estimating the EBSPs' depth resolution.

The present study employed large single crystals; thus, avoiding the significant problem of obtaining a stress-free HR-EBSD reference pattern that typically arises in the analysis of engineering materials [128], which needs to be addressed before the method can be more generally applied. This might be achieved by simulation of reference patterns, but that remains challenging [173]. Cross-correlation of transmission electron microscopy (TEM) acquired nano-diffraction patterns [467], piezospectroscopic (PS) analysis of the cathodoluminescence (CL) emission [468], Laue microdiffraction [469], and dark-field X-ray microscopy [111] are some of the possible high-resolution mapping approaches that can provide absolute strains, which can be used with this method to examine mixed-mode local fracture behaviour (contrary to the well documented global fracture) of brittle inclusions, coatings, interfaces, and grain boundaries in engineering materials. In situ EBSD with a sample geometry that allows examination of the crack under load – such as indentation close to an edge (see [470]) – can benefit from the current analysis.

## 6.5 Conclusion

A novel approach has been formulated to decompose the $J$-integral evaluation of the elastic energy release rate to the three-dimensional stress intensity factors directly from experimental measurements of the elastic deformation gradient tensors of the crack field by in situ high (angular) resolution electron backscatter diffraction (HR-EBSD). An exemplar study is presented of a quasi-static crack, inclined to the observed surface, propagating on low index $\{hkl\}$ planes in (001) single crystal silicon wafers. By applying mode-specific *J*-integral analysis, the overall mechanical conditions present at the tip were investigated and related to theories that deal with mixed-mode fracture criteria. The mixed-mode crack fields were consistent with a constant maximum potential energy release rate criterion for crack propagation, with average mode I fracture toughness, $K_{IC}$ of 0.70 ± 0.02 MPa $m^{0.5}$. This high-resolution approach can potentially study the mixed-mode local fracture resistance of brittle material microstructures at the micron scale.

# Chapter 7. Conclusion

This thesis aimed to develop novel methods to observe and acquire in-situ quantified deformation data of strain localisation at the micro-scale; thus, it concluded the following.

- The availability of electron backscatter diffraction (EBSD) systems, compared to Synchrotron X-ray diffraction, makes it suitable for characterising micro-scale strain localisation with measurement. EBSD provides more information about the out-of-plane deformation of a thin layer of the material, compared to micro-DIC.
- High-resolution (HR) EBSD calculation of the deformation fields depends on selecting the reference pattern ($EBSP_0$). The $EBSP_0$ effect can be minimised by selecting the least strained reference pattern but with an unknown deformation state (Chapter 3).
- The strain energy release rate (i.e., *J*-integral) and decomposed stress intensity factors can describe the localised field at deformation twins (Chapter 4), slip bands (Chapter 5), and micro-cracks (Chapter 6). However, in non-linear elastic materials use of sophisticated finite element solvers to decompose the stress intensity factors is highly recommended. These FE solvers can be accessed by approximating the displacement field (i.e., FE boundary conditions) from the measured deformation field (Chapter 2).
- The deformation field in the membrane measure using HR-EBSD indicated that as the grain responds to the nominal load, it also stretches to accommodate (inclined) deformation twins and slip bands thickening and growth, inducing a compressive or tensile mode I. Once the load was removed, deformation twins and slip bands' elastic recovery were mainly in mode II (in-plane shear) and mode III (out-of-plane shear).

- The three-dimensional stress intensity factors were consistent with the magnitude and mode of the shear of the slip band; the ratio of the mode II to mode III stress intensity factors depended on the slip inclination angle relative to the observed surface.
- The local Schmid factor based on the measured grain stress field is more precise than the Schmid factor calculated assuming uniaxial stress (section 5.2.3).
- Mixed-mode cracks' field, for an inclined crack propagating in a linear-elastic material while changing direction and plane, were consistent with a constant maximum potential energy release rate criterion for crack propagation due to the coupling of the loading modes.

# Chapter 8. Potential future research directions

The experimental techniques and analytical methods explored and developed in this thesis can be generally used for in-situ studies of short fatigue cracks, cracks in films and coatings, deformation-twins and slip-bands in different materials, as well as environment-assisted cracking and intergranular fracture in bulk samples, providing alternatives to micro- pillars and cantilevers experiments, indentation fracture method and analytical solution.

In Chapter 3, the study considered the ferrite phase of the duplex stainless steel in only one condition of age-hardening caused by spinodal decomposition. Further studies with analysis of the strain fields associated with the propagation and thickening of twins in the ferrite as a function of ageing conditions might elucidate whether the transition from spinodal decomposition to precipitation at higher temperatures and longer ageing times influences twin development.

Considering the analysed stress concentration, the measured surface mechanical conditions will change with depth; an in situ three-dimensional strain map will be optimal to fully characterise the concentration field and properly link it to geometry, especially in materials where the local fracture behaviour needs further investigation. Trials were made to measure the elastic field ahead of the deformation twinning from Chapter 4, cracks nucleated from micro-indentation, and intragranular slip band using Laue micro-diffraction combined with differential aperture microscopy (DAXM) for depth-resolved 3D X-ray microscopy at the 34-ID-E beamline, the Advanced Photon Source (APS) [108] using white/pink beam. However, in the deformation twin case, high deformation at the ferrite grain smeared the Laue pattern spots, limiting indexing quality (Figure 8-1). In the case of the indention, Silicon low Z and

consequent X-ray absorption led to detector saturation and difficulties in depth resolving of information [471,472]. In the case of the slip band, the resolution (~0.5 x 0.25 x 0.25 $\mu m^3$) was not enough to capture the minute details of the deformation field ahead of the slip band. Nevertheless, APS is being upgraded to increase brightness, and the 34-ID-E beamline is fitted with new K-B reflective mirrors [473]. Both upgrades are expected to increase the spatial resolution to 0.25 µm by 2025.

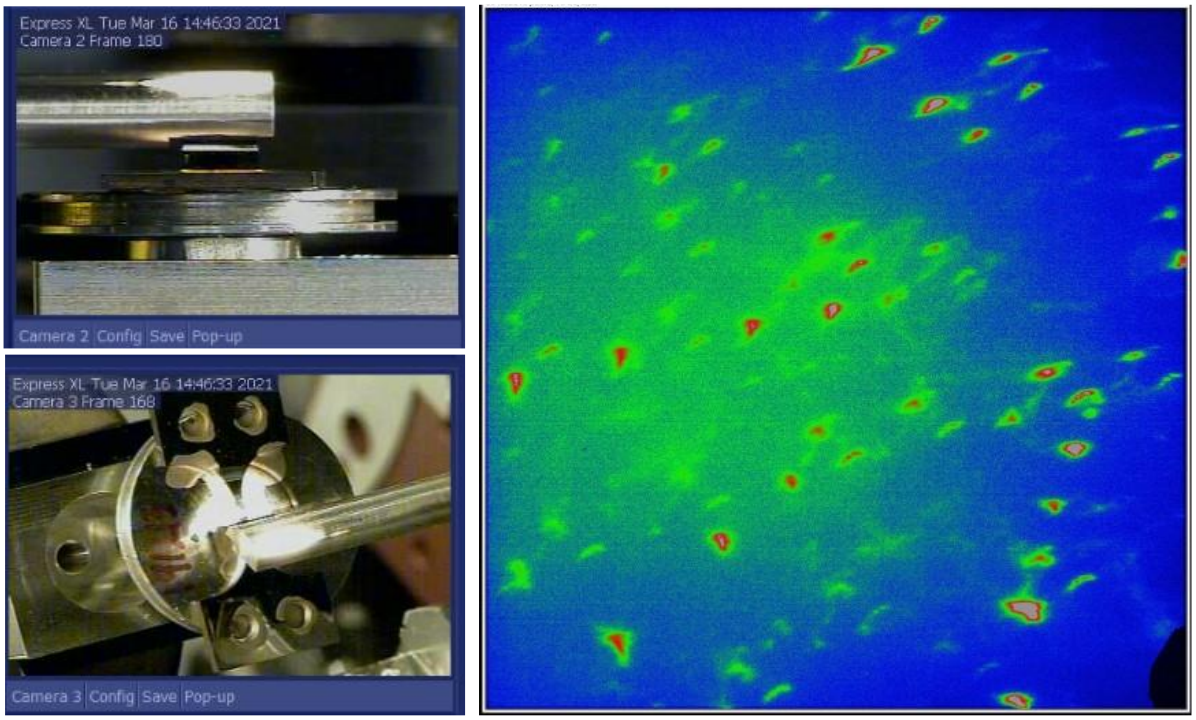


Figure 8-1: (a) Tensile sample contains a deformation twin (Figure 4-7). The scanning wire was brought near the sample surface. (b) Laue pattern collected from the sample, showing smeared spots.

Laue microdiffraction is available in other facilities, such as European Synchrotron Radiation Facility (ESRF) at the BM32 beamline [474]. However, it has lower magnification than APS, which measures only the deviatoric strains (no monochromatic x-rays) and is typically used for 2D measurement. Other facilities capable of Laue micro-diffraction measurement are listed below in Table 8-1 with their resolution as reported on their website.

Table 8-1: List of facilities capable of performing Laue micro-diffraction combined with differential aperture microscopy (DAXM) for depth-resolved elastic strain measurement.

| Facility | Beamline | Resolution |
|---|---|---|
| The Advanced Photon Source (APS), Argonne National Laboratory, Illinois, US | 34-ID-E | ~0.5 x 0.25 x 0.25 $\mu m^3$ (2D and 3D) |
| European Synchrotron Radiation Facility (ESRF), Grenoble, France | BM32 | > 0.5 (2D) |
| National Synchrotron Radiation Research Centre (NSRRC) – Taiwan Photon Source Beamlines (TPS), Hsinchu, Taiwan | 21A[12] | 100 nm (2D and 3D) |
| Canadian Light Source (CLS), Saskatoon, Canada | VESPERS (07B2-1) | 2 – 4 µm |
| Pohang Accelerator Laboratory (PAL) - Pohang Light Source (PLS)-II, Pohang, South Korea | 4B | 3 µm |

Furthermore, newly developed dark-field X-ray microscopy at the ESRF ID06 beamline [111] can measure the full elastic strain tensors at the micro-scale, especially when the sample does not have a trackable volumetric structure suitable for digital volume correlation (DVC) [475].

The *J*-integral was extensively used with the surface measurement; however, volumetric quantification coupled with this approach may provide insights into criteria for deformation-twin/slip-band/micro-cracks propagation, twin/slip thickening and twin variant selection. The

[12] No peer-reviewed publication was found to support the claim of reaching a 100 nm resolution.

method is of interest because, firstly, the *J*-integral can be calculated directly from experimental data without resorting to crystal plasticity models and knowing the loading condition or specimen geometry. Secondly, the mechanical condition of a twin can be readily obtained by decomposing the *J*-integral into opening and shear modes described as stress intensity factors. Thirdly, the nature of the *J*-integral facilitates the employment of finite element (FE) analysis, and its evaluation is implemented natively in most FE solvers. Furthermore, the experimental strain-integrated displacement field used in the *J*-integral evaluation can be easily incorporated with crystal plasticity models, which can simulate twin growth via the extended finite element method (XFEM [476,477]). Such analyses would benefit from advanced strain energy integral definitions that can be applied to linear elastic and elastic-plastic materials to address factors including surface traction [478], loading and internal tractions [74], thermal [72] and electrochemical [73], residual stresses [58] and boundary interactions [479–481], which are natively implemented in commercial Finite element software.

Other path-independent conservation integrals evaluated over a surface that encloses a defect [31,482] can be used to represent a configurational force measured around defects as most of the information required for computing these integrals is either directly obtained from the local measurement (i.e., displacement gradient from HR-EBSD as in Chapter 6) or can be approximated (i.e., integration of strains to displacement as in Chapter 2). For example, the elastic field at a dislocation can be measured using HR-TKD [409] and analysed

using the *J*-, *M*-[13] and *L*-integrals [483,484], dislocations arrangement measured using high-resolution synchrotron diffraction [485] can be parameterised using *M*-integral [486], misfitting inclusions and voids measured using HR-EBSD [487,488] can be evaluated using *Eshelby*-integral [294] or *M*-integral [489], and pile-ups ahead of slip band impinged at grain boundaries measured using HR-EBSD [297] or DAXM [110] and analysed using vectorial *J*-integral and the local Schmid factor ($xSF$) (devolved in 5.2.3) to predict the slip system to nucleate [31].

[13] The M-integral and the interaction (I) integral are two different integrals that are usually confused in literature. M-integral describes energy release rate for uniform expansion of a defect and I-integral is used for SIFs extraction from the *J*-integral assuming small-scale yielding.

# Chapter 9. Appendices

Appendices follow the notation: Appendix (Chapter number.Numbring) – Appendix title.

## Appendix (2.A) – FE-OOM code implementation

The developed method was implemented in MATLAB® using an object-originated programming approach [490]. The developed algorithm uses MATLAB® built-in libraries (e.g., *parpool* for parallelism) to accelerate the process efficiently. We start with a general formulation of numerical integration using Gaussian quadrature for a two-dimensional problem which takes the form of an equation (9—1) and can be easily expanded to the third dimension (illustrated in Figure 9-1).

$$\int_{-a}^{a}\int_{-b}^{b} F(x_1,x_2)dx_1dx_2 = \int_{-1}^{1}\int_{-1}^{1} f(\eta_1,\eta_2)|J|d\eta_1d\eta_2 \qquad 9—1$$

where $(x_1, x_2)$ and $(\eta_1, \eta_2)$ are the coordinates in physical and natural domains, respectively. The scalar of distortion between the two domains takes the form of $|J|$, where Jacobian ($J$). The shape function ($N$) transforms between two domains which simplifies the problem to equation (9—2).

$$\int_{-a}^{a}\int_{-b}^{b} N_iN_jdx_1dx_2 = \int_{-1}^{1}\int_{-1}^{1} N_iN_j|J|d\eta_1d\eta_2 \qquad 9—2$$

Once the transformation between coordinates is achieved, this formulation allows for the use of Gaussian quadrature approximation with a weighted sum over the points (equation 9—3) [490], where $N_k$ is the number of integration points, $W$ is the weighting factor, and $g_2^{i,j}$ is the Gauss point for a 2D element. After this brief introduction to a different aspect of numerical integration, we focus on the numerical integration of elastic deformation fields.

$$\int_{-1}^{1}\int_{-1}^{1} f(\eta_1,\eta_2)d\eta_1 d\eta_2 = \sum_{i=1}^{N_k}\sum_{j=1}^{N_k} W_i W_j f\left(g_2^{i,j}\right) \qquad 9—3$$

A 2D or 3D infinitesimal strain (or deformation gradient) field is provided as an input, with the first columns containing the element coordinate (X, Y for 2D or X, Y and Z for 3D) and the rest for the strain field components ($\varepsilon_{11}$, $\varepsilon_{22}$ and $\varepsilon_{12}$ for 2D or $\varepsilon_{11}$, $\varepsilon_{22}$, $\varepsilon_{33}$, $\varepsilon_{12}$, $\varepsilon_{13}$ and $\varepsilon_{23}$ for 3D). There is the option for the user also to provide a uniform or non-uniform mesh grid (or nodes coordinates) or relay on a custom-made meshing algorithm that uses isoparametric elements to discretise the domain by fitting a uniform 2D four nodes linear or eight nodes quadratic element rectangular (*FE_Mesh_Generator*) mesh or 3D eight nodes hexahedron linear elements (*HexMeshAbaqus* function) mesh grid around measurement points. The Gauss points decide the number of points. For example, full integration using a quadratic element with eight nodes means nine measurement points will be placed inside one element to solve for eight nodal displacements (see Figure 2-1). Due to the uniform spacing between each point, no interpolation was needed. However, in the case of non-uniform spacing or matrix deficiency (the map being non-rectangular), a different meshing algorithm (*Meshing* function) was developed, which places the measurement point at the centre of each element and then interpolates to the Gauss points. The outputs of these functions are the node coordinates and element connectivity matrix.

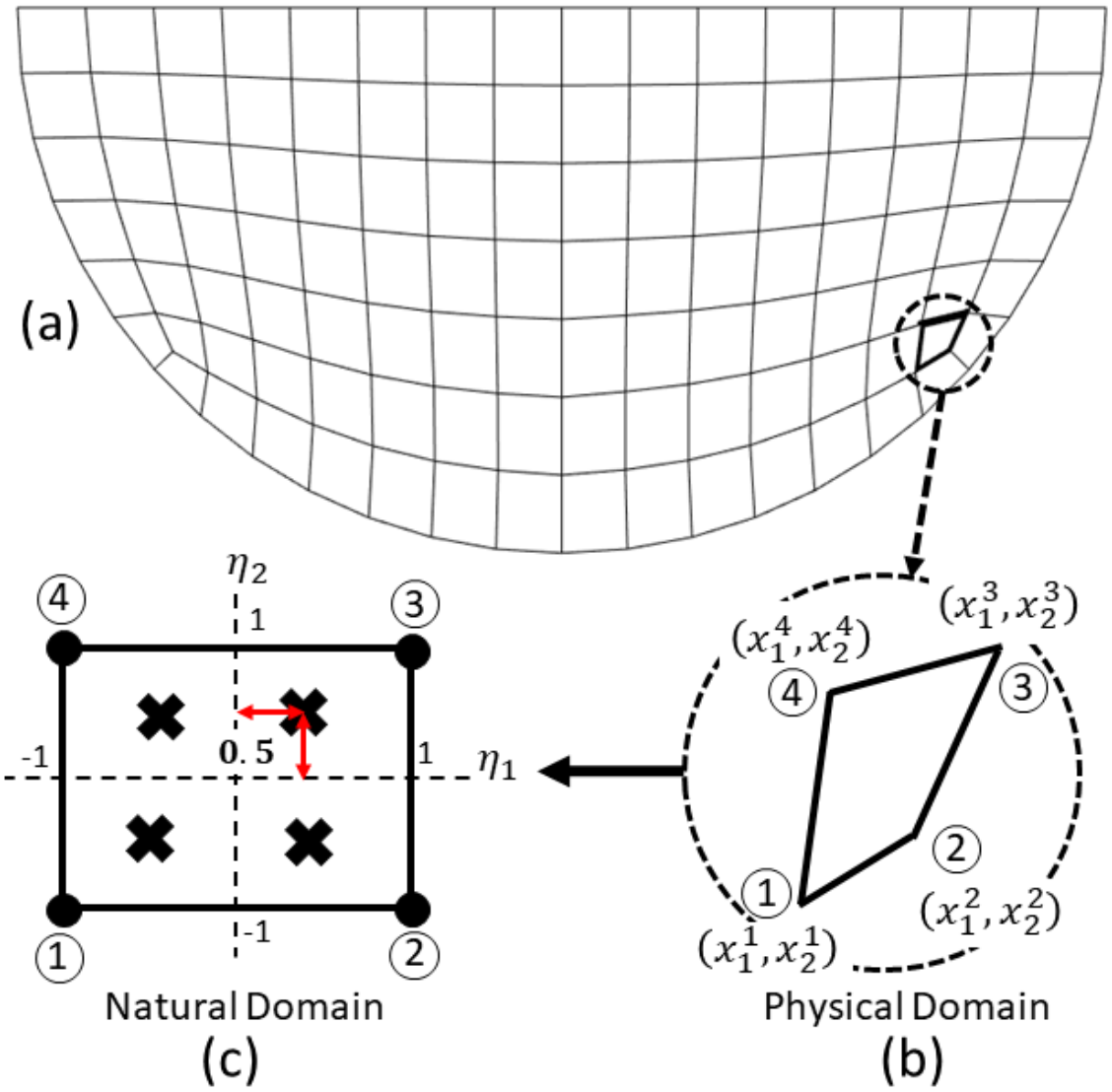


Figure 9-1: (a) A non-uniformly discretising of a physical domain using quadrilateral elements. Elements in the (b) physical and (c) natural domain.

After physical domain discretisation/meshing, the algorithm proceeds to calculate the Jacobian and shape functions based on nodes, elements, number of Gauss points and shape function (*Mesh_Me* function) associated with element type (Liner or Quadratic). The element ($el$) in the physical domain has a nodal coordinate of ($x_1, \dots x_d$), where $d$ notes the domain spatial dimensionality. Each node in the element is numbered counterclockwise. The assembly matrix is then allocated by knowledge of the element coordinate and node conductivity matrix. For example, for a two-dimensional physical domain, for $k$ number of elements, the coordinates can be described as below:

$$el_i = \sum_{i=1}^{N_d} N_i(x_1, x_2)\, x_{i,k} \qquad 9—4$$

The nodal displacement in each can then be expressed as the following:

$$u_i = \sum_{i=1}^{N_d} N_i(x_1, x_2)\, u_{i,k} \qquad 9—5$$

In the natural domain, the element has the following coordinates:

$$el_i = \sum_{I=1}^{N_{\text{nodes}}} N_I(\eta_1, \eta_2)\, x_{I,k} \qquad 9—6$$

The shape function matrix ($N_I$) at the element nodes is then used to transform elements from the physical to the natural domain using a linear geometrical transformation. Then the transformation between domains to solve for $\eta_1, \eta_2$ and the displacement vector is expressed as below:

$$\therefore \eta_i = \sum_{I=1}^{N_{\text{nodes}}} N_I(x_1, x_2)\, \eta_{i,k} \qquad 9—7$$

$$u_i = \sum_{I}^{N_{\text{nodes}}} N_I(\eta_1, \eta_2)\, u_{Ii} \qquad 9—8$$

The node coordinate ($N_d^n$) in the natural domain ($\eta_1, \dots \eta_d$) takes the format expressed in 9—9 for four nodes two-dimensional linear element up to 20 nodes three-dimensional quadratic element. Then the coordinate of the Gauss point ($g$) is definite in the natural frame as expressed for some elements in (9—10) and (9—11), although the position can be shifted from being centric at $1/2$ to $1/\sqrt{3}$ as shown in Figure 2-1 for quadrilateral (i.e. linear and quadratic) elements. Figure 9-1 shows a schematic of the position of each component

discussed earlier for a two-dimensional linear element. Schematics and some information about different elements are also shown in Table 9-1.

$$N_d^n = \underbrace{\begin{bmatrix} -1 & -1 \\ 1 & -1 \\ 1 & 1 \\ -1 & 1 \end{bmatrix}}_{\text{2D Linear}} = \underbrace{\begin{bmatrix} -1 & -1 \\ 1 & -1 \\ 1 & 1 \\ -1 & 1 \\ 0 & -1 \\ 1 & 0 \\ 0 & 1 \\ -1 & 0 \end{bmatrix}}_{\text{2D Quadratic}} = \underbrace{\begin{bmatrix} -1 & -1 & -1 \\ 1 & -1 & -1 \\ 1 & 1 & -1 \\ -1 & 1 & -1 \\ -1 & -1 & 1 \\ -1 & 1 & 1 \\ 1 & -1 & 1 \\ 1 & 1 & 1 \end{bmatrix}}_{\text{3D Linear}} = \underbrace{\begin{bmatrix} -1 & -1 & -1 \\ 1 & -1 & -1 \\ 1 & 1 & -1 \\ -1 & 1 & -1 \\ -1 & -1 & 1 \\ -1 & 1 & 1 \\ 1 & -1 & 1 \\ 1 & 1 & 1 \\ 0 & -1 & -1 \\ 0 & 1 & -1 \\ 0 & -1 & 1 \\ 0 & 1 & 1 \\ -1 & 0 & -1 \\ 1 & 0 & -1 \\ -1 & 0 & 1 \\ 1 & 0 & 1 \\ -1 & -1 & 0 \\ 1 & 1 & 0 \\ -1 & 1 & 0 \\ 1 & -1 & 0 \end{bmatrix}}_{\text{3D Quadratic}} \qquad 9—9$$

$$g_2^n = g^n(\eta_1, \eta_2) = \underbrace{\begin{bmatrix} 0 & 0 \end{bmatrix}}_{\text{2D reduced Linear}} = \underbrace{\frac{1}{2}\begin{bmatrix} -1 & -1 \\ 1 & -1 \\ 1 & 1 \\ -1 & 1 \end{bmatrix}}_{\substack{\text{2D full Linear} \\ \text{2D reduced Quadratic}}} = \frac{1}{2}\underbrace{\begin{bmatrix} -1 & -1 \\ 1 & -1 \\ 1 & 1 \\ -1 & 1 \\ 0 & -1 \\ 1 & 0 \\ 0 & 1 \\ -1 & 0 \\ 0 & 0 \end{bmatrix}}_{\text{2D full Quadratic}} \qquad 9—10$$

$$g_3^n = g^n(\eta_1, \eta_2, \eta_3) = \underbrace{\begin{bmatrix} 0 & 0 & 0 \end{bmatrix}}_{\text{3D reduced Linear}} = \frac{1}{2}\underbrace{\begin{bmatrix} -1 & -1 & -1 \\ 1 & -1 & -1 \\ 1 & 1 & -1 \\ -1 & 1 & -1 \\ -1 & -1 & 1 \\ 1 & -1 & 1 \\ -1 & 1 & 1 \\ 1 & 1 & 1 \end{bmatrix}}_{\substack{\text{3D full Linear} \\ \text{3D reduced Quadratic}}} = \frac{1}{2}\underbrace{\begin{bmatrix} -1 & -1 & -1 \\ 1 & -1 & -1 \\ 1 & 1 & -1 \\ -1 & 1 & -1 \\ -1 & -1 & 1 \\ 1 & -1 & 1 \\ -1 & 1 & 1 \\ 1 & 1 & 1 \\ 0 & -1 & -1 \\ 0 & 1 & -1 \\ 0 & -1 & 1 \\ 0 & 1 & 1 \\ -1 & 0 & -1 \\ 1 & 0 & -1 \\ -1 & 0 & 1 \\ 1 & 0 & 1 \\ -1 & -1 & 0 \\ 1 & -1 & 0 \\ -1 & 1 & 0 \\ 1 & 1 & 0 \\ 0 & 0 & 0 \\ 1 & 0 & 0 \\ -1 & 0 & 0 \\ 0 & 1 & 0 \\ 0 & -1 & 0 \\ 0 & 0 & 1 \\ 0 & 0 & -1 \end{bmatrix}}_{\text{3D full Quadratic}} \quad 9—11$$

Table 9-1: Coded elements type.

| Dimension | ABAQUS equivalent | Element type | Nodes | Integration point | |
|---|---|---|---|---|---|
| | | | | Full | Reduced |
| 2D | CPS4 | Linear | 4 | 4 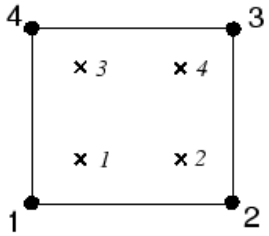 | 1 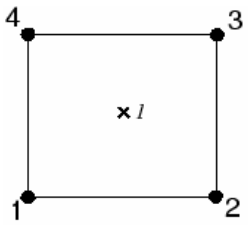 |
| 2D | CPS8 | Quadratic | 8 | 9 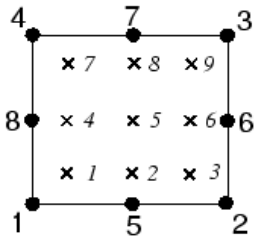 | 4 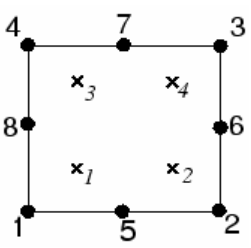 |
| 3D | C3D8 | Linear | 8 | 8 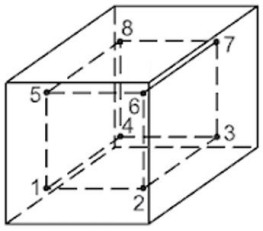 | 1 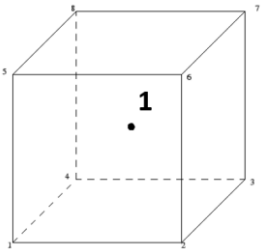 |
| 3D | C3D20 | Quadratic | 20 | 27 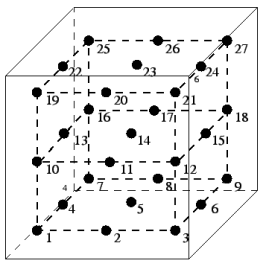 | 8 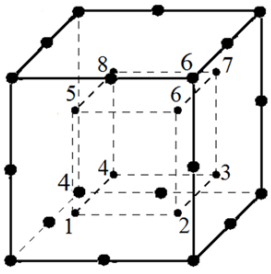 |

The shape function $N_I(\eta_1 \dots \eta_n)$ and shape function derivative is then calculated. Some examples are included below:

$$N_I(\eta_1,\eta_2)=\underbrace{\frac{1}{4}\begin{bmatrix}(1-\eta_1)(1-\eta_2)\\(1+\eta_1)(1-\eta_2)\\(1+\eta_1)(1+\eta_2)\\(1-\eta_1)(1+\eta_2)\end{bmatrix}}_{\text{2D Linear}}=\underbrace{\frac{1}{4}\begin{bmatrix}(1-\eta_1)(1-\eta_2)(-\eta_1-\eta_2-1)\\(1+\eta_1)(1-\eta_2)(\eta_1-\eta_2-1)\\(1+\eta_1)(1+\eta_2)(\eta_1+\eta_2-1)\\(1-\eta_1)(1+\eta_2)(-\eta_1+\eta_2-1)\\2(1-\eta_1^2)(1-\eta_2)\\2(1+\eta_1)(1-\eta_2^2)\\2(1-\eta_1^2)(1+\eta_2)\\2(1-\eta_1)(1-\eta_2^2)\end{bmatrix}}_{\text{2D Quadratic}} \qquad 9—12$$

$$N_I(\eta_1,\eta_2,\eta_3)=\underbrace{\frac{1}{8}\begin{bmatrix}(1-\eta_1)(1-\eta_2)(1-\eta_3)\\(1+\eta_1)(1-\eta_2)(1-\eta_3)\\(1+\eta_1)(1+\eta_2)(1-\eta_3)\\(1-\eta_1)(1+\eta_2)(1-\eta_3)\\(1-\eta_1)(1-\eta_2)(1+\eta_3)\\(1+\eta_1)(1-\eta_2)(1+\eta_3)\\(1+\eta_1)(1+\eta_2)(1+\eta_3)\\(1-\eta_1)(1+\eta_2)(1+\eta_3)\end{bmatrix}}_{\text{3D Linear}}$$

$$=\underbrace{\frac{1}{8}\begin{bmatrix}(1-\eta_1)(1-\eta_2)(1-\eta_3)(-2-\eta_1-\eta_2-\eta_3)\\2(1-\eta_1^2)(1-\eta_2)(1-\eta_3)\\(1+\eta_1)(1-\eta_2)(1-\eta_3)(-2+\eta_1-\eta_2-\eta_3)\\2(1+\eta_1)(1+\eta_2^2)(1-\eta_3)\\(1+\eta_1)(1+\eta_2)(1-\eta_3)(-2+\eta_1+\eta_2-\eta_3)\\2(1-\eta_1^2)(1+\eta_2)(1-\eta_3)\\(1-\eta_1)(1+\eta_2)(1-\eta_3)(-2-\eta_1+\eta_2-\eta_3)\\2(1-\eta_1)(1-\eta_1^2)(1-\xi_3)\\2(1-\eta_1)(1-\eta_2)(1-\eta_3^2)\\2(1+\eta_1)(1-\eta_2)(1-\eta_3^2)\\2(1+\eta_1)(1+\eta_2)(1-\eta_3^2)\\2(1-\eta_1)(1+\eta_2)(1-\eta_3^2)\\(1-\eta_1)(1-\eta_2)(1+\eta_3)(-2-\eta_1-\eta_2+\eta_3)\\2(1-\eta_1^2)(1-\eta_2)(1+\eta_3)\\(1+\eta_1)(1-\eta_2)(1+\eta_3)(-2+\eta_1-\eta_2+\eta_3)\\2(1+\eta_1)(1-\eta_2^2)(1+\eta_3)\\(1+\eta_1)(1+\eta_2)(1+\eta_3)(-2+\eta_1+\eta_2+\eta_3)\\2(1-\eta_1^2)(1+\eta_2)(1+\eta_3)\\(1-\eta_1)(1+\eta_2)(1+\eta_3)(-2-\eta_1+\eta_2+\eta_3)\\2(1-\eta_1)(1-\eta_2^2)(1+\eta_3)\end{bmatrix}}_{\text{3D Quadratic}} \qquad 9—13$$

The element order and the number of Gauss points are optional in the algorithm. However, for 2D analysis, the algorithm is built to adjust the number of Gauss points to achieve higher

accuracy efficiently based on the number of available elements, element uniformity (higher order of Gauss points for non-uniform element distribution) and computer/system cache memory size and the number of available cores. A more advanced method could use the hp-FEM or h-adaptive method.

The relationship between the displacement derivatives in the natural and physical coordinates can be formulated again using the shape function.

$$\frac{\partial u_i}{\partial x_j} = \frac{\partial}{\partial x_j}\left(\sum_{I}^{N_{\text{nodes}}} N_I u_{Ii}\right) = \sum_{I}^{N_{\text{nodes}}} \frac{\partial N_I(\eta_1,\eta_2)}{\partial x_j} u_{Ii} \qquad 9—14$$

Now $\frac{\partial N_I(\eta_1,\eta_2)}{\partial x_j}$ can be determined (for two-dimensional problems)

$$\frac{\partial N_I(\eta_1,\eta_2)}{\partial x_j} = \frac{\partial \eta_i}{\partial x_j}\ \frac{\partial N_I(\eta_1,\eta_2)}{\partial \eta_i} \qquad 9—15$$

$$\begin{bmatrix} \dfrac{\partial N_I(\eta_1,\eta_2)}{\partial x_1} \\ \dfrac{\partial N_I(\eta_1,\eta_2)}{\partial x_2} \end{bmatrix} = \underbrace{\begin{bmatrix} \dfrac{\partial \eta_1}{\partial x_1} & \dfrac{\partial \eta_1}{\partial x_2} \\ \dfrac{\partial \eta_2}{\partial x_1} & \dfrac{\partial \eta_2}{\partial x_2} \end{bmatrix}}_{J^{-1}} \cdot \begin{bmatrix} \dfrac{\partial N_I(\eta_1,\eta_2)}{\partial \eta_1} \\ \dfrac{\partial N_I(\eta_1,\eta_2)}{\partial \eta_2} \end{bmatrix} \qquad 9—16$$

where the $x_i$ or $x_1$ and $x_2$ coordinates for the nodes are defined below

$$x_i = \sum_{I}^{N_{\text{nodes}}} N_I(x_1,x_2)\ .x_{Ii} \qquad 9—17$$

the derivative should be

$$\frac{\partial x_i}{\partial \eta_j} = \sum_{I}^{N_{\text{nodes}}} \frac{\partial N_I(\eta_1,\eta_2)}{\partial \eta_j}.x_{Ii} \qquad 9—18$$

and the coordinate system derivatives relationship using the Jacobian determinant is:

$$\frac{\partial \eta_i}{\partial x_j} = \frac{1}{|J|}\left(\frac{\partial x_i}{\partial \eta_j}\right) \qquad 9—19$$

thus:

$$\frac{\partial u_i}{\partial x_j} = \sum_{I}^{N_{\text{nodes}}} \frac{\partial \eta_k}{\partial x_j}\frac{\partial N_I}{\partial \eta_k}.u_{Ii} \qquad 9—20$$

The elements' (global) stiffness matrix, $K$, which contains the equations to be solved and the element force matrix, $F$, at Gauss points a, are assembled in a sparse matrix (DataUm function) to use the available memory efficiently. This is used to solve for the nodal displacement, $u$, (*Dis_Solver* function), equation (2—11). Solving for the nodal displacement ($u_{Ii}$) require optimisation; thus, the linear least-squares method is used for the whole map.

$$R^2 = \sum_{k}^{N_k} \left| \left(\frac{\partial u_i}{\partial x_j}\right)_k - \frac{\partial u_i(x_k, u_{Ii})}{\partial x_j} \right|^2 \qquad 9—21$$

$$\frac{\partial R^2}{\partial u_{Ii}} = 0 = -2\sum_{k}^{N_k} \left| \left(\frac{\partial u_i}{\partial x_j}\right)_k - \frac{\partial u_i(x_k)}{\partial x_j} \right| \frac{\partial^2 u_i(x_k)}{\partial x_j.\partial u_{Ii}} \qquad 9—22$$

There are several equation solvers built-in MATLAB. The algorithm starts an adaptive trial and error procedure, starting from a more accurate and computationally expensive MATLAB® built-in algorithm while estimating and isolating regions beyond the error tolerance to be solved with other suitable algorithms.

The first attempt uses the MATLAB® built-in *backslash* (/) or *mldivide* algorithm, which gives an exact solution using Orthogonal and upper triangular (QR) decomposition for full rectangular matrices, and other different solvers depending on the matrix density by checking for suitable conditioned method (for more details about *mldivide* and other MATLAB built-in algorithms, please refer to the MATLAB® webpage). In essence, *Backslash* or *mldivide* is

suitable for dense/full matrixes (i.e., uniform square or rectangular grid) with few elements (less than 10,000 elements, depending on the CPU capabilities) because it converts a sparse matrix to a full matrix that occupies far more memory causing the process to fail if the size of the memory required for the full matrix is larger than what is available. This algorithm will also fail if the R decomposition matrix's diagonal elements are zero and found unreliable for deficient (not-full) matrixes.

The second attempt uses MATLAB's built-in Moore-Penrose Pseudoinverse (*pinv*) algorithm that gives a (minimal norm) least-square solution for a system of linear equations using singular value decomposition (SVD) to form the pseudoinverse of $A_{ij}$ in equation 2—11. This algorithm is suitable for non-full and underdetermined/constrained matrixes. However, it is sensitive to noise and discontinuity and relies on singular value decomposition, which is computationally expensive but reliable [491]. That is why, when this method is being used, the number of Gauss points is automatically increased if a high level of discontinuity (i.e., more than 5% of the matrix is empty) and an elevated level of noise is detected (i.e., values which are further away from a local median by more than three scaled median absolute deviation, MAD). Failure of this method usually is due to memory issues because – like *mldivide* – it requires the sparse matrix to be converted to a full matrix and because of error exceeding an adaptive tolerance value at an elevated level of noise.

The third attempt uses the *lsqminnorm* algorithm, suitable for sparse matrixes, which is computationally less expensive as it uses complete orthogonal decomposition (COD) rather than singular value decomposition (SVD) to find an approximate solution. This is sufficient considering the algorithm is on the third attempt, which means the algorithm has already failed the requirement for the previous algorithms due to matrix size, density, shapes, and

noise level. Hough and Vavasis [492] argued for COD's accuracy, simplicity, and efficiency over standard iterative QR decomposition for solving ill-conditioned and rank-deficient linear problems.

The fourth and last attempt uses a custom-made Moore-Penrose pseudo-inverse algorithm [493] that accepts sparse matrices compared to *pinv*. The algorithm incorporates Tikhonov's regularization term to avoid noise problems and compute a stable solution. Failure of this last method will be due to memory issues. The algorithm is configured to automatically reduce the input strain-fields density by 5% and restart the entire process again. This reduction will incrementally increase at 5% intervals until the displacement field is obtained. For a detailed discussion about SVD, QR decomposition and COD, please go to Ref. [494].

The nodal displacement is then corrected for rigid body movement (translations and rotation) by selecting the point with absolute minimum displacement as the origin (*RotRemoving* function for 2D and *shoemake_3D_v04_07_02_Abdo* function for 3D) [112]. The code can be coupled with the algorithm *DIC2ABAQUS* (https://doi.org/10.5281/zenodo.6411605) or *DVC2ABAQUS* (https://doi.org/10.5281/zenodo.6411611) to allow for the 2D or 3D displacement fields, respectively, to be input as a boundary condition in the ABAQUS® finite element solver to find the *J*-integral and stress intensity factor analysis or *AbaqusBC* for crystal plasticity analysis. Code and verification examples are available at https://doi.org/10.5281/zenodo.6411573; see the *input_desk_example* function or directly use *Westergaard_Modes* and *Westergaard_3D* functions to create a 2D and 3D, respectively, mixed-mode crack field based on Westergaard solution

## Appendix (3.A) – Age-hardened duplex stainless steel

Duplex stainless steel (DSS) is a mixture of austenite and ferrite microstructure, not necessarily in equal proportions, where the alloy solidifies as ferrite, and the temperature falls to around 1000 °C, it is partially transformed to austenite [495]. These contain 18-28% Cr and 4-8% Ni and are strong and have good corrosion resistance. More (practical) details are in Ref [496]. DSS is a well-characterised, suitable model material for EBSD analysis as the polished surface does not oxidise further, and high-quality patterns can be acquired reasonably.

Alpha (α) phase is a ferritic phase with body centred cubic (BCC) structure, $Im\bar{3}m$ [229] space group, 2.866 Å lattice parameter, and has one twinning system {112}<111> and three slip systems {110}<111>, {112}<111> and {123}<111>, however, the last system rarely activates [303]. Gamma (γ) phase is austenitic with a face-centred cubic (FCC) structure, $Fm\bar{3}m$ [259] space group, 3.66 Å lattice parameter, typically has more Ni, Cu, and interstitial C and N [497]. Plastic deformation occurs in austenite compared to ferrite and the preferred slip variant to be activated has a low Schmid factor [498]. During deformation, straight slip bands form in austenite that propagate to the ferrite-austenite boundary, assisting in slipping the ferrite phase. Curved slip bands also form due to the bulk ferrite grain deformation [201,503,504].

Duplex stainless is widely used in the industry because it possesses excellent oxidation resistance but can have limited toughness due to its large ferritic grain size, and they have hardened, and embrittlement tendencies at temperatures ranging from 280–500 °C, especially at 475 °C, where spinodal decomposition of the supersaturated solid ferrite solution into Fe-rich nanophase ($\alpha'$) and Cr-rich nanophase ($\alpha''$), occur accompanied by G-phase precipitation occurs [196–198,505], which makes the ferrite phase a preferential

initiation site for micro-cracks [502]. This is because aging encourages ∑3 {112}<111> ferrite deformation twinning at slow strain rate and room temperature in tensile or compressive deformation, nucleating from local stress concentrations sites [196,302], and parent-twinning boundaries, with 60° (in or out) misorientation, are suitable for cleavage crack nucleation [280,300,503].

Spinodal decomposition refers to the spontaneous separation of a phase into two coherent phases via uphill diffusion, i.e., a negative diffusion coefficient $\frac{d^2G}{dX^2} < 0$, without a barrier to nucleation due to the phase being thermodynamically unstable (i.e., miscibility gap, $\alpha'$+ $\alpha''$region in Figure 9-2) [504], where $G$ is the Gibbs free energy per mole of solution and $X$ the composition. It increases hardness and decreases magneticity [203]. The miscibility gap describes the region in a phase diagram below the melting point of each compound where the atom disrupts the solid phase into the liquid of two separated stable phases [505].

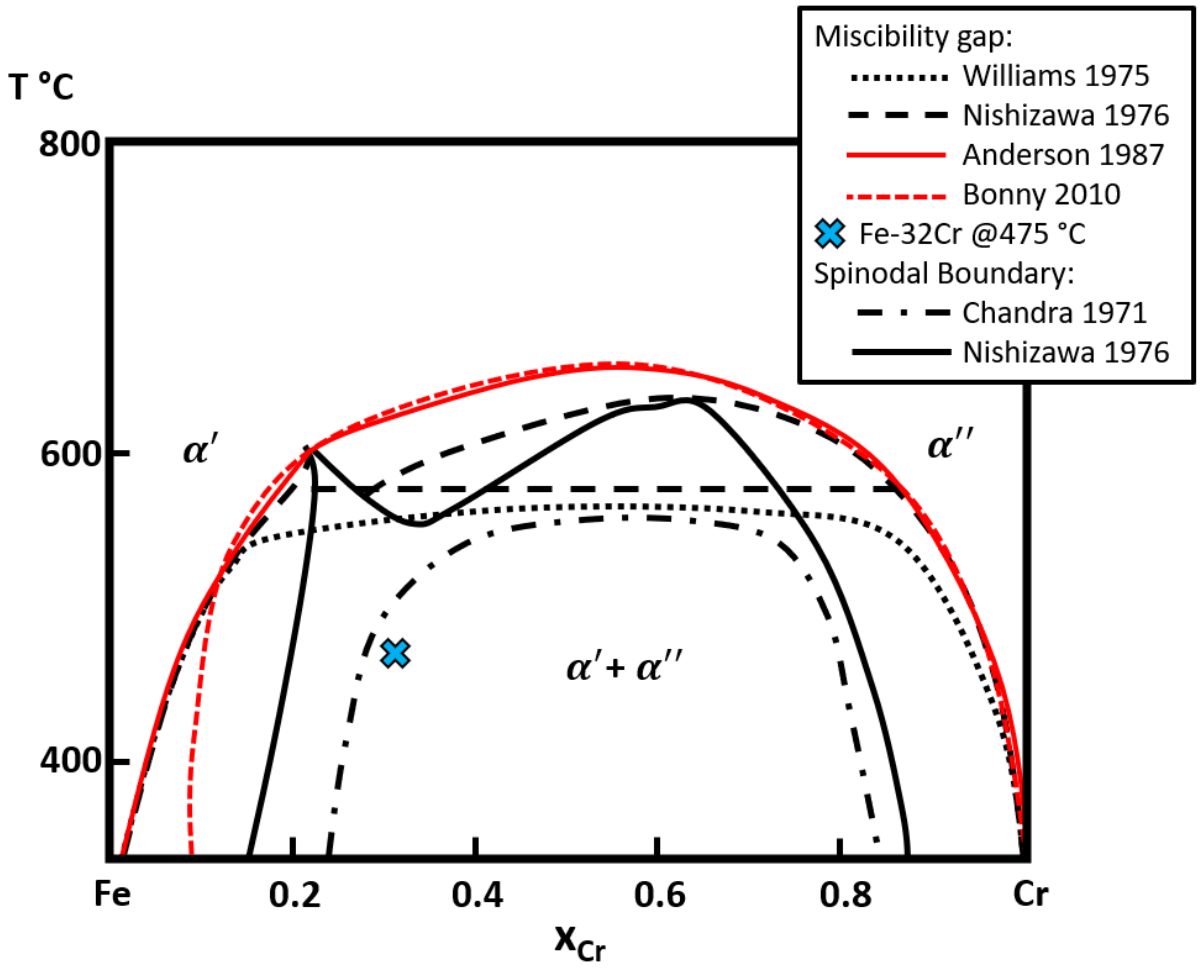


Figure 9-2: Calculated metastable miscibility gap in the Fe-Cr binary system (remake of [506–508]).

Using Field Emission Gun Transmission Electron Microscope FEG-TEM, the nanometre-scaled modulated structure of the decomposed ferrite was revealed as a Cr-rich nanophase gave a bright image and a Fe-rich darker image (Figure 9-3) [509]. It also revealed that these modulated nanophases grow coarser with aging time [509,510]. Decomposed phases start as irregular rounded shapes with no particular arrangement, but with time the Cr-rich nanophase takes a plat shape aligned in the $< 110 >$ directions [510]. Nevertheless, as the ferrite hardness increases with aging time, the hardness of the ductile austenite phase remains nearly unchanged [199–201,301] due to faster diffusivity in ferrite compared to the austenite [203]. Nevertheless, austenite undergoes a substitutional redistribution of elements, enhancing galvanic corrosion between the two phases [512].

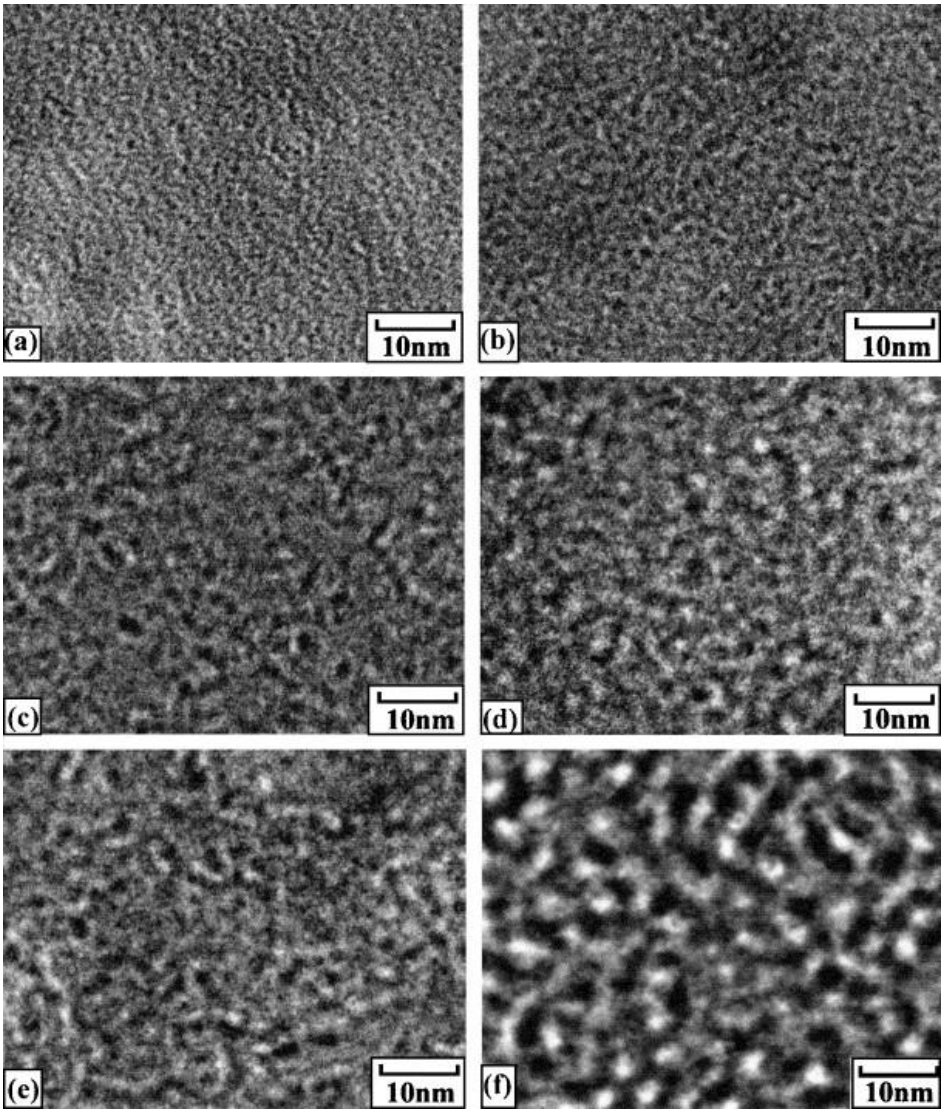


Figure 9-3: FEG-TEM showing the morphology of the modulated microstructure for the specimens aged at 475 °C for different time intervals: (a) 2 h; (b) 4 h; (c) 8 h; (d) 16 h; (e) 32 h and (f) 64 h [509].

Spinodal decompositions increase the hardening of the material due to the misfit between the Cr-rich and Fe-rich nano-phases, internal stress, and variation of elastic modulus. The formation of coherent (i.e., lattice matching) precipitates induces an equal but opposite strain, raising the system's free energy depending on the precipitate shape and matrix and precipitate elastic properties [505,513]. Around a spherical inclusion, the distortion is purely hydrostatic. The embrittlement is caused by dislocations impediment/ locking by (mostly) the spinodal decomposed (modulated) matrix [200,201] and (strain around) G-phase precipitates [514] (i.e., internal stress relaxation by the formation of Cottrell atmosphere [515]).

G-phase precipitates are phase rich in Ni, Ti, and Si [199], but Cr and Mn may substitute Ti sites [516] and be named because it appears prominently at grain boundaries [199]. G-phase precipitates occur during long-term aging, are encouraged by increasing Ni content in the ferrite phase [517], and reduce corrosion resistance significantly [518]. It has ellipsoid morphology, FCC structure ($Fm\bar{3}m$), and 11.4 Å lattice parameter [519], with a diameter < 50 nm that increases with aging [520,521].

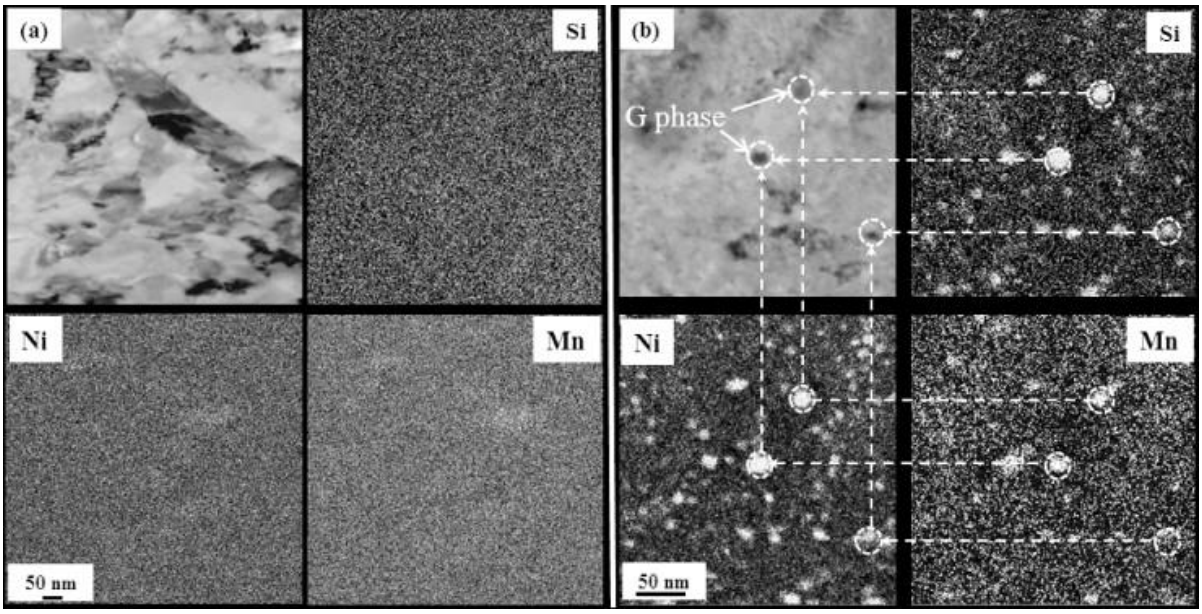


Figure 9-4: STEM image and corresponding Energy Dispersive Spectroscopy (EDS) mapping for SUS304 annealed at 400 °C for (a) 1 h and (b) 500 h [516].

550 °C heat treatment can reverse spinodal decomposition but not affect the G-phase precipitates [522]. The ferrite matrix spinodal decomposition can be substantially reversed by introducing an external pulsed electric current that changes the system's free energy due to the difference in electrical conductivity between the nanophases and the dissolution of G-phase precipitates [523,524]. Cyclic loading suppresses spinodal decomposition [525], and radiation accelerates it but changes its nature from an interconnected network to isolated islands [526]. A very recent and detailed review of aged DSS can be found in Ref [507].

# Appendix (3.B) – Geometrically necessary dislocations (GND) density estimation

Although vulnerable to recovery, irreversible dislocation behaviour acts to decrease dislocation mobility due to multiplication (increase in density) and their interactions (i.e., formation of locks and jogs) which makes continuous plastic deformation more difficult (i.e., strain hardening [527]). The dislocations trapped and accumulated randomly in a uniform shear process are labelled statistically stored dislocations (SSDs) [528]. This is typically associated with normal three-stage strain hardening of a pure single crystal [529]. Still, except in pure single crystals, the strain hardening response to load in almost all metals and alloys is plastically non-homogeneous and influenced by other strengthening mechanisms (e.g., dispersion of particles dislocation-precipitant interactions which increase CRSS, grains size). In plastically non-homogeneous materials, plastic deformation gradients form is imposed by incompatible microstructure (e.g., phases or particles). Thus, to allow a compatible deformation (i.e., maintain lattice continuity) of a heterogeneous specimen, dislocations are stored in these microstructures and are labelled as geometrically necessary dislocations (GND) [529].

The 'geometric slip distance' – a microstructure characteristic – describes the accumulation rate with strain, with a length-scale equivalent to the microstructure (e.g., phases or GB) spacing. Since dislocations (each with a unit Burgers vector) of the same sign do not coalesce and repel one another, dislocations tend to pile-up against a barrier on the slip plane (e.g., phases or GB). Thus, the dislocations individually contribute to hardening (Ashby's hardening) by acting as obstacles to slip and collectively forming a long-range back-stress due to dislocations pile-up, which can monotonically lead to fracture. These long-range internal

stresses are not unique to pile-ups but more of a plastic deformation compatibility requirement, sometimes addressed as 'image stress,' which acts to cancel the imposed stress field at the other side of the interface, with a magnitude inversely proportional to the distance to the interface [258]. The GND density controls the strain hardening process when their density exceeds the SSDs [528,530].

This means plastic deformation is accommodated by dislocation behaviour, and an effective way to analyse the intragranular misorientation can be done by analysing the residual dislocations accumulated during hardening (i.e., GND density). This was achieved by using Nye [531]-Kröner [532]-Bilby [533] framework for EBSD data to estimate the GND content (i.e., density and arrangement), which is linked to the slight local lattice curvature caused by stress incompatibility [216,217]. Individual dislocation content can also be resolved without serial sectioning or knowledge about the sample deformation history [376]. Although the statistically stored dislocations (SSDs) net geometric effect is cancelled by adjacent opposite-sign dislocations within the Burgers circuit (i.e., net Burgers' vector equals zero), extreme care must be exercised when deciding the interaction volume scale for non-redundant-dislocations measurement, as seen in equation (9—24).

$$\alpha_{ij} = \underbrace{\frac{1}{\mathrm{V}}\int_{L} b_i \, \mathrm{t}_j \, ds}_{\text{Avg. Dislocations Properties}} = \underbrace{\frac{1}{\mathrm{V}}\sum_{d=1}^{D} b_i^d \int_{l} t_j^d \, ds^d}_{\text{Retain Dislocations Properties}} = \sum_{d=1}^{D} \rho^d * b_i^d \otimes \mathrm{t}_j^d \qquad 9—23$$

$$\because \rho^d = \frac{1}{\mathrm{V}}\int_{L} ds^d = \frac{l^d}{V_\cdot} = \rho_{GNDs}^d + \underbrace{\rho_{SSDs}^d}_{\sum=0} = \rho_{GNDs}^d \qquad 9—24$$

where $\alpha_{ij}$ is Nye's dislocation tensor, $L$ is the total length of dislocation in reference volume (V), $l$ is the length of dislocation type (d) with Burgers vector $b_i$, $ds$ Length increment along the dislocation line, $\mathrm{t}_j$ is line vector, $\rho^d$ is GND density of dislocation type (d), and D is

all present dislocation types (e.g., 18 for FCC with 12 edges and 6 screw dislocations [530]). And, by considering a continuous displacement field u(x) defined only in an infinitesimal neighbourhood $\left(1 \gg \left|\frac{\partial u}{\partial x}\right|\right)$ of position x around a closed curve (C); a relationship between local lattice curvature (eq. 9—25) and local dislocation network (eq. 9—26) written as the net Burgers' vector (B) over the surface ($s$) can be found [215,216,534].

$$\oint_c du = \oint_c \beta dx = \iint_s \mathrm{curl}(\beta)\, ds = \iint_s \mathrm{curl}\left(\beta^{\mathrm{Plastic}} + \beta^{\mathrm{Elastic}}\right) ds = 0 \qquad 9—25$$

$$\mathrm{B} = -\oint_c \beta^{\mathrm{P}}\, dx = -\iint_s \mathrm{curl}(\beta^{\mathrm{P}})\, ds = \iint_s \alpha_{ij}\, ds \qquad 9—26$$

$$\therefore \alpha_{ij} = -\mathrm{curl}(\beta^{\mathrm{P}}) = \mathrm{curl}(\beta^{\mathrm{E}}) = e_{ikl}\left(\underbrace{\epsilon^{E}_{jl,k}}_{\Sigma\approx 0} + \omega^{E}_{jl,k}\right) \qquad 9—27$$

where $\beta$ is the local lattice distortion or displacement gradient tensor, $e_{kli}$ is Levi–Civita permutation tensor, and $\epsilon_{jl,k}$ and $\omega_{jl,k}$ are the elastic strain and lattice rotation tensors.

With Nye's dislocation tensor ($\alpha$) written as the sum of the gradient of the lattice elastic strain gradient and rotation (nine components); the EBSD technique cannot measure any derivatives normal to the sample surface (i.e., terms containing $\frac{\partial}{\partial x_3}$), and from experiments, the elastic strain gradients were found to be sufficiently smaller compared to the rotation gradients (≈1%); thus, it will be neglected ($\epsilon_{jl,k} \approx 0$). This makes five components of the dislocation tensors accessible ($\alpha_{13}, \alpha_{23}, \alpha_{33}, \alpha_{12}, \alpha_{21}$ and $\alpha_{11}$) with the sixth being calculable ($\alpha_{11} - \alpha_{22}$). These six components (nine in 3D techniques [109,110,405]) can be expressed as a column vector ($\Lambda$) for rotation derivatives and related to each slip system (*D,* with $b_i^d$ and $\mathrm{t}_i^d$) using the matrix (A) multiplied by the dislocation densities matrix ($\rho$) with the matrix size in brackets **()** as in equations (9—28) and (9—29), where the comma indicates the

partial differentiation with respect to Cartesian coordinates [105,205,297,537].

$$A\ (6 * D).\ \rho\ (D * 1) = \Lambda\ (6 * 1) \qquad 9—28$$

$$\begin{pmatrix} b_1^1 t_1^1 - ½ \sum_{i=1}^{3} b_i^1 t_i^1 & \dots & b_1^d t_1^d - ½ \sum_{i=1}^{3} b_i^d t_i^d \\ b_1^1 t_2^1 & \dots & b_1^d t_2^d \\ b_1^1 t_3^1 & \dots & b_1^d t_3^d \\ b_2^1 t_1^1 & \dots & b_2^d t_2^d \\ b_2^1 t_2^1 - ½ \sum_{i=1}^{3} b_i^1 t_i^1 & \dots & b_2^d t_2^d - ½ \sum_{i=1}^{3} b_i^d t_i^d \\ b_2^1 t_3^1 & \dots & b_2^d t_3^d \end{pmatrix} \begin{pmatrix} \rho^1 \\ \vdots \\ \rho^d \end{pmatrix} = \begin{pmatrix} \omega_{23,1} \\ \omega_{31,1} \\ \omega_{12,1} \\ \omega_{23,2} \\ \omega_{31,2} \\ \omega_{12,2} \end{pmatrix} \qquad 9—29$$

The least-square method is then used to solve for $\rho$ using. The solution to the minimisation problem of the values of the dislocation densities is then obtained by the equation 9—30, which is overdetermined when solving for any material except simple cubic materials; thus, a minimisation approach must be employed (i.e., $L_1$ energetically motivated or $L_2$ geometrically motivated) combined with a weighting factor (w) to reflect each system activation probability or (strain) energy [107].

$$\rho = (A^T A)^{-1} A^T \Lambda \qquad 9—30$$

Pantleon [107] argues that Nye's dislocation density tensor is the build-up/summation of the absolute value of single dislocations with different densities to achieve minimum total energy. Thus, here, the edge and screws are being weighted (i.e., used a vector coefficient) as described in 9—31 and 9—32 based on their strain energy [378,535], where the effective Poisson ratio ($v$) is calculated from the Voigt stiffness tensor ($C_{ij}$) of an anisotropic material [536]. The GND density calculated with this method is termed 'a lower- bound GND.' Thus here, the $L_1$ method (natively implanted in MATLAB in the '*linprog'* algorithm) was employed (as in equation 9—31) since it has been widely used and showed high sensitivity in resolving the structure of individual dislocation variants [371,376,530,535]. Also, this study assumed a

direct relationship between dislocation strain energy and dislocation length (through plastic strain gradients, dislocation density and lattice curvature linear relation), irrespective of the negligible elastic strain gradients and dislocation fields interaction influences, which is commonly used in the literature [105,205,533,536,540][14].

$$L_1 = \sum_{\mathrm{i}=1}^{D} |\rho_d * w_d| \,, \qquad w_d^{screw} = (b_d^{\mathrm{screw}})^2, \qquad w_{\mathrm{i}}^{edge} = \frac{\left(b_d^{\mathrm{edge}}\right)^2}{(1-v)} \tag{9—31}$$

$$v = \frac{C_{11} + 4C_{12} - 2C_{44}}{2(2C_{11} + 3C_{12} + C_{44})} \tag{9—32}$$

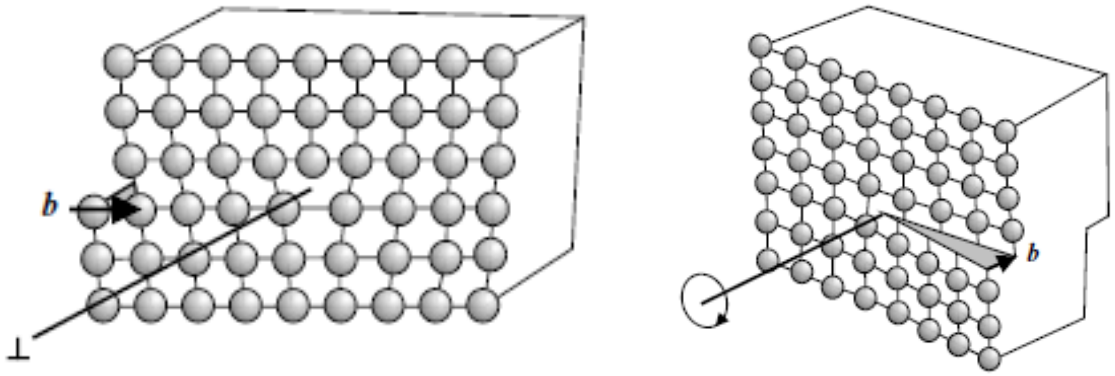


Edge Dislocation Screw Dislocation

Figure 9-5: Schematic of dislocations and associated Burgers' vector ($b$) [538].

GND density calculation based on calculating the local kernel disorientation from HR-EBSD elastic lattice rotation gradient showed less noise level compared to one based on calculating the local kernel[15] average misorientation (KAM) from EBSD Euler angles [179]; this is due to

[14] For $L_2$ method (equation below) can be calculated using Moore-Penrose pseudo-inversion (pinv) or nonnegative least-squares curve fitting problems (*lsqnonneg*).

$$L_2 = \sqrt{\sum_{\mathrm{i}=1}^{D} (\rho_i * w_i)^2} \tag{9—16}$$

[15] A kernel describes a set of points surrounding a centric point of interest.

the increase of the angular resolution when calculating the lattice rotation. However, there is a negligible dependency of the estimated GND distribution on the reference pattern selection [207,541] because only the lattice distortion gradient is needed.

As discussed earlier, GND density estimation is length-scale dependent. The optimum step size can be estimated using Ruggles *et al.* [537] selection criteria, which involve plotting GND density vs step size and selecting the step size where the mean map GND density is almost constant with slight changes in step size. However, this time-consuming method requires multiple iterations of slow pattern acquisition with inevitable carbon deposition accumulation. Instead, Wilkinson and Randman [206] used the below equation to estimate the dislocations density measurement sensitivity limit ($\Delta\rho$), where MAE is the mean angular resolution, and $\lambda$ is the step size.

$$\Delta\rho = \frac{\mathrm{MAE}}{b\,\lambda}, \qquad \mathrm{MAE} = \frac{\text{Shift Sensitivity}}{\text{Pattern Size}} \tag{9—33}$$

This formula suggests that a more significant step size provides higher measurement accuracy, which is not entirely accurate as a too-large step size can lead to missing essential dislocations as one portion is averaged with another portion, and a too-small step size can render the dislocation density to be no longer continuously distributed [215,533,542]. From Ruggles *et al.* [537] comparing different steps and Suchandrima *et al.* [541] comparing (HR) EBSD to micro-beam Laue and crystal plasticity simulation; any step size between 0.5 and 0.05 µm should be adequate to estimate GND density. Plus, Kikuchi patterns binning size inversely affects the estimated GND density and associated noise [207].

## Appendix (4.A) – $EBSP_0$ effect on *J*-integral analysis

The effect of the choice of $EBSP_0$ is shown in Figure 9-6, which presents the *J*-integral, mode I and II stress intensity factor calculated from an HR-EBSD field based on either the '*Chosen*' $EBSP_0$ from the 1st phase and another selected using the conventional criteria from the available $EBSP_0$ (i.e., '*Native*'). The *Native* reference gives a minor change in the magnitude of *J*-integral compared to the '*Chosen*' reference. There is also an effect on mode decomposition to stress intensity factors, whereby the *Native* choice finds no significant change in $K_I$ and $K_{II}$ between the first and second observations at 15% and 20% nominal strain. Using the '*Chosen*' $EBSP_0$ finds increases in $K_I$ and $K_{II}$ that correlate with the observed tensile thickening and shear propagation. This supports the identification of the '*Chosen*' $EBSP_0$ as being more optimal and closer to a strain-free reference.

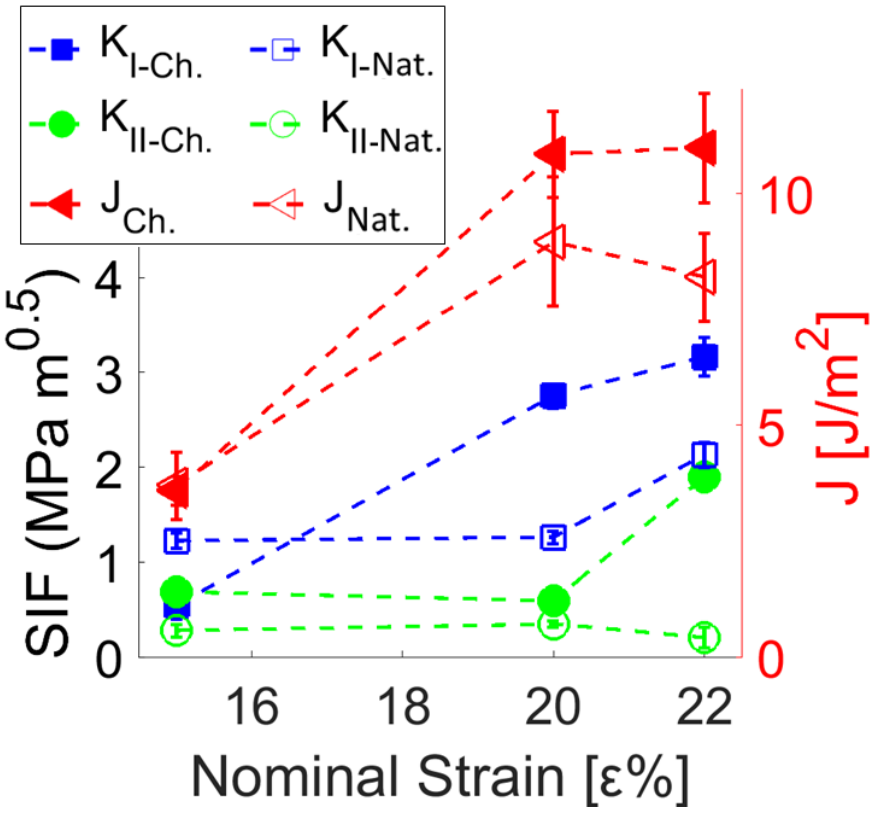


Figure 9-6: *J*-integral, mode I and II stress intensity factor calculated from HR-EBSD field based on an $EBSP_0$ *Chosen* (Ch.) from the 1st phase and another selected using a *Native* criterion from phase-available $EBSP_0$ (Nat.).

To quantify the effects of using non-optimal reference patterns, the *J*-integral analysis (including decomposing $K_I$ and $K_{II}$) for the field ahead of the twin at 15% nominal strain was repeated across the 53 HR-EBSD maps created using the randomly selected reference patterns. Correlations between stress intensity factors and reference patterns were then examined, and the correlation coefficients were tabulated in Table 9-2. Deformed $EBSP_0$ will directly affect these parameters.

Table 9-2: Correlation coefficients for stress intensity factors and components calculated from the EBSPs. The minus sign indicates an inverse relationship.

| $EBSP_0$ | PH | MAE | IQ | $A^0$ | E11 | E22 | E12 | S11 | S22 | S12 |
|---|---|---|---|---|---|---|---|---|---|---|
| J | -0.12 | 0.3 | 0.18 | -0.37 | -0.45 | -0.26 | 0.45 | -0.63 | -0.27 | 0.51 |
| $K_I$ | -0.16 | 0.01 | 0.02 | -0.81 | -0.85 | -0.56 | 0.22 | -0.95 | -0.65 | 0.3 |
| $K_{II}$ | -0.36 | 0.1 | 0.28 | 0.19 | -0.14 | -0.16 | 0.85 | -0.31 | -0.02 | 0.83 |

## Appendix (4.B) – *J*-integral convergence

The initial non-convergence in *J*-integral can be attributed to the high level of plasticity close to the slip band, illustrated by the GND distribution. Convergence also started to fail when the domain expanded to the peripheral fields of other stress raisers, such as the array of slip bands in the adjacent subgrain. As discussed by [40,42], their contribution to the gradient field makes the vector field non-conservative unless fully engulfed by the integration domain, so the integral at the far-field will not be path-independent. Values shown here are the average taken from the stable converged region (between the green lines in Figure 9-7), with the variance indicating the convergence stability.

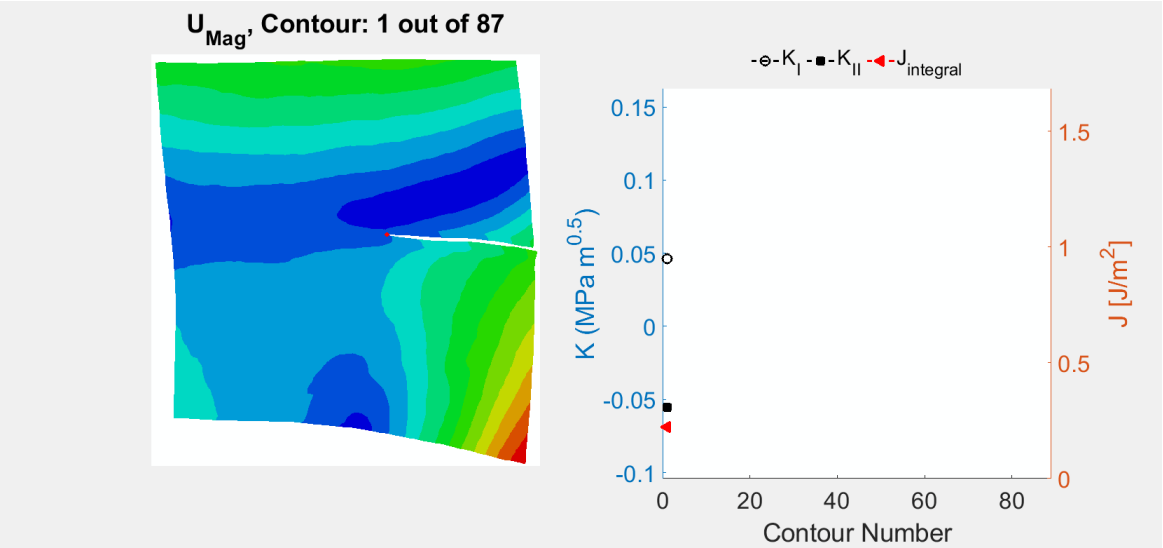


Figure 9-7: Animated *J*-integral domain advancement. The area between the two green dotted lines indicates the stable convergence considered for calculating strain energy-release values and variance.

## Appendix (4.C) – Pattern degradation

The image below shows the effect of carbon deposition on the quality of the patterns, which is caused by the electron-beam-induced decomposition of gaseous hydrocarbons during slow EBSPs acquisition [321]. Carbon depositions degrade the quality of EBSPs inside the probed area compared to the EBSPs outside the acquisition window. The gradient of pattern degradation increases moving inside the probed zone with an apparent accumulation of deposited carbon. The black spots from the beam instant-induced carbon deposition also highlight the immediate deposition even if agglomeration did not happen.

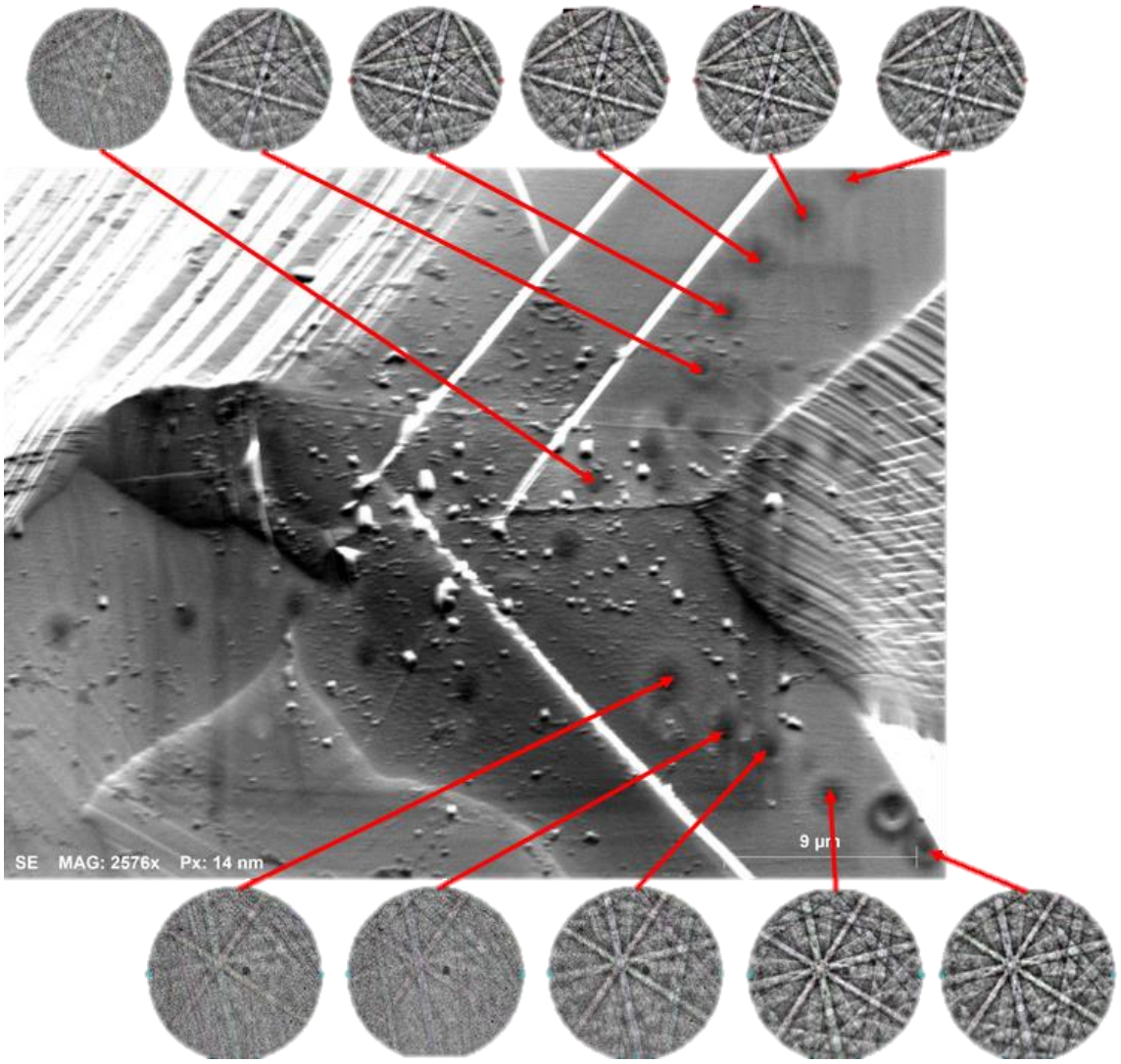


Figure 9-8: Pattern degradation due to carbon deposition in a highly magnified location after 3hr EBSPs acquisition around a deformation twin in the ferrite phase of duplex stainless steel.

# Appendix (5.A) – Additional figures

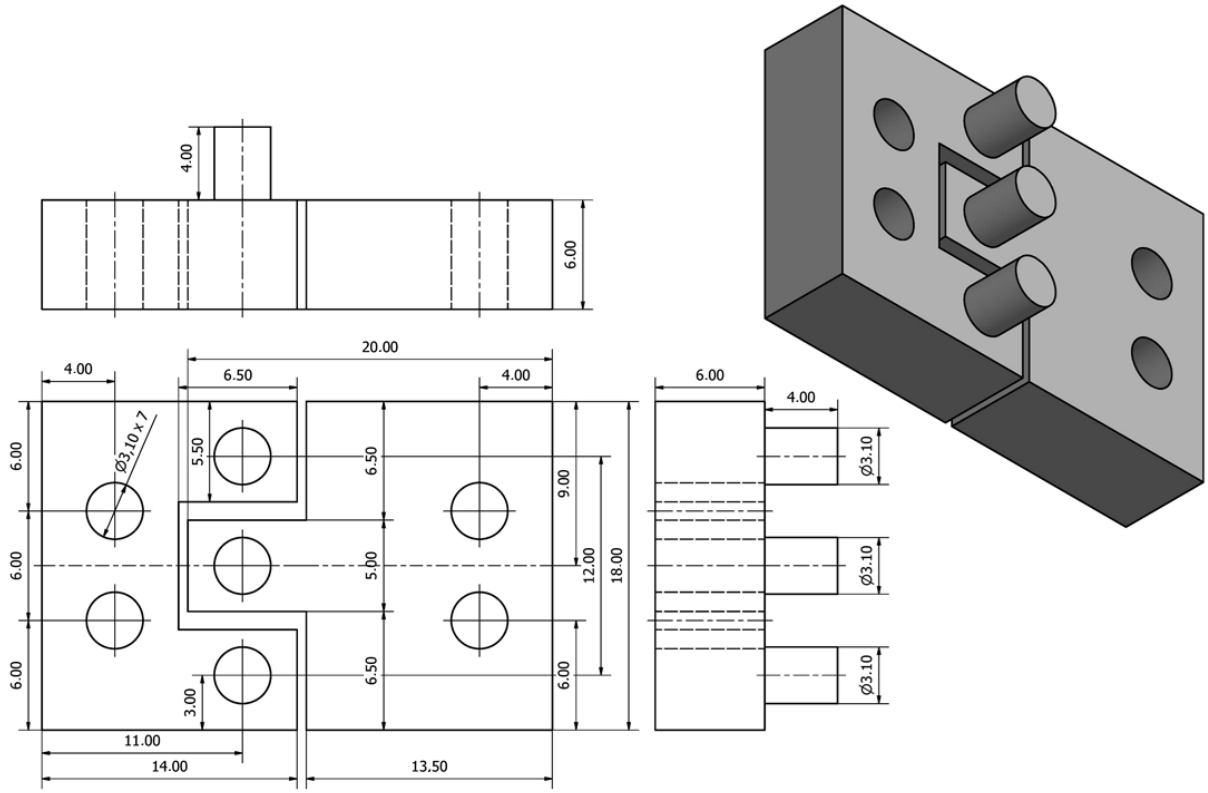


Figure 9-9: The three-point bending grip (made of stainless steel) schematic.

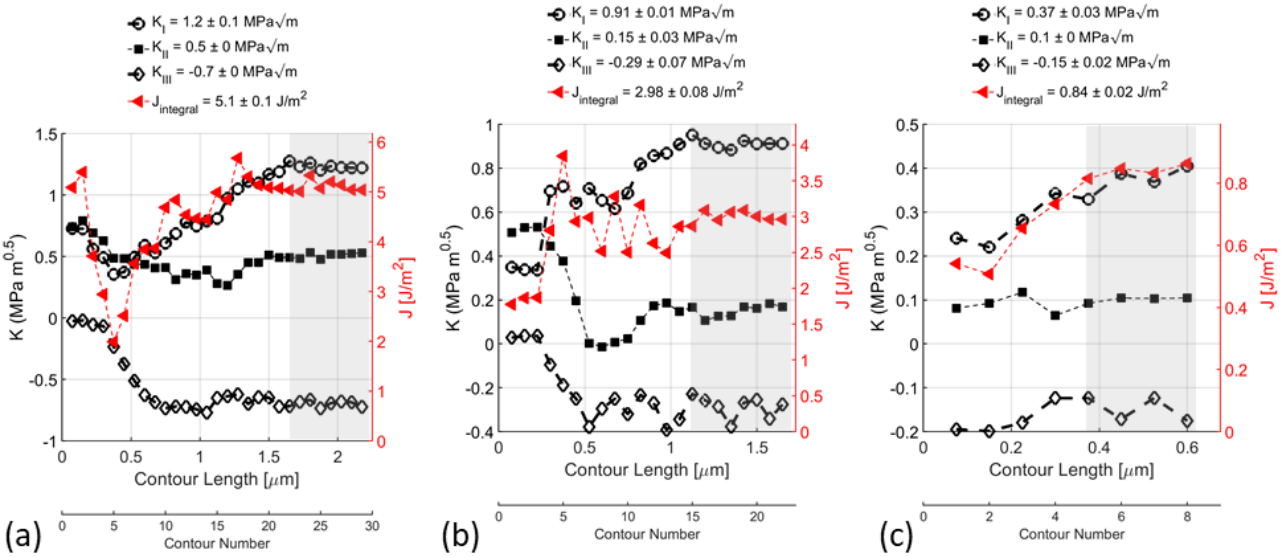


Figure 9-10: Convergence of the *J*-integral and decomposed SIFs for the $[1\bar{1}1](\bar{1}12)$ slip bands numbered (a) 2, (b) 1, (c) 3 in Figure 5-13 of Chapter 5.

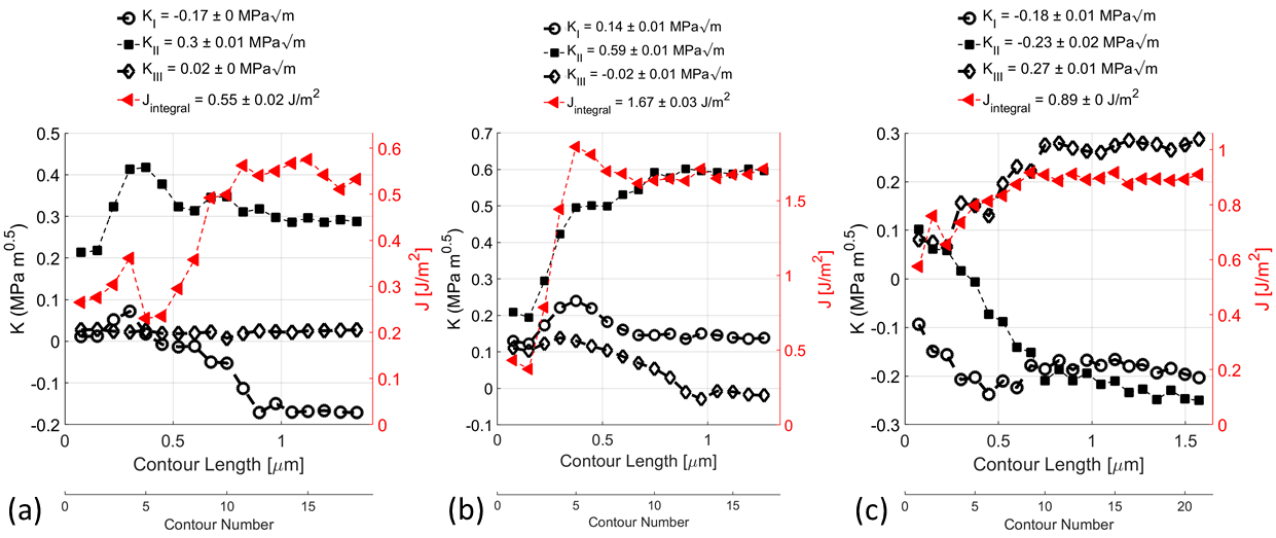


Figure 9-11: Convergence of the *J*-integral and decomposed SIFs for $[\bar{1}11](211)$ slip band with the nominal extension of (a) 1 mm and (b) 1.2 mm, before being (c) unloaded after 1.5 mm extension in Figure 5-18 of Chapter 5.

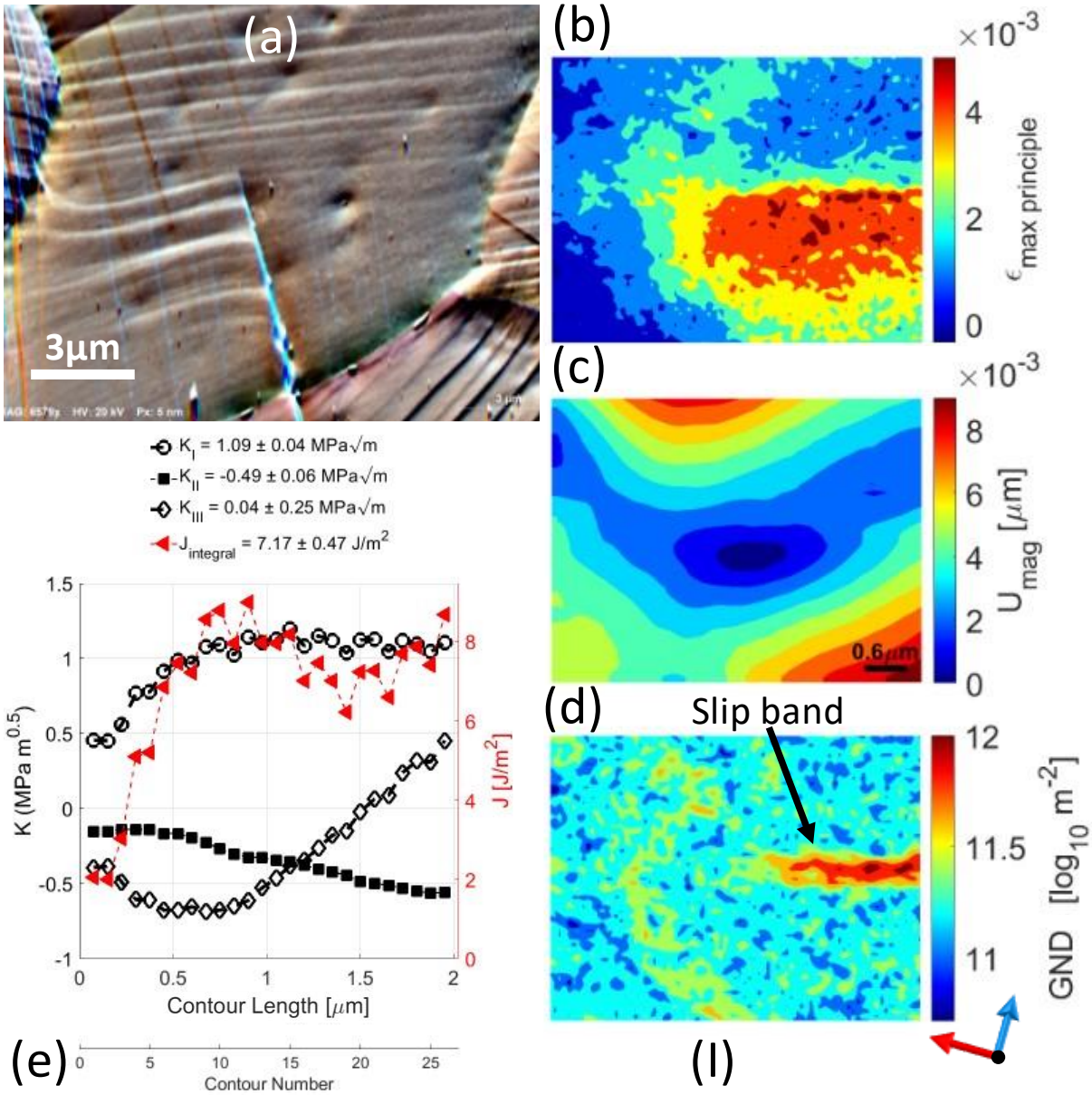


Figure 9-12: (I) $[\bar{1}11](110)$ slip band in ferrite crossing a low-angle GB. (a) FSD image. (b) maximum principal strain. (c) Integrated displacement magnitude. (d) GND density. (e) *J*-integral and stress intensity factors convergence. The slip band is accentuated by high GND density and is placed at the centre of $y$-axis in (b), (c), and (d). The ratio of the mode II to mode III stress intensity factors is included in Figure 5-19. Values are in Table 9-3.

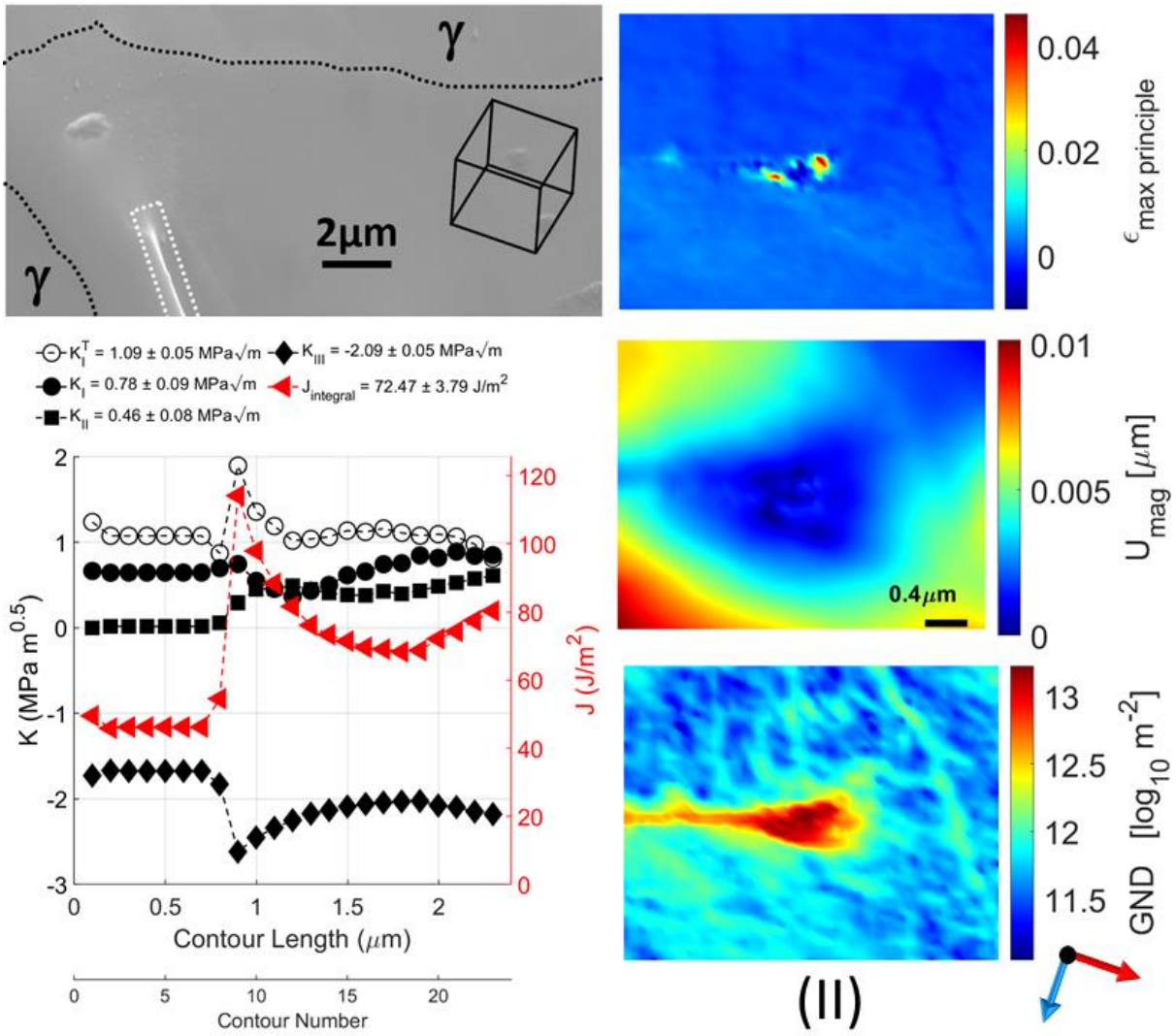


Figure 9-13: (II) $[\bar{1}1\bar{1}](211)$ slip band in ferrite. Same image sequence as Figure 9-12. The ratio of the mode II to mode III stress intensity factors is included in Figure 5-19. Values are in Table 9-3.

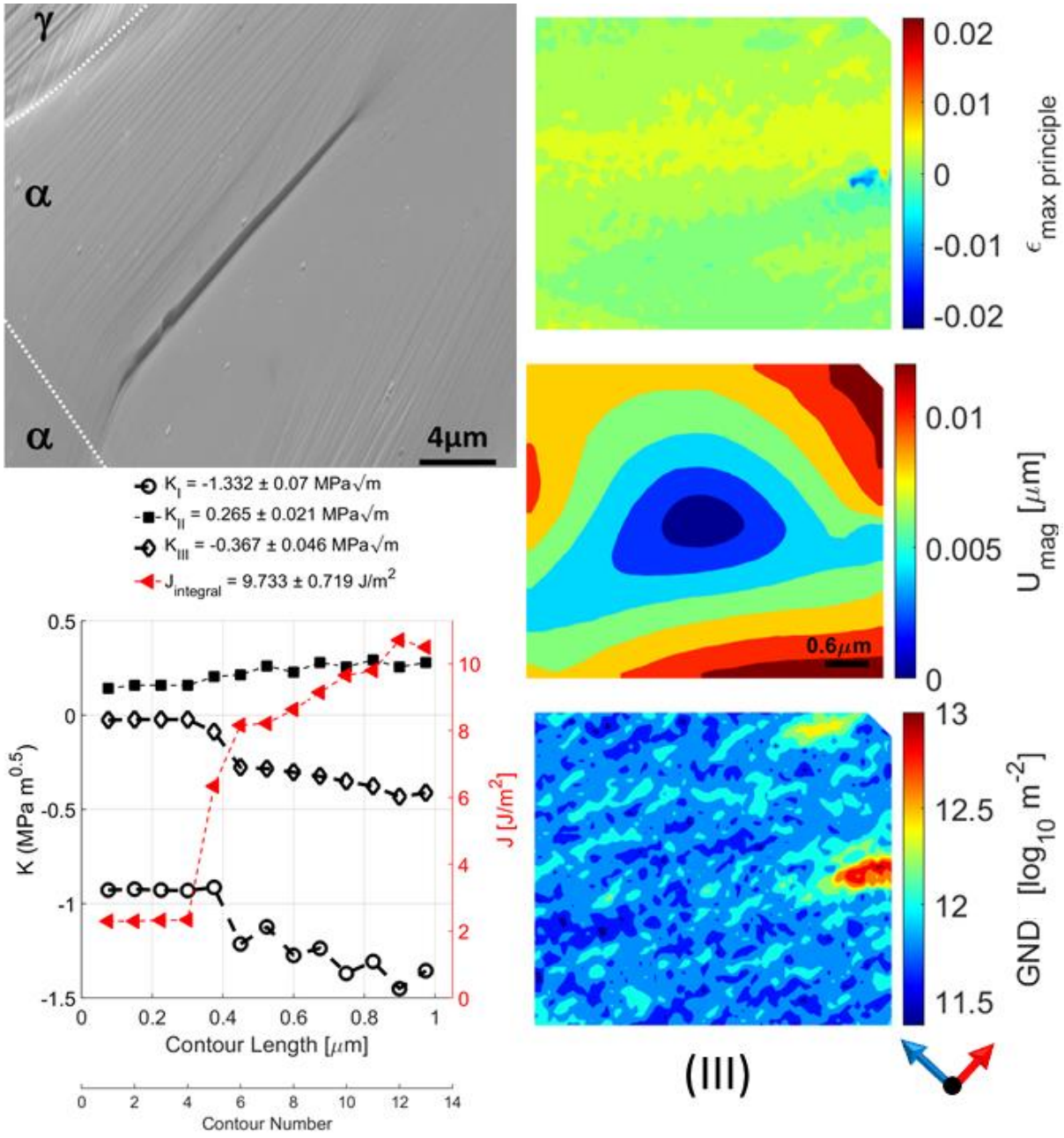


Figure 9-14: (III) $[\bar{1}11](1\bar{1}2)$ slip band in ferrite. Same image sequence as Figure 9-12. The ratio of the mode II to mode III stress intensity factors is included in Figure 5-19. Values are in Table 9-3.

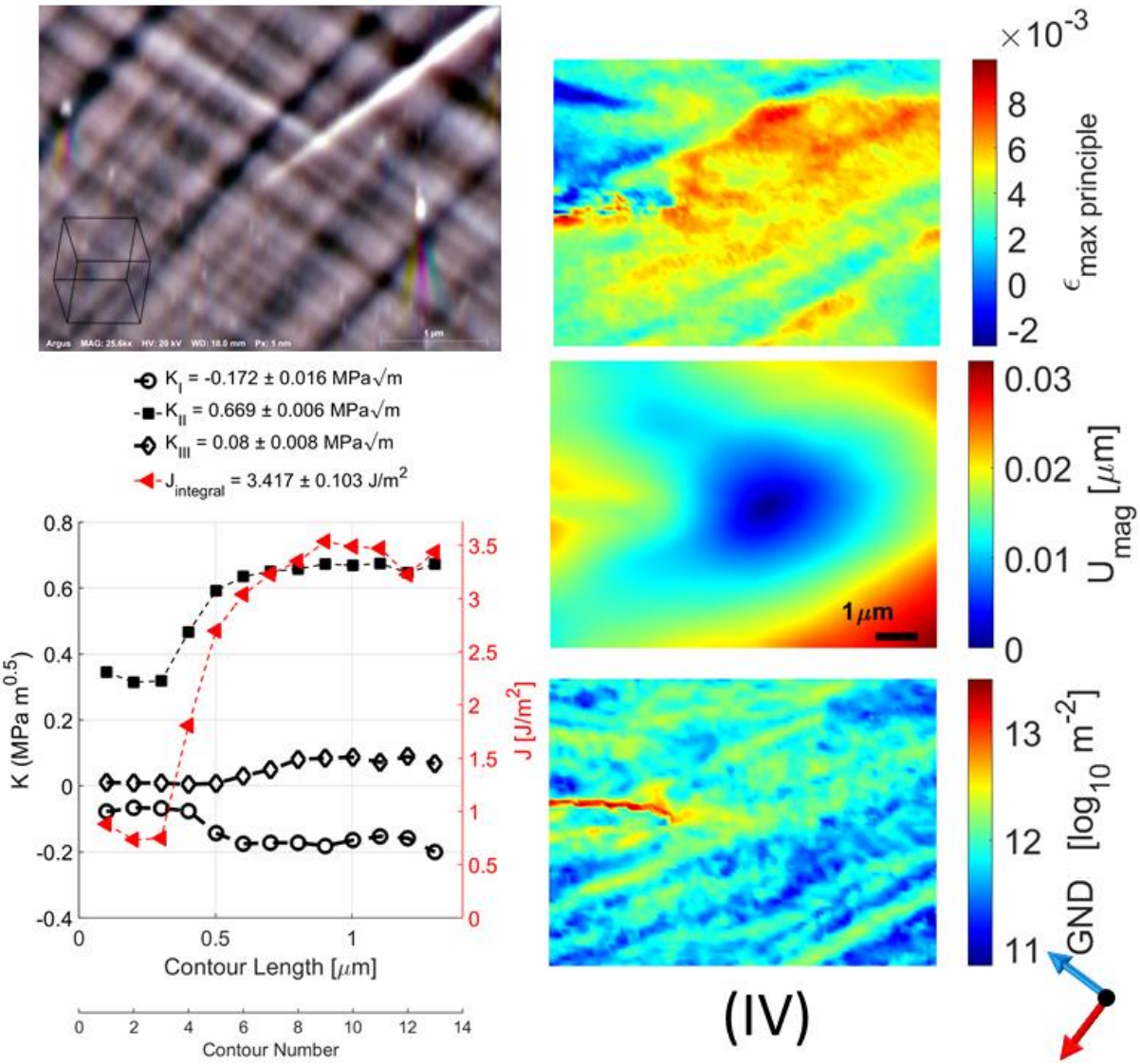


Figure 9-15: (IV) $[\bar{1}11](110)$ slip band in ferrite. Same image sequence as Figure 9-12. The ratio of the mode II to mode III stress intensity factors is included in Figure 5-19. Values are in Table 9-3.

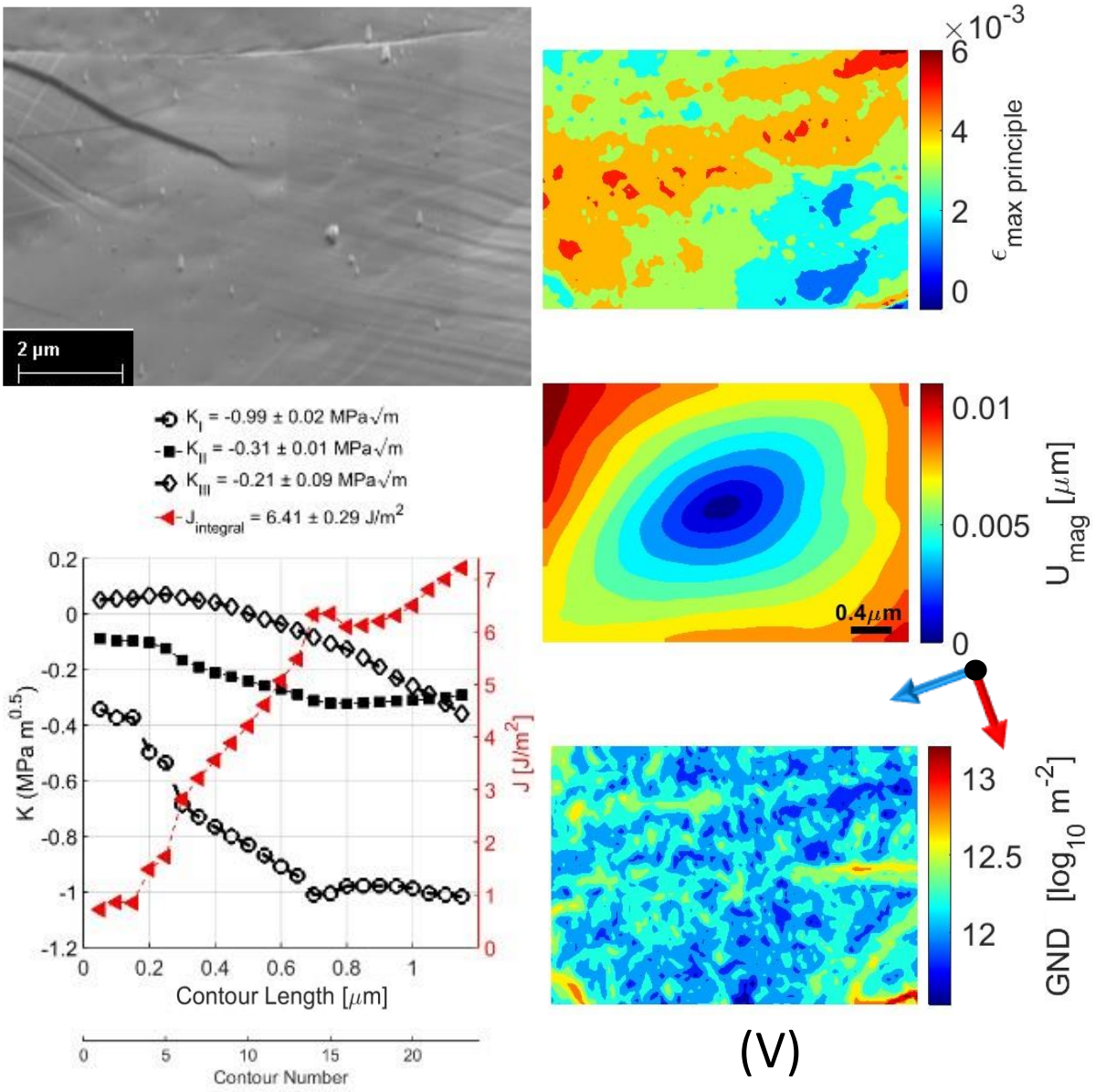


Figure 9-16: (V) $[11\bar{1}](\bar{1}21)$ slip band in ferrite. Same image sequence as Figure 9-12. The ratio of the mode II to mode III stress intensity factors is included in Figure 5-19. Values are in Table 9-3.

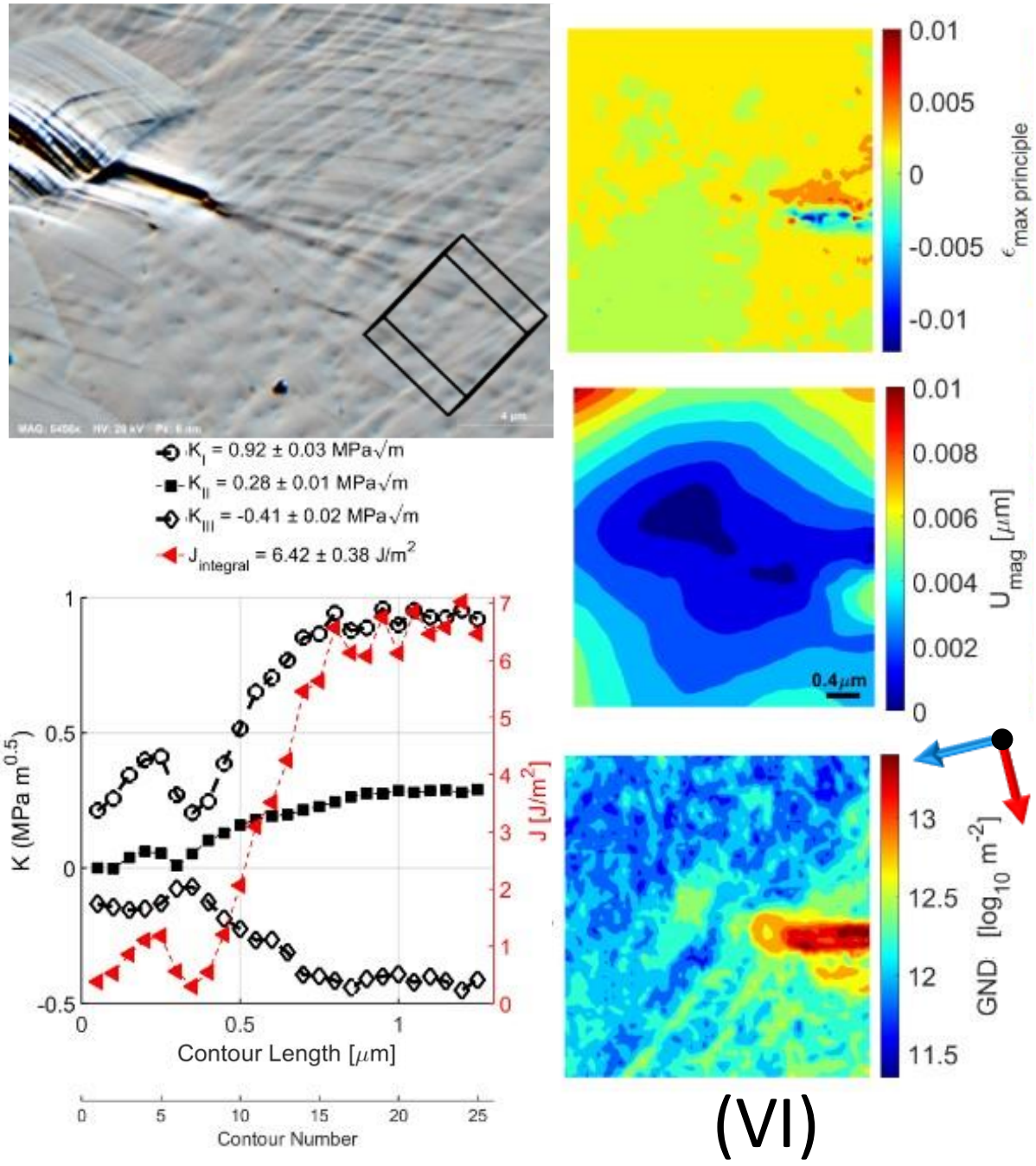


Figure 9-17: (VI) $[11\bar{1}](011)$ slip band in ferrite. Same image sequence as Figure 9-12. The ratio of the mode II to mode III stress intensity factors is included in Figure 5-19. Values are in Table 9-3.

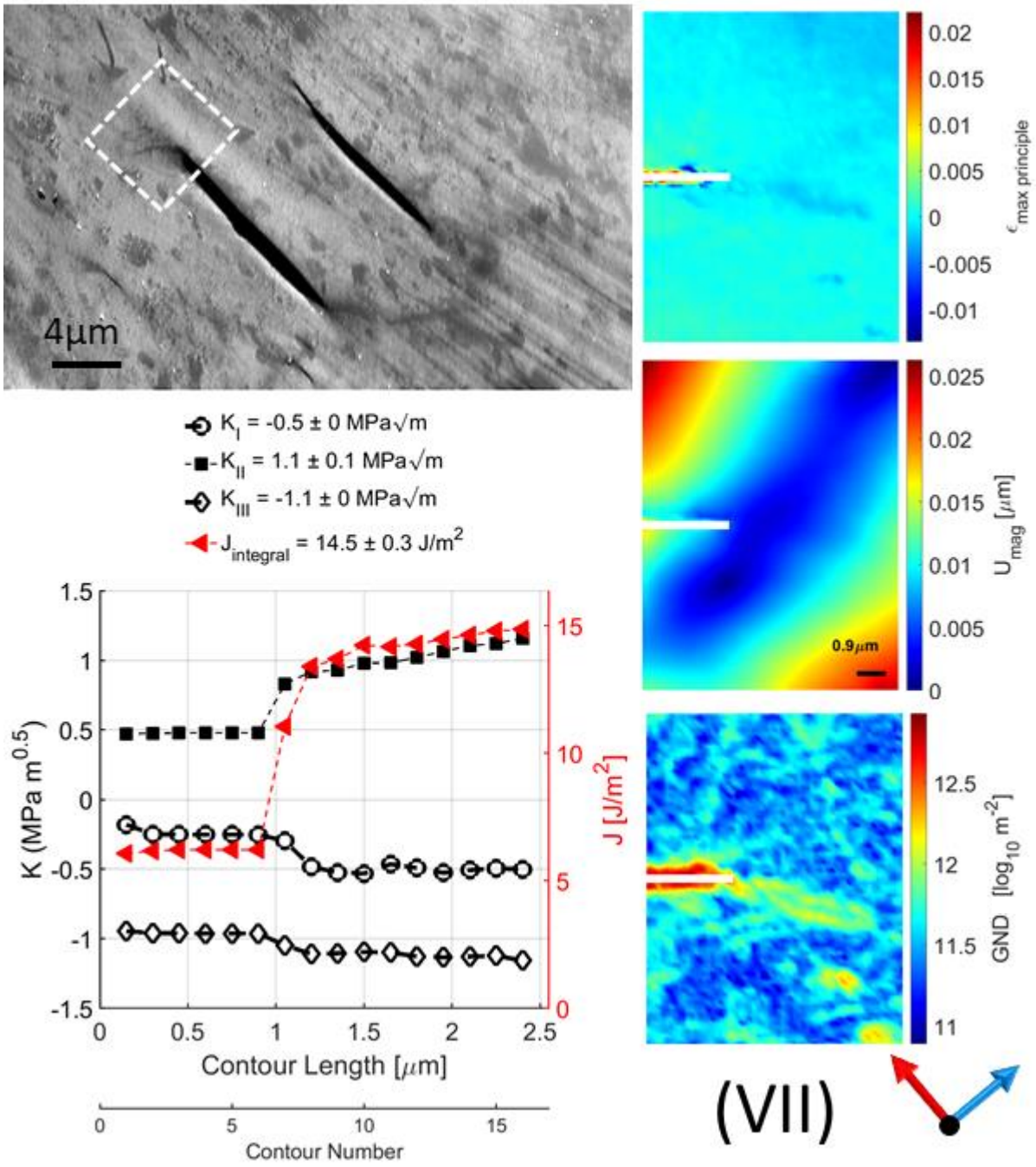


Figure 9-18: (VII) $[11\bar{1}](\bar{1}21)$ slip band in ferrite (inside the dashed white box). Same image sequence as Figure 9-12. The white line marks the slip band in the middle of the strain, displacement and GND density maps. The ratio of the mode II to mode III stress intensity factors is included in Figure 5-19. Values are in Table 9-3.

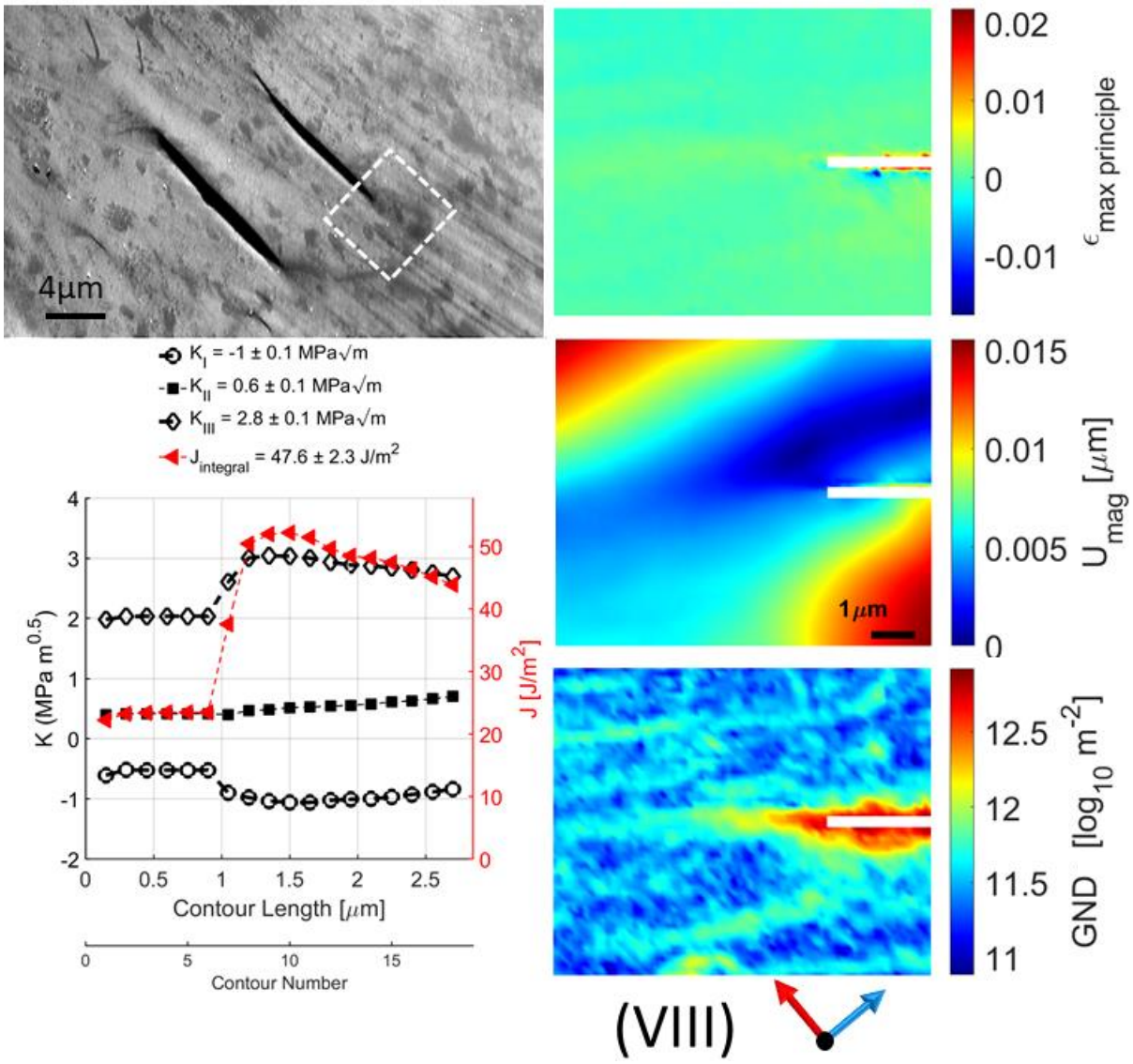


Figure 9-19: (VIII) $[11\bar{1}](\bar{1}21)$ slip band in ferrite (inside the dashed white box). Same image sequence as Figure 9-12. The white line marks the slip band in the middle of the strain, displacement and GND density maps. The ratio of the mode II to mode III stress intensity factors is included in Figure 5-19, and values are in Table 9-3.

Table 9-3: Additional in Situ examples from Figure 9-12 to Figure 9-19.

| Label | $(hkl)$[16] | Trace | $\psi$ | $J$ (J m$^{-2}$) | $K_I$ (MPa m$^{0.5}$) | $K_{II}$ (MPa m$^{0.5}$) | $K_{III}$ (MPa m$^{0.5}$) | No. of Contours |
|---|---|---|---|---|---|---|---|---|
| I | $(1\,\bar{7}\,12)$ | $[\bar{1}11](110)$ | 10.0° | 7.17 ± 0.47 | 1.09 ± 0.04 | -0.49 ± 0.06 | 0.04 ± 0.25 | 26 |
| II | $(3\,\bar{7}\,8)$ | $[\bar{1}1\bar{1}](211)$ | 75.9° | 72.47 ± 3.79 | 0.78 ± 0.09 | 0.46 ± 0.08 | -2.09 ± 0.05 | 23 |
| III | $(1\,6\,6)$ | $[\bar{1}11](1\bar{1}2)$ | 127.9° | 8.98 ± 0.76 | -1.23 ± 0.09 | 0.2 ± 0.05 | -0.28 ± 0.08 | 29 |
| IV | $(4\,\bar{7}\,11)$ | $[\bar{1}11](110)$ | 2.3° | 3.42 ± 0.10 | -0.17 ± 0.02 | 0.67 ± 0.01 | 0.08 ± 0.01 | 13 |
| V | $(0\,2\,11)$ | $[11\bar{1}](\bar{1}21)$ | 146.3° | 6.41 ± 0.29 | -0.99 ± 0.02 | -0.31 ± 0.01 | -0.21 ± 0.09 | 23 |
| VI | $(0\,2\,9)$ | $[11\bar{1}](011)$ | 125.3° | 6.42 ± 0.38 | 0.92 ± 0.03 | 0.28 ± 0.01 | -0.41 ± 0.02 | 25 |
| VII | $(\bar{3}\,0\,8)$ | $[11\bar{1}](\bar{1}21)$ | 119.1° | 14.50 ± 0.30 | -0.50 ± 0.00 | 1.10 ± 0.10 | -1.10 ± 0.00 | 16 |
| VIII | $(\bar{3}\,0\,8)$ | $[11\bar{1}](\bar{1}21)$ | 119.1° | 65.91 ± 12.33 | -2.52 ± 0.08 | 0.96 ± 0.06 | 2.1 ± 0.39 | 27 |

Table 9-4: Crystallographic orientation of the surface plane of the observed ferrite grains in the exemplar studies, rounded to the nearest Miller indices $(hkl)$.

| Dataset | $(hkl)$ | $\psi$ |
|---|---|---|
| Incipient slip band | $(\bar{2}\,0\,11)$ | 79.3° |
| Slip bands array | $(\bar{5}\,\overline{12}\,10)$ | 107.6° |
| Loaded slip band | $(\overline{11}\,\bar{1}\,12)$ | 172.3° |

[16] Parent grain orientation rounded to the nearest Miller indices $(hkl)$.

# Appendix (5.B) – HR-EBSD based Schmid factor ($xSF$)

## 5.B.1. Introduction

Von Mises [542], in 1928, identified that the response and change in shape for a crystal required the plastic deformation to be 'arbitrary'. For a ductile polycrystalline material to accommodate this 'arbitrary shape change,' five independent slip systems must be activated (six if the volume is not conserved). Importantly, in a crystal with an insufficient number of independent slip systems, the crystal may also twin or phase transform to accommodate this 'arbitrary shape change' [238,543]. The word independent here indicates that, in each slip system, the produced strain must be unique and cannot be produced by any combination of other slip systems.

Moreover, Schmid [544], around 1935, related the shear stress tensor of an applied load resolved along a specific slip plane – known as resolved shear stress ($\tau_{rss}$) – using a geometrical factor to describe what is now known as Schmid's law, which is described in equation (9—34) and Figure 9-20 and takes the value between ±0.5 where $\lambda$ and $\varphi$ are the angles between the loading direction ($r$) and the slip direction ($d$), as in eq. (9—35), and the loading direction and the slip plane normal ($n$), as in eq. (9—36), respectively.

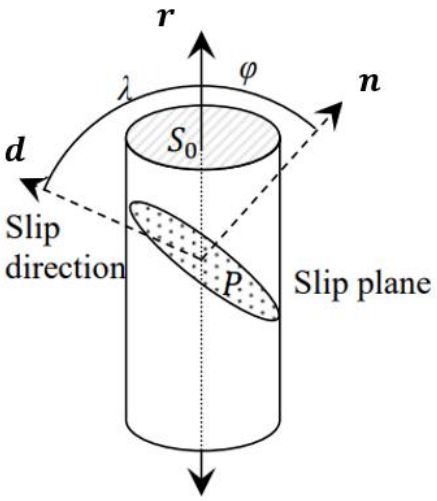


$$\mathrm{SF} = \cos\lambda\cos\varphi \qquad 9—34$$

$$\cos\lambda = \frac{r \cdot d}{|r||d|} \qquad 9—35$$

$$\cos\varphi = \frac{r \cdot n}{|r||n|} \qquad 9—36$$

Figure 9-20: Schematic of slip deformation in a single crystal.

Thus,

"*Of the twelve (Or 24 if shears in opposite senses parallel to the same line be regarded as distinct) crystallographically similar possible modes of shearing, the one for which the component of shear-stress in the direction was greatest was the one which actually occurred*" (Taylor and Elam 1925 [545], p. 28). Nevertheless, ferrite in duplex stainless steel violated this law [396].

With this geometrical analysis, Schmid opened the way to study deformation by activating deformation systems. Nevertheless, obtaining the resolved shear stress is complicated for polycrystalline materials due to the constraints imposed by neighbouring crystals, which led Taylor [316,317] in 1938 to describe the effects of 'random' grains orientations to relate the stress-strain behaviour for a single-crystal to that of poly-crystals using Taylor's orientation factor (Schmid's factor reciprocal) that shows the material global strength dependency on the textured orientation of the crystals [546]. Both Taylor and Schmid analyses (1) assume a uniform uniaxial strain where grain will deform comparatively-to and uniformly-with the applied stress, (2) do not consider the local grain inter/intra interaction, (3) account only for slip as a deformation mode, (4) did not consider local grain behaviour when it starts yielding where deformation via dislocations will cause a small portion of the crystal, under load, to

rotate separately especially at boundaries, acting as a locking key against slip transfer from adjacent crystals; thus, increasing strength [317,547], (5) did not consider the role of elastic anisotropy in regulating deformation localisation [548]. Chin *et al.* [549] and Bilby *et al.* [232] improved Taylor's analysis to include twinning as a deformation mechanism but did not address the other points.

In BCC metals, in the initial stages of deformation, screw dislocations have non-planar cores and will cross-slip (without dissociating) between the many available slip planes, following the most effortless path creating the 'wavy slip' observed at the micro-scale. Eventually, as deformation progresses, applied shear will force dislocations to nearly linear rearrangements (assisted by thermal activation), i.e., slip lines, before they extend to the 3$^{rd}$ dimension, i.e., slip band, by plane-glide in pencil-like shape with dense veins and walls [550,551]. Despite this arrangement being due to shear, the plane of choice does not follow Schmid's law and is affected by tension-compression asymmetry, non-shear stresses [552], and shear and dilatational stress components arise from the fields around spinodal precipitates owing to loops accumulation [553]. The created pencil slip band does not get thick and kept planner due to the spinodal nanostructure obstructing dislocations movement [554] while the external stress intensifies the tip-generated stress field (compared to the matrix), preparing the slip to propagate [399,555]. Thus, it is challenging to determine BCC metals' operatic dislocation slip planes. Therefore, due to the complex multiaxial stress in the current experiment, highlighted in Figure 9-21, a simplistic uniaxial external loading direction cannot be assumed for Schmid factor calculation to predict the operative slip system.

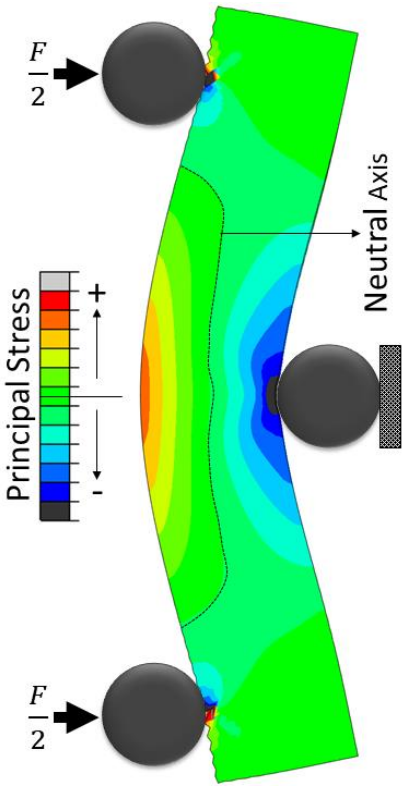


Figure 9-21: Unitless maximum principal stress distribution in the three-point bending test with the black dashed lines highlighting the neutral axis. $F$ is the applied load on the moving two pins.

Although there is an increased focus on EBSD-based trace analysis to identify slip systems [304,556–559], few researchers have envisaged an alternative criterion to the Schmid factor ($SF$). Guo [157] calculated a point-by-point local Schmid factor for (HR)-EBSD stress components mapped at the sample frame and normalised by the highest normal stress components. Hommer *et al.* [560] calculated the resolved shear stress by normalising the diagonal stress components (assumes pure shear) collected using high-energy diffraction microscopy (HEDM) by the maximum eigenvalue of the normalised stress tensor. Li *et al.* [561] optimised SF using experimental data but did not provide a consistent/phenomenological description; instead gave a probabilistic/heuristic formulation based on the available data. In this work, both methods were generalised (expanded and bridged) to describe the probability of slip variants occurring in grain using the stress components calculated by HR-EBSD.

## 5.B.2. Method, see section 5.2.3

## 5.B.3. Results and discussion

The figures below are the analyses included in the main chapter that used the local Schmid Factor method (labelled Calc. in plots below) and consider its effectiveness in determining the probable slip variant to occur compared to the conventional Schmid law that assumed uniaxial stress (labelled X in all plots below). The trace length in these figures is proportional to the SF from the conventional Schmid law calculations. The legends show the Schmid factors calculated using uniaxial stress and the EBSD-measured field.

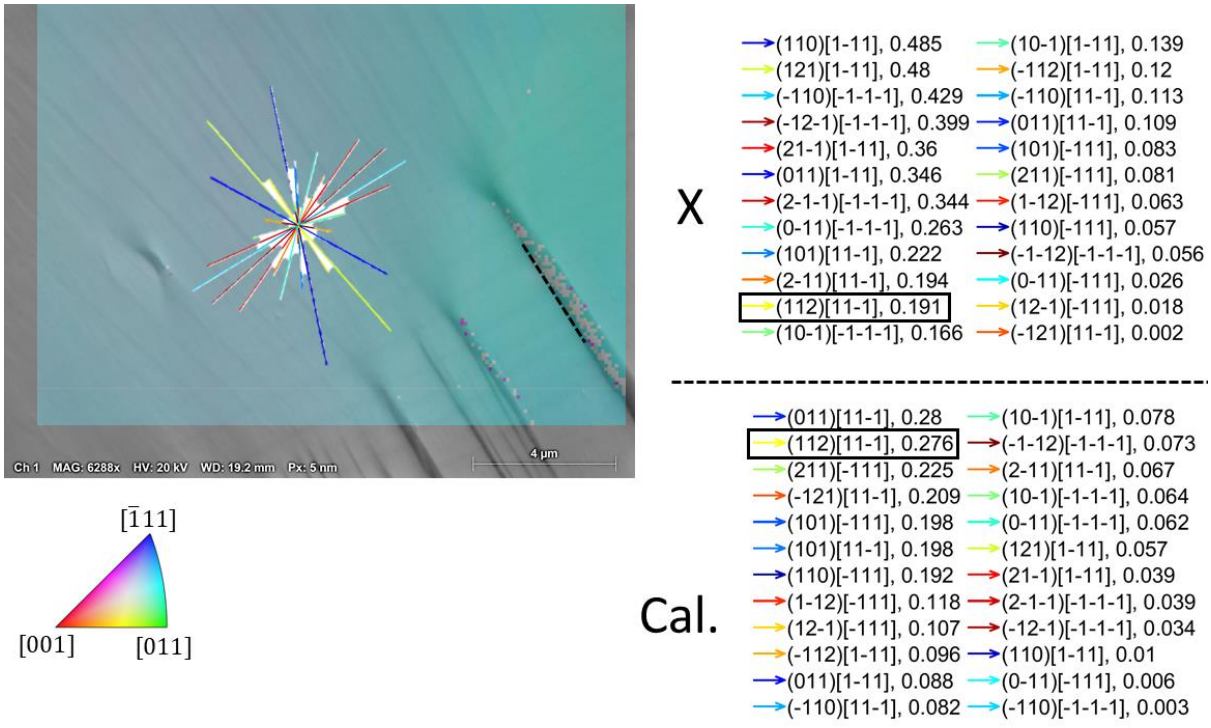


Figure 9-22: Trace and calculated Schmid factor for $[11\bar{1}](112)$ slip bands in ferrite grains separated by a low-angle GB in DSS. Trace length is proportional to Schmid factor (SF) magnitude, where the Schmid factor assumes loading in the x-direction (X). Legend follows the notation (plane)[direction). Results are also shown for a direction matrix calculated from the stress components obtained from HR-EBSD (Cal.).

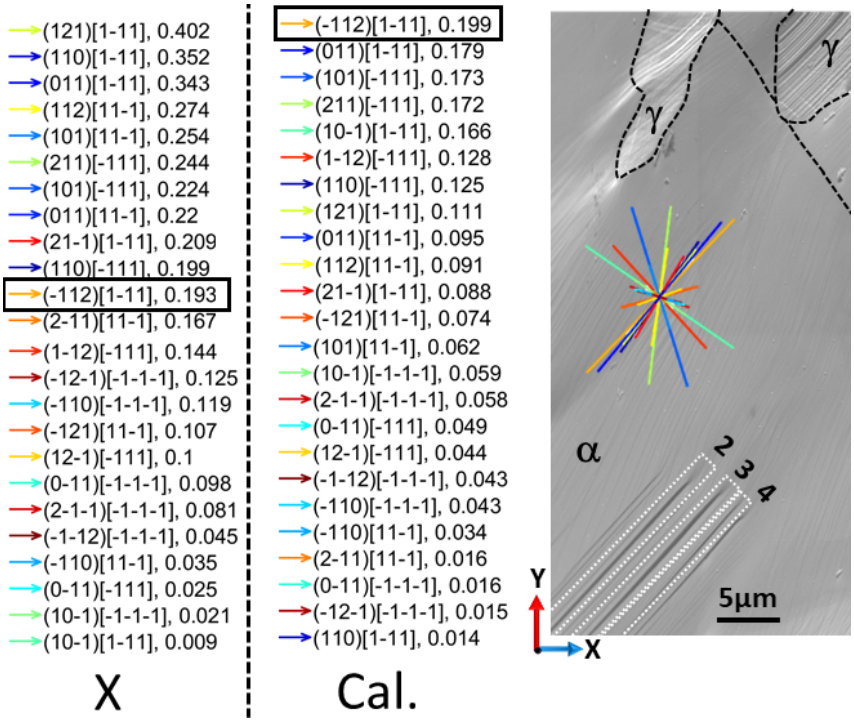


Figure 9-23: Trace and calculated Schmid factor for $[1\bar{1}1](\bar{1}12)$ slip bands in ferrite grains separated by a low-angle GB in DSS. Trace length is proportional to Schmid factor (SF) magnitude, where the SF assumes loading in the x-direction (X). Legend follows the notation (plane)[direction). Results are also shown for a direction matrix calculated from the stress components obtained from HR-EBSD (Cal.).

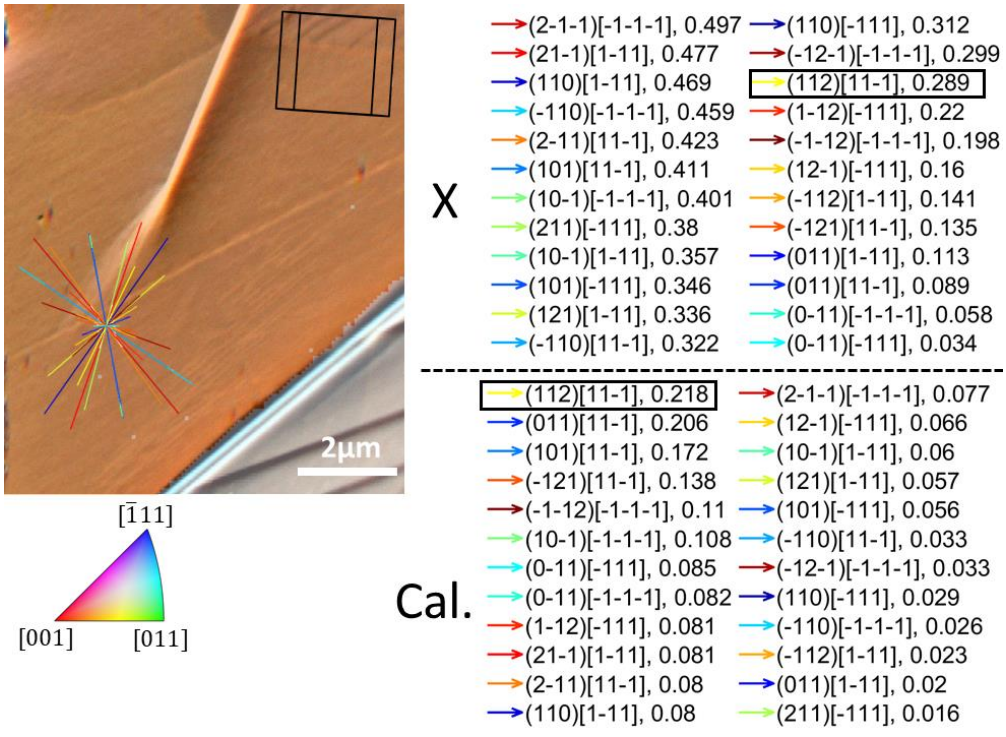


Figure 9-24: Traces of slip variants and EBSD map superimposed on an FSD image of $[11\bar{1}](112)$ slip band in a ferrite. Trace length is proportional to Schmid factor (SF) magnitude, where the SF assumes loading in the x-direction (X). Legend follows the notation (plane)[direction). Results are also shown for a direction matrix calculated from the stress components obtained from HR-EBSD (Cal.).

The same analysis was applied to 18 slip bands, 10 with a deformation field measured in situ, and the other 8 measured ex situ. The occurrence of the traced slip band is then ranked by the SFs calculated assuming i) loading in the x-direction and ii) for the local stress field ($xSF$). These values are plotted in Figure 9-25, which shows a good agreement with the observed slip system (i.e., high occurrence probability) for the relative $xSF$ where the data were obtained in-situ compared to ex-situ, especially for the {112} variants. Here, the probability is ranked from 1 to 28 (the total number of probable slip bands); 1 means the traced slip band is assumed to be the 1st to occur (the most probable).

| No. | Slip Trace |
|---|---|
| 1 | $[1\bar{1}1](\bar{1}12)$ |
| 2 | $[11\bar{1}](112)$ |
| 3 | $[\bar{1}11](110)$ |
| 4 | $[1\bar{1}1](21\bar{1})$ |
| 5 | $[\bar{1}11](12\bar{1})$ |
| 6 | $[\bar{1}11](211)$ |
| 7 | $[\bar{1}11](110)$ |
| 8 | $[1\bar{1}1](110)$ |
| 9 | $[1\bar{1}1](121)$ |
| 10 | $[11\bar{1}](112)$ |
| 11 | $[11\bar{1}](101)$ |
| 12 | $[\bar{1}11](101)$ |
| 13 | $[\bar{1}11](211)$ |
| 14 | $[11\bar{1}](101)$ |
| 15 | $[\bar{1}11](101)$ |
| 16 | $[\bar{1}\bar{1}\bar{1}](\bar{1}2\bar{1})$ |
| 17 | $[\bar{1}\bar{1}\bar{1}](\bar{1}2\bar{1})$ |
| 18 | $[1\bar{1}1](\bar{1}12)$ |

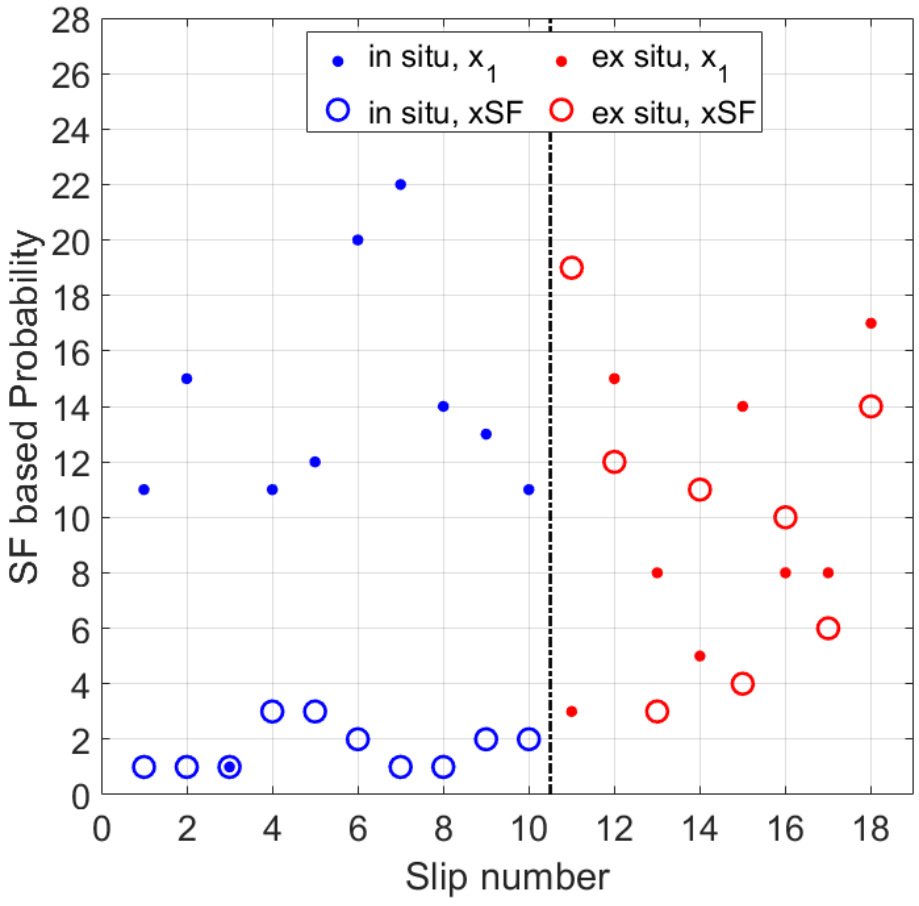


Figure 9-25: Probability of slip band occurrence based on Schmid Factor calculated using tensile x-direction loading ($x_1$) and the current method ($xSF$). The probability is from 1 to 28, with 1 means the traced slip band is assumed as the 1st to occur; thus, the most probable.

## Appendix (5.C) – Decomposed *J*-integral: Error analysis

The stress concentrations of a crack were considered to assess the errors in the J-integral analysis and decomposition of modes, which have been applied in this paper to slip bands. A synthetic displacement field for a mixed-mode crack in an infinite body was created that has a mode I stress intensity factor ($K_I$) of 3 MPa m$^{0.5}$, mode I ($K_{II}$) of 1 MPa m$^{0.5}$, and mode III ($K_{III}$) of 5 MPa m$^{0.5}$, using an analytical solution [28] and assuming plane strain conditions (eq. 9—37). The elastic modulus ($E$) and Poison's ratio ($v$) were 210 GPa and 0.3, respectively. The data are presented in the field of view of 1 x 1 m$^2$, with 0.02 x 0.02 m$^2$ square elements, and the crack tip was placed at the centre (0,0).

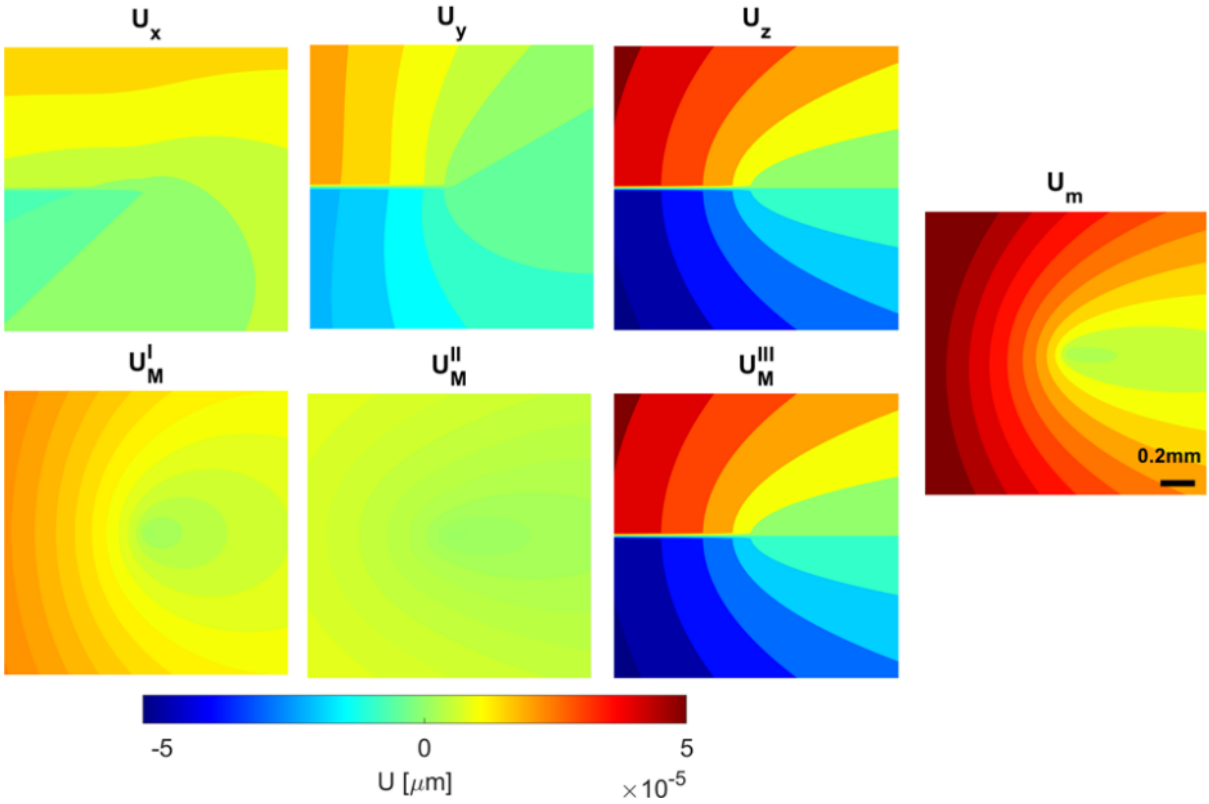


Figure 9-26: Synthetic $U_x$, $U_y$, and $U_z$ displacement field components before being decomposed, and also represented by the displacement magnitude $U_M$ for each decompsoed field.

$$\begin{Bmatrix} U_x \\ U_y \\ U_z \end{Bmatrix} = \frac{1}{\mu}\sqrt{\frac{r}{2\pi}} \begin{bmatrix} \cos\frac{\theta}{2}\left(1-2v+\sin^2\frac{\theta}{2}\right) & \sin\frac{\theta}{2}\left(2-2v+\cos^2\frac{\theta}{2}\right) & 0 \\ \sin\frac{\theta}{2}\left(2-2v-\cos^2\frac{\theta}{2}\right) & \cos\frac{\theta}{2}\left(-1+2v+\sin^2\frac{\theta}{2}\right) & 0 \\ 0 & 0 & 2\sin\frac{\theta}{2} \end{bmatrix} \begin{Bmatrix} K_I \\ K_{II} \\ K_{III} \end{Bmatrix} \quad 9—37$$

$$\text{Shear modulus } (\mu) = \frac{E'}{2(1+v)}, \qquad E' = \frac{E}{1-v^2}$$

Synthetic $U_x$, $U_y$, and $U_z$ displacement fields around the stationary mixed mode crack were decomposed to the in-plane symmetrical field ($U^I$) used to calculate mode I SIF, in-plane asymmetrical ($U^{II}$) used to calculate mode II SIF, and out-of-plane asymmetrical ($U^{III}$) used to calculate mode III SIF (Figure 9-26). The EDI method implemented in ABAQUS® was used on the decomposed fields. Stabilised convergence is achieved as the domain expands, with the calculated *J*-integral and decomposed stress intensity factors matching the values used as inputs to create the field, except for small contours were highly localised fields close to crack tip influenced initial convergence (Figure 9-27).

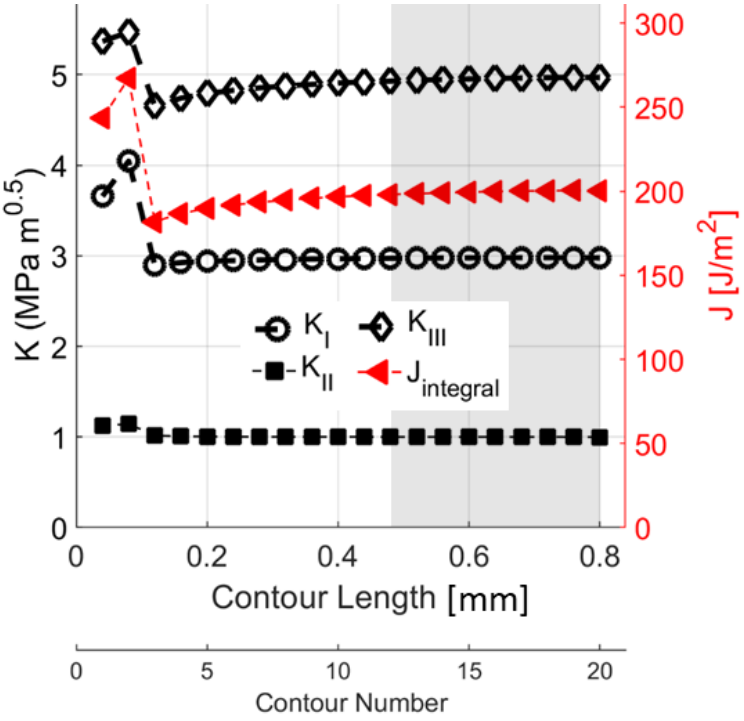


Figure 9-27: *J*-integral and decomposed loading modes as a function of contour distance from the crack tip. The represented values are calculated from the highlighted grey area.

The key sources of errors were assessed. First, a noise signal was randomly distributed to each displacement component. The magnitude of the signal increased from 0.0001% to 1% of the field mean magnitude, and the effect on the *J* and SIFs were then studied. As shown in Figure 9-28, the EDI convergence decreased with increasing noise; hence, the uncertainty error in the value increased. The mean $K_I$ and *J* values decreased, and the $K_{II}$ values increased, although $K_{III}$ was not adversely affected by the noise.

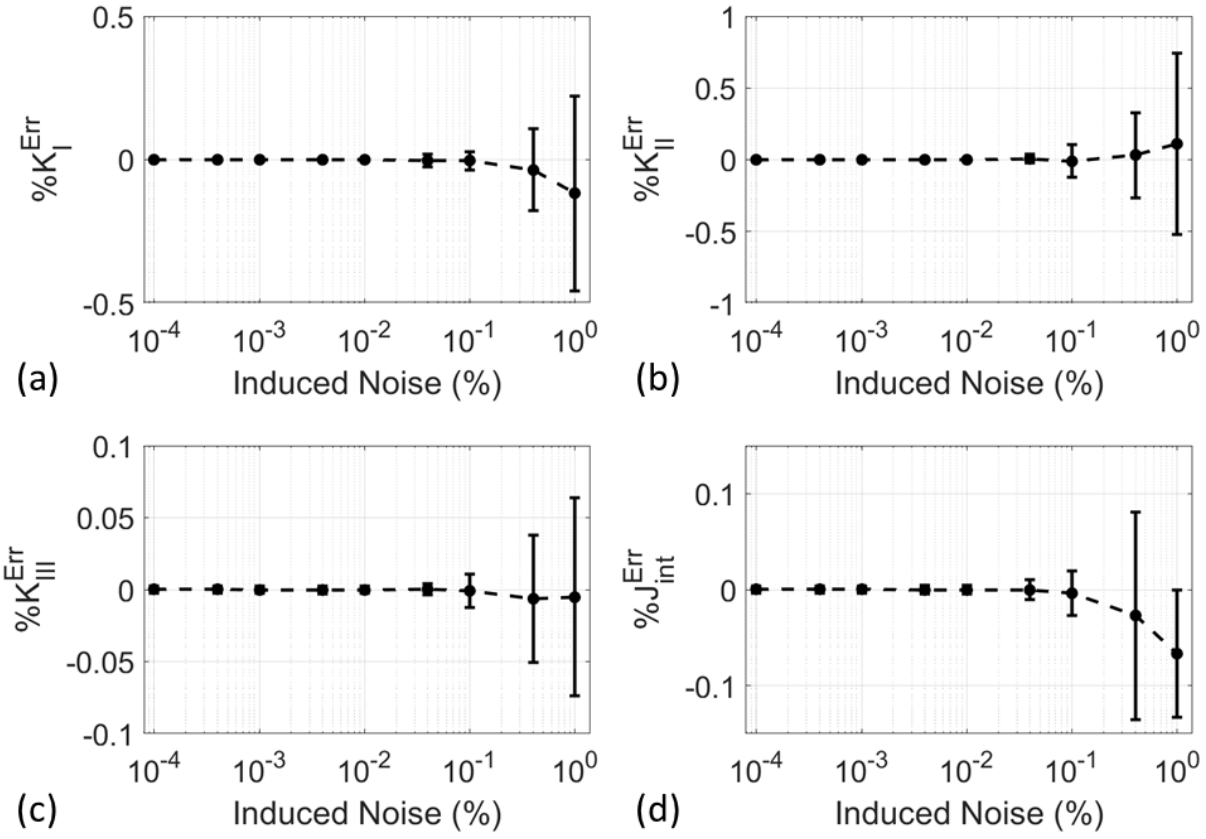


Figure 9-28: (a) $K_I$, (b) $K_{II}$, (c) $K_{III}$, and (d) *J* normalised error analysis with induced random.

Second, the sensitivity of the analysis to crack tip location was assessed relative to the accurate crack tip position, which was at the origin (0,0) coordinate. The (normalised) error in accurately locating the crack increases if the location was assumed to be ahead, relative to assuming the same distance behind the crack (Figure 9-29). In $K_I$ and $K_{II}$ analysis, the values are less affected by inaccuracy along the X-axis. However, for mode I, positional inaccuracies

in Y-axis increase the value if the crack was inaccurately located under its correct position and vice versa compared to mode II, which varies symmetrically as the tip deviates along the Y-axis. In $K_{III}$ analysis, deviation from the tip is more complex but generally increases the value of $K_{III}$. The induced errors in each decomposed field combine and form the complex error (Figure 9-29a). The overall trend of the SIFs is that uncertainties in the Y-axis position relative to the true position of the crack have more adverse effects than X-axis. The sensitivity to the crack position does not affect the EDI convergence for SIF calculation (Figure 9-29e) but mainly affects the value. However, it seems to affect both the convergence and the value for the *J*-integral.

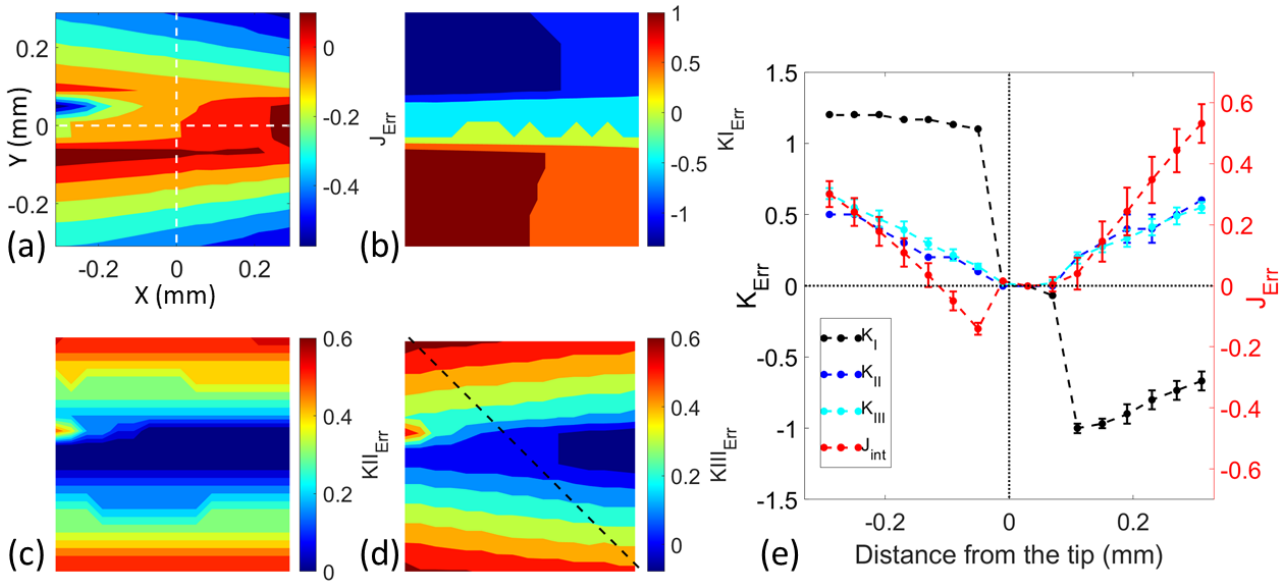


Figure 9-29: (a) J, (b) $K_I$, (c) $K_{II}$ and (d) $K_{III}$ normalised error analysis of the sensitivity to crack tip position originally at (0,0) highlighted by dashed white lines in (a). (e) The diagonal line profile (highlighted by the dashed black line in (d) of the *J*-integral and decomposed SIFs.

Linear gradients caused by pattern centre (PC) shift due to the beam movement during each EBSP acquisition were not assessed, as the magnitude and distribution of this spurious gradient highly depend on the $EBSP_0$ deformation status and position with respect to the beam. In practice, the PC shift can be corrected using AstroEBSD [171], and the remaining rigid

body motions will then be removed from the integrated displacement field by selecting the point with absolute minimum displacement as the origin [112].

To summarise, the proposed method was validated using the synthetic displacement field of a crack under mixed-mode loading. The effect of noise and uncertainty of crack tip on the *J*-integral and SIFs values were also investigated. Noise affects the EDI convergence, and uncertainty in the crack tip position directly affects the value, especially on Y-axis (i.e., perpendicular to the crack direction). Concerning the slip band studies in this work, the effect of the positional error is minimal as the slip band position is defined by the region of high GND density, with the most significant positional uncertainty being along the X-axis, which causes a significant error.

## Appendix (5.D) – 3D integration and EBSP depth resolution

The effect of EBSP depth resolution ($Z$) estimation on the integrated field, which was resolved on the slip geometry, was examined using the experimental data for the $[\bar{1}11](211)$ field (section 5.3.3 at 1 mm extension). The analysis used the full range of the probable depth of information. As shown in Figure 9-30b, the in-plane displacement fields were not affected by the assumption of the effective depth of the interaction volume, but the mean magnitude (and distribution Figure 9-30a) of the out-of-plane displacement ($\langle \|U_z\| \rangle$) is inversely dependent on the magnitude of the assumed depth of information, except for depths smaller than 8 nm. This inverse-power relationship takes the form of $\langle \|\mathrm{U_z}\| \rangle = {}^{a}/_{\mathrm{Z}}$, with *a* being a fitting coefficient.

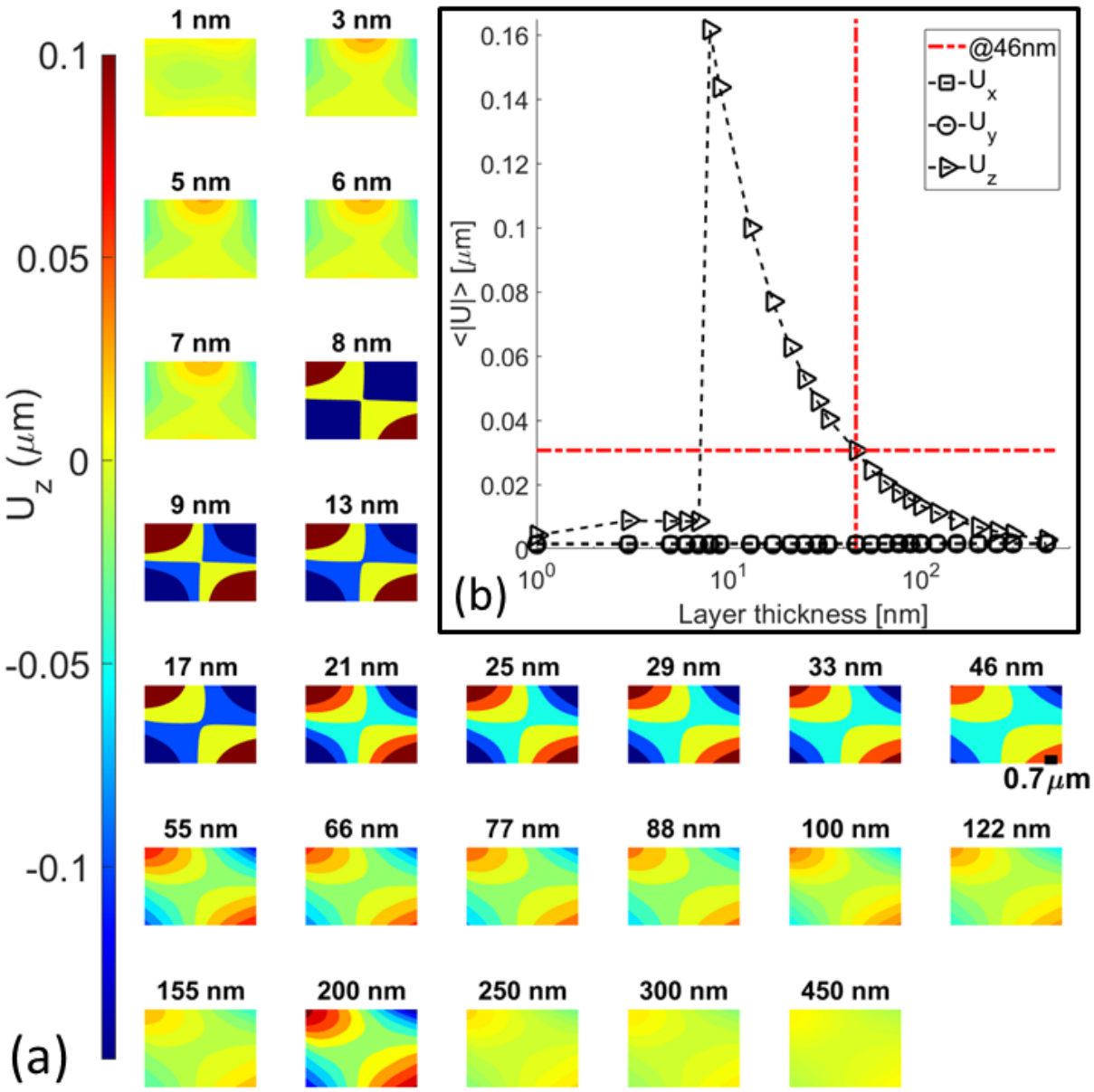


Figure 9-30: (a) Integrated elastic displacement field using different depths of information. (b) The magnitude of the displacement components.

To assess the effect of the (HR)-EBSD map area on the analysis of the stress concentration, the size of the integrated map was reduced progressively by removing the outer 3 pixels in each direction before integrating for the full range of the probable depth of information. In total, 11 sizes across 26 assumed depths were analysed (i.e., a total of 286 maps). The value of $U_z$ was then taken from the same centric point in each map, and its dependence on depth was fitted by the inverse-power relationship to determine the fitting coefficient $a$. Examining

the relation between the fitting coefficient ($a$) and integrated window size revealed a dependence of the out-of-plane displacement on the integrated window size. Note that in inverse-power fitting, $a$ describes the steepness of the relationship, which means that as the integrated window becomes smaller, the change between consecutive $\langle \|U_z\| \rangle$ also becomes smaller.

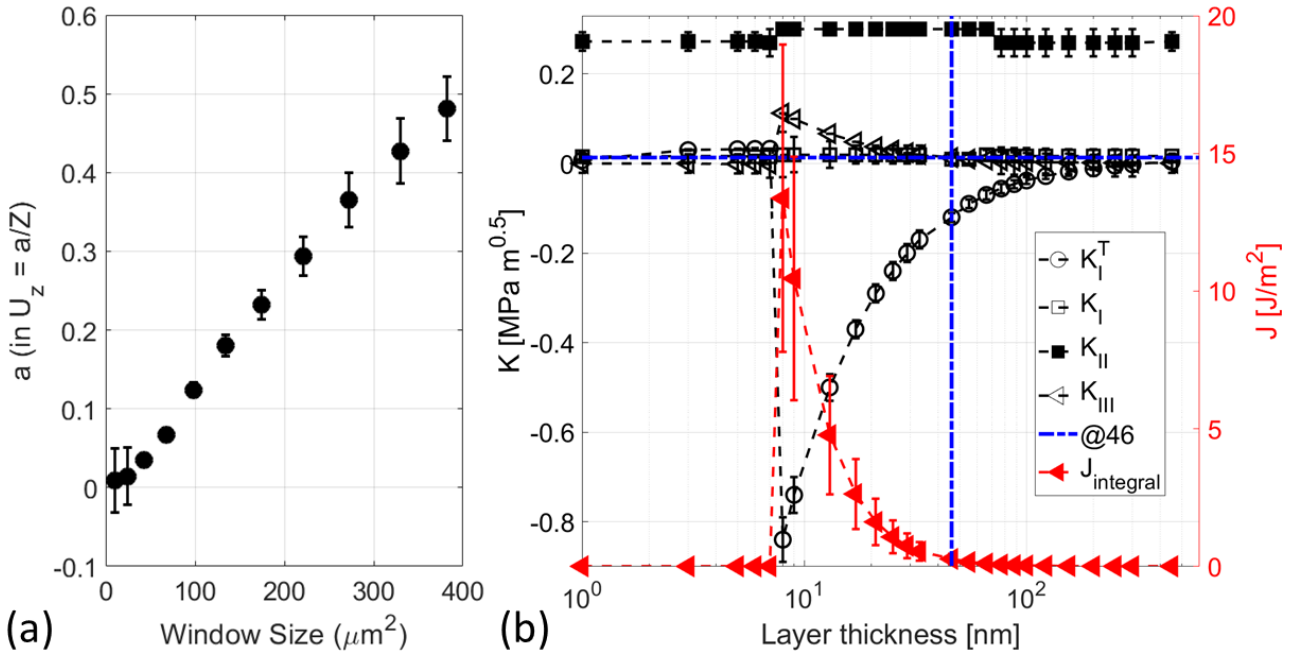


Figure 9-31: (a) Integrated window size and the variable (a) in the inverse-power relationship between the magnitude of out-of-plane displacement ($U_z$) and assumed depth of information ($Z$). The variance is calculated using the goodness of fit ($R^2$). (b) *J*-integral and decomposed stress intensity factors as a function of depth of information for $[\bar{1}11](211)$ Slip bands at 1mm.

This out-of-plane displacement ($U_z$) will not only affect the value of $K_{III}$ that is calculated from the (HR)-EBSD data, but also the symmetrical component of the $K_{III}$ field will affect $K_I^r$, by inducing a compressive mode I field. Thus, in Figure 9-31b, this effect on mode I gradually dissipates as the assumed depth increases and – consequently – the predicted out-of-plane deformation decreases. The in-plane $K_I$ and $K_{II}$ are unaffected by the assumed depth of the information.

The depth resolution of EBSD is widely accepted to vary between 10 to 40 nm, decreasing with the material atomic number [562]. Nevertheless, using a differently thick transparent amorphous layer of Cr coating a mono-Si crystal, experimental measurements indicated that the depth resolution could be as shallow as 2 nm. This was determined by Si pattern quality deteriorating by ~50% when using a FEG-SEM with 15 kV beam conditions and 15 mm working distance between the beam and sample and 65 mm between the sample and the detector and without considering the channelling effect [373]. However, using a similar experimental approach, different results were reported (Table 9-5), e.g., Isabell and David [563] concluded that depth resolution could extend to 1 μm due to inelastic scattering (including tangential smearing and channelling effect).

In Monte Carlo (MC) simulations, the depth resolution for EBSPs formation is estimated using Block wave theory, where backscattered primary electrons, after interacting with the crystal lattice, exit the surface carrying information about the crystallinity of volume interacting with the electrons. The backscattered electrons (BSE) energy distribution depends on the material's characteristics and the beam conditions [564]. This BSE wave field is also affected by the thermal diffuse scattering process that causes incoherent and inelastic (energy loss) scattering – after the Bragg diffraction events – which does not, yet, have a complete physical description that can be related to mechanisms that constitute EBSP depth resolution [565,566].

Table 9-5: EBSP's depth resolution experimentally measured or estimated based on Monte Carlo (MC) simulation.

| Author | Material | Density ($kg/m^3$)[17] | Voltage (kV) | Depth Resolution (nm) |
|---|---|---|---|---|
| Dingley [562] | – | – | – | 10-40 |
| Dingley and Randle [567] | – | – | – | 10 |
| El-Dasher *et al.* [568] | – | – | – | ~20 |
| Bhattacharyya and Eades [569] | – | – | – | < 1000 (MC) |
| Zaefferer [373] | Si | 2.33 | 15 | 3.5 ± 1.5 |
| Yamamoto [570] | Al | 2.70 | 20 | 50 |
| Bhattacharyya and Eades [569] | Al | 2.70 | 20 | 15-40 |
| Baba-Kishi [571] | Al | 2.70 | 20 | > 50 |
| Ren *et al.* [572] | Al | 2.70 | 20 | 115 (MC) |
| Isabell and Dravid [563] | Al | 2.70 | 30 | ~400 |
| Michael and Goehner [121,573] | Al | 2.70 | 40 | 100 |
| Yamamoto [570] | Al | 2.70 | 50 | 120 |
| Isabell and Dravid [563] | Nb | 3.58 | 30 | < 1000 |
| Isabell and Dravid [563] | $SrTiO_3$ | 5.11 | 30 | ~300 |
| Keller *et al.* [574] | GaAs | 5.32 | 15 | 30 |
| Steinmetz and Zaefferer [575] | Fe | 7.87 | 7.5 | 10 |
| Bordín *et al.* [576] | $\sigma$-Fe | 7.87 | 20 | 16 (MC) |
| C. Zhu *et al.* [151] | Ni | 8.91 | 10 | 10 (MC) |

[17] At room temperature.

| Author | Material | Density ($kg/m^3$) | Voltage (kV) | Depth Resolution (nm) |
|---|---|---|---|---|
| Harland *et al.* [577][18] | Ni | 8.91 | 30 | $\lesssim 10$ |
| Kohl [563,578] | Ni | 8.91 | 30 | 5-6 (MC) |
| Michael and Goehner [121,573] | Ni | 8.91 | 40 | 20 |
| Chen *et al.* [123] | Cu | 8.96 | 5 | 38 |
| Chen *et al.* [123] | Cu | 8.96 | 10 | 46 |
| Yamamoto [570] | Cu | 8.96 | 20 | 20 |
| Ren *et al.* [572] | Cu | 8.96 | 20 | 35 (MC) |
| Chen *et al.* [123] | Cu | 8.96 | 30 | 72 |
| Yamamoto [570] | Cu | 8.96 | 50 | 50 |
| Ren *et al.* [572] | Ag | 10.49 | 20 | 30 (MC) |
| Isabell and Dravid [563] | W | 19.30 | 30 | ~50 |
| Ren *et al.* [572] | Au | 19.30 | 20 | 22 (MC) |
| Harland *et al.* [579] | Au | 19.30 | 30 | 80 |
| Michael and Goehner [121,573] | Au | 19.30 | 40 | 10 |

The experimental results summarised in Table 9-5 are not consistent. These experiments are highly cumbersome due to the need for precise and well-calibrated equipment, with the results open to interpretation [580]. This is partially because there is no agreement about the definition of depth resolution. For example, definitions in the literature include those where the depth is where ~92% of the signal is generated [581,582], or defined by pattern quality

[18] Using small angle detector (SAD).

[373], or are as ambiguous as "*where useful information is obtained*" [583]. The reported values in Table 9-5 either do not mention a definition or do not have a rationale for the definition of depth resolution. In addition, most of these experiments do not provide information on the beam size, tilt angle, beam-to-sample and sample-to-detector working distance, and – sometimes – even the beam energy. These are critical parameters for determining (or simulating) the depth resolution of the patterns as the interaction volume, which decreases with the sample atomic number or density, increases with beam energy and size [563]. The beam current is generally not considered to affect the depth resolution in experiments or simulations. However, it affects the beam spot size and pattern signal-to-noise (S/N) ratio [151,584,585], affecting the depth resolution and the details in the pattern. Most importantly, conclusions drawn from both experiments and simulations assume the surface is pristine with homogeneity of the depth resolution, neither of which is valid for a deformed sample [373].

Therefore, determining the depth resolution is challenging, which is clear from the contradicting depth resolutions reported in the literature. The current MC simulation [578,586] gives an approximation based on incorrect assumptions [373]. The depth resolution assumed in this thesis, which is the depth to which 50% of the information is obtained, is consistent with Zaefferer [373].

# Appendix (6.A) – Additional figures

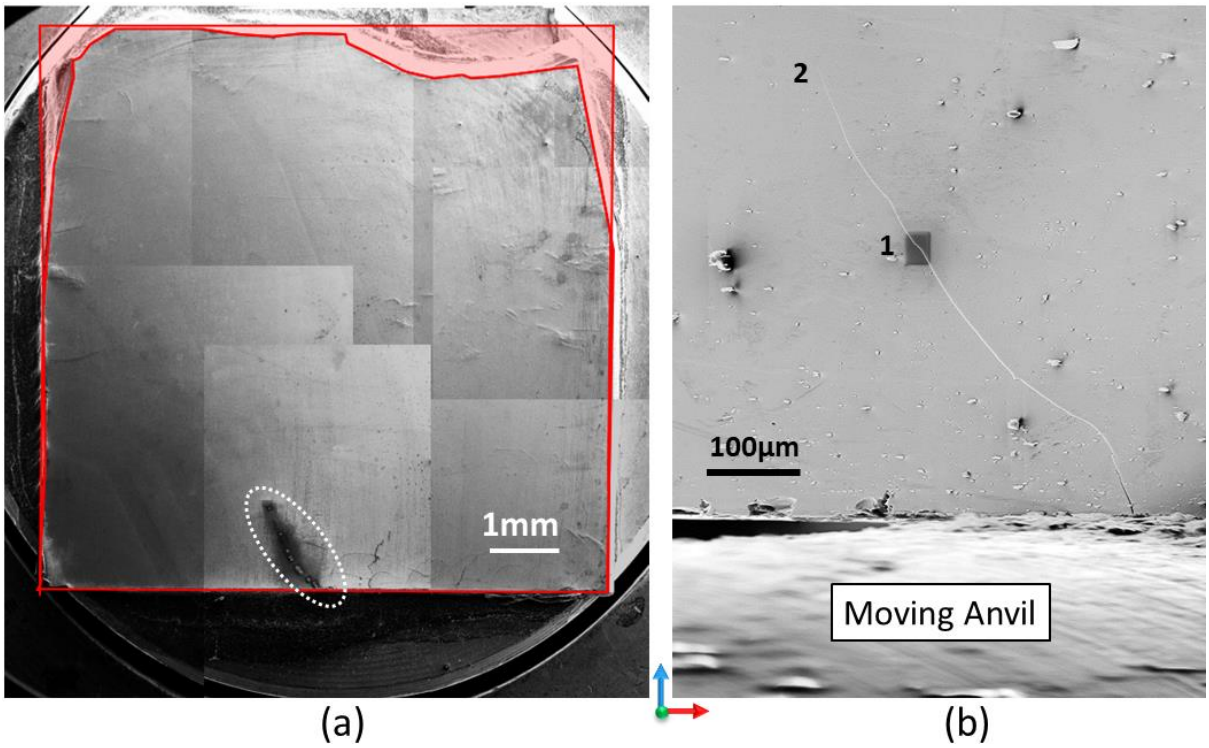


Figure 9-32: (a) The compressed sample (I) after the test with the initial damage that occurred at the beginning of the test, highlighted by the red-shaded area. The area where the crack propagation is highlighted with a dashed white oval. (b) Initial crack propagation. The black rectangle at the point labelled 1 is due to carbon deposition during the (slow) EBSD scan.

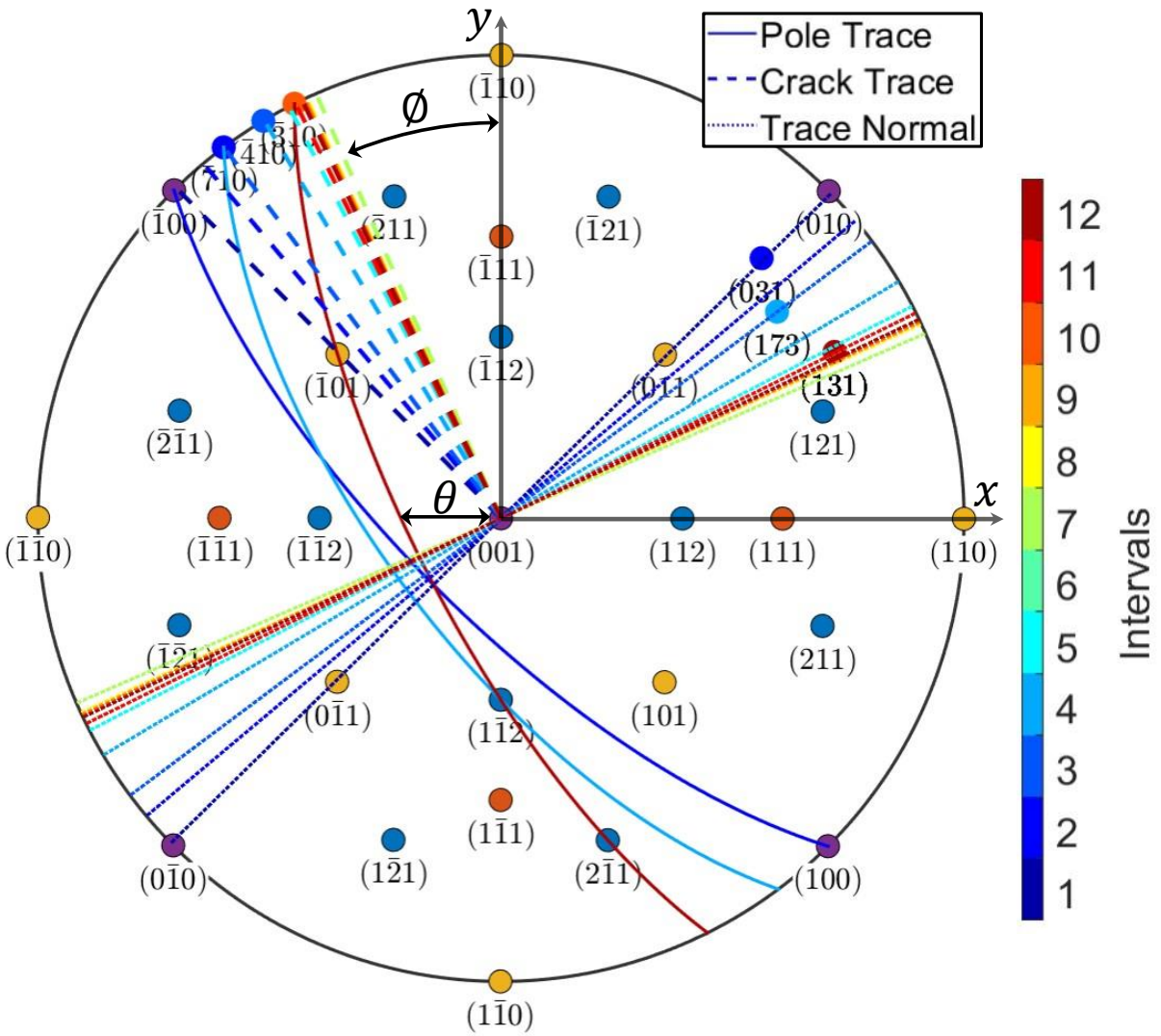


Figure 9-33: (001) stereograph rotated as to the EBSD data for (001) mono-Si crystal wafer (Data I) with the crack trace and trace normal superimposed using dashed and dotted lines, respectively. The crack pole trace was then used to find the crack plane as it moved from (031) to (131) during the experiment. {001}, {110}, {111}, and {112} family of planes are colour coded differently to ease distinctions. Other planes and lines are colour coded to reflect the corresponding interval labelled in Figure 6-4.

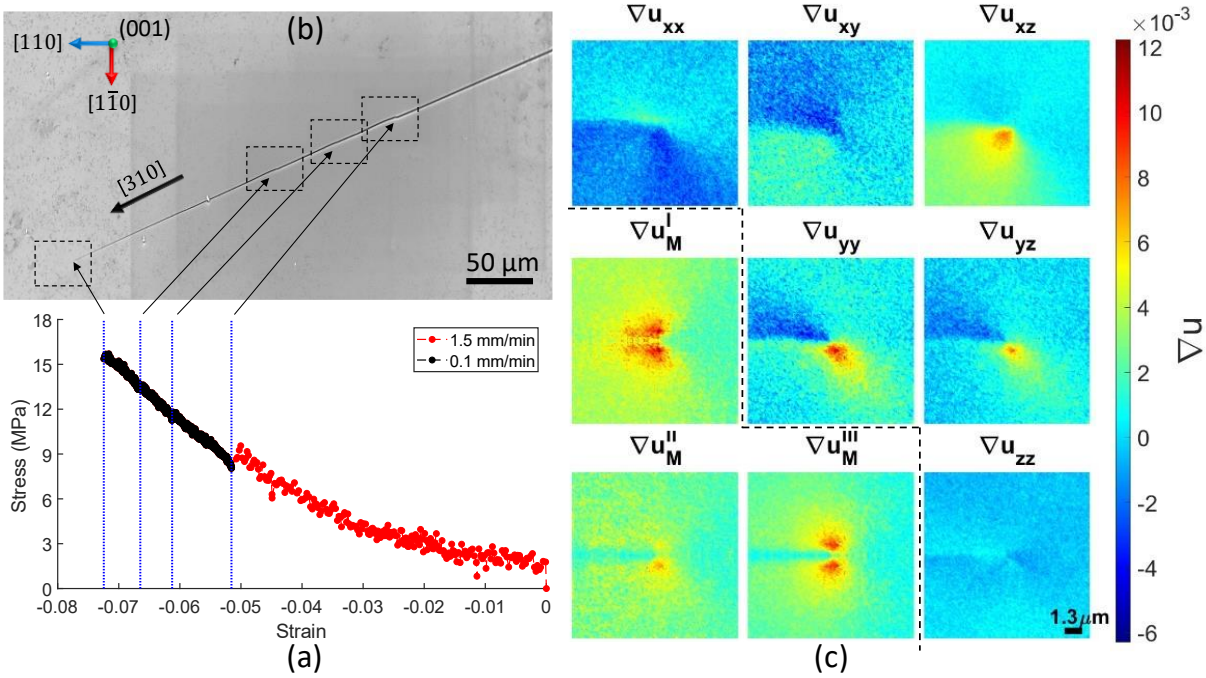


Figure 9-34: (a) Experiment – compressive – nominal strain and stress for Data II in Table 6-2 highlighted with the blue lines. The red points highlight the first rapid loading of the sample to create the initial crack before reducing the compression speed to 0.1 mm min$^{-1}$. (b) SEM image for the $[310](1\bar{3}1)$ crack at its 4$^{th}$ observation propagating in (001) Si wafer. Black dashed boxes highlight where EBSD maps were acquired. (c) The (HR-EBSD) measured and (loading mode) decomposed displacement gradient fields after rotation to the $[310]$ direction for the 1$^{st}$ observation.

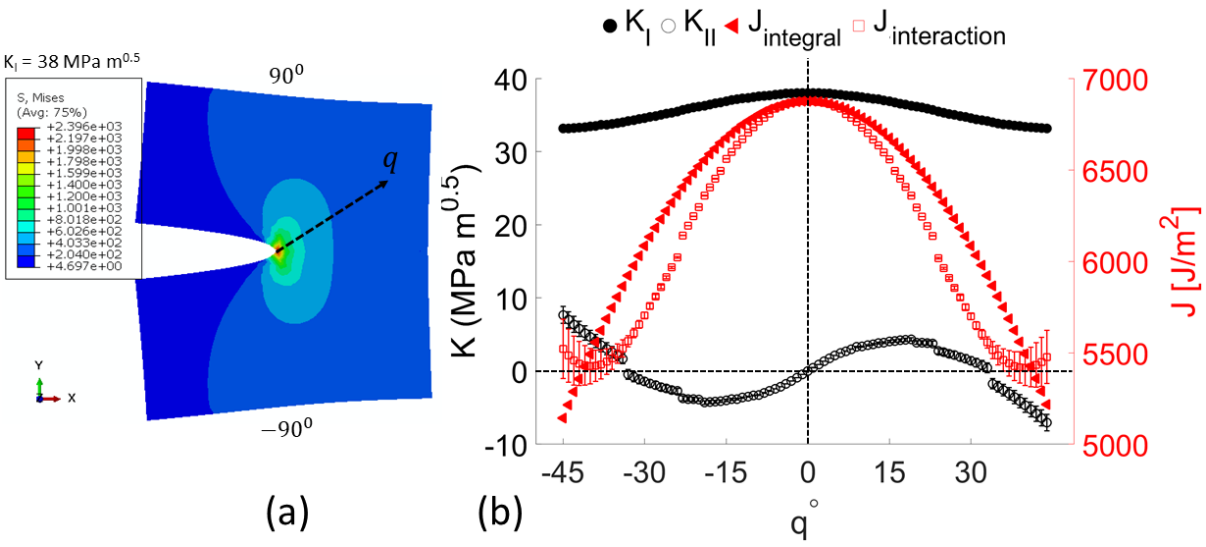


Figure 9-35: (a) ABAQUS® simulation of a two-dimensional crack on an isotropic material (E = 210 GPa), loaded to 38 MPa m$^{0.5}$ in mode I. (b) Calculated mode I and II stress intensity factors have been calculated with the assumption of $q$-vectors that deviate from the actual direction using the interaction integral method [114] natively implemented in ABAQUS®. As the assumed direction deviates from the actual direction with maximum potential strain energy release rate ($J$-integral), the mode II stress intensity factor increases and the mode I stress intensity factor decreases.

## Appendix (6.B) – In situ $EBSP_0$ selection

The effect of using a '*Native*' compared to '*Chosen*' (see Chapter 3) on the correlation parameters was quantified and tabulated in Table 9-6. PH and MAE values are more consistent between maps that used the 'Chosen' approach than those using the '*Native*' approach. The accuracy of the maps was slightly improved using the 'Chosen' $EBSP_0$, which was then used for further *J*-integral analysis.

Table 9-6: Effect of using '*Native*', '*Chosen*', and 8th interval $EBSP_0$ as a reference pattern.

| Interval | *Native* | | *Chosen* | | 8th *Chosen*-$EBSP_0$ | |
|---|---|---|---|---|---|---|
| | PH | MAE ($10^{-4}$) | PH | MAE ($10^{-4}$) | PH | MAE ($10^{-4}$) |
| 1 | 0.75 | 1.8 | 0.74 | 1.6 | 0.75 | 17.9 |
| 2 | 0.75 | 1.8 | 0.74 | 1.6 | 0.73 | 7.9 |
| 3 | 0.69 | 1.9 | 0.71 | 1.7 | 0.74 | 5.1 |
| 4 | 0.74 | 1.9 | 0.74 | 1.6 | 0.74 | 14.8 |
| 5 | 0.74 | 1.8 | 0.74 | 1.6 | 0.74 | 5.3 |
| 6 | 0.74 | 1.8 | 0.73 | 1.6 | 0.74 | 5.0 |
| 7 | 0.74 | 2.1 | 0.73 | 1.7 | 0.78 | 2.3 |
| 8 | 0.73 | 1.8 | 0.73 | 1.6 | 0.73 | 1.6 |
| 9 | 0.74 | 1.9 | 0.74 | 1.7 | 0.74 | 10.8 |
| 10 | 0.74 | 1.8 | 0.73 | 1.6 | 0.76 | 18.7 |
| 11 | 0.75 | 1.9 | 0.75 | 1.6 | 0.76 | 21.1 |
| 12 | 0.74 | 1.7 | 0.74 | 1.6 | 0.74 | 19.6 |
| Average | 0.74 | 1.9 | 0.74 | 1.6 | 0.75 | 10.8 |

Since the beam conditions and experiment geometry were kept the same during the experiment intervals, all maps can be calculated relative to one $EBSP_0$ instead of 12. A synthetic 12 x 12 EBSD map was created using the $EBSP_0$ from each interval, as shown in the

schematic in Figure 9-36, where numbers donate the $EBSP_0$ interval. HR-EBSD analysis was conducted on the data. In the synthetic data, the 8th interval $EBSP_0$ was chosen as the least deformed from the available $EBSP_0$ using conventional selection criteria, i.e., based on pattern quality (IQ) and low kernel average misorientation (KAM).

| | | | | | | | | | | | |
|---|---|---|---|---|---|---|---|---|---|---|---|
| 1 | 2 | 3 | 4 | 5 | 6 | 7 | 8 | 9 | 10 | 11 | 12 |
| 1 | 2 | 3 | 4 | 5 | 6 | 7 | 8 | 9 | 10 | 11 | 12 |
| 1 | 2 | 3 | 4 | 5 | 6 | 7 | 8 | 9 | 10 | 11 | 12 |
| 1 | 2 | 3 | 4 | 5 | 6 | 7 | 8 | 9 | 10 | 11 | 12 |
| 1 | 2 | 3 | 4 | 5 | 6 | 7 | 8 | 9 | 10 | 11 | 12 |
| 1 | 2 | 3 | 4 | 5 | 6 | 7 | 8 | 9 | 10 | 11 | 12 |
| 1 | 2 | 3 | 4 | 5 | 6 | 7 | 8 | 9 | 10 | 11 | 12 |
| 1 | 2 | 3 | 4 | 5 | 6 | 7 | 8 | 9 | 10 | 11 | 12 |
| 1 | 2 | 3 | 4 | 5 | 6 | 7 | 8 | 9 | 10 | 11 | 12 |
| 1 | 2 | 3 | 4 | 5 | 6 | 7 | 8 | 9 | 10 | 11 | 12 |
| 1 | 2 | 3 | 4 | 5 | 6 | 7 | 8 | 9 | 10 | 11 | 12 |
| 1 | 2 | 3 | 4 | 5 | 6 | 7 | 8 | 9 | 10 | 11 | 12 |

Figure 9-36: Schematic of patterns arrangement in the synthetic EBSD map.

Note that a shadow from the stage anvil was cast on the patterns on the first interval (Figure 9-37a) due to the proximity of the crack to the anvil; however, once excluded, it did not affect HR-EBSD cross-correlation (see Table 9-6). From HR-EBSD analysis (Figure 9-37b), the 8th and 7th intervals show a relatively low deformation, but deformation conditions exacerbate with intervals which can be illustrated clearly from the gradient seen in the in-plane components of the normal strain and $\omega_{13}$. The phantom (or artificial) stresses were introduced at each interval can be as high as 2.5 GPa and highly affect the in-plane stress (Figure 9-37c).

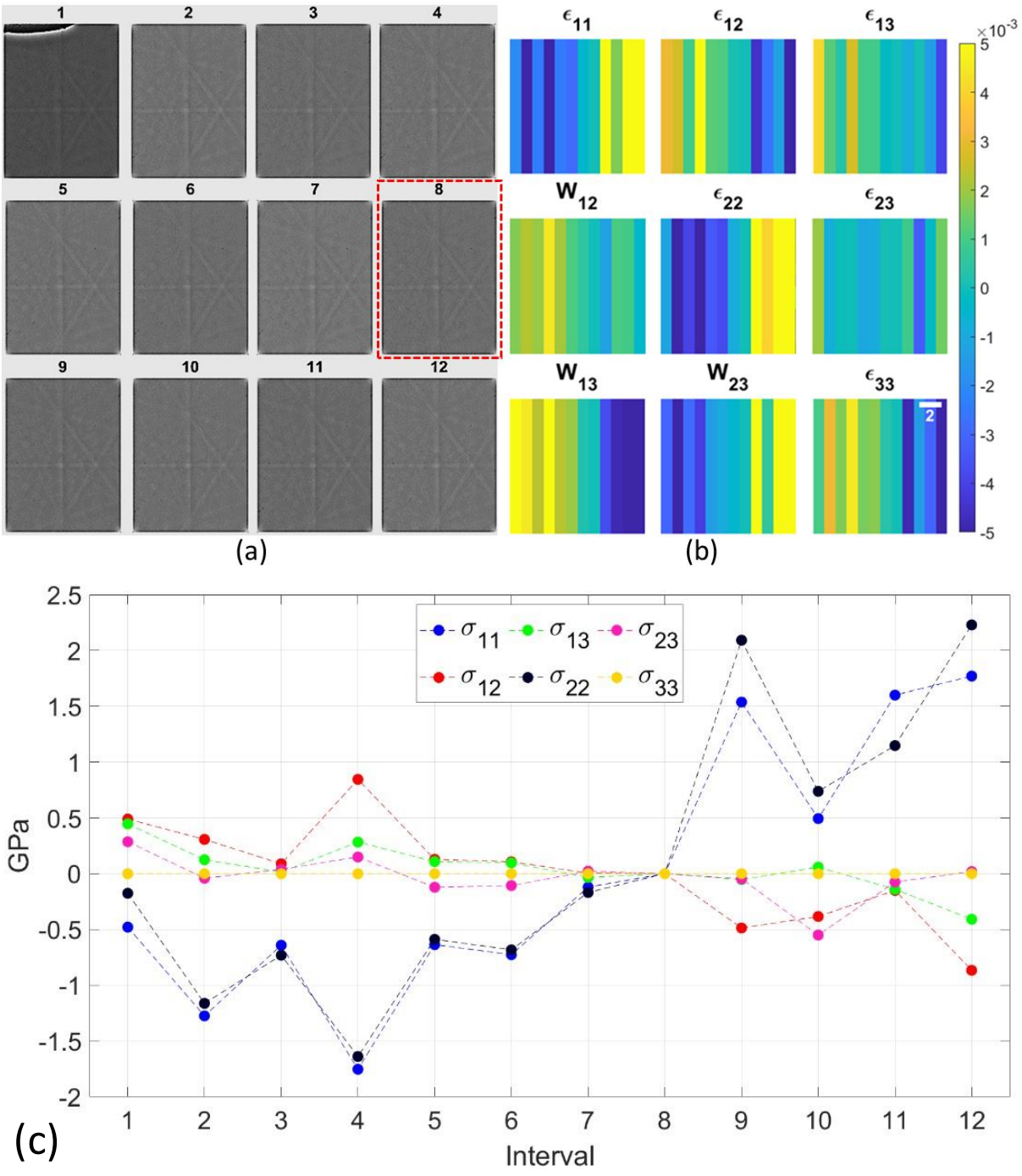


Figure 9-37: (a) In situ crack *Chosen* $EBSP_0$ at different experimental intervals. (b) Elastic deformation component from the *Chosen* $EBSP_0$ from each interval compared to $EBSP_0$ from the 8th interval (red squared in a). (c) Stress tensors relative to the 8th interval were calculated using (001) Silicon anisotropic elastic properties [213]. $\sigma_{33}$ is zero due to the assumed traction-free surface [161].

A closer look can be taken at the effect of swapping EBSPs across scans using the 8th $EBSP_0$ for the 7th and 9th intervals. As indicated by the synthetic EBSD data in Figure 9-37, the 7th interval deformation field slightly changes when using the 8th $EBSP_0$ as a reference pattern, indicated

in Figure 9-37c. As indicated in Figure 9-37c, for the 9th scan, the deformation magnitude (in each tensor) was directly increased, especially in the in-plane components. This clearly shows, and contrary to our expectation, that each EBSD map has a different imaging condition; even when the current, voltage and working distance were kept constant, pattern centre (PC) shift due to beam movement during acquisition was minimised [171], pattern remapping [166], and no further angular effect from drift was expected as the ROI was small (~20 x 15 $\mu m^2$) and the sample was conductive [215].

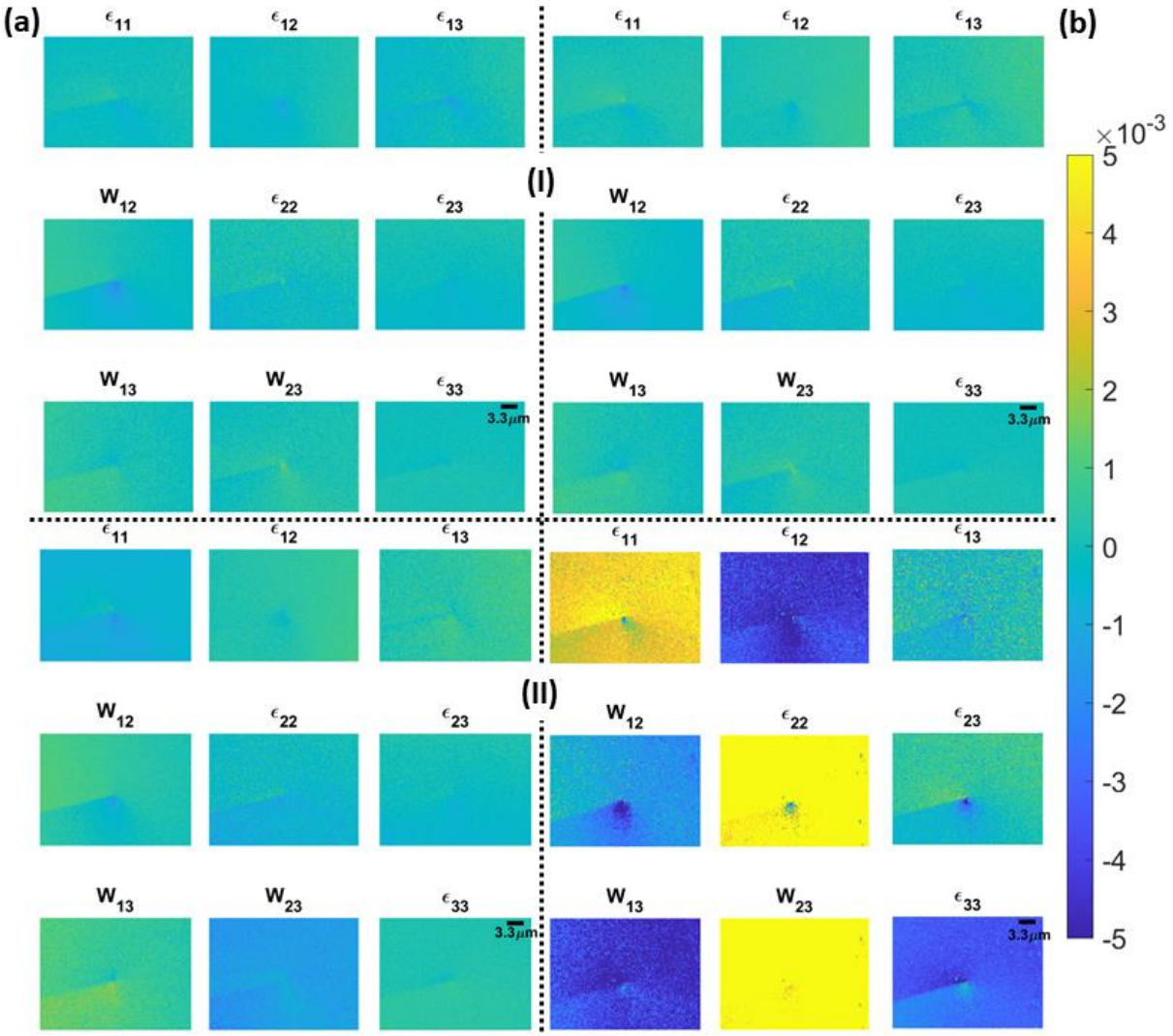


Figure 9-38: Deformation field components for steps (a) 7 and (b) 9 of in situ test using (I) *Chosen* and (II) Swapped (from step 8) $EBSP_0$.

It appears that slight stage movement coupled with minor re-focusing of the field of view (although there is no necking or change of thickness effect here) changed the experiment geometry; thus, impacting the probed EBSPs. This shows that swapping $EBSP_0$ across intervals or finding an $EBSP_0$ for all intervals and relating all 'relative' (or absolute) information to one $EBSP_0$ will yield erroneous results, although it slightly improves the correlation (see Table 9-6).

The results are similar to results using pristine single crystal mounted within the sample for calibration [163] due to the change in projection parameters. When the 1$^{st}$ iteration of HR-EBSD calculates both real and artificial strain, the 2$^{nd}$ iteration will not separate the real strain (Figure 9-38) due to pattern centre variation inducing phantom stress [151]. This directly contradicts Deal *et al*.'s [587] evidence of the feasibility of using a physical reference pattern ($EBSP_0$) library to calculate absolute strains using high (angular) resolution electron backscatter diffraction (HR-EBSD) with 11% repeatability. While the physical reference pattern ($EBSP_0$) library method might work for very limited cases (see Chapter 4), it seriously underestimates the error (or phantom stress) and yet faces the same limitations daunting simulated reference patterns for absolute strain measurement but without providing an understanding of the (physical) building blocks.

## Appendix (6.C) – Analytical field benchmarking

A mixed-mode crack's displacement field that has a mode I stress intensity factor ($K_I$) of 3 MPa $m^{0.5}$, mode II ($K_{II}$) of 1 MPa $m^{0.5}$, and mode III ($K_{III}$) of 2 MPa $m^{0.5}$ were created using an analytical solution [28] and assuming plane stress conditions (eq. 9—38 to 9—42). The elastic modulus ($E$) and Poison's ratio ($v$) were 210 GPa and 0.3, respectively. The field of view was 1*1m, having 0.02*0.02 square elements and a crack tip at the centre (0,0). Then, the (numerical) displacement gradient ($u_{i,j}$) calculated from the displacement (equation 2—16).

$$\mathrm{u}_1 = \frac{K_I}{2\mu}\sqrt{\frac{r}{2\pi}}\cos\left(\frac{\theta}{2}\right)\left[k-1+2\sin^2\left(\frac{\theta}{2}\right)\right] + \frac{K_{II}}{2\mu}\sqrt{\frac{r}{2\pi}}\sin\left(\frac{\theta}{2}\right)\left[k+1+2\cos^2\left(\frac{\theta}{2}\right)\right] \quad 9—38$$

$$\mathrm{u}_2 = \frac{K_I}{2\mu}\sqrt{\frac{r}{2\pi}}\cos\left(\frac{\theta}{2}\right)\left[k+1-2\cos^2\left(\frac{\theta}{2}\right)\right] - \frac{K_{II}}{2\mu}\sqrt{\frac{r}{2\pi}}\cos\left(\frac{\theta}{2}\right)\left[k-1-2\sin^2\left(\frac{\theta}{2}\right)\right] \quad 9—39$$

$$\mathrm{u}_3 = \frac{2K_{III}}{\mu}\sqrt{\frac{r}{2\pi}}\sin\left(\frac{\theta}{2}\right) \quad 9—40$$

$$\text{shear modulus } (\mu) = \frac{E}{2(1+v)} \quad 9—41$$

$$k = \frac{3-v}{1+v} \quad 9—42$$

$$u_{i,j} = \frac{\partial \mathrm{u}_i}{\partial x_j} \quad 9—43$$

Equation (6—9) was then used to decompose the displacement gradient to different modes, and the (infinitesimal) strain was then calculated from each mode with their relationship as expressed below and shown in Figure 9-39a.

$$\varepsilon_{ij} = \frac{1}{2}\left(u_{i,j} + u_{j,i}\right) \quad 9—44$$

Using the displacement derivatives with the method outlined in section 6.2.2, the calculated *J*-integral and decomposed stress intensity factors matched inputted values (Figure 9-39b). Highly localised fields close to crack edges can also influence initial convergence, but convergence stabilises as the domain expands.

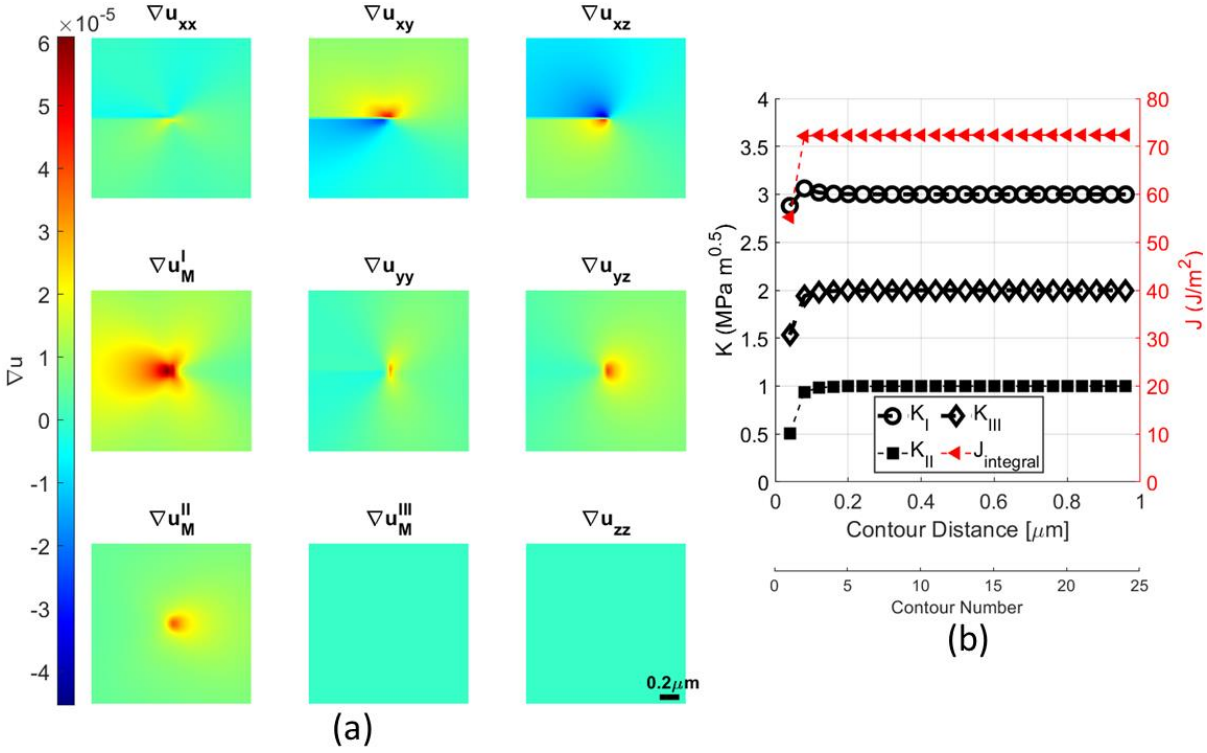


Figure 9-39: (a) The analytical displacement gradient for a stationary mixed loaded crack. (b) *J*-integral and decomposed loading modes as a function of contour distance from the crack tip.

The key sources of errors in this analysis were assessed. First, a normally distributed random noise was incrementally induced from zero to 10% on all the strain components. Figure 9-40a shows the amount of induced error in each component, with $K_{II}$ being highly influenced by noise. The dashed upper pound line indicates that this method is highly vulnerable to noise compared to a method that uses total elastic displacement, e.g., a 6% noise induces a convergence error of 7.6 ± 18.8 %, 16.8 ± 35.5% and 4.2 ± 11.2 % in $K_I$, $K_{II}$ and $K_{III}$, respectively, compared to 3.8%, 3% and 0.8% when using displacement field subjected to same noise [63,588]. This is because the induced noise on three displacement components will be diluted

when the derivatives are calculated, whereas the induced noise on the nine strain components will directly affect the analysis. Calculating the strains next to the crack flanks is critical in mixed mode; this region cannot be masked or excluded, especially in mode I, but can be carefully extrapolated from the displacement gradients [75].

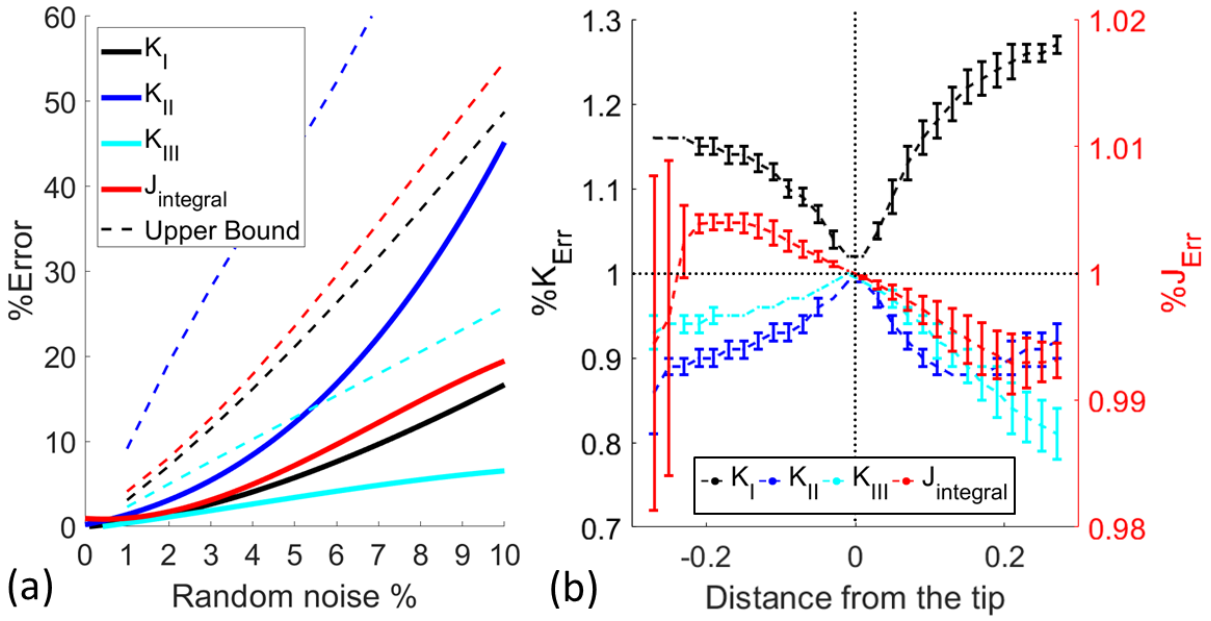


Figure 9-40: Error due to (a) noise and (b) crack tip accuracy.

Second, the analysis sensitivity to crack tip location was assessed using the accurate crack tip positioned at the origin (0,0) coordinate. The error in accurately locating the crack increases if the location was assumed ahead relative to behind the crack (Figure 9-40b). This is due to the nature of the analytical field, as there is symmetry on the crack edges, but the magnitude at the crack tip gradually changes with distance. Detailed analysis of two-dimensional errors reveals a distinct behaviour for each component of SIFs and the sum of all components in the J-integral influencing both magnitude and convergence.

Linear strain and rotation gradient, caused by pattern centre (PC) shift due to the beam movement during each EBSP acquisition, were not assessed as this spurious gradient

magnitude and distribution are highly dependent on the $EBSP_0$ deformation status and position with respect to the beam. Nevertheless, errors due to PC shifts can be reduced using AstroEBSD [171]. To less extent, certain meshing [589] and element/node configurations produce strain singularities [590,591] to improve accuracy; however, the discrepancy in results obtained from different singular elements persists [592,593]. For *J*-integral, comparably coarse meshes are sufficient, with no unique crack tip elements being required, which reduces the need for a high degree of mesh refinement at the crack tip [592].

In addition, this decomposition method is suitable for a regulated mesh and a crack field that is symmetric around the crack with no apparent noise at the crack edges but does not work for other stress raisers with compressive mechanical conditions (especially mode I) as minus values are interpreted as imaginary. Also, the stress field needs to be linearly elastic and have the $r^{-0.5}$ form of singularity, where $r$ is the distance from the crack tip. Complex and computationally expensive methods can be used as an alternative (Chapter 2), which can be coupled with finite element solvers to get the most out of the measured field, including padding noise near the crack [75], calculate the crack probable extension direction (e.g., XFEM ABAQUS®), etc.

# Cited literature


[1] Timoshenko SP. History of Strength of Materials. McGraw-Hill; 1953.

[2] Osakada K. History of plasticity and metal forming analysis. J Mater Process Technol 2010;210:1436–54. https://doi.org/10.1016/j.jmatprotec.2010.04.001.

[3] Savart F. Untersuchungen über das Gefüge der Metalle. Ann Phys 1829;92:248–59. https://doi.org/10.1002/andp.18290920604.

[4] Thorn B. Deformation of perfectly plastic and isotropic linear strain hardening cylindrical shells 1964.

[5] Inglis CE. Stress in a Plate Due to the Presence of Cracks and Sharp Corners. Transactions of the Institute of Naval Architects 1913:219–41.

[6] Griffith AA. VI. The phenomena of rupture and flow in solids. Philosophical Transactions of the Royal Society of London Series A, Containing Papers of a Mathematical or Physical Character 1921;221:163 LP – 198. https://doi.org/10.1098/rsta.1921.0006.

[7] Taylor G, Quinney H. The latent energy remaining in a metal after cold working. Proceedings of the Royal Society A: Mathematical, Physical and Engineering Sciences 1934;143:307 LP – 326. https://doi.org/10.1098/rspa.1934.0004.

[8] Orowan E. Zur Kristallplastizität. I. Zeitschrift Für Physik 1934;89:605–13. https://doi.org/10.1007/BF01341478.

[9] Polanyi M. Über eine Art Gitterstörung, die einen Kristall plastisch machen könnte. Zeitschrift Für Physik 1934;89:660–4. https://doi.org/10.1007/BF01341481.

[10] Norman GE, Yanilkin A V. Homogeneous nucleation of dislocations. Physics of the Solid State 2011;53:1614. https://doi.org/10.1134/S1063783411080221.

[11] Frank FC, Read WT. Multiplication Processes for Slow Moving Dislocations. Physical Review 1950;79:722–3. https://doi.org/10.1103/PhysRev.79.722.

[12] Malis T, Tangri K. Grain boundaries as dislocation sources in the premacroyield strain region. Acta Metallurgica 1979;27:25–32. https://doi.org/10.1016/0001-6160(79)90053-1.

[13] Brentnall WD, Rostoker W. Some observations on microyielding. Acta Metallurgica 1965;13:187–98. https://doi.org/10.1016/0001-6160(65)90195-1.

[14] Irwin GR. Fracturing of Metals. ASM; 1949.

[15] Orowan E. Fracture and strength of solids. Reports on Progress in Physics 1949;12:185.

[16] Irwin GR. NRL Report 4763: Onset of Fast Crack Propagation in High Strength Steel and Aluminum Alloys. Washington, DC, United States: 1956.

[17] Irwin GR. Analysis of Stresses and Strains Near the End of a Crack Traversing a Plate. Journal of Applied Mechanics-Transactions of the ASME 1957;E24:351–69.

[18] Sanders JL. On the Griffith-Irwin fracture theory. Transaction of the ASME 1959:352–3.

[19] Anderson TL. Fracture Mechanics: Fundamentals and Applications. 4th ed. CRC Press; 2017.

[20] Huber MT. Specific work of strain as a measure of material effort (a Translation from the original paper from Polish by Anna Stręk under scientific supervision of Ryszard B. Pęcherski). Archives of Mechanics 1904;56:173–90.

[21] Mises R v. Mechanik der festen Körper im plastisch- deformablen Zustand. Nachrichten von Der Gesellschaft Der Wissenschaften Zu Göttingen, Mathematisch-Physikalische Klasse 1913:582–92.

[22] Westergaard HM. Bearing Pressures and Cracks: Bearing Pressures Through a Slightly Waved Surface or Through a Nearly Flat Part of a Cylinder, and Related Problems of Cracks. J Appl Mech 1939;6:A49–53. https://doi.org/10.1115/1.4008919.

[23] Sneddon IN. The distribution of stress in the neighbourhood of a crack in an elastic solid. Proc R Soc Lond A Math Phys Sci 1946;187:229 LP – 260. https://doi.org/10.1098/rspa.1946.0077.

[24] Williams ML. On the Stress Distribution at the Base of a Stationary Crack. J Appl Mech 1956;24:109–14.

[25] Irwin GR. Plastic Zone Near a Crack and Fracture Toughness. Sagamore Research Conference Proceedings 1961;4:63–78.

[26] Hiroshi Tada; Paul C. Paris; George R. Irwin; The Stress Analysis of Cracks Handbook. 2nd ed. Paris Productions; 1985.

[27] Dugdale DS. Yielding of steel sheets containing slits. J Mech Phys Solids 1960;8:100–4. https://doi.org/10.1016/0022-5096(60)90013-2.

[28] Anderson TL. Elastic-Plastic Fracture Mechanics. Fracture Mechanics - Fundamentals and Applications. 4th ed., CRC Press; 2017, p. 688.

[29] Noether E. Invariante Variationsprobleme. Nachrichten von Der Gesellschaft Der Wissenschaften Zu Göttingen, Mathematisch-Physikalische Klasse 1918:235–57.

[30] Günther W. Über einige randintegrale der elastomechanik. Abh Brauchschw Wiss Ges 1962;14:53–72.

[31] Eshelby JD. The force on an elastic singularity. Philosophical Transactions of the Royal Society of London Series A, Mathematical and Physical Sciences 1951;244:87–112. https://doi.org/10.1098/rsta.1951.0016.

[32] Eshelby JD. The Continuum Theory of Lattice Defects. In: Seitz F, Turnbull DBT-SSP, editors. vol. 3, Academic Press; 1956, p. 79–144. https://doi.org/https://doi.org/10.1016/S0081-1947(08)60132-0.

[33] Rice JR. A Path Independent Integral and the Approximate Analysis of Strain Concentration by Notches and Cracks. J Appl Mech 1968;35:379–86. https://doi.org/10.1115/1.3601206.

[34] Sanders JL. On the Griffith-Irwin Fracture Theory. J Appl Mech 1960;27:352–3. https://doi.org/10.1115/1.3643965.

[35] Cherepanov GP. Crack propagation in continuous media. Journal of Applied Mathematics and Mechanics 1967;31:503–12. https://doi.org/10.1016/0021-8928(67)90034-2.

[36] Hutchinson JW. Singular behaviour at the end of a tensile crack in a hardening material. J Mech Phys Solids 1968;16:13–31. https://doi.org/10.1016/0022-5096(68)90014-8.

[37] Rice JR, Rosengren GF. Plane strain deformation near a crack tip in a power-law hardening material. J Mech Phys Solids 1968;16:1–12. https://doi.org/10.1016/0022-5096(68)90013-6.

[38] Parks DM. The virtual crack extension method for nonlinear material behavior. Comput Methods Appl Mech Eng 1977;12:353–64. https://doi.org/10.1016/0045-7825(77)90023-8.

[39] Brocks W, Olschewski J. On J-dominance of crack-tip fields in largely yielded 3D structures. Int J Solids Struct 1986;22:693–708. https://doi.org/10.1016/0020-7683(86)90114-9.

[40] Shi MX, Huang Y, Gao H. The J-integral and geometrically necessary dislocations in nonuniform plastic deformation. Int J Plast 2004;20:1739–62. https://doi.org/10.1016/J.IJPLAS.2003.11.013.

[41] Theocaris PS. A comparison between the elastic strain energy and the plastic work at the crack tip. Eng Fract Mech 1988;30:767–77. https://doi.org/10.1016/0013-7944(88)90138-5.

[42] Kuang JH, Chen YC. The values of J-integral within the plastic zone. Eng Fract Mech 1996;55:869–81. https://doi.org/https://doi.org/10.1016/S0013-7944(96)00077-X.

[43] Li FZ, Shih CF, Needleman A. A comparison of methods for calculating energy release rates. Eng Fract Mech 1985;21:405–21. https://doi.org/https://doi.org/10.1016/0013-7944(85)90029-3.

[44] Ramberg W, Osgood WR. NACA Technical Note 902: Description of Stress-Strain Curves by Three Parameters. Washington, DC, United States: 1943.

[45] Chen Y-H. Advances in Conservation Laws and Energy Release Rates. Dordrecht: Springer Netherlands; 2002. https://doi.org/10.1007/978-94-015-9908-5.

[46] Budiansky B, Rice JR. Conservation Laws and Energy-Release Rates. J Appl Mech 1973;40:201–3. https://doi.org/10.1115/1.3422926.

[47] Freund LB. Stress intensity factor calculations based on a conservation integral. Int J Solids Struct 1978;14:241–50. https://doi.org/10.1016/0020-7683(78)90028-8.

[48] Shimada T, Ouchi K, Chihara Y, Kitamura T. Breakdown of Continuum Fracture Mechanics at the Nanoscale. Scientific Reports 2015 5:1 2015;5:1–6. https://doi.org/10.1038/srep08596.

[49] Begley JA, Landes JD. The *J* Integral as a Fracture Criterion. In: Corten HT, editor. Fracture Toughness: Part II, West Conshohocken, PA: ASTM International; 1972, p. 1–23. https://doi.org/10.1520/STP38816S.

[50] Agarwal BD, Patro BS, Kumar P. J integral as fracture criterion for short fibre composites: An experimental approach. Eng Fract Mech 1984;19:675–84. https://doi.org/10.1016/0013-7944(84)90100-0.

[51] Mindess S, Lawrence F v., Kesler CE. The J-integral as a fracture criterion for fiber reinforced concrete. Cem Concr Res 1977;7:731–42. https://doi.org/10.1016/0008-8846(77)90057-6.

[52] Singh RK, Parihar KS. The J-integral as a fracture criterion for polycarbonate thermoplastic. J Mater Sci 1986;21:3921–6. https://doi.org/10.1007/BF02431630.

[53] Lee RF, Donovan JA. J-Integral and Crack Opening Displacement as Crack Initiation Criteria in Natural Rubber in Pure Shear and Tensile Specimens. Rubber Chemistry and Technology 1987;60:674–88. https://doi.org/10.5254/1.3536150.

[54] Rice JR, Paris PC, Merkle JG. Some Further Results of J-Integral Analysis and Estimates. Progress in Flaw Growth and Fracture Toughness Testing, vol. 536, 100 Barr Harbor Drive, PO Box C700, West Conshohocken, PA 19428-2959: ASTM International; 1973, p. 231–45. https://doi.org/10.1520/STP49643S.

[55] Yoda M. The J-integral fracture criterion under opening and tearing modes and unloading effects. Eng Fract Mech 1980;13:647–56. https://doi.org/10.1016/0013-7944(80)90093-4.

[56] Becker TH, Mostafavi M, Tait RB, Marrow TJ. An approach to calculate the J-integral by digital image correlation displacement field measurement. Fatigue Fract Eng Mater Struct 2012;35:971–84. https://doi.org/10.1111/j.1460-2695.2012.01685.x.

[57] Jin X, Wade-Zhu J, Chen Y, Mummery PM, Fan X, Marrow TJ. Assessment of the fracture toughness of neutron-irradiated nuclear graphite by 3D analysis of the crack

displacement field. Carbon N Y 2021;171:882–93. https://doi.org/10.1016/J.CARBON.2020.09.072.

[58] Shih CF, Moran B, Nakamura T. Energy release rate along a three-dimensional crack front in a thermally stressed body. Int J Fract 1986;30:79–102. https://doi.org/https://doi.org/10.1007/BF00034019.

[59] Shih CF. Relationships between the J-integral and the crack opening displacement for stationary and extending cracks. J Mech Phys Solids 1981;29:305–26. https://doi.org/10.1016/0022-5096(81)90003-X.

[60] Rice J. Mechanics of Crack Tip Deformation and Extension by Fatigue. Fatigue Crack Propagation, vol. 415, 100 Barr Harbor Drive, PO Box C700, West Conshohocken, PA 19428-2959: ASTM International; 1967, p. 247–65. https://doi.org/10.1520/STP47234S.

[61] Cotterell B, Rice JR. Slightly curved or kinked cracks. Int J Fract 1980;16:155–69. https://doi.org/10.1007/BF00012619.

[62] Shih CF, Asaro RJ. Elastic-Plastic Analysis of Cracks on Bimaterial Interfaces: Part I—Small Scale Yielding. J Appl Mech 1988;55:299–316. https://doi.org/10.1115/1.3173676.

[63] Molteno MR, Becker TH. Mode I-III Decomposition of the J -integral from DIC Displacement Data. Strain 2015;51:492–503. https://doi.org/10.1111/str.12166.

[64] Dhatt G, Lefrançois E, Touzot G. The finite element method. Finite Element Method, London: Wiley-ISTE; 2012, p. 1–7.

[65] Caimmi F, Calabrò R, Briatico-Vangosa F, Marano C, Rink M. J-Integral from Full Field Kinematic Data for Natural Rubber Compounds. Strain 2015;51:343–56. https://doi.org/10.1111/str.12145.

[66] Agiasofitou E, Lazar M. Micromechanics of dislocations in solids: J-, M-, and L-integrals and their fundamental relations. Int J Eng Sci 2017;114:16–40. https://doi.org/https://doi.org/10.1016/j.ijengsci.2017.02.001.

[67] Kim H, Kim S, Kim SY. Lattice-based J integral for a steadily moving dislocation. Int J Plast 2021;138:102949. https://doi.org/https://doi.org/10.1016/j.ijplas.2021.102949.

[68] Markenscoff X, Ni L. The energy-release rate and “self-force” of dynamically expanding spherical and plane inclusion boundaries with dilatational eigenstrain. J Mech Phys Solids 2010;58:1–11. https://doi.org/https://doi.org/10.1016/j.jmps.2009.10.001.

[69] Rice J, Drugan W, Sham T-L. Elastic-Plastic Analysis of Growing Cracks. Fracture Mechanics, 100 Barr Harbor Drive, PO Box C700, West Conshohocken, PA 19428-2959: ASTM International; 1979, p. 189-189–33. https://doi.org/10.1520/STP36972S.

[70] Palmer AC, Rice JR, Hill R. The growth of slip surfaces in the progressive failure of over-consolidated clay. Proceedings of the Royal Society of London A Mathematical and Physical Sciences 1973;332:527–48. https://doi.org/10.1098/rspa.1973.0040.

[71] Rice JR. Dislocation nucleation from a crack tip: An analysis based on the Peierls concept. J Mech Phys Solids 1992;40:239–71. https://doi.org/https://doi.org/10.1016/S0022-5096(05)80012-2.

[72] KC A, Kim J-H. Interaction integrals for thermal fracture of functionally graded materials. Eng Fract Mech 2008;75:2542–65. https://doi.org/https://doi.org/10.1016/j.engfracmech.2007.07.011.

[73] Haftbaradaran H, Qu J. A path-independent integral for fracture of solids under combined electrochemical and mechanical loadings. J Mech Phys Solids 2014;71:1–14. https://doi.org/https://doi.org/10.1016/j.jmps.2014.06.007.

[74] Walters MC, Paulino GH, Dodds RH. Interaction integral procedures for 3-D curved cracks including surface tractions. Eng Fract Mech 2005;72:1635–63. https://doi.org/https://doi.org/10.1016/j.engfracmech.2005.01.002.

[75] Barhli SM, Mostafavi M, Cinar AF, Hollis D, Marrow TJ. J-Integral Calculation by Finite Element Processing of Measured Full-Field Surface Displacements. Exp Mech 2017;57:997–1009. https://doi.org/10.1007/s11340-017-0275-1.

[76] Barhli SM, Saucedo-Mora L, Simpson C, Becker T, Mostafavi M, Withers PJ, et al. Obtaining the J-integral by diffraction-based crack-field strain mapping. Procedia Structural Integrity 2016;2:2519–26. https://doi.org/10.1016/j.prostr.2016.06.315.

[77] Barhli SM, Saucedo-Mora L, Jordan MSL, Cinar AF, Reinhard C, Mostafavi M, et al. Synchrotron X-ray characterization of crack strain fields in polygranular graphite. Carbon N Y 2017;124:357–71. https://doi.org/10.1016/J.CARBON.2017.08.075.

[78] Breitbarth E, Strohmann T, Besel M, Reh S. Determination of Stress Intensity Factors and J integral based on Digital Image Correlation. Frattura Ed Integrità Strutturale 2019;13:12–25. https://doi.org/10.3221/IGF-ESIS.49.02.

[79] McNeill SR, Peters WH, Sutton MA. Estimation of stress intensity factor by digital image correlation. Eng Fract Mech 1987;28:101–12. https://doi.org/10.1016/0013-7944(87)90124-X.

[80] Roux S, Hild F. Stress intensity factor measurements from digital image correlation: post-processing and integrated approaches. Int J Fract 2006;140:141–57. https://doi.org/10.1007/s10704-006-6631-2.

[81] Yoneyama S. Smoothing Measured Displacements and Computing Strains Utilising Finite Element Method. Strain 2011;47:258–66. https://doi.org/10.1111/j.1475-1305.2010.00765.x.

[82] Réthoré J, Gravouil A, Morestin F, Combescure A. Estimation of mixed-mode stress intensity factors using digital image correlation and an interaction integral. Int J Fract 2005;132:65–79. https://doi.org/10.1007/s10704-004-8141-4.

[83] Stern M, Becker EB, Dunham RS. A contour integral computation of mixed-mode stress intensity factors. Int J Fract 1976;12:359–68. https://doi.org/10.1007/BF00032831.

[84] Cinar AF, Barhli SM, Hollis D, Flansbjer M, Tomlinson RA, Marrow TJ, et al. An autonomous surface discontinuity detection and quantification method by digital image correlation and phase congruency. Opt Lasers Eng 2017;96:94–106. https://doi.org/10.1016/J.OPTLASENG.2017.04.010.

[85] Poissant J, Barthelat F. A Novel “Subset Splitting” Procedure for Digital Image Correlation on Discontinuous Displacement Fields. Exp Mech 2010;50:353–64. https://doi.org/10.1007/s11340-009-9220-2.

[86] Systèmes® D. ABAQUS. ABAQUS v66 2009. https://classes.engineering.wustl.edu/2009/spring/mase5513/abaqus/docs/v6.6/index.html.

[87] Mikami Y, Oda K, Kamaya M, Mochizuki M. Effect of reference point selection on microscopic stress measurement using EBSD. Materials Science and Engineering: A 2015;647:256–64. https://doi.org/10.1016/j.msea.2015.09.004.

[88] Coleman TF, Li Y. An Interior Trust Region Approach for Nonlinear Minimization Subject to Bounds. SIAM Journal on Optimization 1996;6:418–45. https://doi.org/10.1137/0806023.

[89] Barhli SM. Advanced quantitative analysis of crack fields, observed by 2D and 3D image correlation, volume correlation and diffraction mapping. Ph.D. University of Oxford, 2017.

[90] Bathe K-J. Appropriate Order of Numerical Integration. Finite Element Procedures. 2nd ed., Watertown, MA: 2016, p. 465–76.

[91] Ciarlet PG. The Finite Element Method for Elliptic Problems. Society for Industrial and Applied Mathematics; 2002. https://doi.org/10.1137/1.9780898719208.

[92] Szabo BA (Barna A, Babuška Ivo. Finite element analysis. 1st ed. John Wiley & Sons; 1991.

[93] Wigger T, Lupton C, Alshammrei S, Tong J, Marrow TJ, Earp P, et al. In situ mapping of normal strains in the field of a growing fatigue crack in a steel weld using digital image

correlation and energy dispersive synchrotron X-ray diffraction. Int J Fatigue 2018;115:11–9. https://doi.org/10.1016/J.IJFATIGUE.2018.05.016.

[94] Drakopoulos M, Connolley T, Reinhard C, Atwood R, Magdysyuk O, Vo N, et al. I12: the Joint Engineering, Environment and Processing (JEEP) beamline at Diamond Light Source. J Synchrotron Radiat 2015;22:828–38. https://doi.org/10.1107/S1600577515003513.

[95] International A. ASTM E647-15e1, Standard Test Method for Measurement of Fatigue Crack Growth Rates. West Conshohocken, PA: 2015. https://doi.org/10.1520/E0647-15E01.

[96] Bachmann F, Hielscher R, Schaeben H. Texture Analysis with MTEX – Free and Open Source Software Toolbox. Solid State Phenomena 2010;160:63–8. https://doi.org/10.4028/www.scientific.net/SSP.160.63.

[97] Hielscher R, Schaeben H. A novel pole figure inversion method: specification of the MTEX algorithm. J Appl Crystallogr 2008;41:1024–37. https://doi.org/10.1107/S0021889808030112.

[98] Simpson C. PyXe: XRD Strain Analysis. 2016. https://doi.org/10.5281/zenodo.49824.

[99] Mostafavi M, Collins DM, Peel MJ, Reinhard C, Barhli SM, Mills R, et al. Dynamic contact strain measurement by time-resolved stroboscopic energy dispersive synchrotron X-ray diffraction. Strain 2017;53:e12221. https://doi.org/10.1111/str.12221.

[100] Pecharsky VK, Zavalij PY. The Powder Diffraction Pattern. Fundamentals of Powder Diffraction and Structural Characterization of Materials. 2nd Editio, Boston, MA: Springer US; 2009, p. 151–202. https://doi.org/10.1007/978-0-387-09579-0_8.

[101] Pan B, Qian K, Xie H, Asundi A. Two-dimensional digital image correlation for in-plane displacement and strain measurement: a review. Meas Sci Technol 2009;20:62001. https://doi.org/10.1088/0957-0233/20/6/062001.

[102] Guizar-Sicairos M, Thurman ST, Fienup JR. Efficient subpixel image registration algorithms. Opt Lett 2008;33:156–8. https://doi.org/10.1364/OL.33.000156.

[103] Peter Kovesi. Image Features from Phase Congruency. Videre: Journal of Computer Vision Research 1999;1:1–26.

[104] Gnäupel-Herold T. ISODEC: software for calculating diffraction elastic constants. J Appl Crystallogr 2012;45:573–4. https://doi.org/10.1107/S0021889812014252.

[105] Weisser MA, Evans AD, Van Petegem S, Holdsworth SR, Van Swygenhoven H. In situ room temperature tensile deformation of a 1% CrMoV bainitic steel using synchrotron and neutron diffraction. Acta Mater 2011;59:4448–57. https://doi.org/10.1016/j.actamat.2011.03.068.

[106] Hill R. The Elastic Behaviour of a Crystalline Aggregate. Proceedings of the Physical Society Section A 1952;65:349–54. https://doi.org/10.1088/0370-1298/65/5/307.

[107] Pantleon W. Resolving the geometrically necessary dislocation content by conventional electron backscattering diffraction. Scr Mater 2008;58:994–7. https://doi.org/10.1016/J.SCRIPTAMAT.2008.01.050.

[108] MacDowell AA, Celestre RS, Tamura N, Spolenak R, Valek B, Brown WL, et al. Submicron X-ray diffraction. Nucl Instrum Methods Phys Res A 2001;467–468:936–43. https://doi.org/https://doi.org/10.1016/S0168-9002(01)00530-7.

[109] Guo Y, Collins DM, Tarleton E, Hofmann F, Tischler J, Liu W, et al. Measurements of stress fields near a grain boundary: Exploring blocked arrays of dislocations in 3D. Acta Mater 2015;96:229–36. https://doi.org/10.1016/J.ACTAMAT.2015.05.041.

[110] Guo Y, Collins DM, Tarleton E, Hofmann F, Wilkinson AJ, Britton T ben. Dislocation density distribution at slip band-grain boundary intersections. Acta Mater 2020;182:172–83. https://doi.org/10.1016/j.actamat.2019.10.031.

[111] Kutsal M, Bernard P, Berruyer G, Cook PK, Hino R, Jakobsen AC, et al. The ESRF dark-field x-ray microscope at ID06. IOP Conf Ser Mater Sci Eng 2019;580:12007. https://doi.org/10.1088/1757-899x/580/1/012007.

[112] Mostafavi M, Collins DM, Cai B, Bradley R, Atwood RC, Reinhard C, et al. Yield behavior beneath hardness indentations in ductile metals, measured by three-dimensional computed X-ray tomography and digital volume correlation. Acta Mater 2015;82:468–82. https://doi.org/https://doi.org/10.1016/j.actamat.2014.08.046.

[113] Walters MC, Paulino GH, Dodds RH. Stress-intensity factors for surface cracks in functionally graded materials under mode-I thermomechanical loading. Int J Solids Struct 2004;41:1081–118. https://doi.org/https://doi.org/10.1016/j.ijsolstr.2003.09.050.

[114] Courtin S, Gardin C, Bézine G, ben Hadj Hamouda H. Advantages of the J-integral approach for calculating stress intensity factors when using the commercial finite element software ABAQUS. Eng Fract Mech 2005;72:2174–85. https://doi.org/10.1016/j.engfracmech.2005.02.003.

[115] Adams BL, Wright SI, Kunze K. Orientation imaging: The emergence of a new microscopy. Metallurgical Transactions A 1993;24:819–31. https://doi.org/10.1007/BF02656503.

[116] Humphreys FJ. Review Grain and subgrain characterisation by electron backscatter diffraction. J Mater Sci 2001;36:3833–54. https://doi.org/10.1023/A:1017973432592.

[117] Wilkinson AJ, Hirsch PB. Electron diffraction based techniques in scanning electron microscopy of bulk materials. Micron 1997;28:279–308. https://doi.org/10.1016/S0968-4328(97)00032-2.

[118] Randle V. Electron backscatter diffraction: Strategies for reliable data acquisition and processing. Mater Charact 2009;60:913–22. https://doi.org/10.1016/j.matchar.2009.05.011.

[119] Goldstein JI, Newbury DE, Michael JR, Ritchie NWM, Scott JHJ, Joy DC. Backscattered Electrons. Scanning Electron Microscopy and X-Ray Microanalysis. 4th ed., New York, NY: Springer; 2018, p. 15–28. https://doi.org/10.1007/978-1-4939-6676-9_2.

[120] Winkelmann A, Nolze G. Analysis of Kikuchi band contrast reversal in electron backscatter diffraction patterns of silicon. Ultramicroscopy 2010;110:190–4. https://doi.org/10.1016/J.ULTRAMIC.2009.11.008.

[121] Schwarzer RA, Field DP, Adams BL, Kumar M, Schwartz AJ. Present State of Electron Backscatter Diffraction and Prospective Developments. In: Schwartz AJ, Kumar M, Adams BL, Field DP, editors. Electron Backscatter Diffraction in Materials Science, vol. 53, Boston, MA: Springer US; 2009, p. 1–20. https://doi.org/10.1007/978-0-387-88136-2_1.

[122] Venables JA, Harland CJ. Electron back-scattering patterns—A new technique for obtaining crystallographic information in the scanning electron microscope. Philosophical Magazine 1973;27:1193–200. https://doi.org/10.1080/14786437308225827.

[123] Chen D, Kuo J-C, Wu W-T. Effect of microscopic parameters on EBSD spatial resolution. Ultramicroscopy 2011;111:1488–94. https://doi.org/10.1016/j.ultramic.2011.06.007.

[124] Field DP. Improving the Spatial Resolution of EBSD. Microscopy and Microanalysis 2005;11:52–3. https://doi.org/DOI: 10.1017/S1431927605506445.

[125] Deal A, Tao X, Eades A. EBSD geometry in the SEM: simulation and representation. Surface and Interface Analysis 2005;37:1017–20. https://doi.org/10.1002/sia.2115.

[126] Randle V. Theoretical Framework for Electron Backscatter Diffraction. In: Schwartz AJ, Kumar M, Adams BL, editors. Electron Backscatter Diffraction in Materials Science. 1st ed., Boston, MA: Springer US; 2000, p. 19–30. https://doi.org/10.1007/978-1-4757-3205-4_2.

[127] Eades A, Deal A, Bhattacharyya A, Hooghan T. Energy Filtering in EBSD. In: Schwartz AJ, Kumar M, Adams BL, Field DP, editors. Electron Backscatter Diffraction in Materials

Science. 2nd ed., Boston, MA: Springer US; 2009, p. 53–63. https://doi.org/10.1007/978-0-387-88136-2_4.

[128] Wilkinson AJ, Britton TBen. Strains, planes, and EBSD in materials science. Materials Today 2012;15:366–76. https://doi.org/10.1016/S1369-7021(12)70163-3.

[129] Sawatzki S, Woodcock TG, Güth K, Müller K-H, Gutfleisch O. Calculation of remanence and degree of texture from EBSD orientation histograms and XRD rocking curves in Nd–Fe–B sintered magnets. J Magn Magn Mater 2015;382:219–24. https://doi.org/10.1016/J.JMMM.2015.01.046.

[130] Maitland T, Sitzman S. Backscattering Detector and EBSD in Nanomaterials Characterization. In: Zhou W, Wang ZL, editors. Scanning Microscopy for Nanotechnology, New York, NY: Springer New York; 2006, p. 41–75. https://doi.org/10.1007/978-0-387-39620-0_2.

[131] Tixier R, Waché C. Kossel patterns. J Appl Crystallogr 1970;3:466–85. https://doi.org/10.1107/S0021889870006726.

[132] Lassen NK. Automated determination of crystal orientations from electron backscattering patterns. 1994.

[133] Dicks K. Introduction to EBSD. 2018.

[134] Alam MN, Blackman M, Pashley DW. High-angle Kikuchi patterns. Proc R Soc Lond A Math Phys Sci 1954;221:224–42. https://doi.org/10.1098/rspa.1954.0017.

[135] Dingley DJ, Wright SI, Nowell MM. Dynamic Background Correction of Electron Backscatter Diffraction Patterns. Microscopy and Microanalysis 2005;11:528–9. https://doi.org/DOI: 10.1017/S1431927605506676.

[136] Hough PVC. Method and Means for Recognizing Complex Patterns, 1962.

[137] Wright SI, Zhao J, Adams BL. Automated Determination of Lattice Orientation From Electron Backscattered Kikuchi Diffraction Patterns. Textures and Microstructures 1991;13:123–31. https://doi.org/10.1155/TSM.13.123.

[138] Wright SI, Adams BL, Kunze K. Application of a new automatic lattice orientation measurement technique to polycrystalline aluminum. Materials Science and Engineering: A 1993;160:229–40. https://doi.org/10.1016/0921-5093(93)90452-K.

[139] Lassen NChrK. Automatic crystal orientation determination from EBSPs. Micron and Microscopica Acta 1992;23:191–2. https://doi.org/10.1016/0739-6260(92)90133-X.

[140] Krieger Lassen, N. C.; Juul Jensen, D.; Conradsen K. Automatic recognition of deformed and recrystallized regions in partly recrystallized samples using electron back scattering patterns. ICOTOM 10 1993.

[141] Wright SI, Nowell MM, Lindeman SP, Camus PP, de Graef M, Jackson MA. Introduction and comparison of new EBSD post-processing methodologies. Ultramicroscopy 2015;159:81–94. https://doi.org/10.1016/J.ULTRAMIC.2015.08.001.

[142] Prior DJ. Problems in determining the misorientation axes, for small angular misorientations, using electron backscatter diffraction in the SEM. J Microsc 2003;195:217–25. https://doi.org/10.1046/j.1365-2818.1999.00572.x.

[143] Wilkinson AJ, Dingley DJ, Meaden G. Strain Mapping Using Electron Backscatter Diffraction. In: Schwartz AJ, Kumar M, Adams BL, Field DP, editors. Electron Backscatter Diffraction in Materials Science. 2nd ed., Boston, MA: Springer US; 2009, p. 231–49. https://doi.org/10.1007/978-0-387-88136-2_17.

[144] Nolze G. Image distortions in SEM and their influences on EBSD measurements. Ultramicroscopy 2007;107:172–83. https://doi.org/10.1016/J.ULTRAMIC.2006.07.003.

[145] Nowell M. How I Prepare Samples for EBSD Analysis. New Jersey, USA: 2017.

[146] Dingley DJ, Randle V. Microtexture determination by electron back-scatter diffraction. J Mater Sci 1992;27:4545–66. https://doi.org/10.1007/BF01165988.

[147] Adams BL. Orientation imaging microscopy: Emerging and future applications. Ultramicroscopy 1997;67:11–7. https://doi.org/10.1016/S0304-3991(96)00103-9.

[148] Winkelmann A, Trager-Cowan C, Sweeney F, Day AP, Parbrook P. Many-beam dynamical simulation of electron backscatter diffraction patterns. Ultramicroscopy 2007;107:414–21. https://doi.org/https://doi.org/10.1016/j.ultramic.2006.10.006.

[149] Lassen NCK, Jensen DJ, Conradsen K. Automatic Recognition of Deformed and Recrystallized Regions in Partly Recrystallized Samples Using Electron Back Scattering Patterns. Materials Science Forum 1994;157–162:149–58. https://doi.org/10.4028/WWW.SCIENTIFIC.NET/MSF.157-162.149.

[150] Wilkinson AJ. Methods for determining elastic strains from electron backscatter diffraction and electron channelling patterns. Materials Science and Technology 1997;13:79–84. https://doi.org/10.1179/mst.1997.13.1.79.

[151] Zhu C, de Graef M. EBSD pattern simulations for an interaction volume containing lattice defects. Ultramicroscopy 2020;218:113088. https://doi.org/10.1016/J.ULTRAMIC.2020.113088.

[152] Troost KZ, van der Sluis P, Gravesteijn DJ. Microscale elastic-strain determination by backscatter Kikuchi diffraction in the scanning electron microscope. Appl Phys Lett 1993;62:1110–2. https://doi.org/10.1063/1.108758.

[153] Wilkinson AJ, Dingley DJ. Quantitative deformation studies using electron back scatter patterns. Acta Metallurgica et Materialia 1991;39:3047–55. https://doi.org/10.1016/0956-7151(91)90037-2.

[154] Wilkinson AJ. Measurement of elastic strains and small lattice rotations using electron back scatter diffraction. Ultramicroscopy 1996;62:237–47. https://doi.org/10.1016/0304-3991(95)00152-2.

[155] Wilkinson AJ, Meaden G, Dingley DJ. High resolution mapping of strains and rotations using electron backscatter diffraction. Materials Science and Technology 2006;22:1271–8. https://doi.org/10.1179/174328406X130966.

[156] Wilkinson AJ, Meaden G, Dingley DJ. High-resolution elastic strain measurement from electron backscatter diffraction patterns: New levels of sensitivity. Ultramicroscopy 2006;106:307–13. https://doi.org/10.1016/j.ultramic.2005.10.001.

[157] Guo Y. The interactions between slip band, deformation twins and grain boundaries in commercial purity titanium. University of Oxford, 2015.

[158] Britton TB, Wilkinson AJ. High resolution electron backscatter diffraction measurements of elastic strain variations in the presence of larger lattice rotations. Ultramicroscopy 2012;114:82–95. https://doi.org/10.1016/J.ULTRAMIC.2012.01.004.

[159] Maurice C, Fortunier R. A 3D Hough transform for indexing EBSD and Kossel patterns. J Microsc 2008;230:520–9. https://doi.org/10.1111/j.1365-2818.2008.02045.x.

[160] Britton TB, Jiang J, Guo Y, Vilalta-Clemente A, Wallis D, Hansen LN, et al. Tutorial: Crystal orientations and EBSD — Or which way is up? Mater Charact 2016;117:113–26. https://doi.org/10.1016/j.matchar.2016.04.008.

[161] Hardin TJ, Ruggles TJ, Koch DP, Niezgoda SR, Fullwood DT, Homer ER. Analysis of traction-free assumption in high-resolution EBSD measurements. J Microsc 2015;260:73–85. https://doi.org/https://doi.org/10.1111/jmi.12268.

[162] Britton TB. A Hight Resolution Electron Backscatter Diffraction Study of Titanium and its Alloys. 2010.

[163] Villert S, Maurice C, Wyon C, Fortunier R. Accuracy assessment of elastic strain measurement by EBSD. J Microsc 2009;233:290–301. https://doi.org/10.1111/j.1365-2818.2009.03120.x.

[164] Plancher E, Petit J, Maurice C, Favier V, Saintoyant L, Loisnard D, et al. On the Accuracy of Elastic Strain Field Measurements by Laue Microdiffraction and High-Resolution EBSD: a Cross-Validation Experiment. Exp Mech 2016;56:483–92. https://doi.org/10.1007/S11340-015-0114-1/FIGURES/8.

[165] Riedl T, Wendrock H. Reliability of high-resolution electron backscatter diffraction determination of strain and rotation variations using phase-only and cross correlation. Crystal Research and Technology 2014;49:195–203. https://doi.org/10.1002/CRAT.201300217.

[166] Maurice C, Driver JH, Fortunier R. On solving the orientation gradient dependency of high angular resolution EBSD. Ultramicroscopy 2012;113:171–81. https://doi.org/10.1016/J.ULTRAMIC.2011.10.013.

[167] Vermeij T, Hoefnagels JPM. A consistent full-field integrated DIC framework for HR-EBSD. Ultramicroscopy 2018;191:44–50. https://doi.org/10.1016/J.ULTRAMIC.2018.05.001.

[168] Ernould C, Beausir B, Fundenberger JJ, Taupin V, Bouzy E. Integrated correction of optical distortions for global HR-EBSD techniques. Ultramicroscopy 2021;221:113158. https://doi.org/10.1016/J.ULTRAMIC.2020.113158.

[169] Shi Q, Loisnard D, Dan C, Zhang F, Zhong H, Li H, et al. Calibration of crystal orientation and pattern center of EBSD using integrated digital image correlation. Mater Charact 2021;178:111206. https://doi.org/10.1016/J.MATCHAR.2021.111206.

[170] Basinger JA. Detail Extraction from Electron Backscatter Diffraction Patterns BYU ScholarsArchive Citation. 2011.

[171] Britton TB, Tong VS, Hickey J, Foden A, Wilkinson AJ. AstroEBSD : exploring new space in pattern indexing with methods launched from an astronomical approach. J Appl Crystallogr 2018;51:1525–34. https://doi.org/10.1107/S1600576718010373.

[172] Pang EL, Larsen PM, Schuh CA. Global optimization for accurate determination of EBSD pattern centers. Ultramicroscopy 2020;209:112876. https://doi.org/10.1016/J.ULTRAMIC.2019.112876.

[173] Tanaka T, Wilkinson AJ. Pattern matching analysis of electron backscatter diffraction patterns for pattern centre, crystal orientation and absolute elastic strain determination – accuracy and precision assessment. Ultramicroscopy 2019;202:87–99. https://doi.org/10.1016/J.ULTRAMIC.2019.04.006.

[174] Foden A, Collins D, Wilkinson A, Britton TB. Indexing Electron Backscatter Diffraction Patterns with a Refined Template Matching Approach 2018.

[175] Jackson MA, Pascal E, de Graef M. Dictionary Indexing of Electron Back-Scatter Diffraction Patterns: a Hands-On Tutorial. Integr Mater Manuf Innov 2019;8:226–46. https://doi.org/10.1007/S40192-019-00137-4/FIGURES/7.

[176] Britton B. Strain Mapping by High Angular Electron Backscatter Diffraction (HR-EBSD). Alabama, US: University of Alabama; 2016.

[177] Jiang J, Zhang T, Dunne FPE, Britton T ben. Deformation compatibility in a single crystalline Ni superalloy. Proceedings of the Royal Society A: Mathematical, Physical and Engineering Sciences 2016;472:20150690. https://doi.org/10.1098/rspa.2015.0690.

[178] Wright SI, Nowell MM. EBSD Image Quality Mapping. Microscopy and Microanalysis 2006;12:72–84. https://doi.org/10.1017/S1431927606060090.

[179] Britton TB, Hickey JLR. Understanding deformation with high angular resolution electron backscatter diffraction (HR-EBSD). IOP Conf Ser Mater Sci Eng 2018;304:012003. https://doi.org/10.1088/1757-899X/304/1/012003.

[180] Maurice C, Fortunier R, Driver J, Day A, Mingard K, Meaden G. Comments on the paper “Bragg’s law diffraction simulations for electron backscatter diffraction analysis” by Josh Kacher, Colin Landon, Brent L. Adams & David Fullwood. Ultramicroscopy 2010;110:758–9. https://doi.org/10.1016/J.ULTRAMIC.2010.02.003.

[181] Britton TB. Comment on “An Experimental Study on Evolution of Grain-Scale Stress/Strain and Geometrical Necessary Dislocations in Advanced TA15 Titanium Alloy during Uniaxial Tension Deformation.” Adv Eng Mater 2017;19:1700051. https://doi.org/10.1002/ADEM.201700051.

[182] Zhang T, Collins DM, Dunne FPE, Shollock BA. Crystal plasticity and high-resolution electron backscatter diffraction analysis of full-field polycrystal Ni superalloy strains and rotations under thermal loading. Acta Mater 2014;80:25–38. https://doi.org/https://doi.org/10.1016/j.actamat.2014.07.036.

[183] Kacher J, Landon C, Adams BL, Fullwood D. Bragg’s Law diffraction simulations for electron backscatter diffraction analysis. Ultramicroscopy 2009;109:1148–56. https://doi.org/10.1016/J.ULTRAMIC.2009.04.007.

[184] Werner AW and GN and MV and FS-P and WSM. Physics-based simulation models for EBSD: advances and challenges. IOP Conf Ser Mater Sci Eng 2016;109:12018.

[185] Alkorta J, Marteleur M, Jacques PJ. Improved simulation based HR-EBSD procedure using image gradient based DIC techniques. Ultramicroscopy 2017;182:17–27. https://doi.org/10.1016/J.ULTRAMIC.2017.06.015.

[186] Winkelmann A, Nolze G, Cios G, Tokarski T, Bała P, Hourahine B, et al. Kikuchi pattern simulations of backscattered and transmitted electrons. J Microsc 2021;284:157–84. https://doi.org/10.1111/JMI.13051.

[187] Winkelmann A, Nolze G, Vos M, Salvat-Pujol F, Werner WSM. Physics-based simulation models for EBSD: advances and challenges. IOP Conf Ser Mater Sci Eng 2016;109:012018. https://doi.org/10.1088/1757-899X/109/1/012018.

[188] Winkelmann A. Principles of depth-resolved Kikuchi pattern simulation for electron backscatter diffraction. J Microsc 2010;239:32–45. https://doi.org/10.1111/J.1365-2818.2009.03353.X.

[189] Vermeij T, de Graef M, Hoefnagels J. Demonstrating the potential of accurate absolute cross-grain stress and orientation correlation using electron backscatter diffraction. Scr Mater 2019;162:266–71. https://doi.org/10.1016/J.SCRIPTAMAT.2018.11.030.

[190] Kacher J, Basinger J, Adams BL, Fullwood DT. Reply to comment by Maurice et al. in response to “Bragg’s Law Diffraction Simulations for Electron Backscatter Diffraction Analysis.” Ultramicroscopy 2010;110:760–2. https://doi.org/10.1016/j.ultramic.2010.02.004.

[191] Fullwood D, Vaudin M, Daniels C, Ruggles T, Wright SI. Validation of kinematically simulated pattern HR-EBSD for measuring absolute strains and lattice tetragonality. Mater Charact 2015;107:270–7. https://doi.org/10.1016/J.MATCHAR.2015.07.017.

[192] Britton TB, Maurice C, Fortunier R, Driver JH, Day AP, Meaden G, et al. Factors affecting the accuracy of high resolution electron backscatter diffraction when using simulated patterns. Ultramicroscopy 2010;110:1443–53. https://doi.org/10.1016/j.ultramic.2010.08.001.

[193] Alkorta J. Limits of simulation based high resolution EBSD. Ultramicroscopy 2013;131:33–8. https://doi.org/10.1016/J.ULTRAMIC.2013.03.020.

[194] Jackson BE, Christensen JJ, Singh S, de Graef M, Fullwood DT, Homer ER, et al. Performance of Dynamically Simulated Reference Patterns for Cross-Correlation Electron Backscatter Diffraction. Microscopy and Microanalysis 2016;22:789–802. https://doi.org/10.1017/S143192761601148X.

[195] Tao X, Eades A. Alternatives to Image Quality (IQ) Mapping in EBSD. Microscopy and Microanalysis 2002;8:692–3. https://doi.org/10.1017/S1431927602106465.

[196] Data Sheet Zeron® 100 (UNS S32760). Temperance, MI: 2000.

[197] Örnek C, Burke MG, Hashimoto T, Engelberg DL. 748 K (475 °C) Embrittlement of Duplex Stainless Steel: Effect on Microstructure and Fracture Behavior. Metallurgical and Materials Transactions A 2017;48:1653–65. https://doi.org/10.1007/s11661-016-3944-2.

[198] Weng KL, Chen HR, Yang JR. The low-temperature aging embrittlement in a 2205 duplex stainless steel. Materials Science and Engineering: A 2004;379:119–32. https://doi.org/10.1016/J.MSEA.2003.12.051.

[199] Beattie HJ, Versnyder FL. A New Complex Phase in a High-Temperature Alloy. Nature 1956;178:208–9. https://doi.org/10.1038/178208b0.

[200] Zhang Q, Singaravelu ASS, Zhao Y, Jing T, Chawla N. Mechanical properties of a thermally-aged cast duplex stainless steel by nanoindentation and micropillar compression. Materials Science and Engineering: A 2019;743:520–8. https://doi.org/10.1016/J.MSEA.2018.11.112.

[201] Lee HJ, Kong BS, Obulan Subramanian G, Heo J, Jang C, Lee KS. Evaluation of thermal aging of δ-ferrite in austenitic stainless steel weld using nanopillar compression test. Scr Mater 2018;155:32–6. https://doi.org/10.1016/J.SCRIPTAMAT.2018.06.016.

[202] Z L, Y H, T C, X W, P L, Y L. Microstructural Evolution and Mechanical Behavior of Thermally Aged Cast Duplex Stainless Steel. Materials (Basel) 2020;13:1–13. https://doi.org/10.3390/MA13245636.

[203] Örnek C, Burke MG, Hashimoto T, Lim JJH, Engelberg DL, Örnek C. 475°C Embrittlement of Duplex Stainless Steel—A Comprehensive Microstructure Characterization Study. Mater Perform Charact 2017;6:409–36. https://doi.org/10.1520/MPC20160088.

[204] Nowell MM, Witt RA, True BW. EBSD Sample Preparation: Techniques, Tips, and Tricks. Micros Today 2005;13:44–9. https://doi.org/DOI: 10.1017/S1551929500053669.

[205] Jiapeng S, Cheng L, Han J, Ma A, Fang L. Nanoindentation Induced Deformation and Pop-in Events in a Silicon Crystal: Molecular Dynamics Simulation and Experiment. Sci Rep 2017;7:10282. https://doi.org/10.1038/s41598-017-11130-2.

[206] Wilkinson AJ, Randman D. Determination of elastic strain fields and geometrically necessary dislocation distributions near nanoindents using electron back scatter diffraction. Philosophical Magazine 2010;90:1159–77. https://doi.org/10.1080/14786430903304145.

[207] Jiang J, Britton TB, Wilkinson AJ. Measurement of geometrically necessary dislocation density with high resolution electron backscatter diffraction: Effects of detector binning and step size. Ultramicroscopy 2013;125:1–9. https://doi.org/10.1016/J.ULTRAMIC.2012.11.003.

[208] Jiang J, Britton TB, Wilkinson AJ. Evolution of dislocation density distributions in copper during tensile deformation. Acta Mater 2013;61:7227–39. https://doi.org/10.1016/J.ACTAMAT.2013.08.027.

[209] Abdolvand H, Wilkinson AJ. On the effects of reorientation and shear transfer during twin formation: Comparison between high resolution electron backscatter diffraction experiments and a crystal plasticity finite element model. Int J Plast 2016;84:160–82. https://doi.org/10.1016/J.IJPLAS.2016.05.006.

[210] Britton TB, Jiang J, Clough R, Tarleton E, Kirkland AI, Wilkinson AJ. Assessing the precision of strain measurements using electron backscatter diffraction – part 1: Detector assessment. Ultramicroscopy 2013;135:126–35. https://doi.org/10.1016/j.ultramic.2013.08.005.

[211] Britton TB, Wilkinson AJ. Measurement of residual elastic strain and lattice rotations with high resolution electron backscatter diffraction. Ultramicroscopy 2011;111:1395–404. https://doi.org/10.1016/j.ultramic.2011.05.007.

[212] Kim SA, Johnson WL. Elastic constants and internal friction of martensitic steel, ferritic-pearlitic steel, and α-iron. Materials Science and Engineering: A 2007;452–453:633–9. https://doi.org/10.1016/j.msea.2006.11.147.

[213] Hopcroft MA, Nix WD, Kenny TW. What is the Young's Modulus of Silicon? Journal of Microelectromechanical Systems 2010;19:229–38. https://doi.org/10.1109/JMEMS.2009.2039697.

[214] Lekhnitskii SG. General Equations of the Theory of Elasticity of an Anisotropic Body. Theory of Elasticity of an Anisotropic Elastic Body. 1st ed., Moscow: MIR Publishers; 1981, p. 15–73.

[215] Britton TB, Jiang J, Guo Y, Vilalta-Clemente A, Wallis D, Hansen LN, et al. Tutorial: Crystal orientations and EBSD — Or which way is up? Mater Charact 2016;117:113–26. https://doi.org/10.1016/j.matchar.2016.04.008.

[216] Sun S, Adams BL, King WE. Observations of lattice curvature near the interface of a deformed aluminium bicrystal. Philosophical Magazine A 2000;80:9–25. https://doi.org/10.1080/01418610008212038.

[217] El-Dasher BS, Adams BL, Rollett AD. Viewpoint: experimental recovery of geometrically necessary dislocation density in polycrystals. Scr Mater 2003;48:141–5. https://doi.org/10.1016/S1359-6462(02)00340-8.

[218] Press WH, Teukolsky SA, Vetterling WT, Flannery BP. Numerical Recipes in C (2nd Ed.): The Art of Scientific Computing. USA: Cambridge University Press; 1992.

[219] Goel S, Haque Faisal N, Luo X, Yan J, Agrawal A. Nanoindentation of polysilicon and single crystal silicon: Molecular dynamics simulation and experimental validation. J Phys D Appl Phys 2014;47:275304. https://doi.org/10.1088/0022-3727/47/27/275304.

[220] Wright SI, Nowell MM, Field DP. A Review of Strain Analysis Using Electron Backscatter Diffraction. Microscopy and Microanalysis 2011;17:316–29. https://doi.org/DOI: 10.1017/S1431927611000055.

[221] Wilkinson AJ, Hirsch PB. Electron diffraction based techniques in scanning electron microscopy of bulk materials. Micron 1997;28:279–308. https://doi.org/10.1016/S0968-4328(97)00032-2.

[222] Abdolvand H, Wilkinson AJ. Assessment of residual stress fields at deformation twin tips and the surrounding environments. Acta Mater 2016;105:219–31. https://doi.org/10.1016/j.actamat.2015.11.036.

[223] Britton TB, Hickey JLR. Understanding deformation with high angular resolution electron backscatter diffraction (HR-EBSD). IOP Conf Ser Mater Sci Eng 2018;304:012003. https://doi.org/10.1088/1757-899X/304/1/012003.

[224] Zhu C, Kaufmann K, Vecchio KS. Novel remapping approach for HR-EBSD based on demons registration. Ultramicroscopy 2020;208:112851. https://doi.org/10.1016/J.ULTRAMIC.2019.112851.

[225] Zhao C, Li X. Quantitative Study of Residual Strain and Geometrically Necessary Dislocation Density Using HR-EBSD Method. Exp Mech 2021;61:1281–90. https://doi.org/10.1007/S11340-021-00741-6/FIGURES/14.

[226] Jiang J, Britton TB, Wilkinson AJ. Mapping type III intragranular residual stress distributions in deformed copper polycrystals. Acta Mater 2013;61:5895–904. https://doi.org/10.1016/J.ACTAMAT.2013.06.038.

[227] Wallis D, Hansen LN, Britton T ben, Wilkinson AJ. Dislocation Interactions in Olivine Revealed by HR-EBSD. J Geophys Res Solid Earth 2017;122:7659–78. https://doi.org/10.1002/2017JB014513.

[228] Kalácska S, Dankházi Z, Zilahi G, Maeder X, Michler J, Ispánovity PD, et al. Investigation of geometrically necessary dislocation structures in compressed Cu micropillars by 3-dimensional HR-EBSD. Materials Science and Engineering: A 2020;770:138499. https://doi.org/10.1016/J.MSEA.2019.138499.

[229] Keller RR, Roshko A, Geiss RH, Bertness KA, Quinn TP. EBSD measurement of strains in GaAs due to oxidation of buried AlGaAs layers. Microelectron Eng 2004;75:96–102. https://doi.org/10.1016/J.MEE.2003.11.010.

[230] Bilby BA, Crocker AG. The Theory of the Crystallography of Deformation Twinning. Proc R Soc Lond A Math Phys Sci 1965;288:240–55. https://doi.org/10.1098/rspa.1965.0216.

[231] Christian JW, Mahajan S. Deformation twinning. Prog Mater Sci 1995;39:1–157. https://doi.org/10.1016/0079-6425(94)00007-7.

[232] Bilby BA, Crocker AG, Cottrell AH. The theory of the crystallography of deformation twinning. Proc R Soc Lond A Math Phys Sci 1965;288:240–55. https://doi.org/10.1098/rspa.1965.0216.

[233] Wang J, Beyerlein IJ, Tomé CN. An atomic and probabilistic perspective on twin nucleation in Mg. Scr Mater 2010;63:741–6. https://doi.org/10.1016/J.SCRIPTAMAT.2010.01.047.

[234] An XH, Han WZ, Huang CX, Zhang P, Yang G, Wu SD, et al. High strength and utilizable ductility of bulk ultrafine-grained Cu–Al alloys. Appl Phys Lett 2008;92:201915. https://doi.org/10.1063/1.2936306.

[235] Sarma VS, Wang J, Jian WW, Kauffmann A, Conrad H, Freudenberger J, et al. Role of stacking fault energy in strengthening due to cryo-deformation of FCC metals. Materials Science and Engineering: A 2010;527:7624–30. https://doi.org/10.1016/J.MSEA.2010.08.015.

[236] Youssef K, Sakaliyska M, Bahmanpour H, Scattergood R, Koch C. Effect of stacking fault energy on mechanical behavior of bulk nanocrystalline Cu and Cu alloys. Acta Mater 2011;59:5758–64. https://doi.org/10.1016/J.ACTAMAT.2011.05.052.

[237] Čapek J. Investigation of basic deformation mechanisms of magnesium alloys by means of advanced in-situ methods and theoretical modeling. Charles Univeristy, 2017.

[238] Cahn RW. Twinned crystals. Adv Phys 1954;3:363–445. https://doi.org/10.1080/00018735400101223.

[239] Wang S, Schuman C, Bao L, Lecomte JS, Zhang Y, Raulot JM, et al. Variant selection criterion for twin variants in titanium alloys deformed by rolling. Acta Mater 2012;60:3912–9. https://doi.org/10.1016/J.ACTAMAT.2012.03.046.

[240] Christian JW. Deformation Twinning. The Theory of Transformations in Metals and Alloys, Elsevier; 2002, p. 859–960. https://doi.org/10.1016/B978-008044019-4/50025-8.

[241] Guo Y, Schwiedrzik J, Michler J, Maeder X. On the nucleation and growth of {112¯2} twin in commercial purity titanium: In situ investigation of the local stress field and dislocation density distribution. Acta Mater 2016;120:292–301. https://doi.org/https://doi.org/10.1016/j.actamat.2016.08.073.

[242] Abdolvand H, Sedaghat O, Guo Y. Nucleation and growth of {112¯2} twins in titanium: Elastic energy and stress fields at the vicinity of twins. Materialia (Oxf) 2018;2:58–62. https://doi.org/10.1016/J.MTLA.2018.06.012.

[243] Paudel Y, Barrett CD, Tschopp MA, Inal K, El Kadiri H. Beyond initial twin nucleation in hcp metals: Micromechanical formulation for determining twin spacing during deformation. Acta Mater 2017;133:134–46. https://doi.org/https://doi.org/10.1016/j.actamat.2017.05.013.

[244] Paramatmuni C, Zheng Z, Rainforth WM, Dunne FPE. Twin nucleation and variant selection in Mg alloys: An integrated crystal plasticity modelling and experimental approach. Int J Plast 2020;135:102778. https://doi.org/https://doi.org/10.1016/j.ijplas.2020.102778.

[245] Paramatmuni C, Guo Y, Withers PJ, Dunne FPE. A three-dimensional mechanistic study of the drivers of classical twin nucleation and variant selection in Mg alloys: A mesoscale modelling and experimental study. Int J Plast 2021;143:103027. https://doi.org/10.1016/J.IJPLAS.2021.103027.

[246] Arul Kumar M, Beyerlein IJ, Tomé CN. Effect of local stress fields on twin characteristics in HCP metals. Acta Mater 2016;116:143–54. https://doi.org/10.1016/J.ACTAMAT.2016.06.042.

[247] Arul Kumar M, Kanjarla AK, Niezgoda SR, Lebensohn RA, Tomé CN. Numerical study of the stress state of a deformation twin in magnesium. Acta Mater 2015;84:349–58. https://doi.org/10.1016/J.ACTAMAT.2014.10.048.

[248] Sheinerman IAO and AG. Nanoscale cracks at deformation twins stopped by grain boundaries in bulk and thin-film materials with nanocrystalline and ultrafine-grained structures. J Phys D Appl Phys 2014;47:15307.

[249] Yu Q, Jiang Y, Wang J. Cyclic deformation and fatigue damage in single-crystal magnesium under fully reversed strain-controlled tension–compression in the [1 0 1¯ 0] direction. Scr Mater 2015;96:41–4. https://doi.org/10.1016/J.SCRIPTAMAT.2014.10.020.

[250] Beyerlein IJ, Zhang X, Misra A. Growth Twins and Deformation Twins in Metals. Annu Rev Mater Res 2014;44:329–63. https://doi.org/10.1146/annurev-matsci-070813-113304.

[251] Mughrabi H. Dislocation wall and cell structures and long-range internal stresses in deformed metal crystals. Acta Metallurgica 1983;31:1367–79. https://doi.org/10.1016/0001-6160(83)90007-X.

[252] Britton TB, Dunne FPE, Wilkinson AJ. On the mechanistic basis of deformation at the microscale in hexagonal close-packed metals. Proceedings of the Royal Society A: Mathematical, Physical and Engineering Sciences 2015;471:20140881. https://doi.org/10.1098/rspa.2014.0881.

[253] Li B, El Kadiri H, Horstemeyer MF. Extended zonal dislocations mediating twinning in titanium. Philosophical Magazine 2012;92:1006–22. https://doi.org/10.1080/14786435.2011.637985.

[254] Britton TB, Dunne FPE, Wilkinson AJ. On the mechanistic basis of deformation at the microscale in hexagonal close-packed metals. Proceedings of the Royal Society A: Mathematical, Physical and Engineering Sciences 2015;471:20140881. https://doi.org/10.1098/rspa.2014.0881.

[255] Liu Y, Tang PZ, Gong MY, McCabe RJ, Wang J, Tomé CN. Three-dimensional character of the deformation twin in magnesium. Nature Communications 2019 10:1 2019;10:1–7. https://doi.org/10.1038/s41467-019-10573-7.

[256] Kannan V, Hazeli K, Ramesh KT. The mechanics of dynamic twinning in single crystal magnesium. J Mech Phys Solids 2018;120:154–78. https://doi.org/10.1016/J.JMPS.2018.03.010.

[257] Barnett MR. Twinning and the ductility of magnesium alloys: Part I: “Tension” twins. Materials Science and Engineering: A 2007;464:1–7. https://doi.org/10.1016/J.MSEA.2006.12.037.

[258] Mughrabi H. Dislocation wall and cell structures and long-range internal stresses in deformed metal crystals. Acta Metallurgica 1983;31:1367–79. https://doi.org/10.1016/0001-6160(83)90007-X.

[259] Beyerlein IJ, Zhang X, Misra A. Growth Twins and Deformation Twins in Metals. Annu Rev Mater Res 2014;44:329–63. https://doi.org/10.1146/annurev-matsci-070813-113304.

[260] Barba D, Alabort E, Pedrazzini S, Collins DM, Wilkinson AJ, Bagot PAJ, et al. On the microtwinning mechanism in a single crystal superalloy. Acta Mater 2017;135:314–29. https://doi.org/10.1016/J.ACTAMAT.2017.05.072.

[261] Barba D, Pedrazzini S, Vilalta-Clemente A, Wilkinson AJ, Moody MP, Bagot PAJ, et al. On the composition of microtwins in a single crystal nickel-based superalloy. Scr Mater 2017;127:37–40. https://doi.org/10.1016/J.SCRIPTAMAT.2016.08.029.

[262] Zhang Y, Tao NR, Lu K. Effect of stacking-fault energy on deformation twin thickness in Cu–Al alloys. Scr Mater 2009;60:211–3. https://doi.org/https://doi.org/10.1016/j.scriptamat.2008.10.005.

[263] Mahajan S, Williams DF. Deformation Twinning in Metals and Alloys. International Metallurgical Reviews 1973;18:43–61. https://doi.org/10.1179/imtlr.1973.18.2.43.

[264] Yu Q, Shan Z-W, Li J, Huang X, Xiao L, Sun J, et al. Strong crystal size effect on deformation twinning. Nature 2010 463:7279 2010;463:335–8. https://doi.org/10.1038/nature08692.

[265] Beyerlein IJ, Capolungo L, Marshall PE, McCabe RJ, Tomé CN. Statistical analyses of deformation twinning in magnesium. Philosophical Magazine 2010;90:2161–90. https://doi.org/10.1080/14786431003630835.

[266] Lloyd JT. A dislocation-based model for twin growth within and across grains. Proceedings of the Royal Society A: Mathematical, Physical and Engineering Sciences 2018;474:20170709. https://doi.org/10.1098/rspa.2017.0709.

[267] Grilli N, Cocks ACF, Tarleton E. A phase field model for the growth and characteristic thickness of deformation-induced twins. J Mech Phys Solids 2020;143:104061. https://doi.org/10.1016/j.jmps.2020.104061.

[268] Venables JA. Deformation twinning in face-centred cubic metals. The Philosophical Magazine: A Journal of Theoretical Experimental and Applied Physics 1961;6:379–96. https://doi.org/10.1080/14786436108235892.

[269] Christian JW. Deformation Twinning. The Theory of Transformations in Metals and Alloys, Elsevier; 2002, p. 859–960. https://doi.org/10.1016/B978-008044019-4/50025-8.

[270] Venables JA. The nucleation and propagation of deformation twins. Journal of Physics and Chemistry of Solids 1964;25:693–700. https://doi.org/https://doi.org/10.1016/0022-3697(64)90178-7.

[271] Kauffmann A, Freudenberger J, Geissler D, Yin S, Schillinger W, Sarma VS, et al. Severe deformation twinning in pure copper by cryogenic wire drawing. Acta Mater 2011;59:7816–23. https://doi.org/10.1016/J.ACTAMAT.2011.08.042.

[272] Song SG, Gray GT. Structural interpretation of the nucleation and growth of deformation twins in Zr and Ti—I. Application of the coincidence site lattice (CSL) theory to twinning problems in h.c.p. structures. Acta Metallurgica et Materialia 1995;43:2325–37. https://doi.org/https://doi.org/10.1016/0956-7151(94)00433-1.

[273] Johansson J, Odén M. Load sharing between austenite and ferrite in a duplex stainless steel during cyclic loading. Metallurgical and Materials Transactions A 2000;31:1557–70. https://doi.org/10.1007/s11661-000-0166-3.

[274] Marrow TJ, King JE. Fatigue crack propagation mechanisms in a thermally aged duplex stainless steel. Materials Science and Engineering: A 1994;183:91–101. https://doi.org/https://doi.org/10.1016/0921-5093(94)90893-1.

[275] Marrow TJ. The fracture mechanism in 475°C embrittled ferritic stainless steels. Fatigue Fract Eng Mater Struct 1996;19:919–33. https://doi.org/10.1111/j.1460-2695.1996.tb01027.x.

[276] Johansson J, Odén M. Load sharing between austenite and ferrite in a duplex stainless steel during cyclic loading. Metallurgical and Materials Transactions A 2000;31:1557–70. https://doi.org/10.1007/s11661-000-0166-3.

[277] Christian JW, Mahajan S. Deformation twinning. Prog Mater Sci 1995;39:1–157. https://doi.org/10.1016/0079-6425(94)00007-7.

[278] Venables JA. The nucleation and propagation of deformation twins. Journal of Physics and Chemistry of Solids 1964;25:693–700. https://doi.org/https://doi.org/10.1016/0022-3697(64)90178-7.

[279] Reid CN. The association of twinning and fracture in bcc metals. Metallurgical Transactions A 1981;12:371–7. https://doi.org/10.1007/BF02648534.

[280] Marrow TJ, Harris C. The fracture mechanism of 475°C embrittlement in a duplex stainless steel. Fatigue Fract Eng Mater Struct 1996;19:935–47. https://doi.org/10.1111/j.1460-2695.1996.tb01028.x.

[281] Sleeswyk AW. Emissary dislocations: Theory and experiments on the propagation of deformation twins in α-iron. Acta Metallurgica 1962;10:705–25. https://doi.org/https://doi.org/10.1016/0001-6160(62)90040-8.

[282] Spreadborough J, Langheinrich D, Anderson E, Brandon D. Etch-Pit Observations Concerning Twins in Iron and Iron Alloys. J Appl Phys 1964;35:3585–7. https://doi.org/10.1063/1.1713275.

[283] Guo Y, Abdolvand H, Britton TB, Wilkinson AJ. Growth of {112¯2} twins in titanium: A combined experimental and modelling investigation of the local state of deformation. Acta Mater 2017;126:221–35. https://doi.org/10.1016/J.ACTAMAT.2016.12.066.

[284] Baxevanakis KP, Gourgiotis PA, Georgiadis HG. Interaction of cracks with dislocations in couple-stress elasticity. Part I: Opening mode. Int J Solids Struct 2017;118–119:179–91. https://doi.org/10.1016/J.IJSOLSTR.2017.03.019.

[285] Kacher J, Sabisch JE, Minor AM. Statistical analysis of twin/grain boundary interactions in pure rhenium. Acta Mater 2019. https://doi.org/10.1016/J.ACTAMAT.2019.04.051.

[286] Lagerlöf KPD, Castaing J, Pirouz P, Heuer AH. Nucleation and growth of deformation twins: A perspective based on the double-cross-slip mechanism of deformation twinning. Philosophical Magazine A 2002;82:2841–54. https://doi.org/10.1080/01418610208240069.

[287] Mahajan S, Williams DF. Deformation Twinning in Metals and Alloys. International Metallurgical Reviews 1973;18:43–61. https://doi.org/10.1179/imtlr.1973.18.2.43.

[288] Wang S, Schuman C, Bao L, Lecomte JS, Zhang Y, Raulot JM, et al. Variant selection criterion for twin variants in titanium alloys deformed by rolling. Acta Mater 2012;60:3912–9. https://doi.org/10.1016/J.ACTAMAT.2012.03.046.

[289] Kacher J, Sabisch JE, Minor AM. Statistical analysis of twin/grain boundary interactions in pure rhenium. Acta Mater 2019. https://doi.org/10.1016/J.ACTAMAT.2019.04.051.

[290] Baxevanakis KP, Gourgiotis PA, Georgiadis HG. Interaction of cracks with dislocations in couple-stress elasticity. Part I: Opening mode. Int J Solids Struct 2017;118–119:179–91. https://doi.org/10.1016/J.IJSOLSTR.2017.03.019.

[291] Gong M, Hirth JP, Liu Y, Shen Y, Wang J. Interface structures and twinning mechanisms of twins in hexagonal metals. Mater Res Lett 2017;5:449–64. https://doi.org/10.1080/21663831.2017.1336496.

[292] Wang Y, Li J. Phase field modeling of defects and deformation. Acta Mater 2010;58:1212–35. https://doi.org/https://doi.org/10.1016/j.actamat.2009.10.041.

[293] Eshelby JD. The force on an elastic singularity. Philosophical Transactions of the Royal Society of London Series A, Mathematical and Physical Sciences 1951;244:87–112. https://doi.org/10.1098/rsta.1951.0016.

[294] Eshelby JD, Peierls RE. The determination of the elastic field of an ellipsoidal inclusion, and related problems. Proc R Soc Lond A Math Phys Sci 1957;241:376–96. https://doi.org/10.1098/rspa.1957.0133.

[295] Venables JA. The electron microscopy of deformation twinning. Journal of Physics and Chemistry of Solids 1964;25:685–92. https://doi.org/10.1016/0022-3697(64)90177-5.

[296] Britton TB, Wilkinson AJ. Stress fields and geometrically necessary dislocation density distributions near the head of a blocked slip band. Acta Mater 2012;60:5773–82. https://doi.org/10.1016/j.actamat.2012.07.004.

[297] Guo Y, Britton TB, Wilkinson AJ. Slip band–grain boundary interactions in commercial-purity titanium. Acta Mater 2014;76:1–12. https://doi.org/10.1016/J.ACTAMAT.2014.05.015.

[298] Stinville JC, Vanderesse N, Bridier F, Bocher P, Pollock TM. High resolution mapping of strain localization near twin boundaries in a nickel-based superalloy. Acta Mater 2015;98:29–42. https://doi.org/https://doi.org/10.1016/j.actamat.2015.07.016.

[299] Earp PD, Barhli SM, Marrow TJ. Full-field characterisation of the stress concentration of blocked twins by high-resolution EBSD in alpha-uranium. ICF 2017 - 14th International Conference on Fracture, vol. 2, Rhodes; Greece: ICF 2017; 2017, p. 128–9.

[300] Marrow TJ, Humphreys AO, Strangwood M. The Crack Initiation Toughness for Brittle Fracture of Super Duplex Stainless Steel. Fatigue Fract Eng Mater Struct 1997;20:1005–14. https://doi.org/https://doi.org/10.1111/j.1460-2695.1997.tb01543.x.

[301] Collins TJ. ImageJ for microscopy. Biotechniques 2007;43:S25–30. https://doi.org/10.2144/000112517.

[302] Arganda-Carreras I, Kaynig V, Rueden C, Eliceiri KW, Schindelin J, Cardona A, et al. Trainable Weka Segmentation: a machine learning tool for microscopy pixel classification. Bioinformatics 2017;33:2424–6. https://doi.org/10.1093/bioinformatics/btx180.

[303] Du C, Maresca F, Geers MGD, Hoefnagels JPM. Ferrite slip system activation investigated by uniaxial micro-tensile tests and simulations. Acta Mater 2018;146:314–27. https://doi.org/https://doi.org/10.1016/j.actamat.2017.12.054.

[304] Cepeda-Jiménez CM, Molina-Aldareguia JM, Pérez-Prado MT. EBSD-Assisted Slip Trace Analysis During In Situ SEM Mechanical Testing: Application to Unravel Grain Size Effects on Plasticity of Pure Mg Polycrystals. JOM 2016;68:116–26. https://doi.org/10.1007/s11837-015-1521-6.

[305] Bond WL. The Mathematics of the Physical Properties of Crystals. Bell System Technical Journal 1943;22:1–72. https://doi.org/10.1002/j.1538-7305.1943.tb01304.x.

[306] Kim SA, Johnson WL. Elastic constants and internal friction of martensitic steel, ferritic-pearlitic steel, and α-iron. Materials Science and Engineering: A 2007;452–453:633–9. https://doi.org/10.1016/j.msea.2006.11.147.

[307] Salvati E, Sui T, Korsunsky AM. Uncertainty quantification of residual stress evaluation by the FIB–DIC ring-core method due to elastic anisotropy effects. Int J Solids Struct 2016;87:61–9. https://doi.org/https://doi.org/10.1016/j.ijsolstr.2016.02.031.

[308] Dunne FPE, Rugg D, Walker A. Lengthscale-dependent, elastically anisotropic, physically-based hcp crystal plasticity: Application to cold-dwell fatigue in Ti alloys. Int J Plast 2007;23:1061–83. https://doi.org/https://doi.org/10.1016/j.ijplas.2006.10.013.

[309] Wawrzynek PA, Carter BJ, Banks-Sills L. The M-integral for Computing Stress Intensity Factors in Generally Anisotropic Materials. Hanover, MD: 2005.

[310] Voigt W. Lehrbuch der kristallphysik:(mit ausschluss der kristalloptik). vol. 34. BG Teubner; 1910.

[311] Reuss A. Berechnung der Fließgrenze von Mischkristallen auf Grund der Plastizitätsbedingung für Einkristalle . ZAMM - Journal of Applied Mathematics and Mechanics / Zeitschrift Für Angewandte Mathematik Und Mechanik 1929;9:49–58. https://doi.org/https://doi.org/10.1002/zamm.19290090104.

[312] Takeuchi T. Dynamic Propagation of Deformation Twins in Iron Single Crystals. J Physical Soc Japan 1966;21:2616–22. https://doi.org/10.1143/JPSJ.21.2616.

[313] Luster J, Morris MA. Compatibility of deformation in two-phase Ti-Al alloys: Dependence on microstructure and orientation relationships. Metallurgical and Materials Transactions A 1995;26:1745–56. https://doi.org/10.1007/BF02670762.

[314] Roters F, Eisenlohr P, Hantcherli L, Tjahjanto DD, Bieler TR, Raabe D. Overview of constitutive laws, kinematics, homogenization and multiscale methods in crystal

plasticity finite-element modeling: Theory, experiments, applications. Acta Mater 2010;58:1152–211. https://doi.org/https://doi.org/10.1016/j.actamat.2009.10.058.

[315] Bieler TR, Eisenlohr P, Roters F, Kumar D, Mason DE, Crimp MA, et al. The role of heterogeneous deformation on damage nucleation at grain boundaries in single phase metals. Int J Plast 2009;25:1655–83. https://doi.org/https://doi.org/10.1016/j.ijplas.2008.09.002.

[316] Taylor GI. The mechanism of plastic deformation of crystals. Part I.—Theoretical. Proceedings of the Royal Society of London Series A 1934;145:362 LP – 387.

[317] Taylor GI. Plastic Strain in Metals. Lecture to the Institute of Metals 1938;62:307–24.

[318] Schneider CA, Rasband WS, Eliceiri KW. NIH Image to ImageJ: 25 years of image analysis. Nat Methods 2012;9:671–5. https://doi.org/10.1038/nmeth.2089.

[319] Yoneyama S, Morimoto Y, Takashi M. Automatic Evaluation of Mixed-mode Stress Intensity Factors Utilizing Digital Image Correlation. Strain 2006;42:21–9. https://doi.org/https://doi.org/10.1111/j.1475-1305.2006.00246.x.

[320] Marshall PE, Proust G, Rogers JT, McCabe RJ. Automatic twin statistics from electron backscattered diffraction data. J Microsc 2010;238:218–29. https://doi.org/https://doi.org/10.1111/j.1365-2818.2009.03343.x.

[321] Griffiths AJ V, Walther T. Quantification of carbon contamination under electron beam irradiation in a scanning transmission electron microscope and its suppression by plasma cleaning. J Phys Conf Ser 2010;241:012017. https://doi.org/10.1088/1742-6596/241/1/012017.

[322] Britton TB, Maurice C, Fortunier R, Driver JH, Day AP, Meaden G, et al. Factors affecting the accuracy of high resolution electron backscatter diffraction when using simulated patterns. Ultramicroscopy 2010;110:1443–53. https://doi.org/10.1016/j.ultramic.2010.08.001.

[323] Jenčuš P, Polák J, Lukáš P, Muránsky O. In situ neutron diffraction study of the low cycle fatigue of the α−γ duplex stainless steel. Physica B Condens Matter 2006;385–386:597–9. https://doi.org/10.1016/J.PHYSB.2006.06.109.

[324] Clausen B, Lorentzen T, Bourke MAM, Daymond MR. Lattice strain evolution during uniaxial tensile loading of stainless steel. Materials Science and Engineering: A 1999;259:17–24. https://doi.org/https://doi.org/10.1016/S0921-5093(98)00878-8.

[325] Chatterjee K, Venkataraman A, Garbaciak T, Rotella J, Sangid MD, Beaudoin AJ, et al. Study of grain-level deformation and residual stresses in Ti-7Al under combined bending and tension using high energy diffraction microscopy (HEDM). Int J Solids Struct 2016;94–95:35–49. https://doi.org/10.1016/j.ijsolstr.2016.05.010.

[326] Gadalińska E, Baczmański A, Wroński S, Le Joncour L, Braham C, François M, et al. Direct determination of phase stress evolution in duplex steel using synchrotron diffraction. Materials Science and Engineering: A 2021;801:140355. https://doi.org/https://doi.org/10.1016/j.msea.2020.140355.

[327] Meyers MA, Vöhringer O, Lubarda VA. The onset of twinning in metals: a constitutive description. Acta Mater 2001;49:4025–39. https://doi.org/10.1016/S1359-6454(01)00300-7.

[328] Song SG, Gray GT. Structural interpretation of the nucleation and growth of deformation twins in Zr and Ti—I. Application of the coincidence site lattice (CSL) theory to twinning problems in h.c.p. structures. Acta Metallurgica et Materialia 1995;43:2325–37. https://doi.org/https://doi.org/10.1016/0956-7151(94)00433-1.

[329] Xu D-S, Chang J-P, Li J, Yang R, Li D, Yip S. Dislocation slip or deformation twinning: confining pressure makes a difference. Materials Science and Engineering: A 2004;387–389:840–4. https://doi.org/https://doi.org/10.1016/j.msea.2004.01.128.

[330] Gao Y, Zhang Y, Wang Y. Determination of twinning path from broken symmetry: A revisit to deformation twinning in bcc metals. Acta Mater 2020;196:280–94. https://doi.org/https://doi.org/10.1016/j.actamat.2020.06.031.

[331] He Z, Kotousov A. On Evaluation of Stress Intensity Factor from In-Plane and Transverse Surface Displacements. Exp Mech 2016;56:1385–93. https://doi.org/10.1007/s11340-016-0176-8.

[332] Wang L, Barabash R, Bieler T, Liu W, Eisenlohr P. Study of $$ \{ 11\bar{2} 1\} $$Twinning in α-Ti by EBSD and Laue Microdiffraction. Metallurgical and Materials Transactions A 2013;44:3664–74. https://doi.org/10.1007/s11661-013-1714-y.

[333] Karlsson A, Bäcklund J. J-integral at loaded crack surfaces. Int J Fract 1978;14. https://doi.org/10.1007/BF00116006.

[334] Song H, Rahman SS. An extended J-integral for evaluating fluid-driven cracks in hydraulic fracturing. Journal of Rock Mechanics and Geotechnical Engineering 2018;10:832–43. https://doi.org/https://doi.org/10.1016/j.jrmge.2018.04.009.

[335] Grilli N, Tarleton E, Edmondson PD, Gussev MN, Cocks ACF. In situ measurement and modelling of the growth and length scale of twins in α-uranium. Phys Rev Mater 2020;4:43605. https://doi.org/10.1103/PhysRevMaterials.4.043605.

[336] Qiao H, Barnett MR, Wu PD. Modeling of twin formation, propagation and growth in a Mg single crystal based on crystal plasticity finite element method. Int J Plast 2016;86:70–92. https://doi.org/https://doi.org/10.1016/j.ijplas.2016.08.002.

[337] Korsunsky AM. Elastic and Inelastic Deformation and Residual Stress. A Teaching Essay on Residual Stresses and Eigenstrains 2017:5–20. https://doi.org/10.1016/B978-0-12-810990-8.00002-1.

[338] Wilson D, Zheng Z, Dunne FPE. A microstructure-sensitive driving force for crack growth. J Mech Phys Solids 2018;121:147–74. https://doi.org/https://doi.org/10.1016/j.jmps.2018.07.005.

[339] Liu J, Lyons J, Sutton M, Reynolds A. Experimental Characterization of Crack Tip Deformation Fields in Alloy 718 at High Temperatures. J Eng Mater Technol 1998;120:71–8. https://doi.org/10.1115/1.2806840.

[340] Réthoré J, Roux S, Hild F. Noise-robust stress intensity factor determination from kinematic field measurements. Eng Fract Mech 2008;75:3763–81. https://doi.org/10.1016/j.engfracmech.2007.04.018.

[341] Panchal JH, Kalidindi SR, McDowell DL. Key computational modeling issues in Integrated Computational Materials Engineering. Computer-Aided Design 2013;45:4–25. https://doi.org/https://doi.org/10.1016/j.cad.2012.06.006.

[342] Chen B, Jiang J, Dunne FPE. Microstructurally-sensitive fatigue crack nucleation in Ni-based single and oligo crystals. J Mech Phys Solids 2017;106:15–33. https://doi.org/https://doi.org/10.1016/j.jmps.2017.05.012.

[343] McDowell DL, Dunne FPE. Microstructure-sensitive computational modeling of fatigue crack formation. Int J Fatigue 2010;32:1521–42. https://doi.org/https://doi.org/10.1016/j.ijfatigue.2010.01.003.

[344] Pokharel R, Lind J, Kanjarla AK, Lebensohn RA, Li SF, Kenesei P, et al. Polycrystal Plasticity: Comparison Between Grain - Scale Observations of Deformation and Simulations. Annu Rev Condens Matter Phys 2014;5:317–46. https://doi.org/10.1146/annurev-conmatphys-031113-133846.

[345] Chandrasekaran D, Nygårds M. A study of the surface deformation behaviour at grain boundaries in an ultra-low-carbon steel. Acta Mater 2003;51:5375–84. https://doi.org/https://doi.org/10.1016/S1359-6454(03)00394-X.

[346] Zhang M, Bridier F, Villechaise P, Mendez J, McDowell DL. Simulation of slip band evolution in duplex Ti–6Al–4V. Acta Mater 2010;58:1087–96. https://doi.org/https://doi.org/10.1016/j.actamat.2009.10.025.

[347] Dunne FPE. Fatigue crack nucleation: Mechanistic modelling across the length scales. Curr Opin Solid State Mater Sci 2014;18:170–9. https://doi.org/10.1016/J.COSSMS.2014.02.005.

[348] Wang Y, Li J. Phase field modeling of defects and deformation. Acta Mater 2010;58:1212–35. https://doi.org/https://doi.org/10.1016/j.actamat.2009.10.041.

[349] Fleck M, Querfurth F, Glatzel U. Phase field modeling of solidification in multi-component alloys with a case study on the Inconel 718 alloy. J Mater Res 2017;32:4605–15. https://doi.org/DOI: 10.1557/jmr.2017.393.

[350] Zheng H, Cao A, Weinberger CR, Huang JY, Du K, Wang J, et al. Discrete plasticity in sub-10-nm-sized gold crystals. Nat Commun 2010;1:144. https://doi.org/10.1038/ncomms1149.

[351] Fisher JC, Hart EW, Pry RH. Theory of Slip-Band Formation. Physical Review 1952;87:958–61. https://doi.org/10.1103/PhysRev.87.958.

[352] Andani MT, Lakshmanan A, Sundararaghavan V, Allison J, Misra A. Quantitative study of the effect of grain boundary parameters on the slip system level Hall-Petch slope for basal slip system in Mg-4Al. Acta Mater 2020;200:148–61. https://doi.org/https://doi.org/10.1016/j.actamat.2020.08.079.

[353] Livingston JD, Chalmers B. Multiple slip in bicrystal deformation. Acta Metallurgica 1957;5:322–7. https://doi.org/10.1016/0001-6160(57)90044-5.

[354] Lee TC, Robertson IM, Birnbaum HK. Prediction of slip transfer mechanisms across grain boundaries. Scripta Metallurgica 1989;23:799–803. https://doi.org/10.1016/0036-9748(89)90534-6.

[355] Koss DA, Chan KS. Fracture along planar slip bands. Acta Metallurgica 1980;28:1245–52. https://doi.org/https://doi.org/10.1016/0001-6160(80)90080-2.

[356] Lukáš P, Klesnil M, Krejčí J. Dislocations and Persistent Slip Bands in Copper Single Crystals Fatigued at Low Stress Amplitude. Physica Status Solidi (b) 1968;27:545–58. https://doi.org/10.1002/pssb.19680270212.

[357] Tu S-T, Zhang X-C. Fatigue Crack Initiation Mechanisms. Reference Module in Materials Science and Materials Engineering, Elsevier; 2016. https://doi.org/10.1016/B978-0-12-803581-8.02852-6.

[358] Rice JR. Tensile crack tip fields in elastic-ideally plastic crystals. Mechanics of Materials 1987;6:317–35. https://doi.org/https://doi.org/10.1016/0167-6636(87)90030-5.

[359] Makin MJ. The mechanism of slip band growth in irradiated crystals. Https://DoiOrg/101080/14786437008238467 2006;21:815–7. https://doi.org/10.1080/14786437008238467.

[360] Anderson PM, Hirth JP, Lothe J. Theory of Straight Dislocations. Theory of dislocations. Third, New York: Cambridge University Press; 2017, p. 85–9.

[361] Agiasofitou E, Lazar M. A new insight into the J-, M-, and L-integrals of dislocations. PAMM 2018;18:e201800159. https://doi.org/10.1002/PAMM.201800159.

[362] Eshelby JD. Energy Relations and the Energy-Momentum Tensor in Continuum Mechanics. In: Ball JM, Kinderlehrer D, Podio-Guidugli P, Slemrod M, editors. Fundamental Contributions to the Continuum Theory of Evolving Phase Interfaces in Solids, Berlin, Heidelberg: Springer Berlin Heidelberg; 1999, p. 82–119. https://doi.org/10.1007/978-3-642-59938-5_5.

[363] Hussain MA, Pu SL, Underwood J. Strain Energy Release Rate for a Crack Under Combined Mode I and Mode II. In: Irwin GR, editor. Fracture Analysis: Proceedings of the 1973 National Symposium on Fracture Mechanics, Part II, West Conshohocken, PA: ASTM International; 1974, p. 2–28. https://doi.org/10.1520/STP33130S.

[364] Golebiewska Herrmann A, Herrmann G. On Energy-Release Rates for a Plane Crack. J Appl Mech 1981;48:525–8. https://doi.org/10.1115/1.3157667.

[365] Park JH, Earmme YY. Application of conservation integrals to interfacial crack problems. Mechanics of Materials 1986;5:261–76. https://doi.org/https://doi.org/10.1016/0167-6636(86)90023-2.

[366] Chen Y-H, Lu TJ. Recent developments and applications of invariant integrals . Appl Mech Rev 2003;56:515–52. https://doi.org/10.1115/1.1582199.

[367] Nishioka T, Atluri SN. On the computation of mixed-mode K-factors for a dynamically propagating crack, using path-independent integrals J'k. Eng Fract Mech 1984;20:193–208. https://doi.org/10.1016/0013-7944(84)90128-0.

[368] Nikishkov GP, Atluri SN. Calculation of fracture mechanics parameters for an arbitrary three-dimensional crack, by the 'equivalent domain integral' method. Int J Numer Methods Eng 1987;24:1801–21. https://doi.org/https://doi.org/10.1002/nme.1620240914.

[369] Richard HA, Schramm B, Schirmeisen NH. Cracks on Mixed Mode loading – Theories, experiments, simulations. Int J Fatigue 2014;62:93–103. https://doi.org/10.1016/J.IJFATIGUE.2013.06.019.

[370] Wright SI, Nowell MM, de Kloe R, Camus P, Rampton T. Electron imaging with an EBSD detector. Ultramicroscopy 2015;148:132–45. https://doi.org/10.1016/j.ultramic.2014.10.002.

[371] Ruggles TJ, Fullwood DT, Kysar JW. Resolving geometrically necessary dislocation density onto individual dislocation types using EBSD-based continuum dislocation microscopy. Int J Plast 2016;76:231–43. https://doi.org/10.1016/J.IJPLAS.2015.08.005.

[372] Bachmann F, Hielscher R, Schaeben H. Grain detection from 2d and 3d EBSD data—Specification of the MTEX algorithm. Ultramicroscopy 2011;111:1720–33. https://doi.org/https://doi.org/10.1016/j.ultramic.2011.08.002.

[373] Zaefferer S. On the formation mechanisms, spatial resolution and intensity of backscatter Kikuchi patterns. Ultramicroscopy 2007;107:254–66. https://doi.org/https://doi.org/10.1016/j.ultramic.2006.08.007.

[374] Weiss S, Klement U. Orientation determination on non planar surfaces. Proceedings of the Channel Users Meeting, Ribe, Denmark 2004:9–11.

[375] Lord JD, Roebuck B, Morrell R, Lube T. 25 year perspective Aspects of strain and strength measurement in miniaturised testing for engineering metals and ceramics. Materials Science and Technology 2010;26:127–48. https://doi.org/10.1179/026708309X12584564052012.

[376] Ruggles TJ, Yoo YSJ, Dunlap BE, Crimp MA, Kacher J. Correlating results from high resolution EBSD with TEM- and ECCI-based dislocation microscopy: Approaching single

dislocation sensitivity via noise reduction. Ultramicroscopy 2020;210:112927. https://doi.org/https://doi.org/10.1016/j.ultramic.2019.112927.

[377] Ruggles T. Characterization of Geometrically Necessary Dislocation Content with EBSD-Based Continuum Dislocation Microscopy. 2015.

[378] Hull D, David J. Bacon. Introduction to dislocations. vol. 37. 2nd ed. Elsevier; 2011.

[379] Tang YT, D'Souza N, Roebuck B, Karamched P, Panwisawas C, Collins DM. Ultra-high temperature deformation in a single crystal superalloy: Mesoscale process simulation and micromechanisms. Acta Mater 2021;203:116468. https://doi.org/10.1016/J.ACTAMAT.2020.11.010.

[380] Bordín SF, Limandri S, Ranalli JM, Castellano G. EBSD spatial resolution for detecting sigma phase in steels. Ultramicroscopy 2016;171:177–85. https://doi.org/https://doi.org/10.1016/j.ultramic.2016.09.010.

[381] Hovington P, Drouin D, Gauvin R. CASINO: A new monte carlo code in C language for electron beam interaction —part I: Description of the program. Scanning 1997;19:1–14. https://doi.org/https://doi.org/10.1002/sca.4950190101.

[382] Schmidt-Rieder E, Ashworth M, Farr JPG. The effect of nitrogen on the stability of the passive film on a zeron 100 super duplex stainless steel. Electrochemical and Solid-State Letters 1999;2:19–21. https://doi.org/10.1149/1.1390720/XML.

[383] Helm JD, McNeill SR, Sutton MA. Improved three-dimensional image correlation for surface displacement measurement. Https://DoiOrg/101117/1600624 1996;35:1911–20. https://doi.org/10.1117/1.600624.

[384] Chen KL, Atluri SN. Comparison of different methods of evaluation of weight functions for 2-D mixed-mode fracture analyses. Eng Fract Mech 1989;34:935–56. https://doi.org/10.1016/0013-7944(89)90230-0.

[385] Nishioka T, Atluri SNN. On the computation of mixed-mode for a dynamically propagating crack, using path-independent integrals. Eng Fract Mech 1984;20:193–208. https://doi.org/10.1016/0013-7944(84)90128-0.

[386] Huber O, Nickel J, Kuhn G. On the decomposition of the J-integral for 3D crack problems. Int J Fract 1993;64:339–48. https://doi.org/10.1007/BF00017849.

[387] Shivakumar KN, Raju IS. An equivalent domain integral method for three-dimensional mixed-mode fracture problems. Eng Fract Mech 1992;42:935–59. https://doi.org/https://doi.org/10.1016/0013-7944(92)90134-Z.

[388] Rigby RH, Aliabadi MH. Decomposition of the mixed-mode J-integral—revisited. Int J Solids Struct 1998;35:2073–99. https://doi.org/https://doi.org/10.1016/S0020-7683(97)00171-6.

[389] Wang SS, Yau JF. Interfacial cracks in adhesively bonded scarf joints. AIAA Journal 1981;19:1350–6. https://doi.org/10.2514/3.7865.

[390] Ishikawa H, Kitagawa H, Okamura H. J integral of a mixed mode crack and its application. Mechanical Behaviour of Materials, vol. 3, Elsevier; 1980, p. 447–55. https://doi.org/10.1016/B978-1-4832-8414-9.50137-1.

[391] Arfken GB, Weber HJ, Harris FE. Rotation in R3. Mathematical Methods for Physicists: A Comprehensive Guide. 7th ed., Academic Press; 2013, p. 139–41.

[392] Melcher A, Unser A, Reichhardt M, Nestler B, Pötschke M, Selzer M. Conversion of EBSD data by a quaternion based algorithm to be used for grain structure simulations. Technische Mechanik 2010;30.

[393] Ben-Ari M. A Tutorial on Euler Angles and Quaternions. 2014.

[394] Schwarzer RA, Hjelen J. Backscattered Electron Imaging with an EBSD Detector. Micros Today 2015;23:12–7. https://doi.org/10.1017/S1551929514001333.

[395] Saylor DM, El-Dasher BS, Adams BL, Rohrer GS. Measuring the five-parameter grain-boundary distribution from observations of planar sections. Metallurgical and Materials Transactions A 2004;35:1981–9. https://doi.org/10.1007/s11661-004-0147-z.

[396] Bartali A El, Aubin V, Degallaix S. Surface observation and measurement techniques to study the fatigue damage micromechanisms in a duplex stainless steel. Int J Fatigue 2009;31:2049–55. https://doi.org/https://doi.org/10.1016/j.ijfatigue.2008.11.003.

[397] Jiang R, Pierron F, Octaviani S, Reed PAS. Characterisation of strain localisation processes during fatigue crack initiation and early crack propagation by SEM-DIC in an advanced disc alloy. Materials Science and Engineering: A 2017;699:128–44. https://doi.org/10.1016/J.MSEA.2017.05.091.

[398] Niblack W. An Introduction to Digital Image Processing. DNK: Strandberg Publishing Company; 1985.

[399] Du J, Mompiou F, Zhang W-Z. In-situ TEM study of dislocation emission associated with austenite growth. Scr Mater 2018;145:62–6. https://doi.org/https://doi.org/10.1016/j.scriptamat.2017.10.014.

[400] Xie KY, Wang Y, Ni S, Liao X, Cairney JM, Ringer SP. Insight into the deformation mechanisms of α-Fe at the nanoscale. Scr Mater 2011;65:1037–40. https://doi.org/https://doi.org/10.1016/j.scriptamat.2011.08.023.

[401] Kiener D, Minor AM. Source-controlled yield and hardening of Cu(100) studied by in situ transmission electron microscopy. Acta Mater 2011;59:1328–37. https://doi.org/https://doi.org/10.1016/j.actamat.2010.10.065.

[402] Howell D, Wood IG, Dobson DP, Jones AP, Nasdala L, Harris JW. Quantifying strain birefringence halos around inclusions in diamond. Contributions to Mineralogy and Petrology 2010;160:705–17. https://doi.org/10.1007/s00410-010-0503-5.

[403] Larrouy B, Villechaise P, Cormier J, Berteaux O. Grain boundary–slip bands interactions: Impact on the fatigue crack initiation in a polycrystalline forged Ni-based superalloy. Acta Mater 2015;99:325–36. https://doi.org/https://doi.org/10.1016/j.actamat.2015.08.009.

[404] Cottrell AH. LX. The formation of immobile dislocations during slip. The London, Edinburgh, and Dublin Philosophical Magazine and Journal of Science 1952;43:645–7. https://doi.org/10.1080/14786440608520220.

[405] Konijnenberg PJ, Zaefferer S, Raabe D. Assessment of geometrically necessary dislocation levels derived by 3D EBSD. Acta Mater 2015;99:402–14. https://doi.org/10.1016/j.actamat.2015.06.051.

[406] Korsunsky AM. Dislocations. A Teaching Essay on Residual Stresses and Eigenstrains 2017:79–92. https://doi.org/10.1016/B978-0-12-810990-8.00007-0.

[407] Pharr GM, Herbert EG, Gao Y. The Indentation Size Effect: A Critical Examination of Experimental Observations and Mechanistic Interpretations 2010. https://doi.org/10.1146/annurev-matsci-070909-104456.

[408] Barabash R, Gao Y, Sun Y, Lee SY, Choo H, Liaw PK, et al. Neutron and X-ray diffraction studies and cohesive interface model of the fatigue crack deformation behavior. Http://DxDoiOrg/101080/09500830802311080 2008;88:553–65. https://doi.org/10.1080/09500830802311080.

[409] Yu H, Liu J, Karamched P, Wilkinson AJ, Hofmann F. Mapping the full lattice strain tensor of a single dislocation by high angular resolution transmission Kikuchi diffraction (HR-TKD). Scr Mater 2019;164:36–41. https://doi.org/https://doi.org/10.1016/j.scriptamat.2018.12.039.

[410] McLean MJ, Osborn WA. In-situ elastic strain mapping during micromechanical testing using EBSD. Ultramicroscopy 2018;185:21–6. https://doi.org/10.1016/J.ULTRAMIC.2017.11.007.

[411] Zielinski W, Lii MJ, Gerberich WW. Crack-tip dislocation emission arrangements for equilibrium —I. In situ TEM observations of Fe2wt%Si. Acta Metallurgica et Materialia 1992;40:2861–71. https://doi.org/https://doi.org/10.1016/0956-7151(92)90451-J.

[412] Bei H, Shim S, Miller MK, Pharr GM, George EP. Effects of focused ion beam milling on the nanomechanical behavior of a molybdenum-alloy single crystal. Appl Phys Lett 2007;91:111915. https://doi.org/10.1063/1.2784948.

[413] Bei H, Shim S, Pharr GM, George EP. Effects of pre-strain on the compressive stress–strain response of Mo-alloy single-crystal micropillars. Acta Mater 2008;56:4762–70. https://doi.org/https://doi.org/10.1016/j.actamat.2008.05.030.

[414] Uchic MD, Shade PA, Dimiduk DM. Plasticity of Micrometer-Scale Single Crystals in Compression. Annu Rev Mater Res 2009;39:361–86. https://doi.org/10.1146/annurev-matsci-082908-145422.

[415] di Gioacchino F, Edwards TEJ, Wells GN, Clegg WJ. A new mechanism of strain transfer in polycrystals. Scientific Reports 2020 10:1 2020;10:1–15. https://doi.org/10.1038/s41598-020-66569-7.

[416] Lauener CM, Petho L, Chen M, Xiao Y, Michler J, Wheeler JM. Fracture of Silicon: Influence of rate, positioning accuracy, FIB machining, and elevated temperatures on toughness measured by pillar indentation splitting. Mater Des 2018;142:340–9. https://doi.org/10.1016/J.MATDES.2018.01.015.

[417] Hofmann F, Tarleton E, Harder RJ, Phillips NW, Ma P-W, Clark JN, et al. 3D lattice distortions and defect structures in ion-implanted nano-crystals. Sci Rep 2017;7:45993.

[418] Sernicola G, Giovannini T, Patel P, Kermode JR, Balint DS, Britton T ben, et al. In situ stable crack growth at the micron scale. Nat Commun 2017;8. https://doi.org/10.1038/s41467-017-00139-w.

[419] Morrell BREBLL; R. Measurement Good Practice Guide No 9: Palmqvist Toughness for Hard and Brittle Materials. Teddington: 2008.

[420] Koko A, Elmukashfi E, Wilkinson AJ, Marrow TJ. J-integral analysis of the strain fields of micro-cracks in single silicon crystal using HR-EBSD 2021.

[421] Luan X, Qin H, Liu F, Dai Z, Yi Y, Li Q. The Mechanical Properties and Elastic Anisotropies of Cubic Ni3Al from First Principles Calculations. Crystals (Basel) 2018;8. https://doi.org/10.3390/cryst8080307.

[422] Rigby RH, Aliabadi MH. Mixed-mode J-integral method for analysis of 3D fracture problems using BEM. Eng Anal Bound Elem 1993;11:239–56. https://doi.org/10.1016/0955-7997(93)90026-H.

[423] Cook RF. Strength and sharp contact fracture of silicon. J Mater Sci 2006;41:841–72. https://doi.org/10.1007/s10853-006-6567-y.

[424] Masolin A, Bouchard P-O, Martini R, Bernacki M. Thermo-mechanical and fracture properties in single-crystal silicon. J Mater Sci 2013;48:979–88. https://doi.org/10.1007/s10853-012-6713-7.

[425] Tanaka M, Higashida K, Nakashima H, Takagi H, Fujiwara M. Orientation dependence of fracture toughness measured by indentation methods and its relation to surface

energy in single crystal silicon. International Journal of Fracture 2006 139:3 2006;139:383–94. https://doi.org/10.1007/S10704-006-0021-7.

[426] Ebrahimi F, Kalwani L. Fracture anisotropy in silicon single crystal. Materials Science and Engineering: A 1999;268:116–26. https://doi.org/10.1016/S0921-5093(99)00077-5.

[427] Danilewsky A, Wittge J, Kiefl K, Allen D, McNally P, Garagorri J, et al. Crack propagation and fracture in silicon wafers under thermal stress. J Appl Crystallogr 2013;46:849–55. https://doi.org/10.1107/S0021889813003695/XZ5004SUP1.WMV.

[428] Deegan RD, Chheda S, Patel L, Marder M, Swinney HL, Kim J, et al. Wavy and rough cracks in silicon. Phys Rev E 2003;67:066209. https://doi.org/10.1103/PhysRevE.67.066209.

[429] Suwito W, Dunn ML, Cunningham SJ. Fracture initiation at sharp notches in single crystal silicon. 1998.

[430] Brede M, Hsia KJ, Argon AS. Brittle crack propagation in silicon single crystals. J Appl Phys 1998;70:758. https://doi.org/10.1063/1.349632.

[431] Zhao C, Cai Y, Ding Y, Yang L, Wang Z, Wang Y. Investigation on the crack fracture mode and edge quality in laser dicing of glass-anisotropic silicon double-layer wafer. J Mater Process Technol 2020;275:116356. https://doi.org/10.1016/J.JMATPROTEC.2019.116356.

[432] Wallner H. Linienstrukturen an Bruchflächen. Zeitschrift Für Physik 1939;114:368–78. https://doi.org/10.1007/BF01337002.

[433] Bonamy D, Ravi-Chandar K. Interaction of shear waves and propagating cracks. Phys Rev Lett 2003;91:235502. https://doi.org/10.1103/PHYSREVLETT.91.235502/FIGURES/5/MEDIUM.

[434] Zhao L, Bardel D, Maynadier A, Nelias D. Velocity correlated crack front and surface marks in single crystalline silicon. Nature Communications 2018 9:1 2018;9:1–8. https://doi.org/10.1038/s41467-018-03642-w.

[435] Fineberg J, Gross SP, Marder M, Swinney HL. Instability in dynamic fracture. Phys Rev Lett 1991;67:457. https://doi.org/10.1103/PhysRevLett.67.457.

[436] Sherman D, Sherman D. Energy considerations in crack deflection phenomenon in single crystal silicon. International Journal of Fracture 2006 140:1 2006;140:125–40. https://doi.org/10.1007/S10704-006-0048-9.

[437] Rack A, Scheel M, Danilewsky AN. Real-time direct and diffraction X-ray imaging of irregular silicon wafer breakage. IUCrJ 2016;3:108–14. https://doi.org/10.1107/S205225251502271X/RO5006SUP1.AVI.

[438] Gleizer A, Sherman D. The cleavage energy at initiation of (110) silicon. Int J Fract 2014;187:1–14. https://doi.org/10.1007/S10704-013-9882-8/FIGURES/7.

[439] Pérez R, Gumbsch P. An ab initio study of the cleavage anisotropy in silicon. Acta Mater 2000;48:4517–30. https://doi.org/10.1016/S1359-6454(00)00238-X.

[440] Bouscaud D, Pesci R, Berveiller S, Patoor E. Estimation of the electron beam-induced specimen heating and the emitted X-rays spatial resolution by Kossel microdiffraction

in a scanning electron microscope. Ultramicroscopy 2012;115:115–9. https://doi.org/10.1016/J.ULTRAMIC.2012.01.018.

[441] Glassbrenner CJ, Slack GA. Thermal Conductivity of Silicon and Germanium from 3°K to the Melting Point. Physical Review 1964;134:A1058–69. https://doi.org/10.1103/PhysRev.134.A1058.

[442] Rubanov S, Munroe PR. FIB-induced damage in silicon. J Microsc 2004;214:213–21. https://doi.org/10.1111/j.0022-2720.2004.01327.x.

[443] Hintsala ED, Bhowmick S, Yueyue X, Ballarini R, Asif SAS, Gerberich WW. Temperature dependent fracture initiation in microscale silicon. Scr Mater 2017;130:78–82. https://doi.org/10.1016/J.SCRIPTAMAT.2016.11.016.

[444] Guan L, Tang G, Chu PK. Recent advances and challenges in electroplastic manufacturing processing of metals 2010. https://doi.org/10.1557/JMR.2010.0170.

[445] Gussev MN, Edmondson PD, Leonard KJ. Beam current effect as a potential challenge in SEM-EBSD in situ tensile testing. Mater Charact 2018;146:25–34. https://doi.org/10.1016/J.MATCHAR.2018.09.037.

[446] Lee S-Y, Park KR, Kang S, Lee J-H, Jeon E, Shim C-H, et al. Selective crack suppression during deformation in metal films on polymer substrates using electron beam irradiation. Nat Commun 2019;10. https://doi.org/10.1038/s41467-019-12451-8.

[447] Higashida K, Narita N, Tanaka M, Morikawa T, Miura Y, Onodera R. Crack tip dislocations in silicon characterized by high-voltage electron microscopy.

Http://DxDoiOrg/101080/01418610208240439 2009;82:3263–73. https://doi.org/10.1080/01418610208240439.

[448] Shlyannikov V, Martínez-Pañeda E, Tumanov A, Khamidullin R. Mode I and mode II stress intensity factors and dislocation density behaviour in strain gradient plasticity. Theoretical and Applied Fracture Mechanics 2021;116:103128. https://doi.org/10.1016/J.TAFMEC.2021.103128.

[449] Dhondt G. Mixed-mode K-calculations in anisotropic materials. Eng Fract Mech 2002;69:909–22. https://doi.org/10.1016/S0013-7944(01)00127-8.

[450] Tanaka M, Tarleton E, Roberts SG. The brittle–ductile transition in single-crystal iron. Acta Mater 2008;56:5123–9. https://doi.org/10.1016/J.ACTAMAT.2008.06.025.

[451] Kalácska S, Ast J, Ispánovity PD, Michler J, Maeder X. 3D HR-EBSD Characterization of the plastic zone around crack tips in tungsten single crystals at the micron scale. Acta Mater 2020;200:211–22. https://doi.org/10.1016/J.ACTAMAT.2020.09.009.

[452] Huang JY, E JC, Huang JW, Sun T, Fezzaa K, Xu SL, et al. Dynamic deformation and fracture of single crystal silicon: Fracture modes, damage laws, and anisotropy. Acta Mater 2016;114:136–45. https://doi.org/10.1016/J.ACTAMAT.2016.05.022.

[453] Erdogan F, Sih GC. On the Crack Extension in Plates Under Plane Loading and Transverse Shear. Journal of Basic Engineering 1963;85:519–25. https://doi.org/10.1115/1.3656897.

[454] Sih GC. Strain-energy-density factor applied to mixed mode crack problems. Int J Fract 1974;10:305–21. https://doi.org/10.1007/BF00035493.

[455] Sih GC. Mechanics of fracture initiation and propagation: surface and volume energy density applied as failure criterion. vol. 11. Springer Science & Business Media; 2012.

[456] Nuismer RJ. An energy release rate criterion for mixed mode fracture. Int J Fract 1975;11:245–50.

[457] Palaniswamy K, Knauss WG. II - On the Problem of Crack Extension in Brittle Solids Under General Loading. In: NEMAT-NASSER SBT-MT, editor., Pergamon; 1978, p. 87–148. https://doi.org/https://doi.org/10.1016/B978-0-08-021792-5.50010-0.

[458] Chang J, Xu J, Mutoh Y. A general mixed-mode brittle fracture criterion for cracked materials. Eng Fract Mech 2006;73:1249–63. https://doi.org/10.1016/J.ENGFRACMECH.2005.12.011.

[459] Smith DJ, Ayatollahi MR, Pavier MJ. The role of T-stress in brittle fracture for linear elastic materials under mixed-mode loading. Fatigue Fract Eng Mater Struct 2001;24:137–50. https://doi.org/10.1046/j.1460-2695.2001.00377.x.

[460] Maiti SK, Smith RA. Comparison of the criteria for mixed mode brittle fracture based on the preinstability stress-strain field Part I: Slit and elliptical cracks under uniaxial tensile loading. Int J Fract 1983;23:281–95. https://doi.org/10.1007/BF00020696.

[461] Richard HA, Kuna M. Theoretical and experimental study of superimposed fracture modes I, II and III. Eng Fract Mech 1990;35:949–60. https://doi.org/10.1016/0013-7944(90)90124-Y.

[462] Schöllmann M, Richard HA, Kullmer G, Fulland M. A new criterion for the prediction of crack development in multiaxially loaded structures. Int J Fract 2002;117:129–41. https://doi.org/10.1023/A:1020980311611.

[463] Richard HA, Fulland M, Sander M. Theoretical crack path prediction. Fatigue Fract Eng Mater Struct 2005;28:3–12. https://doi.org/10.1111/J.1460-2695.2004.00855.X.

[464] Richard HA, Schramm B, Schirmeisen NH. Cracks on Mixed Mode loading – Theories, experiments, simulations. Int J Fatigue 2014;62:93–103. https://doi.org/10.1016/J.IJFATIGUE.2013.06.019.

[465] Richard HA, Eberlein A, Kullmer G. Concepts and experimental results for stable and unstable crack growth under 3D-mixed-mode-loadings. Eng Fract Mech 2017;174:10–20. https://doi.org/10.1016/J.ENGFRACMECH.2016.12.005.

[466] Yu H, Kuna M. Interaction integral method for computation of crack parameters K–T – A review. Eng Fract Mech 2021;249:107722. https://doi.org/10.1016/j.engfracmech.2021.107722.

[467] Gammer C, Kacher J, Czarnik C, Warren OL, Ciston J, Minor AM. Local and transient nanoscale strain mapping during in situ deformation. Appl Phys Lett 2016;109:081906. https://doi.org/10.1063/1.4961683.

[468] Leto A, Munisso MC, Porporati AA, Zhu W, Pezzotti G. Stress Dependence of Paramagnetic Point Defects in Amorphous Silicon Oxide. Journal of Physical Chemistry A 2008;112:3927–34. https://doi.org/10.1021/JP710348V.

[469] Larson BC, Yang W, Ice GE, Budai JD, Tischler JZ. Three-dimensional X-ray structural microscopy with submicrometre resolution. Nature 2002;415:887–90. https://doi.org/10.1038/415887a.

[470] Laurie Palasse; Jaroslav Lukeš. In-situ SEM nanoindentation combined with 3D EBSD. 2021.

[471] Takahashi T, Ishikawa T, Kikuta S. Generation of the X-ray second harmonic under the dynamical diffraction condition. Nucl Instrum Methods Phys Res A 1986;246:768–71. https://doi.org/10.1016/0168-9002(86)90188-9.

[472] Gaines JL, Kissel LD, Catron HC, Hansen RA. Scattering of x rays from low-Z materials. Livermore, CA (United States): 1980. https://doi.org/10.2172/7073743.

[473] Schmidt O. Advanced Photon Source Upgrade (APS-U) Beamline Engineering Overview. Mechanical Engineering Design of Synchrotron Radiation Equipment and Instrumentation (MEDSI), Paris: 2018.

[474] Ulrich O, Biquard X, Bleuet P, Geaymond O, Gergaud P, Micha JS, et al. A new white beam x-ray microdiffraction setup on the BM32 beamline at the European Synchrotron Radiation Facility. Review of Scientific Instruments 2011;82:033908. https://doi.org/10.1063/1.3555068.

[475] Vertyagina Y, Mostafavi M, Reinhard C, Atwood R, Marrow TJ. In situ quantitative three-dimensional characterisation of sub-indentation cracking in polycrystalline alumina. J Eur Ceram Soc 2014;34:3127–32. https://doi.org/10.1016/J.JEURCERAMSOC.2014.04.002.

[476] Mohammadi S. New Frontiers. In: Mohammadi S, editor. Extended Finite Element Method, Oxford, UK: Blackwell Publishing Ltd; 2008, p. 189–217. https://doi.org/10.1002/9780470697795.

[477] Giner E, Sukumar N, Tarancón JE, Fuenmayor FJ. An Abaqus implementation of the extended finite element method. Eng Fract Mech 2009;76:347–68. https://doi.org/https://doi.org/10.1016/j.engfracmech.2008.10.015.

[478] Karlsson A, Bäcklund J. J-integral at loaded crack surfaces. Int J Fract 1978;14. https://doi.org/10.1007/BF00116006.

[479] Ming-Yuan H, Hutchinson JW. Crack deflection at an interface between dissimilar elastic materials. Int J Solids Struct 1989;25:1053–67. https://doi.org/https://doi.org/10.1016/0020-7683(89)90021-8.

[480] Yu H, Wu L, Guo L, He Q, Du S. Interaction integral method for the interfacial fracture problems of two nonhomogeneous materials. Mechanics of Materials 2010;42:435–50. https://doi.org/https://doi.org/10.1016/j.mechmat.2010.01.001.

[481] Yu H, Wu L, Guo L, Du S, He Q. Investigation of mixed-mode stress intensity factors for nonhomogeneous materials using an interaction integral method. Int J Solids Struct 2009;46:3710–24. https://doi.org/https://doi.org/10.1016/j.ijsolstr.2009.06.019.

[482] Knowles JK, Sternberg E. On a class of conservation laws in linearized and finite elastostatics. Arch Ration Mech Anal 1972;44:187–211. https://doi.org/10.1007/BF00250778.

[483] Lazar M, Agiasofitou E. Eshelbian dislocation mechanics: J-, M-, and L-integrals of straight dislocations. Mech Res Commun 2018;93:89–95. https://doi.org/10.1016/J.MECHRESCOM.2017.09.001.

[484] Baxevanakis KP, Giannakopoulos AE. Finite element analysis of discrete edge dislocations: Configurational forces and conserved integrals. Int J Solids Struct 2015;62:52–65. https://doi.org/10.1016/J.IJSOLSTR.2015.01.025.

[485] Muránsky O, Balogh L, Tran M, Hamelin CJ, Park J-S, Daymond MR. On the Measurement of Dislocations and Dislocation Structures using EBSD and HRSD Techniques. Acta Mater 2019. https://doi.org/10.1016/J.ACTAMAT.2019.05.036.

[486] Chang JH, Chien AJ. Evaluation of M-integral for anisotropic elastic media with multiple defects. Int J Fract 2002;114:267–89. https://doi.org/10.1023/A:1015561313059.

[487] Karamched PS, Wilkinson AJ. High resolution electron back-scatter diffraction analysis of thermally and mechanically induced strains near carbide inclusions in a superalloy. Acta Mater 2011;59:263–72. https://doi.org/10.1016/J.ACTAMAT.2010.09.030.

[488] Guo Y, Zong C, Britton TB. Development of local plasticity around voids during tensile deformation. Materials Science and Engineering: A 2021;814:141227. https://doi.org/10.1016/J.MSEA.2021.141227.

[489] Hui T, Chen YH. The M-integral analysis for a nano-inclusion in plane elastic materials under uni-axial or bi-axial loadings. Journal of Applied Mechanics, Transactions ASME 2010;77:1–9. https://doi.org/10.1115/1.3176997/469765.

[490] Pepper DW, Heinrich JC. The Finite Element Method: Basic Concepts and Applications with MATLAB, MAPLE, and COMSOL. 3rd ed. CRC Press; 2017.

[491] Golub GH, Loan CF van. Some Sensitivity Issues. Matrix Computations. 4th ed., Baltimore: The Johns Hopkins University Press; 2013, p. 290–1.

[492] Hough PD, Vavasis SA. Complete Orthogonal Decomposition for Weighted Least Squares. SIAM Journal on Matrix Analysis and Applications 1997;18:369–92. https://doi.org/10.1137/S089547989528079X.

[493] Luong B. Moore-Penrose pseudo-inverse factorization object “PIF.” 25453, 2009.

[494] Trefethen LN, Bau D. Numerical Linear Algebra. vol. 50. 3600 Market Street, 6th Floor Philadelphia, PA 19104-2688: SIAM; 1997. https://doi.org/10.1137/1.9780898719574.

[495] Alvarez-Armas I. Duplex Stainless Steels: Brief History and Some Recent Alloys. Recent Patents on Mechanical Engineeringe 2008;1. https://doi.org/10.2174/2212797610801010051.

[496] TMR Stainless. Practical Guidelines for the Fabrication of Duplex Stainless Steels. 3rd ed. International Molybdenum Assoication (IMOA); 2014.

[497] Nilsson J-O. Super duplex stainless steels. Materials Science and Technology 1992;8:685–700. https://doi.org/10.1179/mst.1992.8.8.685.

[498] Zieliński W, Światnicki W, Barstch M, Messerschmidt U. Non-uniform distribution of plastic strain in duplex steel during TEM in situ deformation. Mater Chem Phys 2003;81:476–9. https://doi.org/10.1016/S0254-0584(03)00059-2.

[499] Serre I, Salazar D, Vogt JB. Atomic force microscopy investigation of surface relief in individual phases of deformed duplex stainless steel. Materials Science and Engineering: A 2008;492:428–33. https://doi.org/10.1016/J.MSEA.2008.04.060.

[500] Zhang Q, Ma S, Jing T. Mechanical Properties of a Thermally-aged Cast Duplex Stainless Steel by in Situ Tensile Test at the Service Temperature. Metals 2019, Vol 9, Page 317 2019;9:317. https://doi.org/10.3390/MET9030317.

[501] Weng KL, Chen HR, Yang JR. The low-temperature aging embrittlement in a 2205 duplex stainless steel. Materials Science and Engineering: A 2004;379:119–32. https://doi.org/https://doi.org/10.1016/j.msea.2003.12.051.

[502] Liu G, Li S-L, Zhang H-L, Wang X-T, Wang Y-L. Characterization of Impact Deformation Behavior of a Thermally Aged Duplex Stainless Steel by EBSD. Acta Metallurgica Sinica (English Letters) 2018 31:8 2018;31:798–806. https://doi.org/10.1007/S40195-018-0708-6.

[503] Kato M. Hardening by spinodally modulated structure in b.c.c. alloys. Acta Metallurgica 1981;29:79–87. https://doi.org/10.1016/0001-6160(81)90088-2.

[504] Mburu S, Kolli RP, Perea DE, Schwarm SC, Eaton A, Liu J, et al. Effect of aging temperature on phase decomposition and mechanical properties in cast duplex stainless steels. Materials Science and Engineering: A 2017;690:365–77. https://doi.org/10.1016/J.MSEA.2017.03.011.

[505] Porter DA, Easterling KE. Phase transformations in metals and alloys. 3rd ed. CRC press; 2009.

[506] Bonny G, Terentyev D, Malerba L. New Contribution to the Thermodynamics of Fe-Cr Alloys as Base for Ferritic Steels. Journal of Phase Equilibria and Diffusion 2010 31:5 2010;31:439–44. https://doi.org/10.1007/S11669-010-9782-9.

[507] Fan Y, Liu TG, Xin L, Han YM, Lu YH, Shoji T. Thermal aging behaviors of duplex stainless steels used in nuclear power plant: A review. Journal of Nuclear Materials 2021;544:152693. https://doi.org/10.1016/J.JNUCMAT.2020.152693.

[508] Bonny G, Terentyev D, Malerba L. New Contribution to the Thermodynamics of Fe-Cr Alloys as Base for Ferritic Steels. Journal of Phase Equilibria and Diffusion 2010 31:5 2010;31:439–44. https://doi.org/10.1007/S11669-010-9782-9.

[509] Weng KL, Chen HR, Yang JR. The low-temperature aging embrittlement in a 2205 duplex stainless steel. Materials Science and Engineering: A 2004;379:119–32. https://doi.org/10.1016/J.MSEA.2003.12.051.

[510] Soriano-Vargas O, Avila-Davila EO, Lopez-Hirata VM, Cayetano-Castro N, Gonzalez-Velazquez JL. Effect of spinodal decomposition on the mechanical behavior of Fe–Cr alloys. Materials Science and Engineering: A 2010;527:2910–4. https://doi.org/10.1016/J.MSEA.2010.01.020.

[511] Godfrey TJ, Smith GDW. The Atom Probe Analysis of a Cast Duplex Stainless Steel. Le Journal de Physique Colloques 1986;47:C7-217-C7-222. https://doi.org/10.1051/jphyscol:1986738.

[512] May JE, de Sousa CAC, Kuri SE. Aspects of the anodic behaviour of duplex stainless steels aged for long periods at low temperatures. Corros Sci 2003;45:1395–403. https://doi.org/10.1016/S0010-938X(02)00244-5.

[513] Cahn JW. On spinodal decomposition. Acta Metallurgica 1961;9:795–801. https://doi.org/10.1016/0001-6160(61)90182-1.

[514] Badyka R, Monnet G, Saillet S, Domain C, Pareige C. Quantification of hardening contribution of G-Phase precipitation and spinodal decomposition in aged duplex stainless steel: APT analysis and micro-hardness measurements. Journal of Nuclear Materials 2019;514:266–75. https://doi.org/10.1016/J.JNUCMAT.2018.12.002.

[515] Calcagnotto M, Adachi Y, Ponge D, Raabe D. Deformation and fracture mechanisms in fine- and ultrafine-grained ferrite/martensite dual-phase steels and the effect of aging. Acta Mater 2011;59:658–70. https://doi.org/10.1016/J.ACTAMAT.2010.10.002.

[516] Shuro I, Kuo HH, Sasaki T, Hono K, Todaka Y, Umemoto M. G-phase precipitation in austenitic stainless steel deformed by high pressure torsion. Materials Science and Engineering: A 2012;552:194–8. https://doi.org/10.1016/J.MSEA.2012.05.030.

[517] Sakata M, Kadoi K, Inoue H. Acceleration of 475 °C embrittlement in weld metal of 22 mass% Cr-duplex stainless steel. Mater Today Commun 2021;29:102800. https://doi.org/10.1016/J.MTCOMM.2021.102800.

[518] Xue F, Shi F, Zhang C, Zheng Q, Yi D, Li X, et al. The Microstructure and Mechanical and Corrosion Behaviors of Thermally Aged Z3CN20-09M Cast Stainless Steel for Primary

Coolant Pipes of Nuclear Power Plants. Coatings 2021, Vol 11, Page 870 2021;11:870. https://doi.org/10.3390/COATINGS11080870.

[519] Li S, Wang Y, Wang X, Xue F. G-phase precipitation in duplex stainless steels after long-term thermal aging: A high-resolution transmission electron microscopy study. Journal of Nuclear Materials 2014;452:382–8. https://doi.org/10.1016/J.JNUCMAT.2014.05.069.

[520] Hamaoka T, Nomoto A, Nishida K, Dohi K, Soneda N. Effects of aging temperature on G-phase precipitation and ferrite-phase decomposition in duplex stainless steel. Http://DxDoiOrg/101080/147864352012707340 2012;92:4354–75. https://doi.org/10.1080/14786435.2012.707340.

[521] MATEO A, LLANES L, ANGLADA M, REDJAIMIA A, METAUER G. Characterization of the intermetallic G-phase in an AISI 329 duplex stainless steel. Journal of Materials Science 1997 32:17 1997;32:4533–40. https://doi.org/10.1023/A:1018669217124.

[522] Lee HJ, Kong BS, Obulan Subramanian G, Heo J, Jang C, Lee KS. Evaluation of thermal aging of δ-ferrite in austenitic stainless steel weld using nanopillar compression test. Scr Mater 2018;155:32–6. https://doi.org/10.1016/J.SCRIPTAMAT.2018.06.016.

[523] Liu X, Zhang X. An ultrafast performance regeneration of aged stainless steel by pulsed electric current. Scr Mater 2018;153:86–9. https://doi.org/10.1016/J.SCRIPTAMAT.2018.05.004.

[524] Liu X, Lu W, Zhang X. Reconstructing the decomposed ferrite phase to achieve toughness regeneration in a duplex stainless steel. Acta Mater 2020;183:51–63. https://doi.org/10.1016/J.ACTAMAT.2019.11.008.

[525] Akita M, Kakiuchi T, Uematsu Y. Microstructural Changes of High-Chromium Ferritic Stainless Steel Subjected to Cyclic Loading in 475°C Embrittlement Region. Procedia Eng 2011;10:100–5. https://doi.org/10.1016/J.PROENG.2011.04.019.

[526] Miller MK, Stoller RE, Russell KF. Effect of neutron-irradiation on the spinodal decomposition of Fe-32% Cr model alloy. Journal of Nuclear Materials 1996;230:219–25. https://doi.org/10.1016/0022-3115(96)80017-1.

[527] Otte HM, Hren JJ. The observation of crystalline imperfections and their role in plastic deformation. Exp Mech 1966;6:177–93. https://doi.org/10.1007/BF02326148.

[528] Ashby MF. The deformation of plastically non-homogeneous materials. The Philosophical Magazine: A Journal of Theoretical Experimental and Applied Physics 1970;21:399–424. https://doi.org/10.1080/14786437008238426.

[529] Mitchell TE, Spitzig WA. Three-stage hardening in tantalum single crystals. Acta Metallurgica 1965;13:1169–79. https://doi.org/10.1016/0001-6160(65)90054-4.

[530] Arsenlis A, Parks DM. Crystallographic aspects of geometrically-necessary and statistically-stored dislocation density. Acta Mater 1999;47:1597–611. https://doi.org/10.1016/S1359-6454(99)00020-8.

[531] Nye JF. Some geometrical relations in dislocated crystals. Acta Metallurgica 1953;1:153–62. https://doi.org/10.1016/0001-6160(53)90054-6.

[532] Kröner E. Continuum theory of dislocations and self-stresses (Translated to English in 1972 by I. Raasch and C.S. Hartley). Ergebnisse Der Angewandten Mathematik 1958;5:1327–47.

[533] Bilby BA, Gardner LRT, Smith E. The relation between dislocation density and stress. Acta Metallurgica 1958;6:29–33. https://doi.org/10.1016/0001-6160(58)90088-9.

[534] Wallis D, Hansen LN, ben Britton T, Wilkinson AJ. Geometrically necessary dislocation densities in olivine obtained using high-angular resolution electron backscatter diffraction. Ultramicroscopy 2016;168:34–45. https://doi.org/10.1016/j.ultramic.2016.06.002.

[535] Kysar JW, Saito Y, Oztop MS, Lee D, Huh WT. Experimental lower bounds on geometrically necessary dislocation density. Int J Plast 2010;26:1097–123. https://doi.org/10.1016/J.IJPLAS.2010.03.009.

[536] Clouet E, Garruchet S, Nguyen H, Perez M, Becquart CS. Dislocation interaction with C in α-Fe: A comparison between atomic simulations and elasticity theory. Acta Mater 2008;56:3450–60. https://doi.org/https://doi.org/10.1016/j.actamat.2008.03.024.

[537] Ruggles TJ, Rampton TM, Khosravani A, Fullwood DT. The effect of length scale on the determination of geometrically necessary dislocations via EBSD continuum dislocation microscopy. Ultramicroscopy 2016;164:1–10. https://doi.org/10.1016/J.ULTRAMIC.2016.03.003.

[538] Dunne F, Petrinic N. Microplasticity. Introduction to computational plasticity, Oxford, UK: Oxford University Press; 2005, p. 3–10.

[539] Britton TB, Hickey JLRR. Understanding deformation with high angular resolution electron backscatter diffraction (HR-EBSD). IOP Conf Ser Mater Sci Eng 2018;304:012003. https://doi.org/10.1088/1757-899X/304/1/012003.

[540] Gao H, Huang Y. Geometrically necessary dislocation and size-dependent plasticity. Scr Mater 2003;48:113–8. https://doi.org/10.1016/S1359-6462(02)00329-9.

[541] Das S, Hofmann F, Tarleton E. Consistent determination of geometrically necessary dislocation density from simulations and experiments. Int J Plast 2018;109:18–42. https://doi.org/https://doi.org/10.1016/j.ijplas.2018.05.001.

[542] Mises R V. Mechanik der plastischen Formänderung von Kristallen. ZAMM - Zeitschrift Für Angewandte Mathematik Und Mechanik 1928;8:161–85. https://doi.org/10.1002/zamm.19280080302.

[543] Buehler WJ, Gilfrich J v, Wiley RC. Effect of Low-Temperature Phase Changes on the Mechanical Properties of Alloys near Composition TiNi. J Appl Phys 1963;34:1475–7. https://doi.org/10.1063/1.1729603.

[544] Schmid E, Boas W. Kristallplastizitaet (Plasticity of crystals). Translation: 1950 1935. https://doi.org/10.1017/S0368393100116219.

[545] Taylor GI, Elam CF. The plastic extension and fracture of aluminium crystals. Proceedings of the Royal Society of London Series A, Containing Papers of a Mathematical and Physical Character 1925;108:28–51. https://doi.org/10.1098/rspa.1925.0057.

[546] Bunge HJ. Some applications of the Taylor theory of polycrystal plasticity. Kristall Und Technik 1970;5:145–75. https://doi.org/10.1002/crat.19700050112.

[547] Harren S v., Dève HE, Asaro RJ. Shear band formation in plane strain compression. Acta Metallurgica 1988;36:2435–80. https://doi.org/10.1016/0001-6160(88)90193-9.

[548] Ming D, Asaro RJ. Localized deformation modes and non-Schmid effects in crystalline solids. Part I. Critical conditions of localization. Mechanics of Materials 1996;23:71–102. https://doi.org/10.1016/0167-6636(96)00012-9.

[549] Chin GY, Hosford WF, Mendorf DR. Accommodation of Constrained Deformation in f.c.c. Metals by Slip and Twinning. Proceedings of the Royal Society A: Mathematical, Physical and Engineering Sciences 1969;309:433–56. https://doi.org/10.1098/rspa.1969.0051.

[550] Mrovec M, Nguyen-Manh D, Pettifor DG, Vitek V. Bond-order potential for molybdenum: Application to dislocation behavior. Phys Rev B 2004;69:94115. https://doi.org/10.1103/PhysRevB.69.094115.

[551] Hsieh YC, Zhang L, Chung TF, Tsai YT, Yang JR, Ohmura T, et al. In-situ transmission electron microscopy investigation of the deformation behavior of spinodal nanostructured δ-ferrite in a duplex stainless steel. Scr Mater 2016;125:44–8. https://doi.org/10.1016/J.SCRIPTAMAT.2016.06.047.

[552] Vitek V, Mrovec M, Gröger R, Bassani JL, Racherla V, Yin L. Effects of non-glide stresses on the plastic flow of single and polycrystals of molybdenum. Materials Science and

Engineering: A 2004;387–389:138–42. https://doi.org/https://doi.org/10.1016/j.msea.2004.04.066.

[553] Verhaeghe B, Louchet F, Doisneau-Cottignies B, Bréchet Y, Massoud J-P. Micromechanisms of deformation of an austenoferritic duplex stainless steel. Philosophical Magazine A 1997;76:1079–91. https://doi.org/10.1080/01418619708200016.

[554] Hsieh Y-C, Zhang L, Chung T-F, Tsai Y-T, Yang J-R, Ohmura T, et al. In-situ transmission electron microscopy investigation of the deformation behavior of spinodal nanostructured δ-ferrite in a duplex stainless steel. Scr Mater 2016;125:44–8. https://doi.org/https://doi.org/10.1016/j.scriptamat.2016.06.047.

[555] Yang J, Li Y, Cai Z, Li S, Ma C, Han E, et al. Evolution of persistent slip bands and simulation of its stress field in a fatigued copper single crystal. Materials Science and Engineering: A 2003;345:164–71. https://doi.org/10.1016/S0921-5093(02)00452-5.

[556] Bridier F, Villechaise P, Mendez J. Analysis of the different slip systems activated by tension in a α/β titanium alloy in relation with local crystallographic orientation. Acta Mater 2005;53:555–67. https://doi.org/10.1016/J.ACTAMAT.2004.09.040.

[557] Hémery S, Villechaise P. Comparison of slip system activation in Ti-6Al-2Sn-4Zr-2Mo and Ti-6Al-2Sn-4Zr-6Mo under tensile, fatigue and dwell-fatigue loadings. Materials Science and Engineering: A 2017;697:177–83. https://doi.org/10.1016/J.MSEA.2017.05.021.

[558] Stinville JC, Vanderesse N, Bridier F, Bocher P, Pollock TM. High resolution mapping of strain localization near twin boundaries in a nickel-based superalloy. Acta Mater 2015;98:29–42. https://doi.org/https://doi.org/10.1016/j.actamat.2015.07.016.

[559] Wang H, Boehlert CJ, Wang QD, Yin DD, Ding WJ. In-situ analysis of the tensile deformation modes and anisotropy of extruded Mg-10Gd-3Y-0.5Zr (wt.%) at elevated temperatures. Int J Plast 2016;84:255–76. https://doi.org/10.1016/J.IJPLAS.2016.06.001.

[560] Hommer GM, Pilchak AL, Stebner AP. Normalized resolved shear stress calculations for single crystals subjected to multiaxial loading. Materialia (Oxf) 2018;2:53–7. https://doi.org/https://doi.org/10.1016/j.mtla.2018.06.009.

[561] Li H, Mason DE, Bieler TR, Boehlert CJ, Crimp MA. Methodology for estimating the critical resolved shear stress ratios of α-phase Ti using EBSD-based trace analysis. Acta Mater 2013;61:7555–67. https://doi.org/10.1016/J.ACTAMAT.2013.08.042.

[562] Dingley D. Progressive steps in the development of electron backscatter diffraction and orientation imaging microscopy. J Microsc 2004;213:214–24. https://doi.org/10.1111/J.0022-2720.2004.01321.X.

[563] Isabell TC, Dravid VP. Resolution and sensitivity of electron backscattered diffraction in a cold field emission gun SEM. Ultramicroscopy 1997;67:59–68. https://doi.org/https://doi.org/10.1016/S0304-3991(97)00003-X.

[564] Brodusch N, Demers H, Gauvin R. Imaging with a Commercial Electron Backscatter Diffraction (EBSD) Camera in a Scanning Electron Microscope: A Review. J Imaging 2018;4. https://doi.org/10.3390/jimaging4070088.

[565] Tanaka M, Terauchi M, Tsuda K, Saitoh K. Convergent-beam electron diffraction IV. vol. 2. Jeol; 2002.

[566] Winkelmann A. Dynamical Simulation of Electron Backscatter Diffraction Patterns BT - Electron Backscatter Diffraction in Materials Science. In: Schwartz AJ, Kumar M, Adams BL, Field DP, editors., Boston, MA: Springer US; 2009, p. 21–33. https://doi.org/10.1007/978-0-387-88136-2_2.

[567] Dingley DJ, Randle V. Microtexture determination by electron back-scatter diffraction. Journal of Materials Science 1992 27:17 1992;27:4545–66. https://doi.org/10.1007/BF01165988.

[568] El-Dasher BS, Adams BL, Rollett AD. Viewpoint: experimental recovery of geometrically necessary dislocation density in polycrystals. Scr Mater 2003;48:141–5. https://doi.org/10.1016/S1359-6462(02)00340-8.

[569] Bhattacharyya A, Eades JA. Use of an energy filter to improve the spatial resolution of electron backscatter diffraction. Scanning 2009;31:114–21. https://doi.org/10.1002/SCA.20150.

[570] Yamamoto T. Experimental aspects of electron channeling patterns in scanning electron microscopy. II. Estimation of contrast depth. Physica Status Solidi (a) 1977;44:467–76. https://doi.org/10.1002/PSSA.2210440208.

[571] Baba-Kishi KZ. Measurement of crystal parameters on backscatter kikuchi diffraction patterns. Scanning 1998;20:117–27. https://doi.org/10.1002/SCA.1998.4950200210.

[572] Ren SX, Kenik EA, Alexander KB, Goyal A. Exploring Spatial Resolution in Electron Back-Scattered Diffraction Experiments via Monte Carlo Simulation. Microscopy and Microanalysis 1998;4:15–22. https://doi.org/10.1017/S1431927698980011.

[573] Engler O, Randle V. Introduction to Texture Analysis. 2nd ed. CRC Press; 2009. https://doi.org/10.1201/9781420063660.

[574] Keller RR, Roshko A, Geiss RH, Bertness KA, Quinn TP. EBSD measurement of strains in GaAs due to oxidation of buried AlGaAs layers. Microelectron Eng 2004;75:96–102. https://doi.org/https://doi.org/10.1016/j.mee.2003.11.010.

[575] Steinmetz DR, Zaefferer S. Towards ultrahigh resolution EBSD by low accelerating voltage. Https://DoiOrg/101179/026708309X12506933873828 2013;26:640–5. https://doi.org/10.1179/026708309X12506933873828.

[576] Bordín SF, Limandri S, Ranalli JM, Castellano G. EBSD spatial resolution for detecting sigma phase in steels. Ultramicroscopy 2016;171:177–85. https://doi.org/10.1016/J.ULTRAMIC.2016.09.010.

[577] Harland CJ, Akhter P, Venables JA. Accurate microcrystallography at high spatial resolution using electron back-scattering patterns in a field emission gun scanning electron microscope. J Phys E 1981;14:175. https://doi.org/10.1088/0022-3735/14/2/011.

[578] Dingley DJ, Field DP. Electron backscatter diffraction and orientation imaging microscopy. Materials Science and Technology 1997;13:69–78. https://doi.org/10.1179/mst.1997.13.1.69.

[579] Harland CJ, Klein JH, Akhter P, Venables JA. Electron back-scattering patterns in a field emission gun scanning electron microscope. Proceedings of the 9th International Congress on Electron Microscopy, Toronto 1981;1:564–5.

[580] Wisniewski W, Rüssel C. An experimental viewpoint on the information depth of EBSD. Scanning 2016;38:164–71. https://doi.org/https://doi.org/10.1002/sca.21251.

[581] Powell CJ, Jablonski A. Surface Sensitivity of Auger-Electron Spectroscopy and X-ray Photoelectron Spectroscopy. Journal of Surface Analysis 2011;17:170–6. https://doi.org/10.1384/JSA.17.170.

[582] PiŇos J, MikmekovÁ, Frank L. About the information depth of backscattered electron imaging. J Microsc 2017;266:335–42. https://doi.org/10.1111/JMI.12542.

[583] ISO 18115:2001/Amd 2:2007 - Surface chemical analysis — Vocabulary — Amendment 2. Geneva: 2007.

[584] Humphreys FJ. Characterisation of fine-scale microstructures by electron backscatter diffraction (EBSD). Scr Mater 2004;51:771–6. https://doi.org/10.1016/J.SCRIPTAMAT.2004.05.016.

[585] Goldstein JI, Newbury DE, Michael JR, Ritchie NWM, Scott JHJ, Joy DC. The Visibility of Features in SEM Images. Scanning Electron Microscopy and X-Ray Microanalysis, New

York, NY: Springer New York; 2018, p. 123–31. https://doi.org/10.1007/978-1-4939-6676-9_8.

[586] Ren SX, Kenik EA, Alexander KB, Goyal A. Exploring Spatial Resolution in Electron Back-Scattered Diffraction Experiments via Monte Carlo Simulation. Microscopy and Microanalysis 1998;4:15–22. https://doi.org/10.1017/S1431927698980011.

[587] Deal A, Spinelli I, Chuang A, Gao Y, Broderick T. Measuring residual stress in Ti-6Al-4V with HR-EBSD, using reference patterns from annealed material. Mater Charact 2021;175:111027. https://doi.org/10.1016/J.MATCHAR.2021.111027.

[588] Amiot F, Bornert M, Doumalin P, Dupré J-C, Fazzini M, Orteu J-J, et al. Assessment of Digital Image Correlation Measurement Accuracy in the Ultimate Error Regime: Main Results of a Collaborative Benchmark. Strain 2013;49:483–96. https://doi.org/https://doi.org/10.1111/str.12054.

[589] Banks-Sills L, Sherman D. On the computation of stress intensity factors for three-dimensional geometries by means of the stiffness derivative and J-integral methods. Int J Fract 1992;53:1–20. https://doi.org/10.1007/BF00032694.

[590] Barsoum RS. Triangular quarter-point elements as elastic and perfectly-plastic crack tip elements. Int J Numer Methods Eng 1977;11:85–98. https://doi.org/10.1002/nme.1620110109.

[591] Banks-Sills L, Sherman D. On quarter-point three-dimensional finite elements in linear elastic fracture mechanics. Int J Fract 1989;41:177–96. https://doi.org/10.1007/BF00018656.

[592] Mohammadi S. Extended Finite Element Method. Oxford, UK: Blackwell Publishing Ltd; 2008. https://doi.org/10.1002/9780470697795.

[593] Owen DRJ, Fawkes AJ. Engineering Fracture Mechanics: Numerical Methods and Applications. Swansea, UK: Pineridge Press Ltd; 1983.